SECTION A

# JOURNAL OF RESEARCH

## of the NATIONAL BUREAU OF STANDARDS

JNBAAR 80A (3) 389–549 (May-June 1976)

U.S. DEPARTMENT OF COMMERCE / National Bureau of Standards

## Physics and Chemistry

**Journal of Research**

**of the**

**National Bureau of Standards**

A. Physics and Chemistry

May–June • 1976

VOLUME • 80A

NUMBER • 3

Associate Editor: D. D. Wagman

Publication dates:
Feb. 1, Apr. 1, June 1, Aug. 1, Oct. 1, Dec. 1, 1976

J. Res. Nat. Bur. Stand. (U.S.), A

**JOURNAL OF RESEARCH**

The National Bureau of Standards Journal of Research reports research and development in the fields of activity shown at right. Also included from time to time are survey articles on topics closely related to the Bureau's scientific and technical program.

The Journal is published in two separate sections as follows:

**A. Physics and Chemistry**

Contains papers of interest primarily to scientists working in these fields. Issued six times a year. Annual subscription: domestic, $17.00; foreign, $21.25. Single copy, varies.

**B. Mathematical Sciences**

Presents studies and compilations designed mainly for the mathematician and the theoretical physicist. Issued quarterly. Annual subscription: domestic, $9.00; foreign, $11.25. Single copy, $2.25.

The National Bureau of Standards[1] was established by an act of Congress March 3, 1901. The Bureau's overall goal is to strengthen and advance the Nation's science and technology and facilitate their effective application for public benefit. To this end, the Bureau conducts research and provides: (1) a basis for the Nation's physical measurement system, (2) scientific and technological services for industry and government, (3) a technical basis for equity in trade, and (4) technical services to promote public safety. The Bureau consists of the Institute for Basic Standards, the Institute for Materials Research, the Institute for Applied Technology, the Institute for Computer Sciences and Technology, and the Office for Information Programs.

**THE INSTITUTE FOR BASIC STANDARDS** provides the central basis within the United States of a complete and consistent system of physical measurement; coordinates that system with measurement systems of other nations; and furnishes essential services leading to accurate and uniform physical measurements throughout the Nation's scientific community, industry, and commerce. The Institute consists of the Office of Measurement Services, the Office of Radiation Measurement and the following Center and divisions:

Applied Mathematics — Electricity — Mechanics — Heat — Optical Physics — Center for Radiation Research: Nuclear Sciences; Applied Radiation — Laboratory Astrophysics[2] — Cryogenics[2] — Electromagnetics[2] — Time and Frequency[2].

**THE INSTITUTE FOR MATERIALS RESEARCH** conducts materials research leading to improved methods of measurement, standards, and data on the properties of well-characterized materials needed by industry, commerce, educational institutions, and Government; provides advisory and research services to other Government agencies; and develops, produces, and distributes standard reference materials. The Institute consists of the Office of Standard Reference Materials, the Office of Air and Water Measurement, and the following divisions:

Analytical Chemistry — Polymers — Metallurgy — Inorganic Materials — Reactor Radiation — Physical Chemistry.

**THE INSTITUTE FOR APPLIED TECHNOLOGY** provides technical services to promote the use of available technology and to facilitate technological innovation in industry and Government; cooperates with public and private organizations leading to the development of technological standards (including mandatory safety standards), codes and methods of test; and provides technical advice and services to Government agencies upon request. The Institute consists of the following divisions and Centers:

Standards Application and Analysis — Electronic Technology — Center for Consumer Product Technology: Product Systems Analysis; Product Engineering — Center for Building Technology: Structures, Materials, and Life Safety; Building Environment; Technical Evaluation and Application — Center for Fire Research: Fire Science; Fire Safety Engineering.

**THE INSTITUTE FOR COMPUTER SCIENCES AND TECHNOLOGY** conducts research and provides technical services designed to aid Government agencies in improving cost effectiveness in the conduct of their programs through the selection, acquisition, and effective utilization of automatic data processing equipment; and serves as the principal focus within the executive branch for the development of Federal standards for automatic data processing equipment, techniques, and computer languages. The Institute consists of the following divisions:

Computer Services — Systems and Software — Computer Systems Engineering — Information Technology.

**THE OFFICE FOR INFORMATION PROGRAMS** promotes optimum dissemination and accessibility of scientific information generated within NBS and other agencies of the Federal Government; promotes the development of the National Standard Reference Data System and a system of information analysis centers dealing with the broader aspects of the National Measurement System; provides appropriate services to ensure that the NBS staff has optimum accessibility to the scientific information of the world. The Office consists of the following organizational units:

Office of Standard Reference Data — Office of Information Activities — Office of Technical Publications — Library — Office of International Relations — Office of International Standards.

[1] Headquarters and Laboratories at Gaithersburg, Maryland, unless otherwise noted; mailing address Washington, D.C. 20234.
[2] Located at Boulder, Colorado 80302.

U.S. DEPARTMENT OF COMMERCE
Elliot L. Richardson, Secretary

NATIONAL BUREAU OF STANDARDS
Ernest Ambler, Acting Director

Order all publications from the Superintendent of Documents
U.S. Government Printing Office, Washington, D.C. 20402

The Secretary of Commerce has determined that the publication of this periodical is necessary in the transaction of the public business required by law of this Department. Use of funds for printing this periodical has been approved by the Director of the Office of Management and Budget through June 30, 1976.

JOURNAL OF RESEARCH of the National Bureau of Standards—A. Physics and Chemistry
Vol. 80A, No. 3, May–June 1976

# Fluorescence Quantum Yield Measurements*

**J. B. Birks**

**University of Manchester, Manchester, U.K.**

**(April 9, 1976)**

Four *molecular fluorescence parameters* describe the behaviour of a fluorescent molecule in very dilute ($\sim 10^{-6}\,M$) solution:

(i) the fluorescence spectrum $F_M(\bar{\nu})$;
(ii) the fluorescence polarization $P_M$;
(iii) the radiative transition probability $k_{FM}$; and
(iv) the radiationless transition probability $k_{IM}$.

These parameters and their temperature and solvent dependence are those of primary interest to the photophysicist and photochemist. $F_M(\bar{\nu})$ and $P_M$ can be determined directly, but $k_{FM}$ and $k_{IM}$ can only be found indirectly from measurements of the secondary parameters,

(v) the fluorescence lifetime $\tau_M$, and
(vi) the fluorescence quantum efficiency $q_{FM}$,

where $k_{FM}=q_{FM}/\tau_M$ and $k_{IM}=(1-q_{FM})\,\tau_M$.

The *real fluorescence parameters* $F(\bar{\nu})$, $\tau$ and $\phi_F$ of more concentrated ($c>10^{-5}\,M$) solutions usually differ from the molecular parameters $F_M(\bar{\nu})$, $\tau_M$ and $q_{FM}$ due to concentration (self) quenching, so that $\tau>\tau_M$ and $\phi_F<q_{FM}$. The concentration quenching is due to excimer formation and dissociation (rates $k_{DM}c$ and $k_{MD}$, respectively) and it is often accompanied by the appearance of an excimer fluorescence spectrum $F_D(\bar{\nu})$ in addition to $F_M(\bar{\nu})$, so that $F(\bar{\nu})$ has two components. The *excimer fluorescence parameters* $F_D(\bar{\nu})$, $P_D$, $k_{FD}$ and $k_{ID}$, together with $k_{DM}$ and $k_{MD}$, and their solvent and temperature dependence, are also of primary scientific interest.

The *observed* (technical) *fluorescence parameters* $F^T(\bar{\nu})$, $\tau^T$ and $\phi_F^T$ in more concentrated solutions usually differ from the real parameters $F(\bar{\nu})$, $\tau$ and $\phi_F$, due to the effects of self-absorption and secondary fluorescence. The technical parameters also depend on the optical geometry and the excitation wavelength. The problems of determining the real parameters from the observed, and the molecular parameters from the real, will be discussed.

Methods are available for the accurate determination of $F^T(\bar{\nu})$ and $\tau^T$. The usual method of determining $\phi_F^T$ involves comparison with a reference solution $R$, although a few calorimetric and other absolute determinations have been made. For two solutions excited under identical conditions and observed at normal incidence

$$\frac{\phi_F^T}{\phi_{FR}^T}=\frac{n^2\int F^T(\bar{\nu})\,d\bar{\nu}}{n_R^2\int F_R^T(\bar{\nu})\,d\bar{\nu}}$$

where $n$ is the solvent refractive index.

Two reference solution standards have been proposed, quinine sulphate in $N$ $H_2SO_4$ which has no self-absorption, and 9,10-diphenylanthracene in cyclohexane which has no self-quenching. The relative merits of these solutions will be discussed, and possible candidates for an "ideal" fluorescence standard with no self-absorption and no self-quenching will be considered.

Key words: Fluorescence lifetime; fluorescence quantum efficiency; fluorescence quantum yields; fluorescence spectrum; fluorescence standards; molecular fluorescence parameters; observed (technical) fluorescence parameters; polarization; radiative and non-radiative transition probabilities; real fluorescence parameters.

*Paper presented at the Workshop Seminar 'Standardization in Spectrophotometry and Luminescence Measurements' held at the National Bureau of Standards, Gaithersburg, Md., Nov. 19–20, 1975.

## 1. Introduction

Most atoms, molecules, polymers and crystals emit ultraviolet, visible or infrared photons following excitation of their electronic energy levels. This emission or *luminescence* is classified according to the mode of excitation:

*photoluminescence* due to optical (non-ionizing) radiation;
*cathodoluminescence* due to cathode rays (electron beams);
*radioluminescence* (*scintillations*) due to ionizing radiation;
*electroluminescence* due to electric fields;
*thermoluminescence* produced thermally after prior irradiation by other means;
*triboluminescence* due to frictional and electrostatic forces;
*sonoluminescence* due to ultrasonic radiation;
*chemiluminescence* due to a chemical process, commonly oxidation;
*electrochemiluminescence* due to a chemical process, initiated by an electric field; and
*bioluminescence* due to a biological process, usually enzymatic in origin.

*Luminescent materials* can be divided into several broad groups.

(i) *Aromatic molecules* constitute the largest group. They emit luminescence in the vapour, liquid, polymer and crystal phases and in fluid and rigid solutions [1][1]. They are used extensively in organic liquid, plastic and crystal scintillators [2], luminescent dyes and paints, detergent and paper whiteners, luminescent screens, dye lasers, etc.

(ii) Many *inorganic crystals*, including diamond, ruby, alkali halides, zinc sulphide and calcium tungstate, luminesce efficiently. The emission is usually from impurity centres (activators) or, in the absence of such impurities, from crystal defects [2]. Luminescent inorganic crystals are used as scintillators [2], luminescent screens, solid-state lasers, jewels, etc.

(iii) *Noble gases* (He, Ne, Ar, Kr, Xe) luminesce in the vapour, liquid, and solid phases and in liquid and solid solutions [2, 3]. They are used in discharge lamps, gas lasers and scintillators.

(iv) Many *simple inorganic molecules* luminesce in the vapour phase [4]. Some, like $H_2$, $D_2$, $N_2$, and Hg are used in discharge lamps; others, like $N_2$, $I_2$, and $CO_2$ are used in gas lasers.

(v) Some *inorganic ions*, notably those of the rare earth elements, are luminescent. They are used as activators in inorganic crystals (see (ii) above), glasses and chelates. Applications include inorganic crystal and glass scintillators and Nd glass lasers.

(vi) Many *biological molecules* are luminescent. These include

(a) *aromatic amino-acids* (tryptophan, tyrosine, phenylalanine) in proteins;
(b) *nucleotides* (adenine, guanine, uracil, cytosine, thymine) in DNA and RNA;
(c) *retinyl polyenes* in the visual pigments;
(d) *chlorophylls* and *carotenoids* in the photosynthetic chloroplast; and
(e) several *vitamins* and *hormones*.

The study of biomolecular luminescence is an important area of biophysical research [5].

(vii) *Aliphatic molecules*, such as the paraffins and cyclohexane, once considered to be nonluminescent, are now known to emit in the far ultraviolet ($\sim 200$ nm) with low quantum yield [6]. This list, which is not exhaustive, illustrates the wide range of luminescent materials and their applications.

## 2. Luminescence of Aromatic Molecules

### 2.1. Radiative transitions

The initial discussion is limited to aromatic molecules (i), but it will be later extended to other luminescent materials (ii)-(vii). Most aromatic molecules have an even number of $\pi$-electrons, giving a ground singlet electronic state $S_0$ in which the electron spins are paired. The *excited* $\pi$ electronic states of the molecule are either

singlet states: $S_1, S_2 \ldots S_p$; or
triplet states : $T_1, T_2 \ldots T_q$.

A spin-allowed radiative transition (luminescence) between two states of the same multiplicity (e.g. $S_1 \rightarrow S_0$, $S_p \rightarrow S_0$, $T_q \rightarrow T_1$) is called *fluorescence* ($F$). A spin-forbidden radiative transition between two states of different multiplicity (e.g. $T_1 \rightarrow S_0$) is called *phosphorescence* ($P$). The energy difference between the initial and final electronic state is emitted as a fluorescence photon ($h\nu_F$) or phosphorescence photon ($h\nu_p$).

The fluorescence occurring immediately after the initial excitation of $S_1$ (or $S_p$) is known as *prompt fluorescence*. In some molecules or molecular systems there are mechanisms by which $S_1$ (or $S_p$) may become excited subsequent to the initial excitation, resulting in *delayed fluorescence*. The two principal mechanisms are as follows [1].

(i) Thermal activation of molecules in the lowest triplet state $T_1$, which is long-lived because the $T_1 \rightarrow S_0$ transition is spin-forbidden, repopulates the fluorescent singlet state $S_1$, resulting in *E-type* (eosin-type) *delayed fluorescence*, so called because it occurs in eosin and other dye molecules.
(ii) Diffusional interaction between pairs of $T_1$-excited molecules in solution or $T_1$ excitons in a crystal creates singlet-excited molecules by the process

$$T_1 + T_1 \rightarrow S_1 \text{ (or } S_p) + S_0 \qquad (1)$$

[1] Figures in brackets indicate the literature references at the end of this paper.

resulting in *P-type* (pyrene-type) *delayed fluorescence*, so called because it occurs in pyrene and other aromatic hydrocarbons.

### 2.2. Radiationless Transitions

Radiative transitions are between electronic states of different energy. In a complex molecule or crystal there are also radiationless transitions between different electronic states of the same energy. These isoenergetic radiationless transitions are induced by molecular or crystal vibrations.

A spin-allowed radiationless transition between two states of the same multiplicity is called *internal conversion* (*IC*). A spin-forbidden radiationless transition between two states of different multiplicity is called *intersystem crossing* (*ISC*).

### 2.3. Vibrational Relaxation

After the initial excitation or after an isoenergetic radiationless transition, the molecule is usually in a vibronic state $S_p^*$ (or $T_q^*$) corresponding to a vibrationally-excited level of a particular electronic state $S_p$ (or $T_q$). In a condensed medium (solution, liquid, polymer, crystal) or a high-pressure vapour the excess vibrational energy $S_p^*-S_p^o$ (or $T_q^*-T_q^o$) is rapidly dissipated collisionally to the environment leading to *vibrational relaxation (VR)*.

The dissipative *VR* process, which is distinct from the nondissipative *IC* and *ISC* processes, plays an essential role in the thermal equilibration of the excited molecules. At normal temperatures *VR* is rapid ($\sim 10^{-12}-10^{-13}$ s, depending on the excess vibrational energy to be dissipated) and much faster than *IC*, *ISC*, *F* or *P*.

Isolated excited molecules in a low-pressure vapour, where *VR* is inhibited by the low collision rate, behave in a different manner than those in the condensed phase [6]. In an isolated molecule the fluorescence occurs from the vibronic state $S_p^*$ initially excited or from isoenergetic vibronic states $S_1^*$, $S_2^*$ . . . . of lower electronic states populated by *IC*. This phenomena is called *resonance fluorescence*. In the condensed phase *VR* brings the excited molecules rapidly into thermal equilibrium and all the processes (*F*, *P*, *IC* and *ISC*) occur from an equilibrated system of molecules.

### 2.4. Photophysical Processes and Parameters

Figure 1 shows schematically the photophysical processes that can occur in an aromatic molecular system in very dilute solution ($\sim 10^{-6}$ *M*) following excitation into $S_2$.

$S_2$ decays by

(a) *IC* to $S_1^*$, followed by *VR* to $S_1$;
(b) *IC* to $S_0^{***}$, followed by *VR* to $S_0$; or
(c) $S_2 \rightarrow S_0$ fluorescence $F_2$.

$S_2 \rightarrow S_1$ fluorescence, which could potentially occur, is forbidden since $S_2$ and $S_1$ have the same parity (*ungerade*) [1].

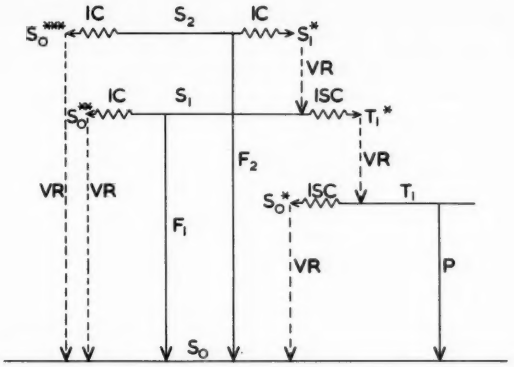


FIGURE 1. *Schematic diagram of radiative (solid vertical lines), radiationless (wavy horizontal lines), and vibrational relaxation (broken vertical lines) transitions between electronic states (solid horizontal lines)* $S_2$, $S_1$, $T_1$ *and* $S_0$ *of an aromatic molecule in a condensed medium.*

*F* = fluorescence, *P* = phosphorescence, *IC* = internal conversion, *ISC* = intersystem crossing, *VR* = vibrational relaxation.

$S_1$, from (a), decays by

(d) $S_1 \rightarrow S_0$ fluorescence $F_1$;
(e) *ISC* to $T_1^*$, followed by *VR* to $T_1$; or
(f) *IC* to $S_0^{**}$, followed by *VR* to $S_0$.

$T_1$, from (e), decays by

(g) $T_1 \rightarrow S_0$ phosphorescence *P*; or
(h) *ISC* to $S_0^*$, followed by *VR* to $S_0$

*F*, *P*, *IC*, and *ISC* are the rate-determining processes, since *VR* is much faster. $k_{AB}$ is defined as the rate parameter of the $B \rightarrow A$ process, where *B* is the initial state and *A* is the product radiation (*F* or *P*) or final state (for *IC* or *ISC*) [1]. Subscripts $G=S_0$, $T=T_1$, $M=S_1$, and $H=S_2$ indicate the different states.

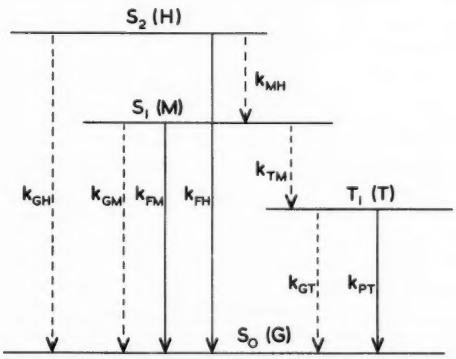


FIGURE 2. *Rate parameters of radiative transitions (solid vertical lines) and radiationless plus vibrational relaxation transitions (broken vertical lines) between electronic states (solid horizontal lines)* $S_2$, $S_1$, $T_1$, *and* $S_0$ *of an aromatic molecule in a condensed medium.*

The notation of the states, radiations and rate parameters is indicated.

Figure 2 shows the rate parameters corresponding to the processes of figure 1. In the rate parameter description the *VR* subsequent to each *IC* or *ISC* is omitted, but the distinction between the isoenergetic radiationless transitions and the vibrational relaxation should not be overlooked.

The $S_2$, $S_1$ and $T_1$ *decay parameters* are given by

$$k_H = k_{FH} + k_{MH} + k_{GH} = 1/\tau_H \tag{2}$$

$$k_M = k_{FM} + k_{TM} + k_{GM} = 1/\tau_M \tag{3}$$

$$k_T = k_{PT} + k_{GT} = 1/\tau_T \tag{4}$$

where $\tau_H$, $\tau_M$ and $\tau_T$ are the $S_2$, $S_1$ and $T_1$ *lifetimes*, respectively.

The *quantum efficiency* $q_{AB}$ of any photophysical process, rate $k_{AB}$, from an excited state $B$ is defined as the fraction of the excited molecules in $B$ that decay by that process, so that

$$q_{AB} = k_{AB}/k_B \tag{5}$$

The $S_2 \rightarrow S_0$ and $S_1 \rightarrow S_0$ *fluorescence quantum efficiencies* are, respectively,

$$q_{FH} = k_{FH}/k_H \tag{6}$$

$$q_{FM} = k_{FM}/k_M \tag{7}$$

the $T_1 \rightarrow S_0$ *phosphorescence quantum efficiency* is

$$q_{PT} = k_{PT}/k_T \tag{8}$$

the $S_2 \rightarrow S_1^*$ *internal conversion quantum efficiency* is

$$q_{MH} = k_{MH}/k_H \tag{9}$$

and the $S_1 \rightarrow T_1^*$ and $T_1 \rightarrow S_0^*$ *intersystem crossing quantum efficiencies* are, respectively,

$$q_{TM} = k_{TM}/k_M \tag{10}$$

$$q_{GT} = k_{GT}/k_T \tag{11}$$

The rate parameters (fig. 2), the decay parameters and lifetimes (2)–(4), and the quantum efficiencies (5)–(11) are *molecular parameters*. They refer to very dilute ($\sim 10^{-6} M$) solutions, containing no dissolved oxygen or other impurity quenchers.

An increase in the solution molar concentration $c$ does not change the unimolecular rate parameters, but it introduces bimolecular processes due to interactions between excited molecules in $S_2$, $S_1$ or $T_1$ and unexcited molecules in $S_0$, producing *concentration quenching*. To a first approximation the $S_2$, $S_1$ and $T_1$ concentration quenching rates may be expressed as $k_{CH}c$, $k_{CM}c$ and $k_{CT}c$, and the $S_2$, $S_1$ and $T_1$ decay parameters become

$$k'_H = k_H + k_{CH}c = 1/\tau'_H \tag{2a}$$

$$k'_M = k_M + k_{CM}c = 1/\tau'_M \tag{3a}$$

$$k'_T = k_T + k_{CT}c = 1/\tau'_T \tag{4a}$$

respectively, where $\tau'_H$, $\tau'_M$ and $\tau'_T$ are the $S_2$, $S_1$ and $T_1$ lifetimes in a solution of molar concentration $c$. An exact treatment also considers the rate parameters of the *excimers* produced by the concentration quenching and their dissociation [1], but the Stern-Volmer approximation of (2a)–(4a) is adequate for the present discussion.

The *quantum yield* $\phi$ of any photophysical process in a solution of concentration $c$ is defined in the same manner as the quantum efficiency, except that the limitation to very dilute solutions is removed. The $S_2 \rightarrow S_0$ and $S_1 \rightarrow S_0$ *fluorescence quantum yields* are, respectively

$$\phi_{FH} = \frac{k_{FH}}{k_H + k_{CH}c} = \frac{q_{FH}}{1 + K_{CH}c} \tag{12}$$

$$\phi_{FM} = \frac{k_{FM}}{k_M + k_{CM}c} = \frac{q_{FM}}{1 + K_{CM}c} \tag{13}$$

and the $T_1 \rightarrow S_0$ *phosphorescence quantum yield* is

$$\phi_{PT} = \frac{k_{PT}}{k_T + k_{CT}c} = \frac{q_{PT}}{1 + K_{CT}c} \tag{14}$$

The parameters $K_{CH}(=k_{CH}/k_H)$, $K_{CM}(=k_{CM}/k_M)$ and $K_{CT}(k_{CT}/k_T)$ are the *Stern-Volmer coefficients of concentration quenching of* $S_2$, $S_1$ and $T_1$, respectively.

The $S_2 \rightarrow S_1^*$ *internal conversion quantum yield* is

$$\phi_{MH} = \frac{k_{MH}}{k_H + k_{CH}c} = \frac{q_{MH}}{1 + K_{CH}c} \tag{15}$$

and the $S_1 \rightarrow T_1^*$ and $T_1 \rightarrow S_0^*$ *intersystem crossing quantum yields* are, respectively,

$$\phi_{TM} = \frac{k_{TM}}{k_M + k_{CM}c} = \frac{q_{TM}}{1 + K_{CM}c} \tag{16}$$

$$\phi_{GT} = \frac{k_{GT}}{k_T + k_{CT}c} = \frac{q_{GT}}{1 + K_{CT}c} \tag{17}$$

The above expressions for quantum efficiencies and yields all refer to direct excitation of the state from which the process occurs, and they require revision when the state is not excited directly. Thus for excitation into $S_2$, the $S_1 \rightarrow S_0$ fluorescence quantum yield is

$$\phi_{FM}^H = \phi_{MH}\phi_{FM} \tag{18}$$

For excitation into $S_1$, the $T_1 \rightarrow S_0$ phosphorescence quantum yield is

$$\phi_{PT}^M = \phi_{TM}\phi_{PT} \tag{19}$$

### 2.5. Vavilov's Law and Kasha's Rules

It is commonly assumed that $\phi_{MH}=1.0$ for $S_2 \rightarrow S_1^*$ *IC* and that $\phi=1$ for *IC* between higher excited states within the singlet ($S_p$) manifold, so that $\phi_{FM}$ is independent of the excitation wavelength $\lambda_{ex}$ up to the ionization potential. This assumption, known as *Vavilov's law*, has been confirmed for many compounds in solution. Major deviations from Vavilov's law have, however, been observed for solutions of benzene, toluene, *p*-xylene, mesitylene, fluorobenzene, naphthalene, 2-methylnaphthalene, 1,6-dimethylnaphthalene [1], tryptophan, tyrosine and phenylalanine [7]. In each case it is observed that $\phi_{FM}^H/\phi_{FM}=\phi_{MH}<1$. In benzene and its derivatives and possibly in the other compounds, the effect is due to efficient $S_2 \rightarrow S_0^{***}$ *IC* ($k_{GH}$) competing with $S_2 \rightarrow S_1^*$ *IC* ($k_{MH}$) [8]. In fluorescence quantum yield measurements it is essential either to verify that Vavilov's law applies, or to limit the excitation to the region of the $S_0 \rightarrow S_1$ absorption spectrum.

*Kasha's rules* [9], another well-known generalization, state that in a complex molecule luminescence occurs only from the lowest excited state of a given multiplicity, i.e., $S_1 \rightarrow S_0$ fluorescence and $T_1 \rightarrow S_0$ phosphorescence. For many years azulene and its derivatives, which emit $S_2 \rightarrow S_0$ fluorescence and negligible $S_1 \rightarrow S_0$ fluorescence, were the main exceptions to Kasha's rules. Recently the picture has changed dramatically.

In addition to the normal $S_1 \rightarrow S_0$ fluorescence, weak $S_2 \rightarrow S_0$ fluorescence has been observed in benzene, toluene, *p*-xylene, mesitylene, naphthalene, pyrene, 1 : 2-benzanthracene, 3:4-benzopyrene, 1:12-benzoperylene and ovalene, weak $S_3 \rightarrow S_0$ fluorescence has been observed in *p*-xylene, mesitylene, naphthalene, pyrene and 1:2-benzanthracene, and weak $S_4 \rightarrow S_0$ fluorescence has been observed in pyrene and fluoranthene [6, 10].

Such fluorescence from higher excited states was predicted by the author in 1954 [11]. Its detection is difficult, since it occurs in the region of the $S_0 \rightarrow S_p$ absorption spectrum, and its quantum yield is only $\sim 10^{-5}$ $\phi_{FM}$ [6]. Subsequent attention will be focused on the main $S_1 \rightarrow S_0$ fluorescence.

### 2.6. The Fluorescence Spectrum

The $S_1 \rightarrow S_0$ fluorescence spectrum occurs from a system of $S_1$ excited molecules in thermal equilibrium in solution. The fraction of these molecules with vibrational energy $E_v$ is proportional to $\exp(-E_v/kT)$, where $k$ is Boltzmann's constant and $T$ is the absolute temperature. A large majority are in the zero point level $S_1^0$, and to a first approximation the fluorescence of the "hot" molecules can be disregarded.

The $S_1^0 \rightarrow S_0$ fluorescence occurs into $S_0^0$, the zero-point level of $S_0$, and into the many vibrational levels of $S_0$. The $S_1^0 \rightarrow S_0^0$ transition, or *0–0 fluorescence transition*, of wavenumber $(\bar{\nu}_{00})_F$ is the highest energy transition in the $S_1^0 \rightarrow S_0$ fluorescence spectrum. In the vapour $(\bar{\nu}_{00})_F$ coincides with $(\bar{\nu}_{00})_A$, the corresponding $S_0^0 \rightarrow S_1^0$ *0–0 absorption transition*. In solution, due to solvent polarization effects

$$(\bar{\nu}_{00})_A-(\bar{\nu}_{00})_F=\Delta\,\bar{\nu}_{00} \qquad (20)$$

where $\Delta\bar{\nu}_{00}$ varies from 0 to a few hundred $cm^{-1}$ depending on the solvent [1]. In benzene the 0–0 fluorescence and absorption transitions are symmetry-forbidden and they are absent from the vapour spectra. They appear as weak solvent-induced bands (the Ham bands) in solution spectra, the intensity depending on the solvent [1].

At low temperatures the $S_1 \rightarrow S_0$ ($=S_1^0 \rightarrow S_0$) *fluorescence spectrum* $F_M(\bar{\nu})$ consists of a complex series of a few hundred narrow lines of different intensities, which may be analysed into progressions and combinations of the different vibrational modes of the unexcited molecule. When the temperature is increased, thermal broadening and solvent-solute interactions obscure most of the vibrational structure. At room temperature $F_M(\bar{\nu})$ commonly consists of a few prominent broad bands with little other structure. Thus $F_M(\bar{\nu})$ for anthracene in cyclohexane solution consists of a progression of 5 broad bands, spaced about 1400 $cm^{-1}$ apart, corresponding to *CC* vibrational modes. Similar vibrational progressions occur in $F_M(\bar{\nu})$ for other condensed hydrocarbons [1]. For large molecules, e.g., dyes, with many degrees of vibrational and/or rotational freedom, $F_M(\bar{\nu})$ at room temperature often consists of a single broad band with no vibrational structure. Berlman [12] has recorded the fluorescence spectra of many aromatic molecules.

The solvent has a strong influence on $F_M(\bar{\nu})$ at room temperature. In a polar solvent like ethanol the vibrational bands are broad and poorly resolved, and the separation $\Delta\bar{\nu}_{00}$ between the absorption and fluorescence 0–0 bands is relatively large. In a non-polar aliphatic hydrocarbon solvent, like cyclohexane or *n*-hexane, the spectral resolution is improved and $\Delta\bar{\nu}_{00}$ is reduced. In a fluorocarbon solvent, like perfluoro-*n*-hexane (PFH), each of the vibrational bands has a well-resolved fine structure, similar to that in the vapour phase, and $\Delta\bar{\nu}_{00}=0$ [13]. PFH is an ideal spectroscopic solvent, apart from cost and the low solubility of aromatic molecules in PFH.

At temperatures above about $-100\,°C$ the "hot" vibrationally-excited $S_1$ molecules with a Boltzmann distribution of energies $S_1^*$ ($=S_1^0+E_v$) also contribute to $F_M(\bar{\nu})$. Each component $S_1^* \rightarrow S_0$ spectrum is similar to the $S_1^0 \rightarrow S_0$ spectrum, except that it is shifted by an amount $E_v$ towards higher energies, and its intensity is proportional to $\exp(-E_v/kT)$. Most of the $S_1^* \rightarrow S_0$ spectral distribution lies below the $S_1^0 \rightarrow S_0$ spectrum and is obscured thereby. However, each component $S_1^* \rightarrow S_0$ spectrum extends beyond $\bar{\nu}_{00}$ to $\bar{\nu}_{00}+E_v$, giving rise to *hot fluorescence bands*, the intensity and extent of which increase with tempera-

ture. These hot fluorescence bands, which are an integral part of the $S_1 \rightarrow S_0$ fluorescence spectrum $F_M(\bar{\nu})$ at room temperature, occur in all aromatic molecules, although they are not often recorded. The emission bands are in the same region as the $S_0 \rightarrow S_1$ absorption, and special care is needed to observe them [6].

### 2.7. The rate parameters

Observations of $q_{FM}$ and $\tau_M$ for a very dilute solution enable

$$k_{FM} = q_{FM}/\tau_M \tag{21}$$

$$k_{IM} = k_{FM} + k_{GM} = (1 - q_{FM})\tau_M \tag{22}$$

to be determined. Birks and Munro [14] have reviewed methods of measuring $\tau_M$. Observations of $q_{TM}$ $(= k_{TM}/k_M)$, by one of the several methods described by Wilkinson [15], enable $k_{TM}$ and $k_{GM}$ to be evaluated. The measurement of $q_{PT}$ and $\tau_T$ permits $k_{PT}$ and $k_{GT}$ to be determined [1]. Thus measurements of five quantities $q_{FM}$, $\tau_M$, $q_{TM}$, $q_{PT}$ and $\tau_T$ are required to determine the five $S_1$ and $T_1$ unimolecular rate parameters $k_{FM}$, $k_{TM}$, $k_{GM}$, $k_{PT}$ and $k_{GT}$.

Observations of $\tau'_M$ and $\tau'_T$ (or $\phi_{FM}$ and $\phi_{PT}$) as a function of the molar concentration $c$ enable the bimolecular rate parameters $k_{CM}$ and $k_{CT}$ to be determined. The observations and analysis may be extended further to obtain the fluorescence ($k_{FD}$), *ISC* ($k_{TD}$), *IC* ($k_{GD}$) and dissociation ($k_{MD}$) rate parameters of the singlet excimer [1]. This involves observations of the molecular ($\phi_{FM}$) and excimer ($\phi_{FD}$) fluorescence quantum yields of concentrated solutions.

It is the *rate parameters* and their dependence on temperature, solvent, substitution etc. that are the quantities of interest to the photophysicist and photochemist, and not the properties from which they are derived. The latter may be of technical interest for particular applications. Of the three quantities $q_{FM}$, $\tau_M$ and $q_{TM}$ required to determine the $S_1$ rate parameters $k_{FM}$, $k_{TM}$ and $k_{GM}$, the published values of $q_{FM}$ (or $\phi_{FM}$, which is often implicitly equated to $q_{EM}$) show the largest scatter. When the solution concentration $c$ is increased, self-absorption effects introduce difficulties in the determination of $\phi_{FM}$. It is hoped that this paper will help to improve the situation.

### 2.8. The Fluorescence Rate Parameter

A theoretical expression for $k_{FM}$ has been derived from the Einstein radiation relation using the zero-order Born-Oppenheimer approximation [16, 17]

$$k'_{FM} = 2.88 \times 10^{-9} \frac{n_F^3}{n_A} \langle \bar{\nu}_F^{-3} \rangle_{\text{Av}}^{-1} \int \frac{\epsilon(\bar{\nu})\, d\bar{\nu}}{\bar{\nu}} \tag{23}$$

where $n_F$ and $n_A$ are the mean refractive indices of the solvent over the $S_1 \rightarrow S_0$ fluorescence and $S_0 \rightarrow S_1$ absorption spectra, respectively, $\langle \bar{\nu}_F^{-3} \rangle_{\text{Av}}^{-1}$ is the reciprocal of the average value of $\bar{\nu}^{-3}$ over the fluorescence spectrum, $\epsilon(\bar{\nu})$ is the decadic molar extinction coefficient, and the integral is taken over the $S_0 \rightarrow S_1$ absorption spectrum. Relation (23) has been tested for a number of molecules, and excellent agreement between $k_{FM}$ and $k'_{FM}$ has been obtained for several molecules in different laboratories [1, 12, 16, 17, 18]. Such molecules may be useful as fluorescence standards.

If the solvent optical dispersion is small $n_F \simeq n_A = n$, and (23) can be simplified to

$$k'_{FM} = n^2 (k'_{FM})_0 \tag{24}$$

where $(k'_{FM})_0$ is a molecular constant, independent of the solvent and the temperature. Relation (24) has been verified for several solutes in different solvents over a wide temperature range [19].

In some molecules there are large discrepancies between $k_{FM}$ and $k'_{FM}$. A detailed study of these anomalies has revealed the presence of electronic states not observed spectroscopically [20, 21]. The nature and origin of such radiative lifetime anomalies are discussed elsewhere [22]. The factors determining the other $S_1$ and $T_1$ rate parameters $k_{TM}$, $k_{GM}$, $k_{PT}$ and $k_{GT}$ have been considered previously [1, 6, 8].

### 2.9. Molecular Fluorescence Parameters

The $S_1 \rightarrow S_0$ fluorescence of an aromatic compound in very dilute solution is characterized by the following molecular parameters.

(a) The fluorescence spectrum $F_M(\bar{\nu})$ depends on the solvent and temperature (see 2.6).

(b) The fluorescence polarization $p_M$ depends on the direction of the transition dipole moment relative to the molecular axes. For a $\pi^* \rightarrow \pi$ electronic transition this lies in the molecular plane along one of two orthogonal axes depending on the symmetry of $S_1$. For naphthalene the fluorescence is long-axis polarized; for anthracene it is short-axis polarized [1].

(c) The fluorescence rate parameter $k_{FM}$ is proportional to the square of the transition dipole moment [1]. In the absence of any anomalies $k_{FM}/n^2$ is independent of the solvent and temperature (24).

(d) The $S_1$ radiationless rate parameter $k_{IM}$ $(= k_{TM} + k_{GM})$ describes the processes competing with the fluorescence. $k_{IM}$ usually depends markedly on the solvent and on the temperature [1].

$F_M(\bar{\nu})$ and $p_M$ can be observed directly. The evaluation of $k_{FM}$ and $k_{IM}$ involves measurements of two secondary parameters:

(e) The fluorescence lifetime $\tau_M$; and

(f) the fluorescence quantum efficiency $q_{FM}$.

Several accurate methods are available for measuring $\tau_M$[14]. Reliable methods are available for measuring $q_{FM}$, but they are often used incorrectly [23].

The molecular fluorescence parameters $F_M(\bar{\nu})$, $p_M$, $k_{FM}$ and $k_{IM}$ are independent of the molar concentration $c$. The secondary fluorescence parameters $\tau_M$ and $\phi_{FM}$ decrease with increase in $c$ due to

(g) the concentration quenching rate parameter $k_{CM}$.

$k_{CM}$, which depends markedly on the solvent viscosity and the temperature, is a further molecular parameter of photophysical interest.

## 3. Other Luminescent Materials

The preceding discussion of the luminescence of aromatic molecules is applicable to the other luminescent materials considered in the Introduction. It applies directly to biological molecules (vi) and aliphatic organic molecules (vii). Noble gases (iii) also have singlet ground states, and there are close analogies between them and the aromatic hydrocarbons, particularly in excimer formation [3]. There are no radiationless transitions in the noble gases ($q_{FM}=q_{FH}=1.0$) because of the absence of internal vibrations. They form excimers in the vapour, liquid, and solid phases, and the vibrational modes of these may generate radiationless transitions and vibrational relaxation in the condensed phase [3].

Simple inorganic molecules (iv) are similar. They normally have singlet ground states and excited singlet and triplet states. Although they have internal vibrations, the vibronic state density is low, and there are normally no radiationless transitions except at high excitation energies, where predissociation may occur [4].

The luminescence of inorganic crystals (ii) and inorganic ions (v) in a solid matrix is closely related to that of aromatic molecular crystals. Unfortunately there are major terminological differences between inorganic crystal photophysics and organic molecular crystal photophysics. Table 1 is based on a brief survey of the inorganic luminescence literature, and may require revision in the light of any recent changes.

TABLE 1. *Terminology of photophysical processes*

| Process | Organic | Inorganic |
|---|---|---|
| 1. Luminescence, | | |
| (a) spin-allowed | Fluorescence (*F*) | Fluorescence |
| (b) spin-forbidden | Phosphorescence (*P*) | Fluorescence |
| (c) thermally-activated delayed | E-type delayed fluorescence | Phosphorescence |
| 2. Radiationless transition | | |
| (a) spin-allowed | Internal conversion (*IC*) | |
| (b) spin-forbidden | Intersystem crossing (*ISC*) | |
| 3. Vibrational relaxation | Vibrational relaxation (*VR*) | |
| 4. Radiationless transition plus vibrational relaxation | *IC* (or *ISC*) and *VR* | Multiphonon process |

The inorganic luminescence terminology predates the discovery of electron spin, and it has not been adjusted to take account of this. Because of spin, processes 1(a) and 1(b) differ in lifetime by a factor of up to $10^8$, and it would seem appropriate to distinguish them. In 1933 Jablonski [24], the originator of figure 1, showed that the two slow emissions 1(b) and 1(c) observed in organic dyes originated from a common metastable state $X$, and he proposed that they be called $\beta$-phosphorescence and $\alpha$-phosphorescence, respectively. Since 1944 when Lewis and Kasha [25] demonstrated that $X=T_1$, the lowest excited triplet state, 1(b) has been called simply phosphorescence, while 1(c) which has the same emission spectrum as 1(a) is called E-type delayed fluorescence.

Standardization of luminescence terminology is long overdue. Those responsible for organizing international luminescence conferences and publishing luminescence journals have unfortunately neglected to formulate a scientific language common to workers in organic and inorganic luminescence. Perhaps the National Bureau of Standards can assist in the matter.

## 4. Fluorescence Measurements

### 4.1. Fluorescence Spectra

A true (corrected) fluorescence spectrum is plotted as the relative quantum intensity $F_M(\bar{\nu})$ (relative number of quanta per unit wave-number interval) against wavenumber $\bar{\nu}$. A few spectrometers have been developed which record directly the true fluorescence spectrum. The majority provide spectra which require correction for the dispersion of the analyzing monochromator, the spectral response of the photomultiplier or detector, and any light losses. This involves the preparation of an *instrumental calibration curve*, by measurements

(a) with a calibrated lamp through a neutral filter;
(b) with a thermopile or bolometer;
(c) of reference solution fluorescence spectra [26]; or
(d) with a fluorescent quantum counter.

A *quantum counter* is a system which has a constant fluorescence quantum yield over a broad spectral range. To achieve this it should have a high and relatively constant absorption over the spectral range of interest, it should have negligible self-absorption (no overlap of fluorescence and absorption spectrum), it should obey Vavilov's law, and it should be stable photochemically. Systems commonly used as quantum counters include:

(i) 3 $gl^{-1}$ Rhodamine B in ethylene glycol (210–530 nm),
(ii) 4 $gl^{-1}$ quinine sulphate in $N$ $H_2SO_4$ (220–340 nm), and
(iii) $10^{-2}M$ 1-dimethylaminonaphthalene 5-(or 7-) sodium sulphonate in 0.1 $N$ $Na_2CO_3$ (210 – 400 nm).

An extension of this list would be advantageous.

Three common optical geometries are used in fluorescence measurements;

(a) front-surface or *reflection geometry*, in which the fluorescence from the irradiated surface of the specimen is observed;

(b) *90° geometry*, in which the fluorescence is observed in a direction normal to the incident beam; and

(c) *transmission geometry*, in which the fluorescence is observed from the opposite side of the speciment to the excitation.

For very dilute solutions ($\sim 10^{-6}M$) the three geometries give the same fluorescence spectrum, quantum efficiency and lifetime. The 90° geometry, used by Birks and Dyson [17] and others, has the advantage of minimizing background incident light and of allowing the fraction of incident light absorbed in the specimen to be monitored directly.

An increase in the solution concentration $c$ reduces $q_{FM}$ and $\tau_M$ to $\phi_{FM}$ and $\tau'_M$, respectively, due to concentration quenching. It also attenuates the high-energy region of $F_M(\bar{\nu})$ due to self-absorption arising from the overlap of the absorption and fluorescence spectra. As $c$ is increased the intensity of the 0–0 fluorescence band decreases towards zero due to its overlap with the 0–0 absorption band. At room temperature and high $c$ the self-absorption may extend to the 0–1 and 0–2 fluorescence bands, which overlap the 1–0 and 2–0 hot absorption bands, due to thermally activated molecules in the first and second vibrational levels of $S_0$. These self-absorption effects are a maximum in the transmission geometry (c), somewhat reduced in the 90° geometry (b), and they are least in the reflection geometry (a), which is normally used for fluorescence studies of more concentrated solutions.

The effect of self-absorption on $F_M(\bar{\nu})$ observed in reflection can be minimized by Berlman's technique [12] of excitation at an intense absorption maximum, thereby minimizing the penetration depth $d_{ex}$ of the exciting light. This technique does not, however, compensate for the secondary fluorescence produced by the self-absorption and which modifies $\phi_{FM}$ and $\tau_M$, as discussed below.

### 4.2. Fluorescence Quantum Yields

Absolute determinations of fluorescence quantum yields have been made using integrating spheres to collect the fluorescence emission over a full $4\pi$ solid angle, by calorimetry to distinguish radiative processes from radiationless processes and vibrational relaxation, by actinometry to integrate light intensities photochemically, and by polarization and scattering measurements. These methods have been reviewed by Lipsett [27] and Demas and Crosby [28].

The superscript $T$ is introduced to refer to the *observed (technical) fluorescence parameters* $F_M^T(\bar{\nu})$, $\phi_{FM}^T$ and $\tau_M^T$, which may differ from the true fluorescence parameters $F_M(\bar{\nu})$, $\phi_{FM}$ and $\tau'_M$, due to self-absorption and secondary fluorescence. Absolute determinations of $\phi_{FM}$ are difficult and uncommon, and it is normal practice to measure $\phi_{FM}^T$ by comparison with a standard of known fluorescence quantum yield $\phi_{FR}^T$. If $F_M^T(\bar{\nu})$ and $F_T^T(\bar{\nu})$ are the corrected fluorescence spectra of the specimen and standard, respectively, excited under identical conditions (same excitation wavelength, optical density and geometry) and observed *at normal incidence in reflection*, then

$$\frac{\phi_{FM}^T}{\phi_{FR}^T} = \frac{n^2 \int_0^\infty F_M^T(\bar{\nu})\,d\bar{\nu}}{n_R^2 \int_0^\infty F_R^T(\bar{\nu})\,d\bar{\nu}} \tag{25}$$

where $n$ and $n_R$ are the refractive indices of the specimen solution and the standard solution, respectively. The integrations are often made using a quantum counter [28].

The refractive index term is a correction for the solution optical geometry. The angular dependence of the fluorescence flux $F(\phi)$ from a small isotropically emitting source behind an infinite plane surface in a medium of refractive index $n$ is

$$F(\phi) = F_0(\cos\phi)n^{-1}(n^2 - \sin^2\phi)^{-1/2} \tag{26}$$

where $F_0$ is a constant ($\propto \phi_M^T$) and $F(\phi)$ is the flux (in quanta $cm^2\ s^{-1}$) falling on a small aperture at an angle $\phi$ from the normal to the face. For $\phi = 0°$ (26) reduces to

$$F(0) = F_0/n^2 \tag{27}$$

leading to (25). Relation (26) has been verified by Melhuish [29] who recommended the use of cuvettes with blackened back and sides for fluorescence yield measurements to minimize internal reflection errors.

Shinitzky [30] has pointed out a further potential source of error in fluorescence quantum yield and lifetime measurements. When a fluorescent system is excited by unpolarized light and its emission is detected without a polarizer, the emission intensity has a typical anisotropic distribution which is directly related to its degree of polarization. This effect can introduce an error of up to 20 percent in all fluorescence quantum yield and lifetime measurements, but it is eliminated when the fluorescence is detected at an angle of 55° or 125° to the direction of excitation, provided that the emission detection system is unbiased with respect to polarization. Procedures for the elimination of polarization errors for partially polarized excitation and biased detection systems were developed by Cehelnik, Mielenz, and Velapoldi [31] and Mielenz, Cehelnik, and McKenzie [32].

If $n$ and $n_R$ differ, it is recommended that the specimen and reference solutions be excited at 55° incidence angle and observed at normal incidence, to eliminate the polarization effect and simplify the refractive index correction. The latter correction disappears if $n = n_R$, and the excitation and front-face observation

directions need only differ by 55°. The angles of incidence and "reflection" should differ to minimize scattered light.

The self-absorption attenuates the high-energy end of $F_M(\bar{\nu})$, but it does not affect the low-energy end. If $F_M(\bar{\nu})$, observed in very dilute solution, and $F_M^T(\bar{\nu})$, observed at molar concentration $c$, are *normalized* in the low-energy region, then the parameter

$$a = \frac{A_M - A_M^T}{A_M} \tag{28}$$

where

$$A_M = \int_0^\infty F_M(\bar{\nu})\, d\bar{\nu} \tag{29}$$

$$A_M^T = \int_0^\infty F_M^T(\bar{\nu})\, d\bar{\nu} \tag{30}$$

represents the *self-absorption probability*. This normalization procedure, introduced for anthracene crystal fluorescence [33], has been applied by Birks and Christophorou [34] to concentrated solutions of aromatic hydrocarbons. Substitution of $A_M$ in place of $A_M^T$ in (25) gives $\phi_{FM}$ in place of $\phi_{FM}^T$. For materials of low $\phi_{FM}$ ($< 0.3$), the linear Stern-Volmer plots of $q_{FM}/\phi_{FM}$ against $c$ of gradient $K_{CM}$ (13) confirm the validity of the procedure, which corresponds to assuming

$$\phi_{FM}^T = (1 - a)\, \phi_{FM} \tag{31}$$

This relation neglects the *secondary fluorescence* resulting from the self-absorption. Allowing for this, the author [11, 35] has shown that

$$\phi_{FM}^T = \frac{(1-a)\phi_{FM}}{1 - a\phi_{FM}} \tag{32}$$

which approximates to (31) when $a\phi_{FM} \ll 1$, and that

$$\tau_M^T = \frac{\tau_M'}{1 - a\phi_{FM}}. \tag{33}$$

Relation (33) is considered to be generally valid. Relation (32) is considered to be valid for the transmission and 90° geometries. It is also valid for the reflection geometry, except for specimens of high $\phi_{FM}$. Under the latter conditions the secondary fluorescence contributes markedly to the observed fluorescence intensity, so that $\phi_{FM}^T > \phi_{FM}$ in reflection, although $\phi_{FM}^T < \phi_{FM}$ in transmission as predicted by (32). Figure 3 plots Melhuish's observations [36] of $\phi_{FM}^T$ as a function of $c$ for 9,10-diphenylanthracene (DPA) in benzene solution, excited at 366 nm with front-face observation. Due to secondary fluorescence $\phi_{FM}^T$ increases from $q_{FM} = 0.83$ in very dilute solution to $\phi_{FM}^T = 1.0$ at $c \geq 1.5 \times 10^{-3} M$. Correction for self-absorption and secondary fluorescence, using a much more complex relation than (32), showed that $\phi_{FM} = 0.83 \pm 0.02$ over the whole range of $c$, thus demonstrating that DPA is immune to concentration quenching [36].

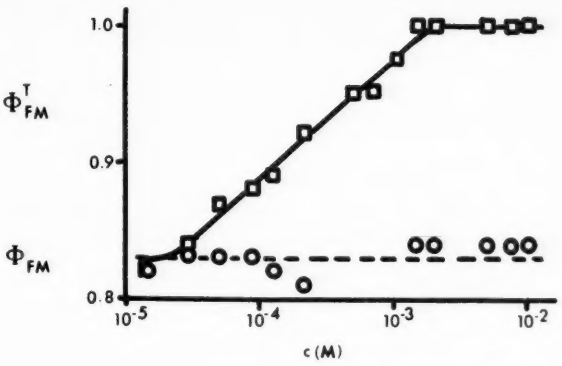


FIGURE 3. *9,10-diphenylanthracene in benzene.*

Front-surface observation at $\lambda_{ex} = 365$ nm. Technical fluorescence quantum yield $\phi_{FM}^T$ (+) and true fluorescence quantum yield $\phi_{FM}$ (o) against molar concentration $c$. Data from Melhuish [36].

The secondary fluorescence contribution to $\phi_{FM}^T$ increases with decrease in the excitation penetration depth $d_{ex}$. Berlman's [12] choice of an intense absorption band for excitation ($\lambda_{ex} = 265$ nm for DPA) minimizes $d_{ex}$. This minimizes the effect of self-absorption on $F_M^T(\bar{\nu})$, but it also maximizes the effect of secondary fluorescence on $\phi_{FM}^T$. To reduce the latter, a weak absorption region should be chosen for excitation, and $c$ should be kept as low as possible.

To summarize, there are no particular problems in determining $\phi_{FM}$ for (a) very dilute solutions (b) more concentrated solutions observed in the transmission or 90° geometries, and (c) more concentrated solutions of $\phi_{FM} < \sim 0.3$ observed in the reflection geometry. The effects of self-absorption and secondary fluorescence are, however, difficult to compensate in concentrated solutions of high $\phi_{FM}$ observed in the reflection geometry. One simple solution is to abandon the reflection geometry and to observe such systems in the more tractable transmission geometry. The alternative is to utilize one of the numerous mathematical relations, some simple [11, 35], some complex [27, 36], which have been developed to describe self-absorption and secondary fluorescence.

### 4.3. Fluorescence Standards

Melhuish [36] proposed the use of a $5 \times 10^{-3} M$ solution of quinine bisulphate (QS) in $1N$ sulphuric acid as a fluorescence standard. From careful measurements he obtained $\phi_{FM} = 0.510$ for $c = 5 \times 10^{-3} M$ increasing to $q_{FM} = 0.546$ at infinite dilution at 25 °C. The value of $\phi_{FM}$ at any other concentration can be evaluated using the Stern-Volmer relation (13). The QS solution is stable under prolonged irradiation, its fluorescence is not quenched by dissolved air (unlike most aromatic molecules), and it has a very small over-

lap of the absorption and fluorescence spectra. It suffers from three minor disadvantages:

(a) concentration quenching;
(b) the temperature coefficient of $\phi_{FM}$ is about $-0.25$ percent per degree over the range 10° to 40° C; and
(c) sulphuric acid is not a conventional solvent for aromatic molecules and this necessitates using the refractive index correction in (25).

Nevertheless the QS standard, and various secondary standards derived therefrom, have been adopted in this and many other laboratories [28, 37]. Quinine is the fluorescent entity, and the use of quinine sulphate in place of the bisulphate does not appear to affect the values of $q_{FM}$ and $\phi_{FM}$ [28]. Unfortunately many authors have chosen to use 0.1 $N$ sulphuric acid as the solvent, rather than 1 $N$ as recommended by Melhuish [36], while assuming his fluorescence quantum yield values to be unchanged. There is evidence that $\phi_{FM}$ increases by 6–8 percent on increasing the solvent normality from 0.1 $N$ to 1 $N$ [28].

Table 2 lists comparative data on $\tau_M$ and $q_{FM}$ for very dilute solutions of several aromatic compounds obtained using the QS standard [16–18]. The consistency of the data from three different laboratories is gratifying. The close agreement between the experiment values of $k_{FM}(=q_{FM}/\tau_M)$ and the theoretical values of $k'_{FM}$ from (23) for several compounds shows the error in $q_{FM}$ for the QS standard to be small. Gelernt et al. [36] have recently calorimetrically determined $q_{FM}$ for QS in 1 $N$ sulphuric acid at 25° C. The calorimetric value of $q_{FM}=0.561$ ($\pm 0.039$) agrees satisfactorily with the fluorimetric value of $q_{FM}=0.546$ [34]. Other fluorescence standards have been discussed by Demas and Crosby [28].

TABLE 2. *Fluorescence lifetimes* ($\tau_M$) *and quantum efficiencies* ($q_{FM}$) *of very dilute solutions*

| Compound | Solvent | $\tau_M$ (ns) | $q_{FM}$ | $k_{FM}/k'_{FM}$ | Ref. |
|---|---|---|---|---|---|
| Quinine Bisulphate | 1$N$ $H_2SO_4$ | 20.1 | 0.54 | 0.73 | [17] |
| | 1$N$ $H_2SO_4$ | 19.4 | .54 | .75 | [18] |
| Perylene | benzene | 4.9 | .89 | .93 | [17] |
| | benzene | 4.79 | .89 | .90 | [16] |
| | benzene | 5.02 | .89 | .90 | [18] |
| Acridone | ethanol | 11.8 | .83 | 1.02 | [16] |
| | ethanol | 12.5 | .825 | 1.05 | [18] |
| 9-Aminoacridine | ethanol | 13.87 | .99 | 1.15 | [16] |
| | ethanol | 15.15 | .99 | 1.02 | [18] |
| 9,10-Diphenyl anthracene | benzene | 7.3 | .85 | 0.99 | [17] |
| | benzene | 7.37 | .84 | .98 | [18] |

Berlman [12] used a $10^{-3}M$ solution of 9,10-diphenylanthracene (DPA) in cyclohexane, excited at 265 nm (an absorption maximum) and observed in reflection, as a fluorescence standard. Under these conditions the DPA solution has a technical fluorescence quantum yield of $\phi^T_{FM}=1.0$, due to self-absorption and secondary fluorescence, although the true fluorescence quantum yield is $\phi_{FM}=q_{FM}=0.83$ ($\pm 0.02$) (fig. 3). Relation (25) requires that the specimen and standard be compared under identical conditions of excitation and optical density, so that the $10^{-3}M$ DPA solution standard is only suitable for observations of $\phi^T_{FM}$ on concentrated solutions in reflection geometry. The QS standard is more versatile since it does not limit the specimen concentration or optical geometry.

Berlman [12] observed $\tau^T_M$ with heterochromatic excitation and $F^T_M(\bar{\nu})$ with monochromatic excitation (these parameters need to be observed under identical conditions for (32) and (33) to be applicable [35]). He evaluated $\phi^T_{FM}$ by comparison with $F^T_R(\bar{\nu})$ for the DPA standard observed under similar conditions, although the optical densities and excitation wavelengths of the specimen and standard appear to have differed. Apart from the usual hot band elimination and some 0–0 band attenuation, $F^T_M(\bar{\nu})$ approximates to the molecular spectrum $F_M(\bar{\nu})$. $\phi^T_{FM}$ and $\tau^T_M$ do not correspond to $q_{FM}$ and $\tau_M$, as implicitly assumed by Berlman [12], who used them to "evaluate" $k_{FM}$. They require correction for self-absorption and secondary fluorescence to obtain $\phi_{FM}$ and $\tau_M$, and these parameters need correction for concentration quenching to obtain $q_{FM}$ and $\tau_M$. Birks [1] tried to correct Berlman's $\phi^T_{FM}$ data [12] by renormalizing them to $q_{FR}=0.83$ for DPA, but this procedure has since been shown to be invalid [23].

It is of interest to note the effect of substituting different fluorescence parameters in the relations used to evaluate $k_{FM}$ and $k_{IM}$. From (3a), (13), (21), (22), (32) and (33)

$$\frac{q_{FM}}{\tau_M}=\frac{\phi_{FM}}{\tau'_M}=k_{FM} \tag{34}$$

$$\frac{\phi^T_{FM}}{\tau^T_M}=(1-a)k_{FM} \tag{35}$$

$$\frac{(1-q_{FM})}{\tau_M}=k_{IM} \tag{36}$$

$$\frac{(1-\phi_{FM})}{\tau'_M}=\frac{(1-\phi^T_{FM})}{\tau^T_M}=k_{IM}+k_{CM}c. \tag{37}$$

An ideal fluorescence standard for aromatic solutions should

(i) have no self-absorption,
(ii) have no concentration quenching,
(iii) be in a common solvent suitable for other aromatic molecules (to eliminate the refractive index correction),
(iv) be readily available as a high-purity material (or be insensitive to impurities), and
(v) be photochemically stable.

QS satisfies (iv) and (v) and it approximates closely to (i), but it does not satisfy (ii) and (iii). DPA meets criteria (ii)–(v), but it exhibits strong self-absorption. To minimize self-absorption in an aromatic hydrocarbon solution it is necessary that $S_1$ is a $^1L_b$ state, so that the $S_0 \rightarrow S_1$ absorption is weak, and not a $^1L_a$ state, giving strong $S_0 \rightarrow S_1$ absorption, as in DPA [1]. There are two hydrocarbons which exhibit no concentration quenching (ii), have $S = {}^1L_b$ so that self-absorption (i) is reduced, and satisfy (iii) and (v). These compounds, *phenanthrene* and *chrysene*, merit consideration as fluorescence standards. They can be obtained, but are not yet readily available, as high-purity materials (iv).

*Aromatic excimers* satisfy all the criteria for a fluorescence standard, since they have no self-absorption (i) or concentration quenching (ii) [1]. In concentrated solutions the excimer spectrum $F_D(\bar{\nu})$ can be readily distinguished from the attenuated monomer spectrum $F_M^T(\bar{\nu})$ [34], although the presence of the latter may be undesirable. It can be eliminated by the use of a pure liquid or crystal. A *pyrene crystal* has $\phi_{FD} = q_{FD} = 1.0$ at low temperatures and $\phi_{FD} = q_{FD} = 0.65$ at room temperature, a broad structureless fluorescence spectrum between 400 and 550 nm with a maximum at 470 nm, and no self-absorption in any optical geometry [1]. It would appear to be an ideal crystal fluorescence standard.

## 5. References


[1] Birks, J. B., Photophysics of Aromatic Molecules, (Wiley-Interscience, London, and New York, 1970).
[2] Birks, J. B., The Theory and Practice of Scintillation Counting (Pergamon Press, Oxford 1964).
[3] Birks, J. B., Excimers. Rpts. Prog. Phys. **38,** 903 (1975).
[4] Herzberg, G., Molecular Spectra and Molecular Structure. I. Spectra of Diatomic Molecules (Van Nostrand, Princeton 1950).
[5] Birks, J. B., (Ed.) Excited States of Biological Molecules. Proc. Intern. Conf. Lisbon 1974 (Wiley-Interscience, London, and New York, 1976).
[6] Birks, J. B., Organic Molecular Photophysics, Vol. II, Ed. Birks, J. B. (Wiley-Interscience, London, and New York, p. 409, 1975).
[7] Tatischeff, I., and Klein, R., ref. [5], p. 375 (1976).
[8] Birks, J. B., Organic Molecular Photophysics, Vol. I, Ed. Birks, J. B. (Wiley-Interscience, London, and New York, p. 1, 1973).
[9] Kasha, M., Disc. Faraday Soc. **9,** 14 (1950).
[10] Nickel, B., Chem. Phys. Letters **27,** 84 (1974).
[11] Birks, J. B., Phys. Rev. **94,** 1567 (1954).
[12] Berlman, I. B., Handbook of Fluorescence Spectra of Aromatic Molecules (Academic Press, New York. 1st edition, 1965; 2nd edition, 1971).
[13] Lawson, C. W., Hirayama, F., and Lipsky, S., J. Chem. Phys. **51,** 1590 (1969).
[14] Birks, J. B., and Munro, I. H., Progress in Reaction Kinetics, **4,** 239 (1967).
[15] Wilkinson, F., Organic Molecular Photophysics, Vol. II, Ed. Birks, J. B. (Wiley-Interscience, London, and New York, p. 95, 1975).
[16] Strickler, S. J., and Berg. R. A., J. Chem. Phys. **37,** 814 (1962).
[17] Birks, J. B., and Dyson, D. J., Proc. Roy. Soc. **A275,** 135 (1963).
[18] Ware, W. R., and Baldwin, B. A., J. Chem. Phys. **40,** 1703 (1964).
[19] Cundall R. B., and Pereira, L. C., J. Chem. Soc. Faraday Trans. II, **68,** 1152 (1972).
[20] Birks, J. B., and Birch, D. J. S., Chem. Phys. Letters, **31,** 608(1975).
[21] Birch, D. J. S., and Birks, J. B., Chem. Phys. Letters, in press.
[22] Birks, J. B., Z. Phys. Chem. (N.F.) submitted for publication.
[23] Birks, J. B., J. Luminescence **9,** 311 (1974).
[24] Jablonski, A., Nature **131,** 839 (1933); Z. Phys. Lpz. **94,** 38 (1935).
[25] Lewis, G. N., and Kasha, M., J. Amer. Chem. Soc. **66,** 2100 (1944).
[26] Melhuish, W. H., J. Phys. Chem. **64,** 792 (1960).
[27] Lipsett, F. R., Progress in dielectrics **7,** 217 (1967).
[28] Demas, J. N., and Crosby, G. A., J. Phys. Chem. **75,** 991 (1971).
[29] Melhuish, W. H., J. Opt. Soc. Amer. **51,** 278 (1961).
[30] Shinitzky, M., J. Chem. Phys. **56,** 5979 (1972).
[31] Cehelnik, E. D., Mielenz, K. D., and Velapoldi, R. A., J. Res. Nat. Bur. Stand. (U.S.), **79A** (Phys. and Chem.), No. 1, 1–15 (Jan.–Feb. 1975).
[32] Mielenz, K. D., Cehelnik, E. D., and McKenzie, R. L., J. Chem. Phys. **64,** 370 (1976).
[33] Birks, J. B., and Little, W. A., Proc. Phys. Soc. **A 66,** 921 (1953).
[34] Birks, J. B., and Christophorou, L. G., Proc. Roy. Soc. **A 274,** 552 (1963).
[35] Birks, J. B., Molec. Cryst. Liq. Cryst. **28,** 117 (1975).
[36] Melhuish, W. H., J. Phys. Chem. **65,** 229 (1961).
[37] Parker, C. A., Photoluminescence of Solutions. (Elsevier, Amsterdam 1968).
[38] Gelernt, B., Findeisen, A., Stein, A., and Poole, J. A., VIII Intern. Conf. Photochemistry, Edmonton, August 1975, Abstract δ10.


(Paper 80A3–890)

JOURNAL OF RESEARCH of the National Bureau of Standards—A. Physics and Chemistry
Vol. 80A, No. 3, May–June 1976

# Some Methods of Luminescence Efficiency Measurements *

**Alfred Bril and A. Willy de Jager-Veenis**

**Philips Research Laboratories, Eindhoven, The Netherlands**

**(April 9, 1976)**

Methods of absolute and relative radiant and quantum efficiency measurements are described for ultraviolet, visible, cathode-ray, and x-ray excitations. Data on some standard luminescent materials are given.

Key words: Cathode-ray excitation; luminescence; luminescence standards; phosphors; quantum efficiencies; radiant efficiencies; UV excitation; x-ray excitation.

## 1. Introduction

Methods of absolute radiant and quantum efficiency measurements are given together with methods of relative efficiency measurements. The methods are especially suitable for powder materials for which the angular distribution of the emitted luminescent radiation is Lambertian.

The relative measurements are performed with the aid of standard phosphors, whose efficiencies have previously been determined by absolute measurements. Methods are given for excitation of the phosphors by ultraviolet and visible radiation, cathode rays and x rays.

For samples with non-Lambertian emission distributions, a method is described in which an Ulbricht's sphere or an elliptical mirror is used.

## 2. Ultraviolet Excitation

All powder phosphors are measured using a thick layer (thickness about 2 mm) at the irradiated side. The detection takes place perpendicular to the plane of the phosphor, the excitation is at an angle of 50° with that plane (see fig. 1). The excitation wavelength ($\lambda_{exc}$) or regions are isolated from a high pressure mercury lamp by interference filters, the arc being focused on the phosphor with a quartz lens. In this way a high excitation density is reached, but generally well below the excitation region where saturation effects start. This is especially advantageous when a relatively insensitive thermoelement is used as a detector.

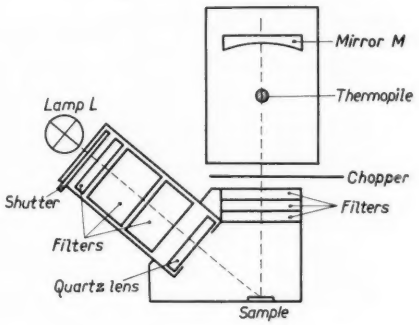


FIGURE 1. *Schematic diagram of the apparatus for the efficiency measurements.*

The radiant efficiencies, from which the quantum efficiencies are calculated, are determined directly (when the spectral power distribution is known).

### 2.1. Relative Measurements, Giving Absolute Efficiency Values

Phosphors can be measured with respect to the following standard samples whose efficiency is generally agreed upon.

(a) The standards issued by the National Bureau of Standards, Washington, D.C. (See ref. [1–4]).

(b) Sodium salicylate (See ref. [5]).
This phosphor is also suitable for excitation

* Paper presented at the Workshop Seminar 'Standardization in Spectrophotometry and Luminescence Measurements' held at the National Bureau of Standards, Gaithersburg, Md., November 19–20, 1975.

in the far ultraviolet (vacuum ultraviolet) because of its constant efficiency as a function of $\lambda_{exc}$ up to 350 nm.

(c) The standard "Ekta S10"[1] proposed by Grum [6].

(d) "Lumogen T red GG," which can be used in the excitation region between 190 and 550 nm [7].

### 2.2. Absolute Measurements

The absolute radiant efficiency can in fact be determined with the aid of a relative measurement, being the ratio of the amount of emitted power and that of the absorbed exciting power [1].[2] For one or two wavelengths the absolute efficiencies can be determined. For other $\lambda_{exc}$ the *relative* excitation spectrum can be determined from which the absolute efficiency at any $\lambda_{exc}$ can be derived.

For this determination three quantities are measured:

(a) The diffuse reflection of the exciting radiation against $BaSO_4$ for which the reflection is known.

(b) The luminescence + reflection of the exciting radiation (without using a filter).

(c) The luminescence of the phosphor, using a filter between phosphor and detector that passes only the luminescence.

From these three measured quantities the reflection and radiant efficiency of the phosphor can be determined.

The expressions found for the radiant efficiency $\eta_p$ and the reflection $r_p$ are given here for the case of using as a detector a thermopile or thermoelement with flat radiant response. Three emf's are measured, viz, $V_R$ due to the reflection standard (e.g., $BaSO_4$ [8], reflection $R$), $V_P$ due to the phosphor (luminescence intensity $L$ + reflected exciting radiation of intensity $I$) and $V_{P,F}$ due to the phosphor when a filter $F$ absorbing the exciting radiation is placed in front of the detector. We assume that the filter has a transmission $\tau$ in the emission region of the phosphor. This leads to the following equations:

$$CV_R = IR$$
$$CV_P = Ir_p + L$$
$$CV_{P,F} = \tau L$$

where $C$ is a constant.

After solving for $r_p$ and $L$ we find

$$\eta_p = \frac{L}{I(1-r_p)} = \frac{R}{\tau(1-r_p)} \frac{V_{P,F}}{V_R}$$

$$r_p = R \frac{V_P - V_{P,F}/\tau}{V_R}$$

As a cross-check the reflection found in this way can be compared with that measured directly with a spectrophotometer.

The method described can be used in the same way for the case of a varying spectral response of the detector and/or a varying spectral transmission of the filter, even when the filter transmits partly in the region of the exciting radiation. Of course the equations become somewhat more complicated in this case.

The quantum efficiency $q_p$ is found from the radiant efficiency by

$$q_p = \eta_p \frac{\int \lambda_p(\lambda)\, d\lambda}{\lambda_{exc} \int p(\lambda)\, d\lambda}$$

where $p(\lambda)$ is the emitted luminescent power and $\lambda_{exc}$ is the exciting wavelength.

The NBS standards mentioned in 2.1 are not excited in the visible (only No. 1030 would be suitable in the blue-violet) region. Therefore, other standards are necessary in the visible region. These can be found among the "lumogen" phosphors. A yellow luminescent lumogen was described by Kristianpoller and Dutton [9], yellow and red ones by Vavilov [10], Morgenshtern, Neustruev and Epshtein [11] and Küttner, Selzle and Schlag [12]. The latter used 5-(p-dimethylaminobenzyliden)-barbituric acid as a red lumogen; they found a quantum efficiency of 45 percent at $\lambda_{exc} = 405$ nm.

We chose the red luminescent "Lumogen T red GG" which was already mentioned in section 2.1. It is commercially available from the Badische Anilin und Soda Fabrik (Ludwigshafen, Germany). The properties of the phosphor are described in reference [7]. It has a red luminescence and shows a quantum efficiency which is not quite constant but varies in a limited range between 40 percent and 60 percent in the spectral region between 220 nm and 550 nm (see fig. 2).

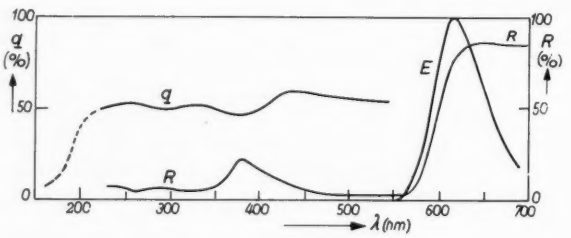


FIGURE 2. *"Lumogen T red GG"*

$q$ = quantum efficiency, $R$ = diffuse reflection and $E$ = spectral power distribution.

The spectral power distributions at room temperature and liquid nitrogen temperature are given in figures 3 and 4. The temperature dependence curve is given in figure 5 for $\lambda_{exc} = 365$ nm. The quantum efficiency

[1] In order to describe materials and experimental procedures adequately, it is occasionally necessary to identify commercial products by manufacturer's name or label. In no instance does such identification imply endorsement by the National Bureau of Standards, nor does it imply that the particular product or equipment is necessarily the best available for that purpose.

[2] Figures in brackets indicate the literature references at the end of this paper.

together with the diffuse spectral reflection are given in figure 2. An important advantage of this phosphor over liquid standards like rhodamine B is that the absorption is high in the whole region, the lowest value being 78 percent near $\lambda = 380$ nm (diffuse reflection $\approx 22$ percent).

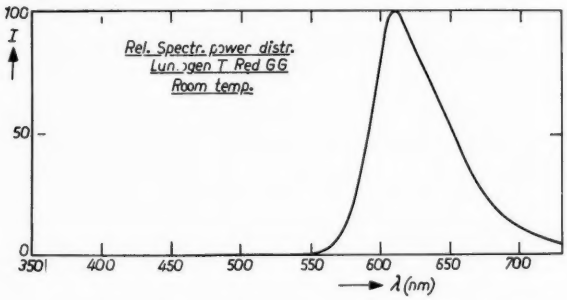


FIGURE 3. *Spectral power distribution of "Lumogen T red GG" at room temperature.*

*I* denotes the spectral radiant power in arbitrary units.

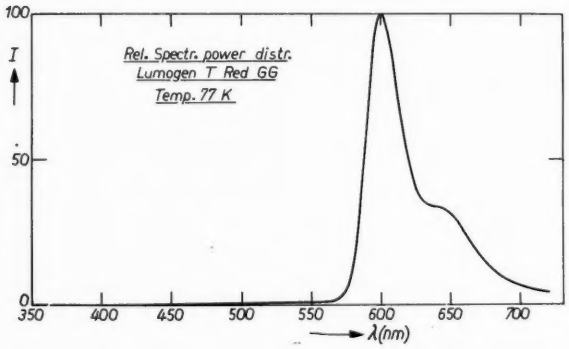


FIGURE 4. *Spectral power distribution of "Lumogen T red GG" at liquid nitrogen temperature.*

See further subscript fig. 3.

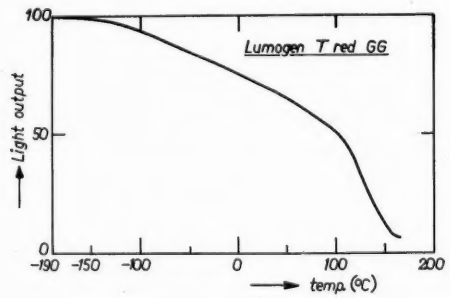


FIGURE 5. *Temperature dependence of the luminescence of "Lumogen T red GG" for $\lambda_{exc} = 365$ nm.*

The absorption of rhodamine B is given in figure 6, showing the enormous variation through the spectrum leading to a similar large variation in light output. Another drawback of liquid samples is the different geometry of the set-up needed for the measurement.

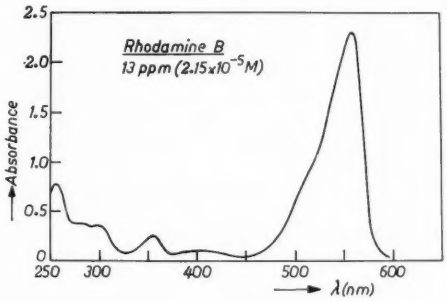


FIGURE 6. *Spectral absorbance of rhodamine B.*

Various authors have reported measurements using 254 nm mercury vapour discharge excitation. Here we give additional measurements on some standards for longer wavelength excitation at $\lambda_{exc} = 365$ nm. The phosphors measured were sodium salicylate, the "Ekta S10" sample, introduced by Grum [6] and "Lumogen T red GG" [7] (see tables 1 and 2).

The results for diffuse reflection at the exciting and emission wavelength, the practical and intrinsic radiant efficiencies, and the practical and intrinsic quantum efficiencies are given.

TABLE 1. *Efficiencies at $\lambda_{exc} = 365$ nm*

| Phosphor | Diffuse reflection at | | Radiant efficiency | | Quantum efficiency | |
|---|---|---|---|---|---|---|
| | $\lambda = 365$ nm % | $\lambda_{em}$ % | $\eta_p$ % | $\eta_i$ % | $q_p$ % | $q_i$ % |
| Na-salicylate | 30 | 80 | 33 | 37 | 37 | 41 |
| "Ekta S10" | 15 | 67 | 37 | 45 | 41 | 50 |
| "Lumogen T red GG" | 13 | | 25 | | 41 | |

TABLE 2. *Efficiencies at $\lambda_{exc} = 260$ nm*

| Phosphor | Diffuse reflection at | | Radiant efficiency | | Quantum efficiency | |
|---|---|---|---|---|---|---|
| | $\lambda = 260$ nm % | $\lambda_{em}$ % | $\eta_p$ % | $\eta_i$ % | $q_p$ % | $q_i$ % |
| Na-salicylate | 7 | 80 | 34 | 37 | 55 | 60 |
| "Lumogen T red GG" | 6 | | 22 | | 53 | |

Because of the thick layer used, a correction has to be made for the loss of the light absorbed in the layer. The intrinsic radiant efficiency $\eta_i$ can then be approximated by [2]

$$\eta_i = \frac{2}{1 + r_\infty}\,\eta_p$$

where $r_\infty$ is the reflection coefficient of the phosphor for an infinitely thick layer.

The diffuse reflection of "Ekta S10" is given in figure 7, the spectral power distribution in figure 8.

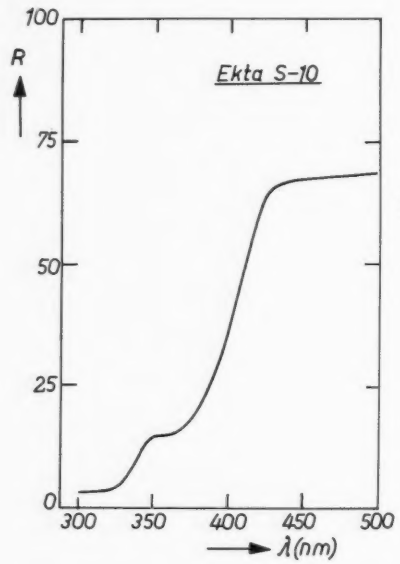


FIGURE 7. *Diffuse reflection of "Ekta S10."*

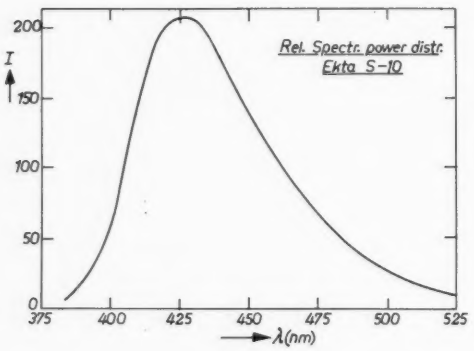


FIGURE 8. *Spectral power distribution of "Ekta S10."*

See further subscript fig. 3.

The efficiency data for Na-salicylate at $\lambda_{exc} = 260$ nm can be compared with the data given in Samson's book (ref. [3]) which are discussed by us in reference [7], together with some additional data.

Polarization effects in our measurements proved to be negligible, as may be expected for powder materials. Measurements were carried out with incident polarized UV radiation, in two directions perpendicular to each other.

The stability of the lumogen was also tested as well as the dependence on excitation density. During one month the efficiency of the lumogen was measured every two days. The stability in time proved to be very good; no changes were observed within the error of measurement, which was of the order of $\pm 10$ percent.

The efficiency values were not affected even when the intensity of the UV-radiation was attenuated a thousand times.

## 3. Excitation in Selected Narrow Absorption Peaks

A method to determine the efficiencies of phosphors that have a small absorption of a few percent in narrow, well defined excitation levels (for the normal case of $\lambda_{exc} \leqslant \lambda_{em}$) was described earlier by us [13, 14]. Examples of these powders are rare-earth activated phosphors, such as $YVO_4-Eu^{3+}$ and $NaYF_4-Er^{3+}$, where the (visible) excitation peaks are those of the rare-earth ion. The host lattice absorbs in the UV region.

A diagram of the set-up is shown in figure 9. The phosphor is irradiated via a scanning monochromator. Two measurements have to be carried out, differing only in the filter used in front of the photomultiplier.

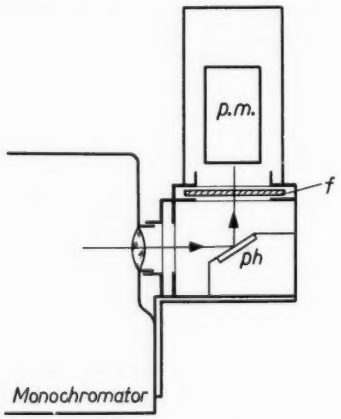


FIGURE 9. *Schematic diagram of the experimental set-up: ph = phosphor sample, f = filters, pm = photomultiplier.*

One filter transmits only the light reflected from the sample, giving the absorption spectrum. In the second measurement the other filter selects the emission wavelength region, thus obtaining the excitation spectrum of that emission. The curves are of the type shown in figure 10 for $YVO_4-Eu^{3+}$. The efficiency is calculated as follows.

The radiant efficiency is the ratio of the emitted power $E$ to the absorbed exciting power $A$. The latter is determined by the area under the absorption curve of a certain peak with correction for the transmission $\tau_A$ of the filter used and for the photomultiplier response $G(\lambda_A)$ in the absorption region. The emitted

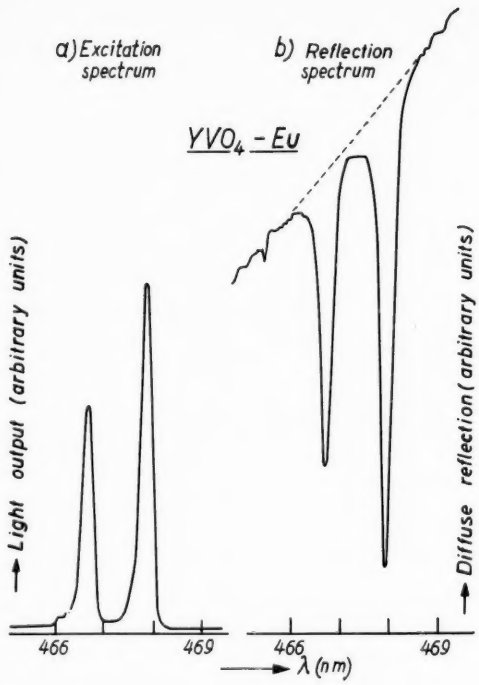


FIGURE 10. *Relative light output of $Eu^{3+}$-emission (curve a) and diffuse reflection (curve b) as a function of wavelength for $YVO_4$-Eu.*

For curve b the zero line is suppressed (the absorption peak has a depth of about 13 percent).

power $E$ is determined by the corresponding area under the excitation curve with correction for the transmission $\tau_E$ of the filter used in this case and the response $G(\lambda_E)$ in the emission region. For single narrow peaks we can take the ratio of the ordinate maxima in the absorption and excitation spectra $U_A$ and $U_E$, respectively, instead of the area. We then find for the emitted power

$$E = U_E \frac{\int p(\lambda_E)\,d\lambda_E}{\int p(\lambda_E) G(\lambda_E)\tau_E(\lambda_E)\,d\lambda_E}$$

where $p(\lambda_E)d\lambda_E$ is the relative emitted power in a region $d\lambda_E$ (integration extended over the total spectral region of the emission). The absorbed power is given by

$$A = \frac{U_A}{G(\lambda_A)\tau_A}.$$

Then the radiant efficiency $\eta$ is

$$\eta = \frac{E}{A} = \frac{U_E \tau_A G(\lambda_A) \int p(\lambda_E)\,d\lambda_E}{U_A \int p(\lambda_E) G(\lambda_E)\tau_E(\lambda_E)\,d\lambda_E}.$$

The quantum efficiency $q$ is derived from the radiant efficiency by

$$q = \eta \frac{\int \lambda_E p(\lambda_E)\,d\lambda_E}{\lambda_A \int p(\lambda_E)\,d\lambda_E}.$$

The error in this type of measurement may be of the order of 10–25 percent, depending on the value of the absorption. This large error is caused by the low value of the absorption in the rare-earth ion.

## 4. Cathode-Ray Excitation

The radiant efficiency $\eta_p$ for cathode-ray excitation [2–4, 15, 16] is generally defined as the ratio of the amount of emitted luminescent power in the spectral region under consideration to the power of the incident cathode-ray beam (and not to the power *absorbed* by the phosphor layer). Thus no correction is made for the loss due to reflection of primary electrons [2, 15, 16].

In this case two really absolute measurements are necessary, viz., that of the emitted power and that of the power of the cathode-ray beam (fig. 11).

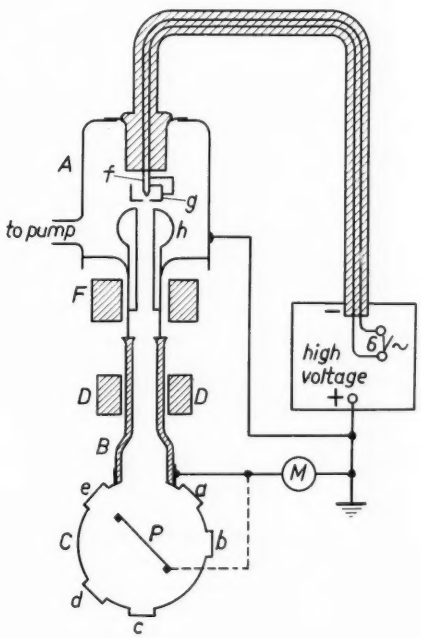


FIGURE 11. *Experimental set-up for efficiency measurements with C. R. excitation.*

A. metal chamber, h. anode, f. filament, g. cap, F. focusing coil, D. deflection coils, B. glass tube, C. metal cylinder, P. target plate, a, b, c, and d quartz windows, M. microammeter.



206-267 OL - 76 - 2

The measurements are carried out on thick layers at the irradiated side. Precautions should be taken to ensure that charging up of the layer is negligible.

The radiant output of the phosphor was compared with the radiation of a standard lamp which was diffusely reflected by a MgO layer. A thermopile was used [2] as a detector.

## 5. X-Ray Excitation

To measure radiant efficiencies with x-ray excitation [17–19] *thin* phosphor layers are used ($\approx 100\,\mu$m). This is necessary to minimize the loss in light output due to scattering and absorption of the emitted luminescence. The total back-screen emission is collected by a $2\pi$-geometry elliptical mirror and focused onto the photomultiplier detector (see fig. 12),

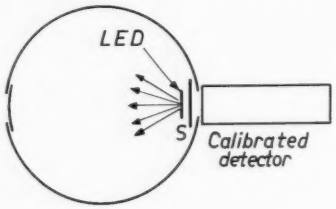


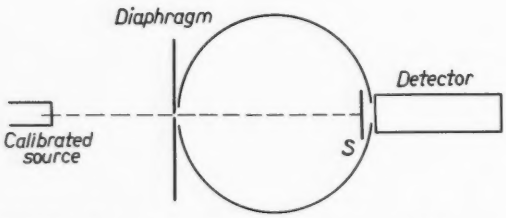


FIGURE 12. *Diagram for efficiency measurement of light emitting diodes.*

which is calibrated in absolute units (A/W). The x-ray absorption coefficients are measured with a scintillation crystal as well as calculated from the tables of Storm and Israel [20].

## 6. Measurements of Light-Emitting Diodes, Crystals, etc

In cases where the angular distribution of the emitted radiation does not obey Lambert's law it is not sufficient to measure the emitted radiation in one direction but the total radiation should be determined. This can be carried out with the aid of an Ulbricht's sphere or with an elliptical mirror.

The absolute output can be calibrated in two ways (see fig. 13):

(1) the luminescent output is measured with a calibrated detector (A/W · cm²). e.g., a 150 CV or 150 UV photocell (calibration National Physical Laboratory, Teddington, England).

(2) the luminescent output is compared with the output of a calibrated standard lamp, e.g., a 200 W or 1000 W tungsten - halogen lamp; calibrated by the National Bureau of Standards in Washington, D.C. (W/nm · cm²). In this case the diode to be measured is replaced by a $BaSO_4$-coated screen S.

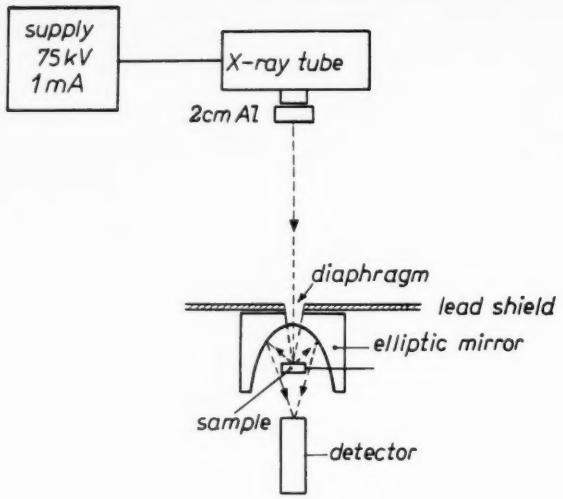


FIGURE 13. *Experimental set-up for x-ray efficiency measurements.*

The use of a $2\pi$-geometry elliptical mirror [21] instead of an Ulbricht's sphere gave nearly the same results.

## 7. References


[1] Nat. Bur. Stand. (U.S.), Tech. News Bull. **42**, 145 (1958) Bril, A., and Hoekstra, W., Philips Res. Repts. **16**, 356, (1961) and Philips Res. Repts. **19**, 296 (1964).

[2] Bril, A., in Kallman-Spruch, Luminescence of Organic and Inorganic Materials, p. 479 (John Wiley and Sons. Inc. New York 1962).

[3] Ludwig, G. W., and Kingsley, J. D., J. Electrochem. Soc. **117**, 348 (1970).

[4] Kingsley, J. D., and Ludwig, G. W., J. Electrochem. Soc. **117**, 353 (1970).

[5] See e.g. Samson, J. A. R., Techniques of Vacuum Ultraviolet Spectroscopy, p. 216 (John Wiley and Sons. Inc., New York. 1967).

[6] Grum, F., C.I.E.-Report of Subcommittee on Luminescence, 18th Session, London, 1975.

[7] Bril, A., and de Jager-Veenis, A. W., The Electrochemical Society, Spring Meeting at Toronto, May 1975; J. Electrochem. Soc. **123**, 396 (1976).

[8] Grum, F., and Luckey, G. W., App. Optics **7**, 2289 (1968).

[9] Kristianpoller, N., and Dutton, D., Appl. Opt. **3**, 287 (1964).

[10] Vavilov, V. S., J. Chem. Phys. Solids **8**, 223 (1959).

[11] Morgenshtern, Z. L., Neustruev, V. B., and Epshtein, M. I., J. Appl. Spectros. **3**, 35 (1965).

[12] Küttner, H. G., Selzle, A. L., and Schlag, E. W., Z. Naturf. **29a,** 224 (1974).
[13] Bril, A., Blasse, G., and Bertens, J. A. A., J. Electrochem. Soc., **115,** 395 (1968).
[14] Bril, A., Sommerdijk, J. L., and de Jager, A. W., J. Electrochem. Soc. **122,** 5 (1975).
[15] Lehmann, W., J. Electrochem. Soc. **118,** 1164 (1971).
[16] Meyer, V. D., J. Electrochem. Soc. **119,** 920 (1972).
[17] de Poorter, J. A., and Bril, A., J. Electrochem. Soc. **122,** 1086 (1975).
[18] Ludwig, G. W., J. Electrochem. Soc. **118,** 1152 (1971).
[19] Grum, F., Costa, L. F., Donovan, J. L., J. Opt. Soc. Am. **59,** 848 (1969).
[20] Storm, E., and Israel, H. I., Report LA 3753, Los Alamos Scientific Laboratory of the University of California, 1967.
[21] van der Does de Bye, J. A. W., Rev. Sci. Instrum. **40,** 320 (1969)

(Paper 80A3–891)

JOURNAL OF RESEARCH of the National Bureau of Standards—A. Physics and Chemistry
Vol. 80A, No. 3, May–June 1976

# On the Actinometric Measurement of Absolute Luminescence Quantum Yields*

**J. N. Demas and B. H. Blumenthal**

**Chemistry Department, University of Virginia, Charlottesville, Virginia 22901**

**(April 9, 1976)**

The theory of the measurement of luminescent quantum yields using chemical actinometry is described. The sample's emission intensity is measured by nearly completely surrounding the sample with an actinometer solution, and the excitation intensity is directly measured with the same type of actinometer. The ratio of the measured sample emission intensity corrected for the fraction escaping through the excitation ports to the measured excitation intensity is the absolute luminescence yield. Equations, a suitable cell design, and computer calculated correction factors for different cell dimensions and optical densities are given. The absolute yield of the actinometer is not needed, only its relative response with wavelength. New quantum-flat actinometers which should greatly simplify the measurements are described.

Key words: Absolute yield; chemical actinometry; correction factors; luminescence; quantum-flat actinometer; quantum yield.

## 1. Introduction

The measurement of absolute luminescence quantum yields is an important but experimentally difficult area [1, 2, 3].[1] Most yield measurements are made relative to a luminescence standard rather than by an "absolute" method. It is thus imperative for good accuracy that the luminescent standards be accurately calibrated. To date, these standards have been derived almost exclusively from calorimetry or by reference to a standard scatterer, usually with a luminescent quantum counter detector.

The history of quantum yield measurements has demonstrated quite painfully that it is exceedingly difficult to detect and eliminate all systematic errors. Thus, materials selected for standards should be tested by as many independent and presumably reliable "absolute" methods as possible and rechecked as new techniques become available.

We describe here the theory of a conceptually new "absolute" method for measuring luminescence quantum yields based on chemical actinometers. The technique avoids many of the intrinsic error sources of the other methods and thus promises to be a useful check on existing and new standards. The current availability of numerous lasers with both high intensites and a wide range of wavelengths ranging from $< 250$ nm to $> 800$ nm coupled with new broadband, quantum-flat actinometers make the actinometric method most attractive. In addition to the theory we present a suitable cell design, tabular correction factors, and describe suitable actinometers.

## 2. Theory

The actinometric approach for determining yields measures the excitation intensity and the sample emission intensity by chemical actinometry; the ratio of the emission to excitation intensity, both corrected for the fraction of the excitation beam absorbed, is the absolute quantum yield. The total emitted intensity is measured by nearly completely surrounding the sample with the actinometer solution except for a small excitation port and correcting for the small port losses. The same type of actinometer is then used to measure the excitation beam intensity.

For the actinometer monitoring the emission intensity of the luminescent unknown, the amount of reaction in the actinometer, $D_x$ (mol of product), is given by

*Paper presented at the Workshop Seminar 'Standardization in Spectrophotometry and Luminescence Measurements' held at the National Bureau of Standards, Gaithersburg, Md., November 19–20, 1975.

[1] Figures in brackets indicate the literature references at the end of this paper.

$$D_x = I_0 t_x F_x \phi F'_E \bar{\Theta}_x$$

$$F_x = T(1 - 10^{-A_x}) \qquad (1)$$

where $I_0$ (einstein/s) is the incident excitation intensity, $t_x$(s) is the irradiation time, $F_x$ is the fraction of incident excitation light absorbed by the unknown, $T$ is the effective transmittance of the entrance window, $A_x$ is the absorbance of the solution to the excitation beam, $\phi$ is the sample's absolute luminescence efficiency, $F'_E$ is the fraction of emitted light captured by the actinometer, and $\bar{\Theta}_x$(mol/einstein) is the actinometer's effective photochemical quantum yield for the emission band. It is assumed that the excitation beam is monochromatic, all of the emission passing into the actinometer is absorbed, and reabsorption-reemission corrections are negligible. $\bar{\Theta}_x$ is given by

$$\bar{\Theta}_x = \frac{\int_0^\infty F(\bar{\nu})\Theta_x(\bar{\nu})\,d\bar{\nu}}{\int_0^\infty F(\bar{\nu})\,d\bar{\nu}} \qquad (2)$$

where $\bar{\nu}$ is energy in $cm^{-1}$, $F(\bar{\nu})$ (relative quanta/$cm^{-1}$ of bandwidth) is the corrected relative emission spectrum and $\Theta_x(\bar{\nu})$ (mol/einstein) is the variation of the actinometer yield with excitation energy.

In the measurement of the excitation beam intensity, the amount of reaction in the actinometer, $D_s$(mol), is given by

$$D_s = I_0 t_s F_s \Theta_s$$

$$F_s = T(1 - 10^{-A_s}) \qquad (3)$$

where $t_s$(s) is the irradiation time, $F_s$ is the fraction of the excitation beam absorbed by the actinometer, $T$ is the same as eq 1, $A_s$ is the absorbance of the actinometer solution to the laser, and $\Theta_s$ (mol/einstein) is the actinometer's yield at the excitation wavelength. The absolute luminescence quantum yield is then given by

$$\phi = \left(\frac{D_x}{D_s}\right)\left(\frac{t_s}{t_x}\right)\left(\frac{1-10^{-A_s}}{1-10^{-A_x}}\right)\left(\frac{\Theta_s}{\bar{\Theta}_x}\right)\left(\frac{1}{F'_E}\right). \qquad (4)$$

The $D$'s, $A$'s and $t$'s are directly measurable and $F'_E$ can be evaluated from geometric considerations (see below). At first it might appear that this method can be no more accurate than the absolute accuracy of the evaluation of the actionometer's yield, $\Theta(\bar{\nu})$, a process which is rarely good to better than 10 percent. In reality since eq 4 uses the ratio of $\Theta_s$ to $\bar{\Theta}_x$, only the variation of $\phi(\bar{\nu})$ with $\bar{\nu}$ need be known accurately. As long as data from the same workers are used, this error is likely to be substantially smaller than 10 percent and quite possibly less than 5 percent. Also, as we shall show, actinometers with intrinsically quantum-flat responses are becoming available which will make $\Theta_s/\bar{\Theta}_x = 1.000$ within ~1-2 percent, regardless of how accurately the absolute yield is known.

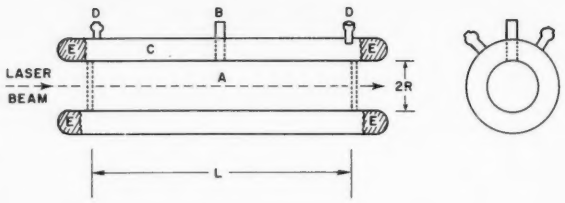


FIGURE 1. *Cell design for luminescence quantum yield measurements by actinometry.*

a. Luminescent sample. b. Filling stem for sample. c. Actinometer solution compartment. d. Filling stems for actinometer which are also suitable for a flow actinometer system. e. Silvering on actinometer jacket ends to reflect emission transmitted down glass walls back into solution. To extend the maximum wavelength of the actinometer, the entire actinometer jacket could be silvered to double the absorption path for emission.

## The Model

Figure 1 shows an easily fabricated cell suitable for measuring absolute yields by actinometry. The cell, built much like a reflux condenser, has a long, central irradiation volume with a small diameter filling stem. The outer jacket contains the actinometer solution which intercepts and absorbs a large fraction of the emitted light. The two filling ports on the actinometer jacket facilitate filling and permit the use of flow actinometers.

This cell design has numerous advantages. The system is only suitable for use with laser excitation; therefore, the monochromatic laser light eliminates, in virtually all solution cases, the need for effective absorbance corrections arising from variation of absorbance over the excitation band [4]. Questionable refractive index corrections are also eliminated. The high symmetry and entering and exiting excitation ports simplify evaluation of $F_x$ and $F'_E$; further, the exit port removes unabsorbed excitation light from the system so that it cannot affect the actinometer. By silvering the ends of the actinometer jacket, radiation light piped down the glass walls can be directed back into the actinometer. By making $L/R$ large, $F'_E$ can be made to approach unity as closely as desired. By choosing a large $L/R$, one can easily absorb a large fraction of the exciting light and still keep the reabsorption-reemission correction small. Thus, the system combines some of the best features of the optically dense and dilute approaches.

### Evaluation of $F'_E$

To evaluate $F'_E$ we make several assumptions, all of which will be quite accurate or will introduce negligible errors in a well-designed cell. These assumptions are: (1) the laser beam is centered and its diameter is small compared to $R$, (2) all emission not directly striking the windows is absorbed by the actinometer, (3) all of the emission transmitted by the cell windows is lost, (4) reabsorption-reemission corrections are negligible, and (5) the windows and cell walls are nonabsorbing.

$F'_E$ is divided into two terms, a geometric factor for direct capture of the emitted light and a correction for

the emitted light reflected by the windows back into the cell which is subsequently absorbed by the actinometer. $F'_E$ is given by

$$F'_E = F_E + (1 - F_E) r_{eff} F_{RA} \tag{5}$$

where $F_E$ is the fraction of primary emission that would be absorbed if the windows were perfectly transparent with no reflection losses, $r_{eff}$ is the fraction of primary emitted radiation reflected back into the cell by the windows, and $F_{RA}$ is that fraction of this reflected radiation which is eventually absorbed by the actinometer, the remainder eventually escaping. $F_E$ can be evaluated by

$$F_E = \left(\frac{1}{2B}\right) \int_0^L \left\{\cos\left[\arctan\left(\frac{R}{\ell}\right)\right] + \cos\left[\arctan\left(\frac{R}{(L-\ell)}\right)\right]\right\} A\, d\ell \tag{6}$$

$$A = \frac{\epsilon C \exp\left[-\ln(10)\,\epsilon C \ell\right]}{\{1 - \exp\left[-\ln(10)\,\epsilon C \ell\right]\}}$$

$$B = 1 - \exp\left[-\ln(10)\,\epsilon C L\right]$$

where $\epsilon$ is the sample's molar extinction coefficient at the excitation wavelength and $C$ is the sample concentration. The first and second cosine terms account for the fraction of radiation striking the entrance and exit windows respectively as a function of position in the cell. The $A$ term accounts for the decrease in emission intensity along the tube caused by absorption. The $B$ term corrects for the total fraction of excitation light absorbed in the cell.

For a very large $L/R$ and not too high an optical density, $F_E$ will approach unity. For extremely high optical densities, however, the emission front surfaces at the entrance window where half the radiation could escape, and $F_E$ approaches 0.5.

Equation 6 has no obvious analytical solution and was evaluated numerically using Simpson's rule. Because of the discontinuities in the integrand at $\ell = 0$ and $\ell = L$, the evaluation limits were just set very near both windows. Initially calculations were done on a Hewlett Packard 2000 [2] system in time sharing BASIC, but its $\sim 6-7$ significant figures proved inadequate. All calculations presented here were done on a Hewlett Packard 9100 B programmable desk calculator which has 10–12 significant figures; there were no problems with convergence. Integration was performed over the range $\ell/L = 10^{-5}$ to 0.99999 with 200 subdivisions. Increasing the number of divisions to 1000 caused no changes in the fifth significant figure. Our calculated $F_E$'s are thus accurate to better than 0.1 percent. Calculated results for $F_E$'s as a function of $L/R$ and $A_x$ are given in table 1.

[2] In order to describe materials and experimental procedures adequately, it is occasionally necessary to identify commercial products by manufacturer's name or label. In no instance does such identification imply endorsement by the National Bureau of Standards, nor does it imply that the particular product or equipment is necessarily the best available for that purpose.

## 3. Discussion

Table 1 reveals that, as expected, $F_E$ approaches unity for large values of $L/R$ with low to intermediate values of $A_x$. Also, for very large values of $A_x$, $F_E$ seems to approach 0.5. $F_E$ decreases as $A_x$ increases because of the movement of the emission towards one end where the escape factor is greater.

TABLE 1. *Emission absorption fraction*, $F_E$

| $A_x$ \ $L/R$ | 5 | 10 | 20 | 50 | 100 | 200 |
|---|---|---|---|---|---|---|
| 0.5 | 0.8141 | 0.9001 | 0.9479 | 0.9786 | 0.9892 | 0.9946 |
| 1.0 | .7986 | .8866 | .9385 | .9738 | .9865 | .9932 |
| 1.5 | .7776 | .8681 | .9255 | .9670 | .9828 | .9912 |
| 2.0 | .7551 | .8478 | .9109 | .9593 | .9785 | .9889 |
| 2.5 | .7333 | .8277 | .8960 | .9513 | .9739 | .9864 |
| 3.0 | .7136 | .8089 | .8818 | .9434 | .9693 | .9839 |
| 3.5 | .6962 | .7916 | .8683 | .9357 | .9648 | .9814 |
| 4.0 | .6808 | .7760 | .8556 | .9282 | .9604 | .9790 |
| 5.0 | .6555 | .7488 | .8327 | .9141 | .9585 | .9741 |
| 6.0 | .6357 | .7263 | .8125 | .9010 | .9437 | .9694 |
| 7.0 | .6199 | .7072 | .7947 | .8887 | .9359 | .9649 |
| 8.0 | .6071 | .6910 | .7786 | .8773 | .9284 | .9604 |
| 9.0 | .5964 | .6770 | .7642 | .8665 | .9212 | .9561 |
| 10.0 | .5875 | .6647 | .7512 | .8564 | .9143 | .9518 |

As a practical consideration $F_E$ should be as close as possible to unity. Fortunately this is not difficult. Even for a cell which is only 2.5 times longer than its diameter ($L/R = 5$), $F_E$ is $> 75$ percent for $A_x \leq 2$, an acceptable value. More realistic values of $L/R$ for actinometer cells would be 20–50 which yield $F_E > 90$ percent for $A_x \leq 2.0$. Even values of $L/R$ of 100–200 are feasible; a 50 cm cell would be 0.5–1 cm in diameter; in these cases $F_E$ would exceed 90 percent for $A_x \leq 3$. It is thus clear that excellent collection efficiency of the emission can be readily obtained.

In the evaluation of $\emptyset$, $F'_E$ rather than $F_E$ is actually required. We have not done a quantitative analysis for $F'_E$ because $r_{eff}$ and $F_{RA}$ are quite difficult to evaluate, but in a well-designed cell the error associated with replacing $F'_E$ by $F_E$ is quite small. For example, in a cell with a large $L/R$, most of the emission incident on the cell windows will be at near normal incidence; thus, we can use $r_{eff} \sim 0.04$ for a glass-air interface. For $F_E = 90$ percent, $F'_E$ will be $< 0.5$ percent greater than $F_E$, and the error falls for larger $F_E$'s.

Until recently the potential choices of actinometers were limited to ferrioxalate and Reinecke's salt. The ferrioxalate actinometer will yield total absorption of the emitted radiation up to $\sim 480$ nm using a 5 cm thick actinometer solution (0.15 F). The yield is not strongly wavelength dependent from 254 nm to 480 nm, and calibration is sufficiently detailed to permit accurate evaluation of $\bar{\Theta}_x$.

Reinecke's salt offers much deeper red penetration, $\sim 610$ nm for $2 \times 10^{-2} M$ solution and a 5 cm minimum cell length. The yield is more nearly constant than ferrioxalate over the 390–620 nm range. Unfortunately

Reinecke's salt has serious disadvantages. The yield changes sharply below 390 nm, and detailed data in this region are lacking. The complex is difficult to dissolve at high concentrations and undergoes a relatively rapid thermal reaction ($\sim 0.6\%$/h). Although it is about an order of magnitude less sensitive than ferrioxalate, this is not likely to be a problem with a high intensity laser excitation source.

New photosensitized actinometers promise to eliminate the previous difficulties. For example, the tris-(2,2-bipyridine)ruthenium(II) photooxidation of tetramethylethylene has been developed as an actinometer for high power lasers [5]. The system should be intrinsically quantum flat, because the lowest excited state is responsible for the sensitization; luminescence experiments have verified that the efficiency of population of the emitting state is constant to $\sim \pm 2$ percent over this region [6]. A solution $10^{-3}M$ in the ruthenium complex will absorb all radiation below $\sim 520$ nm in a 2 cm pathlength. By using similar osmium(II) complexes as the sensitizer [6, 7, 8], total absorption of the emission and a quantum flat response below $\sim 700$ nm should be realized. These systems use volumetric monitoring of the consumed $O_2$ and are thus not very sensitive, but laser excitation supplies adequate intensity. Finally, because the consumed $O_2$ must be replaced and inhomogeneity of the reactants can be a problem in a static system, these actinometers must be operated in a flow system.

An analogous system which also shows promise is the methylene blue sensitized photooxidation of tetramethylethylene. Solutions can easily be made totally absorbing to beyond 700 nm in a 1 cm pathlength, and the yield is comparable to the Ru(II) and Os(II) systems. The quantum yields may, however, not be perfectly flat, and minor corrections may be required.

In summary, we feel that the actinometric method, although too complex for routine measurements, will prove especially useful in developing primary luminescence quantum yield standards. This method eliminates most of the error sources inherent in other absolute techniques, and thus supplies a valuable check. The technique is currently feasible for compounds emitting below 520 nm, and with the natural evolution of actinometry, operation to 700 nm and beyond should soon be feasible.

---

Acknowledgment is made to the National Science Foundation, the donors of the Petroleum Research Fund, administered by the American Chemical Society, and to the Research Corporation for support of this work.

## 4. References

[1] Lipsett, F. R., Progr. Dielectrics, **7,** 217 (1967).
[2] Demas, J. N., and Crosby, G. A., J. Phys. Chem. **75,** 991 (1971).
[3] Crosby, G. A., Demas, J. N., and Callis, J. B., J. Res. Nat. Bur. Stand. (U.S.), **76A** (Phys. and Chem.), No. 6, 561–577 (Nov.–Dec. 1972).
[4] Demas, J. N., Anal. Chem. **45,** 992 (1973).
[5] (a) Demas, J. N., Harris, E. W., and McBride, R. P., Lasers in Physical Chemistry and Biophysics (Elsevier, New York, N.Y., 1975), p. 477.
(b) Demas, J. N., McBride, R. P., and Harris, E. W., J. Phys. Chem., accepted.
[6] Demas, J. N., and Crosby, G. A., J. Am. Chem. Soc. **93,** 2841 (1971).
[7] Demas, J. N., Harris, E. W., Flynn, Jr., C. M., and Diemente, D., J. Am. Chem. Soc. **97,** 3838 (1975).
[8] Demas, J. N., Harris, E. W., and McBride, R. P., submitted.

(Paper 80A3–892)

JOURNAL OF RESEARCH of the National Bureau of Standards—A. Physics and Chemistry
Vol. 80A, No. 3, May–June 1976

# The Calorimetric Detection of Excited States*

**James B. Callis**

**Department of Pathology, University of Washington Medical School, Seattle, Washington 98195**

**(April 9, 1976)**

Calorimetric techniques offer the photophysicist and photochemist the opportunity to measure a number of parameters of excited states which may be difficult to obtain by other techniques. The calorimetric strategy seeks to measure the heating of a sample resulting from radiationless decays or chemical reactions of excited states. Heating is best measured through volume and pressure transducers, and four calorimeters based on these are described. With calorimetric instrumentation one can perform measurements on samples in the gas, liquid and solid phases over a wide temperature range. Moreover time dependent processes with time constants ranging from microseconds to seconds are amenable to study. Examples of the application of calorimetric techniques to the determination of quantum yields of fluorescence, triplet formation and photochemistry are given.

Key words: Absolute quantum efficiency; absolute quantum yield; calorimetry; luminescence; photoacoustic spectrometer; piezocalorimeter; transducers; triplet formation

## 1. Introduction

In understanding the nature of excited electronic states it is well appreciated that a wide variety of parameters are accessible to photometric measurement. Among them are the absorption spectrum of the excited state, the excitation spectrum, and the lifetime. If the excited state decays by emission of photons, one can also measure the spectral distribution of emission, the polarization, and the quantum yield of emitted photons. Unfortunately, it is not so generally appreciated that a number of parameters of an excited state are also accessible to calorimetric measurement. The calorimetric strategy seeks to measure how much of the light absorbed by a sample is converted to heat energy by radiationless processes and/or photochemistry. Parameters which can be measured include: the lifetime of an excited state, the excitation spectrum for a particular process, the energy yield of a radiationless process, and the enthalpy of a photochemical process.

A simple example illustrates how calorimetric measurements can complement photometric measurements. Most air saturated liquid solutions of luminescent organic molecules exhibit only fluorescence at room temperature. By measuring the ratio of the heating of the fluorescent substance in response to photoexcitation to that of a non-fluorescent but equally absorbing substance, one obtains the energy yield of radiationless processes $Y_h$ [1, 2].[1] In the absence of photochemistry, the fluorescence energy yield is the complement of $Y_h$, and the quantum yield of fluorescence $\Phi_f$ is related to it by the formula

$$\Phi_f = (\bar{\nu}_a/\bar{\nu}_f)(1-Y_h) \tag{1}$$

where $\bar{\nu}_a$ and $\bar{\nu}_f$ are the average frequencies of absorbed and emitted photons respectively. Calorimetric quantum yields determined in this manner [1, 2, 3] are among the most precise and accurate reported in the literature, and in addition provide a valuable independent technique for verifying the many assumptions that go into the derivation of quantum yields from photometric measurements [4, 5]. Despite these advantages, very few quantum yields have been measured calorimetrically. This unfortunate situation exists because most workers in the field are unfamiliar with calorimetric techniques, and moreover, the measurements are time consuming and tedious to perform. It is the purpose of this paper to point out some recent work which shows that using capacitor microphones and piezoelectric crystals as heat flow transducers, calorimetry can be a rapid, simple and sensitive technique for use in measuring a wide variety of parameters of excited states. Also, samples in the gas, liquid and solid phases, including thin films and monolayers are amenable to study.

*Paper presented at the Workshop Seminar 'Standardization in Spectrophotometry and Luminescence Measurements' held at the National Bureau of Standards, Gaithersburg, Md., November 19–20, 1975.

[1] Figures in brackets indicate the literature references at the end of this paper.

## 2. Types of Calorimeters Suitable for Measuring Photochemical and Photophysical Processes

The most obvious approach for detection of heat production is to use a conventional calorimeter based upon the usual temperature sensors: thermistors and thermopiles. We will not discuss these instruments here because they have already been reviewed [3, 4, 5] and because they have inherent disadvantages in sensitivity, risetime and speed at which measurements can be made. Instead, we will concentrate on alternative strategies for measuring heat flow based on volume and pressure changes produced in the sample.

In general, addition of an amount of heat $dQ$ to the sample gives rise to both a pressure change $dP$ and a volume change $dV$ according to the thermodynamic relationship [6]

$$dQ=\frac{C_P dV}{\alpha V}+C_v\frac{\beta}{\alpha}dP \tag{2}$$

where $C_P$ and $C_v$ are the heat capacities at constant pressure and constant volume, $V$ the volume of the solution, $\alpha=V^{-1}(\partial V/\partial T)_P$ is the coefficient of thermal expansion, and $\beta=-V^{-1}(\partial V/\partial P)_T$ is the compressibility of the sample. Three of the calorimeters we will describe use the capacitor microphone to detect volume changes in the sample. In all of these devices the sample is enclosed in a cell with rigid walls. One of these walls, generally normal to the direction of propagation of exiting light is replaced by the compliant diaphragm of a capacitor microphone. Because of the diaphragm, a second relationship between $dP$ and $dV$ must be simultaneously obeyed:

$$dP=\kappa dV/V. \tag{3}$$

We have assumed that the changes are small so that a linear relationship exists, and $\kappa$, the linear constant, is approximately given for a cubic cell by $k/\ell$ where $k$ is the force constant for displacing the diaphragm, and $\ell$ is the linear dimension of the cell. Combining eq (2) and (3) we have

$$dV=\alpha V dQ/(C_P+C_V\kappa\beta). \tag{4}$$

Equation (4) shows that: (a) the volume change is independent of any gradients in the distribution of energy in the cells; (b) the largest volume changes are obtained for samples which have the highest values of $\alpha$ and the lowest heat capacities (gases give the largest signals; water gives low signals); (c) the compliance of the diaphragm must be kept low enough so that the product $\kappa\beta$ is as small as possible.

The capacitor microphone for measuring the volume changes consists of the diaphragm and a stationary electrode spaced a small distance apart; together they form a capacitor whose capacitance $C$ is given by

$$C=\epsilon A/x \tag{5}$$

where $\epsilon$ is the dielectric constant, $A$ is the area of the electrodes, and $x$ is the spacing between them, and edge effects were neglected. If the change in spacing of the electrodes is small enough, the capacitance will be related to it linearly. Several methods have been used successfully for the detection of the capacitance change. In the most common method [7], the microphone is polarized either with an externally supplied dc voltage or by placing an electret [8] in the gap between the electrodes; when the capacitance changes, charge flows to maintain a constant voltage. The charge flow is then converted to a voltage change by a charge sensitive pre-amp [9]. Capacitance changes can also be detected with an ac bridge circuit [10]. Even with simple detection systems, a displacement of the diaphragm of the order of one angstrom is easily measured with a bandwidth of 10 kHz [6]. The frequency response of the microphone is linear over a very wide range; the upper limit is set by the lowest mechanical resonance of the diaphragm (10–20kHz), and the lower limit is determined by the low frequency cut-off of the electronics or the thermal instabilities of the system.

With these fundamental considerations in mind, we may now discuss three types of calorimeters based upon the use of capacitor microphone pressure transducers: the "acoustic spectrophone" for study of gas phase systems, the "optoacoustic cell" for study of thin films and thin sections of solid materials, and the "flash calorimeter" for studies of liquid samples.

The acoustic spectrophone has been widely used as a technique for infrared gas analysis [12] and for measuring vibrational relaxation rates [13]. A typical acoustic spectrophone [11] consists of a cylindrical cell with transparent windows at each end to allow radiation to enter and leave; the microphone is generally mounted on the cylindrical wall with the diaphragm normal to the direction of propagation of the excitation beam. Often, a regulated leak is provided so that long term pressure drifts can be relieved.

The design of acoustic spectrophones is discussed in detail by Rosengren [14], Parker and Ritke [11] and Kerr and Atwood [15]. The ultimate limit of signal to noise arises from the Brownian motion of the gas molecules. Present designs can come within two orders of magnitude of this limit at reasonable gas pressures. The present limitations arise from noise in the detection electronics, temperature instabilities (especially at low frequencies) and spurious contributions to the signal arising from gas adsorbed on the windows [14]. Even with these limitations, energy inputs as small as one microwatt may be easily detected. Parker has shown [11] that the rise time for the volume change is set by the lowest acoustical resonance frequency in the cavity whose frequency is given by $c/2l$, where $c$ is the speed of sound in the gas, and $l$ is the length of the cavity.

A device similar to the acoustic spectrophone has been developed by Rosencwaig [17] for the study of radiationless processes and photochemistry in thin films of solids, and semisolid materials such as crystals, evaporated films, powders, gels, thin layer

chromatography plates, and even thin layers of tissue. The photoacoustic cell is quite similar to the acoustic spectrophone of Parker, except it is much shorter in cavity length. The thin sample is simply mounted flush with the exit window, and the cell is filled with a suitable gas which is transparent to the exciting radiation.

The origin of the photoacoustic effect is believed to be as follows [11, 18]: irradiation of the sample with pulsed or chopped steady state light results in a localized heating due to non-radiative decay processes by the excited states. Some of the heating is transferred via diffusion from the solid to a thin boundary layer of gas adjacent to the solid. Adiabatic expansion of the gas then gives rise to a pressure wave in the gas which is detected by a capacitor microphone. A quantitative version of this process has been proposed [11, 18]. Like the acoustic spectrophone this device can easily detect microwatts of absorbed radiation, and the risetime is set by the transit time for sound in the cavity.

The third device based on the use of the capacitor microphone is the flash calorimeter of Callis, Gouterman and Danielson [6]. A schematic of the device is given in Figure 1. The sample cell is constructed from $25 \times 25$ mm square Pyrex[2] tubing. Joined to the sides are two 4-mm Pyrex-Teflon vacuum stopcocks. One of these provides connection to a vacuum line, allowing for introduction of degassed samples. The other stopcock opens into a small relief reservoir. It provides a controlled leak so that liquid can slowly enter or leave the cell, thus preventing slow pressure changes that would occur in a completely closed cell subject to temperature drifts. To allow use of a circular diaphragm a short piece of 25-mm Pyrex tubing is fused to the top of the cell. The diaphragm is made from 1 mm aluminum, which is sufficiently thick so that it does not deform permanently under vacuum, yet not so thick that the product $\kappa\beta$ exceeds unity. The microphone consists of the diaphragm, an epoxy glass circuit board spacer, and a stationary electrode-guard ring assembly fabricated from brass and epoxy glass circuit board material. The spacer ring is ground down until the gap between diaphragm and stationary electrode is approximately 0.25 mm and the entire assembly is potted with epoxy cement. The cell is mounted in a brass block which is temperature stabilized by means of a thermoelectric heat pump. The entire assembly is mounted in an acoustically shielded aluminum box which rests on a vibration isolation table.

As with other devices based on the use of microphones, the rise time of the flash calorimeter is determined by the transit time for sound in the cavity. This limits the use of the instrument in kinetic studies to phenomena with time constants longer than $100\mu$s. The sensitivity of the flash calorimeter is quite remarkable; a displacement of the diaphragm of $10^{-8}$ cm is easily detected with a bandwidth of 10 kHz. For ethanol this corresponds to a temperature rise of $\sim 10^{-6}$ °C or an energy input of $\sim 64\mu$J. The limits of detection at high frequencies are largely due to the noise in the preamplifier stage; we are presently many orders of magnitude above the limit imposed by the thermal noise of the sample.

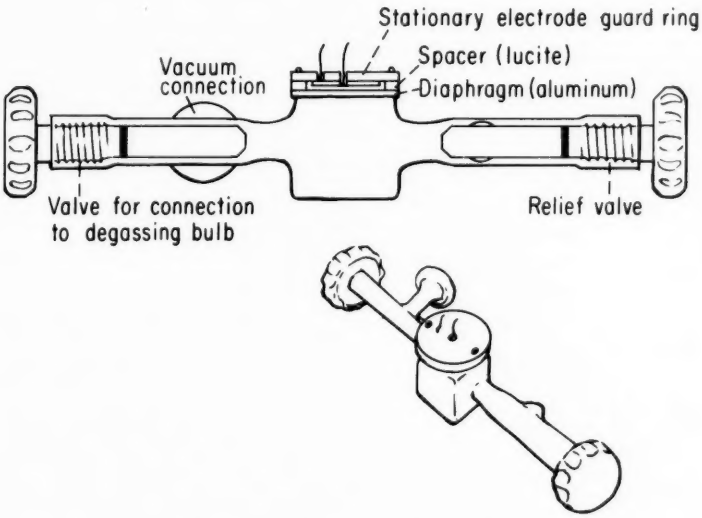


FIGURE 1. *Flash calorimeter schematic.*

[2] In order to adequately describe materials and experimental procedures, it is occasionally necessary to identify commercial products by manufacturer's name or label. In no instance does such identification imply endorsement by the National Bureau of Standards, nor does it imply that the particular product or equipment is necessarily the best available for that purpose.

We now describe an instrument which is particularly well suited for measurement of radiationless processes in bulk solids. This device, the piezoelectric calorimeter, uses a piezoelectric crystal to measure pressure changes in the sample. In certain crystals and polycrystalline materials with assymetric charge distribution, an applied pressure results in displacement of the positive and negative charges relative to each other. The displacement of the charges can be measured by applying electrodes to the surfaces and measuring the potential difference between them caused by charge migration. Piezoelectric crystals are available which are rugged, inexpensive, and linear and which will perform at temperatures from 4 K to 700 K.

A simple piezoelectric calorimeter is shown in figure 2. It consists of a cylindrical sample (we have used polymethyl methacrylate samples in which the organic compound of interest is dissolved), and a cylindrical piezoelectric transducer of the same radius as the sample. The transducer and sample are clamped rigidly together by an aluminum frame.

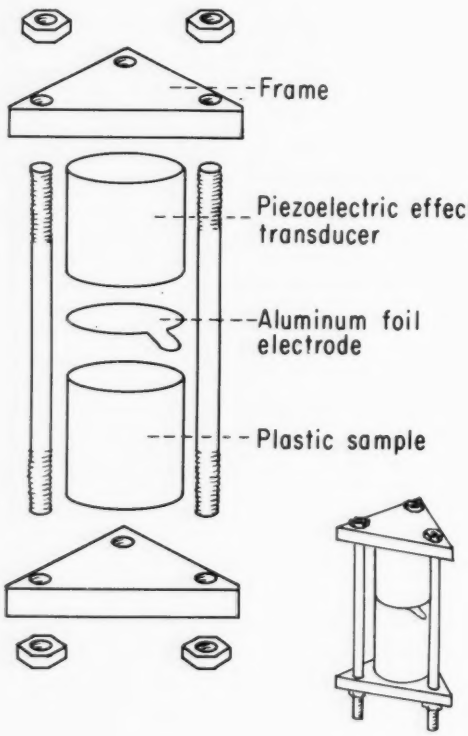


FIGURE 2. *Piezocalorimeter schematic.*

The piezoelectric crystal may be conveniently thought of as measuring the pressure generated by heating at constant volume. Equation (4) then becomes

$$dP = dQ\alpha/\beta C_V. \tag{6}$$

The open circuit voltage response to a pressure change is given by:

$$E = gtdP \tag{7}$$

where $g$ is the open circuit voltage constant in units of $m^2/C$, $t$ is the thickness of the crystal in m, and $E$ is the voltage produced [7]. The simplest method for operating these devices is to use a charge sensitive preamplifier, as with the capacitor microphone. The upper end of the frequency response will then be limited by the lowest acoustic resonance, while the lower end will be limited by the low frequency response of the preamplifier.

The response of the piezoelectric calorimeter to an infrared heating flash shows characteristics similar to that of the flash calorimeter. The ring period is shorter due to the higher speed of sound in the cavity, but is not damped as effectively. With the present apparatus we can easily detect a step rise of $E \leq 10^{-3}$V which corresponds to a pressure change of 0.073 dyn/cm$^2$ for a lucite rod of 1 cm thickness, which in turn corresponds to a temperature change of $6.7 \times 10^{-7}$ °C. For our samples we find that $dQ \sim 4.7$ $\mu$cal is easily detected.

In addition to the calorimeter, the measurement of calorimetric parameters also requires a light source, a means for selecting a bandwidth of the radiation, and suitable signal processing electronics. The ideal light source for calorimetry must be of high intensity, stable with time, and of high spectral purity. Clearly the laser approaches most closely this ideal, and a number of authors have employed both cw and pulsed lasers. For excitation spectrum studies a Xenon arc lamp-monochromator combination possesses the one advantage of infinite wavelength tunability and the capability of ultraviolet irradiation. Since the calorimeters are ac coupled, the light source must be intensity modulated. For a cw light source, a simple and common method to achieve intensity modulation is with a mechanical chopper. In this case, the most attractive form of signal processing is to use a phase sensitive amplifier, operated in synchrony with the chopper. If all of the heating from the sample appears with a rate constant greater than the chopping rate, then all of the signal will be in phase with the chopper. However, if some of the heating arises from processes which have rate constants comparable to or less than the chopping rate, then some of the heating will be out of phase. Quantitation of these effects leads to methods for measuring rates of relaxation of excited states and the yield of heating of a particular process. The disadvantages of modulation of a cw source and phase sensitive detection is that the signal decreases linearly with the frequency, and that a series of measurements must be made at a number of different frequencies if the order of the kinetics is to be specified.

For the measurement of the time dependence of the heating, the use of a pulsed light source is advantageous. Large amounts of energy can be output in very short times, thus providing a good signal to noise ratio for fast time dependent processes, as well as giving the heating curve directly. This technique re-

quires some method for transient recording and signal averaging is often desirable. A potential problem with pulsed excitation is that it strongly excites the lowest cavity resonance of the chamber. The resultant oscillation is superimposed on the signal and often obscures the heating curve at short times.

## 3. Applications of Calorimetric Techniques

### 3.1. Fluorescence Quantum Yields

In the introduction, we noted the advantages of the calorimetric strategy for determination of quantum yields. Thus far, all of these measurements have been done on dilute liquid solutions which are easily done photometrically. In contrast determination of quantum yields from thin layers of powdered samples is a very difficult procedure to perform photometrically [19, 20]. Some pioneering work by Rosencwaig [17, 21] illustrates how the optoacoustic spectrometer can be used to advantage on these systems. A number of trivalent rare earth ions show narrow absorption bands in the visible and ultraviolet which arise from inner shell $f$–$f^*$ transitions. Some of these levels exhibit fluorescence, and the fluorescence quantum yield of a particular level exhibits a marked dependence upon which level is excited [22]. Rosencwaig studied the photoacoustic excitation spectrum of samples of powdered holmium oxide. The first sample contained cobalt and fluorine impurities in sufficient quantity to quench all of the luminescence. He found that the photoacoustic spectrum, when corrected for the wavelength dependence of the relative output of the excitation beam, corresponded well with the observed absorption spectrum. In contrast, the photoacoustic spectrum of pure $Ho_2O_3$ exhibited a spectrum in which some of the lines were greatly diminished in intensity; the latter of course involve excited states which decay by radiative processes. The information contained in these two scans, together with lifetimes and luminescence spectra taken by exciting at each major absorbance would provide, for the first time, a complete picture of the dynamic interrelationships of these excited states.

### 3.2. Quantum Yields of Triplet Formation

A knowledge of quantum yields of triplet formation is important in understanding the intersystem crossing process, and also in understanding the many photochemical reactions and energy transfer process which take place through the intermediacy of a triplet state. A number of ingenious methods exist for determination of triplet yields [23] but all are based on the use of various assumptions which are difficult to verify experimentally. The calorimetric strategy offers an attractive alternative to the other techniques, and also provides an independent check on the assumptions used in the other methods.

The calorimetric method is based on the fact that the lifetime of the lowest triplet state of an organic molecule is long compared to that of its excited singlet states. Thus, we expect that a delta function excitation pulse will produce fast heating due to relaxation of the singlet states, and slow heating due to relaxation of the triplet states. The heating may then be partitioned into

$$Q_{\text{tot}} = Q_{\text{fast}} + Q_{\text{slow}}. \tag{8}$$

It has been shown (6) that $\Phi_t$ can be obtained from the relation:

$$\Phi_t = Q_{\text{slow}}[h\bar{\nu}_{in} - \Phi_f h\bar{\nu}_f]/Q_{\text{tot}}E_t \tag{9}$$

where $\Phi_f$ and $\Phi_t$ are the quantum yields for fluorescence and triplet yields, $\bar{\nu}_f$ and $\bar{\nu}_{in}$ are the average fluorescence and absorbed frequencies, and $E_t$ is the energy of the triplet state.

As an example of the use of the flash calorimeter we show the heating response of $10^{-4}$ $M$ acridine orange to flash excitation in figure 3. The results are the average of 100 flashes. Clearly, there are two kinds of heating, as expected. Furthermore, the observed heating obeys the expected [6] time dependent form,

$$Q(t) = [Q_{\text{fast}} + Q_{\text{slow}}(1 - e^{-k_p^* t})]e^{-t/RC} \tag{10}$$

where $k_p^*$ is the triplet decay time, and $RC$ is the decay time of the ac coupled electronics. For comparison, in figure 4 we show the heating response of $10^{-4}M$ anthracene in polymethyl methacrylate as studied with the piezoelectric calorimeter. It also shows the

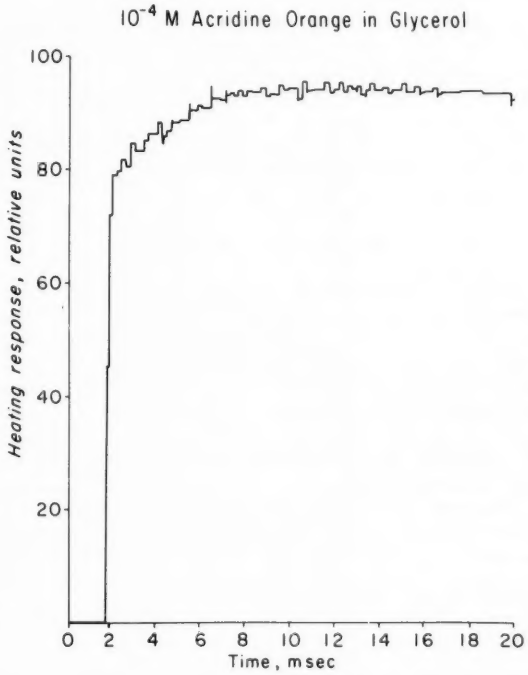


FIGURE 3. *Calorimetric response of degassed acridine orange in glycerol at room temperature.*

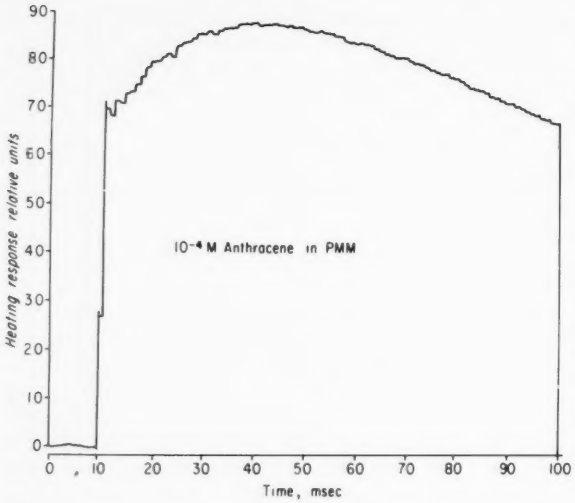


FIGURE 4. *Calorimetric response of anthracene in polymethyl methacrylate at room temperature.*

same type of heating response as predicted by eq (10). The value $\Phi_f = 0.72$ for anthracene in plastic compares well with that determined in mineral oil by other methods [23].

### 3.3. Applications to Photochemistry and Photobiology

In addition to heating from radiationless transitions, one may also detect heating from photochemical processes. Suppose that the sample is excited by $N_{ex}$ photons of energy $E_{in}$, and either decays radiationlessly to the ground state, or by photochemistry with a probability $\Phi_P$ to a stable product state of energy $E_P$ above the ground state. The total heating $dQ$ will then be given by

$$dQ = N_{ex}(E_{in} - \Phi_P E_P). \tag{11}$$

Equation (11) shows that energy levels of photochemical products can be obtained if the yields are known, or the yields can be determined if the energy levels are known. Also, the rates of formation of the photochemical products can be measured or deduced and finally, as Rosencwaig has pointed out [17], the excitation spectrum of the photochemical process can be obtained, and compared with the conventional absorption spectrum.

The work of deGroot et al. [24] illustrates the use of the acoustic spectrophone to study photochemical processes of acetaldehyde. These authors find that at pressures below a few torr the optoacoustic spectrum in the region 230–360 nm resembles the normal absorption spectrum of the compound. When the pressure is increased, however, a minimum appears in the spectrum at 290 nm which indicates that at least some of the absorbed light energy is no longer converted to heat on the time scale of chopping. The authors ascribe this phenomenon to the efficient formation of a high energy unstable intermediate, a dioxetene. Studies with a pulsed light source shows that the intermediate decays to stable low energy products with a time constant of 2 ms. At wavelengths shorter than 290 nm the heating is again rapid; this is ascribed to the rapid decomposition of vibrationally hot dioxetene to low energy products.

Another interesting study using the acoustic spectrophone has been reported by Kaya, Harshbarger and Robin [25]. These investigators observed the gas phase optoacoustic excitation spectrum of biacetyl under a wide variety of conditions. They were able to demonstrate that the lowest excited triplet could be populated only by excitation at wavelengths longer than 443 nm; irradiation at shorter wavelengths resulted in intersystem crossing to the second excited triplet which then decayed rapidly and directly to the ground state. In mixtures of benzene and biacetyl, the authors were able to show that energy transfer from benzene to the biacetyl triplet manifold takes place only when exciting into the lowest vibronic bands of the lowest excited singlet of the donor. In pyridine-biacetyl mixtures, the lowest $n-\pi^*$ state of pyridine was found to transfer to the triplet manifold of biacetyl, but the lowest $\pi-\pi^*$ state does not.

A final study by Callis, Parson and Gouterman [26] illustrates the potential application of calorimetric techniques to the study of photobiological systems. A very useful model system for the study of the bioenergetics of photosynthesis is the chromatophore of photosynthetic bacteria. The chromatophores are vesicular fragments of the bacterial membrane, which contain the photosensitive pigments and most of the enzymes necessary for light induced electron transport and coupled phosphorylation. In the chromatophore light induces a cyclic electron flow which is coupled in some unknown manner to the formation of high energy phosphate bonds, in which the free energy available from the photons are stored.

In the study of photochemical reactions in the liquid and solid phases using a volume transducer we must include the possibility of a volume difference $\Delta V_r$ between reactants and products, as well as a contribution from heating. For a system which either returns radiationlessly to the ground state or converts to a product state $E_p$ with efficiency $\Phi_p$, the total volume change $\Delta V$ will be

$$\Delta V = N_{ex}(E_{in} - \Phi_p E_p)(\alpha/\rho C_p) + N_{ex}\Phi_p \Delta V_r. \tag{12}$$

If $E_p$ and $\Delta V_r$ are temperature independent, the measurement of $\Delta V$ at two different temperatures allows one to obtain $E_p$ and $\Delta V_r$.

Figure 5 shows the volume response of *Chromatium* chromatophores to weak flashes at temperatures of 23 °C and 4 °C. The traces labeled "light" were obtained in the presence of a strong cw light which saturated all photochemical processes, and resulted in the conversion of all of the input energy to heat. The light response at 4 °C is much smaller due to the

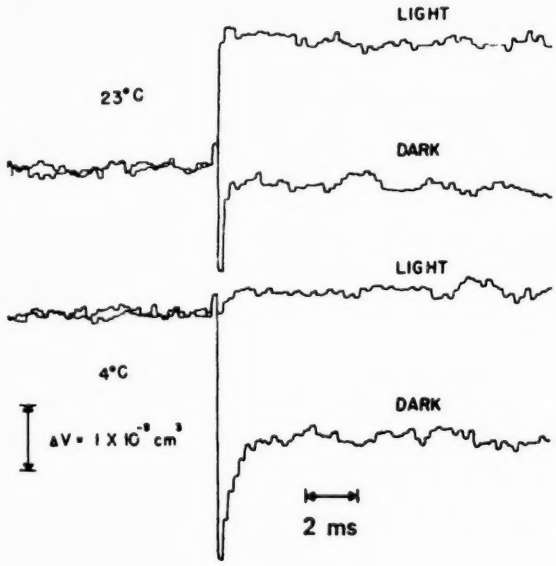


FIGURE 5. *Volume changes of Chromatium chromatophores in response to flash excitation.*

reduced magnitude of $\alpha/\rho C_p$ at this temperature. In the dark at 23 °C, a weak flash causes an instantaneous volume decrease which is then followed by a fast recovery almost to the base line. In the dark at 4 °C we observe an instantaneous volume decrease which recovers about half way with a time constant of 250 $\mu s$. From a quantitative evaluation of these data, we have concluded that: (a) the initial high energy state of the photosynthetic apparatus does not possess a significant enthalpy change from the ground state, and thus the free energy change available from the photon is stored in an excited state characterized by negative entropy; (b) the high energy state also has a decreased volume from the ground state. Further studies have shown that the volume changes are altered by the presence of ion transporting antibiotics, and uncouplers of phosphorylation. The flash calorimeter thus appears to be a valuable tool for the study of energy conservation in photosynthetic systems.

## 4. Conclusions

Calorimetric techniques can be used to measure a number of parameters of excited states such as lifetimes, excitation spectra, energy yields of radiationless and photochemical processes, and enthalpies of photochemical reactions. Simple calorimeters capable of measuring these parameters have been developed for the study of molecules in the gas, solid and liquid phases. A wide variety of measurements now exist which show the usefulness of calorimetric techniques for studies of absolute fluorescence quantum efficiencies, quantum yields of triplet formation, photochemical processes in the gas phase, and for studies of energy storage in photosynthesis. As more investigators realize how simple and convenient these measurements are, we can expect an increase in the use of calorimetric techniques in photophysical and photochemical studies.

## 5. References

[1] Alenstev, M. A., National Research Council of Canada Technical Translation TT-433, Zh. Eksp. Fiz. **21,** 133 (1951).
[2] Seybold, P. G., Gouterman, M., and Callis, J. B., Photochem. Photobiol. **9,** 229 (1969).
[3] Gelernt, B., Findeisen, A., and Poole, J., J. Chem. Soc. Faraday Trans. II, **70,** 939 (1974).
[4] Demas, J. N., and Crosby, G. A., J. Phys. Chem. **75,** 991 (1971).
[5] Crosby, G. A., Demas, J. N., and Callis, J. B., J. Res. Nat. Bur. Stand. (U.S.), **76A** (Phys. and Chem.), No. 6, 561–577 (Nov.–Dec. 1972).
[6] Callis, J. B., Gouterman, M., and Danielson, J. D. S., Rev. Sci. Inst., **40,** 1599 (1969).
[7] Lion, K. S., Instrumentation in Scientific Research (McGraw-Hill, New York, 1959).
[8] Sessler, G. M., and West, J. E., J. Acoust. Soc. Am., **40,** 1433 (1966).
[9] McCray, J. A., and Cahill, T. A., Electronic Circuit Analysis for Scientists (Wiley and Sons, New York, 1973).
[10] Koidan, W., J. Acoust. Soc. Am. **29,** 813 (1957).
[11] Parker, J. G., and Ritke, D. N., J. Chem. Phys., **59,** 3713 (1973).
[12] Hill, D. W., and Powell, T., Non Dispersive Infra-Red Gas Analysis in Science, Medicine, and Industry (Plenum, New York, 1968).
[13] Cottrell, T. L., and McCoubrey, J. C., Molecular Energy Transfer in Gases (Butterworths, London, 1961), pp. 64–73.
[14] Rosengren, L., Appl. Opt. **14,** 1960 (1975).
[15] Kerr, E. L., and Atwood, J. G., Appl. Opt. **7,** 915 (1968).
[16] Patel, C. K., Burkhardt, E. G., and Lambert, C. A., Science, **184,** 1173 (1974).
[17] Rosencwaig, A., Anal. Chem. **47,** 592A (1975).
[18] Rosencwaig, A., and Gersho, A., Science, **190,** 557 (1975).
[19] Wrighton, M. S., J. Phys. Chem. **78,** 2229 (1974).
[20] Bril, A., Somerdijk, J. A., and de Jager-Veenis, A. W. J., Electrochem. Soc. **122,** 660 (1975).
[21] Rosencwaig, A., Physics Today, **28,** 23 (1975).
[22] Wybourne, G. G., Ed., Spectroscopic Properties of the Rare Earths (Inter-science Publ., New York, 1965).
[23] Callis, J. B., Ph.D. Thesis, University of Washington, Seattle, 1970.
[24] deGroot, M. S., Emeis, C. A., Hesselman, I. A. M., Drent, E., and Farenhorst, E., Chem. Phys. Lett. **17,** 332 (1975).
[25] Kaya, K., Harshbarger, W., and Robin, M., J. Chem. Phys., **60,** 4231 (1974).
[26] Callis, J. B., Parson, W. W., and Gouterman, M., Biochem. Biophys. Acta, **267,** 348 (1972).

(Paper 80A3–893)

JOURNAL OF RESEARCH of the National Bureau of Standards—A. Physics and Chemistry
Vol. 80A, No. 3, May–June 1976

# Fluorescence Efficiency of Laser Dyes *

**K. H. Drexhage**

**Research Laboratories, Eastman Kodak Company, Rochester, New York 14650**

**(April 9, 1976)**

The fluorescence efficiency of xanthene dyes, oxazine dyes, and 7-aminocoumarins is discussed. Relations with the molecular structure are pointed out and dependence on solvent and temperature is explained. Several new fluorescence standards are suggested.

Key words: Aminocoumarins; carbazine dyes; deuterium effect; fluorescence quantum yield; laser dyes; molecular structure; oxazine dyes; quenching; xanthene dyes.

## 1. Introduction

The recent development of the dye laser [1] [1] has opened up an important new field of applications for organic dyes. This has led to a renewed interest in the theory of nonradiative transitions in dyes and also to the synthesis of new highly fluorescent dyes. In this article we review briefly the relations between fluorescence and molecular structure in the most important classes of laser dyes: xanthenes, oxazines, and 7-aminocoumarins. Following this discussion specific suggestions for improved fluorescence standards are made. [2]

## 2. Xanthene Dyes

The chromophore of xanthene dyes has typically the following structures

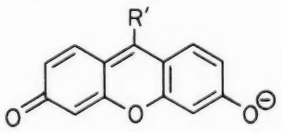


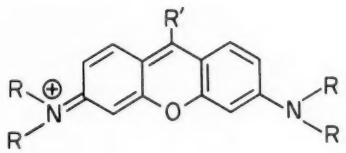


Depending on the end groups, in particular number and type of the substituents $R$, the maximum of the main absorption band falls somewhere in the range 480–580 nm. The transition moment is parallel to the long axis of the molecule [2]. With $R' = H$ and amino end groups the dyes are called pyronins. Due to a convenient syntheses with phthalic anhydride many xanthene dyes have $R' =$ carboxyphenyl and are called fluorescein or rhodamines (fig. 1). The methyl substituents of Rhodamine 6G have practically no influence on the optical properties of the dye except for the dimerization in aqueous solution which we are not concerned with here. The absorption maximum of the main band occurs almost at the same wavelength in pyronins and rhodamines, if the end groups are identical. The absorption band near 350 nm is stronger in rhodamines than in pyronins, and rhodamines show a slightly larger Stokes shift than pyronins. The chemical stability of rhodamines is generally superior, as pyronins in alkaline solution are readily oxidized by dissolved oxygen to form a colorless, blue fluorescing xanthone.

* Paper presented at the Workshop Seminar 'Standardization in Spectrophotometry and Luminescence Measurements' held at the National Bureau of Standards, Gaithersburg, Md., November 19–20, 1975.

[1] Figures in brackets indicate the literature references at the end of this paper.

[2] In order to describe materials and experimental procedures adequately, it is occasionally necessary to identify commercial products by manufacturer's name or label. In no instance does such identification imply endorsement by the National Bureau of Standards, nor does it imply that the particular product or equipment is necessarily the best available for that purpose.



206-267 OL - 76 - 3

FIGURE 1. *Molecular structure of rhodamine dyes; absorption maximum in ethanol.*

Rhodamines like Rhodamine B react to pH variations in an interesting manner. The carboxyl group is completely protonated in acidic solution, but dissociates in alkaline solution. The negative charge has an inductive effect on the central carbon atom of the chromophore. The maxima of the main absorption band and of the fluorescence are shifted to shorter wavelengths, and the extinction coefficient at the absorption maximum is slightly reduced. While these effects are rather weak in aqueous solution [3], the wavelength shift amounts to about 10 nm in polar organic solvents (methanol, ethanol, etc.) [4, 5, 6, 7]. When Rhodamine B, which is usually obtained as the hydrochloride,

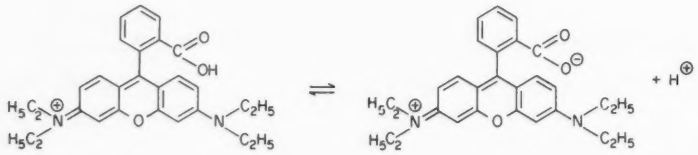

is dissolved in ethanol, the relative amounts of the two forms of the dye are determined by this acid-base equilibrium. The dissociation increases on dilution causing a shift of absorption and fluorescence to shorter wavelengths. This concentration dependence of the spectra is therefore not due to a monomer-dimer equilibrium, as was claimed in recent papers [8, 9]. In less polar organic solvents (e.g., acetone) the unprotonated (zwitterionic) dye undergoes a reversible conversion to a lactone:

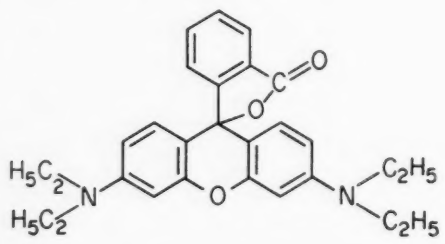

Because the conjugation of the chromophore is interrupted, this is a colorless compound. On addition of acid or complex-forming metal ions the chromophore is regenerated. If the carboxyl group is esterified as in Rhodamine 6G, all these reactions do not take place, and the absorption maximum is independent of pH and concentration (except for aqueous solutions, where aggregation takes place, and for strongly acidic conditions, where protonation of the amino groups occurs).

Because of the symmetry of the rhodamine chromophore, there is no dipole moment parallel to its long axis. As a consequence, the Stokes shift is small, and the fluorescence band overlaps strongly the absorption band (fig. 2) [10]. Also, there is only little variation of absorption and fluorescence maxima with solvent polarity [4, 5]. Provided there are no heavy-atom substituents, the rate of intersystem crossing from $S_1$ is very low in xanthene dyes, which is in accordance with our loop rule [11]. Phosphorescence is weak even in low temperature glasses and has a lifetime in the order of 0.1 s, which is short compared with, for instance, acriflavine and some aromatic compounds.

The fluorescence of rhodamines is quenched externally by $I^-$ and $SCN^-$, less efficiently by $Br^-$ and $Cl^-$. No quenching was observed by $ClO_4^-$ and $BF_4^-$ [4, 5]. The quenching process apparently involves a charge transfer from the anion to the excited dye molecule. It is not a heavy-atom effect. In polar solvents like ethanol, Rhodamine 6G-iodide is completely dissociated at a concentration of $10^{-4}$ mol/l and no quenching takes place, because the lifetime of the excited state is of the order of a few nanoseconds, much shorter than the diffusion time the quencher would need to reach an excited dye molecule. In less polar solvents like chloroform the dye salt does not dissociate and its fluorescence is totally quenched. The perchlorate of Rhodamine 6G behaves strikingly differently: its fluorescence efficiency is independent [12] of solvent polarity (0.95 based on the value 0.90 for fluorescein). It is, however, reduced by heavy-atom solvents (0.40 in iodomethane), and the fluorescence of this dye is completely quenched by nitrobenzene, presumably due to the high electron affinity of this solvent.

There are two structural features that influence the rate of internal conversion in xanthene dyes: mobility of the amino groups and hydrogen vibrations.

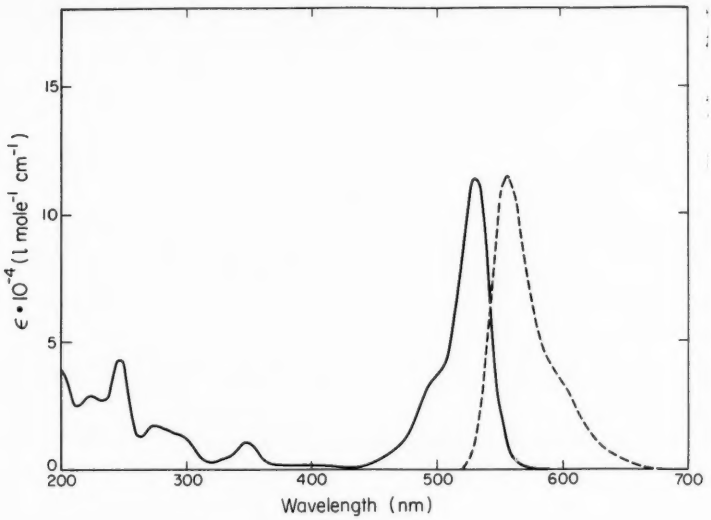


FIGURE 2. *Rhodamine 6G in ethanol.*

Absorption spectrum ($\epsilon$ molar decadic extinction coefficient); quantum spectrum of fluorescence (arbitrary units).

We found that the fluorescence efficiency of rhodamines that carry two alkyl substituents at each nitrogen, e.g., Rhodamine B, varies strongly with solvent and temperature [4, 5, 11]. We ascribe this to mobility of the amino groups. If the amino groups are rigidized as in the new dye Rhodamine 101 ($\lambda_{abs}=577$ nm in ethanol) the quantum efficiency is practically unity,

Rhodamine 101

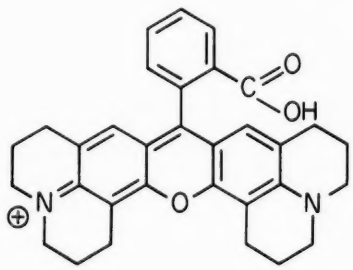

independent of solvent and temperature. It is interesting that the amino groups are not mobile when they are less than fully alkylated (Rhodamine 6G, Rhodamine 110). However, in such dyes there is a probability that the electronic excitation energy is funneled into *N-H* vibrations, causing nonradiative decay to $S_0$. Although this effect is rather weak in xanthene dyes, it is noticeable for instance in Rhodamine 6G. On solution in *O*-deuterated ethanol, *H* is exchanged for *D* in the amino groups of the dye. With the greater mass of deuterium the nonradiative decay is less likely and the fluorescence efficiency increases from 0.95 to 0.99.

## 3. Oxazine Dyes

When the central carbon atom in the xanthene chromophore is replaced by nitrogen, the chromophore of an oxazine dye is obtained. The central *N*-atom acts as a sink for the $\pi$-electrons, causing a wavelength shift of about 80 nm to the red. As within the xanthene class the absorption of oxazines also shifts to the red with increasing alkylation of the amino groups (fig. 3). Apart from the pronounced red shift of the $S_0-S_1$ transition there is little difference between the electronic transitions of oxazines and rhodamines [2]. The electron-withdrawing effect of the central *N*-atom causes the amino groups to be more acidic. Thus addition of a little base to a solution of Oxazine 4 in ethanol changes the color from blue to red due to deprotonation of one of the amino groups:

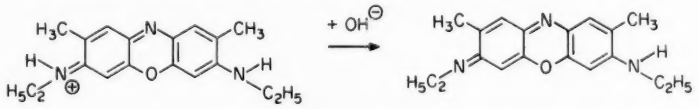


Oxazines with fully alkylated amino groups do not undergo any change on addition of base. On the other hand, all oxazines are protonated in strong acids.

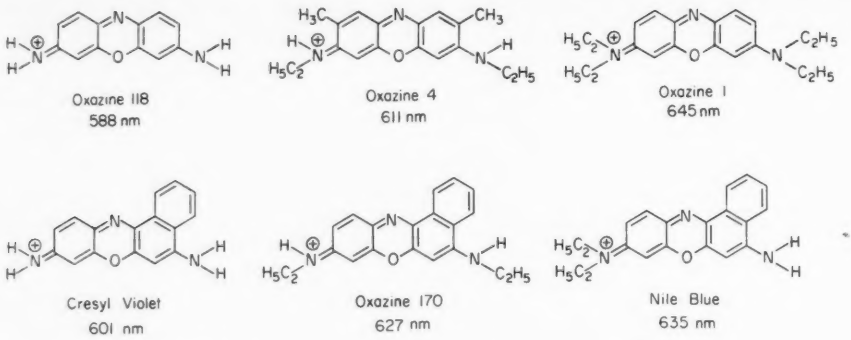


FIGURE 3. *Molecular structure of oxazine dyes; absorption maximum in ethanol.*

Some oxazine dyes have a structure modified by an added benzo group (fig. 3). This causes a slight red shift of absorption and fluorescence. Furthermore, the shape of the absorption spectrum is different than in other oxazine dyes and depends on the temperature [13]. These effects are probably caused by steric interference of the amino group with a hydrogen of the added benzo group [11].

The triplet yield of oxazines is generally very low in accordance with the loop rule. No phosphorescence has been observed in these dyes. The fluorescence quenching processes, discussed for xanthene dyes, are also found with oxazines. Owing to the smaller energy difference between $S_1$ and $S_0$, internal conversion plays a greater role in oxazines than in rhodamines. Thus the fluorescence efficiency of Oxazine 1-perchlorate is less than 0.1 in ethanol, but much higher in dichloromethane and in 1,2-dichlorobenzene. Likewise, the effect of hydrogen vibrations is much more pronounced. The fluorescence efficiency of Oxazine 4 is a factor of 2 higher in *O*-deuterated ethanol than in normal ethanol.

## 4. 7-Aminocoumarins

The most important laser dyes in the blue and green region of the spectrum are coumarin derivatives that have an amino group in 7-position:

The chromophore is not symmetric as in the xanthenes and oxazines discussed above. The ground state can be described by structure A, the excited state $S_1$ by B. While there is some dipole moment in the ground state, it is much greater in the excited state. As a consequence these compounds show a large Stokes shift, in particular in polar solvents (fig. 4). Absorption and fluorescence maxima depend much more on solvent polarity than is the case with xanthenes and oxazines [4, 5]. A large number of highly fluorescent derivatives have been synthesized in recent years [4, 5, 14–18]. Here we can give only a few examples (fig. 5). Absorption and fluorescence of 7-aminocoumarins are not influenced by a small amount of base present in the solution. However, they react with strong acids in a variety of ways [4, 5, 11]. The amino group of Coumarin 1, for instance, is easily protonated and thus decoupled from the chromophore. As a consequence the absorption band at 373 nm disappears. This reaction is inhibited, if the amino group is rigidized as in Coumarin 102. In the excited state $S_1$, the keto group is more basic than the amino group and thus is protonated if sufficient acid is present so that the diffusion is faster than the decay of $S_1$. Frequently a new fluorescence band appears due to the protonated form. Most coumarins are very soluble in organic solvents, but insoluble in water. However, derivatives have been reported recently that are highly soluble in water (fig. 6) [18].

## 5. Fluorescence Standards

The optical properties of an ideal fluorescence standard should be independent of the environment (solvent composition, temperature, etc.). This means, among other things, that the compound should not be involved in chemical equilibria. Alkaline solutions are to be avoided, because their alkalinity changes gradually due to absorption of carbon dioxide. Furthermore the fluorescence should not be quenched by oxygen and the fluorescence efficiency should be independent of temperature variations. The commonly used fluorescence standards fail badly on one or more of these requirements. A number of better standards can be suggested on the basis of the foregoing discussions.

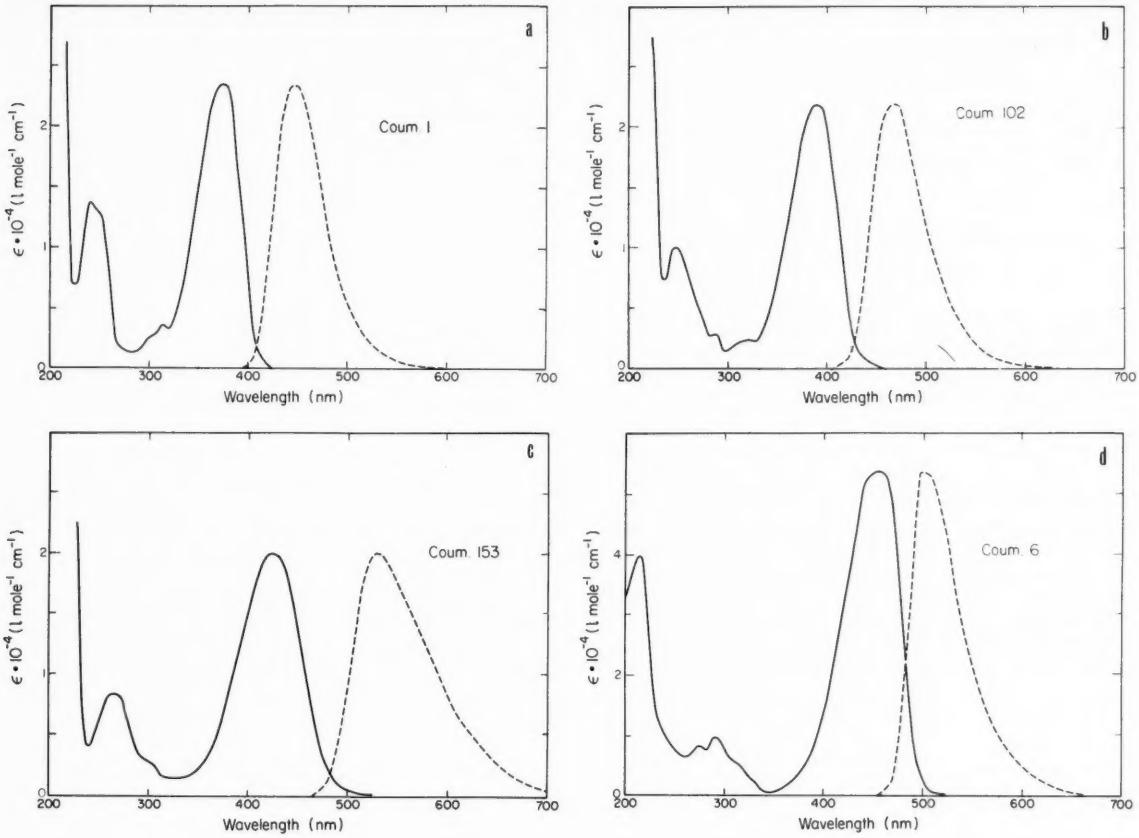


**FIGURE 4a, b, c, and d.** *7-Aminocoumarins in ethanol.*

Absorption spectrum ($\epsilon$ molar decadic extinction coefficient); quantum spectrum of fluorescence (arbitrary units).

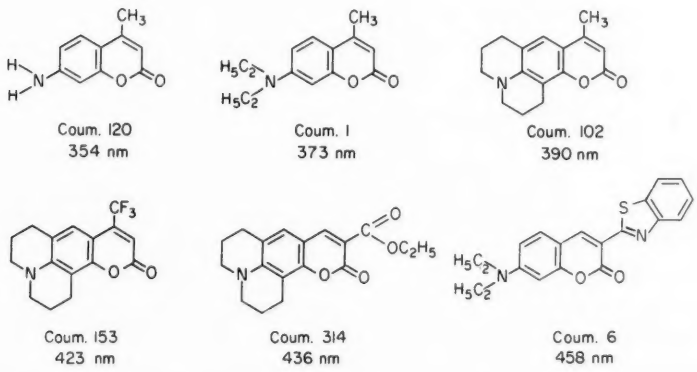


**FIGURE 5.** *Molecular structure of 7-aminocoumarin derivatives; absorption maximum in ethanol.*

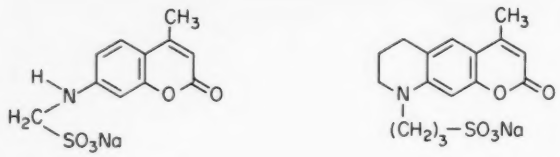


Coum. 175
353 nm

Coum. 386
388 nm

FIGURE 6. *Molecular structure of water-soluble 7-aminocoumarins; absorption maximum in water.*

*Coumarin 1.* This compound (7-diethylamino-4-methylcoumarin) is the most readily available 7-aminocoumarin. It is easily purified by recrystallization from ethanol. It is highly soluble in most organic solvents, but not in water. The fluorescence quantum efficiency is about 0.5 in ethanol, generally higher in less polar solvents, and is almost independent of temperature. There is little or no quenching by oxygen. A disadvantage is the possible protonation in acidic solvents. If this is a problem, Coumarin 102 or Coumarin 153 may be used. The latter compound is particularly interesting because of its large Stokes-shift and the very broad fluorescence spectrum. The fluorescence efficiency of Coumarin 102 was measured as 0.6 and that of Coumarin 153 as 0.4 (both in ethanol). Another compound, possibly useful as a standard, is Coumarin 6 (quantum efficiency 0.8 in ethanol), which absorbs at longer wavelengths than most other coumarin derivatives. The latter compounds are commercially available, but the price is still high. However, this should not be a deterrent, as the price will certainly come down and generally only a few milligrams are required. We feel that Coumarin 1 is superior to quinine bisulfate in every respect. It can be used in almost any solvent except water.

*Rhodamine 6G-$ClO_4$.* As was pointed out previously in this article, the frequently used standard Rhodamine B undergoes acid-base reactions that affect its optical properties. Its fluorescence efficiency depends strongly on type of solvent and temperature. Therefore it is not surprising that the quantum yield values reported in the literature vary considerably. As discussed above, Rhodamine 6G-perchlorate is superior to Rhodamine B, because its quantum efficiency has the value 0.95 almost independent of solvent and temperature. The dye chloride is readily available in rather pure form. It can be further purified by column chromatography on basic alumina with ethanol or methanol as the solvent. The perchlorate is insoluble in water and is easily prepared by adding $HClO_4$ to an aqueous solution of the dye chloride. It can be recrystallized from alcohol-water mixtures. The ethyl ester perchlorate of Rhodamine 101 has the same useful properties as Rhodamine 6G-perchlorate, while absorption and fluorescence are shifted about 50 nm to the red. However, this dye is not yet commercially available.

*Oxazine 170-$ClO_4$.* Of all available oxazines this derivative has the highest fluorescence efficiency ($\sim 0.5$ in ethanol). Its fluorescence properties are closely related to those of Rhodamine 6G-$ClO_4$. Absorption and fluorescence are shifted by about 100 nm to the red (fig. 7). As in the case of Oxazine 4, the fluorescence efficiency increases nearly a factor of 2 on deuteration of the amino groups. Apart from this effect, it is almost independent of solvent and temperature. However, variations of temperature have some effect on the absorption spectrum due to the annellated benzo group. In this respect Oxazine

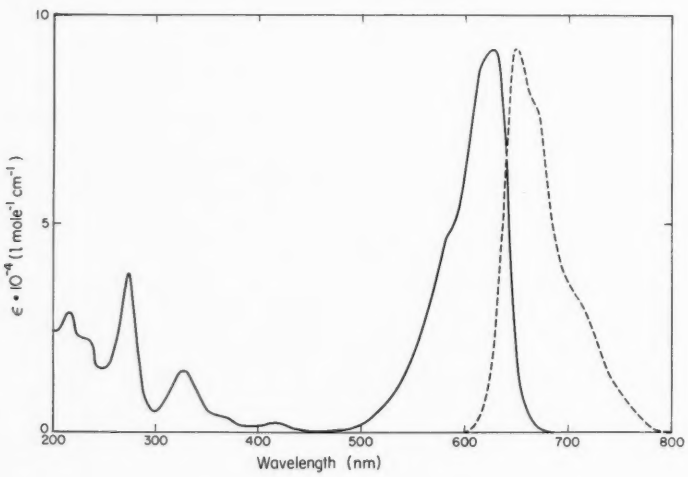


FIGURE 7. *Oxazine 170 in ethanol.*

Absorption spectrum (ε molar decadic extinction coefficient); quantum spectrum of fluorescence (arbitrary units).

4-$ClO_4$ would be preferable. As pointed out earlier, these dyes cannot be used in basic solution. Being perchlorates, they are practically insoluble in water.

*Hexamethylindodicarbocyanine (HIDC) and Hexamethylindotricarbocyanine (HITC).* Very few dyes are known that are relatively stable and fluoresce well in the infrared region of the spectrum. Of the commercially available materials, the cyanine dyes 1,1′,3,3,3′,3′-hexamethylindodicarbocyanine (HIDC) iodide and 1,1′,3,3,3′,3′-hexamethylindotricarbocyanine (HITC) iodide stand out on both counts. Contrary to the other compounds

HIDC (n = 2)
HITC (n = 3)

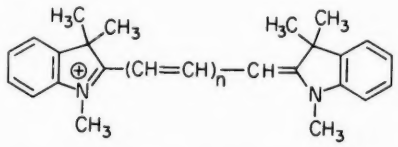

suggested here, the fluorescence efficiency of these dyes depends markedly on type of solvent and temperature. It appears to be highest in sulfoxides (dimethyl sulfoxide, tetramethylene sulfoxide). As shown in figure 8, the fluorescence of HITC extends to 900 nm. The photochemical stability is much higher than in related thiacarbocyanines. A concentrated solution of HIDC-iodide in dimethyl sulfoxide is currently in use in our laboratory as a photon counter that operates up to 700 nm. It is much more sensitive than equally concentrated solutions of methylene blue as this has a lower fluorescence efficiency.

The fluorescence spectra and efficiencies of the suggested dyes need to be determined accurately. To us this seems to be of greater benefit than perpetuating bad standards whose only justification today is their common usage.

## 6. References and Notes


[1] Dye Lasers (F. P. Schäfer, Ed.) Topics in Applied Physics, Vol. 1 (Springer, Berlin, 1973).

[2] Jakobi, H., and Kuhn, H., Z. Elektrochem. Ber. Bunsenges. Phys. Chem. **66**, 46 (1962).

[3] Ramette, R. W., and Sandell, E. B., J. Am. Chem. Soc. **78**, 4872 (1956).

[4] Drexhage, K. H., VII Intern. Quant. Electron. Conf., Montreal, Canada, paper B.5 (1972).

[5] Drexhage, K. H., Laser Focus **9**(3), 35 (1973).

[6] Ferguson, J., and Mau, A. W. H., Chem. Phys. Lett. **17**, 543 (1972).

[7] Ferguson, J., and Mau, A. W. H., Austral. J. Chem. **26**, 1617 (1973).

[8] Selwyn, J. E., and Steinfeld, J. I., J. Phys. Chem. **76**, 762 (1972).

[9] Wong, M. M., and Schelly, Z. A., J. Phys. Chem. **78**, 1891 (1974).

[10] The absorption of Rhodamine 6G (2g/l in ethanol), whose maximum is at 530 nm, is still noticeable at 633 nm, far beyond the fluorescence maximum of 555 nm: a 5mW He-Ne laser excites yellow anti-Stokes fluorescence that can be observed visually.


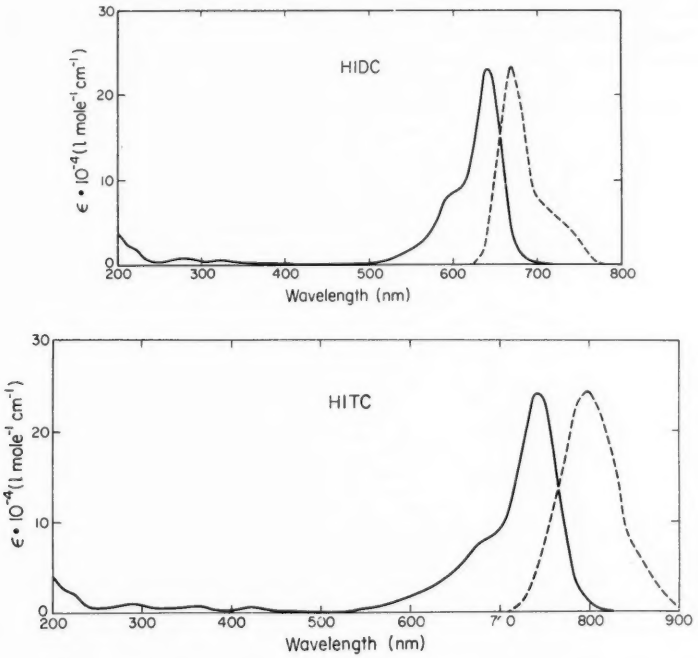


FIGURE 8a. and b. *HIDC and HITC in ethanol.*

Absorption spectrum (ε molar decadic extinction coefficient); quantum spectrum of fluorescence (arbitrary units).

[11] Drexhage, K. H., Structure and properties of laser dyes, in: Dye Lasers (F. P. Schäfer, Ed.), Topics in Applied Physics, Vol. 1, p. 144 (Springer, Berlin, 1973).
[12] This statement has to be taken with a grain of salt. We found indeed variations up to 10 percent with solvent. But the accuracy of our quantum efficiency measurements was probably less than this, when solvents with widely varying refractive index were involved. We feel, however, that the accuracy of the measurements was sufficient to justify the interpretations given here and elsewhere in this article.
[13] Gacoin, P., and Flamant, P., Opt. Commun. **5,** 351 (1972).
[14] Tuccio, S. A., Drexhage, K. H., and Reynolds, G. A., Opt. Commun. **7,** 248 (1973).
[15] Drexhage, K. H., and Reynolds, G. A., VIII Intern. Quant. Electron. Conf., San Francisco, Calif., paper F.1 (1974).
[16] Schimitschek, E. J., Trias, J. A., Hammond, P. R., and Atkins, R. L. Opt. Commun. **11,** 352 (1974).
[17] Reynolds, G. A., and Drexhage, K. H., Opt. Commun. **13,** 222 (1975).
[18] Drexhage, K. H., Erikson, G. R., Hawks, G. H., and Reynolds, G. A., Opt. Commun. **15,** 399 (1975).

(Paper 80A3–894)

JOURNAL OF RESEARCH of the National Bureau of Standards—A. Physics and Chemistry
Vol. 80A, No. 3, May–June 1976

# Oscillator Strengths for Lines of Ionized Uranium (U II)

**Charles H. Corliss**

**Institute for Basic Standards, National Bureau of Standards, Washington, D.C. 20234**

**(March 29, 1976)**

Oscillator strengths for 49 lines of U II recently measured by Voight can be used to calibrate the intensity scale of the U II lines in the NBS Tables of Spectral-Line Intensities and derive a larger set of oscillator strengths of lower precision but consistent with the new measurements. The standard deviation of the differences between the two sets of *gf*-values for the 49 lines is 29 percent. Oscillator strengths of that precision are given for 776 additional lines from the NBS Intensity Tables. The uncertainty in absolute value is 67 percent.

Key words: Oscillator strengths for U II; transition probabilities for U II; uranium spectrum.

## 1. Introduction

Recently Voigt [1975][1] measured oscillator strengths for 49 lines of U II in a wall-stabilized argon arc. His analysis of errors leads to the conclusion that, on a relative scale, his errors do not exceed 10 percent. In his table III of results for U II lines he compares his values with *gf*-values from Corliss and Bozman [1962]. The well-known energy dependent error of their values is clearly exhibited in this table. Nearly all the old values for lines originating from levels above 25 000 $cm^{-1}$ are larger than Voigt's values, while for lines originating from levels below 25 000 $cm^{-1}$ the old values are nearly all smaller. A new calibration of the level populations in the copper arc of Meggers, Corliss, and Scribner [1975] is clearly required.

## 2. Comparison of Intensities with Oscillator Strengths

We compare the intensities from Meggers, Corliss, and Scribner with the new oscillator strengths by the usual population plot of log $I\lambda^3/gf_v$ versus upper energy level. The standard deviation of the residuals from the least-squares line fitted to the 49 points was 0.20 dex ($\pm 58\%$). Since Voigt's *gf*-values have a relative error of only 10 percent, we may interpret the residuals as mostly error in the intensities.

The errors in the intensities may be random, systematic or both. Random errors cannot be removed but systematic errors can be removed if they can be specified. There seem to be two possibilities of systematic error in the intensities, i.e., as a function of wavelength or of intensity. The residuals from the plot were plotted against both quantities and there was correlation in each case. It is not surprising that if one quantity were to show correlation the other would also, since atomic spectra usually show a correlation between wavelength and intensity. However, in this case the correlation of the residuals with intensity was better than with wavelength. This correlation plot and its least-squares fitted line are shown in figure 1. The line can be represented by the equation $R = -0.894 + 0.323 \log I$. The only badly outlying point represents the spectrum line at 2941 Å.

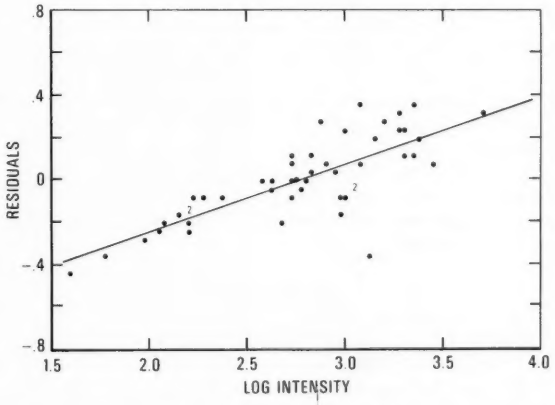


FIGURE 1. *Residuals from a plot of log* $I\lambda^3/gf_v$ *versus energy level plotted versus log* I

The intensity correlation shown above implies either that the intensity scale of Meggers, Corliss, and

[1] Years in brackets indicate the literature reference at the end of this paper.

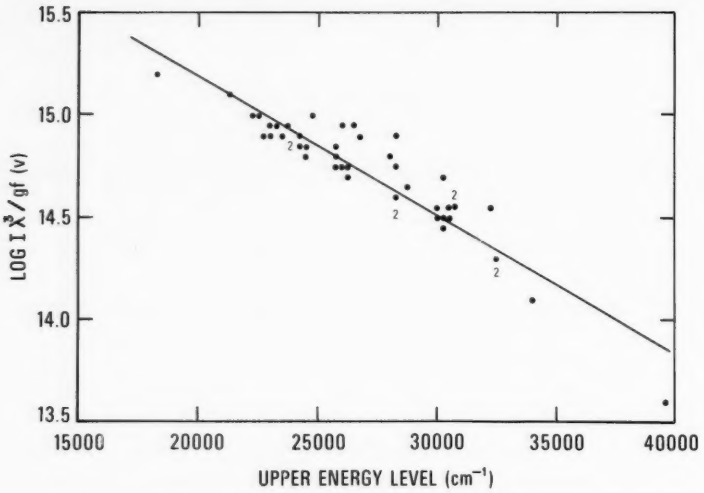


FIGURE 2. *Population plot for the copper arc with the intensities adjusted according to the line in figure 1*

Scribner is too expanded or that Voigt's scale is too compressed.[2]

## 3. Derivation of New Values

Figure 1 clearly demonstrates a systematic discrepancy between the intensity scale of U II lines in Meggers, Corliss, and Scribner and Voigt's *gf*-values. To derive from our intensities *gf*-values consistent with Voigt's we should remove this systematic effect. By subtracting $R$ from log $I$ we obtain a corrected intensity which has the systematic error removed. Log $I\lambda^3/gf_v$ is then recomputed using the corrected intensity and plotted in figure 2. The standard deviation of the residuals is now reduced to 0.11 dex ($\pm 29\%$), which in fact represents also the standard deviation of the differences between Voigt's *gf*-values and *gf*-values derived from the corrected intensity scale of U II lines in the Tables of Spectral-Line Intensities.

The equation of the least-squares fitted line in figure 2 is $\log I\lambda^3/gf = 16.531 - 0.00006717\ E$. With this equation we calculate *gf* for the 49 lines measured by Voigt and for 776 others.

## 4. Results

The results are given in the tables. In table 1 we give log *gf* as measured by Voigt and as calculated from the Tables of Spectral-Line Intensities. The differences for the 49 lines are given in the fourth column. The standard deviation of the differences is

TABLE 1. *Comparison of log gf for lines of* U II

| Wavelength Å | Log *gf* (*v*) | Log *gf* (*c*) | Difference |
|---|---|---|---|
| 2941.92 | −0.18 | −0.47 | −0.29 |
| 3111.62 | −0.72 | −0.86 | −0.14 |
| 3305.90 | −0.92 | −0.99 | −0.07 |
| 3550.82 | −1.28 | −1.01 | 0.27 |
| 3670.07 | −0.59 | −0.72 | −0.13 |
| 3700.58 | −1.34 | −1.21 | 0.13 |
| 3701.52 | −0.62 | −0.69 | −0.07 |
| 3746.41 | −1.00 | −0.84 | 0.16 |
| 3748.68 | −0.64 | −0.73 | −0.09 |
| 3782.84 | −1.06 | −0.89 | 0.17 |
| 3826.51 | −1.39 | −1.17 | 0.22 |
| 3831.46 | −0.70 | −0.59 | 0.11 |
| 3854.66 | −0.59 | −0.54 | 0.05 |
| 3859.58 | −0.62 | −0.62 | 0.00 |
| 3865.92 | −0.85 | −0.77 | 0.08 |
| 3881.46 | −1.00 | −0.80 | 0.20 |
| 3890.36 | −1.00 | −0.86 | 0.14 |
| 3932.03 | −0.82 | −0.89 | −0.07 |
| 3985.80 | −0.72 | −0.71 | 0.01 |
| 3992.54 | −1.13 | −1.02 | 0.11 |
| 4017.72 | −0.96 | −0.91 | 0.05 |
| 4050.04 | −1.11 | −0.99 | 0.12 |
| 4051.91 | −0.92 | −0.95 | −0.03 |
| 4062.55 | −1.12 | −1.17 | −0.05 |
| 4067.76 | −1.03 | −0.90 | 0.13 |
| 4090.14 | −0.70 | −0.78 | −0.08 |
| 4116.10 | −1.19 | −1.19 | 0.00 |
| 4124.73 | −1.26 | −1.28 | −0.02 |
| 4128.34 | −1.15 | −1.10 | 0.05 |
| 4141.23 | −0.70 | −0.80 | −0.10 |
| 4171.59 | −0.96 | −0.92 | 0.04 |
| 4241.67 | −0.68 | −0.83 | −0.15 |
| 4244.37 | −1.28 | −1.33 | −0.05 |
| 4341.69 | −1.21 | −1.24 | −0.03 |
| 4372.57 | −1.54 | −1.63 | −0.09 |
| 4373.41 | −1.62 | −1.68 | −0.06 |
| 4472.34 | −1.18 | −1.28 | −0.10 |
| 4515.28 | −1.54 | −1.56 | −0.02 |
| 4538.19 | −1.55 | −1.53 | 0.02 |
| 4543.63 | −1.16 | −1.24 | −0.08 |

[2] Bell and Upson [1971] investigated the intensity scale of Meggers, Corliss, and Scribner for the case of Fe I and concluded that the Fe I scale was too compressed. That conclusion does not support the present result.

TABLE 1. *Comparison of log gf for lines of* U II—Continued

| Wavelength Å | Log $gf$ (*v*) | Log $gf$ (*c*) | Difference |
|---|---|---|---|
| 4567.69 | −1.64 | −1.73 | −0.09 |
| 4569.91 | −1.68 | −1.72 | −0.04 |
| 4570.99 | −1.64 | −1.68 | −0.04 |
| 4573.69 | −1.48 | −1.54 | −0.06 |
| 4641.65 | −1.43 | −1.42 | 0.01 |
| 4689.07 | −1.68 | −1.68 | 0.00 |
| 4722.73 | −1.55 | −1.58 | −0.03 |
| 4731.60 | −1.48 | −1.48 | 0.00 |
| 5492.97 | −1.60 | −1.70 | −0.10 |

0.11 dex (±29%). In table 2 we list the wavelength in Angstroms, energy levels in $cm^{-1}$, the weighted transition probability $gA$ in units of $10^8$ transitions per second, the weighted oscillator strength, and log $gf$ for 825 lines of U II from Meggers, Corliss, and Scribner. Classifications for 680 of these lines are given in the Intensity Tables and 145 more were classified with new levels kindly sent to us by Jean Blaise and Leon Radziemski from the Los Alamos Scientific Laboratory. Earlier references for levels are given in the Intensity Tables.

In a number of cases the intensities in Meggers, Corliss, and Scribner represent the summation of unresolved pairs of lines. When both of the lines originate from the ion, we divided the intensity according to the ratio given in Steinhaus et al. [1972]. The remaining unresolved pairs were not used in this paper.

The error in the relative scale of $gf$ as determined above is about 30 percent. To calculate the error in the absolute scale, we add (quadratically) the absolute error of 60 percent determined by Voigt for his absolute scale with which we are calibrated. The uncertainty in our absolute scale is thus about 67 percent. This large absolute error arises from the uncertainty in the continuous background which had to be subtracted from a faint U I line during Voigt's measurement of the relative intensity of a U I and a U II line in his wall-stabilized arc. A direct measurement of a lifetime in U II would avoid this source of error.

TABLE 2. *Oscillator strengths for lines of* U II

| Wavelength Å | Energy levels $cm^{-1}$ | gA $10^8/s$ | gf | log gf | Wavelength Å | Energy levels $cm^{-1}$ | gA $10^8/s$ | gf | log gf |
|---|---|---|---|---|---|---|---|---|---|
| 2419.57 | 0–41317 | .50 | .044 | −1.36 | 2778.45 | 9553–45533 | .91 | .11 | −.98 |
| 2498.83 | 5526–45533 | .41 | .038 | −1.42 | 2780.04 | 0–35960 | .39 | .045 | −1.35 |
| 2514.77 | 4420–44173 | .72 | .069 | −1.16 | 2784.67 | 289–36189 | .37 | .043 | −1.36 |
| 2549.30 | 4420–43635 | .68 | .066 | −1.18 | 2784.92 | 8276–44173 | .74 | .086 | −1.07 |
| 2556.19 | 0–39108 | .74 | .072 | −1.14 | 2793.94 | 289–36070 | 1.1 | .13 | −.90 |
| 2565.41 | 0–38968 | 1.0 | .099 | −1.00 | 2797.30 | 0–35738 | .22 | .026 | −1.59 |
| 2568.98 | 5259–44173 | .37 | .036 | −1.44 | 2802.56 | 289–35960 | 1.1 | .13 | −.89 |
| 2569.71 | 0–38903 | .84 | .083 | −1.08 | 2805.24 | 914–36551 | .40 | .047 | −1.33 |
| 2584.42 | 0–38681 | .42 | .043 | −1.37 | 2810.35 | 2294–37867 | .39 | .046 | −1.34 |
| 2616.07 | 0–38213 | .33 | .034 | −1.46 | 2811.38 | 1749–37308 | .64 | .076 | −1.12 |
| 2621.81 | 0–38130 | .25 | .025 | −1.59 | 2813.04 | 4706–40244 | .71 | .084 | −1.08 |
| 2639.84 | 0–37869 | .38 | .040 | −1.40 | 2815.98 | 289–35790 | .35 | .042 | −1.38 |
| 2641.55 | 5790–43635 | .58 | .061 | −1.21 | 2821.12 | 914–36351 | 1.2 | .14 | −.86 |
| 2644.12 | 0–37808 | .38 | .040 | −1.40 | 2824.37 | 289–35684 | .61 | .073 | −1.13 |
| 2645.47 | 0–37789 | .90 | .095 | −1.02 | 2832.06 | 5259–40559 | 2.3 | .28 | −.55 |
| 2647.02 | 914–38681 | .18 | .019 | −1.73 | 2834.55 | 914–36183 | .26 | .031 | −1.51 |
| 2659.02 | 0–37596 | .23 | .024 | −1.61 | 2839.89 | 289–35491 | .67 | .081 | −1.09 |
| 2660.14 | 289–37869 | .39 | .041 | −1.39 | 2845.96 | 914–36042 | .34 | .042 | −1.38 |
| 2665.87 | 289–37789 | .32 | .034 | −1.47 | 2846.14 | 8510–43635 | .81 | .099 | −1.01 |
| 2675.88 | 1749–39108 | .47 | .050 | −1.30 | 2849.98 | 5259–40337 | .49 | .060 | −1.23 |
| 2676.41 | 6283–43635 | 1.4 | .15 | −.84 | 2850.82 | 5526–40594 | .51 | .062 | −1.21 |
| 2683.28 | 8276–45533 | 3.0 | .33 | −.48 | 2852.75 | 5526–40570 | .81 | .099 | −1.00 |
| 2685.98 | 1749–38968 | .76 | .082 | −1.09 | 2853.57 | 1749–36782 | .45 | .055 | −1.26 |
| 2691.80 | 8394–45533 | 1.1 | .12 | −.94 | 2854.92 | 1749–36766 | .28 | .034 | −1.46 |
| 2705.19 | 914–37869 | .52 | .058 | −1.24 | 2860.47 | 0–34949 | .55 | .068 | −1.17 |
| 2709.51 | 4420–41317 | .56 | .062 | −1.21 | 2862.62 | 4585–39508 | .43 | .053 | −1.27 |
| 2711.10 | 914–37789 | .24 | .027 | −1.57 | 2865.68 | 0–34885 | 1.0 | .13 | −.90 |
| 2715.54 | 2295–39108 | .40 | .044 | −1.36 | 2869.37 | 1749–36589 | .44 | .054 | −1.26 |
| 2725.94 | 2294–38968 | .47 | .052 | −1.28 | 2874.08 | 1749–36532 | .48 | .060 | −1.22 |
| 2739.39 | 289–36782 | .40 | .045 | −1.34 | 2875.20 | 914–35684 | .42 | .053 | −1.28 |
| 2746.16 | 1749–38152 | .42 | .047 | −1.33 | 2886.45 | 289–34923 | .34 | .043 | −1.37 |
| 2750.13 | 0–36351 | .17 | .019 | −1.73 | 2887.59 | 9553–44173 | 1.2 | .15 | −.82 |
| 2754.16 | 914–37212 | .86 | .098 | −1.01 | 2888.26 | 0–34612 | .55 | .069 | −1.16 |
| 2766.88 | 0–36131 | .40 | .045 | −1.34 | 2889.63 | 289–34885 | 1.2 | .15 | −.83 |
| 2776.29 | 4585–40594 | .46 | .053 | −1.27 | 2894.14 | 5259–39801 | 1.0 | .13 | −.88 |

TABLE 2. *Oscillator strengths for lines of* U II—Continued

| Wavelength Å | Energy levels $cm^{-1}$ | gA $10^8/s$ | gf | log gf | Wavelength Å | Energy levels $cm^{-1}$ | gA $10^8/s$ | gf | log gf |
|---|---|---|---|---|---|---|---|---|---|
| 2898.13 | 5259–39754 | .62 | .078 | −1.11 | 3046.46 | 289–33104 | .27 | .038 | −1.42 |
| 2898.71 | 2294–36782 | .39 | .049 | −1.31 | 3050.20 | 0–32775 | .55 | .077 | −1.11 |
| 2902.81 | 0–34439 | .20 | .025 | −1.60 | 3056.72 | 289–32994 | .27 | .038 | −1.42 |
| 2904.51 | 289–34708 | .39 | .049 | −1.31 | 3062.54 | 1749–34392 | .75 | .11 | −.97 |
| 2912.58 | 289–34612 | .28 | .036 | −1.45 | 3063.88 | 2295–34923 | .23 | .032 | −1.49 |
| 2914.25 | 289–34593 | .47 | .060 | −1.22 | 3066.87 | 8755–41352 | .72 | .10 | −.99 |
| 2918.97 | 5260–39508 | .65 | .083 | −1.08 | 3068.65 | 5790–38368 | .79 | .11 | −.95 |
| 2923.17 | 0–34199 | .19 | .025 | −1.60 | 3075.45 | 289–32795 | .19 | .027 | −1.56 |
| 2925.98 | 1749–35915 | .38 | .048 | −1.32 | 3081.19 | 8510–40956 | .86 | .12 | −.91 |
| 2927.38 | 289–34439 | .46 | .059 | −1.23 | 3084.24 | 2295–34708 | .26 | .037 | −1.43 |
| 2930.59 | 0–34112 | .22 | .029 | −1.54 | 3086.70 | 5401–37789 | .36 | .051 | −1.29 |
| 2931.89 | 0–34097 | .34 | .044 | −1.36 | 3086.80 | 11787–44173 | .96 | .14 | −.86 |
| 2936.45 | 2294–36339 | .55 | .071 | −1.15 | 3087.11 | 2294–34678 | .26 | .037 | −1.43 |
| 2936.78 | 1749–35790 | .25 | .032 | −1.49 | 3088.99 | 1749–34112 | .38 | .054 | −1.27 |
| 2937.35 | 914–34949 | .26 | .033 | −1.48 | 3090.36 | 289–32638 | .26 | .037 | −1.43 |
| 2939.49 | 9626–43635 | .98 | .13 | −.89 | 3094.83 | 289–32591 | .19 | .027 | −1.57 |
| 2941.92 | 5527–39508 | 2.6 | .34 | −.47 | 3095.04 | 1749–34049 | .43 | .061 | −1.21 |
| 2942.12 | 2294–36273 | .48 | .062 | −1.21 | 3095.23 | 2295–34593 | .35 | .050 | −1.30 |
| 2942.85 | 915–34885 | .44 | .057 | −1.24 | 3095.75 | 5259–37552 | .79 | .11 | −.95 |
| 2943.40 | 4420–38385 | .44 | .057 | −1.25 | 3098.01 | 5716–37985 | .84 | .12 | −.92 |
| 2945.89 | 1749–35684 | .43 | .057 | −1.25 | 3103.77 | 914–33124 | .20 | .030 | −1.53 |
| 2948.09 | 289–34199 | .46 | .060 | −1.22 | 3105.10 | 2294–34490 | .29 | .042 | −1.37 |
| 2949.61 | 4420–38313 | .65 | .085 | −1.07 | 3105.65 | 5526–37716 | .42 | .060 | −1.22 |
| 2955.65 | 289–34112 | .36 | .048 | −1.32 | 3111.62 | 1749–33877 | .95 | .14 | −.86 |
| 2957.74 | 4585–38385 | .56 | .073 | −1.14 | 3112.25 | 289–32410 | .29 | .043 | −1.37 |
| 2959.85 | 2294–36070 | .49 | .065 | −1.19 | 3119.35 | 5260–37308 | 1.1 | .16 | −.81 |
| 2962.78 | 1749–35491 | .45 | .059 | −1.23 | 3121.09 | 4663–36694 | .36 | .052 | −1.28 |
| 2966.66 | 914–34612 | .39 | .052 | −1.28 | 3121.33 | 0–32028 | .20 | .029 | −1.53 |
| 2967.94 | 289–33972 | .65 | .086 | −1.07 | 3124.43 | 8347–40344 | .86 | .13 | −.90 |
| 2968.40 | 914–34593 | .31 | .041 | −1.39 | 3126.70 | 4663–36637 | .45 | .066 | −1.18 |
| 2970.48 | 6283–39938 | .56 | .074 | −1.13 | 3129.73 | 7166–39108 | .71 | .10 | −.98 |
| 2976.35 | 289–33877 | .51 | .067 | −1.17 | 3130.73 | 289–32221 | .15 | .023 | −1.65 |
| 2980.28 | 5259–38803 | .47 | .063 | −1.20 | 3131.99 | 5716–37635 | .57 | .083 | −1.08 |
| 2982.74 | 289–33805 | .42 | .057 | −1.25 | 3133.42 | 2295–34199 | .21 | .031 | −1.51 |
| 2984.61 | 2295–35790 | .81 | .11 | −.97 | 3133.92 | 1749–33648 | .26 | .038 | −1.42 |
| 2987.80 | 289–33748 | .27 | .037 | −1.44 | 3136.89 | 6283–38152 | .52 | .077 | −1.11 |
| 2989.88 | 1749–35185 | .49 | .066 | −1.18 | 3138.51 | 4420–36273 | .34 | .050 | −1.30 |
| 2999.22 | 2294–35627 | .37 | .050 | −1.30 | 3139.60 | 5716–37558 | 1.1 | .17 | −.78 |
| 3000.09 | 4420–37743 | .51 | .069 | −1.16 | 3141.95 | 2294–34112 | .28 | .042 | −1.38 |
| 3001.21 | 1749–35059 | .27 | .036 | −1.44 | 3144.96 | 5716–37504 | .94 | .14 | −.86 |
| 3007.91 | 5667–38903 | 1.0 | .14 | −.86 | 3145.56 | 5527–37308 | 1.0 | .15 | −.82 |
| 3010.75 | 289–33493 | .27 | .036 | −1.44 | 3146.75 | 4663–36433 | .40 | .060 | −1.22 |
| 3012.45 | 289–33475 | .13 | .024 | −1.61 | 3148.56 | 0–31751 | .20 | .029 | −1.54 |
| 3012.71 | 914–34097 | .29 | .040 | −1.40 | 3151.08 | 1749–33475 | .25 | .038 | −1.42 |
| 3013.37 | 4420–37596 | .63 | .086 | −1.06 | 3153.12 | 8853–40559 | 1.8 | .27 | −.57 |
| 3016.96 | 1749–34885 | .47 | .065 | −1.19 | 3155.41 | 4663–36346 | .40 | .059 | −1.23 |
| 3018.10 | 5259–38383 | .52 | .071 | −1.15 | 3155.86 | 2294–33972 | .41 | .061 | −1.21 |
| 3020.24 | 4663–37764 | .41 | .056 | −1.25 | 3160.77 | 5716–37345 | .55 | .082 | −1.09 |
| 3022.21 | 1749–34827 | .80 | .11 | −.96 | 3165.28 | 6283–37867 | .37 | .056 | −1.25 |
| 3031.99 | 4663–37635 | 1.2 | .17 | −.77 | 3165.50 | 2294–33876 | .35 | .053 | −1.28 |
| 3033.19 | 1749–34708 | .66 | .091 | −1.04 | 3170.86 | 5716–37244 | .46 | .069 | −1.16 |
| 3035.96 | 1749–34678 | .25 | .035 | −1.45 | 3171.37 | 5260–36782 | .43 | .065 | −1.19 |
| 3038.05 | 0–32905 | .26 | .037 | −1.44 | 3173.71 | 0–31499 | .14 | .021 | −1.68 |
| 3039.14 | 4663–37558 | .54 | .075 | −1.12 | 3175.36 | 8853–40337 | .74 | .11 | −.95 |
| 3039.26 | 5259–38152 | .70 | .096 | −1.02 | 3176.21 | 1749–33224 | .43 | .065 | −1.19 |
| 3040.46 | 914–33794 | .22 | .031 | −1.51 | 3177.33 | 5716–37180 | .79 | .12 | −.92 |
| 3043.79 | 1749–34593 | .34 | .048 | −1.32 | 3179.04 | 289–31736 | .25 | .039 | −1.41 |
| 3044.16 | 4663–37504 | 1.0 | .14 | −.85 | 3179.83 | 914–32353 | .28 | .042 | −1.37 |

TABLE 2. *Oscillator strengths for lines of* U II—Continued

| Wavelength Å | Energy levels $cm^{-1}$ | gA $10^8/s$ | gf | log gf | Wavelength Å | Energy levels $cm^{-1}$ | gA $10^8/s$ | gf | log gf |
|---|---|---|---|---|---|---|---|---|---|
| 3180.20 | 1749–33184 | .32 | .048 | −1.32 | 3370.13 | 5260–34923 | .29 | .050 | −1.30 |
| 3185.71 | 1749–33130 | .36 | .055 | −1.26 | 3372.01 | 289–29936 | .20 | .035 | −1.46 |
| 3188.34 | 1749–33104 | .32 | .048 | −1.32 | 3375.78 | 8853–38468 | .77 | .13 | −.88 |
| 3190.89 | 5259–36589 | .26 | .040 | −1.40 | 3376.55 | 2294–31902 | .18 | .031 | −1.50 |
| 3191.76 | 4663–35985 | .24 | .036 | −1.44 | 3382.68 | 2294–31848 | .13 | .023 | −1.64 |
| 3200.14 | 5716–36956 | .61 | .094 | −1.03 | 3384.45 | 289–29827 | .20 | .035 | −1.46 |
| 3206.05 | 914–32096 | .36 | .056 | −1.25 | 3386.13 | 914–30438 | .22 | .038 | −1.42 |
| 3206.23 | 2295–33475 | .26 | .040 | −1.40 | 3392.99 | 4585–34049 | .19 | .032 | −1.49 |
| 3213.09 | 8394–39508 | .41 | .064 | −1.19 | 3393.91 | 2294–31751 | .33 | .057 | −1.25 |
| 3218.34 | 5526–36589 | .55 | .085 | −1.07 | 3394.78 | 5260–34708 | .58 | .10 | −1.00 |
| 3219.17 | 6283–37338 | .47 | .074 | −1.13 | 3395.32 | 1749–31193 | .30 | .052 | −1.28 |
| 3224.26 | 5526–36532 | .58 | .090 | −1.05 | 3398.26 | 5259–34678 | .33 | .057 | −1.24 |
| 3226.17 | 914–31902 | .28 | .044 | −1.36 | 3401.01 | 289–29683 | .24 | .041 | −1.38 |
| 3232.16 | 289–31219 | .51 | .080 | −1.09 | 3401.87 | 4585–33972 | .19 | .032 | −1.49 |
| 3235.23 | 8853–39754 | .43 | .068 | −1.17 | 3403.55 | 5259–34632 | .51 | .089 | −1.05 |
| 3238.46 | 914–31784 | .13 | .020 | −1.70 | 3406.27 | 915–30263 | .22 | .038 | −1.42 |
| 3240.35 | 8347–39199 | .40 | .063 | −1.20 | 3411.53 | 2294–31598 | .32 | .056 | −1.25 |
| 3241.99 | 914–31751 | .26 | .041 | −1.39 | 3412.10 | 8853–38152 | .89 | .16 | −.81 |
| 3244.79 | 2295–33104 | .25 | .039 | −1.41 | 3421.69 | 8379–37596 | .68 | .12 | −.92 |
| 3246.39 | 289–31083 | .24 | .037 | −1.43 | 3422.35 | 5401–34612 | .21 | .036 | −1.44 |
| 3253.75 | 289–31014 | .18 | .029 | −1.54 | 3423.01 | 5526–34732 | .44 | .077 | −1.12 |
| 3257.26 | 8276–38968 | .39 | .061 | −1.21 | 3424.56 | 1749–30941 | .47 | .082 | −1.09 |
| 3261.72 | 1749–32399 | .35 | .056 | −1.25 | 3426.39 | 11382–40559 | .90 | .16 | −.80 |
| 3265.81 | 914–31526 | .34 | .054 | −1.26 | 3430.48 | 6283–35425 | .23 | .041 | −1.38 |
| 3269.78 | 289–30863 | .11 | .018 | −1.75 | 3431.54 | 5791–34923 | .35 | .061 | −1.21 |
| 3270.12 | 289–30860 | .37 | .059 | −1.23 | 3433.71 | 289–29403 | .093 | .016 | −1.79 |
| 3271.45 | 5401–35960 | .24 | .039 | −1.41 | 3434.15 | 1749–30860 | .28 | .049 | −1.31 |
| 3280.00 | 914–31393 | .19 | .031 | −1.51 | 3436.78 | 4706–33794 | .29 | .052 | −1.29 |
| 3282.48 | 0–30455 | .17 | .027 | −1.57 | 3451.21 | 1749–30716 | .18 | .033 | −1.49 |
| 3283.10 | 914–31364 | .22 | .036 | −1.44 | 3453.57 | 8853–37801 | .99 | .18 | −.75 |
| 3285.22 | 1749–32179 | .34 | .055 | −1.26 | 3453.78 | 5667–34612 | .33 | .060 | −1.22 |
| 3288.21 | 289–30691 | .36 | .058 | −1.24 | 3454.23 | 5790–34732 | .57 | .10 | −.99 |
| 3294.44 | 8521–38867 | .53 | .086 | −1.07 | 3455.74 | 1749–30678 | .25 | .045 | −1.35 |
| 3299.70 | 2294–32591 | .30 | .049 | −1.31 | 3457.05 | 5716–34634 | .56 | .10 | −1.00 |
| 3303.60 | 289–30550 | .27 | .043 | −1.36 | 3457.71 | 5526–34439 | .54 | .097 | −1.01 |
| 3305.90 | 0–30240 | .62 | .10 | −.99 | 3458.68 | 2294–31199 | .12 | .022 | −1.66 |
| 3307.55 | 5526–35751 | .24 | .039 | −1.41 | 3472.51 | 11797–40586 | 1.6 | .29 | −.54 |
| 3311.67 | 1749–31936 | .33 | .054 | −1.27 | 3472.56 | 2295–31083 | .19 | .035 | −1.45 |
| 3313.94 | 289–30455 | .26 | .043 | −1.36 | 3474.99 | 914–29683 | .16 | .028 | −1.55 |
| 3318.79 | 4585–34708 | .20 | .034 | −1.47 | 3476.44 | 8423–37180 | .50 | .090 | −1.04 |
| 3319.32 | 12549–42666 | 1.1 | .18 | −.74 | 3477.50 | 4663–33411 | .17 | .032 | −1.50 |
| 3322.12 | 4585–34678 | .42 | .069 | −1.16 | 3482.49 | 1749–30455 | .49 | .089 | −1.05 |
| 3325.66 | 0–30060 | .16 | .026 | −1.58 | 3486.30 | 7598–36273 | .37 | .068 | −1.17 |
| 3327.50 | 914–30958 | .18 | .030 | −1.52 | 3489.57 | 5791–34439 | .42 | .078 | −1.11 |
| 3329.92 | 2294–32316 | .35 | .058 | −1.23 | 3490.24 | 914–29557 | .24 | .044 | −1.36 |
| 3332.42 | 5791–35790 | .24 | .040 | −1.40 | 3493.33 | 5259–33877 | .57 | .11 | −.98 |
| 3336.68 | 5790–35751 | .38 | .064 | −1.19 | 3494.84 | 10198–38803 | 1.1 | .20 | −.71 |
| 3337.79 | 289–30240 | .31 | .052 | −1.28 | 3495.60 | 4585–33184 | .17 | .031 | −1.51 |
| 3338.48 | 915–30860 | .18 | .030 | −1.52 | 3495.75 | 1749–30347 | .11 | .020 | −1.70 |
| 3341.66 | 2295–32211 | .46 | .077 | −1.11 | 3496.42 | 1749–30341 | .41 | .075 | −1.12 |
| 3342.68 | 1749–31656 | .32 | .053 | −1.27 | 3497.62 | 8755–37338 | .51 | .094 | −1.03 |
| 3344.87 | 5526–35414 | .37 | .061 | −1.21 | 3499.33 | 2295–30863 | .26 | .048 | −1.32 |
| 3354.50 | 2294–32096 | .33 | .055 | −1.26 | 3505.07 | 5259–33781 | .50 | .091 | −1.04 |
| 3355.11 | 289–30085 | .10 | .017 | −1.77 | 3505.45 | 0–28518 | .13 | .024 | −1.61 |
| 3357.93 | 289–30060 | .24 | .040 | −1.39 | 3508.85 | 1749–30240 | .29 | .053 | −1.28 |
| 3361.73 | 2294–32032 | .22 | .037 | −1.43 | 3509.67 | 8853–37338 | .99 | .18 | −.74 |
| 3367.90 | 0–29683 | .13 | .022 | −1.65 | 3511.58 | 289–28758 | .14 | .025 | −1.60 |
| 3368.81 | 6283–35958 | .52 | .088 | −1.05 | 3513.37 | 8853–37308 | .51 | .095 | −1.02 |

TABLE 2. *Oscillator strengths for lines of* U II—Continued

| Wavelength Å | Energy levels $cm^{-1}$ | gA $10^8/s$ | gf | log gf | Wavelength Å | Energy levels $cm^{-1}$ | gA $10^8/s$ | gf | log gf |
|---|---|---|---|---|---|---|---|---|---|
| 3515.24 | 4420–32860 | .22 | .041 | −1.39 | 3672.58 | 8853–36074 | .52 | .11 | −.98 |
| 3516.35 | 5667–34097 | .31 | .058 | −1.24 | 3674.99 | 8755–35958 | .23 | .048 | −1.32 |
| 3517.05 | 6283–34708 | .34 | .064 | −1.19 | 3675.08 | 5259–32462 | .23 | .047 | −1.33 |
| 3519.96 | 914–29316 | .29 | .053 | −1.28 | 3676.56 | 6283–33475 | .43 | .087 | −1.06 |
| 3520.79 | 6283–34678 | .40 | .075 | −1.13 | 3677.64 | 11784–38968 | .82 | .17 | −.78 |
| 3521.48 | 5259–33648 | .25 | .047 | −1.33 | 3678.75 | 8347–35523 | .77 | .16 | −.81 |
| 3523.33 | 4663–33037 | .17 | .031 | −1.51 | 3682.04 | 5259–32410 | .34 | .069 | −1.16 |
| 3523.57 | 11382–39754 | 1.0 | .19 | −.72 | 3691.92 | 4706–31784 | .55 | .11 | −.95 |
| 3525.73 | 9241–37596 | .34 | .063 | −1.20 | 3693.70 | 7547–34612 | .61 | .12 | −.91 |
| 3526.60 | 289–28636 | .19 | .035 | −1.46 | 3697.93 | 8755–35790 | .55 | .11 | −.94 |
| 3528.69 | 10198–38529 | .86 | .16 | −.80 | 3700.58 | 915–27929 | .30 | .062 | −1.21 |
| 3529.77 | 0–28322 | .081 | .015 | −1.82 | 3701.52 | 5527–32535 | 1.0 | .20 | −.69 |
| 3531.11 | 1749–30060 | .32 | .060 | −1.22 | 3705.04 | 2294–29277 | .18 | .036 | −1.44 |
| 3533.57 | 915–29206 | .39 | .073 | −1.14 | 3705.97 | 10740–37716 | .47 | .096 | −1.02 |
| 3537.45 | 5259–33520 | .29 | .054 | −1.27 | 3707.65 | 9626–36589 | .39 | .081 | −1.09 |
| 3540.46 | 5716–33953 | .72 | .14 | −.87 | 3714.76 | 2295–29206 | .21 | .043 | −1.37 |
| 3543.16 | 5260–33475 | .39 | .074 | −1.13 | 3717.42 | 8521–35414 | .65 | .13 | −.87 |
| 3544.21 | 6283–34490 | .34 | .063 | −1.20 | 3718.11 | 1749–28636 | .25 | .052 | −1.28 |
| 3546.68 | 1749–29936 | .23 | .043 | −1.37 | 3718.61 | 5526–32410 | .27 | .055 | −1.26 |
| 3547.19 | 1749–29932 | .32 | .060 | −1.22 | 3724.98 | 1749–28587 | .17 | .036 | −1.45 |
| 3550.82 | 0–28154 | .52 | .097 | −1.01 | 3725.07 | 5526–32364 | .25 | .053 | −1.28 |
| 3551.04 | 289–28441 | .13 | .025 | −1.60 | 3725.65 | 7166–33999 | .28 | .058 | −1.23 |
| 3552.17 | 2294–30438 | .30 | .057 | −1.25 | 3730.13 | 5790–32591 | .23 | .047 | −1.33 |
| 3560.44 | 1749–29827 | .16 | .031 | −1.51 | 3731.67 | 5526–32316 | .20 | .043 | −1.37 |
| 3564.59 | 8347–36393 | .62 | .12 | −.93 | 3732.62 | 914–27698 | .22 | .046 | −1.34 |
| 3564.88 | 9553–37596 | .55 | .10 | −.98 | 3737.25 | 10740–37490 | .75 | .16 | −.80 |
| 3570.93 | 4420–32416 | .15 | .029 | −1.53 | 3738.05 | 5791–32535 | .67 | .14 | −.85 |
| 3571.56 | 5790–33781 | .26 | .050 | −1.30 | 3744.24 | 7598–34298 | .55 | .12 | −.94 |
| 3571.69 | 4420–32410 | .25 | .047 | −1.33 | 3746.41 | 5527–32211 | .69 | .15 | −.84 |
| 3576.22 | 10198–38152 | .82 | .16 | −.80 | 3747.14 | 8521–35201 | .70 | .15 | −.83 |
| 3578.72 | 8276–36211 | 1.2 | .22 | −.65 | 3748.68 | 5716–32384 | .89 | .19 | −.73 |
| 3581.84 | 5716–33627 | .54 | .10 | −.99 | 3752.66 | 5526–32166 | .44 | .093 | −1.03 |
| 3590.32 | 5260–33104 | .43 | .083 | −1.08 | 3754.31 | 0–26628 | .12 | .026 | −1.58 |
| 3590.50 | 915–28758 | .23 | .045 | −1.34 | 3755.48 | 5790–32410 | .46 | .097 | −1.01 |
| 3594.95 | 1749–29557 | .25 | .048 | −1.32 | 3756.92 | 4706–31316 | .30 | .063 | −1.20 |
| 3596.88 | 1749–29543 | .12 | .023 | −1.63 | 3759.23 | 5667–32261 | .45 | .095 | −1.02 |
| 3599.84 | 8347–36118 | .44 | .085 | −1.07 | 3759.88 | 5259–31848 | .20 | .043 | −1.37 |
| 3605.48 | 1749–29476 | .14 | .026 | −1.58 | 3760.88 | 0–26581 | .14 | .031 | −1.52 |
| 3606.32 | 4663–32384 | .45 | .087 | −1.06 | 3761.96 | 914–27489 | .13 | .027 | −1.57 |
| 3608.96 | 8510–36211 | .45 | .087 | −1.06 | 3762.11 | 1749–28322 | .14 | .030 | −1.52 |
| 3609.68 | 5716–33411 | .40 | .078 | −1.11 | 3764.57 | 5716–32272 | .56 | .12 | −.92 |
| 3610.49 | 6283–33972 | .32 | .062 | −1.21 | 3768.80 | 5790–32316 | .35 | .075 | −1.13 |
| 3611.24 | 2294–29978 | .11 | .021 | −1.68 | 3772.82 | 8347–34845 | .44 | .094 | −1.02 |
| 3612.67 | 915–28587 | .16 | .032 | −1.50 | 3780.72 | 915–27357 | .22 | .048 | −1.32 |
| 3616.76 | 289–27930 | .21 | .041 | −1.39 | 3782.84 | 289–26716 | .60 | .13 | −.89 |
| 3618.49 | 9553–37181 | .52 | .10 | −.99 | 3783.84 | 5791–32211 | .51 | .11 | −.96 |
| 3623.06 | 915–28507 | .26 | .051 | −1.29 | 3786.57 | 8521–34923 | .33 | .071 | −1.15 |
| 3628.35 | 8521–36074 | .27 | .054 | −1.27 | 3787.23 | 5259–31656 | .27 | .058 | −1.23 |
| 3632.87 | 10198–37716 | .35 | .070 | −1.15 | 3790.22 | 5790–32166 | .22 | .046 | −1.33 |
| 3635.40 | 0–27499 | .12 | .023 | −1.64 | 3790.33 | 914–27290 | .10 | .022 | −1.66 |
| 3640.95 | 1749–29206 | .21 | .042 | −1.38 | 3793.10 | 4585–30941 | .51 | .11 | −.96 |
| 3644.85 | 2294–29722 | .078 | .016 | −1.81 | 3793.57 | 914–27267 | .22 | .048 | −1.32 |
| 3645.03 | 914–28341 | .22 | .043 | −1.36 | 3795.13 | 2294–28636 | .19 | .041 | −1.39 |
| 3649.51 | 4706–32099 | .16 | .032 | −1.49 | 3796.54 | 4663–30996 | .29 | .062 | −1.21 |
| 3659.01 | 4706–32028 | .26 | .052 | −1.29 | 3796.84 | 6445–32775 | .38 | .082 | −1.09 |
| 3662.33 | 4663–31961 | .24 | .049 | −1.31 | 3799.20 | 8394–34708 | .51 | .11 | −.96 |
| 3666.21 | 8521–35790 | .34 | .069 | −1.16 | 3802.27 | 2294–28587 | .20 | .043 | −1.37 |
| 3670.07 | 915–28154 | .95 | .19 | −.72 | 3803.35 | 0–26285 | .087 | .019 | −1.72 |

TABLE 2. *Oscillator strengths for lines of* U II—Continued

| Wavelength Å | Energy levels $cm^{-1}$ | gA $10^8/s$ | gf | log gf | Wavelength Å | Energy levels $cm^{-1}$ | gA $10^8/s$ | gf | log gf |
|---|---|---|---|---|---|---|---|---|---|
| 3809.22 | 5716–31961 | .46 | .10 | −1.00 | 3927.76 | 6283–31736 | .33 | .077 | −1.11 |
| 3813.79 | 2295–28507 | .27 | .059 | −1.23 | 3930.98 | 289–25720 | .20 | .045 | −1.34 |
| 3814.07 | 915–27126 | .22 | .047 | −1.33 | 3932.03 | 289–25714 | .55 | .13 | −.89 |
| 3818.46 | 1749–27930 | .11 | .025 | −1.61 | 3933.03 | 5259–30678 | .18 | .041 | −1.39 |
| 3822.54 | 4706–30859 | .18 | .039 | −1.41 | 3935.38 | 2294–27698 | .29 | .067 | −1.17 |
| 3826.51 | 289–26415 | .31 | .068 | −1.17 | 3940.49 | 914–26285 | .18 | .042 | −1.38 |
| 3829.03 | 915–27023 | .16 | .035 | −1.46 | 3942.55 | 8755–34112 | .41 | .096 | −1.02 |
| 3829.39 | 4585–30691 | .24 | .052 | −1.28 | 3944.13 | 4585–29932 | .25 | .059 | −1.23 |
| 3831.46 | 4663–30756 | 1.2 | .26 | −.59 | 3953.58 | 2294–27581 | .21 | .048 | −1.32 |
| 3835.92 | 7598–33660 | .39 | .086 | −1.07 | 3954.62 | 5716–30996 | .25 | .058 | −1.24 |
| 3838.15 | 2294–28341 | .17 | .038 | −1.42 | 3954.67 | 8347–33627 | .59 | .14 | −.86 |
| 3845.12 | 5526–31526 | .20 | .044 | −1.36 | 3962.77 | 4706–29934 | .22 | .051 | −1.29 |
| 3845.26 | 7547–33546 | .37 | .082 | −1.09 | 3964.67 | 7166–32382 | .37 | .088 | −1.06 |
| 3845.37 | 8394–34392 | .42 | .093 | −1.03 | 3964.96 | 0–25213 | .093 | .022 | −1.66 |
| 3848.60 | 5259–31235 | .49 | .11 | −.96 | 3966.40 | 2295–27499 | .18 | .041 | −1.38 |
| 3849.71 | 8522–34490 | .31 | .070 | −1.16 | 3966.52 | 289–25492 | .24 | .056 | −1.25 |
| 3849.85 | 0–25967 | .12 | .026 | −1.58 | 3969.02 | 8400–33588 | .28 | .066 | −1.18 |
| 3854.66 | 4663–30599 | 1.3 | .29 | −.54 | 3978.80 | 8394–33520 | .38 | .090 | −1.04 |
| 3859.58 | 289–26191 | 1.1 | .24 | −.62 | 3985.80 | 5260–30341 | .81 | .19 | −.71 |
| 3864.30 | 4585–30455 | .27 | .060 | −1.22 | 3988.64 | 8276–33340 | .21 | .049 | −1.31 |
| 3864.48 | 4663–30533 | .27 | .061 | −1.21 | 3988.89 | 2295–27357 | .15 | .035 | −1.46 |
| 3865.92 | 2295–28154 | .77 | .17 | −.77 | 3990.42 | 915–25967 | .22 | .052 | −1.29 |
| 3866.80 | 914–26768 | .21 | .047 | −1.33 | 3992.54 | 5716–30756 | .40 | .095 | −1.02 |
| 3868.42 | 4421–30263 | .16 | .037 | −1.43 | 3994.29 | 289–25317 | .079 | .019 | −1.73 |
| 3870.02 | 5667–31499 | .32 | .071 | −1.15 | 4002.34 | 4706–29684 | .15 | .037 | −1.43 |
| 3871.88 | 8347–34167 | .26 | .058 | −1.24 | 4003.20 | 2294–27267 | .11 | .026 | −1.59 |
| 3874.04 | 289–26094 | .26 | .059 | −1.23 | 4004.06 | 1749–26716 | .20 | .049 | −1.31 |
| 3876.59 | 9626–35414 | .36 | .082 | −1.09 | 4009.17 | 6283–31219 | .20 | .047 | −1.32 |
| 3878.09 | 8853–34632 | .98 | .22 | −.66 | 4011.45 | 5401–30323 | .16 | .039 | −1.41 |
| 3881.46 | 4585–30341 | .70 | .16 | −.80 | 4014.16 | 8755–33660 | .22 | .053 | −1.28 |
| 3882.36 | 1749–27499 | .28 | .063 | −1.20 | 4017.72 | 5716–30599 | .51 | .12 | −.91 |
| 3883.28 | 8423–34167 | .66 | .15 | −.83 | 4018.99 | 289–25163 | .14 | .035 | −1.46 |
| 3884.68 | 8755–34490 | .51 | .11 | −.94 | 4026.02 | 2295–27126 | .080 | .019 | −1.71 |
| 3887.70 | 10198–35913 | .52 | .12 | −.93 | 4031.31 | 914–25713 | .10 | .025 | −1.60 |
| 3890.36 | 289–25986 | .61 | .14 | −.86 | 4033.43 | 4421–29206 | .18 | .043 | −1.37 |
| 3891.68 | 8510–34199 | .30 | .069 | −1.16 | 4033.73 | 7598–32382 | .32 | .079 | −1.10 |
| 3892.41 | 8755–34439 | .50 | .11 | −.94 | 4044.42 | 5259–29978 | .44 | .11 | −.97 |
| 3892.68 | 5260–30941 | .56 | .13 | −.90 | 4050.04 | 0–24684 | .42 | .10 | −.99 |
| 3895.27 | 4421–30085 | .23 | .052 | −1.29 | 4051.91 | 5260–29932 | .45 | .11 | −.95 |
| 3896.78 | 4585–30240 | .43 | .097 | −1.01 | 4053.03 | 1749–26415 | .12 | .031 | −1.51 |
| 3897.05 | 10740–36393 | .68 | .15 | −.81 | 4054.31 | 6283–30941 | .35 | .087 | −1.06 |
| 3897.69 | 5667–31316 | .19 | .044 | −1.35 | 4058.19 | 289–24923 | .18 | .044 | −1.36 |
| 3899.07 | 4421–30060 | .22 | .050 | −1.30 | 4060.10 | 4706–29329 | .11 | .028 | −1.55 |
| 3899.48 | 4663–30301 | .27 | .061 | −1.22 | 4061.74 | 7598–32211 | .22 | .054 | −1.27 |
| 3899.78 | 2295–27929 | .35 | .080 | −1.10 | 4062.55 | 0–24608 | .28 | .068 | −1.17 |
| 3902.56 | 289–25906 | .19 | .044 | −1.35 | 4066.80 | 8521–33104 | .25 | .062 | −1.20 |
| 3904.30 | 8347–33953 | .73 | .17 | −.78 | 4067.76 | 6283–30860 | .51 | .13 | −.90 |
| 3904.56 | 5260–30863 | .29 | .066 | −1.18 | 4071.11 | 12033–36589 | 1.1 | .26 | −.58 |
| 3904.85 | 8510–34112 | .30 | .069 | −1.16 | 4074.49 | 1749–26285 | .17 | .043 | −1.37 |
| 3908.47 | 8394–33972 | .29 | .067 | −1.17 | 4076.69 | 914–25437 | .16 | .040 | −1.39 |
| 3909.06 | 5790–31364 | .20 | .045 | −1.35 | 4080.61 | 12033–36532 | .90 | .23 | −.65 |
| 3911.67 | 4420–29978 | .31 | .072 | −1.14 | 4084.93 | 5791–30263 | .24 | .059 | −1.23 |
| 3914.20 | 12055–37596 | .70 | .16 | −.79 | 4088.25 | 0–24453 | .12 | .031 | −1.51 |
| 3915.88 | 8423–33953 | .64 | .15 | −.83 | 4090.14 | 1749–26191 | .66 | .17 | −.78 |
| 3918.06 | 4421–29936 | .12 | .028 | −1.56 | 4091.49 | 10198–34632 | .51 | .13 | −.89 |
| 3921.55 | 0–25492 | .11 | .025 | −1.60 | 4094.62 | 11544–35960 | .32 | .080 | −1.10 |
| 3923.05 | 8394–33877 | .29 | .067 | −1.17 | 4095.75 | 6283–30691 | .28 | .070 | −1.15 |
| 3924.27 | 4585–30060 | .22 | .051 | −1.29 | 4098.03 | 289–24684 | .18 | .046 | −1.34 |

TABLE 2. *Oscillator strengths for lines of* U II—Continued

| Wavelength Å | Energy levels $cm^{-1}$ | gA $10^8/s$ | gf | log gf | Wavelength Å | Energy levels $cm^{-1}$ | gA $10^8/s$ | gf | log gf |
|---|---|---|---|---|---|---|---|---|---|
| 4106.38 | 1749–26094 | .20 | .050 | −1.30 | 4373.41 | 1749–24608 | .073 | .021 | −1.68 |
| 4106.93 | 0–24342 | .098 | .025 | −1.60 | 4402.30 | 9075–31784 | .077 | .022 | −1.65 |
| 4113.11 | 0–24305 | .065 | .017 | −1.78 | 4402.44 | 8510–31219 | .11 | .033 | −1.48 |
| 4116.10 | 0–24288 | .25 | .064 | −1.19 | 4415.24 | 0–22642 | .064 | .019 | −1.73 |
| 4124.73 | 1749–25986 | .21 | .053 | −1.28 | 4426.68 | 4706–27290 | .082 | .024 | −1.62 |
| 4128.34 | 4420–28636 | .31 | .080 | −1.10 | 4427.65 | 289–22868 | .056 | .017 | −1.78 |
| 4133.20 | 5790–29978 | .19 | .048 | −1.32 | 4433.89 | 8394–30941 | .14 | .043 | −1.37 |
| 4135.76 | 6283–30455 | .15 | .039 | −1.40 | 4434.53 | 1749–24293 | .070 | .021 | −1.68 |
| 4136.81 | 4421–28587 | .15 | .038 | −1.41 | 4462.97 | 915–23315 | .075 | .022 | −1.65 |
| 4138.66 | 9626–33781 | .26 | .066 | −1.18 | 4465.13 | 2295–24684 | .055 | .017 | −1.78 |
| 4139.14 | 0–24152 | .093 | .024 | −1.62 | 4472.34 | 289–22642 | .17 | .052 | −1.28 |
| 4141.23 | 8394–32535 | .62 | .16 | −.80 | 4477.71 | 915–23241 | .044 | .013 | −1.87 |
| 4144.70 | 2295–26415 | .11 | .029 | −1.54 | 4490.84 | 1749–24010 | .068 | .021 | −1.69 |
| 4145.39 | 8521–32638 | .15 | .038 | −1.41 | 4510.32 | 0–22165 | .038 | .012 | −1.94 |
| 4155.41 | 6283–30341 | .31 | .080 | −1.10 | 4515.28 | 289–22429 | .091 | .028 | −1.56 |
| 4163.68 | 0–24010 | .14 | .036 | −1.44 | 4538.19 | 1749–23778 | .096 | .030 | −1.53 |
| 4164.79 | 289–24293 | .049 | .013 | −1.90 | 4543.63 | 915–22917 | .19 | .058 | −1.24 |
| 4165.68 | 289–24288 | .12 | .032 | −1.50 | 4545.58 | 2295–24288 | .089 | .028 | −1.56 |
| 4171.59 | 1749–25714 | .46 | .12 | −.92 | 4553.86 | 915–22868 | .029 | .0091 | −2.04 |
| 4172.97 | 6283–30240 | .20 | .051 | −1.29 | 4555.10 | 8394–30341 | .15 | .046 | −1.34 |
| 4174.19 | 5527–29476 | .24 | .062 | −1.21 | 4567.69 | 1749–23635 | .059 | .019 | −1.73 |
| 4179.00 | 4585–28507 | .15 | .039 | −1.41 | 4569.91 | 289–22165 | .061 | .019 | −1.72 |
| 4184.89 | 8521–32410 | .19 | .049 | −1.31 | 4570.99 | 6283–28154 | .066 | .021 | −1.68 |
| 4188.07 | 289–24159 | .094 | .025 | −1.61 | 4573.69 | 2295–24152 | .091 | .029 | −1.54 |
| 4189.28 | 289–24152 | .13 | .034 | −1.47 | 4584.85 | 1749–23553 | .041 | .013 | −1.89 |
| 4197.52 | 8394–32211 | .32 | .083 | −1.08 | 4601.13 | 915–22642 | .035 | .011 | −1.95 |
| 4200.10 | 6283–30085 | .10 | .027 | −1.57 | 4603.66 | 2295–24010 | .082 | .026 | −1.58 |
| 4204.37 | 0–23778 | .086 | .023 | −1.64 | 4605.15 | 5791–27499 | .075 | .024 | −1.62 |
| 4210.45 | 1749–25492 | .065 | .017 | −1.76 | 4609.86 | 289–21975 | .026 | .0082 | −2.09 |
| 4211.66 | 4585–28322 | .21 | .056 | −1.25 | 4622.43 | 5260–26887 | .055 | .018 | −1.75 |
| 4212.26 | 4421–28154 | .14 | .038 | −1.42 | 4627.08 | 4585–26191 | .17 | .054 | −1.27 |
| 4214.42 | 289–24010 | .052 | .014 | −1.86 | 4641.65 | 8394–29932 | .12 | .038 | −1.42 |
| 4227.33 | 6283–29932 | .12 | .032 | −1.50 | 4646.60 | 915–22429 | .088 | .029 | −1.54 |
| 4228.76 | 4706–28347 | .10 | .027 | −1.57 | 4666.86 | 289–21710 | .058 | .019 | −1.72 |
| 4232.04 | 289–23911 | .047 | .013 | −1.90 | 4671.41 | 4585–25986 | .090 | .030 | −1.53 |
| 4240.59 | 5259–28834 | .085 | .023 | −1.64 | 4689.07 | 0–21320 | .063 | .021 | −1.68 |
| 4241.67 | 4585–28154 | .54 | .15 | −.83 | 4700.98 | 289–21555 | .027 | .0088 | −2.05 |
| 4244.37 | 0–23553 | .17 | .046 | −1.33 | 4702.05 | 4706–25967 | .057 | .019 | −1.73 |
| 4252.43 | 4420–27930 | .15 | .041 | −1.38 | 4702.52 | 2295–23553 | .062 | .021 | −1.68 |
| 4267.30 | 915–24342 | .080 | .022 | −1.66 | 4722.73 | 1749–22917 | .078 | .026 | −1.58 |
| 4268.85 | 2294–25713 | .068 | .019 | −1.73 | 4731.60 | 4585–25714 | .099 | .033 | −1.48 |
| 4269.61 | 1749–25163 | .10 | .027 | −1.56 | 4755.73 | 0–21021 | .043 | .014 | −1.84 |
| 4273.98 | 915–24305 | .055 | .015 | −1.82 | 4769.26 | 0–20961 | .035 | .012 | −1.92 |
| 4276.47 | 5259–28636 | .11 | .029 | −1.53 | 4772.70 | 2295–23241 | .060 | .021 | −1.69 |
| 4282.03 | 289–23635 | .092 | .025 | −1.60 | 4779.63 | 914–21831 | .030 | .010 | −1.98 |
| 4282.46 | 4585–27929 | .15 | .042 | −1.37 | 4819.54 | 4421–25163 | .051 | .018 | −1.75 |
| 4287.87 | 0–23315 | .088 | .024 | −1.62 | 4847.65 | 2295–22917 | .048 | .017 | −1.77 |
| 4297.11 | 289–23553 | .075 | .021 | −1.68 | 4858.08 | 4585–25163 | .074 | .026 | −1.58 |
| 4301.47 | 0–23241 | .061 | .017 | −1.77 | 4859.68 | 0–20571 | .033 | .012 | −1.93 |
| 4310.39 | 6283–29476 | .095 | .027 | −1.58 | 4861.02 | 5402–25967 | .094 | .033 | −1.48 |
| 4313.88 | 1749–24923 | .080 | .022 | −1.65 | 4883.78 | 2294–22764 | .033 | .012 | −1.92 |
| 4319.78 | 2294–25437 | .041 | .012 | −1.94 | 4886.33 | 5527–25986 | .040 | .014 | −1.85 |
| 4325.90 | 5526–28636 | .099 | .028 | −1.56 | 4899.29 | 915–21320 | .043 | .015 | −1.81 |
| 4341.69 | 289–23315 | .20 | .057 | −1.24 | 4913.16 | 2295–22642 | .044 | .016 | −1.79 |
| 4347.19 | 915–23911 | .080 | .023 | −1.64 | 4924.64 | 5667–25967 | .051 | .019 | −1.73 |
| 4362.26 | 0–22917 | .081 | .023 | −1.64 | 4933.66 | 4421–24684 | .033 | .012 | −1.92 |
| 4362.93 | 4585–27499 | .084 | .024 | −1.62 | 4950.17 | 5791–25986 | .040 | .015 | −1.83 |
| 4372.57 | 915–23778 | .082 | .024 | −1.63 | 4972.10 | 915–21021 | .024 | .0089 | −2.05 |

TABLE 2. *Oscillator strengths for lines of* U II—Continued

| Wavelength Å | Energy levels $cm^{-1}$ | gA $10^8/s$ | gf | log gf | Wavelength Å | Energy levels $cm^{-1}$ | gA $10^8/s$ | gf | log gf |
|---|---|---|---|---|---|---|---|---|---|
| 4986.90 | 915–20961 | .024 | .0089 | −2.05 | 5602.90 | 6445–24288 | .031 | .014 | −1.84 |
| 5008.22 | 1749–21710 | .053 | .020 | −1.70 | 5603.97 | 5401–23241 | .019 | .0088 | −2.06 |
| 5047.41 | 2295–22101 | .020 | .0076 | −2.12 | 5628.02 | 5791–23553 | .020 | .0094 | −2.03 |
| 5077.82 | 289–19977 | .014 | .0055 | −2.26 | 5638.00 | 8394–26126 | .029 | .014 | −1.85 |
| 5085.86 | 915–20571 | .021 | .0081 | −2.09 | 5644.21 | 12629–30341 | .042 | .020 | −1.70 |
| 5117.25 | 2294–21831 | .041 | .016 | −1.80 | 5653.77 | 2294–19977 | .016 | .0076 | −2.12 |
| 5137.05 | 6445–25906 | .031 | .012 | −1.92 | 5654.39 | 4421–22101 | .022 | .011 | −1.97 |
| 5145.08 | 6283–25714 | .035 | .014 | −1.85 | 5664.86 | 5667–23315 | .019 | .0092 | −2.04 |
| 5154.04 | 2294–21691 | .022 | .0086 | −2.06 | 5674.88 | 9882–27499 | .027 | .013 | −1.88 |
| 5160.33 | 5791–25163 | .075 | .030 | −1.52 | 5683.33 | 9553–27143 | .041 | .020 | −1.70 |
| 5184.59 | 5402–24684 | .055 | .022 | −1.66 | 5691.40 | 6445–24010 | .044 | .021 | −1.67 |
| 5204.32 | 6283–25492 | .054 | .022 | −1.66 | 5704.07 | 8379–25906 | .040 | .020 | −1.71 |
| 5225.12 | 5790–24923 | .032 | .013 | −1.89 | 5706.99 | 9626–27143 | .046 | .022 | −1.65 |
| 5238.61 | 9553–28636 | .048 | .020 | −1.71 | 5723.63 | 5401–22868 | .037 | .018 | −1.74 |
| 5247.35 | 5402–24453 | .025 | .010 | −1.99 | 5733.21 | 8276–25714 | .039 | .019 | −1.71 |
| 5247.75 | 4585–23635 | .041 | .017 | −1.77 | 5748.10 | 0–17392 | .010 | .0051 | −2.30 |
| 5257.04 | 5667–24684 | .048 | .020 | −1.70 | 5748.44 | 8276–25667 | .024 | .012 | −1.93 |
| 5278.18 | 5402–24342 | .029 | .012 | −1.91 | 5776.87 | 9626–26931 | .029 | .015 | −1.84 |
| 5288.40 | 5402–24305 | .025 | .010 | −1.99 | 5788.59 | 6283–23553 | .028 | .014 | −1.85 |
| 5310.04 | 0–18827 | .012 | .0050 | −2.30 | 5791.74 | 9626–26887 | .048 | .024 | −1.62 |
| 5311.88 | 4421–23241 | .036 | .015 | −1.82 | 5798.54 | 5401–22642 | .052 | .026 | −1.58 |
| 5312.73 | 5791–24608 | .024 | .010 | −1.99 | 5811.27 | 8510–25714 | .037 | .019 | −1.72 |
| 5321.60 | 5667–24453 | .023 | .010 | −2.00 | 5827.99 | 4706–21860 | .019 | .0095 | −2.02 |
| 5327.76 | 6283–25047 | .044 | .019 | −1.73 | 5832.37 | 9882–27023 | .041 | .021 | −1.68 |
| 5349.92 | 4420–23107 | .023 | .0099 | −2.01 | 5837.70 | 4585–21710 | .039 | .020 | −1.70 |
| 5362.40 | 9690–28333 | .047 | .020 | −1.70 | 5839.04 | 7166–24288 | .019 | .010 | −2.00 |
| 5363.82 | 5667–24305 | .025 | .011 | −1.97 | 5841.82 | 8379–25492 | .033 | .017 | −1.78 |
| 5368.43 | 9075–27698 | .057 | .025 | −1.61 | 5843.29 | 6445–23553 | .029 | .015 | −1.83 |
| 5373.45 | 1749–20353 | .0098 | .0042 | −2.37 | 5843.82 | 11787–28894 | .040 | .020 | −1.69 |
| 5386.19 | 15392–33953 | .24 | .10 | −.99 | 5845.25 | 289–17392 | .015 | .0075 | −2.12 |
| 5403.20 | 5790–24293 | .030 | .013 | −1.89 | 5853.91 | 1749–18827 | .016 | .0081 | −2.09 |
| 5405.98 | 8394–26887 | .044 | .019 | −1.71 | 5859.16 | 13015–30078 | .048 | .025 | −1.61 |
| 5444.48 | 5791–24152 | .039 | .017 | −1.76 | 5870.93 | 5402–22429 | .032 | .017 | −1.78 |
| 5465.68 | 9626–27917 | .070 | .031 | −1.50 | 5886.93 | 8510–25492 | .024 | .012 | −1.91 |
| 5475.72 | 9241–27499 | .11 | .052 | −1.29 | 5895.32 | 6283–23241 | .028 | .014 | −1.84 |
| 5480.27 | 12513–30756 | .17 | .078 | −1.11 | 5932.44 | 5791–22642 | .020 | .010 | −1.98 |
| 5481.21 | 6445–24684 | .068 | .031 | −1.51 | 5934.46 | 8510–25356 | .022 | .012 | −1.94 |
| 5482.54 | 15392–33627 | .20 | .091 | −1.04 | 5952.05 | 6445–23241 | .026 | .014 | −1.86 |
| 5484.55 | 1749–19977 | .0094 | .0042 | −2.37 | 6004.83 | 9933–26581 | .044 | .024 | −1.62 |
| 5487.00 | 5791–24010 | .038 | .017 | −1.76 | 6017.39 | 4706–21320 | .024 | .013 | −1.89 |
| 5491.22 | 8510–26716 | .058 | .026 | −1.58 | 6051.74 | 914–17434 | .021 | .011 | −1.94 |
| 5492.97 | 0–18200 | .044 | .020 | −1.70 | 6059.73 | 5667–22165 | .020 | .011 | −1.95 |
| 5494.66 | 4420–22615 | .027 | .012 | −1.92 | 6067.23 | 914–17392 | .018 | .010 | −2.00 |
| 5501.49 | 9553–27725 | .040 | .018 | −1.74 | 6087.34 | 6445–22868 | .031 | .017 | −1.77 |
| 5504.13 | 6445–24608 | .046 | .021 | −1.68 | 6110.91 | 2294–18654 | .0074 | .0042 | −2.38 |
| 5527.83 | 12513–30599 | .17 | .078 | −1.11 | 6164.77 | 10198–26415 | .037 | .021 | −1.68 |
| 5535.78 | 2294–20353 | .013 | .0059 | −2.23 | 6181.37 | 8510–24684 | .018 | .010 | −1.99 |
| 5538.53 | 9075–27126 | .047 | .022 | −1.66 | 6254.22 | 6445–22429 | .020 | .012 | −1.93 |
| 5544.81 | 4585–22615 | .027 | .012 | −1.91 | 6279.64 | 5791–21710 | .014 | .0083 | −2.08 |
| 5548.05 | 12513–30533 | .063 | .029 | −1.54 | 6280.20 | 5402–21320 | .025 | .015 | −1.83 |
| 5551.42 | 6445–24453 | .036 | .017 | −1.78 | 6291.48 | 914–16804 | .0049 | .0029 | −2.54 |
| 5552.60 | 6283–24288 | .026 | .012 | −1.92 | 6322.37 | 0–15812 | .0067 | .0040 | −2.40 |
| 5570.66 | 9553–27499 | .073 | .034 | −1.47 | 6330.77 | 914–16706 | .0057 | .0034 | −2.46 |
| 5580.81 | 5402–23315 | .025 | .012 | −1.94 | 6336.55 | 8510–24288 | .016 | .0094 | −2.03 |
| 5581.23 | 914–18827 | .015 | .0070 | −2.15 | 6346.27 | 5401–21154 | .0096 | .0058 | −2.24 |
| 5581.61 | 289–18200 | .019 | .0088 | −2.06 | 6374.78 | 10285–25967 | .028 | .017 | −1.77 |
| 5587.17 | 8521–26415 | .026 | .012 | −1.92 | 6375.98 | 0–15679 | .0037 | .0023 | −2.64 |
| 5597.37 | 6445–24305 | .035 | .017 | −1.78 | 6378.52 | 289–15962 | .011 | .0067 | −2.17 |



206-267 OL - 76 - 4

TABLE 2. *Oscillator strengths for lines of* U II—Continued

| Wavelength Å | Energy levels $cm^{-1}$ | gA $10^8/s$ | gf | log gf | Wavelength Å | Energy levels $cm^{-1}$ | gA $10^8/s$ | gf | log gf |
|---|---|---|---|---|---|---|---|---|---|
| 6379.64 | 5716–21387 | .022 | .014 | −1.86 | 6776.89 | 10740–25492 | .016 | .011 | −1.96 |
| 6386.84 | 5667–21320 | .013 | .0082 | −2.08 | 6796.43 | 6445–21154 | .0058 | .0040 | −2.40 |
| 6391.32 | 8510–24152 | .014 | .0085 | −2.07 | 6808.76 | 8423–23106 | .0078 | .0055 | −2.26 |
| 6400.36 | 5402–21021 | .010 | .0064 | −2.20 | 6876.75 | 8379–22917 | .041 | .029 | −1.54 |
| 6424.89 | 5402–20961 | .013 | .0079 | −2.10 | 6948.58 | 16211–30599 | .061 | .045 | −1.35 |
| 6448.04 | 9933–25437 | .015 | .0094 | −2.03 | 6987.72 | 10740–25047 | .015 | .011 | −1.95 |
| 6470.55 | 10740–26191 | .017 | .011 | −1.97 | 7020.71 | 10444–24684 | .029 | .022 | −1.66 |
| 6485.38 | 6445–21860 | .0087 | .0055 | −2.26 | 7073.61 | 4663–18797 | .0059 | .0044 | −2.35 |
| 6495.23 | 4585–19977 | .0065 | .0041 | −2.38 | 7082.11 | 5401–19517 | .011 | .0085 | −2.07 |
| 6534.60 | 18654–33953 | .057 | .036 | −1.44 | 7183.47 | 2294–16211 | .0060 | .0046 | −2.33 |
| 6535.46 | 914–16211 | .0062 | .0040 | −2.40 | 7218.04 | 5667–19517 | .0085 | .0066 | −2.18 |
| 6536.58 | 5667–20961 | .0096 | .0061 | −2.21 | 7379.63 | 10740–24288 | .029 | .024 | −1.63 |
| 6549.88 | 7166–22429 | .012 | .0078 | −2.11 | 7454.03 | 10740–24152 | .024 | .020 | −1.69 |
| 6557.58 | 10740–25986 | .021 | .013 | −1.87 | 7510.08 | 8379–21691 | .0098 | .0083 | −2.08 |
| 6587.83 | 5526–20702 | .0093 | .0060 | −2.22 | 7580.91 | 7166–20353 | .010 | .0087 | −2.06 |
| 6590.05 | 5402–20571 | .0082 | .0053 | −2.27 | 7668.73 | 5790–18827 | .0055 | .0049 | −2.31 |
| 6603.34 | 2294–17434 | .0032 | .0021 | −2.68 | 7669.69 | 9882–22917 | .010 | .0092 | −2.04 |
| 6621.77 | 2294–17392 | .0098 | .0064 | −2.19 | 7802.40 | 10740–23553 | .017 | .016 | −1.81 |
| 6622.82 | 7547–22642 | .013 | .0083 | −2.08 | 7837.71 | 9075–21831 | .016 | .014 | −1.84 |
| 6640.50 | 9553–24608 | .0097 | .0064 | −2.19 | 7976.88 | 5667–18200 | .0091 | .0086 | −2.06 |
| 6671.21 | 8276–23262 | .0079 | .0053 | −2.28 | 8040.10 | 8423–20857 | .0065 | .0063 | −2.20 |
| 6676.92 | 18654–33627 | .082 | .055 | −1.26 | 8074.03 | 6445–18827 | .010 | .0099 | −2.01 |
| 6701.68 | 9690–24608 | .012 | .0080 | −2.10 | 8188.20 | 6445–18654 | .010 | .010 | −2.00 |
| 6707.59 | 5667–20571 | .0074 | .0050 | −2.30 | 8210.27 | 10740–22917 | .015 | .015 | −1.83 |
| 6710.57 | 914–15812 | .0035 | .0024 | −2.62 | 8307.56 | 1749–13783 | .0028 | .0028 | −2.55 |
| 6717.45 | 7547–22429 | .014 | .0092 | −2.04 | 8337.50 | 5401–17392 | .012 | .013 | −1.89 |
| 6720.76 | 6445–21320 | .0083 | .0056 | −2.25 | 8618.96 | 914–12513 | .0023 | .0026 | −2.58 |
| 6726.89 | 8379–23241 | .011 | .0076 | −2.12 | 8702.08 | 2294–13783 | .0034 | .0038 | −2.42 |
| 6742.47 | 5526–20353 | .0051 | .0035 | −2.46 | 8787.37 | 4585–15962 | .0065 | .0075 | −2.12 |
| 6771.03 | 914–15679 | .0030 | .0021 | −2.68 | | | | | |

## 5. References


Bell, R. A. and Upson, W. L. (1971). Astrophys. Lett. **9**, 109.

Corliss, C. H. and Bozman, W. R. (1962). Experimental transition probilities for spectral lines of seventy elements. Nat. Bur. S and. (U.S.), Monogr. 53, 583 pages.

Meggers, W. F., Corliss, C. H. and Scribner, B. F. (1975) Tables of spectral-line intensities. Nat. Bur. Stand. (U.S.) Monogr. 145. Part I. 403 pages.

Steinhaus, D. W., Phillips, M. V., Moody, J. B., Radziemski, L. J., Fisher, K. J., and Hahn, D. R., [1972] Los Alamos Report LA4977.

Voigt. P. A., [1975] Phys. Rev. A **11**, 1845.


(Paper 80A3–895)

JOURNAL OF RESEARCH of the National Bureau of Standards—A. Physics and Chemistry
Vol. 80A, No. 3, May–June 1976

# Cancer Detection by NMR in the Living Animal

**I. D. Weisman* and L. H. Bennett**

**Institute for Materials Research, National Bureau of Standards, Washington, D.C. 20234**

**L. R. Maxwell, Sr.**

**5204 Moorland Lane, Bethesda, Md. 20014**

**and D. E. Henson**

**Laboratory of Pathology, National Cancer Institute, Bethesda, Md. 20014**

**(March 6, 1976)**

The purpose of this paper is to review *in vivo* NMR experiments [1, 2] on a transplantable tumor in mice and to discuss the feasibility of using noninvasive NMR for cancer detection in humans.

Key words: Cancer; mice; NMR; spin-lattice relaxation; spin-spin relaxation.

## 1. Introduction

Recently, pulsed nuclear magnetic measurements have been made on biological tissues, with the observation first by Damadian [3, 4][1] and subsequently by others [1, 2, 5–9] that a variety of neoplasms display different spin-lattice ($T_1$) and spin-spin ($T_2$) relaxation times than corresponding normal tissue. These different relaxation times occur with tumors of diverse histologic type, with tumors of human and animal origin, and for tumors transplanted in the live animal or for tumors which have been excised before measurement. Although the physical mechanism of these $T_1$ and $T_2$ values has not yet been determined and is still a matter of controversy, these findings raise the possiblity that the principles and techniques of pulsed NMR might be adapted to detection and diagnosis of cancer without the need for surgical intervention.

The technique utilizes the magnetic resonance properties of the atomic nucleus (in this case protons) when subjected to a steady polarizing magnetic field and radio frequency exciting pulse at the appropriate frequency. Two important processes, spin-lattice relaxation and spin-spin relaxation, characterize the resonant nucleus and are measured in a pulsed NMR experiment. Spin-lattice relaxation is the process in which the spin of the nucleus reaches an equilibrium orientation in the polarizing field after being perturbed by the radio frequency pulse. Spin-spin relaxation is the process in which resonant nuclear spins, initially precessing coherently in the polarizing field, lose synchronization with each other. Both processes are mediated by interactions between the nuclear spin and its static and dynamic atomic environment, which includes motion of other nuclear spins. In simple cases the relaxation processes are each charac-

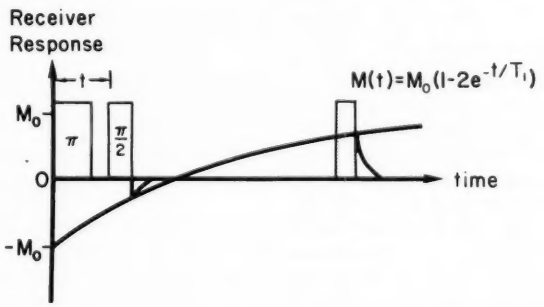


FIGURE 1. *π−t−π/2 pulse sequence for measuring* $T_1$.

* Ph.D. → M.D. Program, University Miami, Florida

[1] Figures in brackets indicate the literature references at the end of this paper.

terized mathematically by a single exponential decay or recovery, in which case a single characteristic time, $T_1$, describes spin-lattice relaxation, and a single time, $T_2$, describes spin-spin relaxation.

Experience suggests that it is often possible to associate a single relaxation time with a particular tissue or tumor. For spin-lattice relaxation measurements using a $\pi - t - \pi/2$ pulse sequence, as indicated in figure 1, the recovery of the nuclear magnetization $M(t)$ as a function of the time $t$ between the two pulses is

$$M(t) = M_0 (1 - 2e^{-t/T_1}) \cdot \quad (1)$$

Frequently the point at which the recovery curve crossed the 0 axis is used for determining $T_1$. This is often referred to as the null-point method.

For spin-spin relaxation, using the Carr-Purcell-Meiboom-Gill (CPMG) pulse sequence, the magnetization $M(t)$ decays with time $t$ according to

$$M(t) = M_0 e^{-t/T_2} \cdot \quad (2)$$

In general, the stronger the interaction between the nuclear spin and other nuclear spins, the shorter the relaxation times. Pure water is an example where eqs (1) and (2) apply and in which a specific value of $T_1$ and of $T_2$ are appropriate. Strong diffusional motion of the protons in water leads to a relatively weak interaction between protons and thus long values of $T_1$ and $T_2$ (2 to 4 s). As discussed below, it is important that the full relaxation curve be measured in both spin-lattice and spin-spin measurements to ascertain if there is a unique $T_1$ or $T_2$ before final conclusions are drawn with regard to the significance of the numbers measure. [1, 2, 10–12].

## 2. NMR Studies on Biological Tissue

### 2.1. Spin-Lattice Relaxation

For biological tissue more than one time constant may be involved because of the complex nature of the specimen. It is thus desirable to generalize eq (1) as follows.

$$M(t) = \sum_{i=1}^{n} M_i(t) = \sum_{i=1}^{n} M_i \, (1 - 2e^{-t/(T_1)i}) \quad (3)$$

where $n$ is the number of different types of tissue in the sample being studied. $M_i$ and $(T_1)_i$ are independent variables; $M_i$ is proportional to the volume of tissue with time constant $(T_1)_i$. $(T_1)_i$ may or may not change with tumor growth. The equilibrium magnetization $M_0 = \Sigma M_i$.

In the event of two or more terms in eq (1) it is necessary to determine the various corresponding values of $T_1$. First it may not be immediately clear as to the value of $n$ and the range of $T_1$'s encountered. For this reason it becomes important to obtain data covering a large range of values for $M(t)$ from $t = 0$ to a time long enough to reduce the signal $M(t)$ until it is comparable with the background noise. The initial signal-to-noise ratio must be high at least 100 to 1. In the case that there is only a small amount of tissue with a long relaxation time, then even this criterion may not be satisfactory. Such a situation would require even weaker signals to be measured and higher signal-to-noise for the combined tissues. Then, using semilogarithmic plots it should be possible to extract the true values of $T_1$. This involves, of course, the corresponding amplitudes that are also unknown *a priori*. It is believed that this type of analysis can be successfully carried out for $n = 2$ and $n = 3$ and possibly for higher values provided that the $T_1$ constants are sufficiently separated. Analysis could result in the detection and identification of one or possibly more neoplasms existing in a host or environment of normal tissue, provided that the individual tissues had different relaxation times, $T_1$. Furthermore, repetitive measurements taken as a function of time can reveal the growth of the tumor as a relative change in the volume of tumor which shows up as an increase or decrease in amplitude $M_i$ associated with the particular $(T_1)_i$ and normal tissue. A change from benign to malignant might be revealed as a change or appearance of a $T_1$ associated with the tumor.

The type of response that would be obtained by the use of $\pi - t - \pi/2$ pulse sequence illustrated in figure 1 has been calculated for single and multiple spin-lattice relaxation times, as shown in figure 2. The assumed values of $T_1$ were 0.3 s and 0.7 s in the various proportions indicated. It is difficult to distinguish, by visual observation, the single-exponential curves (*a* and *e*) from the double-exponential ones (*b*, *c*, *d*). It is obvious that a double-exponential curve cannot be appropriately described by a single spin-lattice relaxation time, but if it is insisted that a single

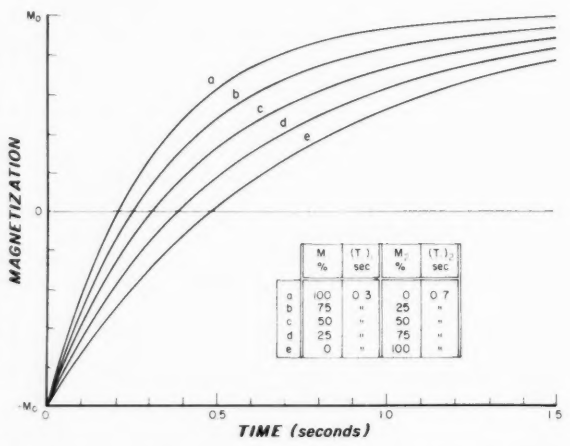


FIGURE 2. *Theoretical curves representing response to the $\pi - t - \pi/2$ pulse sequence illustrated in figure 1 for $T_1 = 0.30$ s, and 0.70 s as single exponentials, and in various combinations as indicated.*

number be assigned, then there are various ways in which this can be done. Some of these ways are given in table 1 which analyzes the $\pi - t - \pi/2$ pulse sequence curves of figure 2 for various combinations of single and double exponential responses for $T_1 =$ 0.3 and 0.7 s. The $1/e$ values derived from the null point are indicated together with the observed $1/e$ values. There is good but not exact agreement between the derived and observed values of $1/e$. It is obvious, however, that the information contained in curves *b*, *c*, and *d* of the two existing time constants of 0.3 and 0.7 s is completely lost.

A useful approach to the analysis of the magnetization recovery of the type shown in figure 2 is to replot the data on semilogarithmic graphs. In figures 3–5, the logarithm of

$$\frac{\Sigma M_i - M(t)}{\Sigma 2M_i}$$

versus $t$ is plotted for various choices of percent of tissue, $M_i$ and their corresponding relaxation time $(T_1)_i$. This procedure may be useful, as indicated in the specific cases described further in this chapter, for analysis of combined tissues and tumors.

In figure 3 theoretical semilogarithmic curves are plotted for the same parameters that were used in the set of curves illustrated in figure 2. There is a progression from a single "fast" exponential for $T_1 = 0.3$ s (curve *a*) to the introduction of a second "slow" exponential for $T_1 = 0.7$ s in increasing amounts (curves *b*, *c*, and *d*) until the single slow exponential

TABLE 1. *Analysis of $\pi - t - \pi/2$ pulse sequence curves of figure 2 for spin-lattice relaxation information*

| Curve No. | Relative amplitudes $M_i$ (%) for | | "$T_1$" values obtained by using various procedures | | |
|---|---|---|---|---|---|
| | $T_1 = 0.3$ s | $T_1 = 0.7$ s | Weighted average[a] | Derived from null point[b] | "Observed" $1/e$ Value[c] |
| a | 100 | 0 | 0.30 | 0.30 | 0.30 |
| b | 75 | 25 | .40 | .35 | .36 |
| c | 50 | 50 | .50 | .43 | .45 |
| d | 25 | 75 | .60 | .56 | .57 |
| e | 0 | 100 | .70 | .70 | .70 |

[a] The weighted average is given by $\dfrac{M_1(T_1)_1 + M_2(T_1)_2}{M_1 + M_2}$.

[b] These values are obtained by dividing the value of $t$ at the null point by the natural logarithm of 2 in analogy with eq (1).

[c] These observed values are obtained by finding the value of $t$ when the magnetization $M(t) = M_0(1 - 2/e)$.

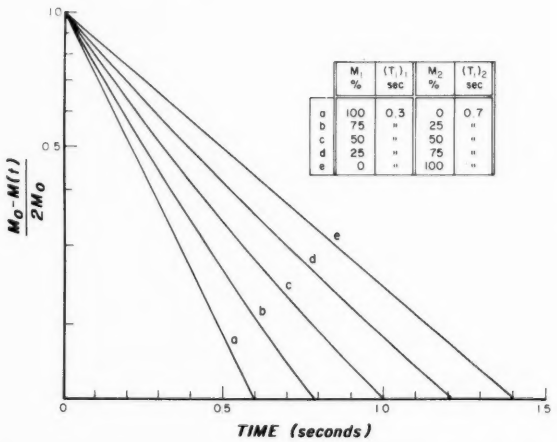


FIGURE 3. *Theoretical exponential curves illustrating changes from a single exponential for $T_1 = 0.3$ s by the introduction of a second exponential with a $T_1 = 0.7$ s in successive strengths until a single exponential for $T_1 = 0.7$ is obtained.*

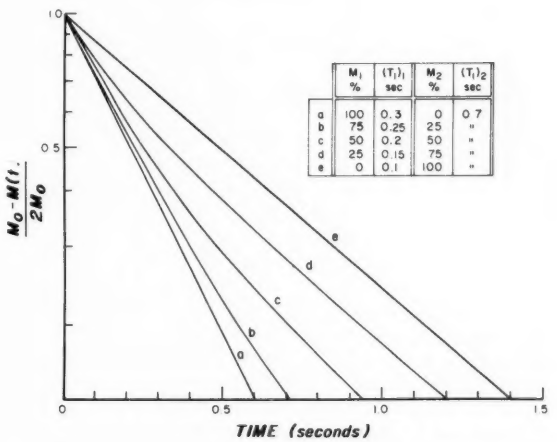


FIGURE 4. *Theoretical exponential curves illustrating a comparison of a single exponential for (a) $T_1 = 0.3$ s and (e) $T_1 = 0.7$ s with combinations of two exponentials (b, c, d) with the values of $T_1$ shown.*

(curve *e*) is reached. In contrast to figure 2b, c, d, the departure from a single exponential response can be discerned in figure 3b, c, d by a simple visual observation. Furthermore, by the use of a straight edge, an approximate estimate can be obtained of the "slow" time constant involved in this figure along with its relative amplitude.

It is clear in the experimental data which we present below in this chapter that there is at least an additional faster relaxation occuring than that associated with the normal tissue. For this reason additional curves have been synthesized to indicate the effect on the spin-lattice relaxation behavior. It would require exceedingly careful measurements, high sensitivity, and data acquisition over a wide time scale to distinguish between relaxation of the types shown in figures 4 and 5.

In figure 4 more than two time constants are introduced, as shown, but still restricting the calculations to two exponentials. The slow component maintains an unchanging value of $T_1 = 0.7$ s. The fast component, however, was made to vary linearly from $T_1 = 0.3$ s for 100 percent fast component to $T_1 = 0.1$ s for zero amplitude. Again the two single exponentials are for $T_1 = 0.7$ and 0.3 s as is readily observed visually.

In figure 5, the time constants $T_1 = 0.3$ s and $T_1 = 0.7$ s are again maintained as the starting and ending single exponentials (curves *a* and *e*), but a third time constant $T_1 = 0.1$ is introduced in varying strengths (curves *b*, *c*, and *d*). Figure 5, as a result, illustrates the relaxation behavior to be expected for tissues with three different time constants and the difficulty in resolving them into their separate exponentials. The similarity of the 3-exponential curves of figure 5 to the 2-exponential curves of figure 4 is striking.

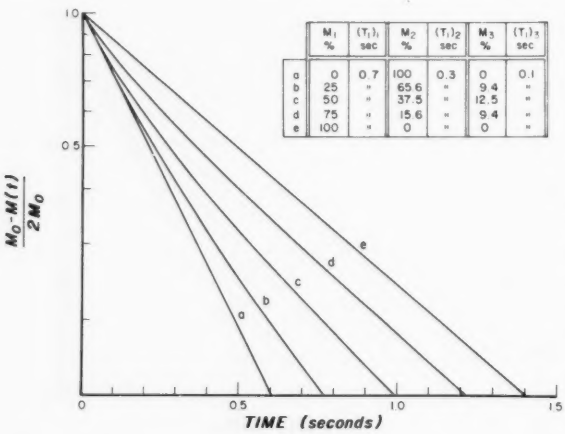


FIGURE 5. *Theoretical exponential curves illustrating a comparison of a single exponential for* $T_1 = 0.3$ *s and* $T_1 = 0.7$ *s with combinations of three exponentials that introduce* $T_1 = 0.3$ *s, 0.7 s with* $T_1 = 0.1$ *s in various proportions.*

### 2.2. Spin-Spin Relaxation

In analogy with the spin-lattice relaxation case the data for spin-spin relaxation might be analyzed in terms of exponentials of the form

$$\frac{M(t)}{M_0} = \sum_{i=1}^{n} A_i e^{-t/(T_2)i} \tag{4}$$

in which $(T_2)_i$ are the component spin-spin times and $A_i$ the corresponding fractional amplitudes which depend upon the amounts of particular tissue with time constants $(T_2)_i$. However, there is evidence [2] that even a tissue that is characterized by a single $T_1$, can not be characterized by a single $T_2$. As in the case of spin-lattice relaxation, it is mathematically possible [10] to analyze the nonexponential part of spin-spin relaxation into $n$ parts each with amplitude $A_i$ and time constant $(T_2)_i$. The analysis to be followed is then similar to that described above for spin-lattice relaxation. It is not clear that the $(T_2)_i$ thus obtained are physically meaningful, but such an analysis into parameters may be useful for monitoring tumor growth. Further work is necessary in order to correlate tumor growth with these parameters.

## 3. Brief Review of *In Vitro* Experiments

Damadian [3] (See also this volume) compared relaxation measurements that he made *in vitro* on various normal and malignant tissues from rats. He reported that the $T_1$ and $T_2$ values obtained by the null and $1/e$ methods respectively were larger in the malignant than in the normal tissues. In some cases these differences were of the order of 10–20 percent, in others factors of 2 or 3. For example, values of $T_1$ for normal tissue from rats varied from 0.3–0.6 s, whereas the $T_1$ values for two typical malignant tissures was in the neighborhood of 0.7–0.8 s. Similarly, the $T_2$ value was about 0.05 s for normal tissue and was 0.1 s for malignant tissue. Note that it was assumed that relaxation was a single exponential in these cases and the values reported were measured using the null method.

Further work has been reported [4] in humans in which $T_1$ measurements on excised normal and malignant tissue have been compared for breast, lung, muscle, skin, and intestine. Again $T_1$ was found to increase in the tumor tissue relative to corresponding normal tissue by factors of 1.5 to 3, with breast showing the biggest difference. A singular exception was found for melanomas where the $T_1$ values were depressed relative to the host tissue (normal lymph node).

Comparisons of $T_1$ and $T_2$ for mammary glands removed from mice by Hazlewood et al. [6] have shown a lengthening of both relaxation times in the preneoplastic nodules and neoplastic tissue relative to normal tissue. In this case full spin-lattice relaxation curves were plotted and found to be described by a single exponential decay. Spin-spin relaxation

was separated from diffusion effects using a measurement technique that did not show the full relaxation curve. The diffusion constants were found to increase along with $T_1$ and $T_2$ in preneoplastic and neoplastic tissues compared to the diffusion constant in normal tissue. This observation supports the model proposed by Damadian in which tumor tissue has less intracellular water structure than normal tissue (hence more diffusion and less interaction between protons and their surroundings resulting in longer relaxation times). The strong interactions between proton spins in normal tissue as evidenced by the measured $T_1$ and $T_2$ being shorter than the corresponding parameters in pure water had been attributed to a majority fraction of bound water molecules [3–5, 13]. Other work [14–18] is not in agreement with this theory of relaxation in normal cells. Some recent work [19] indicates a lack of correlation between diffusion times and spin-lattice and spin-spin relaxation times in normal rabbit lens tissue suggesting that structure or crystallinity of a large fraction of cell water does not account for the observed shortening of relaxation times in tissue relative to ordinary distilled water.

Pulsed NMR studies have also been made on cells in terms of diffusion [20] and of diffusion and molecular exchange [21].

Hollis and coworkers [8, 9] have also found that spin-lattice relaxation times, as measured using the null method, in malignant tumors are in general longer than the corresponding normal tissue. In one study these authors associated differences in tumor growth rates (slow versus fast) with the relative magnitude of $T_1$. For example, the more rapidly growing tumors have the longer $T_1$ values whereas the slower growing tumors tend to overlap the $T_1$ values for normal tissue. Hollis et al. [8] have carried out a more extensive study on a large number of tumors in animals and humans. While the animal tumors showed spin-lattice relaxation times well in excess of those for normal tissues the differences in four human tumors relative to normal tissue was less clear cut. According to these authors it is necessary to explore further the optimization of factors which enhance the relaxation time differences between normal and malignant tissues such as temperature and frequency dependences and a more complete study of the full relaxation curves. They point out that there are alternatives, such as the effect of bound paramagnetic impurities [10], to the mechanism proposed by Damadian (i.e., crystallinity of cellular water) to explain the differences between normal and malignant tissues.

The value of *in vitro* determination is clearly evident from the correlation of the NMR data with neoplasms and non-neoplasms. In addition, such information is then available for *in vivo* studies where applicable. This is obviously important for its use for noninvasive diagonosis of cancer.

Certain limitations exists, however, for *in vitro* applications. An obvious one is concerned with what new and possibly unknown variables are introduced by the incision and the removal of the specimen for examination. In what manner, if any, is the water configuration and behavior altered by this process? It is necessary to make measurements on the same tissue, normal or tumor, before and after removal from the living animal to determine whether in fact there is a difference.

## 4. Neoplasms *In Vivo*

We now report on the investigation which shows that it is possible to detect and monitor the growth of cancer in a live animal by means of nuclear spin-lattice and spin-spin relaxation measurements. Deleterious effects introduced by the removal of the specimen from the host including special preparation of the sample are obviously absent.

Studies on tissue removed from the body have the advantage of selectivity in that the investigator can carefully dissect out the tissue of interest and observe resonances from only its protons. It is a much more difficult task to perform and analyze nuclear magnetic relaxation experiments on live animals because in general many kinds of tissues, only a few of which are of interest) contribute to the resonance signal. It is possible, however, to obtain useful spin-lattice and spin-spin relaxation data from protons in the living animal. For example, such data was obtained by transplanting a Cloudman melanoma into the tails of DBA/2 mice. [1, 2].

One problem is that of sensitivity, i.e. detecting in the human body a relaxation time difference from a relatively small number of malignant cells. It is important to determine, in detail, the time-dependent changes in relaxation that may distinguish between normal and malignant tissues in live animals. For this purpose, it is absolutely essential that the full relaxation curves be examined. Although the motion of the animal contributed to the noise, it was possible to obtain significant data without the use of anesthesia.

### 4.1. Experimental Conditions

Because of the size limitations of the available magnet, it was most convenient to perform this initial experiment on the tail of a mouse, which being long, cylindrical, and narrow, is easily inserted in a small probe. A schematic diagram of a mouse being confined to a small plastic cage is shown in figure 6. The tail is taped to an extension to be inserted in the rf coil. The rf coil is in a probe assembly placed between the poles of an electromagnet, shown in figure 7.

An example of the neoplasm studied is illustrated in figure 8. A Cloudman S91 malignant melanoma was transplanted into the tails of DBA mice. The NMR response of the tumor, as well as the behavior of the immediate and adjoining tissue in the tail, could therefore be ascertained as the tumor grew. Histologically, the Cloudman melanoma is a pleomorphic anaplastic tumor which exhibits extensive areas of necrosis. The necrosis tends to occur centrally while peripherally the tumor contains viable cells which proliferate and

expand the tumor mass (fig. 9). Melanin pigment is not present in the tumor cells. Occasionally in necrotic areas, viable tumor cells remain circumjacent to vascular channels. Clearly, the NMR curves represent contributions from both the viable and necrotic parts of the tumor. In large tumor masses, greater than 60% of the tumor becomes necrotic.

Measurements were made at ambient temperature with a phase-coherent and pulse-coherent 5-kW spectrometer using the laboratory magnet illustrated in figure 7. The amplified nuclear signal voltage fed to the phase detector, was maintained at a value much less than the detector rf reference voltage in order to insure linearity. The magnet was a water-cooled 4 in laboratory electromagnet. Measurements were made at field strengths corresponding to proton frequencies ranging from 8 to 24 MHz. A rotating frame $H_1 \sim 25$G was sufficient to saturate the protons in the mouse tail with a single $\pi$ turning-angle pulse. Either a $\pi - t - \pi/2$ sequence as shown in figure 1 or a $\pi - t -$ echo sequence in which the echo-forming pulses had a spacing$\ll T_1$, was used to measure $T_1$. For the measurements of $T_2$, a Carr-Purcell-Meiboom-Gill sequence consisting of a $\pi/2$ pulse followed by a chain of $\pi$ pulses (phase shifted by $\pi/2$ with respect to the first pulse) was employed. In order to avoid nonexponential behavior associated with diffusion in a magnetic field gradient, the $\pi$ pulses were kept closely spaced ($\sim 1$ ms apart). Signal averaging was accomplished with a gated integrator and with a digital signal averager. In many experiments the data gathering and storage was automated. In this arrangement recording of spin-lattice relaxation could be accomplished quite simply. The pulse sequence programmer would sequentially advance the delay between the $\pi$ saturating pulse and

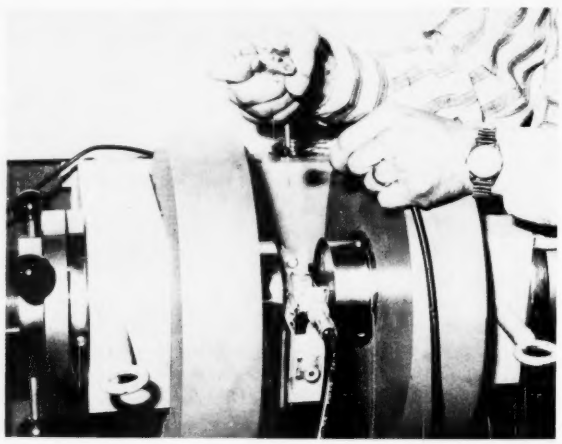

FIGURE 7. *Laboratory electromagnet used for* in vivo *pulsed NMR experiment. RF coil around tail of mouse is for illustration only.*

Actual coil used in study must be shielded against RF leakage and hence would be unobservable when probe is in place.

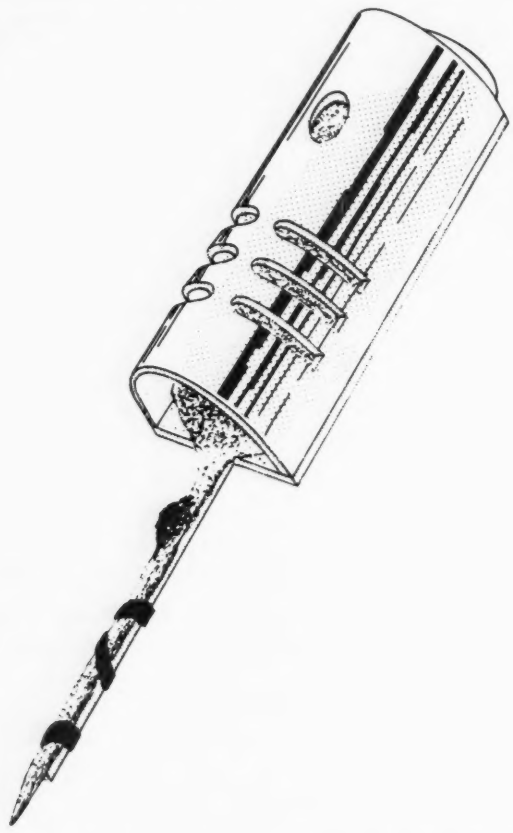

FIGURE 6. *A diagramatic sketch showing the arrangement used for holding mouse with Cloudman S91 tumor in the tail to reduce motion of the animal.*

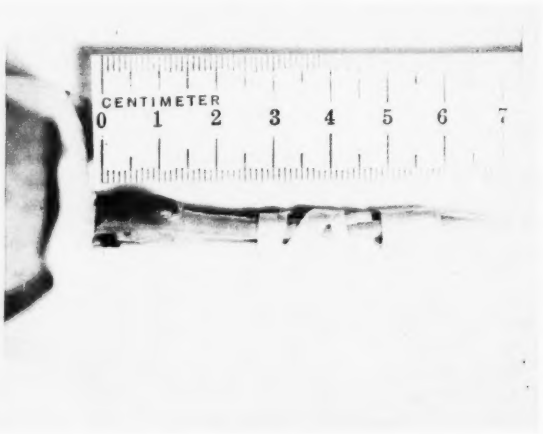


FIGURE 8. *Typical tumor on tail of DBA mouse.*

The mouse is in the small cage at the left (obscured).

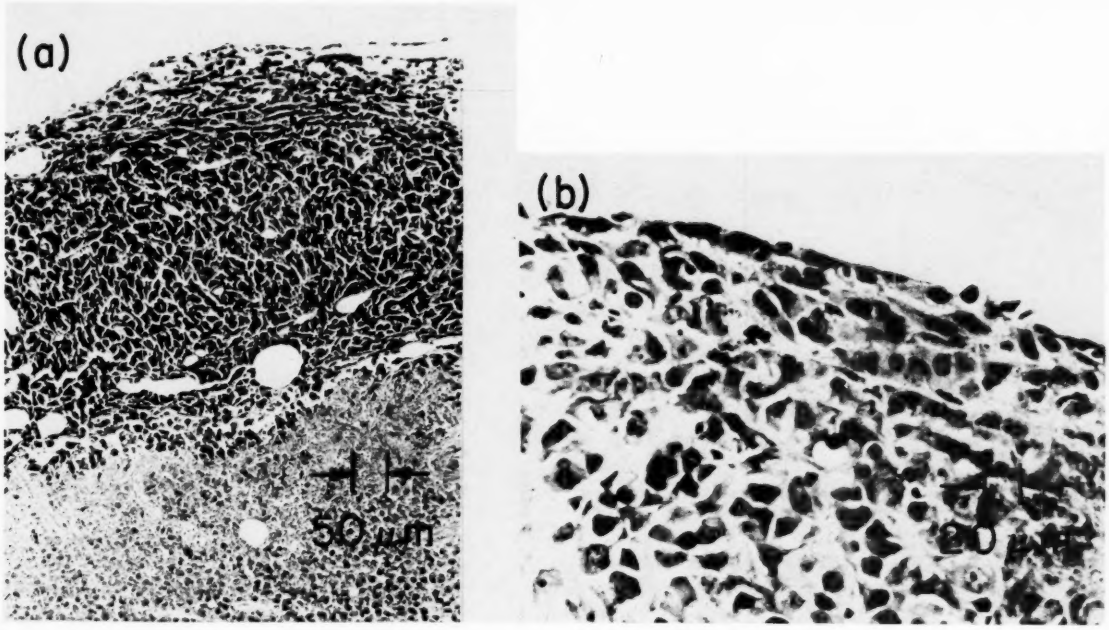


FIGURE 9. *Microphotographs of section through periphery of Cloudman melanoma. Hematoxylin and Eosin stains.*

(a) Rim of viable tumor cells beneath which is an area of necrosis. (b) Viable cells at edge of tumor showing pleomorphic cells with no specific pattern.

echo monitoring signal a small increment of time $\Delta t$ with each repetition of the $\pi - t -$ echo sequence. The echo amplitude corresponding to each spacing $t$ was stored synchronously in an appropriate channel of a signal averager. By repetitively recycling the programmer, many sweeps through the full spin-lattice relaxation (with 100 point resolution) could be added together and appropriate relaxation times derived.

In the case of spin-spin relaxation the signal averager was externally advanced in synchronism with the pulse programmer so as to sequentially store the echo amplitudes appearing between 180° pulses in the Carr-Purcell chain. Many repetitions of the chain were averaged together to obtain the transverse relaxation curve.

### 4.2. Spin-Lattice Relaxation

There exists a distinct difference between the spin-lattice relaxation behavior of normal tail and of melanoma tissue in the mice. The spin-lattice relaxation was measured on the tails of a number of normal mice and in every such case was found to be characterized by a single time $T_1$. The value of $T_1$, depended on frequency or magnetic field, as shown in figure 10. Similar frequency dependence was reported for *in vitro* measurements by Outhred and George [18], and for higher frequencies by Damadian et al. [4]. The latter results are shown in figure 11, where an increase in $T_1$ was found for increasing frequency, both for neoplasms and for control tissue.

The scatter shown for our data (fig. 10) may be in part instrumental, since it includes results obtained before automation of the data gathering and storage, but it also may be due to biological variability.

In protein solutions $T_1$ was found [22, 23] to be dependent upon frequency as well as other parameters such as temperature and existing paramagnetic properties. $T_1$ was found to decrease markedly with decreasing frequencies below 2 MHz.

Just as the spin-lattice relaxation was exponential for normal tissue, so it was exponential for a well-developed melanoma, as is evident from figure 12, where the data extends over two orders of magnitude. The relaxation time associated with the tumor is about twice that of the normal tail, for each frequency (see fig. 10).

The relaxation behavior was investigated for several growing tumors. The time for tumor development in the tails was from 1 to 3 months. If the data were treated as if it were a single exponential, then a "$T_1$" would be obtained, whose value increases as the size of the tumor increases. This method of obtaining a "$T_1$" would correspond to the procedures illustrated in table 1 and might be a weighted average. It is better however to analyze the relaxation behavior into two, or perhaps three, relaxation times, as explained in conjunction with figures 3–5. This preferred procedure leads to a constant $T_1$ for the tumor as it grows.

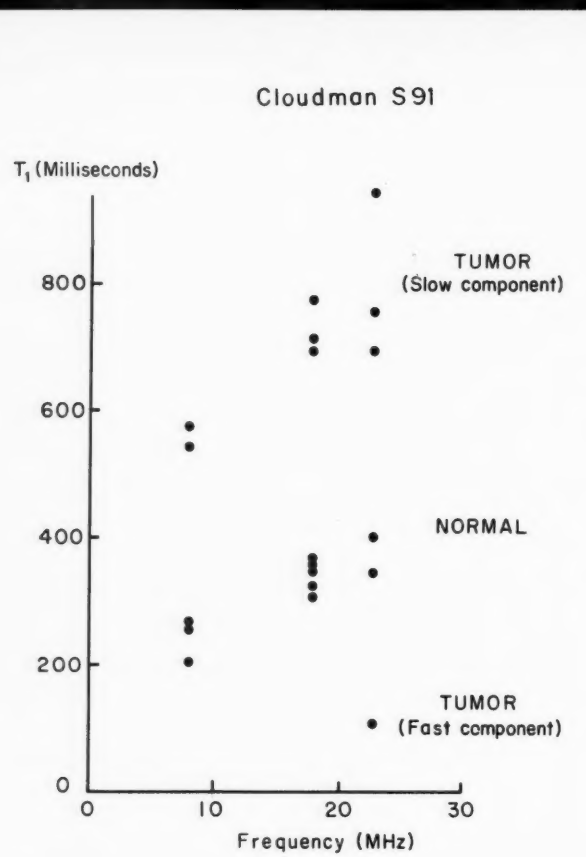


FIGURE 10. *Frequency dependence obtained for Cloudman S91 tumor and normal tissue* in vivo.

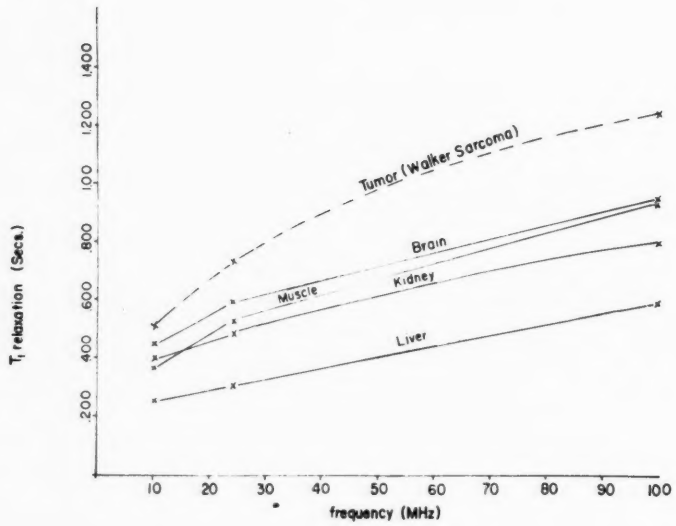


FIGURE 11. *Frequency dependence of* $T_1$ *in tumors and control tissue in vitro by Damadian et al.* [4]

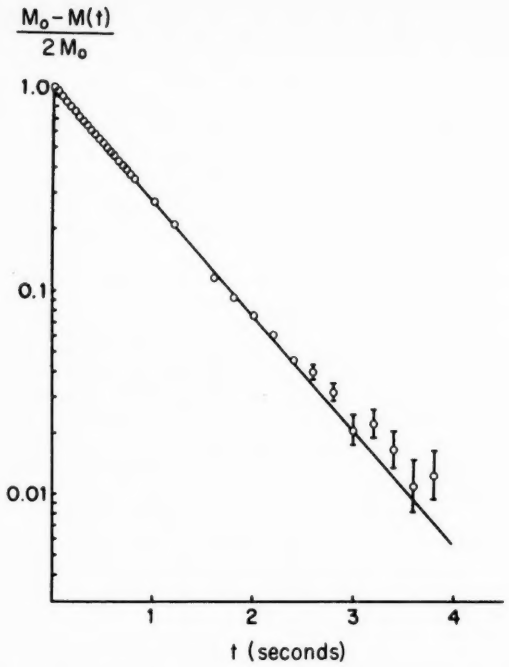


FIGURE 12. *Spin-lattice relaxation from mouse tail with well-developed (86 days after implantation) melanoma.*

Best straight line fit is shown and corresponds to $T_1$ of 0.78 s.

As an example of such an analysis, consider the case, shown in figure 13, where the tumor in the tail was necrotic and extended into the adjoining tail. The measurement was made with the rf coil surrounding the tail at the position of the arrow. The results are shown in figure 14. A "best" straight line to the data

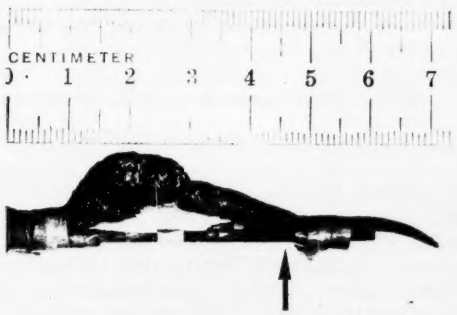


FIGURE 13. *Tumor in tail of mouse, Cloudman S91 in advanced stage with tumor extending beyond original site into normal tissue.*

Arrow indicates region where measurements were made.

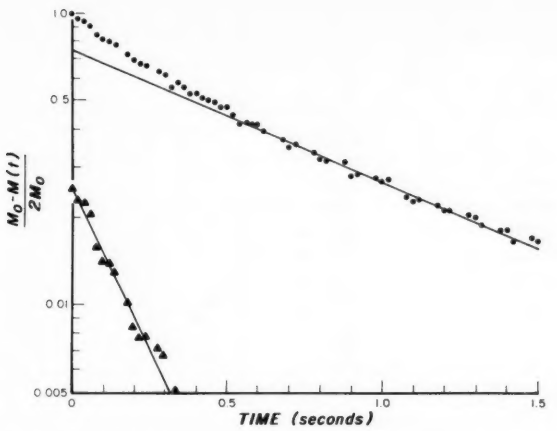


FIGURE 14. *Spin-lattice relaxation of mouse with extended tumor illustrated in fig. 13.*

The data points are shown as solid circles, with the straight line defining a single slow exponential response. A fast single relaxation (triangles) is obtained, as described in the text.

for times $>0.3$ sec establishes the slow relaxation at about $0.95 \pm 0.10$ s. The fast relaxation can then be obtained by subtracting out the slow relaxation component and replotting the difference. The result is about $0.20 \pm 0.05$ s. The data are not good enough in this case to attempt to analyze the fast component further into two times. The fast time then is either a change in the "normal" tissue near the tumor or an average between the normal tissue value of 0.35 to 0.40 s and a faster relaxation time associated with the tumor. We favor this latter interpretation, and a value of about 0.11 s at 23 MHz appears to be appropriate from data we have shown elsewhere [2] for the "fast" component associated with the tumor. We discuss below the experiments necessary to relate the relaxation times to the appropriate cells. For example, can the slow relaxation component of the tumor be associated with the necrotic cells of figure 9, while the fast component corresponds to the viable cells, or is some other explanation correct?

### 4.3. Spin-Spin Relaxation

Spin-spin relaxation curves, *in vivo*, measured for normal and for tails with transplanted tumors are shown in figure 15. The data in figure 15a were obtained from the tail of a normal mouse. The tumor in the tail was monitored at regular intervals from the time that tumor growth was visible to the naked eye (67 days after transplanting) until the tumor was 2 cm in diameter (compared to the normal tail diameter of $\sim 0.5$ cm). In contrast to the spin-lattice relaxation case, the spin-spin relaxation is seen to be more complex: a fit to the normal mouse data of figure 15a requires a superposition of 3 or more exponentials of the form of eq (4). Well-developed tumor relaxation remains complicated although fewer terms are required for fitting than for a normal tail. For example, in

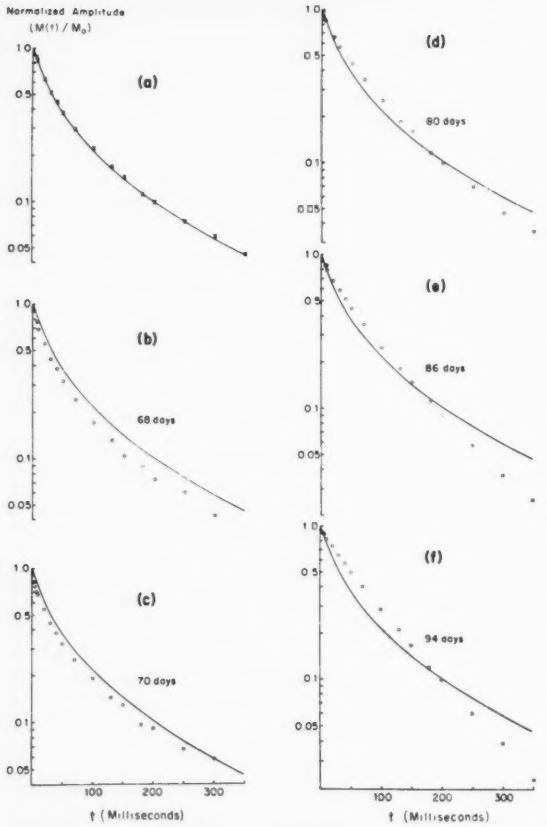


FIGURE 15. *Normalized spin-spin relaxation at 23 MHz in sequence of increasing melanoma size.*

The effects of magnetic field gradients were minimized by using closely spaced (2 ms) pulses. Solid curve in (a) is fit to data from normal tail. In (b)-(f) the open circles are data taken from tail with melanoma as it increased in size. The solid curve represents superimposed normal data from (a) for visual comparison.

figure 15 (d, f) the initial decay of the well-developed tumor is less rapid than the corresponding part of the normal curve whereas the slope of the tumor curve at long times is more rapid than the same portion of the normal curve. Taking the 1/*e* point of the normal curve gives the number shown in table 2, but this sheds little light on the nature of the normal relaxation. The intermediate curve, representing tumor growth at 70 days after transplantation deviates from simple exponential behavior even more than the normal curve. Spin-spin relaxation actually again resembles the normal curve at about 74 days (not shown). Although the curves of figure 15 are not single exponentials, even by the normal tissue, table 2 was prepared to shown the loss of information accompanying conventional 1/*e* data. For early stages of the tumor the 1/*e* value was slightly less than the normal while for the latter stages the 1/*e* became greater than the normal. The usual larger difference found between tumor and normal is clearly absent. This is not surprising in view of the complexity of the responses observed.

TABLE 2. *Spin-spin relaxation values obtained by the* 1/e *procedure for Cloudman S91 from the curves illustrated in figure 15*

| | | "$T_2$" (ms) |
|---|---|---|
| Normal | | 52.5 |
| Tumors | 68 days | 40 |
| | 70 days | 42.5 |
| | 80 days | 65 |
| | 86 days | 65 |
| | 94 days | 77.4 |

### 4.4. Further Work Needed on Mice

The studies on the tails of mice discussed above should be extended to transplantable sarcomas, lymphomas, and carcinomas. The correct assignment should be made of relaxation times of the appropriate tissue in the tails of live mice. This would involve measuring spin-lattice and spin-spin relaxation of protons in the tails of the live animals as the tumor develops. Then, at various stages of development, animals would be sacrificed and the tumors should be taken for pathological and further NMR examination. All NMR measurements should be accompanied by pathological examination and perhaps by measurements of the water content. If it is then determined by following this procedure that the behavior in the live animal is, in fact, the sum of the behavior for representative tissues examined by NMR outisde the body, then the information available from experiments on tissues removed from the animal may be utilized to detect and monitor many tumors in the live animal, without detailed repetition of the *in vitro* standardization procedure for each case.

The Cloudman melanoma S91 contains both necrotic and viable cells which introduces the question as to whether the relaxation times, both $T_1$ and $T_2$, are different for these cells. In fact are the data given here for the tumor representative of one or the other or some average of the two? This introduces a new scope to NMR investigation to study both the necrotic and viable regions of the tumor separately and to compare the results between the two regions and with normal cells.

## 5. New Measurement Techniques

### 5.1. Probe Design

A surface type of NMR probe could be used for monitoring, in live animals and humans, tumors that are not accessible to the conventional geometry NMR probes, such as general body cavity tumors (including breast and liver tumors). A surface type of probe is not a standard item in NMR spectroscopy. A flat coil may serve as a probe for NMR detection on a surface layer near the coil. The sensitivity would be very low because of the gross inhomogeneous distribution of radio frequency magnetic fields over the region of interest from a single planar coil. It should be possible, however, to design the winding so as to focus a homogeneous rf magnetic field into a relatively small region

(<1/2 cubic centimeter) which would produce a considerable improvement in sensitivity. If such a surface probe design is successful, consideration should then be given to designing a scanning type of spectrometer (where the probe is slowly moved over the volume of interest) to search for tumors perhaps as deep as an inch below the surface of the skin.

We feel that ultimately, the use of NMR as a diagnostic tool depends on the successful use of a surface probe.

### 5.2. NMR Zeugmatography

In the area of techniques of measurement, there is a new development involving NMR in a magnetic field gradient which offers promise in its ability to map our the spatial extent of differing nuclear environments in various materials, including biological tissues. This technique has been called NMR "diffraction" [24] or NMR zeugmatography [25, 26]. Whether this technique can supplement the development of a surface probe, as discussed above, requires further investigation.

## 6. Discussion

There have been several explanations given to account for the differences in proton spin-lattice and spin-spin relaxation between living tissue (normal and tumor) and in water. We have not focused on mechanisms here because we were more interested in utilizing of the relaxation time difference between normal and tumor tissue for possible *in vivo* diagnosis of cancer in humans.

An important question remains to be answered for both normal and malignant tissue:

Does tissue spin-lattice and spin-spin relaxation behave the same in the live animal as in the biopsied tissue [27]?

It is important to establish the correspondence between relaxation in the component tissues and relaxation in the tissues acting collectively in the body because this knowledge simplifies the search for subtle changes in the relaxation that may signal early signs of tumor growth. It may also be possible to monitor tumor behavior after treatments such as radio- or chemotherapy.

Our ultimate goal is to apply NMR for the diagnosis of primary and metastatic cancer in humans without the necessity of surgical intervention. For example, NMR might be used to determine if metastatic tumor exists in the axillary lymph nodes upon discovery of a cancer in the breast. For this reason some precautions and thought should be given to the possibility of any adverse effects that might arise during conventional use of NMR on humans of all ages. The influences of the D.C. and A.C. magnetic fields are of possible concern.

It has never been shown that constant D.C. magnetic fields even to high field strengths, greater and of longer duration than that used for NMR, are injurious. There are some reports [28] however, of detectable effects of D.C. magnetic fields on biological organisms but even these reports are not generally accepted.

Of greater concern are the possible side effects of the alternating electromagnetic fields. The harmful effects (e.g. heating) of rf fields [28] are greater at higher frequencies, and thus it is favorable that the frequencies at which the NMR would be performed are definitely below the microwave range where some damage has been shown to occur. Another favorable aspect of the pulsed NMR is that the average power expended is low. In critical regions, special shielding could be used to protect nearby parts from the A.C. radiation.

---

We are grateful to Dr. D. Burk and Dr. M. W. Woods of the National Cancer Institute for their participation in the *in vivo* studies reported in this chapter, to C. M. Mladen for his assistance in the synthesis and analysis of data and to R. L Parke for important technical aid with the measurements.

## 7. References

[1] Weisman, I. D., Bennett, L. H., Maxwell, L. R., Sr., Woods, M. W., and Burk, D., Recognition of cancer in vivo by nuclear magnetic resonance, Science, **178**, 1288–1290 (1972).

[2] Weisman, I. D., Bennett, L. H., and Maxwell, L. R., Sr., In vivo NMR relaxation studies of tumors, IEEE Transactions on Magnetics, **MAG–9**, 454–456 (1973).

[3] Damadian, R., Tumor detection by nuclear magnetic resonance, Science, **171**, 1151–1153 (1971).

[4] Damadian, R., Zaner, K. S., and Minkoff, L. Invited Talk to the New York Academy of Sciences–International Conf. on Electron Spin Resonance and Nuclear Magnetic Resonance in Biology and Medicine, December 4–8, 1972. See also Damadian, R., Zaner, K., Hor, D., DiMaio, T., Minkoff, L., and Goldsmith, M., Nuclear magnetic resonance as a new tool in cancer research: human tumors by NMR, Annals N.Y. Acad. Sci. **222**, 1048–1076 (1973). Also Damadian, R., Zaner, K. S., Hor, D., and DiMaio, T., Human tumors detected by nuclear magnetic resonance, Proc. Nat. Acad. Sci. **71**, 1471–1473 (1974). Damadian, R., Zaner, K., Hor, D., and DiMaio, T., Human tumors by NMR, Physiol. Chem. and Phys. **5**, 381–402 (1973).

[5] Chang, D. C., Rorschach, H. E., Nichols, B. L., and Hazlewood, C. F., Pulsed NMR studied on water in biological tissues, Bull. Am. Phys. Soc. Series II, **17**, no. 3, 328 (1972) and Spin Echo Studies on Cellular Water, Nature, **235**, 170–171 (1972).

[6] Hazlewood, C. F., Chang, D. C., Medina, D., Cleveland, G., and Nichols, B. L., Distinction between the preneoplastic and neoplastic state of murine mammary glands, Proc. Nat. Acad. Sci. USA **69**, no. 6, 1478–1480 (1972).

[7] Iijima, N., Yoshida, Y., Fujii, N., Koike, T., Osanai, K., and Hayashi, S., Spin echo nuclear magnetic resonance in cancerous tissue, IEEE Transactions on Magnetics, **MAG–8**, 415 (1972).

[8] Hollis, D. P., Economou, J. S., Parks, L. C., Eggleston, J. C., Saryan, L. A., and Czeisler, J. L., Nuclear magnetic resonance studies of several experimental and human malignant tumors, Cancer Research, **33**, 2156–2160 (1973).

[9] Hollis, D. P., Saryan, L. A., and Morris, H. P., A nuclear magnetic resonance study of water in two Morris hepatomas, Johns Hopkins Medical Journal, **131**, 441–444 (1972).

[10] Swift, T. J., and Fritz, O. G., A proton spin-echo study of the state of water in frog nerves, Biophys. J., **9**, 54–59 (1969).

[11] Hazlewood, C. F., Nichols, B. L., and Chamberlain, N. F., Evidence for the existence of a minimum of two phases of ordered water in skeletal muscle, Nature, **222**, 747–750 (1969).

[12] Hazlewood, C. F., Chang, D. C., Nichols, B. L., and Woessner, D. E., Nuclear magnetic resonance transverse relaxation times of water protons in skeletal muscle, Biophys. J. **14,** 583–606 (1974).

[13] Cope, F. W., Nuclear magnetic resonance evidence using $D_2O$ for structured water in muscle and brain, Biophys. J. **9,** 303–308 (1969).

[14] Finch, E. D., Harmon, J. F., and Muller, B. H., Pulsed NMR measurements of the diffusion constant of water in muscle. Archives of Biochemistry and Biophysics, **147,** 299–310 (1971).

[15] Bratton, C. B., Hopkins, A. L., and Weinberg, J. W., Nuclear magnetic resonance studies of living muscle, Science, **147,** 738–739 (1965).

[16] Woessner, D. E., Snowden, B. S., Jr. and Chiu, Y. C., Pulsed NMR study of the temperature hysteresis in the agar-water system, J. of Colloid and Interface Sci. **34,** 283–289 (1970).

[17] Woessner, D. E., and Snowden, B. S., Jr., Pulsed NMR study of water in agar gels, J. of Colloid and Interface Sci. **34,** 290–299 (1970).

[18] Outhred, R. K., and George, E. P., Water and ions in muscle and model systems, Biophys. J. **13,** 97–103 (1973).

[19] Neville, M. C., Patterson, C. A., Rae, J. L., and Woessner, D. E., Carbonate ion-selective membrane electrode, Science, **184,** 1072–1074 (1974).

[20] Cooper, R. L., Chang, D. B., Young, A. C., Martin, C. J., and Ancker-Johnson, B., Restricted diffusion in biophysical systems: experiment. Biophys. J. **14,** 161–177 (1974).

[21] Walter, J. A., and Hope, A. B., Nuclear magnetic resonance and the state of water in cells, Prog. in Biophysics and Molecular Biology, **23,** 3–20 (1971).

[22] Koenig, S. H., and Schillinger, W. E., Nuclear magnetic relaxation dispersion in protein solutions, H. J. Biol. Chem. **244,** 3283–3289 (1969).

[23] Koenig, S. H., and Schillinger, W. E., Nuclear magnetic relaxation dispersion in protein solutions, II, J. Biol. Chem. **244,** 6520–6526 (1969).

[24] Mansfield, P., and Grannell, P. K., NMR 'diffraction' in solids, J. Phys. C: Solid State Phys., **6,** L422–L426 (1973).

[25] Lauterbur, P. C., Image formation by induced local interactions: examples employing nuclear magnetic resonance, Nature, **242,** 190–191 (1973).

[26] Lauterbur, P. C., Stable isotope distributions by NMR zeugmatography, Proc. of the First International Conference on Stable Isotopes in Chemistry, Biology, and Medicine, May 9–11, Argonne National Laboratory, CONF.–730525. 255–260 (1973).

[27] Barroilhet, L. E., has recently reported (private communication) that a significant difference in $T_1$ occurs when a test specimen undergoes a change from *in vivo* to *in vitro*.

[28] Pressman, A. S., Electromagnetic Fields and Life, Translated from Russian by F. L. Sinclair, Edited by F. A. Brown, Jr., (Plenum Press, New York–London, 1970).

(Paper 80A3–896)

JOURNAL OF RESEARCH of the National Bureau of Standards—A. Physics and Chemistry
Vol. 80A, No. 3, May–June 1976

# Modulus of Natural Rubber Cross-Linked by Dicumyl Peroxide III. Some Molecular Interpretations, Possible Refinements of Theory, and Conclusions

**Lawrence A. Wood**

**Institute for Materials Research, National Bureau of Standards, Washington, D.C. 20234**

**(March 6, 1976)**

The shear modulus $G = 5.925 \times 10^{-3}(fp - 0.45)T + G^*$ (Part I), its energy component $G^* = 0.0684(fp - 0.45) + 2.70$ (Part II), and the number of effective sub-chains per unit volume $\nu_e = (G - G^*)/RT$ are given detailed molecular consideration. $G$ is given in Mdyn cm$^{-2}$ for rubber cross-linked by adding $p$ parts of dicumyl peroxide per hundred of rubber, and heating until a fraction $f$ of the peroxide is decomposed. $\nu_e$ is found to be approximately twice the density of cross-links, after a correction for impurities and chain ends is made. It can not be computed as $G/RT$, since only the entropy component of modulus is related to $\nu_e$. The sub-chains for the most highly cross-linked rubbers studied had a molecular weight of about 575 g mol$^{-1}$, corresponding to about 8 isoprene units. The modulus corresponding to no added cross-links is not zero. It is determined chiefly by the energy component of the modulus; it does not arise from entanglements. The "front factor" is found to be unity.

An extensive literature survey yields values of the quantity $RT\Psi(v_2)$, where $\Psi(v_2)$ is the Flory-Rehner equation function of $v_2$, the equilibrium volume fraction obtained by swelling the cross-linked rubber. $RT\Psi(v_2)$ is found to be greater than $G - G^*$, but not as large as $G$ itself.

Key words: Cross-linking of rubber; dicumyl peroxide; elasticity theory of rubber; entanglements in rubber; gel point; molecular interpretation of rubber elasticity; modulus of rubber; rubber elasticity; statistical theory of rubber elasticity; swelling of rubber network.

## 1. Introduction

The first paper in this series Part I [1][1] presented experimental data on the change of modulus with temperature and cross-linking for natural rubber cross-linked by dicumyl peroxide.

The results were presented in the form of the following equation:

$$G = S(fp + B)T + H(fp + B) + A = 5.925 \times 10^{-3}(fp - 0.45)T + 0.0684(fp - 0.45) + 2.70 \qquad (1.1)$$

$S$, $B$, $H$, and $A$ are constants having the values shown, while $G$ is the shear modulus (limit of the ratio of shear stress to strain at zero deformation, in Mdyn cm$^{-2}$ or 0.1 MPa) at a temperature $T$ in kelvins, for natural rubber cross-linked by adding $p$ parts of dicumyl peroxide per hundred of rubber (phr) and heating until a fraction $f$ of the peroxide was decomposed. The actual behavior of the system at very low degrees of cross-linking deviated from that given by the equation, and is discussed in a later section of the present paper.

The second paper Part II [2] applied thermodynamical considerations to the experimental results to determine the relative importance of $G^*$ $(= H(fp + B) + A)$—the energy component of the modulus—and $(G - G^*)$—the entropy component. The experimental entropy component was then compared with that predicted by the statistical theory of rubber elasticity in an extremely simplified presentation.

The general concepts outlined in the books of Flory [3], Treloar [4], and Ferry [5] were utilized, largely using the form and symbolism employed in the book by Meares [6].

The present paper makes much more detailed molecular interpretations of the results than the second paper and examines the consequences of several refinements which might be made in the application of the theory.

## 2. Molecular Interpretations

### 2.1. The Gel Point

The gel point or degree of cross-linking just neces-

[1] Figures in brackets indicate the literature references at the end of this paper.

sary for the formation of a network has been determined experimentally in Parts I and II by noting the degree of cross-linking at which there is no change of modulus with temperature (i.e., $\partial G/\partial T = 0$). At lower degrees of cross-linking this derivative is negative, as normally observed for uncross-linked polymers [7–9]. At higher degrees it is positive, as is normal for cross-linked polymers.

The gel point is reached only when the cross-linking has attained some characteristic value. In the present study it was found experimentally that 0.45 phr of dicumyl peroxide must be added to attain the proper degree of cross-linking. Some of this represents dicumyl peroxide wasted by reaction with impurities in the rubber, and the remainder is required to produce, on the average, one cross-link per rubber molecule.

Our calculations of the relative sizes of these components have been based on an assumption regarding the amount of impurities in the rubber. However, the total amount of added dicumyl peroxide required in our work is 0.45 phr regardless of the relative sizes of the components and regardless of the value of the constant $H$ in eq (1.1)

No attempt was made in Part II in the section dealing with the theory of rubber elasticity to predict a value for $G^*$, the modulus of the rubber at the gel point. The theory was used to predict only $G - G^*$, the increase of modulus caused by the addition of active sub-chains beyond this critical amount of cross-linking.

The modulus of the network at the gel point at all temperatures in the present study is found by direct experiment to be equal to $A = 2.70$ Mdyn cm$^{-2}$ regardless of whether the constant $H$ is zero, as in eq (1.2) of Part II; or 0.0684 Mdyn cm$^{-2}$ (phr)$^{-1}$ as in eq (1.1) of Part II (eq (1.1) of this paper).

The statement may be readily verified by an examination of figure 2 of Part II. The modulus at the gel point is likewise independent of the value assumed for the dicumyl peroxide wasted by reaction with impurities, although this is one of the factors determining the abscissa of the gel point.

It is quite surprising that many previous workers have generally neglected consideration of the gel point and its effects on modulus. Most authors, with certain notable exceptions [10–18] have even failed to mention its existence. Charlesby [12] has given one of the most extensive discussions of the subject.

The nonzero value of the modulus near the gel point has likewise not been clearly demonstrated previously, although the experimental evidence has been available.

### 2.2. Alternative Methods of Expressing Added Cross-Linking and Related Quantities

In Parts I and II, the amount of added cross-linking has been expressed in terms of the quantity $fp$, since that is the independent variable directly observed experimentally. It is of course pertinent only to the system of natural rubber cross-linked by dicumyl peroxide. For comparison with other systems and other measured properties the cross-linking can be alternatively expressed in terms of other quantities also closely related to $X$, the number of added cross-links.

Utilizing the numerical values found in Part I for the constants, we shall give the expression for calculating each of these quantities in turn in terms of the quantity $fp$. For convenient reference all the numerical values used in the present paper are summarized in the Appendix. Some of the new expressions have a greater significance in terms of molecular considerations than those using $fp$. However, the values are dependent on the validity of the theory outlined in Part II and on the constants which have been determined from it. Some of the values of course apply only to the particular sample of rubber studied here. Unlike $fp$, the values considered here are not directly observable quantities.

One of the most fundamental of these quantities is $X/N$, the number of added cross-links per rubber molecule. With the insertion of the values of:

$fw$ (amount of dicumyl peroxide wasted by reaction with impurities)
$M$ (average molecular weight of uncured rubber), and
$M_d$ (molecular weight of dicumyl peroxide)
eq (3.7) of Part II becomes

$$X/N = (M/100M_d)\ (fp - fw) = 7.14\ (fp - 0.31). \tag{2.2.1}$$

Table 1 shows values of $X/N$ calculated from this equation for values of $fp$ up to 23.8 phr, the highest degree of cross-linking reached in the present study. It will be noted that there is one added cross-link per molecule at the gel point ($fp = 0.45$ phr) as expected. At the highest cross-linking, there are 168 cross-links per molecule on the average.

The cross-linking can also be expressed in terms of the number of moles of unwasted decomposed dicumyl peroxide per unit volume, which has been assumed to be the same as the number of moles of added cross-links per unit volume. This quantity is found from eq (3.6) of Part II to be

$$X/(A_1 V_r) = [1/(100 M_d \bar{v}_r)]\ [fp - fw] =$$

$$33.399(fp - 0.31) \times 10^{-6} \tag{2.2.2}$$

where $A_1$ is Avogadro's Number, $V_r$ the volume of rubber considered and $\bar{v}_r$ the specific volume of the rubber.

The values are given in table 1 in units of $\mu$mol cm$^{-3}$—numerically equal to the SI units of mol m$^{-3}$.

This quantity may also be weritten as $(1/2)\bar{v}_r^{-1} M_{c\,chem}^{-1}$ where $M_{c\,chem}$ is the molecular weight of a sub-chain (i.e., between cross-links), as determined from stoichiometry. Thus

$$(1/2)\, M_{c\,chem}^{-1} = (1/100M_d)\,(fp - fw)$$

$$= 36.986\ (fp - 0.31) \times 10^{-6} \tag{2.2.3}$$

Values calculated from this equation are also shown in table 1.

TABLE 1.—*Calculated measures of added cross-linking*

| *fp* phr | *X*/*N* added cross-links per molecule | $X/(A_1V_r)$ μmol added cross-links per cm³ | $(1/2)\,\bar{M}_{c\,chem}^{-1}$ μmol g⁻¹ | $M_{c\,chem}$, mol wt between added cross-links g mol⁻¹ |
|---|---|---|---|---|
| 0 | | | | |
| .31 | 0 | 0 | 0 | ∞ |
| .45 | 1.00 | 4.68 | 5.18 | 96,500 |
| 1 | 4.93 | 23.0 | 25.5 | 19,610 |
| 2 | 12.1 | 56.4 | 62.5 | 8,000 |
| 3 | 19.2 | 89.8 | 99.5 | 5,030 |
| 4 | 26.3 | 123 | 136 | 3,680 |
| 5 | 33.5 | 157 | 173 | 2,890 |
| 10 | 69.2 | 324 | 358 | 1,400 |
| 15 | 105 | 491 | 543 | 921 |
| 20 | 141 | 658 | 728 | 687 |
| 23.8 | 168 | 784 | 869 | 575 |

At the highest cross-linking the molecular weight of an average sub-chain is seen to be 575 g mol⁻¹. Each average sub-chain would thus be made up of 8.44 isoprene units and would contain about 34 main-chain carbon atoms.

For comparison with cross-linking produced by systems other than dicumyl peroxide the quantity $X/(A_1V_r)$, the number of moles of added cross-links per unit volume of rubber is preferred. This is shown in figures 1, 2, and 3 as the upper scale of abscissas.

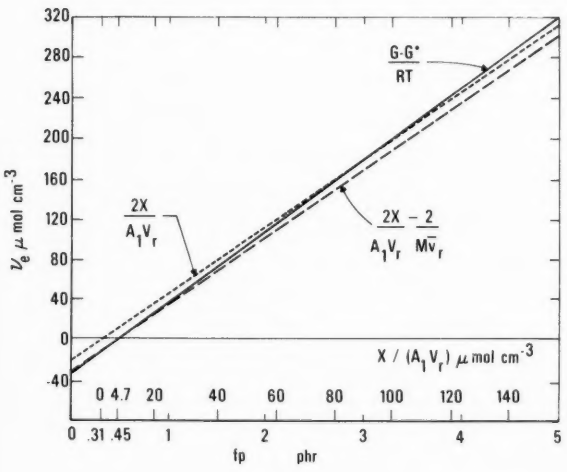


FIGURE 1. *Effective sub-chain density (moles of effective sub-chains per unit volume) as a function of amount of decomposed dicumyl peroxide or as a function of added cross-linking.*

——— Continuous line represents eq (2.3.2)

..... Dotted line corresponds to 2 sub-chains for each added cross-link, uncorrected for chain ends.

- - - - - Dashed line represents eq (2.3.1).

Lower scale of abscissas shows values of *fp* for system of natural rubber cross-linked by dicumyl peroxide.

Upper scale of abscissas shows number of moles of added cross-links per unit volume $X/(A_1V_r)$ or $1/2\bar{v}_r^{-1}\bar{M}_c^{-1}{}_{chem}$, derived from eq (2.2.2).

### 2.3. Number of Effective Sub-chains

Aside from the energy component of the modulus, the fundamental quantity governing the physical properties of the cross-linked network is the number of effective sub-chains. This may be expressed in terms of the calculated number of effective sub-chains per molecule, $(2X/N-2)$, given in table 2 and calculated from eq (2.2.1), furnishing the figures given in table 1. However, for many purposes it is most convenient to express this dependent variable as $\nu_e$, the number of moles of effective sub-chains per unit volume, which may be calculated from *fp* by inserting in eq (3.8) of Part II the values of the constants determined in Part II.

$$\begin{aligned}\nu_e &= [2/\bar{v}_r][(1/100M_d)(fp-fw)-1/M]\\ &= [66.798(fp-0.31)-9.36]10^{-6} \qquad (2.3.1)\\ &= 66.798(fp-0.45)10^{-6}.\end{aligned}$$

From this we conclude that in our rubber there are 9.36 μmol of dangling ineffective loose ends in each cubic centimeter (equivalent to one added cross-link per rubber molecule or 2 sub-chains per molecule) at all degrees of cross-linking. Figure 1 presents a graph (dashed line) of this equation and table 2 shows values calculated from it. It can be seen that the line is displaced from the origin by an amount $fp = 0.45$ phr, corresponding to the sum of the shifts, 0.31 phr due to impurities in the rubber and 0.14 phr due to dangling loose ends of rubber molecules.

We find that $\nu_e$ is zero for $fp = 0.45$ phr, where one cross-link per molecule has been added. Above this point it increases linearly with *fp*.

The dotted line in figure 1 shows the result of omitting completely any correction for the end-effect. It represents the behavior expected if the molecular weight of the polymer had been assumed to be infinite.

For comparison with these values predicted by cross-linking considerations from simple theory, the observed value of $\nu_e$ may be obtained directly experimentally



206-267 OL - 76 - 5

from the observations of the modulus increase $(G-G^*)$. With the insertion of the constants from eqs (1.1) and (2.3) of Part II, eq (3.9) of Part II becomes

$$\nu_{eG} = (G-G^*)/RT = (S/R)\ (fp+B)$$
$$= 71.26\ (f-0.45)\times 10^{-6}. \qquad (2.3.2)$$

The subscript $G$ has been added temporarily at this point to emphasize that this $\nu_e$ has been obtained experimentally from the observed values of $(G-G^*)$ and not from cross-linking considerations. This equation is represented by a continuous line in figure 1. The positive ordinate values are 6.7 percent higher than those given by eq (2.3.1). The discrepancy arises from the 6.7 percent difference in the observed and predicted values of the constant $S$, already mentioned in Part II and tentatively ascribed to the effect of entanglements. These lines illustrate graphically the extent of the agreement between the number of effective sub-chains calculated from the observed modulus and that calculated from the added cross-links. With the correction for wasted dicumyl peroxide and for the chain ends, the relation is surprisingly close to demonstrating the production of two effective sub-chains for each cross-link formed over the range shown in figure 1. This was of course assumed in the derivation of $\nu_e$ in eq (2.3.1) by cross-linking considerations, but this assumption has sometimes been questioned.

The conclusion may also be phrased in slightly different terms. The equation of the continuous line in figure 1 in terms of the upper abscissa is obtained by combining eqs (2.2.2) and (2.3.2) to give

$$\nu_{eG} = 2.134\,(X/A_1V_r) - 10\times 10^{-6}. \qquad (2.3.3)$$

Each mole of added cross-links thus leads to 2.134 moles of effective sub-chains. If 6.7 percent of these are ascribed to entanglements it may be concluded that our experiments show that each molecule of decomposed dicumyl peroxide gives rise directly to exactly one new cross-link and two new sub-chains.

While one is justified in calculating $\nu_e$ by dividing $(G-G^*)$ (the entropy component of the modulus) by $RT$, as has just been done, no significant information regarding the number of effective sub-chains can be obtained from $G$ or $G^*$ alone. The ratio of either of these single quantities to $RT$ is not a proper measure of any kind of sub-chain density, since the component $G^*$ is not related to entropy. Unfortunately most previous authors have based calculations of physically effective sub-chain density on the ratio $G/(RT)$. This can be valid only if $G^*$ is neglible compared with $G$. Table 1 of Part II shows that this is far from true in the present investigation. This point deserves special emphasis because of the confusion in the literature.

It is clear that eqs (2.3.1) and (2.3.2) predict no variation of $\nu_e$ itself with temperature. However its efficiency in producing an entropy component of the modulus is proportional to the temperature, falling to zero at O K, as is obvious from eq (2.3.2). The entropy component of modulus at a given temperature then bears a close relation to the number of moles of effective sub-chains per unit volume and is in fact equal to $RT$ times this number. $G^*$, on the other hand, is an energy component related to intramolecular or intermolecular forces. It is assumed that its magnitude does not vary with temperature, and its variation with cross-linking is found to be very small, arising only from the presence of the term involving the constant $H$ in eq (1.1).

A quantity $M_{c\,phys}^{-1} = \bar{v}_r\nu_e$ has also been used by some previous workers to express the concentration of effective sub-chains. From eqs (3.2) and (3.6) of Part II and (2.2.3) of this paper one finds

$$M_{c\,phys}^{-1} = M_{c\,chem}^{-1} - 2M^{-1}$$
$$= 2(100M_d)^{-1}(fp-fw) - 2M^{-1}$$
$$= [73.972\,(fp-0.31) - 10.36]\,10^{-6}$$
$$= 73.972\,(fp-0.45)\,10^{-6}. \qquad (2.3.4)$$

Table 2 shows values calculated by this equation. Similarly one may utilize $\nu_{eG}$ instead of $\nu_e$ to calculate corresponding values for a molecular weight between cross-links as calculated from $(G-G^*)$.

TABLE 2.—*Calculated measures of effective sub-chains*

| $fp$ phr | $(2X/N)-2$ effective sub-chains per molecule | $\nu_e$ $\mu$moles of effective sub-chains per cm$^3$ | $M_{c\,phys}^{-1}$ $\mu$ mol g$^{-1}$ | $M_{c\,phys}$ mol wt of effective sub-chains, g mol$^{-1}$ |
|---|---|---|---|---|
| 0 | ..... | ..... | ..... | ..... |
| 0.31 | ..... | ..... | ..... | ..... |
| 0.45 | 0 | 0 | 0 | $\infty$ |
| 1 | 7.86 | 36.7 | 40.7 | 24,600 |
| 2 | 22.2 | 104 | 115 | 8,700 |
| 3 | 36.4 | 170 | 189 | 5,290 |
| 4 | 50.6 | 237 | 263 | 3,800 |
| 5 | 65.0 | 304 | 337 | 2,970 |
| 10 | 136 | 638 | 706 | 1,420 |
| 15 | 208 | 972 | 1080 | 926 |
| 20 | 280 | 1306 | 1450 | 690 |
| 23.8 | 334 | 1560 | 1730 | 578 |

In most of our work we prefer to follow the practice shown in figure 1, where the dependent variable is $\nu_e$, the number of moles of effective sub-chains per unit volume, and where the independent variable is the cross-linking expressed in terms of $fp$ for the dicumyl peroxide system or in terms of $X/A_1V_r$ in general. In this way one avoids the reciprocal quantities and possible confusion involved in using $M_{c\ phys}$ and $M_{c\ chem}$.

A comparison of the respective values of $M_{c\ \mathrm{chem}}$ in the last column of table 1 with those of $M_{c\ \mathrm{phys}}$ in the last column of table 2 shows the necessity for making a careful distinction between these two quantities. The distinction is always important conceptually and is quantitatively most significant at low degrees of cross-linking. The distinction would disappear for a polymer of infinite molecular weight as can be noted from eq (2.3.4).

### 2.4. Determination of Modulus Components by Measurements of Equilibrium Swelling

As an alternative to experiments involving deformation of cross-linked polymers by mechanical stress, many other investigators, [10–16, 19–39] have measured the swelling of the system by a liquid. The internal stresses arising from the swelling are balanced by the reaction of the extended network. This is observable as an increase of volume, approaching a limiting equilibrium value.

Flory and Rehner [40–42] have utilized statistical considerations to derive a relation intended to permit the calculation of the apparent number of effective sub-chains from the observed limiting equilibrium swelling. Alternatively this number can be expressed as $\nu_e$, $\bar{v}_r^{-1}M_c^{-1}{}_{phys}$ or $(G-G^*)/RT$, as discussed in section 2.3 and plotted in figure 1.

For reasons that will soon become evident, the dependent variable in this section will first be taken, not as $\nu_e$, but as $(G-G^*)$, the entropy component of the modulus at a temperature of 298.15 K. This variable must be divided by the factor $RT$ to obtain $\nu_e$ itself.

In terms of modulus components, then, the Flory-Rehner equation can be written:

$$G-G^*=\nu_eRT=\bar{v}_r{}^{-1}M_{c\,phys}^{-1}\ RT$$

$$=R\dot{T}\left[-ln\ (1-v_2)-v_2\ -\mu v_2{}^2\right]\left[V_1{}^{-1}\right]\left[v_2{}^{1/3}-v_2/2\right]^{-1} \tag{2.4.1}$$

where $v_2$ is the measured volume-fraction of rubber in the swollen material, $V_1$ is the molar volume of the swelling liquid, and $\mu$ is the Flory-Huggins interaction parameter characteristic of the rubber and swelling liquid. It is normally about 0.4. We shall denote the right-hand member of the equation as $RT\Psi(v_2)$ for brevity.

Values of $RT\Psi(v_2)$, the right-hand member of eq (2.4.1), calculated from equilibrium swelling data reported by five different observers are plotted as experimental points in figure 2. The results of van der Hoff [21], Chasset and Thirion [23], Plazek [29], and Allen and co-workers [36] are reasonably well represented by the dotted line, which has been drawn to represent them. Similar results (not plotted) were also obtained by Angerer [37]. The results of Tamura and Murakami [38] are consistently somewhat below the dotted line and show a somewhat smaller change with increase of cross-linking.

The data plotted in figure 2 are also typical of the results obtained by many other observers [13–16, 19, 20, 22, 24–28, 30–35]. The latter results are not plotted here in order to avoid complexity. However, the points are generally found to lie near or below the dotted line. In no case do they fall below the plotted results of Tamura and Murakami [38], which are reproduced here to typify the extreme case. Most of the differences among these results can probably be explained in terms of differences in the molecular weight of the rubber, its impurities, or the conditions of cure and swelling.

The continuous line in figure 2 represents a plot of $(G-G^*)$ at 298.15 K. in accordance with eq (2.3.2). It represents the entropy component obtained in part 1 of the present study, and differs from the continuous line in figure 1 only by the constant factor $RT$ in the scale of ordinates. As already demonstrated in figure 1 the values of $\nu_e$ calculated from cross-linking considerations differ only slightly from those corresponding to this continuous line. The negative intercept can be ascribed to the presence of chain ends and impurities in the rubber, while the slightly greater slope can be ascribed to the presence of entanglements.

It is clear from figure 2 that the values of $RT\Psi(v_2)$, the right-hand member of eq (2.4.1), obtained from swelling measurements are systematically substantially larger than the values of $(G-G^*)$. In other words we find that the entropy component of the modulus effective in limiting swelling is larger than the entropy component measured by the other methods.

The conclusion then is that the number of sub-chains limiting swelling is larger than the number calculated from cross-linking considerations or its approximate equivalent number effective in the mechanical measurements of the present work.

Furthermore the slope of the dotted line in figure 2 representing the results of the five investigations [21, 23, 29, 36, 37] is about 16 percent greater than that of the continuous line. The comparable figures obtained from the observations of Meissner [14], Manik and Banerjee [31], Mullins [20], and Redding and Smith [32] are 10, 7, 6 and 3 percent respectively. The data of Mason [25] and Tamura and Murakami [38] show even lower slopes, nearly the same as that of the continuous line. Added cross-links are apparently slightly more effective in increasing the entropy component of the swelling modulus than they are in increasing the corresponding entropy component of the mechanical modulus at a given temperature.

These two discrepancies of ordinate values and slopes of the lines in figure 2 are not due to differences

in specimens, differences in calculating abscissa values, or difference in the methods used in measuring the modulus by mechanical means, since values of $G$ calculated from stress relaxation observations of Chasset and Thirion [23], from creep observations of Dickie and Ferry [30] or from torsion pendulum measurements of Plazek [29] on specimens representing the same samples as those used in their swelling experiments are in excellent agreement with our values. This comparison is shown in figure 8 of Part I. Additional experimental points in good agreement with this figure have been obtained more recently by Gent and Kuan [43] in torsional experiments and by Tamura and Murakami [38] by linear extension.

For comparative purposes figure 2 shows also as ordinate a plot (dashed line) of $G$, the sum of the energy and entropy components of the mechanical modulus at 298.15 K, as obtained earlier by indentation measurements. This, of course, corresponds to eq (1.1) and to one of the lines in figure 2 of Part II. Its slope is about 3.8 percent greater than that of the plot of $(G-G^*)$ because of the presence of the term containing the constant $H$. No points in figure 2 and (with scarcely any exceptions) none of the unplotted observations of equilibrium swelling previously mentioned lie above the dashed line. In other words $RT\psi(v_2)$ over the range

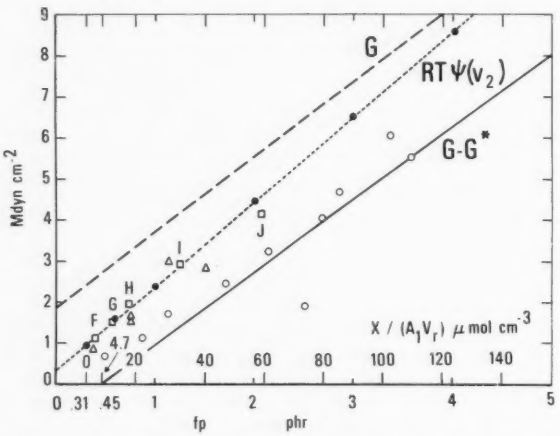


FIGURE 2. *Modulus G at 298.15 K or its entropy component* (G − G*) *from indentation measurements as a function of cross-linking.*

*Comparison with equilibrium swelling results*

..... Dashed line represents the equation $G = 1.835\ (fp - 0.45) + 2.70$, obtained from eq (1.1) at 298.15 K

_____ Continuous line represents the entropy component $G - G^* = 1.766\ (fp - 0.45)$, obtained from eq (2.3.2) at 298.15 K.

..... Dotted line represents $RT\Psi(v_2)$ namely $RT[-\ln(1-v_2) - v_2 - \mu v_2^2]\ [V_1{}^s]\ [v_2{}^{1/3} - v_2/2]^{-1}$, right-hand member of Flory-Rehner equation, eq (2.4.1) at 298.15 K with $v_2$ data from equilibrium swelling measurements of van der Hoff [21].

Empirical equation of line: $RT\Psi(v_2) = 2.05fp + 0.347$.

Data points from equilibrium swelling measurements of:

● van der Hoff [21] (unpurified sample)

⊙ Chasset and Thirion [23] or Plazek [29]

△ Allen et al. [36].

○ Tamura and Murakami [38].

Lower scale of abscissas shows values of $fp$ for system of natural rubber cross-linked by dicumyl peroxide.

Upper scale of abscissas shows number of moles of added cross-links per unit volume $X/(A_1V_r)$ or $1/2\bar{v}_r{}^{1}M_r{}^{-1}{}_{theor}$ derived from eq (2.2.2).

shown never exceeds the total modulus obtained by mechanical measurements. It should be noted that there is no justification for drawing a line in figure 1 to correspond to the line $G$ in figure 2, since the energy component of $G$ does not arise from any definite number of cross-links, as emphasized in section 2.3.

This same discrepancy of ordinates has already been pointed out by other authors. Dickie and Ferry [30] present a graph (their fig. 2) showing that the equilibrium compliance observed in their creep measurements was smaller by a factor of 0.71 than that calculated by eq (2.4.1) from Chasset and Thirion's swelling measurements [23]. In terms of the quantities we have used, this means that the directly-observed modulus $G$ was found to be greater then $RT\Psi(v_2)$ by about the same factor as we note in the region where $fp$ is between 1 and 2 phr. Similar results for natural rubber and polybutadiene in this range were reported by Shen, Chen, Gebhard, and Cirlin [35] and for styrene-butadiene rubber and butyl rubber by Nielsen [44].

Murakami and Hsiue [39] extended the observations on natural rubber to higher degrees of cross-linking than the other observers. They confirmed previous work at low values, but in addition they found that $\Psi(v_2)$ from swelling measurements (which they denoted as $n_S$) was less than $G/RT$ (which they denoted as $n_M$) only as long as the value of $G/RT$ was less than 420 $\mu$mol cm$^{-3}$ corresponding to a $G$ value of 10.4 Mdyn cm$^{-2}$ at 298.15 K. Beyond this point the reverse was true.

The relative slopes of the dotted and dashed lines in figure 2 would also indicate the possibility of such a reversal if extrapolation of the lines is justified. The intersection of the lines occurs at an abscissa where $fp = 7.08$ phr ($X/A_1V_r = 226$ $\mu$mol cm$^{-3}$) corresponding to an ordinate of 14.9 Mdyn cm$^{-2}$. This is not greatly different from the value 10.4 Mdyn cm$^{-2}$ found by Murakami and Hsiue.

In contrast with the precent paper, most previous publications have neglected to include $G^*$ in the Flory-Rehner equation and thus have considered its left-hand member to be simply $G$, the sum of the entropy and energy components. If this should be correct, $RT\Psi(v_2)$ ought to be compared with $G$ rather than with $G-G^*$, and it would not be necessary to conclude that there were more cross-links effective in limiting swelling than those calculated by the other methods. From figure 2 one would then conclude that $RT\Psi(v_2)$ could now be taken as a total modulus including an energy component which is roughly only about half that effective in the mechanical measurements. If it is assumed that in the swollen system inter-chain forces are very greatly reduced, while the intra-chain forces are not much affected, a tentative guess could be made that these types of forces would be approximately equal in the unswollen rubber. On the other hand, most previous workers consider that the intra-chain forces are strongly predominant. However, the present work yields no information about these forces if the left-hand member of eq (2.4.1) is taken as $(G-G^*)$, as we have done.

## 3. Possible Refinements of Simple Theory

### 3.1. Impurities and Sol Content

Specific impurities in the rubber which would react with the dicumyl peroxide rendering some of it unavailable for cross-linking have been discussed in sections 3.2 and 4 of Part II. In the absence of direct measurements, the equivalent amount of these impurities in pale crepe rubber was taken as 0.31 phr, as found in swelling measurements made by van der Hoff [21]. Similar measurements on samples of several extracted and unextracted natural rubbers by Bristow, Moore, and Russell [28] and other measurements reported by Bristow [27] yielded values ranging from 0.2 to 0.45 phr, in approximate agreement with van der Hoff's figure. This number would be expected to vary with the type of rubber studied.

Degradation of the rubber is much more likely with extracted samples, since extraction removes the natural antioxidants. Consequently in most instance preference should be given to results obtained with unextracted samples, making the necessary corrections.

In general, all impurities in the rubber, both reactive and nonreactive, would also act as diluents, for which an additional correction might be made. A similar correction might be made for impurities in the dicumyl peroxide itself. In each case the mass should be multiplied by the corresponding purity.

The purity of the pale crepe rubber may be estimated as normally about 93 percent. The purity of the "recrystallized" dicumyl peroxide was not measured here, but values near 95 percent have been reported [14, 31, 37, 45–48].

The relations derived here are expressed in terms of the ratios

$$p = 100 m_d / m_r \text{ [eq (3.3) of Part II]}$$

and

$$w = 100 m_o / m_r \text{ [eq (3.4) of Part II]}.$$

Therefore the correction factor would involve only the ratio of the purities. It would be unity if the purities of the rubber and dicumyl peroxide should be the same. Since these purities probably were nearly the same in the present work, no correction for diluent effect was made.

The reaction products of the decomposition of the dicumyl peroxide are $\alpha$-$\alpha'$-dimethyl benzyl alcohol, acetophenone, and methane. It is expected that a portion of the first two products will remain as a residue in the rubber. No significant anomalies due to the presence of these residues were noted in the experimental portion of the present study, and no account was taken of them in the simple theory outlined here. However, a more detailed investigation of the most highly cross-linked specimens might be warranted in order to determine quantitatively the fate of these reaction products and their influence on the properties of the rubber.

The sol content of the cross-linked rubber consists of molecules which never become a part of the network. K. W. Scott [47] measured a sol content of about 1 percent for natural rubber cross-linked with 1 phr of dicumyl peroxide and about 0.1 percent when the amount was 3 phr. Similar results were reported by Glaser and Eirich [33]. Still smaller amounts were found when larger amounts of dicumyl peroxide were used. Consequently the sol content was assumed to be negligible in all the present work.

### 3.2. Specific Volume of Rubber

The specific volume of the unvulcanized rubber (NBS Standard Reference Material 385b) at 298.15 K was 1.1074 $cm^3\ g^{-1}$. For simplicity this value has been used for $\bar{v}_r$ throughout the present study. The actual specific volume of the cross-linked rubber would be expected to be less than this value because of the diluent effect of the dicumyl peroxide and the change of volume on cross-linking. A decrease of about 10 percent would be expected at the highest degrees of cross-linking. The specific volume would also be expected to vary about 5 percent above and below the value at 298.15 K at the extremes of temperature used in the present study.

### 3.3. Chain-End Correction

The correction for dangling chain ends ineffective for supporting a stress is discussed in Section 3.1 of Part II [2]. The form of correction used there is exactly the same as that proposed by Flory [49]. He used the quantity $M_{c\,chem}^{-1}$ as a measure of cross-linking and so one finds by the use of eq. (2.2.3) in eq (2.3.1)

$$\nu_e = M_c^{-1}{}_{chem} / \bar{v}_r [1 - 2/(M M_c^{-1}{}_{chem})]. \quad (3.3.1)$$

Differentiation of this equation gives

$$\partial \nu_e / \partial M^{-1} = -2/\bar{v}_r. \quad (3.3.2)$$

In terms of the entropy component of modulus this becomes

$$\partial (G - G^*)/\partial M^{-1} = -2RT/\bar{v}_r. \quad (3.3.3)$$

Later workers [50, 51] have proposed slightly different forms of the second term in brackets in eq (3.3.1) [52], while Mullins [20] gives experimental evidence that the factor should be

$$[1 - 2.3/(M M_c^{-1}{}_{chem})].$$

It is likely that the factor in this form takes account of the effects of nonload-bearing loops, hitherto neglected, as well as chain ends. Use of the revised factor would increase the calculated value of effective molecular weight by about 15 percent. It would still be in the range of reasonable values. Other refinements also give only small variations in calculated molecular weight.

In figure 1 the whole chain-end correction can be seen to result in shifting the line to the right along the abscissa axis by only 0.14 phr, equivalent to a decrease of 9.36 $\mu$mol cm$^{-3}$ on the ordinate axis. This shift is so small that determining the validity of the exact form of correction would require data of high precision extending over a wide range of molecular weights. It would seem that more attention has been given to this correction than would normally be justified by its magnitude. The dotted line in figure 1 is drawn neglecting the correction completely, thus corresponding to an assumption that the polymer was of infinite initial molecular weight. The calculation for a finite molecular weight is of course greatly influenced by the correction for impurities, which in our work was more than twice that ascribed to chain ends.

### 3.4. Modulus at Low Degrees of Cross-Linking

In the experimental portion of the present study (Part I [1]), the conclusions have been based on measurements where $fp$ was greater than 0.45 phr, namely beyond the gel point. When $\nu_e$ is plotted against $fp$, as in figure 1, the considerations already outlined yield the straight lines shown. The value of $fp$ at which $\nu_e$ is zero corresponds to the amount of cross-linking agent which must be introduced to account for that required to establish a network. Only after this amount has been added can any additional cross-linking agent become effective.

At the gel point the number of moles of effective sub-chains in zero (fig. 1) and the modulus $G$ is equal to $G^*$, the energy component alone, so that $G-G^*=0$, as seen in figure 2.

In the remainder of this section we shall consider for the first time the actual observed behavior of the system at low degrees of cross-linking. Below the gel point the network theory outlined previously can make no predictions and we have been guided only by extrapolation. In this region experimental values are less reliable, since the creep rate becomes high [53, 54], and the "equilibrium" modulus is obtainable only by extrapolation to infinite time, for example by the method of Chasset and Thirion [23, 55]. The modulus-temperature relation here is found experimentally to have a negative slope, as predicted by extrapolation from high degrees of cross-linking. This is evident in figures 2 and 7 of Part I.

Results reported by other observers [13, 15–20, 32–34, 36, 48, 56–65] agree with the present work in showing that the modulus increases linearly with cross-linking for the higher degrees of cross-linking. The line likewise almost invariably has a slope greater than that predicted from the cross-linking. In the present work this slope was about 10.5 percent greater than predicted [2], while the literature values in the references just given range from 5 to 31 percent greater.

The line invariably has a positive intercept, ranging from 0.5 to 2 Mdyn cm$^{-2}$. This is in accordance with figure 8 of Part I, figure 2 of Part II, and figure 2 of the present work. Our work shows a value of $G_0=1.87$ Mdyn cm$^{-2}$ at 298.15 K.

The positive intercept and increased slope of the line are evident even when the carbon-carbon cross-links are formed by exposure to radiation [17, 18, 66] rather than by free radicals resulting from the decomposition of a peroxide. Similar effects are evident in studies of silicone rubber cross-linked by radiation [57, 58].

At the lower degrees of cross-linking the actual measured values of modulus lie consistently below the line, the deviation increasing as the cross-linking is reduced. This behavior can be seen in the modulus of Chasset and Thirion's Specimen F, plotted in figure 8 of Part I. It is well verified by other observers [13, 15, 17–20, 31, 32, 56, 57, 60, 61, 64]. The experimental values of modulus often appear to decline to zero at a finite positive value of cross-linking, and sometimes are even calculated as a negative modulus for the material to which no cross-links have been added [13, 32].

An examination of the data suggests that as the cross-linking is reduced, the value at which the deviation from linearity first occurs may be the gel point. However, it is possible that the gel point is that at which the modulus actually becomes zero. The experimental and theoretical difficulties associated with consideration of the region near the gel point and below have already been mentioned.

It is interesting to compare our time-independent modulus value of $G_0=1.87$ Mdym cm$^{-2}$ at 298.15 K, as measured on cross-linked specimens and extrapolated to zero cross-linking, with those derived from observations of a time-dependent modulus obtained from stress relaxation or shear creep experiments on rubber actually containing no cross-linking agent. The latter values have usually been obtained from a point of inflection in the plateau region of a plot of the logarithm of the ratio of stress to strain (or its reciprocal) against the logarithm of the time. Shear creep studies on narrow-distribution synthetic *cis*-isoprene polymers by Nemoto and co-workers [68] yielded shear modulus values of about 0.8 Mdyn cm$^{-2}$ with a plateau centered near $-30$ °C (243 K). Stress relaxation studies by investigators in the Polytechnic Institute of Milan on various polyisoprenes [69, 70] showed modulus values of 3 − 4 Mdyn cm$^{-2}$. Such non-zero values of modulus when no cross-links have been added have usually been ascribed to entanglements, which will be discussed in section 3.5.

### 3.5. Entanglements

The linear relation between modulus and cross-linking discussed in the preceding section has a positive intercept $G_0$, the extrapolated modulus corresponding to no added cross-linking agent. $G_0$ has often been ascribed [19–21, 24, 31, 57, 63, 67, 68] simply to entanglements functioning as effective cross-links, additional to but not much different in character from those which have been introduced by the cross-linking

agent. It would seem that this simple explanation must be abandoned in view of the present work, which has now shown that the modulus has a very appreciable energy component $G^*$ and that this is the chief factor determining $G_0$.

The relation between these quantities is given by eq (2.5) of Part II

$$G_0 = G^* + SBT = A + BH + SBT$$

$$= 2.67 - 2.666 \times 10^{-3} T. \qquad (3.5.1)$$

The values of the intercept $G_0$ calculated from this equation range from 2.67 Mdyn cm$^{-2}$ at 0 K to 2.07 Mdyn cm$^{-2}$ at 223.15 K and 1.67 Mdyn cm$^{-2}$ at 373.15 K. They can be noted in figure 2 of Part II.

We are led to conclude that $G_0$ arises from interatomic forces. The consensus of opinion [71–75] has been that these forces are largely intrachain ("intramolecular") in origin.

The data indicate that these forces (whatever their origin) increase slightly with increasing cross-linking, as might be expected. If entanglements serve to increase these forces, they may well have an important part in giving rise to the intercept.

On the other hand if entanglements act merely as pseudo effective cross-links, they can contribute only to the entropy component of the modulus. In experimental terms, they can increase the slopes of the $G$, $T$ lines of figure 1 of Part II but would not affect the intercepts of these lines.

Previous observations of the relation between modulus and cross-linking, with a few exceptions [29, 76, 77] have been limited to measurements at a single temperature or over a small range. Consequently they have not furnished information regarding the relative contributions of energy and entropy.

The theory of entanglements has been extensively discussed in recent years [78–87]. The considerations have now progressed considerably beyond the simple idea of pseudo cross-links just mentioned. For example topological entanglements have been distinguished from coupling loci arising from interatomic forces, and some entanglements are regarded as trapped between cross-links while others are untrapped. Furthermore entanglements are important in determining the viscoelastic and other properties of a given polymer. We restrict ouselves here to considering their effect on the modulus.

Some theoretical treatments predict that the number of entanglements should increase linearly with an increase in the number of cross-links, while others conclude that it should be independent of the cross-linking. The present work would favor the former conclusion, in view of the fact that the observed value of the constant $S$ in eq (1.1) is greater than that computed from the molecular constants in Part II. If this increase is indeed due to entaglements and not to some defect in the assumptions, one would conclude that the number of entanglements is consistently about 6.7 percent of the number of cross-links. We know of no independent method by which to verify this conclusion.

If entanglements are regarded as temporary cross-links [30, 67, 88] which are effective only for a limited time after the application of a stress, they need be considered only when there is appreciable creep. The significant portions of the present work were done under conditions where the creep was negligible. Consequently, here we can neglect the effect of such temporary cross-links.

The scope of the present paper does not permit further discussion of entanglements, other than to repeat that they are not functioning as pseudo cross-links making a major contribution to the value of $G_0$.

### 3.6. "Front Factor" and Efficiency

One of the most significant conclusions of the present work is the prediction of the value of the constant $S$ in eq (1.1) as equal to $2\ R/(100 M_d \bar{v}_r)$, by eq 4.3 of Part II.

Regardless of whether the 6.7 percent excess of the measured over the calculated value is ascribed to defective assumptions or to the presence of entanglements, as has been done in a previous section, it is clear that the extent of the numerical agreement apparently eliminates the necessity for several refinements and corrections which might be made in the simple theory outlined here.

There has been considerable discussion regarding a "front factor" $\phi$, [89–91] which might be used in calculating modulus change from $\nu_e$, the number of added effective sub-chains per unit volume. James and Guth [10, 91, 92] associate $\phi$ with the details of the reaction producing cross-links and suggest a value of about 0.5 as most reasonable. Others [93] have criticized this treatment and predict a value near unity.

Most recent authors have included a different "front factor" $\langle \bar{r}_i^2 \rangle / \langle \bar{r}_0^2 \rangle$ where $\langle \bar{r}_i^2 \rangle$ is the mean square value of the displacement length of the sub-chain in the isotropic unstrained state and $\langle \bar{r}_0^2 \rangle$ is the mean-square value of the displacement length in the unperturbed state [74]. The latter quantity varies with temperature.

The assumption that each molecule of decomposed dicumyl peroxide gives rise to one cross-link in natural rubber is generally accepted [21, 31, 94–97] but the efficiency $\epsilon$ has occasionally been stated to be less than unity under certain circumstances [27, 28, 60], (especially if no account is taken of the amount wasted by reaction with impurities). Scission during cure would also reduce the efficiency, but has recently been shown to be negligible [28].

The introduction of a "front-factor," $\phi$ whatever its origin, and an efficiency factor $\epsilon$ into eq (3.9) of Part II or eq (2.3.2) of the present paper would result in the substitution of $\phi\epsilon R$ for $R$, the gas constant, in all the relations containing $R$. The present results indicate that the product $\phi\epsilon$, even without the entanglement correction, could not differ from unity by more than about 7 percent. A significant variation of this quantity

with temperature would have been observable as a deviation from linearity in the graph of $\partial G/\partial fp$ against $T$ and of $\partial G/\partial T$ against $fp$ (figs. 6 and 7 respectively of Part I).

If the front factor $\phi$ is taken as 0.5 the efficiency would have to be an unlikely 200 percent (i.e., each molecule of decomposed peroxide would have to furnish two cross-links yielding four additional sub-chains). Such a counterbalance of factors does not seem probable and we prefer to consider that the present results indicate values of unity for both $\phi$ and $\epsilon$ under our conditions of cure.

## 4. Resolution of Components of Modulus

Many of the concepts developed here can be more readily understood when they are utilized to resolve the modulus at $fp = 1$ phr, and $T = 298.15$ K, into four components, as shown in figure 3. The first and largest component, corresponding to the constant $A$ in eq (1.1), is an energy component arising from interatomic or intermolecular forces. It is represented by a vertical displacement of 2.70 Mdyn cm$^{-2}$ from the origin. The

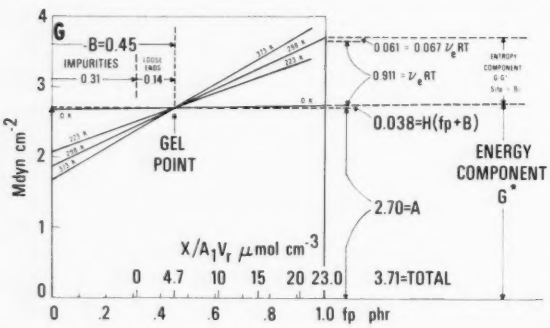


FIGURE 3. *Resolution of modulus* G (*for* T = *298.15 K and* fp = *1 phr*) *into components.*

amount of dicumyl peroxide wasted by reaction with impurities is shown as a horizontal displacement of 0.31 phr, while the effect of dangling loose ends of the rubber molecules is given by an additional horizontal displacement of 0.14 phr to the gel point. The second component, also an energy term independent of temperature, corresponds to the term containing the constant $H$ and is the smallest of the four components. The third term, an entropy term proportional to the temperature, is the one which can be calculated as $RT$ times the density of effective sub-chains attributable to the added dicumyl peroxide. Finally, there is a fourth term, which is also an entropy term proportional to the temperature and the cross-linking. This term can probably be ascribed to the effect of entanglements, functioning as pseudo cross-links.

The lines shown in figure 3 are to be regarded as schematic, since they are the extrapolations of lines determined largely at higher values of cross-linking. In the present work (except in sec. 3.4), little significance has been attached to actual experimental values in the region of the gel point and below.

In view of the fact that a large portion of the modulus arises from an energy component $G^*$ (especially at low degrees of cross-linking), it is not surprising that the form of stress-strain relation derived from entropy considerations alone gives only an approximation to the experimental data [63, 73, 90], the value predicted being consistently higher than the observed stress [98, 99]. It will be noted that the present work has required no assumptions whatever about the equation of state or form of the stress-strain relation outside the range of infinitesimal deformations.

## 5. Conclusions

The qualitative and quantitative agreement of predictions and results demonstrated in the previous sections is a strong confirmation of the essential validity of all the extremely simplified molecular considerations involved, including the general aspects of the statistical theory of rubber elasticity. We know of no previous experimental study extending over as wide ranges of cross-linking and temperature. In fact the cross-linking and temperature have been varied simultaneously on only a few occasions in previous work.

An important advantage of the present work over many previous studies is the fact that measurements are made at very small deformations. Thus the results are expressed in terms of the modulus, defined as the limiting value of the ratio of stress to strain at zero deformation. Consequently, the results are independent of the stress-strain relation or equation of state. This means that no consideration needs to be given here, for example to the difference between the stress-strain relation predicted by the statistical theory of rubber elasticity and that given by the Mooney-Rivlin equation or the empirical equation of Martin, Roth, and Stiehler [99].

The present study has shown that the modulus $G$ includes a considerable component arising from internal energy changes as well as that arising from entropy changes. The energy component at room temperature is of the order of half the total when the degree of cross-linking is that normally used with dicumyl peroxide rubbers.

It is concluded that the nonzero value of the modulus when extrapolated to zero cross-linking is due to the energy component of the modulus rather than to entanglements. Entanglements acting as pseudo-cross-links would serve to increase only the entropy component.

The gel point, defined as the minimum degree of cross-linking required to form a network, may be located experimentally as the cross-linking at which the slope of the modulus-temperature relation is zero. The value of the modulus $G$ at the gel point is not zero, but is the energy component under this condition; the entropy component of $G$ at the gel point is zero.

The amount of dicumyl peroxide required to cross-link rubber to the gel point is the sum of that wasted by reaction with impurities in the rubber and that required to give one cross-link for each rubber molecule. The former quantity was about twice the latter in the work reported here.

The entropy component of the modulus as determined from reported values of equilibrium swelling by the Flory-Rehner equation, is found to be significantly larger than that determined from mechanical measurements. However, the quantity computed is smaller than the sum of the entropy and energy components as determined from cross-linking considerations or from mechanical measurements. It increases linearly with increase of cross-linking at a slightly greater rate than the modulus or the entropy component of the modulus.

It is concluded that the "front factor" sometimes introduced in statistical theory considerations cannot differ from unity by more than about 7 percent. The difference is even less than this if allowance is made for entanglements functioning as pseudo-cross-links.

## 6. Appendix

### Numerical Values of Constants

For convenient reference all the numerical values used in calculations in the present paper are given here.

GIVEN VALUES

From Tables

Molecular Weight of dicumyl peroxide $= M_d = 270.37$ g mol$^{-1}$
Gas Constant $= R = 8.31441 \times 10^7$ erg mol$^{-1}$ K$^{-1}$

Observed Values—Part I

$\bar{v}_r = 1.1074$ cm$^3$ g$^{-1}$; $\bar{v}_r^{-1} = 0.90302$ g cm$^{-3}$
$100M_d/M = -B - fw = 0.45 - 0.31 = 0.14$
$S = 5.925 \times 10^{-3}$ Mdyn cm$^{-2}$ K$^{-4}$ phr$^{-1}$
$A = 2.70$ Mdyn cm$^{-2}$
$H = 0.0684$ Mdyn cm$^{-2}$ phr$^{-1}$

VALUES CALCULATED FROM GIVEN VALUES

| | | Used in eq |
|---|---|---|
| $(100M_d)^{-1}$ | $= 36.986$ $\mu$mol g$^{-1}$ | 2.2.3 |
| $2(100M_d)^{-1}$ | $= 73.972$ $\mu$mol g$^{-1}$ | 2.3.4 |
| $\bar{v}^{-1}(100M_d)^{-1}$ | $= 33.399$ $\mu$mol cm$^{-3}$ | 2.2.2 |
| $2\bar{v}_r^{-1}(100Md)^{-1}$ | $= 66.798$ $\mu$mol cm$^{-3}$ | 2.3.1 |
| $2R\bar{v}_r^{-1}(100M_d)^{-1}$ | $= 5.5539 \times 10^{-3}$ Mdyn cm$^{-2}$ K$^{-1}$ phr$^{-1}$ | 4.3. of Part II |
| $0.14(100M_d)^{-1} = M^{-1}$ | $= 5.18$ $\mu$mol g$^{-1}$ | ..... |
| $2M^{-1}$ | $= 10.36$ $\mu$mol g$^{-1}$ | 2.3.4 |
| $2\bar{v}_r^{-1}M^{-1}$ | $= 9.36$ $\mu$mol cm$^{-3}$ | 2.3.1 |
| $M$ | $= 193{,}000$ g mol$^{-1}$ | ..... |
| $M(100M_d)^{-1}$ | $= 7.14$ | 2.2.1 |
| $S/R$ | $= 71.26$ $\mu$mol cm$^{-3}$ phr$^{-1}$ | 2.3.2 |

## 7. References


[1] Wood, L. A., Bullman, G. W., and Decker, G. E., Modulus of natural rubber cross-linked by dicumyl peroxide. I. Experimental observations, J. Res. Nat. Bur. Stand (U.S.). **76A** (Phys. and Chem.), No. 1, 51–59 (Jan.–Feb. 1972). Rubber Chem. Technol. **45,** 1388 (1972).

[2] Wood, L. A., Modulus of natural rubber cross-linked by dicumyl peroxide II. Comparison with theory, J. Res. Nat. Bur. Stand. **77A,** No. 1, 171–177 (Jan.–Feb. 1973): Rubber Chem. Technol., **46,** 1287 (1973).

[3] Flory, P. J., Principles of Polymer Chemistry (Cornell University Press, Ithaca, N.Y. 1953).

[4] Treloar, L. R. G., The Physics of Rubber Elasticity, 2d Edition (Oxford University Press, London, 1958).

[5] Ferry, J. D., Viscoelastic Properties of Polymers, 2d Edition (John Wiley and Sons, New York, 1970).

[6] Meares, P., Polymers: Structure and Bulk Properties (D. van Nostrand, London, 1965) p. 173.

[7] Nielsen, L. E., Mechanical Properties of Polymers (Reinhold, New York 1962) pp. 108, 109.

[8] Sauer, J. A., and Woodward, A. E., Stress-strain-temperature relations in high polymers, Chapter 3 in book Thermal Characterization Techniques, P. E. Slade, Jr., and L. T. Jenkins (Marcel Dekker, New York, 1970).

[9] Caspary, R., New results for the modulus-temperature characterization of elastomers, Kautschuk and Gummi, Kunstoffe, **25,** 249 (1972).

[10] James, H. M., and Guth, E. Theory of the increase in rigidity of rubber during cure, J. Chem. Physics, **15,** 669 (1947).

[11] Reference [3], p. 459.

[12] Charlesby, A., Atomic Radiation and Polymers (Pergamon Press, New York, 1960).

[13] Russell, R. M., Smith, D. A., and Welding, G. N., Estimation from swelling of the structural contribution of chemical reactions in the vulcanization of natural rubber III, Techniques of Polymer Science. SCI Monograph 17, Society of Chemical Industry, London 1963; Rubber Chem. Technol. **37,** 576 (1964).

[14] Meissner, B., Structure and properties of rubber networks, Part I, J. Polym. Sci. Part C, No. **16,** 781 (1967).

[15] Meissner, B., Klier, I., and Kucharik, S., Structure and properties of rubber networks II, J. Polym. Sci. part C, No. **16** 793, (1967).

[16] Reference [5], page 435.

[17] Steiner, N., The significance of entanglements and network density for the description of the elastic properties and degradation of elastomeric networks, BAM-Berichte, No. 5, Bundesanstalt für Materialprüfung, Berlin March (1971).

[18] Steiner, N., Influence of secondary cross-linking, functionality of chemical cross-links, and of physical cross-links on stress relaxation of elastomers, Kautschuk und Gummi, Kunststoffe, **26** (4), 141 (1973).

[19] Moore, C. G., and Watson, W. F., Determination of degree of cross-linking in natural rubber vulcanizates II, J. Polym. Sci. **19,** 237 (1956).

[20] Mullins, L., Determination of degree of cross-linking in natural rubber vulcanizates III, J. Applied Polymer Sci. **2,** 1 (1959), Rubber Chem. Technol. **34,** 279 (1961).

[21] van der Hoff, B. M. E., Reactions between peroxide and diolefins. I. & E. C. Product Research & Development **2,** 273 (1963); Rubber Chem. Technol. **38,** 560 (1965).

[22] Bristow, G. M. Use of sol-gel analysis to estimate chain scission during vulcanization I. Peroxide vulcanization of natural rubber, J. Applied Polymer Sci. **7,** 1023 (1963).

[23] Chasset, R., and Thirion, P., Viscoelastic relaxation of rubber vulcanizates between the glass transition and equilibrium. Proc. Int. Conf. Non-Crystalline Solids. Delft 1964, J.A. Prins. Ed., p. 345, (North-Holland Publishing Co., Amsterdam, Interscience Publishers, New York); Rubber Chem. Technol. **39,** 870 (1966); Rev. Gen. Caoutchouc **44,** 1041 (1967).

[24] Ferry, J. D., and Macke, R. G., Maekawa, Etsuji, Oyanagi, Yasuji, and Dickie, R. A., Dynamic mechanical properties of cross-linked rubbers I. Effects of cross-link spacing in natural rubber, J. Phys. Chem. **63,** 3413 (1964); Rubber Chem. Technol. **39,** 897 (1966).

[25] Mason, P., Thermal expansion and viscoelasticity of rubber in relation to cross-linking and molecular packing, Polymer **5,** 625 (1964); Rubber Chem. Technol. **39,** 408 (1966).

[26] Bristow, G. M., Relation between stress-strain behavior and equilibrium volume swelling for peroxide vulcanizates of natural rubber and *cis*-14-polyisoprene, J. Applied Polymer Sci. **9,** 1571 (1965).

[27] Bristow, G. M., Estimation of chain scission during vulcanization III. Temperature effect in the peroxide vulcanization of natural rubber, J. Applied Polymer Sci. **9,** 3255 (1965).
[28] Bristow, G. M., Moore, C. G., and Russell, R. M., Determination of degree of cross-linking in natural rubber vulcanizates VII. Cross-linking efficiencies of di-tert butyl and dicumyl peroxide in the vulcanization of natural rubber and their dependence on the type of rubber, J. Polym. Sci. **A3,** 3893 (1965).
[29] Plazek, D. J., Effect of cross-link density on the creep behavior of natural rubber vulcanizates, J. Polym. Sci. A-2, **4,** 745 (1966).
[30] Dickie, R. A., and Ferry, John D., Mechanical properties of substances of high molecular weight. L. Dynamic Mechanical Properties of Cross-linked Rubbers, III. Dicumyl peroxide vulcanizates of natural rubber, J. Phys. Chem. **70** (8), 2594 (1966).
[31] Manik, S. P. and Banerjee, S., Determination of chemical cross-links in rubbers, Angew, Makromol. Chem. **6,** 171 (1969).
[32] Redding, R. B. and Smith, D. A., Rapid measurement of the chemical contribution to network chain density for natural rubber, J. Polym. Sci. **C., 30,** 491 (1970).
[33] Glaser, Z. R., and Eirich, F. R., Thermo-mechanics and structure of elastomers, PIBAL Report 69-38, Polytechnic Institute of Brooklyn, September 1969.
[34] Glaser, Z. R., and Eirich, F. R., Thermal behavior of elastomers at high rates of stretching, J. Polym. Sci. **C, 31,** 275 (1970).
[35] Shen, M., Chen, T. Y., Cirlin, E. H., and Gebhard, H. M., Thermoelasticity of cross-linked rubber networks in book Polymer Networks: Structure and Mechanical Properties, ACS Symposium, September 1970, A. J. Chompff and S. Newman, Ed. (Plenum Press, New York 1971) p. 47.
[36] Allen, G., Kirkham, M. J., Padget, J., and Price, C., Thermodynamics of rubber elasticity at constant volume, Trans. Faraday Soc. **67,** 1278 (1971).
[37] Angerer, G., Continuous measurement of the swelling- and diffusion-behavior of rubber vulcanizates with the aid of the self-recording swelling tester, Kolloid Zeits, und Z für Polymere, **245,** 369 (1971).
[38] Tamura, S., and Murakami, K., Determination of network chain density and the chemical stress relaxation of cross-linked polymers, J. Applied Polymer Sci. **16,** 1149 (1972); Rubber Chem. Technol. **46,** 477 (1973).
[39] Murakami, K., and Hsiue, G. H., Cross-linking density of $n_M(0)$ by mechanical method and that of $n_S(0)$ by swelling method, J. Polymer Sci. Part B. Polymer Letters **10,** 253 (1972); Murakami, K., Chemorheological studies, Rubber Chem. Technol. **4,** 913 (1975).
[40] Flory. P. J., and Rehner. J., Jr., Statistical mechanics of cross-linked polymer networks, J. Chem. Phys. **11,** 521 (1943).
[41] Flory, P. J., Statistical mechanics of swelling of network structures, J. Chem. Phys. **18,** 108 (1950).
[42] Reference [3], p. 576.
[43] Gent, A. N., and Kuan, T. H., Thermoelasticity of stretched elastomers under small torsions: effects of cross-linking, extension, and swelling, J. Polym. Sci. Phys. Ed. **11,** 1723 (1973).
[44] Nielsen, L. E., Mechanical behavior of some lightly cross-linked rubbers, J. Applied Polymer Sci. **8,** 511 (1964).
[45] Smith, D. A., Micromethod for estimation of the degree of cross-linking in elastomers from compression modulus of swollen vulcanizates, J. Polym. Sci. Part C, **16,** 525 (1967).
[46] Hummel, K., Scheele, W., and Hillmer, K. H., Vulcanization of natural rubber by dicumyl perioxide in the absence of additives, Kautschuk und Gummi, **14,** (6), WT171 (1967).
[47] Scott, K. W., An experimental verification of gel network formation theories, J. Polym. Sci. **58,** 517 (1962).
[48] Melley, R. E., and Stuckey, J. E., Determination of cross-link density from compression modulus data, J. Applied Polym. Sci. **14,** 2327 (1970).
[49] Reference [3], p. 463.
[50] Mullins L. and Thomas, A. G., Determination of degree of cross-linking in natural rubber vulcanizates V effect of network flaws due to free chain ends, J. Polym. Sci. **43,** 13 (1960).
[51] Scanlan, J., The effect of network flaws on the elastic properties of vulcanizates, J. Polym. Sci. **43,** 501 (1960).
[52] Reference [6], p. 208.
[53] Wood, L. A. Creep of "pure-gum" vulcanizates of natural rubber, J. Rubber Res. Inst. Malaya, **22** (3), 309 (1969); Rubber Chem. Technol. **43,** 1482 (1970).
[54] Wood, L. A., and Bullman, G. W., Creep and other tensile properties of rubber cross-linked by dicumyl peroxide, J. Polym. Sci. **A-2, 10,** 43 (1972).
[55] Thirion, P., and Chasset, R., Relative contributions of viscoelasticity and aging to the relaxation of rubber vulcanizates, Proc. 4th Rubber Technol. Conference London, May 1962, p. 338 (Inst. of Rubbér Ind. London 1963), Rev. Gen. Caoutchouc, **41,** 271 (1964), Rubber Chem. Technol. **36,** 50 (1963).
[56] Flory, P. J., Rabjohn, N., and Shaffer, M. C., Dependence of elastic properties of rubber on the degree of cross-linking J. Polym. Sci. **4,** 225 (1949).
[57] Bueche, A. M., An investigation of the theory of rubber elasticity using irradiated polydimethylsiloxanes, J. Polym. Sci. **19,** 297 (1956).
[58] St. Pierre, L. E., Dewhurst, H. A., and Bueche, A. M., Swelling and elasticity of irradiated polydimethylsiloxanes. J. Polym. Sci. **36,** 105 (1959).
[59] Mullins, L., Determination of degree of cross-linking in natural rubber vulcanizates IV, Stress-strain behavior at large extensions, J. Applied Polym. Sci. **2,** 257 (1959); Rubber Chem. Technol. **34,** 290 (1961).
[60] Moore, C. G., and Scanlan, J., Determination of degree of cross-linking in natural rubber vulcanizates VI Evidence of chain scission during the cross-linking of natural rubber with organic peroxides, J. Polym. Sci. **43,** 23 (1960).
[61] Bobear, W. J., Elastic properties and network structure in silicone gum vulcanizates, J. Polym. Sci. **4,** Pt. A-2, 299 (1966) Rubber Chem. Technol. **40,** 722 (1966).
[62] Barrie, J. A. and Standen, J. Thermoelastic measurements on some elastomers, Polym. **8,** (2) 97 (1967).
[63] van der Hoff, B. M. E., and Buckler, E. J., Transient changes in topology and energy on extension of polybutadiene networks, J. Macromol. Sci. Chem. **A1** (4), 747 (1967).
[64] Treloar, L. R. G. Introduction to Polymer Science (Wykeham Publications Ltd. London Springer-Verlag New York 1970), p. 58.
[65] Angerer, G., and Ng, T. S., On the possibility of determining network density of vulcanizates from measurements with the oscillating elastometer, Kautschuk und Gummi Kunststoffe **26** (6), 245 (1973).
[66] Reference [12], page 263.
[67] Thirion, P. and Chasset, R., Recent observations on the mechanical properties of polymer networks, Pure and Applied Chemistry **23** (2, 3) 183 (1970); Rubber Chem. Technol. **44,** 1256 (1971).
[68] Nemoto, N., Moriwaki, M., Odami, H., and Kurata, M., Shear creep studies of narrow-distribution poly (*cis*-isoprene), Macromolecules **4,** 215 (1971).
[69] Baresova, V., Szilagyi, L. and Danusso, F., Influence of entanglements on viscoelastic properties of polyisoprenes, J. Polym. Sci. **A-2, 10** 945 (1972).
[70] Szilagyi, L., Ricco. T. and Danusso, F., Characterization of viscoelastic behavior of stereoregular poly(isoprenes) by relaxation experiments, La Chimica E. Industria **55** 417, (1973); Rubber Chem. Technol. **47,** 1 (1974).
[71] Shen, M. C., McQuarrie, D. A. and Jackson, J. L., Thermoelastic behavior of natural rubber, J. Applied Phys. **38,** 791 (1967).
[72] Shen, M. Internal energy contribution to the elasticity of natural rubber, Macromolecules **2,** 358 (1969).
[73] van der Hoff, B. M. E., Relation between energy contribution to elastic force and strain dependence of modulus for polybutadiene vulcanizates, J. Macromol. Sci.-Chem. **A5** (4), 661 (1971).
[74] Mark, J. E., Thermoelastic properties of rubberlike networks and their thermodynamic and molecular interpretation, Rubber Chem. Technol. **46,** 593 (1973).
[75] Göritz, D., and Müller, F. H., Change of state of polymer networks on orientation, I. Energy-elastic contribution to rubber elasticity for cross-linked natural rubber, Koll. Zeits u. Z. Polymere **261,** 679 (1973).
[76] Kruse, J. and Timm T., Temperature dependence of the mech-

anical and stress-optical behavior of elastomers, Kautschuk und Gummi **12,** WT 83 (1959).
[77] Schäfer, E. E., and Rehage, G., On the entropy- and energy-elasticity of cross-linked high polymers, Makromolecular Chem. **123,** 91 (1969).
[78] Ferry, J. D., Mechanical properties of polymer networks, Proc. Int. Conf. Non-crystalline Solids Delft 1964, J. A. Prins Ed. p. 333 (North-Holland Publishing Co., Amsterdam Interscience New York, 1965).
[79] Porter, R. S., and Johnson, J. F., The entanglement concept in polymer systems, Chem. Rev. **66** 1 (1966).
[80] Porter, R. S., MacKnight, W. J., and Johnson, J. F., Viscous and elastic behavior attributed to polymer entanglements Rubber Chem. Technol. (Rubber Reviews) **41** (1), 1 (1968).
[81] Langley, N. R., Elastically effective strand density in polymer networks, Macromolecules **1,** 348 (1968).
[82] Langley, N. R., and Ferry J. D., Dynamic mechanical properties of cross-linked rubbers VI. Polydimethylsiloxane networks, Macromolecules **1,** 353 (1968).
[83] Reference [5], pages 441 ff.
[84] Langley, N. R., Polmanteer, K. E., Relation of elastic modulus to cross-link and entanglement concentrations in rubber networks, J. Polym. Sci.-Phys. Ed. **12,** 1023 (1974).
[85] Langley, N. R., and Polmanteer, K. E., The relation of elastic modulus to cross-links and entanglement concentration in rubber networks, Polymer Preprints (Am. Chem. Soc.) **15** (1) 47 (1974).
[86] Aharoni, S. M., Segmental interpenetrations and entanglements, J. Polym. Sci.-Polym. Lett. Ed. **12,** 549 (1974).
[87] Graessley, W. W., The entanglement concept in polymer rheology, Advances in Polymer Science (Fortschritte der Hochpolymeren Forschung) **16,** 1 (1974).
[88] Nielsen, L. E., Cross-linking—effect on physical properties of polymers, J. Macromol. Sci.-Rev. Macromol. Chem. **C3,** (1) 69 (1969).
[89] Tobolsky, A. V., Carlson, D. W., and Indictor, N., Rubber elasticity and chain configuration, J. Polym. Sci. **54,** 175 (1961).
[90] Krigbaum, W. R., and Roe, R. J., Survey of the theory of rubber-like elasticity, Rubber Chem. Technol. **38,** 1039 (1965).
[91] James, H. M., and Guth, E., Statistical thermodynamics of rubber elasticity J. Chem. Phys. **21,** 1039 (1953).
[92] Guth, E., Recent developments in the statistical mechanics of polymers, J. Polym. Sci. **C, 31,** 267 (1970).
[93] Wall, F. T., and Flory, P. J., Statistical thermodynamics of rubber elasticity J. Chem. Phys. **19,** 1435 (1951).
[94] Lorenz, O. and Parks, C. R., Cross-linking efficiency of some vulcanizing agents in natural rubber, J. Polym. Sci. **50,** 299 (1961).
[95] Thomas, D. K., Cross-linking efficiency of dicumyl peroxide in natural rubber, J. Applied Polymer Sci. **6,** 613 (1962).
[96] Loan, L. D., Cross-linking efficiencies of cumyl peroxide in unsaturated synthetic rubbers, J. Applied Polymer Sci. **7,** 2259 (1963); Rubber Chem. Technol. **38,** 573 (1965).
[97] Loan, L. D., Mechanism of the peroxide vulcanization of elastomers, Rubber Chem. Technol. **40,** 149 (1967).
[98] Treloar, L. R. G., Stress-strain data for vulcanized rubber under various types of deformation, Trans. Faraday Soc. **40,** 59 (1944); Rubber Chem. Technol. **17,** 813 (1944).
[99] Wood, L. A., Stress-strain relation of pure-gum rubber vulcanizates in compression and tension, J. Res. Nat. Bur. Stand. **60,** 193 (1958); Rubber Chem. Technol. **32,** 1 (1959).

(Paper 80A3–897)

JOURNAL OF RESEARCH of the National Bureau of Standards—A. Physics and Chemistry
Vol. 80A, No. 3, May-June 1976

# Calculations of Configurations of Doubly Ionized Copper (Cu III)

**J. Sugar and W. C. Martin**

**Institute for Basic Standards, National Bureau of Standards, Washington, D.C. 20234**

**(March 29, 1976)**

The energy levels belonging to the configurations $3d^74s^2$ and $3d^8n\ell$ ($n\ell = 4s$, $5s$, $4p$, $5p$, $4d$, $5d$, $4f$, and $5g$) have been calculated. The radial energy integrals were treated as parameters and adjusted to give a least-squares fit to the observed levels. Two- and three-body effective electrostatic interactions for equivalent electrons were included, as well as two-body effective interactions for inequivalent electrons. Strong configuration interaction between $3d^74s^2$ and $3d^84d$ was taken into account. Values of the parameters are given for all the above configurations, and the calculated levels are given for all except $3d^84s$ and $3d^84p$ (for which essentially equivalent results have been published). Leading eigenvector percentages are given in appropriate coupling schemes.

Key words: Atomic energy levels; atomic spectra; atomic theory; copper; doubly ionized copper; electron configuration.

## 1. Introduction

A great extension of the analysis of Cu III has recently been achieved by Shenstone [1].[1] In this work he determined nearly all the levels of the configurations $3d^74s^2$ and $3d^8n\ell$ for $n\ell = 4d$, $5d$, $5s$, $6s$, $5p$, $4f$, and much of $3d^85g$. In the course of this analysis we provided calculations of the level structures and continually refined them as new data were obtained. The final result is a set of calculations for all the known configurations of this ion (with the exception of $3d^74s4p$) that are internally consistent so far as common radial integrals (parameters) are concerned and that include all the effective electrostatic interactions, as well as the usual Slater and spin-orbit interactions, that have so far been considered in the iron group.

## 2. Method

Calculations of the energy matrices for these configurations, as well as the matrix diagonalizations and level fitting, were carried out on the NBS Univac 1108 computer. The computer programs were originally obtained from the Laboratoire Aimé Cotton (Orsay, France). Successive diagonalizations and variations of the radial parameters were performed until a least-squares fit of the energy levels was achieved. Final values for the parameters, the standard error for each parameter, and the rms error of the least-squares fit for each configuration are given in table 1. (See ref. [2], for example, for more details of the general procedure.) The rms error is defined as

$$\left[ \sum_{i=1}^{n} \delta_i^2/(n-m) \right]^{1/2},$$

where $\delta$ is the difference between the experimental and calculated positions for a level, $n$ is the number of levels used in the fitting, and $m$ is the number of free parameters. The standard error for a parameter value (in parentheses following the value) indicates how well the value is "defined" by the equations and the experimental levels.

In our initial calculations we were guided by the theoretical study of the even configurations of the third spectra of the iron group by Shadmi, Caspi, and Oreg [3] and by a similar work on the odd configurations by Roth [2]. These papers included claculations of the almost completely known $3d^84s$ and $3d^84p$ configurations of Cu III. Most of the parameters we use, including the effective two-body interactions ($\alpha$ and $\beta$) and three-body interactions ($T$ and $T_x$) for equivalent electrons, are defined in these papers or in reference [4]. In addition we introduced the two-body effective interactions for inequivalent electrons, denoted here as $D^k$ and $X^k$

[1] Figures in brackets indicate literature references given at the end of this paper.

TABLE 1. *Fitted radial parameters for configurations of Cu* III. *Units are* $cm^{-1}$. *Standard errors are given in parentheses except for those parameters whose values were fixed in the least-squares calculation.*

| Parameter | $3d^8 4s$ | $3d^8 5s$ | $3d^8 6s$ | $3d^8 4p$ | $3d^8 5p$ | $3d^8 4d$ | $3d^8 5d$ | $3d^8 4f$ | $3d^8 5g$ | $3d^7 4s^2$ |
|---|---|---|---|---|---|---|---|---|---|---|
| $A$ | 74956(28) | 204843(40) | 249188(41) | 145275(67) | 231897(38) | 208143(74) | 251277(37) | 245483(25) | 268357(17) | 186606(98) |
| $B$ | 1207.4(3.4) | 1234.3(4.3) | 1231.1(3.7) | 1217.9(3.8) | 1237.3(1.9) | 1235.5(2.9) | 1237.9(1.8) | 1247.1(1.0) | 1247 | 1294.9(7.5) |
| $C$ | 5024(28) | 5059(36) | 5115(24) | 5097(21) | 5066(11) | 5051(24) | 5073(13) | 5067.4(7.2) | 5067 | 5316(49) |
| $\alpha$ | 48.8(3.4) | 50.4(4.6) | 49.8(2.4) | 41.0(2.8) | 48.9(1.3) | 48.3(2.5) | 50.2(1.2) | 49.2(0.9) | 49 | 33(11) |
| $\beta$ | −496(36) | −496 | −496 | −583(28) | −496 | −496 | −496 | −496 | −496 | −496 |
| $T$ | −5.63 | −5.63 | −5.63 | −5.63 | −5.63 | −5.63 | −5.63 | −5.63 | −5.63 | −5.63 |
| $T_x$ | | | | | | | | | | −2.88 |
| $F^2$ | | | | 17510(110) | 4777(61) | 8390(130) | 3306(60) | 2047(49) | 1220(110) | |
| $F^4$ | | | | | | 3460(150) | 1320(94) | 292(92) | | |
| $G^0$ | | | | | | 1617(17) | 874.6(8.8) | | | |
| $G^1$ | | | | 6250(55) | 1643(35) | | | 285(35) | | |
| $G^2$ | 9488(60) | 2292(95) | 819(80) | | | 2820(140) | 1412(62) | | 460(64) | |
| $G^3$ | | | | 4580(180) | 1260(110) | | | 87(120) | | |
| $G^4$ | | | | | | 2030(270) | 1220(93) | | 0 | |
| $G^5$ | | | | | | | | 195(91) | | |
| $G^6$ | | | | | | | | | 0 | |
| $D^1$ | | | | −648(98) | −313(50) | −390(110) | | | | |
| $D^3$ | | | | | | −990(280) | | | | |
| $X^2$ | | | | 1420(580) | −1450(520) | | | | | |
| $\zeta(3d)$ | 901(15) | 901(24) | 918(10) | 903(14) | 910.8(6.7) | 906(13) | 911.7(5.1) | 907.7(3.4) | 913.7(6.0) | 973(25) |
| $\zeta(4d)$ | | | | | | 41(13) | | | | |
| $\zeta(5d)$ | | | | | | | 9.2(6.3) | | | |
| $\zeta(4p)$ | | | | 940(27) | | | | | | |
| $\zeta(5p)$ | | | | | 298(12) | | | | | |
| $\zeta(4f)$ | | | | | | | | 1.9(2.6) | | |
| $\zeta(5g)$ | | | | | | | | | 0 | |
| $R^2(dd', ss)$ | | | | | | 4930(170) | | | | 4930(170) |
| rms dev. | 53 | 32 | 10 | 72 | 34 | 77 | 35 | 28 | 41 | 77 |

for the direct and exchange parts [5].[2] We found these to be significant for the $3d^84p$, $3d^85p$ and $3d^84d$ configurations.

## 3. Parameters of the $3d^8$ Core

All configurations treated except $3d^74s^2$ are built on the $3d^8$ core. It is evident from the parameter values (table 1) that the core parameters are little affected by the additional outer electron of these configurations. The electrostatic parameters $B$, $C$, and $\alpha$ were freely varied in all cases except $3d^85g$; their fitted values are nearly identical for each configuration. The seniority parameter $\beta$ could be meaningfully evaluated only for $3d^84s$ and $3d^84p$, for which the doublet built on the $3d^8$ $^1$S core state is now known [1]. Its value was nearly the same in both cases and was also close to the value derived by Shadmi et al. [3] in their general treatment of the third spectra. It was therefore fixed at the value $-496$ cm$^{-1}$, derived from $3d^84s$, in all configurations of Cu III. Since most of the $3d^85g$ levels known with certainty are based on the $^3$F core term, all core parameters except the spin-orbit parameter $\zeta(3d)$ were fixed at average values derived from the other configurations. The fitted value of $\zeta(3d)$ for each of the $3d^8nl$ configurations was practically unchanged.

The effective 3-body parameter $T$ includes the interaction of $3s^23d^8$ with $3s3d^9$ and has a non-zero matrix element only for the $^1$D state of $3d^8$. This parameter cannot be freely determined for $3d^8$ because the number of core parameters exceeds the number of core terms; we therefore fixed it at the value $-5.63$ cm$^{-1}$ deduced by Shadmi et al. [3]. The significance of $T$ is demonstrated by the fact that the omission of this parameter leads to values for the parameters $C$, $\alpha$, and $\beta$ of the $3d^8nl$ configurations that are totally inconsistent with those derived from the general treatment of third spectra in references [2] and [3].[3] The second three-body parameter [4], $T_x$, had no effect on the $d^8nl$ configurations and was omitted. This parameter was included for $3d^74s^2$, where (along with $T$) it is an independent interaction. It was not possible to obtain meaningful fitted values for $T$ and $T_x$ in $3d^74s^2$, probably because their effect is small and this configuration is strongly distorted by near-configuration interaction. The fixed values used for them were estimated from the results of Shadmi et al. [3].

## 4. The Two-Body Effective Interaction for Inequivalent Electrons

The interaction is represented here by the parameters $D^k$ and $X^k$ calculated according to the formulas of Goldschmidt and Starkand [5].[2] They are the coefficients of the scalor products of unit operators, $D^k$ for the direct and $X^k$ for the exchange interaction. The allowed parameters for $d^8p$ are $D^1$ and $X^2$, and for $d^8d$ they are $D^1$, $D^3$, $X^1$, and $X^3$. In the case of $3d^84p$ and $3d^85p$ both effective parameters are well defined by a least-squares fit. Only $D^1$ and $D^3$ were defined for $3d^84d$, perhaps because the far-configuration effects were partly masked by the interaction with $3d^74s^2$. Our attempts to include this type of interaction by least-squares fits in the other configurations of Cu III were unsuccessful, but it is surely important for all $3d^n4p$ and $3d^n4d$ configurations of the iron period.

## 5. Results

An indication of the success of these calculations is the low rms error reached for all configurations (table 1), always less than 100 cm$^{-1}$ and usually much less. This is particularly significant for the highly mixed $3d^84d$ and $3d^74s^2$ configurations where large deviations present in single-configuration calculations are considerably reduced by the introduction of a single parameter $R^2(dd',ss)$ for configuration interaction. The inclusion of the effective parameters $D^k$ and $X^k$ in the $3d^84d$ configuration appears to be their first use for $3d^n4d$. As a further test we introduced them in a calculation[4] of $3d^24d$ of V III and found a reduction of the rms error from 117 cm$^{-1}$ reported by Spector [6] to 67 cm$^{-1}$. We repeated the calculation of $3d^84p$ of Cu III by Roth [2] who obtained an rms error of 126 cm$^{-1}$; with the inclusion of $D^1$ and $X^2$ the rms error was reduced to 72 cm$^{-1}$ (table 1).

Tables 2 through 8 contain the calculated levels obtained with the parameters of table 1. (The $3d^84s$ and $3d^84p$ results are not included because they are essentially the same as appear in references [2] and [3].)

All observed levels are from Shenstone [1], the values being rounded off to the nearest cm$^{-1}$. Observed levels followed by a question mark were so denoted by Shenstone to indicate that these levels may not be real. The "Leading Percentages" refer to squared eigenvector components given as percentages following the term symbols, and rounded off to the nearest percent. The "average %" given at the end of a "Leading Percentage" column is the average purity of the levels for the indicated coupling scheme. The $3d^8$ parent terms for $LS$-coupling designations are given in parentheses.

### 5.1. $(3d^84d+3d^74s^2)$ and $3d^85s$

The calculated levels for these even configurations are in tables 2 and 3, respectively. The two leading percentages in $LS$ coupling are given for each level, any second percentage less than 0.5 percent being omitted. In table 2, the two $3d^74s^2$ $^2$D terms are labeled 1 and 2 as in Nielson and Koster [7].

Shenstone [1] has described his method of assigning $LS$ names to the levels, beginning with the $3d^9$, $3d^84s$, and $3d^84p$ levels and proceeding to name the levels

[2] These authors use the notations $-F^k$ and $-G^k$ for the parameters here designated $D^k$ and $X^k$, respectively ($k=t$).

[3] With $T$ omitted, these parameters take the following values for Cu III $3d^84s$: $C=4686$ (28) cm$^{-1}$, $\alpha=91(3)$ cm$^{-1}$, and $\beta=-45(36)$ cm$^{-1}$.

[4] The following values were obtained for V III by least-squares fitting: $D^1=-728(88)$ cm$^{-1}$, $D^3=-1099(200)$ cm$^{-1}$, $X^1=-327(100)$ cm$^{-1}$, and $X^3=-678(170)$ cm$^{-1}$.

TABLE 2. *Calculated energy levels and leading percentages (LS coupling) for the interacting* $3d^84d$ *and* $3d^74s^2$ *configurations. States of* $3d^74s^2$ *are distinguishable by the absence of parentage. The meaning of the letters under "Remarks" is explained in the text (5.1)*

| J | Levels ($cm^{-1}$) | | O−C ($cm^{-1}$) | Leading percentages | | | | Remarks |
|---|---|---|---|---|---|---|---|---|
| | Observed | Calculated | | | | | | |
| 1/2 | | 186965 | | $^4P$ | 95 | $^2P$ | 3 | |
| | | 193945 | | $^2P$ | 91 | ($^3F$)$^2P$ | 5 | |
| | 195723 | 195743 | −20 | ($^3F$)$^4D$ | 84 | ($^3F$)$^4P$ | 9 | A |
| | 197200 | 197198 | 2 | ($^3F$)$^4P$ | 77 | ($^3F$)$^4D$ | 12 | A |
| | 198034 | 198041 | −7 | ($^3F$)$^2P$ | 81 | ($^3F$)$^4P$ | 13 | |
| | 211286 | 211296 | −10 | ($^1D$)$^2P$ | 62 | ($^3P$)$^4D$ | 29 | |
| | 212209 | 212137 | 72 | ($^1D$)$^2S$ | 85 | ($^3P$)$^4P$ | 10 | |
| | 213142 | 213148 | −6 | ($^3P$)$^4D$ | 70 | ($^1D$)$^2P$ | 27 | |
| | 215762 | 215730 | 32 | ($^3P$)$^4P$ | 86 | ($^1D$)$^2S$ | 11 | |
| | 216834 | 216794 | 40 | ($^3P$)$^2P$ | 89 | ($^1D$)$^2P$ | 7 | |
| 3/2 | 169608 | 169571 | 37 | $^4F$ | 99 | | | |
| | | 186134 | | $^4P$ | 91 | $^2P$ | 8 | |
| | | 192540 | | $^2P$ | 76 | $^2D2$ | 9 | |
| | 194684 | 194670 | 14 | ($^3F$)$^4D$ | 51 | ($^3F$)$^2P$ | 23 | A |
| | 196100 | 196095 | 5 | ($^3F$)$^2P$ | 51 | ($^3F$)$^4D$ | 39 | |
| | 196806 | 196745 | 61 | ($^3F$)$^4P$ | 69 | ($^3F$)$^2P$ | 16 | A |
| | 197986 | 198005 | −19 | ($^3F$)$^4F$ | 93 | ($^3F$)$^4D$ | 4 | |
| | | 198507 | | $^2D2$ | 54 | $^2P$ | 14 | |
| | 201732 | 201751 | −19 | ($^3F$)$^2D$ | 74 | $^2D2$ | 10 | |
| | 211124 | 211073 | 51 | ($^1D$)$^2D$ | 48 | ($^3P$)$^2D$ | 27 | |
| | 211652 | 211634 | 18 | ($^1D$)$^2P$ | 62 | ($^3P$)$^4D$ | 26 | |
| | 213312 | 213264 | 48 | ($^3P$)$^4D$ | 57 | ($^1D$)$^2P$ | 26 | |
| | 215197 | 215172 | 25 | ($^3P$)$^4F$ | 97 | ($^3P$)$^2D$ | 1 | |
| | 215807 | 215758 | 49 | ($^3P$)$^4P$ | 74 | ($^3P$)$^2D$ | 8 | |
| | 216235 | 216063 | 172 | ($^3P$)$^2D$ | 35 | ($^1G$)$^2D$ | 23 | B |
| | | 216818 | | ($^3P$)$^2P$ | 92 | ($^1D$)$^2D$ | 4 | |
| | 224504 | 224479 | 25 | ($^1G$)$^2D$ | 68 | ($^3P$)$^2D$ | 20 | |
| | | 240176 | | $^2D1$ | 80 | $^2D2$ | 20 | |
| | | 256250 | | ($^1S$)$^2D$ | 99 | | | |
| 5/2 | 168857 | 168834 | 23 | $^4F$ | 99 | | | |
| | | 185783 | | $^4P$ | 98 | ($^3F$)$^4P$ | 2 | |
| | 193885 | 193911 | −26 | ($^3F$)$^4D$ | 56 | ($^3F$)$^4P$ | 40 | A |
| | 195340 | 195255 | 85 | ($^3F$)$^4P$ | 51 | ($^3F$)$^4D$ | 28 | A |
| | [a] 196220 | 196232 | −12 | $^2D2$ | 59 | $^2D1$ | 18 | |
| | 196731 | 196768 | −37 | ($^3F$)$^4F$ | 34 | ($^3F$)$^2F$ | 30 | B |
| | 197901 | 197932 | −31 | ($^3F$)$^4G$ | 49 | ($^3F$)$^2F$ | 45 | B, C |
| | 198061 | 198078 | −17 | ($^3F$)$^4F$ | 56 | ($^3F$)$^4G$ | 24 | A, C |
| | 201215 | 201118 | 97 | ($^3F$)$^2D$ | 79 | ($^3F$)$^2F$ | 6 | |
| | 210159 | 210295 | −136 | ($^1D$)$^2F$ | 63 | ($^3P$)$^4D$ | 13 | |
| | 211680 | 211772 | −92 | ($^1D$)$^2D$ | 34 | ($^3P$)$^4D$ | 30 | B |
| | 213134 | 213117 | 17 | ($^3P$)$^4D$ | 51 | ($^1D$)$^2D$ | 30 | |
| | 213515 | 213317 | 198 | $^2F$ | 73 | ($^3P$)$^2F$ | 20 | |
| | 214990 | 214952 | 38 | ($^3P$)$^2D$ | 45 | ($^1G$)$^2D$ | 16 | A, C |
| | 215100 | 215042 | 58 | ($^3P$)$^4F$ | 83 | ($^1D$)$^2F$ | 4 | A, C |
| | 216145 | 216146 | −1 | ($^3P$)$^4P$ | 77 | ($^3P$)$^4F$ | 10 | |
| | 216376 | 216448 | −72 | ($^3P$)$^2F$ | 68 | $^2F$ | 14 | |
| | 221879 | 221882 | −3 | ($^1G$)$^2F$ | 98 | $^2F$ | 1 | |
| | 223787 | 223869 | −82 | ($^1G$)$^2D$ | 73 | ($^3P$)$^2D$ | 19 | |
| | | 240945 | | $^2D1$ | 76 | $^2D2$ | 23 | |
| | | 256273 | | ($^1S$)$^2D$ | 99 | | | |
| 7/2 | 167739 | 167741 | −2 | $^4F$ | 100 | | | |
| | 189603 | 189616 | −13 | $^2G$ | 98 | ($^3F$)$^2G$ | 2 | |
| | 193521 | 193536 | −15 | ($^3F$)$^4D$ | 93 | ($^3F$)$^4F$ | 5 | |
| | 195344 | 195374 | −30 | ($^3F$)$^2F$ | 53 | ($^3F$)$^4F$ | 24 | A |
| | 196742 | 196740 | 2 | ($^3F$)$^4G$ | 36 | ($^3F$)$^4H$ | 34 | B |
| | 197055 | 197063 | −8 | ($^3F$)$^4F$ | 47 | ($^3F$)$^4H$ | 28 | A |
| | 197594 | 197605 | −11 | ($^3F$)$^4G$ | 40 | ($^3F$)$^4H$ | 35 | B |
| | 198930 | 198988 | −58 | ($^3F$)$^2G$ | 81 | ($^3F$)$^4G$ | 8 | |
| | 210240 | 210309 | −69 | ($^1D$)$^2F$ | 69 | ($^3P$)$^4D$ | 24 | |

TABLE 2. *Calculated energy levels and leading percentages (LS coupling) for the interacting* $3d^84d$ *and* $3d^74s^2$ *configurations. States of* $3d^74s^2$ *are distinguishable by the absence of parentage. The meaning of the letters under "Remarks" is explained in the text (5.1)*—Continued

| J | Levels ($cm^{-1}$) | | O−C ($cm^{-1}$) | Leading percentages | | Remarks |
|---|---|---|---|---|---|---|
| | Observed | Calculated | | | | |
| | 211271 | 211217 | 54 | $(^1D)^2G$ 83 | $(^3P)^2F$ 10 | |
| | 212752 | 212860 | −108 | $(^3P)^4D$ 72 | $(^1D)^2F$ 19 | |
| | 213816 | 213988 | −172 | $^2F$ 56 | $(^3P)^2F$ 23 | |
| | 214845 | 214901 | −56 | $(^3P)^4F$ 90 | $(^1D)^2G$ 3 | |
| | 215977 | 216090 | −113 | $(^3P)^2F$ 65 | $^2F$ 29 | |
| | 221861 | 221876 | −15 | $(^1G)^2F$ 98 | $^2F$ 2 | |
| | 223174 | 223198 | −24 | $(^1G)^2G$ 99 | $(^1D)^2G$ 1 | |
| 9/2 | 166160 | 166210 | −50 | $^4F$ 99 | | |
| | 188098 | 188116 | −18 | $^2G$ 94 | $^2H$ 3 | |
| | 195062 | 195086 | −24 | $(^3F)^4G$ 39 | $(^3F)^4F$ 36 | B |
| | 195518 | 195415 | 103 | $(^3F)^4F$ 33 | $(^3F)^2H$ 21 | B |
| | 196029 | 196167 | −138 | $^2H$ 30 | $(^3F)^4G$ 23 | B |
| | 196796 | 196675 | 121 | $(^3F)^4H$ 65 | $(^3F)^2G$ 18 | A |
| | 197376 | 197573 | −197 | $(^3F)^2G$ 49 | $(^3F)^4G$ 26 | |
| | 198687 | 198561 | 126 | $(^3F)^2H$ 60 | $^2H$ 26 | |
| | 211314 | 211259 | 55 | $(^1D)^2G$ 82 | $(^3P)^4F$ 16 | |
| | 214748 | 214782 | −34 | $(^3P)^4F$ 83 | $(^1D)^2G$ 16 | |
| | 223090 | 223101 | −11 | $(^1G)^2H$ 91 | $(^1G)^2G$ 9 | |
| | 223201 | 223217 | −16 | $(^1G)^2G$ 90 | $(^1G)^2H$ 9 | |
| 11/2 | 194033 | 194017 | 16 | $(^3F)^2H$ 51 | $^2H$ 35 | B |
| | 194818 | 194816 | 2 | $(^3F)^4G$ 68 | $(^3F)^4H$ 27 | |
| | 195758 | 195745 | 13 | $(^3F)^4H$ 41 | $^2H$ 31 | B |
| | 197039 | 197000 | 39 | $(^3F)^2H$ 47 | $^2H$ 31 | B |
| | 220311 | 220291 | 20 | $(^1G)^2I$ 100 | | |
| | 223175 | 223173 | 2 | $(^1G)^2H$ 100 | | |
| 13/2 | 194332 | 194320 | 12 | $(^3F)^4H$ 100 | | |
| | 220414 | 220379 | 35 | $(^1G)^2I$ 100 | | |

[a] This level was found by Shenstone after publication of his paper [1]. The more exact value is 196220.49 $cm^{-1}$.

TABLE 3. *Calculated energy levels and leading percentages (LS coupling) for the* $3d^85s$ *configuration.*

| J | Levels ($cm^{-1}$) | | O−C ($cm^{-1}$) | Leading percentages | |
|---|---|---|---|---|---|
| | Observed | Calculated | | | |
| 1/2 | 213418 | 213408 | 10 | $(^3P)^4P$ 98 | $(^3P)^2P$ 2 |
| | 214730 | 214709 | 23 | $(^3P)^2P$ 98 | $(^3P)^4P$ 2 |
| | | 254805 | | $(^1S)^2S$ 100 | |
| 3/2 | 196442 | 196406 | 36 | $(^3F)^4F$ 99 | $(^1D)^2D$ 1 |
| | 210033 | 210035 | −2 | $(^1D)^2D$ 86 | $(^3P)^2P$ 10 |
| | 213127 | 213155 | −28 | $(^3P)^4P$ 94 | $(^1D)^2D$ 5 |
| | 214265 | 214236 | 29 | $(^3P)^2P$ 90 | $(^1D)^2D$ 8 |
| 5/2 | 195555 | 195524 | 31 | $(^3F)^4F$ 89 | $(^3F)^2F$ 11 |
| | 197400 | 197444 | −44 | $(^3F)^2F$ 88 | $(^3F)^4F$ 11 |
| | 209875 | 209860 | 15 | $(^1D)^2D$ 77 | $(^3P)^4P$ 22 |
| | 212951 | 212995 | −44 | $(^3P)^4P$ 78 | $(^1D)^2D$ 22 |
| 7/2 | 194117 | 194140 | −23 | $(^3F)^4F$ 64 | $(^3F)^2F$ 36 |
| | 195789 | 195792 | −3 | $(^3F)^2F$ 64 | $(^3F)^4F$ 36 |
| | 220569 | 220566 | 3 | $(^1G)^2G$ 100 | |
| 9/2 | 193371 | 193363 | 8 | $(^3F)^4F$ 100 | |
| | 220564 | 220565 | −1 | $(^1G)^2G$ 100 | |
| Average %..... | | | | 89 | |



206-267 OL - 76 - 6

TABLE 4. *Calculated energy levels and leading percentages for the* $3d^8 5p$ *configuration.*

| $J$ | Levels ($cm^{-1}$) | | O−C ($cm^{-1}$) | Leading percentages | | | |
|---|---|---|---|---|---|---|---|
| | Observed | Calculated | | LS | | $(L_1S_1)J_1j$ | |
| 1/2 | 215161 | 215155 | 6 | $(^3F)^4D$ | 99 | $^3F_2, 3/2$ | 99 |
| | 229054 | 229142 | −88 | $(^1D)^2P$ | 75 | $^1D_2, 3/2$ | 75 |
| | 231298? | 231304 | −6 | $(^3P)^4P$ | 91 | $^3P_1, 1/2$ | 57 |
| | | 232620 | | $(^3P)^4D$ | 97 | $^3P_0, 1/2$ | 65 |
| | | 233591 | | $(^3P)^2P$ | 86 | $^3P_1, 3/2$ | 51 |
| | | 234189 | | $(^3P)^2S$ | 95 | $^3P_2, 3/2$ | 53 |
| | | 273668 | | $(^1S)^2P$ | 100 | $^1S_0, 1/2$ | 100 |
| 3/2 | 214358 | 214351 | 7 | $(^3F)^4D$ | 88 | $^3F_3, 3/2$ | 73 |
| | 215783 | 215777 | 6 | $(^3F)^4F$ | 90 | $^3F_2, 3/2$ | 51 |
| | 216449 | 216463 | −14 | $(^3F)^2D$ | 90 | $^3F_2, 1/2$ | 39 |
| | 228469 | 228465 | 4 | $(^1D)^2D$ | 57 | $^1D_2, 1/2$ | 69 |
| | 229505 | 229430 | 75 | $(^1D)^2P$ | 55 | $^1D_2, 3/2$ | 82 |
| | 231458 | 231429 | 29 | $(^3P)^4P$ | 73 | $^3P_2, 1/2$ | 39 |
| | 232478? | 232499 | −21 | $(^3P)^4D$ | 87 | $^3P_1, 1/2$ | 77 |
| | 232814 | 232847 | −33 | $(^3P)^2P$ | 85 | $^3P_2, 3/2$ | 69 |
| | 233654 | 233581 | 73 | $(^3P)^2D$ | 87 | $^3P_1, 3/2$ | 54 |
| | 234036 | 234059 | −23 | $(^3P)^4S$ | 90 | $^3P_0, 3/2$ | 26 |
| | | 274085 | | $(^1S)^2P$ | 100 | $^1S_0, 3/2$ | 100 |
| 5/2 | 213026 | 213024 | 2 | $(^3F)^4D$ | 73 | $^3F_4, 3/2$ | 67 |
| | 214703 | 214704 | −1 | $(^3F)^2D$ | 39 | $^3F_3, 1/2$ | 69 |
| | 214766 | 214768 | −2 | $(^3F)^2D$ | 38 | $^3F_3, 3/2$ | 65 |
| | 215417 | 215410 | 7 | $(^3F)^4G$ | 60 | $^3F_2, 1/2$ | 55 |
| | 216566 | 216583 | −17 | $(^3F)^2F$ | 76 | $^3F_2, 3/2$ | 66 |
| | 228424 | 228436 | −12 | $(^1D)^2D$ | 52 | $^1D_2, 1/2$ | 58 |
| | 228960 | 228962 | −2 | $(^1D)^2F$ | 62 | $^1D_2, 3/2$ | 59 |
| | 231333 | 231371 | −38 | $(^3P)^4P$ | 72 | $^3P_2, 3/2$ | 42 |
| | 232458 | 232391 | 67 | $(^3P)^4D$ | 71 | $^3P_2, 1/2$ | 50 |
| | [a](232990) | 233057 | (67) | $(^3P)^2D$ | 75 | $^3P_1, 3/2$ | 53 |
| | 239149 | 239125 | 24 | $(^1G)^2F$ | 99 | $^1G_4, 3/2$ | 99 |
| 7/2 | 211821 | 211821 | 0 | $(^3F)^4D$ | 91 | $^3F_4, 1/2$ | 76 |
| | 213312 | 213313 | −1 | $(^3F)^4F$ | 36 | $^3F_4, 3/2$ | 63 |
| | 214328 | 214327 | 1 | $(^3F)^4G$ | 59 | $^3F_3, 1/2$ | 73 |
| | 215000 | 214998 | 2 | $(^3F)^4F$ | 46 | $^3F_3, 3/2$ | 84 |
| | 216018 | 216030 | −12 | $(^3F)^2G$ | 65 | $^3F_2, 3/2$ | 95 |
| | 229098 | 229074 | 24 | $(^1D)^2F$ | 81 | $^1D_2, 3/2$ | 81 |
| | 232436 | 232488 | −52 | $(^3P)^4D$ | 82 | $^3P_2, 3/2$ | 82 |
| | 238834 | 238829 | 5 | $(^1G)^2F$ | 98 | $^1G_4, 1/2$ | 68 |
| | 240786 | 240786 | 0 | $(^1G)^2G$ | 99 | $^1G_4, 3/2$ | 69 |
| 9/2 | 212415 | 212418 | −3 | $(^3F)^4G$ | 42 | $^3F_4, 1/2$ | 98 |
| | 212995 | 213004 | −9 | $(^3F)^4F$ | 67 | $^3F_4, 3/2$ | 99 |
| | 214588 | 214581 | 7 | $(^3F)^4G$ | 56 | $^3F_3, 3/2$ | 98 |
| | 238788 | 238807 | −19 | $(^1G)^2H$ | 99 | $^1G_4, 1/2$ | 81 |
| | 240853 | 240853 | 0 | $(^1G)^2G$ | 99 | $^1G_4, 3/2$ | 81 |
| 11/2 | 212525 | 212510 | 15 | $(^3F)^4G$ | 100 | $^3F_4, 3/2$ | 100 |
| | 239142 | 239154 | −12 | $(^1G)^2H$ | 100 | $^1G_4, 3/2$ | 100 |
| Average %..... | | | | | 77 | | 71 |

[a] This tentative level was not entered into the least-squares adjustment of the parameters. See text (5.2).

TABLE 5. *Calculated energy levels and leading percentages for the* $3d^8 6s$ *configuration*

| $J$ | Levels ($cm^{-1}$) | | O–C ($cm^{-1}$) | Leading percentages | |
|---|---|---|---|---|---|
| | Observed | Calculated | | $LS$ | $(L_1S_1)J_1j$ |
| 1/2 | | 258291 | | $(^3P)^4P$ 88 | $^3P_1$, 1/2 67 |
| | | 258785 | | $(^3P)^2P$ 88 | $^3P_0$, 1/2 67 |
| | | 299795 | | $(^1S)^2S$ 100 | $^1S_0$, 1/2 100 |
| 3/2 | 241392 | 241385 | 7 | $(^3F)^4F$ 99 | $^3F_2$, 1/2 99 |
| | 254694 | 254703 | −9 | $(^1D)^2D$ 82 | $^1D_2$, 1/2 82 |
| | | 258046 | | $(^3P)^4P$ 83 | $^3P_1$, 1/2 52 |
| | | 258380 | | $(^3P)^2P$ 79 | $^3P_1$, 1/2 48 |
| 5/2 | 240326 | 240330 | −4 | $(^3F)^4F$ 73 | $^3F_3$, 1/2 97 |
| | 241694 | 241699 | −5 | $(^3F)^2F$ 72 | $^3F_2$, 1/2 96 |
| | 254640 | 254630 | 10 | $(^1D)^2D$ 78 | $^1D_2$, 1/2 78 |
| | 257886 | 257887 | −1 | $(^3P)^4P$ 79 | $^3P_2$, 1/2 79 |
| 7/2 | 238638 | 238629 | 9 | $(^3F)^2F$ 63 | $^3F_4$, 1/2 98 |
| | 240303 | 240306 | −3 | $(^3F)^4F$ 63 | $^3F_3$, 1/2 98 |
| | | 265294 | | $(^1G)^2G$ 100 | $^1G_4$, 1/2 100 |
| 9/2 | 238280 | 238289 | −9 | $(^3F)^4F$ 100 | $^3F_4$, 1/2 100 |
| | 265293 | 265293 | 0 | $(^1G)^2G$ 100 | $^1G_4$, 1/2 100 |
| Average % | | | | 84 | 85 |

TABLE 6. *Calculated energy levels and leading percentages for the* $3d^8 5d$ *configuration*

| $J$ | Levels ($cm^{-1}$) | | O–C ($cm^{-1}$) | Leading percentages | |
|---|---|---|---|---|---|
| | Observed | Calculated | | LS | $(L_1S_1)J_1j$ |
| 1/2 | 240764 | 240806 | −42 | $(^3F)^4D$ 56 | $^3F_3$, 5/2 93 |
| | 241900 | 241901 | −1 | $(^3F)^4P$ 60 | $^3F_2$, 5/2 87 |
| | 242247 | 242272 | −25 | $(^3F)^2P$ 74 | $^3F_2$, 3/2 83 |
| | | 255515 | | $(^1D)^2P$ 79 | $^1D_2$, 3/2 48 |
| | | 255831 | | $(^1D)^2S$ 83 | $^1D_2$, 5/2 51 |
| | | 258312 | | $(^3P)^4D$ 90 | $^3P_1$, 3/2 69 |
| | | 259312 | | $(^3P)^4P$ 84 | $^3P_2$, 3/2 62 |
| | | 259847 | | $(^3P)^2P$ 86 | $^3P_2$, 5/2 61 |
| 3/2 | 239327 | 239311 | 16 | $(^3F)^2P$ 53 | $^3F_4$, 5/2 93 |
| | 240795 | 240834 | −39 | $(^3F)^4D$ 45 | $^3F_3$, 3/2 94 |
| | 241328 | 241334 | −6 | $(^3F)^4P$ 65 | $^3F_3$, 5/2 61 |
| | 242219 | 242222 | −3 | $(^3F)^4F$ 80 | $^3F_2$, 5/2 60 |
| | 244619 | 244535 | 84 | $(^3F)^2D$ 89 | $^3F_2$, 3/2 51 |
| | | 255562 | | $(^1D)^2D$ 62 | $^1D_2$, 5/2 48 |
| | 255750 | 255755 | −5 | $(^1D)^2P$ 71 | $^1D_2$, 3/2 42 |
| | | 258336 | | $(^3P)^4D$ 81 | $^3P_2$, 3/2 32 |
| | | 259301 | | $(^3P)^4F$ 81 | $^3P_1$, 3/2 53 |
| | | 259370 | | $(^3P)^4P$ 66 | $^3P_2$, 5/2 34 |
| | | 259957 | | $(^3P)^2P$ 87 | $^3P_0$, 3/2 29 |
| | | 260426 | | $(^3P)^2D$ 71 | $^3P_1$, 5/2 33 |
| | 267310 | 267320 | −10 | $(^1G)^2D$ 89 | $^1G_4$, 5/2 89 |
| | | 300578 | | $(^1S)^2D$ 100 | $^1S_0$, 3/2 100 |
| 5/2 | 238819 | 238835 | −16 | $(^3F)^4P$ 65 | $^3F_4$, 3/2 91 |
| | 240063 | 240042 | 21 | $(^3F)^4D$ 34 | $^3F_4$, 5/2 55 |
| | 240995 | 240982 | 13 | $(^3F)^2F$ 39 | $^3F_3$, 5/2 87 |
| | 242007 | 241987 | 20 | $(^3F)^2F$ 38 | $^3F_2$, 3/2 38 |
| | 242290 | 242279 | 11 | $(^3F)^4G$ 56 | $^3F_2$, 5/2 63 |
| | 243780 | 243755 | 25 | $(^3F)^2D$ 77 | $^3F_3$, 3/2 29 |
| | | 255176 | | $(^1D)^2F$ 67 | $^1D_2$, 3/2 79 |
| | 256093 | 256086 | 7 | $(^1D)^2D$ 61 | $^1D_2$, 5/2 80 |
| | | 258307 | | $(^3P)^4D$ 72 | $^3P_2$, 5/2 32 |
| | | 259097 | | $(^3P)^4F$ 72 | $^3P_1$, 3/2 43 |
| | | 259365 | | $(^3P)^4P$ 34 | $^3P_2$, 5/2 37 |
| | | 259587 | | $(^3P)^2F$ 60 | $^3P_1$, 5/2 85 |
| | | 260089 | | $(^3P)^2D$ 44 | $^3P_0$, 5/2 47 |

TABLE 6. *Calculated energy levels and leading percentages for the $3d^8 5d$ configuration—Cont.*

| J | Levels ($cm^{-1}$) | | O−C ($cm^{-1}$) | Leading percentages | |
|---|---|---|---|---|---|
| | Observed | Calculated | | LS | $(L_1S_1)J_1j$ |
| | 266092 | 266088 | 4 | $(^1G)^2F$ 99 | $^1G_4, 5/2$ 72 |
| | 267031 | 267094 | −63 | $(^1G)^2D$ 91 | $^1G_4, 3/2$ 67 |
| | | 300561 | | $(^1S)^2D$ 100 | $^1S_0, 5/2$ 100 |
| 7/2 | 238731 | 238774 | −43 | $(^3F)^4D$ 86 | $^3F_4, 3/2$ 49 |
| | 239441 | 239439 | 2 | $(^3F)^2F$ 59 | $^3F_4, 5/2$ 49 |
| | 241074 | 241069 | 5 | $(^3F)^4G$ 44 | $^3F_3, 3/2$ 91 |
| | 241250 | 241250 | 0 | $(^3F)^4F$ 46 | $^3F_3, 5/2$ 88 |
| | 242089 | 242053 | 36 | $(^3F)^4H$ 71 | $^3F_2, 3/2$ 68 |
| | 242610 | 242666 | −56 | $(^3F)^2G$ 69 | $^3F_2, 5/2$ 69 |
| | 255173 | 255162 | 11 | $(^1D)^2F$ 77 | $^1D_2, 5/2$ 66 |
| | 255487 | 255496 | −9 | $(^1D)^2G$ 83 | $^1D_2, 3/2$ 71 |
| | 258199 | 258199 | 0 | $(^3P)^4D$ 80 | $^3P_2, 5/2$ 54 |
| | 259018 | 258986 | 32 | $(^3P)^4F$ 80 | $^3P_2, 3/2$ 53 |
| | | 259333 | | $(^3P)^2F$ 81 | $^3P_1, 5/2$ 44 |
| | 266080 | 266087 | −7 | $(^1G)^2F$ 100 | $^1G_4, 5/2$ 52 |
| | 266643 | 266649 | −6 | $(^1G)^2G$ 100 | $^1G_4, 3/2$ 52 |
| 9/2 | 239290 | 239293 | −3 | $(^3F)^4F$ 58 | $^3F_4, 3/2$ 75 |
| | 239569 | 239609 | −40 | $(^3F)^2G$ 51 | $^3F_4, 5/2$ 74 |
| | 240973 | 240970 | 3 | $(^3F)^4H$ 60 | $^3F_3, 3/2$ 80 |
| | 241216 | 241229 | −13 | $(^3F)^4G$ 37 | $^3F_3, 5/2$ 82 |
| | 242298 | 242320 | −22 | $(^3F)^2H$ 62 | $^3F_2, 5/2$ 96 |
| | 255459 | 255464 | −5 | $(^1D)^2G$ 81 | $^1D_2, 5/2$ 81 |
| | 258855 | 258886 | −31 | $(^3F)^4F$ 82 | $^3P_2, 5/2$ 82 |
| | 266653 | 266624 | 29 | $(^1G)^2H$ 99 | $^1G_4, 3/2$ 81 |
| | 266597 | 266646 | −49 | $(^1G)^2G$ 99 | $^1G_4, 5/2$ 81 |
| 11/2 | 239112 | 239109 | 3 | $(^3F)^4G$ 51 | $^3F_4, 3/2$ 75 |
| | 239240 | 239252 | −12 | $(^3F)^2H$ 53 | $^3F_4, 5/2$ 75 |
| | 240961 | 240932 | 29 | $(^3F)^4H$ 55 | $^3F_3, 5/2$ 99 |
| | 265544 | 265508 | 36 | $(^1G)^2I$ 100 | $^1G_4, 3/2$ 87 |
| | 266637 | 266640 | −3 | $(^1G)^2H$ 100 | $^1G_4, 5/2$ 87 |
| 13/2 | 238994 | 238922 | 72 | $(^3F)^4H$ 100 | $^3F_4, 5/2$ 100 |
| | 265590 | 265528 | 62 | $(^1G)^2I$ 100 | $^1G_4, 5/2$ 100 |
| Average % | | | | 72 | 68 |

TABLE 7. *Calculated energy levels and leading percentages for the $3d^8 4f$ configuration*

| J | Levels ($cm^{-1}$) | | O−C ($cm^{-1}$) | Leading percentages | |
|---|---|---|---|---|---|
| | Observed | Calculated | | $(L_1S_1)J_1l[K]$ | LS |
| 1/2 | 234531 | 234510 | 21 | $^3F_4$ [1] 100 | $(^3F)^2S$ 45 |
| | 236324 | 236319 | 5 | $^3F_3$ [1] 75 | $(^3F)^4D$ 45 |
| | 236371 | 236368 | 3 | $^3F_3$ [0] 74 | $(^3F)^4P$ 42 |
| | 237591 | 237586 | 5 | $^3F_2$ [1] 99 | $(^3F)^2P$ 36 |
| | | 251062 | | $^1D_2$ [1] 83 | $(^1D)^2P$ 83 |
| | | 254662 | | $^3P_2$ [1] 84 | $(^3P)^4D$ 84 |
| | | 260986 | | $^1G_4$ [1] 100 | $(^1G)^2P$ 100 |
| 3/2 | 234427 | 234458 | −31 | $^3F_4$ [1] 84 | $(^3F)^4P$ 49 |
| | 234661 | 234649 | 12 | $^3F_4$ [2] 84 | $(^3F)^2P$ 48 |
| | 236395 | 236405 | −10 | $^3F_3$ [1] 71 | $(^3F)^4D$ 36 |
| | 236485 | 236488 | −3 | $^3F_3$ [2] 71 | $(^3F)^4F$ 39 |
| | 237539 | 237563 | −24 | $^3F_2$ [1] 74 | $(^3F)^4P$ 36 |
| | 237734 | 237733 | 1 | $^3F_2$ [2] 74 | $(^3F)^2D$ 41 |
| | | 250942 | | $^1D_2$ [2] 81 | $(^1D)^2D$ 81 |
| | | 251070 | | $^1D_2$ [1] 83 | $(^1D)^2P$ 83 |
| | | 254178 | | $^3P_2$ [2] 72 | $(^3P)^4F$ 87 |
| | 254673? | 254681 | −8 | $^3P_2$ [1] 81 | $(^3P)^4D$ 59 |
| | | 254832 | | $^3P_1$ [2] 79 | $(^3P)^2D$ 61 |
| | | 260953 | | $^1G_4$ [1] 100 | $(^1G)^2P$ 100 |
| | | 261210 | | $^1G_4$ [2] 100 | $(^1G)^2D$ 100 |
| 5/2 | 234491 | 234489 | 2 | $^3F_4$ [2] 88 | $(^3F)^4D$ 45 |
| | 234775 | 234771 | 4 | $^3F_4$ [3] 88 | $(^3F)^2D$ 50 |

TABLE 7. *Calculated energy levels and leading percentages for the* $3d^84f$ *configuration*—Con.

| $J$ | Levels ($cm^{-1}$) | | O−C ($cm^{-1}$) | Leading percentages | |
|---|---|---|---|---|---|
| | Observed | Calculated | | $(L_1S_1)J_1l[K]$ | $LS$ |
| | 236471 | 236465 | 6 | $^3F_3[2]$ 99 | $(^3F)^4P$ 37 |
| | 236590 | 236588 | 2 | $^3F_3[3]$ 99 | $(^3F)^4G$ 37 |
| | 237674 | 237686 | −12 | $^3F_2[2]$ 72 | $(^3F)^4F$ 36 |
| | 237831 | 237836 | −5 | $^3F_2[3]$ 72 | $(^3F)^2F$ 39 |
| | 250732 | 250778 | −46 | $^1D_2[3]$ 81 | $(^1D)^2F$ 81 |
| | 250955? | 250973 | −18 | $^1D_2[2]$ 82 | $(^1D)^2D$ 82 |
| | 254126 | 254142 | −16 | $^3P_2[3]$ 45 | $(^3P)^4F$ 80 |
| | | 254384 | | $^3P_2[2]$ 46 | $(^3P)^2F$ 74 |
| | 254794 | 254807 | −13 | $^3P_1[2]$ 89 | $(^3P)^4D$ 72 |
| | | 254907 | | $^3P_1[3]$ 95 | $(^3P)^4G$ 69 |
| | | 255133 | | $^3P_0[3]$ 93 | $(^3P)^2D$ 50 |
| | | 261199 | | $^1G_4[2]$ 100 | $(^1G)^2D$ 100 |
| | | 261510 | | $^1G_4[3]$ 100 | $(^1G)^2F$ 100 |
| | | 296001 | | $^1S_0[3]$ 100 | $(^1S)^2F$ 100 |
| 7/2 | 234562 | 234566 | −4 | $^3F_4[3]$ 94 | $(^3F)^4D$ 57 |
| | 234813 | 234802 | 11 | $^3F_4[6]$ 94 | $(^3F)^2F$ 53 |
| | 236512 | 236494 | 18 | $^3F_3[3]$ 93 | $(^3F)^4D$ 31 |
| | 236611 | 236607 | 4 | $^3F_3[4]$ 93 | $(^3F)^4G$ 33 |
| | 237751 | 237761 | −10 | $^3F_2[4]$ 79 | $(^3F)^4H$ 54 |
| | 237815 | 237803 | 11 | $^3F_2[3]$ 79 | $(^3F)^2G$ 47 |
| | 250734 | 250732 | 2 | $^1D_2[4]$ 69 | $(^1D)^2G$ 69 |
| | 250818 | 250859 | −41 | $^1D_2[3]$ 69 | $(^1D)^2F$ 69 |
| | 254132 | 254103 | 29 | $^3P_2[3]$ 65 | $(^3P)^4F$ 76 |
| | | 254221 | | $^3P_2[4]$ 67 | $(^3P)^2F$ 75 |
| | 254772 | 254737 | 35 | $^3P_1[4]$ 97 | $(^3P)^4G$ 60 |
| | 254927 | 254914 | 13 | $^3P_1[3]$ 98 | $(^3P)^2G$ 40 |
| | | 255131 | | $^3P_0[3]$ 96 | $(^3P)^4D$ 50 |
| | 261563 | 261508 | 55 | $^1G_4[3]$ 100 | $(^1G)^2F$ 100 |
| | 261763 | 261798 | −35 | $^1G_4[4]$ 100 | $(^1G)^2G$ 100 |
| | | 296004 | | $^1S_0[3]$ 100 | $(^1S)^2F$ 100 |
| 9/2 | 234655 | 234674 | −19 | $^3F_4[6]$ 99 | $(^3F)^4F$ 68 |
| | 234775 | 234753 | 22 | $^3F_4[5]$ 99 | $(^3F)^2G$ 58 |
| | 236537 | 236529 | 8 | $^3F_3[5]$ 88 | $(^3F)^4H$ 45 |
| | 236550 | 236565 | −15 | $^3F_3[4]$ 88 | $(^3F)^4G$ 38 |
| | 237645 | 237613 | 32 | $^3F_2[5]$ 99 | $(^3F)^4I$ 78 |
| | 237779 | 237789 | −10 | $^3F_2[4]$ 99 | $(^3F)^2H$ 44 |
| | 250734 | 250730 | 4 | $^1D_2[4]$ 81 | $(^1D)^2G$ 81 |
| | 251000 | 250946 | 54 | $^1D_2[5]$ 83 | $(^1D)^2H$ 83 |
| | 254031 | 254070 | −39 | $^3P_2[4]$ 80 | $(^3P)^4F$ 80 |
| | 254449 | 254508 | −59 | $^3P_2[5]$ 83 | $(^3P)^2G$ 55 |
| | 254784 | 254729 | 55 | $^3P_1[4]$ 94 | $(^3P)^4G$ 60 |
| | 261757 | 261800 | −43 | $^1G_4[4]$ 100 | $(^1G)^2G$ 100 |
| | 261996 | 261966 | 30 | $^1G_4[5]$ 100 | $(^1G)^2H$ 100 |
| 11/2 | 234681 | 234695 | −14 | $^3F_4[6]$ 93 | $(^3F)^2H$ 46 |
| | 234717 | 234752 | −35 | $^3F_4[5]$ 93 | $(^3F)^4G$ 69 |
| | 236419 | 236407 | 12 | $^3F_3[6]$ 100 | $(^3F)^2I$ 55 |
| | 236532 | 236540 | −8 | $^3F_3[5]$ 100 | $(^3F)^4H$ 42 |
| | 237641 | 237645 | −4 | $^3F_2[5]$ 99 | $(^3F)^2I$ 50 |
| | 251011 | 250949 | 62 | $^1D_2[5]$ 83 | $(^1D)^2H$ 83 |
| | 254468 | 254492 | −24 | $^3P_2[5]$ 84 | $(^3P)^4G$ 84 |
| | 261820 | 261837 | −17 | $^1G_4[6]$ 100 | $(^1G)^2I$ 100 |
| | 261998 | 261969 | 29 | $^1G_4[5]$ 100 | $(^1G)^2H$ 100 |
| 13/2 | 234533 | 234553 | −20 | $^3F_4[7]$ 99 | $(^3F)^2I$ 67 |
| | 234671 | 234670 | 1 | $^3F_4[6]$ 99 | $(^3F)^4H$ 85 |
| | 236418 | 236403 | 15 | $^3F_3[6]$ 100 | $(^3F)^4I$ 60 |
| | 261170 | 261159 | 11 | $^1G_4[7]$ 100 | $(^1G)^2K$ 100 |
| | 261812 | 261843 | −31 | $^1G_4[6]$ 100 | $(^1G)^2I$ 100 |
| 15/2 | 234537 | 234520 | 17 | $^3F_4[7]$ 100 | $(^3F)^4I$ 100 |
| | 261168 | 261165 | 3 | $^1G_4[7]$ 100 | $(^1G)^2K$ 100 |
| Average % | | | | 82 | 67 |

TABLE 8. *Calculated energy levels and leading percentages for the* $3d^8 5g$ *configuration*

| $J$ | Levels ($cm^{-1}$) | | O−C ($cm^{-1}$) | Leading percentages | |
|---|---|---|---|---|---|
| | Observed | Calculated | | $(L_1S_1)J_1l[K]$ | $LS$ |
| 1/2 | 257495 | 257407 | 88 | $^3F_4[0]$ 63 | $(^3F)^4P$ 86 |
| | | 257491 | | $^3F_4[1]$ 63 | $(^3F)^2P$ 73 |
| | | 259319 | | $^3F_3[1]$ 99 | $(^3F)^4D$ 61 |
| | | 284186 | | $^1G_4[0]$ 99 | $(^1G)^2S$ 99 |
| | | 284229 | | $^1G_4[1]$ 99 | $(^1G)^2P$ 99 |
| 3/2 | | 257430 | | $^3F_4[1]$ 69 | $(^3F)^4P$ 51 |
| | 257603 | 257584 | 19 | $^3F_4[2]$ 69 | $(^3F)^2D$ 43 |
| | | 259363 | | $^3F_3[2]$ 90 | $(^3F)^4F$ 53 |
| | 259433 | 259376 | 57 | $^3F_3[1]$ 90 | $(^3F)^4D$ 33 |
| | | 260612 | | $^3F_2[2]$ 98 | $(^3F)^2P$ 36 |
| | | 273899 | | $^1D_2[2]$ 82 | $(^1D)^2D$ 82 |
| | | 277499 | | $^3P_2[2]$ 83 | $(^3F)^4F$ 83 |
| | | 284219 | | $^1G_4[1]$ 100 | $(^1G)^2P$ 100 |
| | | 284303 | | $^1G_4[2]$ 100 | $(^1G)^2D$ 100 |
| 5/2 | 257489 | 257464 | 25 | $^3F_4[2]$ 74 | $(^3F)^4D$ 53 |
| | 257672 | 257673 | −1 | $^3F_4[3]$ 74 | $(^3F)^2D$ 37 |
| | | 259411 | | $^3F_3[2]$ 86 | $(^3F)^4P$ 34 |
| | 259470 | 259463 | 7 | $^3F_3[3]$ 88 | $(^3F)^4G$ 50 |
| | | 260545 | | $^3F_2[2]$ 76 | $(^3F)^4D$ 34 |
| | | 260724 | | $^3F_2[3]$ 77 | $(^3F)^2F$ 34 |
| | | 273812 | | $^1D_2[3]$ 79 | $(^1D)^2F$ 79 |
| | | 273899 | | $^1D_2[2]$ 81 | $(^1D)^2D$ 81 |
| | | 277215 | | $^3P_1[3]$ 57 | $(^3P)^4G$ 79 |
| | | 277466 | | $^3P_2[2]$ 81 | $(^3P)^4F$ 48 |
| | | 277653 | | $^3P_2[3]$ 55 | $(^3P)^2F$ 50 |
| | | 284291 | | $^1G_4[2]$ 100 | $(^1G)^2D$ 100 |
| | | 284410 | | $^1G_4[3]$ 100 | $(^1G)^2F$ 100 |
| 7/2 | 257515 | 257506 | 9 | $^3F_4[3]$ 80 | $(^3F)^4F$ 52 |
| | 257668? | 257701 | −33 | $^3F_4[4]$ 80 | $(^3F)^2F$ 44 |
| | | 259421 | | $^3F_3[3]$ 98 | $(^3F)^4D$ 44 |
| | | 259505 | | $^3F_3[4]$ 99 | $(^3F)^4H$ 45 |
| | 260633? | 260625 | 8 | $^3F_2[3]$ 57 | $(^3F)^4G$ 36 |
| | | 260741 | | $^3F_2[5]$ 58 | $(^3F)^2G$ 39 |
| | | 273724 | | $^1D_2[4]$ 81 | $(^1D)^2G$ 81 |
| | 273801 | 273843 | −42 | $^1D_2[3]$ 82 | $(^1D)^2F$ 82 |
| | | 277176 | | $^3P_2[4]$ 28 | $(^3P)^4G$ 73 |
| | | 277360 | | $^3P_2[3]$ 33 | $(^3P)^2G$ 55 |
| | | 277650 | | $^3P_1[3]$ 58 | $(^3F)^4F$ 61 |
| | | 277744 | | $^3P_0[4]$ 90 | $(^3P)^4H$ 57 |
| | | 277996 | | $^3P_1[4]$ 78 | $(^3P)^2F$ 35 |
| | | 284403 | | $^1G_4[3]$ 100 | $(^1G)^2F$ 100 |
| | | 284542 | | $^1G_4[4]$ 100 | $(^1G)^2G$ 100 |
| | | 318914 | | $^1S_0[4]$ 100 | $(^1S)^2G$ 100 |
| 9/2 | 257574? | 257546 | 28 | $^3F_4[4]$ 87 | $(^3F)^4G$ 46 |
| | 257626 | 257655 | −29 | $^3F_4[5]$ 87 | $(^3F)^2G$ 51 |
| | 259403? | 259414 | −11 | $^3F_3[4]$ 92 | $(^3F)^4F$ 38 |
| | | 259480 | | $^3F_3[5]$ 92 | $(^3F)^4H$ 29 |
| | | 260654 | | $^3F_2[5]$ 74 | $(^3F)^4I$ 48 |
| | 260676? | 260684 | −8 | $^3F_2[4]$ 74 | $(^3F)^2H$ 42 |
| | 273739? | 273692 | 47 | $^1D_2[5]$ 70 | $(^1D)^2H$ 70 |
| | 273807 | 273807 | 0 | $^1D_2[4]$ 70 | $(^1D)^2G$ 70 |
| | | 277141 | | $^3P_2[4]$ 49 | $(^3P)^4G$ 67 |
| | | 277236 | | $^3P_2[5]$ 53 | $(^3P)^2G$ 62 |
| | | 277630 | | $^3P_1[5]$ 69 | $(^3P)^4H$ 49 |
| | | 277727 | | $^3P_0[4]$ 90 | $(^3P)^4F$ 48 |
| | | 277986 | | $^3P_1[4]$ 77 | $(^3P)^4F$ 39 |
| | | 284539 | | $^1G_4[4]$ 100 | $(^1G)^2G$ 100 |
| | | 284662 | | $^1G_4[5]$ 100 | $(^1G)^2H$ 100 |
| | | 318908 | | $^1S_0[4]$ 100 | $(^1S)^2G$ 100 |
| 11/2 | 257531 | 257575 | −44 | $^3F_4[5]$ 100 | $(^3F)^4G$ 60 |
| | [a] 257556 | 257586 | −30 | $^3F_4[6]$ 100 | $(^3F)^2H$ 52 |
| | 259404 | 259415 | −11 | $^3F_3[6]$ 99 | $(^3F)^4I$ 33 |
| | 259418 | 259434 | −16 | $^3F_3[5]$ 100 | $(^3F)^4G$ 35 |
| | 260591 | 260564 | 27 | $^3F_2[6]$ 98 | $(^3F)^4K$ 79 |

TABLE 8. *Calculated energy levels and leading percentages for the* $3d^85g$ *configuration*—Continued

| $J$ | Levels ($cm^{-1}$) | | O−C ($cm^{-1}$) | Leading percentages | | | |
|---|---|---|---|---|---|---|---|
| | Observed | Calculated | | $(L_1S_1)J_1l[K]$ | | $LS$ | |
| | 260646? | 260656 | −10 | $^3F_2[5]$ | 99 | $(^3F)^2I$ | 39 |
| | 273733? | 273692 | 41 | $^1D_2[5]$ | 82 | $(^1D)^2H$ | 82 |
| | 273800? | 273821 | −21 | $^1D_2[6]$ | 82 | $(^1D)^2I$ | 82 |
| | | 277126 | | $^3P_2[5]$ | 46 | $(^3P)^4G$ | 75 |
| | | 277364 | | $^3P_2[6]$ | 83 | $(^3P)^2H$ | 60 |
| | | 277605 | | $^3P_1[5]$ | 59 | $(^3P)^4H$ | 61 |
| | | 284662 | | $^1G_4[5]$ | 100 | $(^1G)^2H$ | 100 |
| | | 284702 | | $^1G_4[6]$ | 100 | $(^1G)^2I$ | 100 |
| 13/2 | 257540 | 257554 | −14 | $^3F_4[7]$ | 99 | $(^3F)^2I$ | 60 |
| | 257565 | 257586 | −21 | $^3F_4[6]$ | 100 | $(^3F)^4H$ | 71 |
| | 259372 | 259335 | 37 | $^3F_3[7]$ | 100 | $(^3F)^4K$ | 52 |
| | 259404 | 259415 | −11 | $^3F_3[6]$ | 99 | $(^3F)^4I$ | 39 |
| | 260591 | 260564 | 27 | $^3F_2[6]$ | 98 | $(^3F)^2K$ | 49 |
| | 273802? | 273821 | −19 | $^1D_2[6]$ | 82 | $(^1D)^2I$ | 82 |
| | | 277364 | | $^3P_2[6]$ | 83 | $(^3P)^4H$ | 83 |
| | | 284572 | | $^1G_4[7]$ | 100 | $(^1G)^2K$ | 100 |
| | | 284702 | | $^1G_4[6]$ | 100 | $(^1G)^2I$ | 100 |
| 15/2 | 257505 | 257460 | 45 | $^3F_4[8]$ | 100 | $(^3F)^2K$ | 71 |
| | 257540 | 257554 | −14 | $^3F_4[7]$ | 100 | $(^3F)^4I$ | 84 |
| | 259372 | 259335 | 37 | $^3F_3[7]$ | 100 | $(^3F)^4K$ | 60 |
| | 284098 | 284194 | −96 | $^1G_4[8]$ | 100 | $(^1G)^2L$ | 100 |
| | | 284572 | | $^1G_4[7]$ | 100 | $(^1G)^2K$ | 100 |
| 17/2 | 257505 | 257460 | 45 | $^3F_4[8]$ | 100 | $(^3F)^4K$ | 100 |
| | 284096 | 284194 | −98 | $^1G_4[8]$ | 100 | $(^1G)^2L$ | 100 |
| Average %..... | | | | | 85 | | 66 |

[a] The value of this level is 257556.45 $cm^{-1}$. It was listed incorrectly as 257566.45 $cm^{-1}$ in Shenstone's publication [1].

of the higher configurations on the basis of the relative intensities of their transitions. His designations are usually in agreement with our calculations for those levels whose assigned eigenvectors yield meaningful $LS$ names. As examples of the nature of such discrepancies as exist, we have added a column to table 2 for remarks on the designations of the levels. (Shenstone draws attention to the $(3d^84d+3d^74s^2)$ group in this connection.) The eigenvectors for the observed levels in table 2 given without a letter in the final column confirm the names assigned by Shenstone.[5] The letters in the final column have the following meanings:

A. The leading component of the eigenvector indicates a designation different from that assigned by Shenstone.
B. The eigenvector yields no theoretically satisfactory single-configuration single-term designation.[5]
C. Indicates pairs of neighboring levels whose eigenvectors might possibly be interchanged.

The low $3d^8(^3F)4d$ $^4P$ and $^4D$ terms overlap, but the $^4D$ term is lower according to our calculations; this accounts for the first six "A" notations in the table. The several B notations for the $J=9/2$ and $J=11/2$ levels mainly arise because of the strong admixtures of $3d^74s^2$ $^2H$ components, which are so distributed amongst these levels that no level for either $J$ value can meaningfully be assigned to this term. The very similar compositions of the $J=11/2$ levels at 194033 and 197039 $cm^{-1}$ may be noted; these prevent a designation for either level according to our criteria.

### 5.2. $3d^85p$, $3d^86s$, and $3d^85d$.

The results for these configurations are given in tables 4, 5, and 6. The leading percentage for each level is given in $LS$ coupling and in a $(L_1S_1)J_1j$ coupling scheme. The notations for the latter scheme have the

[5] Our conditions for a name are that the leading percentage be near 50 percent or greater; and for a leading percentage near 50 percent, the second percentage must be significantly smaller (second designations clearly less appropriate), and no other eigenvector should have a comparable leading percentage ( ~ 50%) for the same designation.

$3d^8$ parent level (in *LS* coupling) followed by the *j* value of the outer electron. Most of the levels have meaningful names in either scheme. The average purity in *LS* coupling is a little higher than the $J_1j$ purity ($3d^85p$ and $3d^85d$), or the purities in the two schemes are practically equal ($3d^86s$); the *LS* names are probably more generally useful.

Shenstone assigned some 25 odd levels to the $3d^74s4p$ configuration [1]. We calculated this large configuration, but the results of the level fitting were inconclusive because of the lack of sufficient data. Shenstone assigned a tentative level at 232 990 $cm^{-1}$ to $3d^7(^4F)4s4p(^3P^\circ)\ ^2D^\circ_{5/2}$ and a level at 233 286 $cm^{-1}$ to $3d^8(^3P)5p\ ^2D^\circ_{5/2}$. The lower of these levels is closer to our prediction for $3d^8(^3P)5p\ ^2D^\circ_{5/2}$, but we used neither level in the least-squares calculations. Although the good fit obtained for the $3d^85p$ levels indicates that the general configuration interaction with $3d^74s4p$ is weak, the closeness of these two $^2D^\circ_{5/2}$ levels might result in significant configuration mixing.

### 5.3. $3d^84f$ and $3d^85g$

Shenstone pointed out that the level structure of the $3d^8$ parent configuration could usually be discerned in the pattern of the $3d^8nl$ levels. "In $5g$ the scheme [in which the parent *J* value is defined] reaches an extreme which makes it possible to identify some, but not all of the levels. In fact, the number of combinations of a level is reduced in most cases to just two..." A small number of combinations is one effect of pair coupling and, as is evident from tables 7 and 8, the $3d^84f$ and $3d^85g$ configurations are best described by the $J_1l$ coupling scheme. The designations for this scheme have the $3d^8$ parent level ($L_1$,$S_1$, and $J_1$) preceding the bracketed *K* value (obtained by coupling $J_1$ and the *l* vector of the outer electron) [8]. Shenstone was able to deduce *LS* names for the $4f$ and $5g$ levels in some accordance with the intensities of their transitions, but many of the *LS* designations have meaning only in that connection. Only two of the eigenvectors for $3d^84f$ have leading percentages less than 50 percent in $J_1l$ coupling, whereas there are 23 such eigenvectors in *LS* coupling; for $3d^85g$, the equivalent numbers are 4 and 26.

## 6. References


[1] Shenstone, A. G., J. Res. Nat. Bur. Stand. (U.S.), **79A** (Phys. and Chem.), No. 3, 497–521 (May–June 1975).
[2] Roth, C., J. Res. Nat. Bur. Stand. (U.S.), **72A** (Phys. and Chem.), No. 5, 505–520 (Sept.–Oct. 1968).
[3] Shadmi, Y., Caspi, E., and Oreg, J., J. Res. Nat. Bur. Stand. (U.S.), **73A** (Phys. and Chem.), No. 2, 173–189 (Mar.–Apr. 1969).
[4] Shadmi, Y., Oreg, J., and Stein, J., J. Opt. Soc. Am. **58**, 909 (1968).
[5] Goldschmidt, Z. B., and Starkand, J., J. Phys. B **3**, L141 (1970).
[6] Spector, N., Opt. Pura Aplic. **3**, 33 (1970).
[7] Nielson, C. W., and Koster, G. F., Spectroscopic Coefficients for the $p^n$, $d^n$, and $f^n$ Configurations (M.I.T. Press, Cambridge, Mass., 1963), 275 pp.
[8] Racah, G., Phys. Rev. **61**, 537 (1942).


(Paper 80A3–898)

JOURNAL OF RESEARCH of the National Bureau of Standards—A. Physics and Chemistry
Vol. 80A, No. 3, May–June 1976

# The International Practical Temperature Scale of 1968 in the Region 90.188 K to 903.89 K as Maintained at the National Bureau of Standards

**George T. Furukawa, John L. Riddle, and William R. Bigge**

**Institute for Basic Standards, National Bureau of Standards, Washington, D.C. 20234**

**(March 16, 1976)**

The reproducibility of the International Practical Temperature Scale of 1968 (IPTS–68) in the region 90.188 K to 903.89 K as maintained at the National Bureau of Standards is discussed. The realizations of the triple point of water, the freezing points of zinc and tin, and the boiling point of oxygen are described. The average of the standard deviations of the resistance measurements at the triple point of water of 213 platinum resistance thermometers received for calibration over a two-year period corresponds to ±0.15 mK. The standard deviations of the resistance ratio $R(T)/R(0\,°C)$ obtained with check thermometers employed for monitoring the zinc, tin, and oxygen point measurements correspond to ±0.28 mK, ±0.30 mK, and ±0.16 mK, respectively; the results of repeated calibrations with five thermometers show comparable reproducibility at the tin and oxygen points but the reproducibility is worse by a factor of two at the zinc point. When suitably packed for protection from possible mechanical shock platinum resistance thermometers can be shipped by common carrier and retain their calibrations.

Key words: Comparator; International Practical Temperature Scale of 1968; IPTS–68; oxygen point; platinum resistance thermometer; temperature standard; tin point; triple point of water; zinc point.

## 1. Introduction

From 13.81 K (−259.34 °C) to 903.89 K (630.74 °C) the International Practical Temperature Scale of 1968 [1,2],[1] referred to hereafter as IPTS–68, is based on nine defining fixed points, the platinum resistance thermometer (PRT) calibrated at these fixed points, and specified interpolation equations to relate the temperature and the resistance ratio,

$$W(T) = R(T)/R(0\,°C), \tag{1}$$

where $R(T)$ is the thermometer resistance at temperature $T$ and $R(0\,°C)$ is the resistance at 0 °C. The defining fixed points are equilibrium states between phases of pure substances to which values of temperature have been assigned. (The isotopic composition is generally specified wherever it may vary sufficiently to have a significant effect on the equilibrium temperature.) The thermometer resistor must be annealed pure platinum, supported in a "strain-free" manner and have a value of $W(100\,°C)$ not less than 1.39250. (Henceforth any reference to PRT indicates a thermometer of standards quality that meets the IPTS–68 specifications.) Below 0 °C the $W$ versus $T$ relation of the PRT is given by

$$W(T) = W^*(T) + \Delta W(T), \tag{2}$$

where $W^*(T)$ is the reference function defined by

$$T = \sum_{j=0}^{20} a_j \left[\frac{\ln W^*(T) + 3.28}{3.28}\right]^j \mathrm{K} \tag{3}$$

and $\Delta W(T)$ is a deviation function which is a polynomial in $T$[3]. (The coefficients $a_j$ of eq (3) are given in reference [2].) The range from 13.81 K to 273.15 K is divided into four subranges, each with its specified deviation function of the general form

$$\Delta W(T) = \sum_{i=0}^{n} k_i T^i \tag{4}$$

where $n \leq 4$. In the subrange 13.81 to 20.28 K, $n=3$; 20.38 to 54.361 K, $n=3$; 54.361 to 90.188 K, $n=2$; and 90.188 to 273.15 K, $n=4$. The coefficients $k_i$ are determined by calibration at the fixed points and by the requirement that the first derivative, $d\Delta W(T)/dT$, be continuous at the junction with the next higher subrange.

From 0 °C to 630.74 °C the values of temperature $t$ are defined by

[1] Figures in brackets indicate the literature references at the end of this paper.

$$t = t' + 0.045\left(\frac{t'}{100\ °C}\right)\left(\frac{t'}{100\ °C} - 1\right)$$

$$\left(\frac{t'}{419.58\ °C} + 1\right)\left(\frac{t'}{630.74\ °C} + 1\right)\ °C, \quad (5)$$

where $t'$ is defined by

$$W(t') = R(t')/R(0\ °C) = 1 + At' + Bt'^2. \quad (6)$$

By definition $t$ and $T$ are related by $t = T - 273.15$ K [2]. Equation (6) is equivalent to

$$t' = \left\{\frac{1}{\alpha}\left[W(t') - 1\right] + \delta\left(\frac{t'}{100\ °C}\right)\left(\frac{t'}{100\ °C} + 1\right)\right\}°C, \quad (7)$$

where

$$\alpha = A + B \times 100\ °C \quad (8)$$

and

$$\delta = -\frac{B(100\ °C)^2}{A + B \times 100\ °C}. \quad (9)$$

The thermometer constants $R(0\ °C)$, $A$, and $B$ are determined from resistance measurements at the triple point of water, the steam point or the tin point, and the zinc point. The constants $\alpha$ and $\delta$ are derived from the constants $A$ and $B$ according to eqs (8) and (9), respectively.

The accuracy of thermometry employing a well calibrated PRT depends primarily upon precise measurements of relative resistances to determine $W(T)$ accurately. In the calibration of PRT's, there are required, in addition, accurate realizations of the defining fixed points to obtain the thermometer constants. At the National Bureau of Standards (NBS) the defining fixed points: the triple point of water, the tin point, and the zinc point are maintained and are employed regularly in the calibration of PRT's. The defining fixed points below 0 °C are "maintained" at present by reference standard PRT's of the capsule type. In an earlier paper, the NBS–IPTS–68 scale between 13.81 and 90.188 K maintained by the reference standard PRT's was described and the reproducibility of the calibrations, in terms of the NBS–IPTS–68 scale, of capsule type PRT's received for calibration during a 2½-year period was shown [4]. The present paper deals with the calibration of long-stem type PRT's (and some capsule type PRT's in special holders) in the range 90.188 to 903.89 K. The fixed points that are maintained, the method of calibration, and the reproducibility of the results are discussed.

## 2. Fixed Points

### 2.1 Triple Point of Water

Of the thirteen defining fixed points[2] that are specified in the text of the IPTS–68 the triple point of water, henceforth referred to as TP, is the most important. (The Thermodynamic Kelvin Temperature Scale is defined by assigning 273.16 K to the temperature of the *TP* and the thermodynamic unit of temperature, kelvin, is defined as 1/273.16 of the thermodynamic temperature of the *TP* [2].) The PRT temperature scale as defined by the IPTS–68 utilizes the resistance ratio, $R(T)/R(0\ °C)$; consequently, the accuracy of every temperature measurement depends on the accuracy of two observations, $R(T)$ and $R(0\ °C)$. Above 0 °C, any errors in $R(0\ °C)$ are amplified in the resistance ratio $R(T)/R(0\ °C)$. (Hereafter, the resistance ratio $R(T)/R(0\ °C)$ will be referred to as $W(T)$.) In practice, the $R(0\ °C)$ of the PRT is determined from measurements at the TP; hence, the accuracy of $R(0\ °C)$ of the PRT ultimately depends on the accuracy of the measurements at the temperature of the TP and on the reproducibility of the TP. In a recent intercomparison of the TP temperatures of a bank of fifteen TP cells at the NBS, six observations were made on each cell over a period of three days; the averages of temperatures observed on each cell were within ±0.1 mK [5].

Figure 1 shows the design of the TP cell employed at the NBS. The sealed borosilicate glass cell contains only ice, water, and water vapor. The thermometer well is constructed of precision bore tubing. The extension at the top serves as a handle or as a support, as shown in the figure. By suitably positioning the cell most of the "gas" can be trapped in the extension and the amount of air can be estimated from the size of the bubble, if any, that remains. (At room temperature when the TP cell is positioned with the bottom end up, the bubble trapped in the extension is under a hydrostatic head of water that corresponds to a pressure slightly higher than the vapor pressure of water. Hence, if the bubble contains only water vapor, it should collapse when the TP cell is turned bottom end up.)

To prepare the TP cell for use, the cell is first cooled by immersing it in a bath of shaved ice for about one-half hour or so. The cell is then mounted in the ice bath with the opening of the reentrant thermometer well above the ice-water level and the thermometer well is wiped dry, e.g., by using absorbent paper on the end of a rod or a tube. A mantle of ice is frozen around and immediately next to the thermometer well by filling the thermometer well with crushed Dry Ice. The well is maintained full of Dry Ice for about 20 min, after which all of the Dry Ice is allowed to evaporate. (It is important to keep the well completely full of Dry Ice during the 20-min period. If the Dry Ice level in the well is allowed to fall several inches and then the well is refilled, the ice mantle is apt to crack. Although the crack often "heals," the desired triple-point temperature of the "inner melt" may not be achieved if a crack in the ice mantle later extends from the well surface into the surrounding liquid water of the cell. The impurities, if any, in the water are expected to become concentrated in the remaining liquid water that surrounds the ice mantle of the cell. This less pure liquid water should not be allowed to mix with the inner melt near the level of the

[2] The tin point (231.9681 °C) is an alternative to the steam point (100 °C) and the argon triple point (−189.352 °C) is an alternative to the oxygen normal boiling point (−182.962°C).

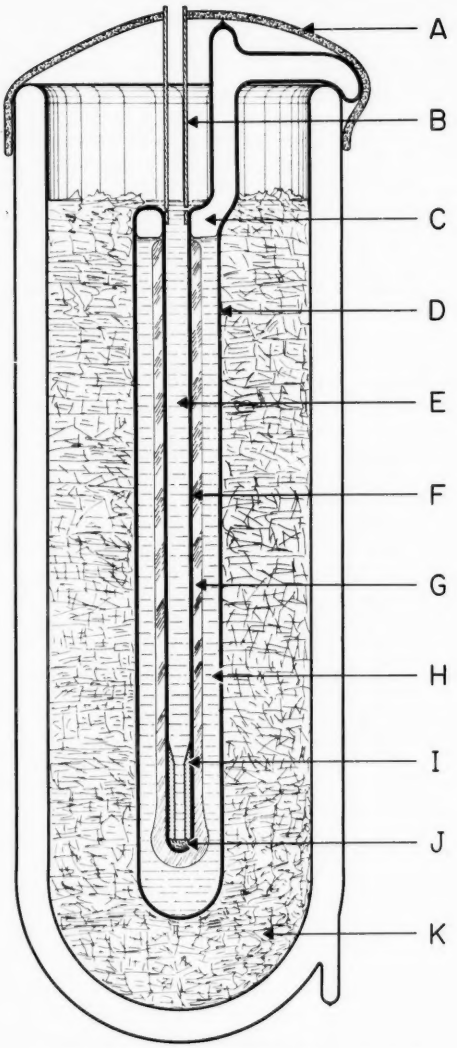


FIGURE 1. *Water triple point cell in an ice bath.*

A. Heavy black felt for shielding against ambient radiation.
B. Polyethylene tube for guiding the SPRT into the thermometer well.
C. Water vapor.
D. Borosilicate glass cell.
E. Water from ice bath.
F. Thermometer well (precision bore).
G. Ice mantle.
H. Air-free water.
I. Aluminum bushing with internal taper at upper end to guide the SPRT into the close-fitting inner bore.
J. Polyurethane sponge.
K. Finely divided ice and water.

thermometer resistor.)[3] Usually dendritic ice crystals form around the bottom of the well on the introduction of the first few pieces of Dry Ice. As more Dry Ice is introduced to fill the thermometer well, a clear coating of ice forms around the well and gradually grows to about 7-mm thickness during the 20 min the well is maintained full of Dry Ice. About 1-mm additional thickness of ice is formed when the remaining Dry Ice, after the 20-min period, is allowed to evaporate. Also, the ice mantle around the bottom end of the well, where the thermometer coil is normally located, becomes somewhat thicker (see fig. 1). After the Dry Ice is completely gone the cell is lowered deeper into the ice bath and the thermometer well is allowed to fill with ice water.

During the 20 min when the thermometer well is maintained full of Dry Ice, there is a strong tendency for the water to freeze solidly across at the top surface of the water in the cell. If this layer of ice forms a strong bond with the thermometer well and the outer cell, subsequent freezing of the water below this layer can develop enough pressure to possibly rupture the glass cell.[4] Therefore, whenever a layer of ice is about to bridge (or has bridged) between the thermometer well and the outer cell wall, the outer cell wall near the upper water surface should be warmed to melt the surface ice. This may be accomplished by raising the cell out of the ice bath briefly and warming the cell near the unwanted ice with the hands while gently shaking the cell sideways to wash and, therefore, melt the ice with the warmer water of the cell. During this time the Dry Ice level in the thermometer well should not be allowed to fall too low.

If the cell is raised high enough to see the mantle during the freezing process, the magnification by the cylinder of water will give the appearance that the ice mantle is thick enough to contact the outer wall although the mantle may actually be much thinner (1 or 2 mm thick).[5] During the freezing of the mantle, if the cell has enough vapor space, the cell may be momentarily inverted, while keeping the Dry Ice from falling out of the thermometer well, to see the mantle without the effect of magnification and, therefore, see the true thickness of the mantle. The cell should be inverted only when the thermometer well is cold enough so that the ice mantle would remain fast to the wall and, therefore, would not float upward against the "bottom" of the cell. If the cell is inverted after the inner melt is made the ice mantle will float upward to the bottom of the cell and the chemical composition of the inner liquid would be expected to be altered by the outer liquid.[6]

The temperature of the water-ice interface of an inner melt is the fixed-point temperature of the TP cell. The inner melt is formed by inserting a solid glass rod at ambient temperature into the thermometer well of the TP cell filled with ice-bath water; thereby, a thin

[3] In an experiment where the ice mantles of five cells were intentionally cracked during the preparation of the cells, the TP temperatures observed for the cells did not differ significantly, if at all, from the temperatures that were obtained when the cells were prepared without cracking the mantles. This indicates that the crack healed sufficiently so that it did not cause the water outside the mantle to mix with that in the inner melt or that the water of the TP cell is highly pure.

[4] On occasions when a layer of ice formed across the top, the internal pressure that was formed broke the ice layer instead of the glass cell. The water that escaped through the break in the ice immediately became an "ice fountain."

[5] The water level in the cell serves as an indicator of whether an adequate (or an excessive) amount of ice is formed around the thermometer well.

[6] Of the five TP cells where the inner and the outer water were intentionally mixed by alternately inverting and uprighting the cells, the TP temperatures that were observed for four of the cells were essentially the same as those before mixing. For the fifth cell the TP temperature after mixing was about 0.04 to 0.05 mK lower than before mixing [5].

layer of ice adjacent to the thermometer well is melted. The existence of this inner melt is tested by giving the cell a sharp rotatory impulse about the axis of the well and observing if the ice mantle spins or moves freely around the thermometer well. The TP cell usually equilibrates to essentially constant temperature within 30 min to 1 h. after preparation using Dry Ice. In most applications at the NBS the TP cell is prepared at least one day prior to use.

During storage of the TP cell in the ice bath, the frozen mantle of ice grows slowly and irregularly until it contacts and attaches itself to the outer walls of the cell. The cell is occasionally removed from the ice bath and the excess ice melted by warming with the hands or with water. (As mentioned earlier the extension on the type of TP cells used at the NBS serves as an indicator of the amount of water frozen in the cell. When the water level reaches the vertical extension, the amount of ice formed is usually considered excessive.) The growth of ice in the TP cell while stored in the ice bath can be reduced by insulating the TP cell with a sheet of plastic foam or by placing the TP cell in a Dewar flask which is in turn immersed in the ice bath. By means of a suitable insulation and occasional melting of excess ice the same freeze of the TP cell may be used in an ice bath for a number of months withoug freezing a new mantle. Moreover, in the PRT calibration laboratory of the NBS the ice bath for the TP cells is installed inside a small freezer chest to reduce the melting of the ice and, thereby, reduce the frequency of replenishing of the ice in the ice bath.

The TP cell is employed with the PRT as follows. Referring to figure 1, a small soft plastic foam (J) is first placed at the bottom of the thermometer well to reduce the mechanical shock when the PRT is inserted. A closely fitting aluminum bushing (I) about 5 cm long is placed above the foam to reduce the external self heating of the PRT (see sec. 4 on self heating). The bushing is constructed of aluminum instead of the heavier copper so that the bushing would gently sink to the bottom on top of the foam when it is inserted into the thermometer well full of water. The bushing has a tapered hole at the top to gently center the PRT when it is inserted into the thermometer well. To avoid upward displacement of the bushing by a "pumping" action when the PRT is inserted, the bushing is not too close fitting with the PRT sheath. To eliminate the effect of the room radiation (particularly the ceiling lights) a heavy black felt cloth (A) is placed over the top of the cell and ice bath except for a hole through which the PRT is inserted.[7] The PRT is precooled in the ice bath that surrounds the TP cell before it is inserted into the cell. A polyethylene plastic tube (B) helps to guide the PRT gently into the thermometer well. Before the final measurements on the PRT are made the thermometer current is on continuously for at least 5 min (with the Mueller bridge nearly balanced) for the thermometer to come to temperature equilibrium.

[7] Visible and near-infrared radiations transmitted through the ice bath could easily cause errors as large as 0.5 mK [6]. The aluminum sleeve can help shield the PRT sensor from the radiation.

The temperature of the water-ice interface of the inner melt where the PRT resistor is immersed (more precisely, the location of the mid-point of the resistor) is slightly lower than the temperature of the TP. The temperature depression is $7 \times 10^{-6}$ K per cm of water column [2]. The depth of immersion of the PRT is taken to be the distance between the upper water surface of the TP cell to the mid-point of the PRT resistor. The TP cells in use at the NBS have well depths of 32 cm or 36 cm, the TP cells with 32 cm wells being the most common and most recent. The depth of immersion of the PRT is about 29 cm or 33 cm, which corresponds to the temperature depression of the TP of 200 $\mu$K or 230 $\mu$K, respectively; therefore, the temperature of the TP cell at the mid-point of the PRT resistor is either 0.00980 °C or 0.00977 °C, depending upon the immersion depth of the TP cell being used.

The value of $R$ (0 °C) is obtained by converting the observed values of $R$(TP) employing equation (6) (see sec. 1, Introduction). Because of the small value of $t'$ at the TP ($t = 0.00980$ °C $\cong t'$ or $t = 0.00977$ °C $\cong t'$), the term containing $t'^2$ is negligible and the average value of $A$ ($3.98485 \times 10^{-3}$ °C$^{-1}$), found for PRT's calibrated at the NBS in the past years, is employed in the conversion. The uncertainty in the adjustments of the value from $R$(TP) to $R$ (0 °C) in this manner is less than $\pm 1 \times 10^{-8}$ $R$(0 °C) for PRT's that meet the IPTS–68 specification that $W$ (100 °C) be not less than 1.39250. Hence, in obtaining $R$(0 °C) from $R$(TP), the uncertainty contributed by this procedure is negligible.

### 2.2. Zinc Point

In place of the normal boiling point (NBP) of sulfur or the sulfur point the equilibrium state between the solid and liquid phases of zinc at 1 standard atmosphere (henceforth referred to as the freezing point of zinc or the zinc point) was recommended as a defining fixed point with the value of 419.505 °C on the IPTS–48 (Revised 1960) [7, 8]. The presently used IPTS–68 assigns the value 419.58 °C to the freezing point of zinc. Prior to 1966 the sulfur point was maintained at the NBS for the calibration of PRT's; however, since 1966 the zinc point has been maintained instead of the sulfur point.[8]

#### 2.2.1. Zinc-Point Cell

The freezing-point cell employed to realize the zinc point is illustrated in figure 2.[9] A bank of such cells assembled from zinc samples (SRM–740) of greater than 99.9999 percent purity is available for the calibration work. The freezing points of these zinc-point cells agree within ±0.1mK. The residual resistivity ratios

[8] In 1966 the PRT Calibration Laboratory of the NBS was moved from Washington, D.C. to the new NBS laboratories in Gaithersburg, Md. The zinc point and the tin point were activated instead of the sulfur point and the steam point, respectively.

[9] Certain commercial materials and instruments are identified in this paper in order to adequately specify the experimental procedure. Such identification does not imply recommendation or endorsement by the National Bureau of Standards.

(the ratio of the electrical resistance at 273 K to that at 4 K) of specimens taken from zinc bars from which the SRM 740 zinc samples were prepared ranged from 33,000 to 38,000 [9], indicating that the zinc samples have very high purity.

The zinc samples had been prepared from a starting material that was selected from a lot of electrolytic zinc of 99.99+ percent purity. The material was vacuum distilled twice and zone refined with 20 passes. After the leading and trailing ends of the zone refined bars were cropped, they were homogenized and cast in fused quartz boats in the form of semicylindrical bars about 5 cm across the flat side. The bars (approximately 61 cm long) were delivered to the National Bureau of Standards—Office of Standard Reference Materials (NBS–OSRM) individually sealed in argon-filled polyethylene bags. The zinc samples (1250 g) for each of the freezing-point cells were received from the NBS–OSRM in the form of two half cylinders (each about 8 cm long) sealed in a polyethylene bag. The samples had been cut from the bars with a carbide tipped tool; they were then etched in high-purity dilute nitric acid, rinsed with distilled water, and air dried.

Because of the relatively high vapor pressure of zinc at its melting point {about 13 Pa (0.1 Torr) [10][10]}, the zinc samples were melted into the high-purity graphite crucibles by induction heating under purified argon atmosphere. The graphite thermometer well was then inserted and the cell was assembled in the form shown in figure 2. Details of the assembly procedure are the same as those described for tin in references [11, 12].

#### 2.2.2. Furnace for the Zinc-Point Cell

The design of the furnace employed with zinc-point cell is shown in figure 3. The furnace core consists of cylindrical blocks of aluminum [top (G), center or main (L), and bottom (T)]. The space surrounding the core is packed with Fiberfrax insulation. The temperature of the center core (L) is controlled by means of an absolute thermocouple and the main heater (O). The temperatures of the top (G) and bottom (T) blocks are controlled relative to the center block temperature by means of differential thermocouples and heaters [(F) and (U), respectively] in the blocks. The electric power to the heaters is controlled automatically from the indication of the corresponding thermocouples.

#### 2.2.3 Preparation of Zinc-Point Freeze

Liquid zinc is found to supercool only 0.02 to 0.06 °C. On the day prior to the zinc-point calibration of the PRT's the furnace control is set at a temperature about 5 °C above the zinc point and the zinc sample is melted overnight. The following morning after inserting a monitoring PRT in the cell, the furnace control is reset to a temperature about 4 °C below the zinc point. After the PRT indicates that recalescence has occurred and about 10 min have passed, the monitoring

[10] 1 Torr = 133.322 Pa.

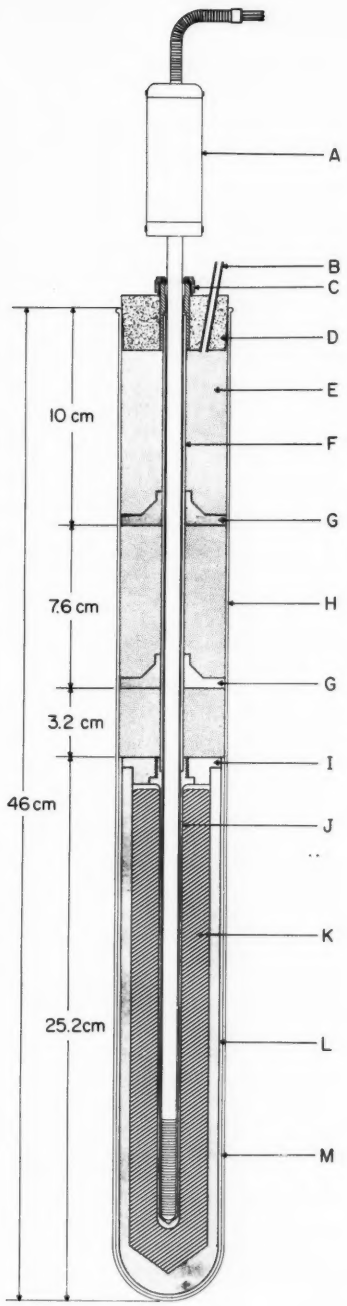


FIGURE 2. *Metal freezing-point cell.*

A. Platinum resistance thermometer.
B. To helium gas supply and pressure gauge.
C. Thermometer stem seal with silicone rubber gasket.
D. Silicone rubber stopper.
E. Insulation, washed Fiberfrax.
F. Thermometer guide tube, borosilicate glass.
G. Heat shunt, graphite.
H. Borosilicate glass cell.
I. Graphite cap (lid).
J. Graphite thermometer well.
K. Metal sample, zinc or tin.
L. Graphite crucible.
M. Insulation, Fiberfrax paper.

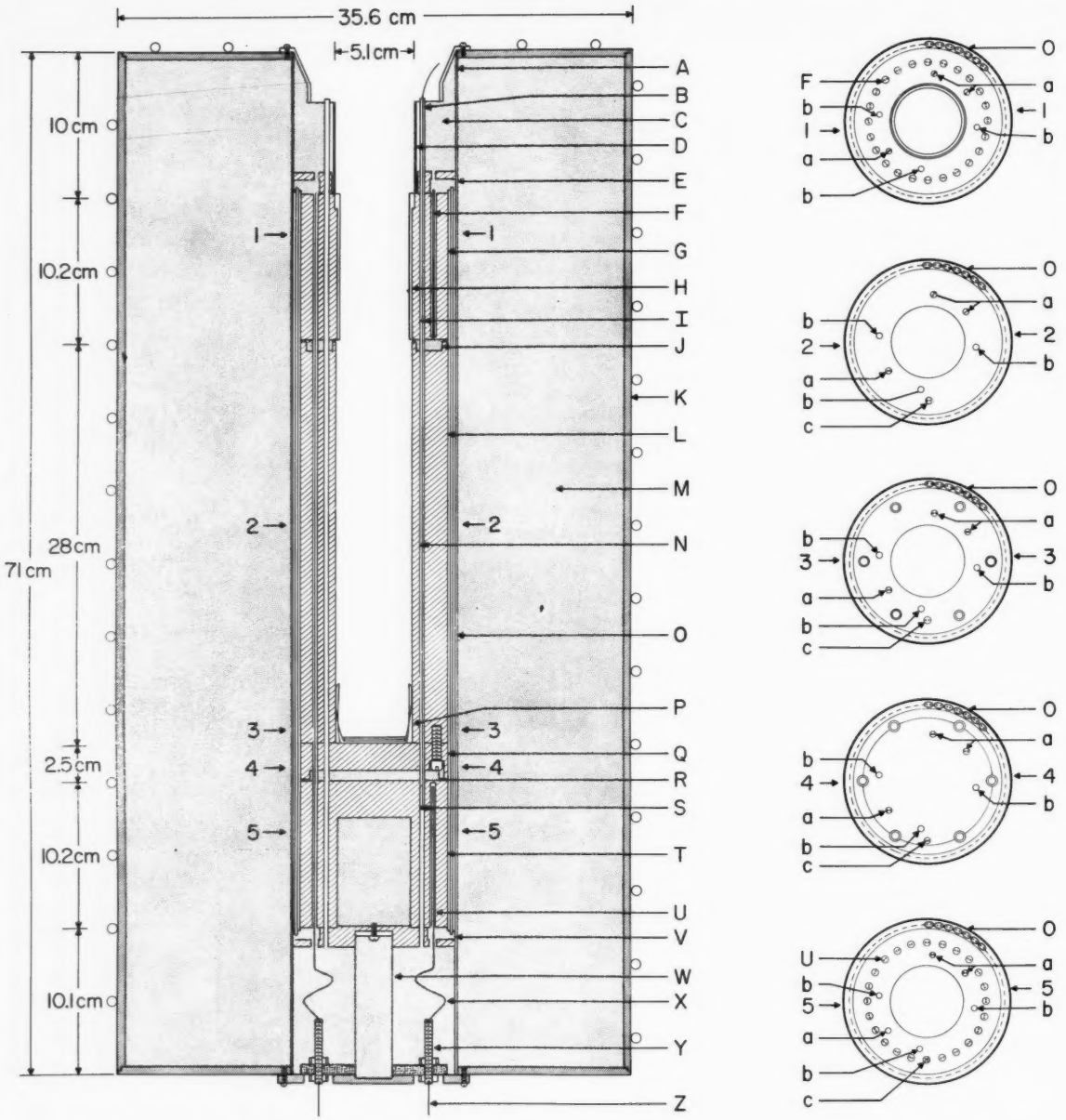


FIGURE 3. *Schematic of furnace body and core.*

A. Stainless steel tube, 11.4 cm o.d. × 0.76 mm wall.
B. Stainless steel tubes (6) : 3.20 mm o.d. × 0.013 mm wall.
C. Insulation, Fiberfrax mats.
D. Stainless steel tube.
E. Insulation, Fiberfrax mats and mica sheets.
F. Control heaters for top core block.
G. Top core block.
H. Sleeve (aluminum or Inconel) for metal freezing point cell.
I. Elevation of thermocouple junction (Chromel-P/Alumel), top core block. (See **a.**)
J. Insulation, Fiberfrax sheets.
K. Brass shell, 4.8 mm thick.
L. Center core block.
M. Insulation, bulk Fiberfrax.
N. Elevation of thermocouple junction (Chromel-P/Alumel), center core block. (See **a.**)
O. Main heaters, held on with Inconel "garters."
P. "Spider" for centering the freezing point cell.
Q. Center core block end plate.
R. Insulation, Fiberfrax sheets.
S. Elevation of thermocouple junction (Chromel-P/Alumel) bottom core block. (See **a.**)
T. Bottom core block.
U. Control heaters for bottom core block.
V. Insulation, Fiberfrax mats and mica sheets.
W. Stainless steel tube support, 2.5 cm o.d. × 0.51 mm wall × 11.4 cm long.
X. Heater leads.
Y. Posts for heater leads.
Z. To electric power.
a. Wells (B) for control thermocouples (See I, N, and S.)
b. Wells (B) for testing the temperature profile of furnace core.
c. Leads from top core block heaters.

PRT is removed and two borosilicate glass rods are inserted successively into the thermometer well for about 3 min each to induce an inner freeze immediately next to the thermometer well. Also, the furnace control is reset to a temperature 1 °C below the zinc point. After withdrawing the second borosilicate glass rod, the cold monitoring PRT is inserted into the thermometer well. By following this procedure freezes of 12 to 14 h. durations are obtained. With cells assembled using SRM–740 zinc standard the change observed in the freezing point while the first 50 percent is frozen is less than 0.2 mK.

The resistance of the monitoring or check PRT is determined approximately 45 min after inserting it cold into the zinc-point cell. (Meanwhile the test PRT is being preheated in an auxiliary furnace held about 20 °C above the zinc point.) After completion of the measurements on the check PRT it is removed from the zinc-point cell and the test PRT is withdrawn from the preheating furnace and quickly inserted into the zinc-point cell so that the thermometer temperature during the insertion would be slightly below that of the cell. (The PRT is inserted slightly colder than the cell temperature to avoid melting and loosening the solid zinc mantle around the thermometer well.) When the PRT is preheated to a temperature close to that of the cell temperature it reaches temperature equilibrium within a few minutes (see fig. 35, Monograph 126 [12]). The resistance readings of the test PRT are started about 15 min after inserting it into the zinc-point cell. (Meanwhile, the second test PRT is being preheated in the auxiliary furnace.) After completion of the measurements on the first test PRT, it is replaced in the zinc-point cell by the second test PRT. A maximum of six test PRT's are calibrated in any single zinc freeze. After the last test PRT is calibrated it is replaced with the preheated check PRT. This second reading with the check PRT must not differ from the first reading by more than 0.5 mK; if the difference is larger, the measurements on some of the test PRT's that were calibrated last will be repeated using another zinc freeze. The test PRT's on which the measurements are to be repeated are decided on the basis of the elapsed time since the start of the freeze and the change in the freezing temperature that is observed with the check PRT.

Because of the effect of the hydrostatic head of liquid zinc, the temperature at the height where the mid-point of the PRT sensor is located in the zinc-point cell is slightly hotter than the equilibrium freezing temperature of zinc at 1 atm pressure as defined in the IPTS–68. (The effect of the hydrostatic head is 27 $\mu$K per cm of liquid zinc [2].) For the NBS zinc-point cell the height of the liquid zinc column above the mid-point of the sensor is 18 cm; therefore, the temperature at the height of the mid-point of the PRT sensor is 419.5805 °C.

## 2.3. Tin Point

The equilibrium state between the solid and liquid phases of tin at 1 standard atmosphere (231.9681 °C, henceforth referred to as the freezing point of tin or the tin point) is an alternative to the normal boiling point of water (steam point) as a defining fixed point on the IPTS–68. Prior to 1966 the steam point was maintained at the NBS for the calibration of PRT's; however, since 1966 the tin point has been maintained instead of the steam point.

### 2.3.1. Tin-Point Cell

The freezing-point cell employed to realize the tin point is designed similar to the zinc-point cell (see fig. 2). A bank of tin-point cells assembled from tin samples (SRM–741) of nominally 99.9999 percent purity is available for the calibration work. The freezing points of these cells agree within $\pm 0.1$ mK [11]. The residual resistivity ratios of specimens taken from tin bars from which SRM–741 tin samples were prepared varied from 28,000 to 43,000 [13], indicating that the tin samples have very high purity.

The tin samples had been prepared by initially electrolyzing commercially refined tin and zone refining the electrolyzed product by at least 20 zone passes. The purified samples were homogenized and cast into semicylindrical bars about 5 cm across the flat side and about 60 cm long. Each of the tin samples (1300 g each) were received from the NBS–OSRM in the form of two half cylinders (each about 10 cm long) sealed in a polyethylene bag. The samples had been cut from the bars with a carbide tipped tool. To remove surface contamination they were etched first in 40 percent hydrochloric acid solution and then in a solution of 40 percent hydrochloric acid plus 10 percent nitric acid; they were washed in distilled water and in ethyl alcohol and air dried.

The tin samples were melted into the high-purity graphite crucible by induction heating under high vacuum. (The vapor pressure of tin at its melting point is estimated to be about $6 \times 10^{-21}$ Pa [10].) The graphite thermometer well was then inserted and the cell was assembled in the form similar to that of the zinc cell shown in figure 2. Details of the assembly procedure are given in references [11, 12].

### 2.3.2. Furnace for the Tin-Point Cell

The design of the furnace employed with the tin-point cell is the same as that used with the zinc-point cell (see fig. 3). Initially the sleeve (H) for enhancing the thermal contact between the heat shunts (G, fig. 2) of the tin-point cell and the furnace was aluminum; however, in recent measurements an Inconel sleeve, similar to that used in the zinc-point furnace, has been used in the tin-point furnace.

### 2.3.3. Preparation of the Tin-Point Freeze

Liquid tin has been found to supercool as much as 25 °C, depending upon the temperature and length of time the metal was allowed to remain melted. Impurities (e.g., Fe) seem to reduce the degree of supercool [14]. If the freeze were initiated with the tin-point cell

in the furnace, the furnace block temperature could not then be raised fast enough to avoid excessive freezing of tin. Therefore, the tin freeze is initiated by employing the "outside nucleated freeze" technique described by McLaren [15]. The tin sample is melted overnight in the furnace held at a temperature about 3 °C above the freezing point. In the morning after inserting a monitoring PRT in the thermometer well, the furnace control is reset down to a temperature 1 °C below the tin point. (A different monitoring PRT is used with the tin-point cell from that used wtih the zinc-point cell, so that any possible effect on the PRT when used at another fixed point would be avoided. As with the zinc-point cell the monitoring PRT used with the tin-point cell serves also as the check PRT.) When the monitoring PRT indicates that the tin sample has cooled to near the freezing point, the cell is withdrawn from the furnace and held out in room temperature. When the PRT indicates that the sample has started to recalesce, the cell is quickly reinserted into the furnace. Following this procedure a freeze duration of 12 to 14 h is obtained. With the tin-point cells containing SRM–741 tin standard, after about 5 percent of the initial "freeze," the temperature change in the following 50 percent of the freeze is less than 0.1 mK. The resistance of the monitoring or the check PRT is determined approximately 45 min after reinserting the tin-point cell into the furnace. (Meanwhile a test PRT is being preheated in an auxiliary furnace held 20 °C above the tin point.) After completion of the measurements on the check PRT it is removed from the tin-point cell and the test PRT is withdrawn from the preheating furnace and quickly inserted into the tin-point cell so that the thermometer temperature during the insertion is slightly above that of the cell. In actual practice it is not certain whether any melting or any additional freezing occurs upon insertion of the PRT. In either event the preheated PRT reaches temperature equilibrium within a few minutes (see fig. 31 Monograph 126 [12]). The resistance readings of the test PRT are started 15 min after inserting it into the tin-point cell. (Meanwhile the second test PRT is being preheated in the auxiliary furnace.) After completion of the measurements on the first test PRT it is replaced in the tin-point cell by the second test PRT. As with the zinc-point cell a maximum of six test PRT's are calibrated in any single tin freeze. After the last test PRT is calibrated it is replaced with the check PRT. The requirement of the second reading of the check PRT is that it shall not differ from the first reading by more than 0.5 mK; if the difference is larger, the measurements on some of the test PRT's that were calibrated last will be repeated using another tin freeze. The test PRT's on which the measurements are to be repeated are decided on the basis of the elapsed time since the start of the freeze and the change in the freezing temperature that is observed with the check PRT.

Because of the effect of the hydrostatic head of liquid tin, the temperature where the midpoint of the PRT sensor is located during measurements in the tin-point cell is slightly higher than the equilibrium freezing temperature of tin at 1 atm pressure as defined in the IPTS–68. (The effect of the hydrostatic head is 22 $\mu$K per cm of liquid tin [2].) For the NBS tin-point cell the height of liquid tin column above the midpoint of the PRT sensor is 18 cm; therefore, the temperature at the midpoint of the PRT sensor is 231.9685 °C.

### 2.4 Normal Boiling Point of Oxygen

The calibration of the PRT's at the normal boiling point of oxygen ( −182.962, oxygen point) is realized by reference to the NBS–1955 temperature scale adjusted to correspond to the IPTS–68 (see reference [4] for the discussion of this NBS–IPTS–68 scale between 13.81 and 90.188 K maintained on capsule-type reference standard PRT's). The temperature (hotness) assigned to the oxygen point is also maintained by long-stem type reference standard PRT's which are intercompared with the capsule type PRT reference standards. Calibrations near the oxygen point are obtained by intercomparing the test PRT's with a long-stem type reference standard PRT in the apparatus shown in figure 4. Eight thin-walled Monel tubes (A) extend into the copper block (P); five tubes are 7.9 mm o.d. to accommodate regular long-stem type PRT's, one is 10.3 mm o.d. for 9 mm PRT's, and two tubes are 12.7 mm o.d. to accommodate capsule type PRT's in holders. The tubes are soldered to the copper block as well as to the copper flanges at the various stages of the apparatus shown in figure 4. The thermometer stems are sealed at the top of the wells by a molded band of soft silicone rubber. The thermometer wells are filled with helium gas to a pressure that is slightly above atmospheric (see helium gas distributing manifold (D) in fig. 4). The helium gas enhances the thermal contact between the thermometer and the wall of the well and reduces the chance of condensible gases entering the wells.

The apparatus is prepared for calibration by evacuating through (J) and immersing in liquid nitrogen to the level shown in figure 4. The copper block (P) and shields (F and L) are cooled by admitting nitrogen gas and/or liquid nitrogen through valve (K) just below the liquid nitrogen surface. The cool nitrogen vapor flows through coils (N) attached to the two top shields and to the copper block and exits through (B) to a large-capacity vacuum pump. When the temperature of the copper block (P) is cooled nearly to the oxygen point, the valve (K) is closed and the nitrogen in the cooling coils is removed by pumping. The temperature of the copper block is adjusted to within 1 K of the oxygen point [either by heating or, if necessary, by opening valve (K)] and the two shields are controlled at the temperature of the block. (Calibrations of the PRT's are performed within 1 K of the oxygen point.) When the temperatures of the copper block and the two shields are nearly the same, the inner shield is allowed to "float" without electric power input. The outer shield is controlled relative to the temperature of the copper block by means of differential thermo-

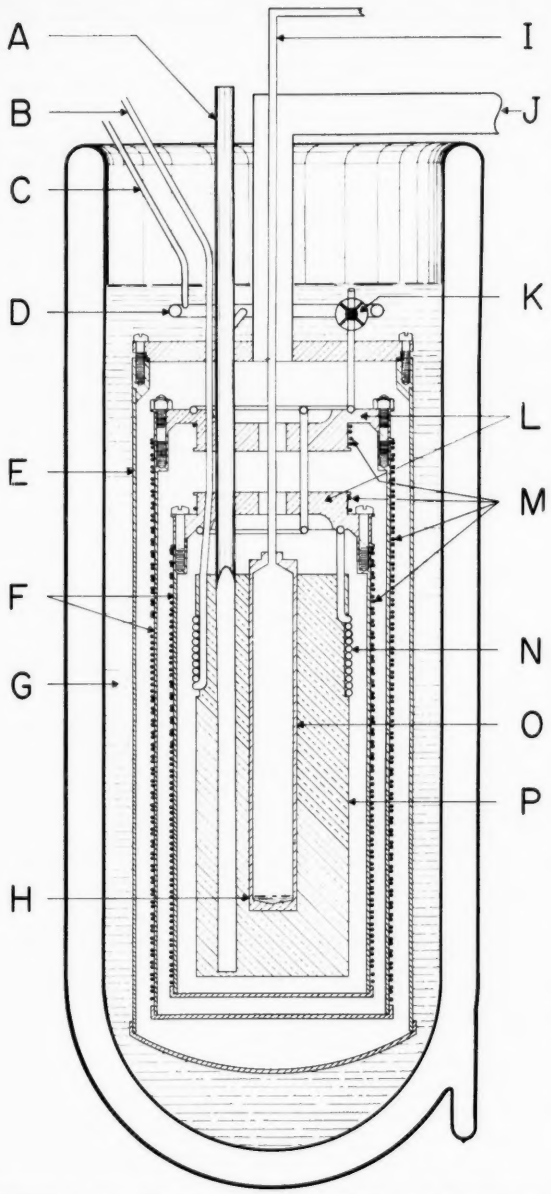


FIGURE 4. *Cryostat for comparison calibration of thermometers with reference standards at the oxygen normal boiling point.*

A. Thermometer well; eight wells are located around the copper block. The SPRT's are sealed at the top with molded silicone rubber.
B. Tube to vacuum pump to draw liquid nitrogen through cooling tubes.
C. Tube to helium gas supply.
D. Manifold for distributing helium gas to the thermometer wells.
E. Envelope (brass).
F. Radiation shields (copper).
G. Liquid nitrogen.
H. Liquid oxygen. (Not employed in comparison calibrations.)
I. Vapor-pressure tube, to differential pressure diaphragm and manometer.
J. High vacuum line.
K. Valve to control the liquid nitrogen input for cooling.
L. Top heat shields, to control thermometer well and thermometer stem temperatures.
M. Heaters.
N. Cooling tubes (thin-wall Monel).
O. Oxygen bulb.
P. Copper block.

couples and shield heaters. The floating shield tends to dampen the effects of temperature gradients and short term variations in the control of the outer shield. The electric power in the shield heaters is controlled automatically from the emf output of the thermocouples. The PRT's are tempered where the tubes pass through liquid nitrogen and where the two shields are soldered to the tubes (A) before entering the copper block (P).

In the calibration of the PRT's the resistance measurements are carried out on the test PRT and the reference standard PRT simultaneously using two Mueller bridges. Measurements are made as rapidly as possible with the commutating switching order NRRNNRRN of the Mueller bridges. As a part of the calibration process the reference standard PRT is checked by comparing with a second reference standard PRT. The temperature at which the resistance of the test thermometer is observed is calculated from the observed resistance of the reference standard PRT and its $R$ versus $T$ relation. (Actually, the analysis is performed in terms of the $W$ versus $T$ relation.)

## 3. Resistance Measurements

The resistance measurements are performed with Mueller bridges. The bridge is basically an equal-arm Wheatstone bridge with modifications to permit commutation of the four PRT leads so that the lead resistances cancel when two bridge readings are averaged. Other modifications include a provision for adjusting the ratio arms to equality and a provision for commutating the ratio arm connections at the same time the PRT leads are commutated, so that small deviations from unity of the ratio arms would be negligible. (For details of the bridge design see reference [12].) A galvanometer photocell amplifier plus a secondary "display" galvanometer are used for balance detection. Under favorable circuit conditions the unbalance can be detected within a few nanovolts. In the process of determining the resistance of the PRT the bridge current is reversed to eliminate the effects of any spurious emf's. The current reversal method also doubles the apparent null detector sensitivity. The observations are made to the nearest 10 $\mu\Omega$ in the following sequence of commutator switch positions: NRRN. (At the oxygen point, observations in this sequence are obtained twice.)

The Mueller bridges are calibrated once a year. (Previously the bridges were calibrated twice a year.) First the bridge is internally calibrated for linearity in terms of the resistance X(10) of the 1-$\Omega$ dial switch. The resistance of a standard resistor (close to 10 $\Omega$), which had been calibrated in terms of the absolute ohm maintained at the NBS, is then measured using the bridge [11]. These data are used to obtain corrections to the nominal values of the switch positions in terms of the absolute ohm. Bridge calibrations are obtained to $10^{-7}$ $\Omega$ for the 1-ohm dial switch and for

[11] More recently the Mueller bridge resistance has been based on the average comparison with four 100-$\Omega$ resistors which had been calibrated in terms of the NBS absolute ohm.

the lower dial switches and to $10^{-6}$ Ω for 10 and 100-ohm dial switches. For details of the Mueller bridge calibration see the appendix of reference [12].

A small residual unbalance exists in the Mueller bridge even with all measuring switches set on zero because of the resistances of the leads that connect the resistor network and the resistances of the switch contacts. The Waidner-Wolff elements [16] contribute also to the residual resistance. In the bridge design a resistor (about 0.98 Ω) is placed in series with the 0.1-ohm decade resistors (which operates "subtractively," see reference [12]) to balance the remainder of the residual resistance of the Waidner-Wolff elements in the adjacent arm and the necessary copper connecting wires in the bridge when all switches are set to zero. The deviation from balance is the "bridge zero." The bridge zero is subtracted algebraically from the dial readings of all measurements. Because of the changes in the switch contact resistance and changes in the temperature of some bridge components the bridge zero varies during the day. Each day the bridge is used the wiping contacts of the switches are exercised, the mercury contacts are cleaned and the mercury replaced, and the bridge zero is read and estimated to $10^{-7}$ Ω. During the day two or three bridge zero measurements are obtained.

## 4. Self-Heating Effects

The measurement of the PRT resistance involves passing an electric current through the resistor. The Joule heating (or $i^2R$ heating) raises the temperature of the resistor, its support, and its leads above that of the surrounding until a steady state condition is reached where the Joule heating equals the rate heat is dissipated to the surrounding medium. (If the temperature of the surrounding medium remains or becomes constant, e.g., as in a fixed-point cell, a steady PRT resistance reading can be attained. Otherwise, the PRT resistance will continue to change depending upon the Joule heating in the PRT resistor and upon other sources of energy exchange of the system.) The time required to reach the steady state condition depends upon the thermal diffusivities of the thermometer components and of the surroundings and upon the thermal resistances between them. In some situations as much as 5 min or longer may be required to reach the steady state condition. The magnitude of the self heating depends upon the Joule heating and upon the rate of heat transfer from the PRT resistor. At a given temperature the heat conduction from the thermometer resistor to the outer surface of the protective sheath remains essentially constant since the geometry and the thermal conductivity of the thermometer components usually remain unchanged with use. However, the heat conduction from the outer surface of the thermometer sheath to the surrounding medium depends upon the degree of thermal contact of the thermometer with the "surrounding heat sink." Therefore, the heat conduction external to the thermometer depends upon the conditions of use. The self heating that is intrinsic to the thermometer is referred to as the *internal* self heating of the PRT. The self heating that is associated with the heat conduction external to the thermometer is referred to as the *external* self heating. The combined self heating is referred to as the *total* self heating. The total self heating may be expressed as a resistance change or as a temperature change corresponding to the resistance change and, strictly speaking, at a given temperature and specified surroundings.

At low electric power levels the total self heating is very nearly linear with respect to the power that is generated in the PRT resistor. At the NBS, measuring currents of 1 and 2 mA are usually used with PRT's of $R(0\ °C)$ of about 25 Ω to determine the total self heating. If $R_1$ is the resistance reading at a current of $i_1$ and $R_2$ is the reading at a current of $i_2$, the resistance $R_0$ at zero current is given by

$$R_0 = R_1 - i_1^2(R_2 - R_1)/(i_2^2 - i_1^2). \tag{10}$$

For $i_1$ and $i_2$ of 1 and 2 mA, respectively,

$$R_0 = R_1 - (R_2 - R_1)/3. \tag{11}$$

Thus, at 1 mA thermometer current the total self heating is $(R_2 - R_1)/3$ Ω; at 2 mA thermometer current it is $4(R_2 - R_1)/3$ Ω. The $R_0$ corresponds to the PRT resistance with no self heating. For temperature measurements of the highest accuracy values of $R_0$ should be used. (The PRT must have also been calibrated for "zero current" measurements.)

The total self heating of the PRT is described also in terms of the change in the observed resistance caused by the change in the Joule heating or the change in the observed resistance caused by the change in the square of the electric current in the PRT. In this paper this latter coefficient of total self heating will be referred to as the total *self-heating effect*. Referring to eq (10), the total self-heating effect is given by $(R_2 - R_1)/(i_2^2 - i_1^2)$. At the NBS the total self-heating effect is expressed as $\Omega/(\text{mA})^2$. As given in eq (10) the product of this coefficient and the square of the current being used gives the total self-heating of the PRT.

A typical steady-state profile of the radial temperature distribution that is expected to result from a current of 1 mA flowing in a 25-Ω PRT (a PRT with the $R(0\ °C)$ of about 25.5 Ω) immersed in an ice bath and in a TP cell (with and without an aluminum bushing) is shown in figures 5 and 6, respectively. [The profile was calculated from $R_0$ and $R_1$ (see eq 11) and the thermal conductivities and thickness of the various parts.] When the outer surface of the protective sheath of the PRT is in direct contact with the surrounding heat sink, the condition closely represented by the PRT immersed in an ice bath (fig. 5) or in a stirred liquid bath, the total self-heating is very nearly the internal self-heating of the PRT. There is no tempera-

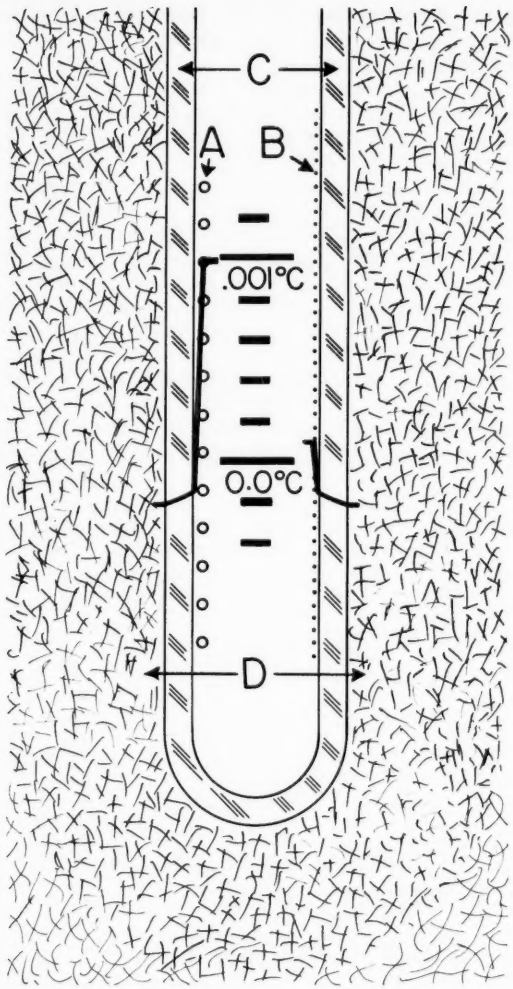


FIGURE 5. *Platinum resistance thermometers at 33 cm immersion in an ice bath.*

Temperature profile from the midpoint of thermometer coil out to the ice bath with 1 milliampere current.

A. Platinum coils of coiled filament thermometer; only coils of one side are indicated.
B. Platinum coils of single layer helix thermometer; only turns of one side are indicated.
C. Borosilicate glass thermometer envelope.
D. Finely divided ice and water.

ture drop beyond the outer surface of the PRT immersed in the ice bath. However, in the TP cell (fig. 6) the PRT is not in direct contact with the heat sink and, therefore, there is an additional temperature drop from the outer surface of the PRT to the water-ice interface (heat sink) of the inner melt where the temperature is very nearly that of the TP except, as previously mentioned in section 2.1, for the effect of the hydrostatic head of water. The external self heating of the PRT in the TP cell is the difference between the total self heating of the PRT in the TP cell and in the ice bath.

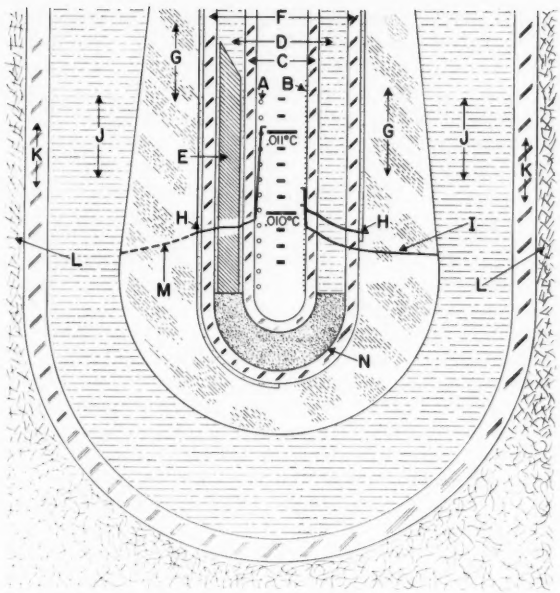


FIGURE 6. *Platinum resistance thermometers at 33 cm immersion in a water triple point cell.*

Temperature profile from the midpoint of thermometer coil out to the ice-water interface with 1 milliampere current.

A. Platinum coils of coiled filament thermometer; only coils of one side are indicated.
B. Platinum coils of single layer helix thermometer; only turns of one side are indicated.
C. Borosilicate glass thermometer envelope.
D. Water from ice bath.
E. Aluminum bushing (length not to scale).
F. Borosilicate glass thermometer well.
G. Ice mantle.
H. Inner melt.
I. No inner melting; temperature profile relative to the temperature of outer ice-water interface.
J. Water in cell.
K. Cell well (borosilicate glass).
L. Outside ice-water bath.
M. Temperature profile of the ice mantle.
N. Polyurethane sponge.

At the NBS, unless requested otherwise, the PRT's are calibrated with a continuous current of 1 mA. The calibration (or the observed resistance) is related to the temperature of the outer surface of the protective sheath of the PRT adjacent to the resistor. In the TP cell this temperature corresponds to the temperature of the water-ice interface at the level of immersion of the PRT adjusted for the external self heating of the PRT. In the calibrations at the other fixed points (tin, zinc, and oxygen) the observed resistances of the PRT at a continuous current of 1 mA are also correlated with the temperature of the outer surface of the PRT, i.e., the temperature of the fixed point is adjusted for the external self heating of the PRT in the fixed-point apparatus. Therefore, to employ the PRT calibrations obtained at the NBS directly in temperature measurements, a continuous current of 1 mA must be used and the PRT must be in good thermal contact with the system of which the temperature is being determined so that the external self heating is negligible. Otherwise, a correction must be made for the external self

heating. Wherever the highest accuracy is desired or the external self heating is difficult to determine, the two-current method (described earlier) should be used to obtain the zero current value of the PRT resistance. Again the calibration of the PRT must have been determined for zero thermometer current.

## 5. Thermometer Immersion

A PRT is sufficiently immersed in the bath when there is no net heat flow between the sensor and its environment (i.e., the environment external to the bath) through the thermometer leads and the sheath that extends from the region of the sensor. The adequacy of thermometer immersion can be readily checked by measurements at two or three different depths of immersion, allowing for the difference in temperature of the bath at different depths. If the temperatures at different depths do not agree within the desired limits, then the immersion of the PRT is inadequate.

The required immersion (or the heat conduction along the PRT stem) can be reduced by choosing materials of poor thermal conductivity for the leads from the PRT sensor and for the PRT sheath and by keeping their cross section as small as practicable. The thermometer sensor and its leads (gold or platinum for standards- type PRT) should make as good a thermal contact as possible with the sheath. The convection in the thermometer exchange gas should be localized (e.g., by means of baffles). In use, as previously emphasized, the thermal contact between the PRT sheath and the system of interest should be made as good as practicable. Figure 7 illustrates the case where the PRT sheath is in good thermal contact with the bath (ice-bath heat sink); the figure shows on a logarithmic scale the difference between the ice-bath temperature and the indicated temperature as a function of immersion for two PRT's of different sheath materials and internal construction. (The measurements shown in figs. 7 and 8 are zero-current values.) For thermometer G, the temperature difference between the thermometer and the bath is reduced by a factor of 10 for each 3.3 cm increase in immersion; for thermometer M, the temperature difference is reduced by a factor of 10 for each 1.4 cm increase in immersion. The relation may be approximated by

$$D = N \log_{10}(\theta/\delta T), \tag{12}$$

where $\delta T$ is the desired limit of immersion error, $\theta$ is the difference between the ambient temperature and the bath temperature, $N$ is the change in the immersion that is required to change the temperature difference relative to the ice point by a factor of 10, and $D$ is the immersion that is necessary to limit the immersion error to $\delta T$. Thus, in the case of the thermometers shown in figure 7 with the ambient temperature of 25 °C, in order for the immersion error to be 0.025 mK or less, the thermometer must be immersed enough so that the temperature difference of 25 °C is reduced by six orders of magnitude; i.e., thermometer G must be immersed 19.8 cm and thermometer M must be immersed 8.4 cm in the ice bath.

Figure 8 shows the immersion characteristics of the same thermometers G and M in a TP cell where the thermal contact between the PRT sheath and the heat sink is slightly inferior than in the ice bath. The immersion characteristics of both PRT's are different from those in the ice bath, particularly for thermometer M where the total immersion must now be about 13.5 cm instead of 10 cm in order for the temperature difference between the observed value and TP temperature to be 0.01 mK. For thermometer G the total immersion required remains nearly the same. The reduction in the thermal contact (see fig. 6) is caused principally by the thermal resistance of the layer of water in the thermometer well and of the glass wall of the well. The relation between the radial and vertical heat flow conditions for thermometer G was not affected as much as in thermometer M by immersion

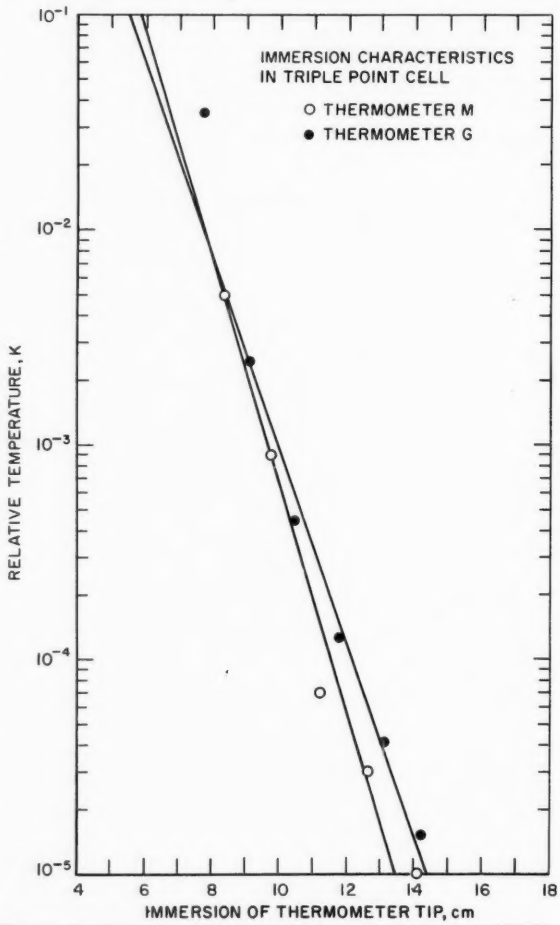


FIGURE 7. *Immersion characteristics in an ice bath of two SPRT's with different sheath materials and internal construction.*

The data show the nearly linear relationship between the logarithm of the relative temperature and the depth of thermometer immersion.

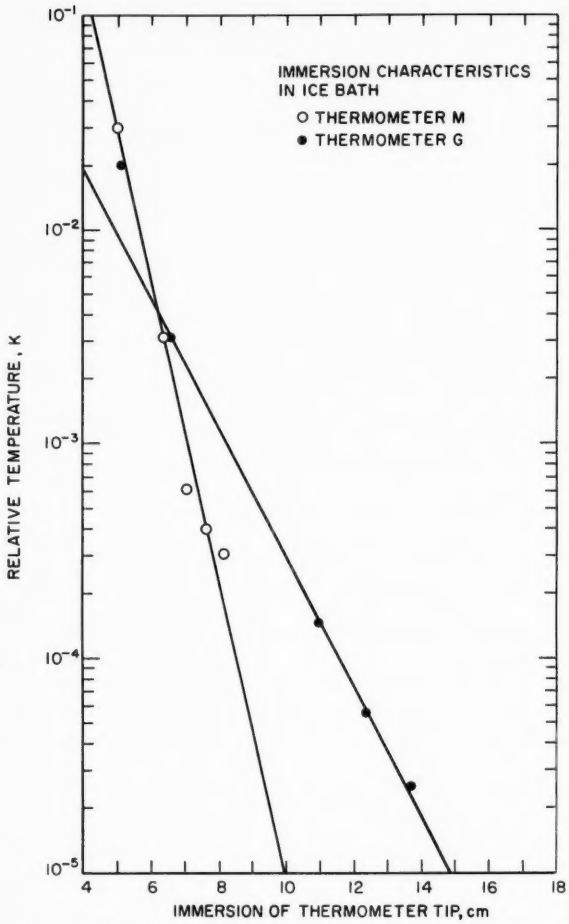


FIGURE 8. *Immersion characteristics in the triple point of water cell of two SPRT's with different sheath materials and internal construction.*

The plot shows the relationship between the logarithm of relative temperature and the depth of thermometer immersion. Comparison with figure 7 shows that the immersion characteristics of the thermometers are poorer in the triple-point cell than those in the ice bath. This degradation in the immersion characteristics is caused by the higher resistance to radial heat flow in the triple-point cell.

in the TP cell. The radial heat conduction within thermometer G is relatively low; hence, the change in thermal contact from that in the ice bath to that in the TP cell does not result in a large change in the immersion characteristics of the PRT. However, in the case of thermometer M with relatively good radial heat conduction the lower radial heat conduction in the TP cell caused the immersion characteristics of thermometer M to become poorer.

The adequacy of immersion of the PRT in a TP cell can be best checked by measurements at three depths of immersion, e.g., at the bottom, 3 cm up, and 6 cm up from the bottom. If the immersion is adequate at the bottom and at 3 and 6 cm up from the bottom, the PRT readings should track the effect of the hydrostatic head of water in the TP cell, i.e., the readings at 3 and 6 cm up from the bottom should be about 21 and 42 $\mu$K, respectively, higher than that at the bottom. The relatively small effect of the hydrostatic head in the TP cell may be obscured by the variations in the total self heating (see sec. 4 on self-heating effects) because of the variations in the thermal contact of the PRT in the TP cell when the vertical location of the PRT is adjusted. Hence, it is essential to carry out two-current measurements and obtain the zero-current resistance readings, which eliminates the effects of self heating, to test the effect of hydrostatic head of water in the TP cell. (At the NBS, as mentioned previously, the PRT's are immersed 29 or 33 cm depending upon the depth of the thermometer well of the TP cell.)

The adequacy of immersion in the tin-point cell or the zinc-point cell can be checked by the same procedure as employed with the TP cell. In the case of the tin-point cell [12] the reading at 3 and 6 cm up from the bottom should be about 66 and 132 $\mu$K, respectively, lower than that at the bottom and in the case of the zinc-point cell the reading at 3 and 6 cm up from the bottom should be about 81 and 162 $\mu$K, respectively, lower than that at the bottom, if the immersion of the PRT is adequate at the three levels in the cells. (At the NBS the mid-points of the PRT sensors are immersed about 18 cm below the liquid surface of the tin and zinc cells. Moreover, to improve the "immersion characteristics" the PRT's are tempered by the graphite heat shunts located above the graphite crucible containing the metal sample; see fig. 2.)

In the oxygen point apparatus, the copper block ((P), fig. 4) is very nearly isothermal. The adequacy of immersion can be checked by reducing the immersion of the PRT in the copper block. If the "combined immersion" (the tempering through the liquid nitrogen and at the shields and the immersion in the copper block) is adequate the readings at two levels of immersion in the copper block should be essentially the same.

## 6. PRT Calibration Procedure

Unless specifically instructed otherwise by the owner of the PRT, all long-stem type PRT's that are received for calibration at the NBS are first annealed for about 4 h in a tube furnace held at 480 °C. After annealing, the PRT's are removed from the furnace and allowed to cool in air at the ambient conditions. (Henceforth, unless indicated otherwise, the long-stem type PRT that meets the IPTS–68 specifications [2] will be referred to as SPRT. The platinum resistance thermometers in general will continue to be referred to as PRT.) The calibration measurements are then obtained at the fixed points in the following sequence: TP, zinc point, TP, tin point, and TP. As mentioned earlier, the

[12] At the NBS the tin-point cell is used without the inner freeze immediately next to the thermometer well. Because of the liquid-solid interface not being close to the thermometer well the temperature gradient expected from the change in pressure with depth is somewhat obscured; the temperature observed at 3 and 6 cm up from the bottom is very nearly the same as that at the bottom. However, the temperature observed at the bottom is essentially the same as that observed at the bottom with an inner freeze immediately next to the well.

SPRT's are usually calibrated in groups of six. The six SPRT's are first successively calibrated at the TP, then at the zinc point, and so forth. The calibration at the oxygen point is carried out by the comparison method, employing reference SPRT's which, as mentioned earlier, are periodically checked to be consistent with the oxygen point maintained on the capsule type reference PRT's that are used to maintain the NBS–IPTS–68 scale in the region from 13.81 K to 90.188 K [4]. After the oxygen point calibration, another measurement is made on the SPRT at the TP. (Henceforth, for convenience, the four SPRT resistance readings at the TP will be referred to as $R(\mathrm{TP})_\mathrm{I}$, $R(\mathrm{TP})_\mathrm{Z}$, $R(\mathrm{TP})_\mathrm{T}$, and $R(\mathrm{TP})_\mathrm{O}$, respectively, and, when necessary, the values of $R(0\,^\circ\mathrm{C})$ obtained from these values of $R(\mathrm{TP})$ will be given the corresponding subscripts.) Whenever the change in the resistance of the SPRT at the TP is greater than what corresponds to about 0.75 mK during the course of calibration the complete calibration process, including the initial annealing at 480 °C, is repeated. In some thermometer designs the changes in the $R(\mathrm{TP})$ readings have been found to be on the average greater than in other designs. For these SPRT's a change in resistance at the TP corresponding to 1 mK is allowed.

Above 0 °C, the constants $A$ and $B$ of eq (6) are obtained by simultaneous solution from the resistance measurements at the TP, the zinc point, and the tin point. The values of the resistance ratio $W(T)$ corresponding to those at the zinc point and the tin point are calculated using the values of $R(\mathrm{TP})$ obtained after the measurements at the metal fixed points; i.e., $W(\mathrm{Zn})=R(\mathrm{Zn})/R(0\,^\circ\mathrm{C})_\mathrm{Z}$ and $W(\mathrm{Sn})=R(\mathrm{Sn})/R(0\,^\circ\mathrm{C})_\mathrm{T}$. (For the calculation of $R(0\,^\circ\mathrm{C})$ from $R(\mathrm{TP})$, see section 2.1.) Employing eqs (5) and (6) and the constants $A$ and $B$, tables of $W(t)$ are calculated at integral values of $t$ from 0 °C to 631 °C for SPRT's with a fused quartz sheath or from 0 °C to 500 °C for SPRT's with borosilicate glass or stainless steel sheaths. If a SPRT is also calibrated at the oxygen point, the constants $A_4$ and $C_4$ of the deviation function (see eq (4)):

$$\Delta W(t)=A_4 t+C_4 t^3(t-100\,^\circ\mathrm{C}) \tag{13}$$

are calculated from the relations:

$$A_4=\alpha-\alpha^* \tag{14}$$

and

$$C_4=[\Delta W(t_{0_2})-A_4 t_{0_2}]/t_{0_2}^3(t_{0_2}-100\,^\circ\mathrm{C}), \tag{15}$$

where $\alpha^*(=3.9259668\times10^{-3}\,^\circ\mathrm{C}^{-1})$ is the $\alpha$ that corresponds to the IPTS–68 reference function [2]. From eq (2)

$$\Delta W(t_{0_2})=W(t_{0_2})-W^*(t_{0_2}), \tag{16}$$

where

$$W(t_{0_2})=R(t_{0_2})/R(0\,^\circ\mathrm{C})_\mathrm{O}. \tag{17}$$

Tables of $W(t)$ are calculated at integral values of $t$ from −183 °C to 0 °C using eq (13), the constants $A_4$ and $C_4$, and the reference function (eq (3)). The above relations for the SPRT are extrapolated to −200 °C for those laboratories that employ the normal boiling point of nitrogen instead of that of oxygen in calibrating other PRT's. (In such tables the values of $t$ below −183 °C are fictitious and serve primarily as artifices for calibrating other PRT's for use above −183 °C.)

When the SPRT is calibrated only at the TP, tin point, and zinc point, the tables of $W(t)$ start from −50 °C. The extrapolation of $W(t)$ downward to −50 °C is obtained by assuming a value for $C_4(\approx 1.7\times10^{-14}\,^\circ\mathrm{C}^{-4})$ in the deviation function (eq (13)). The variation in $C_4$ of SPRT's is not more than $\pm1\times10^{-14}\,^\circ\mathrm{C}^{-4}$. By differentiating eq (13) and substituting −50 °C for $t$ there is obtained:

$$d\Delta W=1.875\times10^7 dC_4. \tag{19}$$

Since $dt/d\Delta W$ at −50 °C is about 247 °C, the uncertainty in the tabulated value of $W(-50\,^\circ\mathrm{C})$, because of the assumed value of $C_4$, corresponds to 0.05 mK, which is negligible.

During the course of calibration large changes in the SPRT resistance can arise from a number of sources. If the SPRT is insufficiently annealed prior to the measurements at the zinc point, the $R(\mathrm{TP})_\mathrm{Z}$ reading can be smaller than the $R(\mathrm{TP})_\mathrm{I}$ reading because of some annealing that could occur at the zinc point. Also, if the SPRT were "bumped" against an object during or after removal from the annealing furnace but prior to the $R(\mathrm{TP})_\mathrm{I}$ reading, the $R(\mathrm{TP})_\mathrm{Z}$ reading would be expected to be smaller than the $R(\mathrm{TP})_\mathrm{I}$ reading on account of the extra strain resistance that was introduced by the bumping of the SPRT but was later partially removed by annealing at the zinc point. On the other hand, if the SPRT were bumped immediately after the $R(\mathrm{TP})_\mathrm{I}$ reading, all of the extra strain resistance introduced by the bumping is most likely not removed by annealing at the zinc point; therefore, the $R(\mathrm{TP})_\mathrm{Z}$ reading could then be expected to be slightly higher than the $R(\mathrm{TP})_\mathrm{I}$ reading. If any large strains are introduced into the SPRT just prior to the $R(\mathrm{TP})_\mathrm{Z}$ reading, the $R(\mathrm{TP})_\mathrm{Z}$ reading should be larger than the $R(\mathrm{TP})_\mathrm{I}$ reading. If any strong bumping occurs after the $R(\mathrm{TP})_\mathrm{Z}$ reading, the $R(\mathrm{TP})_\mathrm{T}$ and the $R(\mathrm{TP})_\mathrm{O}$ readings should reflect the effect. If the platinum wire were wound too tightly around the coil form, strains can be introduced when the SPRT is cooled to the oxygen point and the $R(\mathrm{TP})_\mathrm{O}$ reading could be relatively higher than the other $R(\mathrm{TP})$ readings. Any changes in the $R(\mathrm{TP})$ readings smaller than what correspond to 0.75 mK are considered to arise from the general instability of the SPRT and the limit of precision of routine calibration measurements. Obviously, errors of observations, including errors of recording of data, will be superimposed upon the final data.

Berry [17] recently reported that with PRT's containing oxygen[13] in the protective sheath the $R(TP)$ readings, following the annealing at 450 °C, increased up to 3 or 4 ppm when exposed to temperatures of 200 to 250 °C over a period of seven days. Depending upon the PRT an increase of 1 to 3 ppm is shown to occur within the first hour of exposure to 200 to 250 °C. Accordingly, the $R(TP)_T$ readings would be expected to be higher than the $R(TP)_I$ and $R(TP)_Z$ readings, the increase being dependent upon how long the PRT was in the tin-point cell. It will be shown later that in general the observed $R(TP)_T$ readings are indeed somewhat higher than the $R(TP)_I$ and $R(TP)_Z$ readings in SPRT calibrations. This oxygen-activated thermal effect on the resistance of the PRT seems to impose a limitation on the precision that can be obtained with PRT's. However, a change of 3 ppm in the $R(TP)$ readings corresponds closely to 0.8 mK; such a large increase in the $R(TP)$ readings after the resistance readings at the tin point has seldom been observed. It seems that the length of time (approximately 30 min including the time in the preheating furnace) the SPRT is at the tin-point temperature during calibration is not enough to convert the SPRT to a noticeably higher value of the $R(TP)$.[14] Work is planned to investigate further this recently observed oxygen-activated thermal effect.

Capsule type PRT's are calibrated as received without annealing. The PRT's are installed in holders shown schematically in figure 9 for calibration in the

[13] Dry air is sealed in the protective sheath of most SPRT's. Most capsule-type PRT's have helium gas with a small amount of oxygen sealed in the capsule. Where pure helium gas was initially used, it is possible that the gas would eventually become contaminated with some oxygen.

[14] In an earlier investigation on the freezing point of tin [11] the SPRT that was employed was initially annealed at 480 °C. Before the intercomparison measurements of tin-points were started the SPRT was probably used in preliminary experiments at the tin point for a total of about 6 h. The subsequent measurement described in reference [11] shows that $R(TP)$ increased by an amount corresponding to about 0.01 to 0.02 mK per 1 h and 40 min exposure at the tin point.

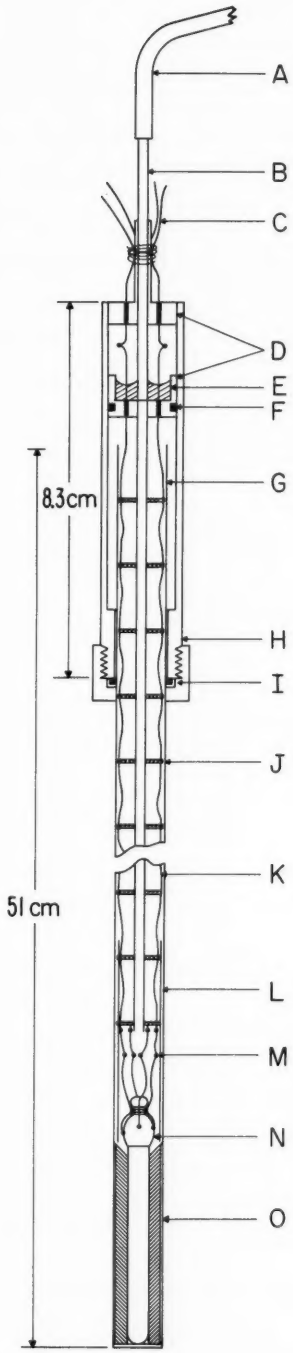


FIGURE 9. *Holder for capsule-type platinum resistance thermometers. Calibration measurements are performed in the holder at the triple point of water, tin point, and the normal boiling point of oxygen.*

A. Elastomer tubing to helium gas source.
B. Thin (0.13 mm) wall stainless steel tubing for purging the holder with helium gas before the vacuum tubing connector (I) is sealed.
C. Leads to measurement equipment (Mueller bridge).
D. Sections (brass) of mechanical tie-down, soldered to the stainless purge tube, for guiding and fastening the incoming thermometer leads.
E. Hard wax for holding and sealing the 0.13 mm gold leads that extend down to the thermometer.
F. "O" ring vacuum seal to brass tube (H).
G. Thin wall stainless steel tube (11.1 mm o.d. × 0.11 mm wall) closed at the bottom.
H. Brass tube with lead seal at top and vacuum tubing connector (I) at the bottom.
I. Vacuum tubing connector for sealing the tube (G).
J. Polytetrafluoroethylene plastic lead spacers.
K. Insulated gold leads (4) passing through holes close to the outer diameter of the spacers (J) to attain good tempering. The lead insulation (not shown) is polytetrafluoroethylene tubing cut into a helix and held in tension to eliminate buckling. The four gold leads are welded at the bottom end to short sections of platinum leads.
L. Thin polytetrafluoroethylene sheet rolled into a cylinder to insulate the exposed leads (near the connections to the capsule thermometer) against the stainless steel tubing.
M. Connections between the short sections of platinum leads of the holder and the platinum leads of the capsule thermometer.
N. Capsule thermometer.
O. Aluminum sleeve to fit the thermometer and the stainless steel tube. The sleeve reduces the external self-heating of the thermometer.

TP cell, in the tin-point cell, or in the oxygen-point apparatus. Because of possible damage and the electrical leakage across the metal-glass lead seal at the high temperatures, the capsule type PRT's are not calibrated at the zinc point as is routinely done with SPRT's. The capsule type PRT (platinum case with soft-glass lead seal) should not be used at temperatures much higher than about 300 °C. If the PRT is to be used between −183 °C and 300 °C the calibration measurements are made at the fixed points in the following sequence: TP, tin point, TP, oxygen point, and TP. When calibration in the range 13 K to 90 K is requested, the measurement sequence is TP, tin point, and TP, followed by comparison calibration between 13 K and 90 K (see ref. [4] for details of calibration in this range). If the PRT is to be used between −50 °C and 300 °C, the calibration sequence is TP, tin point, and TP.

The tables of $W(t)$ at integral values of temperature between 0 °C and 300 °C are calculated for capsule type thermometers from the calibration measurements at the TP and the tin point and an average value for the coefficient $B$ (approximately $5.8755\times10^{-7}$ °C$^{-2}$) based on values of about 200 SPRT's. The range of values of $B$ of SPRT's is about $5\times10^{-10}$ °C$^{-2}$. From eq (6)

$$\frac{dW}{dB}=\frac{dA}{dB}t'+t'^2. \tag{20}$$

The coefficient $A$ is obtained from the measurements at the TP and the tin point and from the average value of $B$. Assuming that there is no measurement error at the tin point,

$$\frac{dA}{dB}=-231.9292\ °C; \tag{21}$$

then,

$$\frac{dW}{dB}=-231.9292\,t'+t'^2. \tag{22}$$

At $t'=300$ °C, an uncertainty of $\pm2.5\times10^{-10}$ °C$^{-2}$ in $B$ corresponds to an uncertainty in the value of temperature of about ±1.4 mK. (A survey of values of $B$ obtained on SPRT's received recently shows the average to be closer to $-5.8768\times10^{-7}$ °C$^{-2}$ and the range to be about $4\times10^{-10}$ °C$^{-2}$.) The tables of $W(t)$ between −183 and 0 °C are calculated for capsule type PRT's by procedures similar to those described earlier for SPRT's.

## 7. Results of the NBS calibration of PRT's

### 7.1 R(0 °C) of PRT's

As indicated earlier, the PRT's are calibrated after annealing by measuring the thermometer resistances at the fixed points in the following sequence: TP, zinc point, TP, tin point, TP, oxygen point, and TP. Figures 10 and 11 show the variation of the values of $R(0\,°C)$ for each thermometer about its mean for PRT's that were received for calibration during a two-year period (June 1972 through July 1974). The symbols ○, △, □, and ◇ correspond to $R(0\,°C)_I$, $R(0\,°C)_Z$, $R(0\,°C)_T$ and $R(0\,°C)_O$,[15] respectively, that were calculated from the corresponding values of $R(TP)$'s. For most SPRT's four measurements at the TP are shown. For some SPRT's the measurements at the oxygen point were not requested; therefore, the $R(TP)_O$ measurements were not obtained. For capsule type PRT's, data are shown only when the calibration was requested for the range −183 °C to 300 °C; therefore, the plots correspond to $R(TP)_I$, $R(TP)_T$, and $R(TP)_O$. The standard deviations of the observed $R(TP)$'s for the PRT's are on the average ±0.15 mK. (As previously mentioned, whenever the range of the observed $R(TP)$'s for the PRT corresponds to 0.75 mK or greater in the initial calibration the PRT is recalibrated; the rejected measurements are not shown in the plot. Also, as previously mentioned, a range of 1 mK in the observed values of $R(TP)$'s is accepted as not atypical for certain designs of PRT's.) An error in $R(TP)$ of ±0.15 mK corresponds to an error in the value of $W$ at the tin point of ±0.30 mK and at the zinc point of ±0.44 mK, assuming that $R(Sn)$ and $R(Zn)$, respectively, have been determined without error.

The relative values of $R(TP)$'s show certain tendencies; e.g., $R(TP)_Z$ is more often lower than $R(TP)_I$, approximately twice as often lower than higher.[15] However, $R(TP)_T$ is more often higher than both $R(TP)_I$ and $R(TP)_Z$, almost twice as often higher than lower. $R(TP)_O$ is more often higher than $R(TP)_T$, approximately 1⅓ as often higher than lower. These observations suggest that either in cooling from the annealing temperature of 480°C some strains are quenched in, which are removed when heated at the zinc point, or else that the additional heating at the zinc point, following the heating at 480 °C for 4 h, caused more annealing of the PRT. However, the latter seems more consistent since the work of Berry [18] suggests that in cooling rapidly from 500 °C only about 0.1 ppm of $R(0\,°C)$ of strain resistance (a change that corresponds to 0.02 mK) can be quenched in. The observation that values of $R(TP)_T$ were twice as often higher than those of $R(TP)_I$ and $R(TP)_Z$ seem to support the work of Berry [17] that when an annealed SPRT is exposed to temperatures of 200 to 250 °C the $R(TP)$ increases 3 or 4 ppm over a period of seven days. Since $R(TP)_O$ is 1⅓ times as often higher than it is lower than $R(TP)_T$, some SPRT's could have been slightly strained between these two measurements.

[15] Since $R(TP)$ was actually observed, reference is made here to $R(TP)$. In figs. 10 and 11 the plot is in terms of $R(0\,°C)$. However, in this discussion and in the plot $R(TP)$ and $R(0\,°C)$ are interchangeable since only their relative values are being examined.

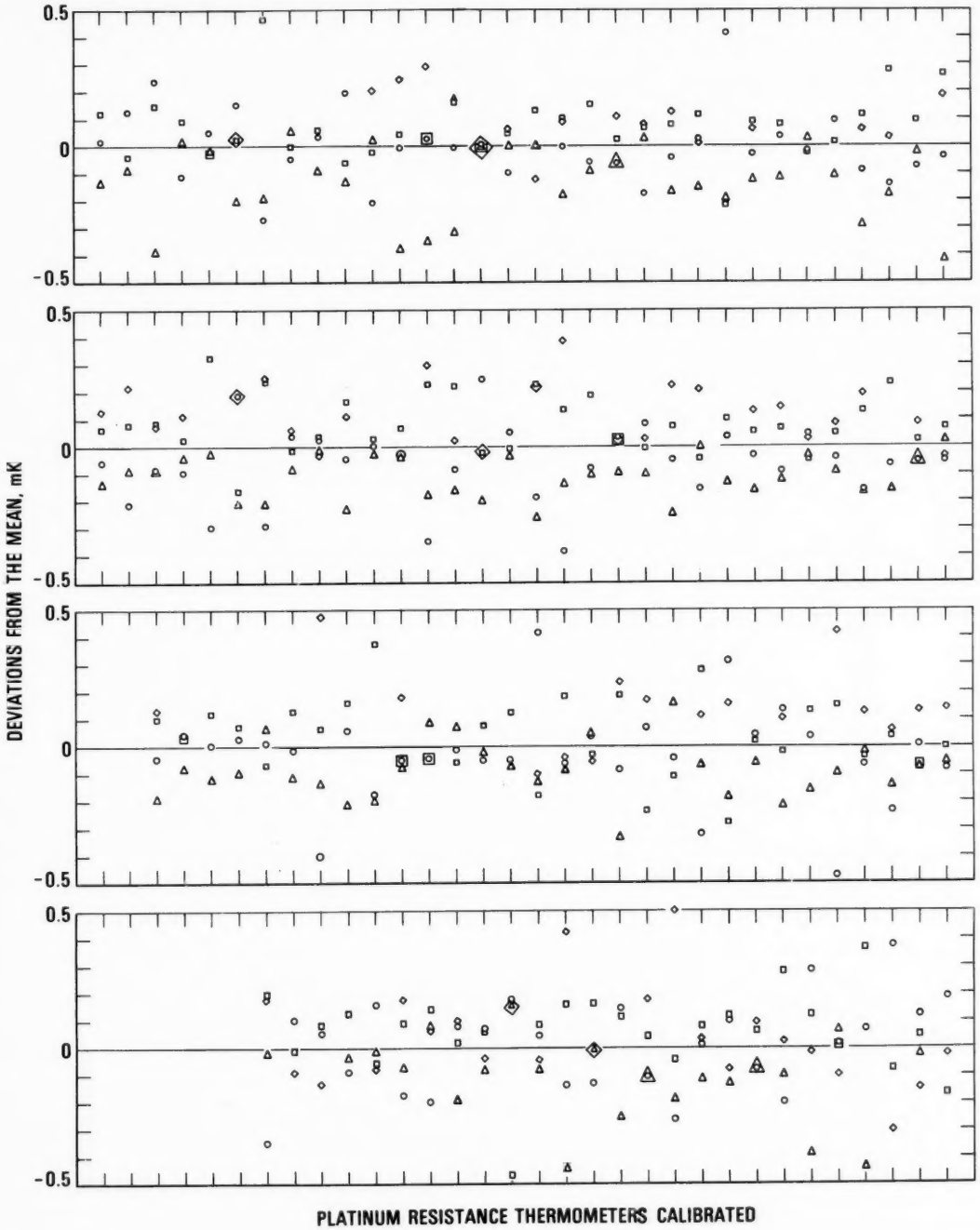


FIGURE 10. *Deviations (in terms of the corresponding values of temperature) from the average value of* R(0 °C) *for each PRT calculated from the observed values of* R(*TP*) *for PRT's calibrated between June 1972 and July 1973.*

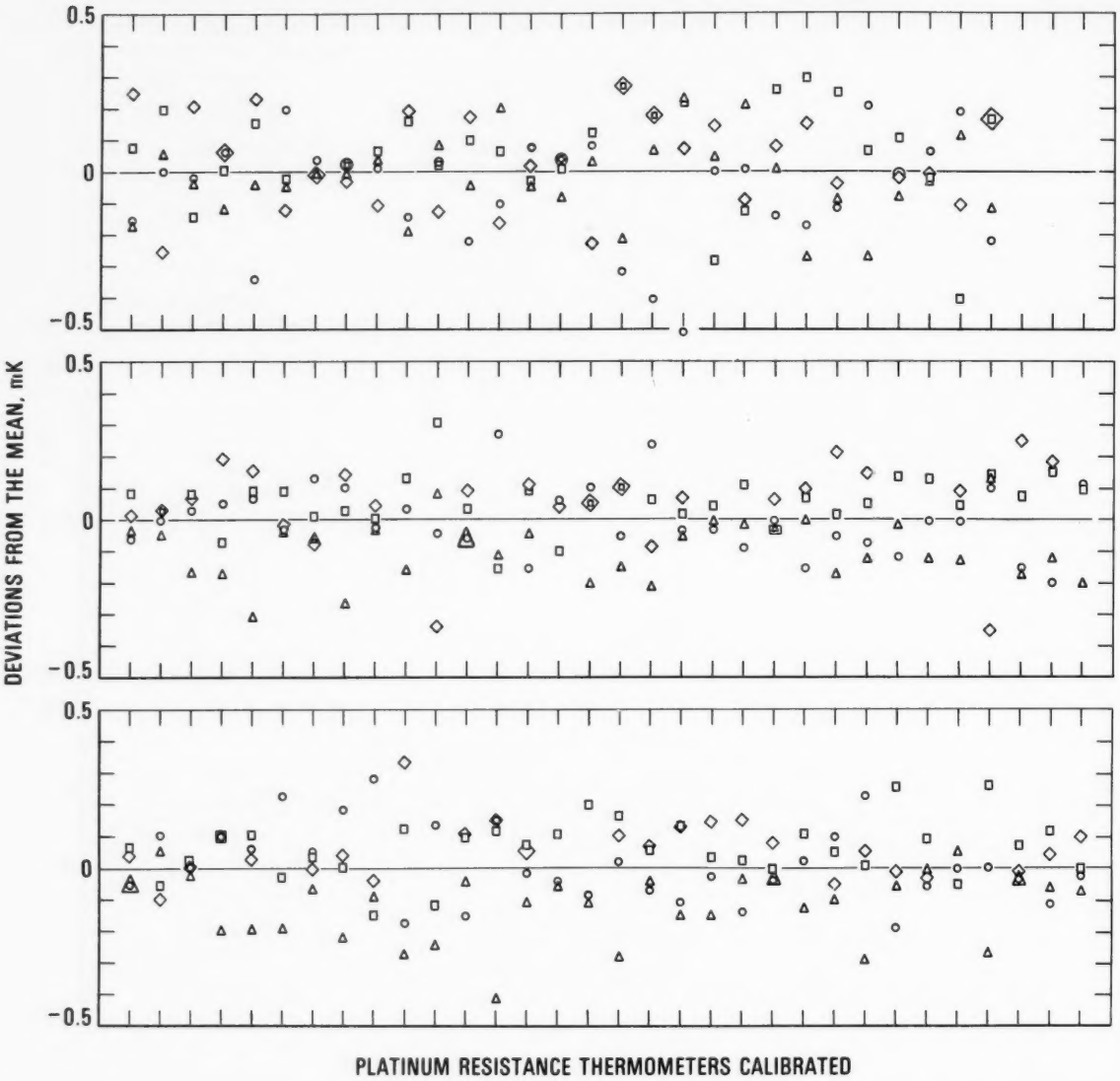


FIGURE 11. *Deviations (in terms of the corresponding values of temperature) from the average value of* R(0 °C) *for each PRT calculated from the observed values of* R(TP) *for PRT's calibrated between August 1973 and July 1974.*

### 7.2 Check PRT's

As part of the calibration process at the NBS, separate check SPRT's are employed to monitor the constancy of the temperature of each of the fixed points. In the cases of the freezing-point cells of tin and zinc, although the metals employed in the cells are of high purity, the equilibrium temperature of the liquid-solid phases is somewhat dependent upon the relative amounts of the two phases. Usually the SPRT's are calibrated during the period in which the first 50 percent of the metal is being frozen. Of a group of SPRT's to be calibrated, the first and the last measurements in each freeze are obtained with the check SPRT. If the second reading on the check SPRT is lower than the first by what corresponds to 0.5 mK some of the SPRT's being calibrated, based on the time of the measurements that were obtained, are recalibrated employing a new freeze with the cell. The first and the last measurements on the new freeze are again obtained with the check SPRT. The comparison of the results of the repeat calibration with those of previous freeze will show whether SPRT's calibrated earlier in the sequence with the previous freeze should also be recalibrated.

The measurements with the check SPRT of every new freeze are compared with those of the previous freezes. The check SPRT's employed with the zinc and tin point cells are usually about 1.5 and 2 h at their respective fixed points during each freeze. The check SPRT for the tin point cell is near the tin point longer because of the preparation and manipulation that are followed for initiating the freeze by withdrawing the cell from the furnace well (see sec. 2.3).

For the oxygen point comparison calibration (see sec. 2.4) a second reference standard SPRT is used as the check SPRT to monitor the consistency of the "working" reference standard SPRT. The value of $W(O_2)$ obtained for the check SPRT is compared with those of previous calibrations.

With each of the readings of the check SPRT's at the fixed points there are also obtained readings at the TP. Thus, there is collected a history of measurements with check SPRT's and fixed points.

Figure 12 shows the observed $R(\mathrm{Zn})$ and $R(0\,^{\circ}\mathrm{C})$ for the check SPRT (designated 200) used with the zinc-point cell. The symbols ○ and △ indicate in most cases the $R(\mathrm{Zn})$ readings at the beginning and end, respectively, of a group of SPRT's that were calibrated. Occasionally additional $R(\mathrm{Zn})$ readings have been obtained, the sequence being ○, △, □, and ◇. When the first reading ○ is suspected and the second reading △ is obtained, the symbols △ and □ indicate the beginning and end readings, respectively, of a group of SPRT's that were calibrated. The fourth reading, indicated by the symbol ◇, is a check, if considered necessary, on the previous reading indicated by □. In calibration batches 72J and 73D the difference in the beginning and end readings of the check SPRT are shown to be excessive. Some of the test SPRT's were recalibrated in the next batch. The symbol + indicates the $R(0\,^{\circ}\mathrm{C})$ readings obtained after the $R(\mathrm{Zn})$ readings. There is shown a definite increase in the values of $R(\mathrm{Zn})$ and $R(0\,^{\circ}\mathrm{C})$ associated with each freeze. (Because of possible strains that are introduced, the resistance of PRT's usually increases with use.) The sharp decrease shown at 74C resulted principally from

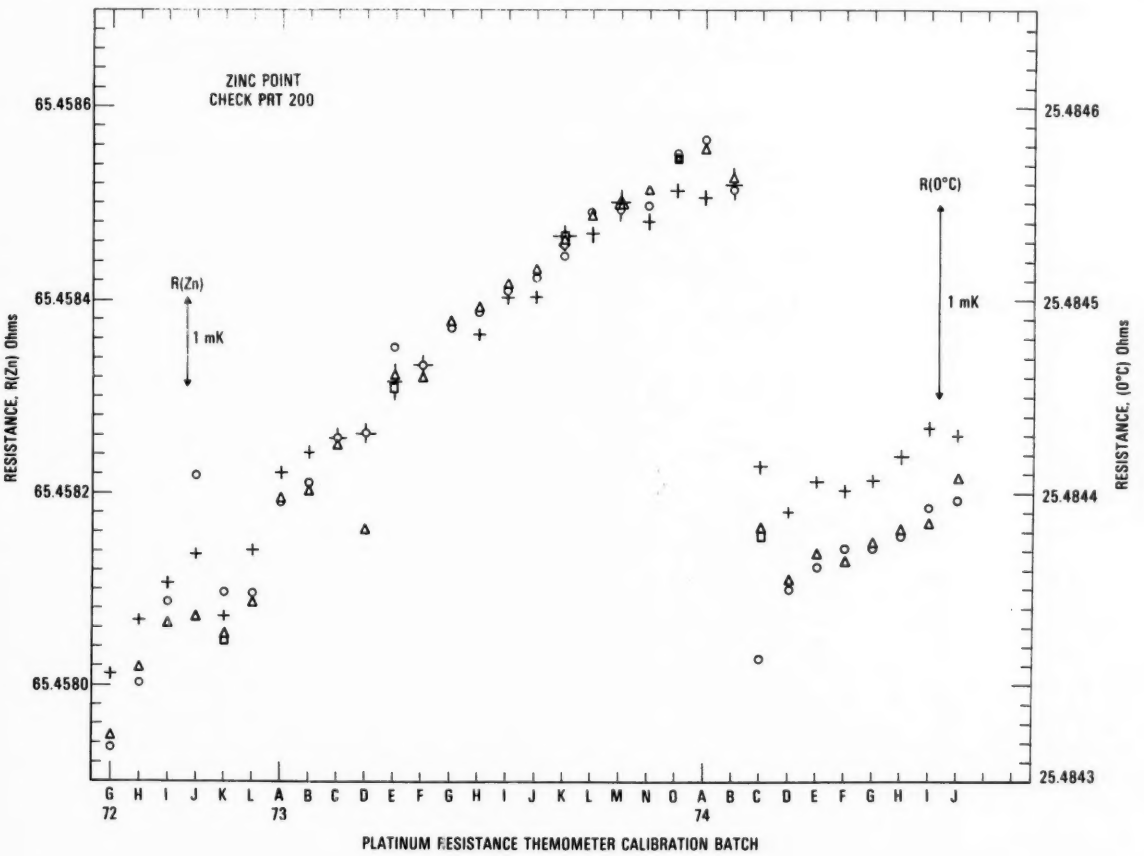


FIGURE 12. *Observed values of resistances for the check SPRT 200 at the zinc freezing point and at the TP (converted to R(0 °C)).*

The sequence of zinc-point observations is represented by the symbols in the order ○, △, □, and ◇; the $R(0\,^{\circ}\mathrm{C})$ values are represented by the symbol +.

the change in the Mueller bridge resistance unit which was previously based on one standard resistor. The new resistance unit is based on the average of four standard resistors. However, since the Mueller bridge is calibrated to be "linear," the values of $R(\mathrm{Zn})/R(0\,^{\circ}\mathrm{C})$ or $W(\mathrm{Zn})$ for the check PRT should be independent of the resistance unit (see fig. 13). The downward trend in the $W(\mathrm{Zn})$ reflects the change in the SPRT with use. However, the total change over the two-year period corresponds to not more than 1 mK. In the interval from the calibration batch 74C to 74J (approximately one-half year) $W(\mathrm{Zn})$ was found to be fairly constant and its range corresponds to about 0.4 mK. The standard deviation of the values of $W(\mathrm{Zn})$ was computed after dividing the data into three intervals: 72G to 72K, 72L to 73J, and 73K to 74J. (Between the intervals the values of $W(\mathrm{Zn})$ seem to show a large change possibly from slight bumping of the check SPRT.) The pooled standard deviation was found to correspond to $\pm 0.28$ mK.

Figure 14 shows the observed $R(\mathrm{Sn})$ and $R(0\,^{\circ}\mathrm{C})$ for the check SPRT (designated 199) used with the tin-point cell. The symbols have the same significance as those used with the readings obtained with the check SPRT for the zinc-point cell. In two cases 73H and 73I, a set of symbols is "flagged." These indicate readings with a second freeze that was used in the calibration of the group of SPRT's. Up to calibration batch 74C the trend of the $R(\mathrm{Sn})$ and $R(0\,^{\circ}\mathrm{C})$ readings is shown to increase, but not as rapidly as in the case with check SPRT 200 for the zinc-point cell. As shown in the measurements with the zinc point check SPRT (see fig. 12), a sudden change in $R(\mathrm{Sn})$ and $R(0\,^{\circ}\mathrm{C})$ occurs at calibration batch 74C because of the change in the Mueller bridge resistance unit. The reason for the relatively constant readings obtained starting from the calibration batch 74C is at present not known. Perhaps the oxygen activated change in $R(0\,^{\circ}\mathrm{C})$ reported by Berry [17] finally reached an equilibrium state for the tin point. (Berry did not report how the thermometer resistances changed at the higher temperatures at which the thermometers were "soaked." In a more

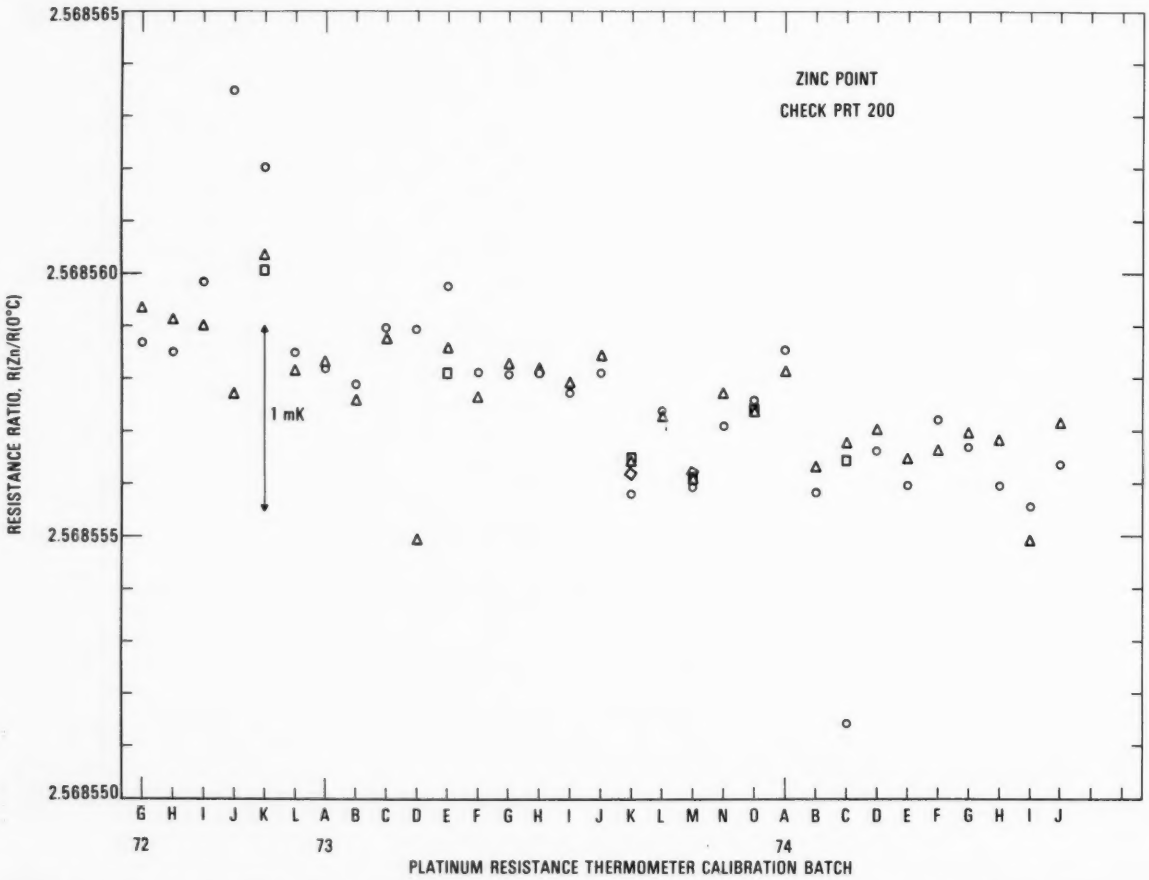
ZINC POINT
CHECK PRT 200
1 mK
RESISTANCE RATIO, R(Zn)/R(0°C)
2.568565
2.568560
2.568555
2.568550
G H I J K L A B C D E F G H I J K L M N O A B C D E F G H I J
72
73
74
PLATINUM RESISTANCE THERMOMETER CALIBRATION BATCH

FIGURE 13. *Values of* W *for the check SPRT 200 from observations of the resistances at the zinc freezing boint and at the TP.*

The sequence of zinc-point observations is represented by the symbols in the order ○, △, □, and ◇.

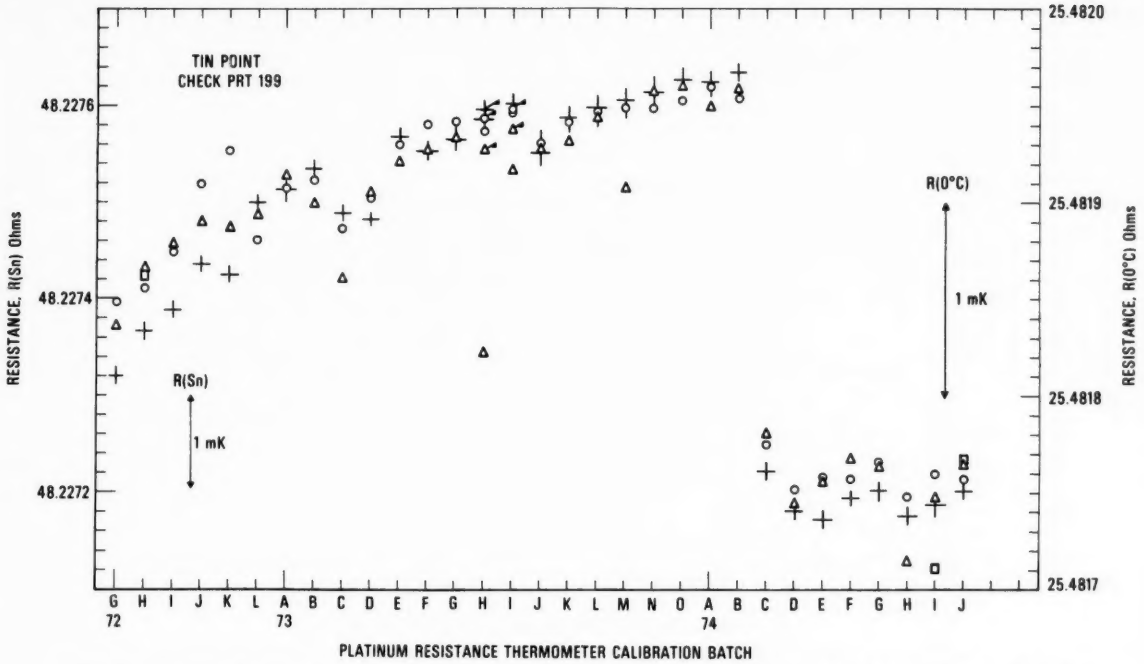


FIGURE 14. *Observed values of resistances for the check SPRT 199 at the tin freezing point and at the TP (converted to* R*(0 °C)).*
The sequence of tin-point observations is represented by the symbols in the order ○, △, and □; the $R(0\,°C)$ values are represented by the symbol +.

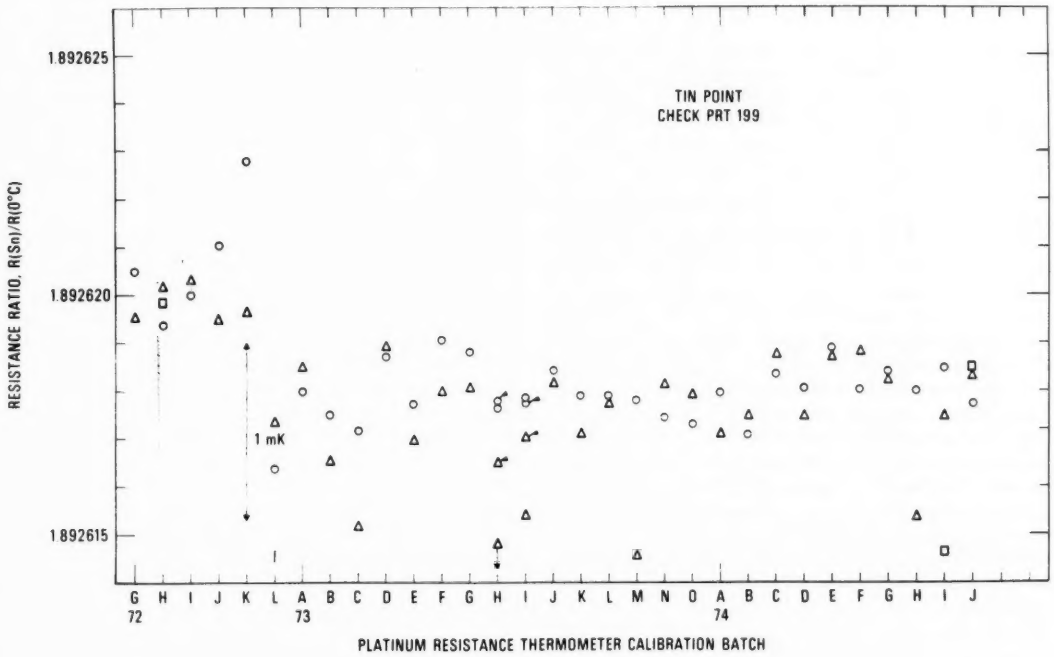
1.892625
1.892620
1.892615
TIN POINT
CHECK PRT 199
1 mK
RESISTANCE RATIO, R(Sn)/R(0°C)
G H I J K L A B C D E F G H I J K L M N O A B C D E F G H I J
72
73
74
PLATINUM RESISTANCE THERMOMETER CALIBRATION BATCH

FIGURE 15. *Values of* W *for the check SPRT 199 from observations of the resistance at the tin freezing point and at the TP.*
The sequence of tin-point observations is represented by the symbols in the order ○, △, and □.

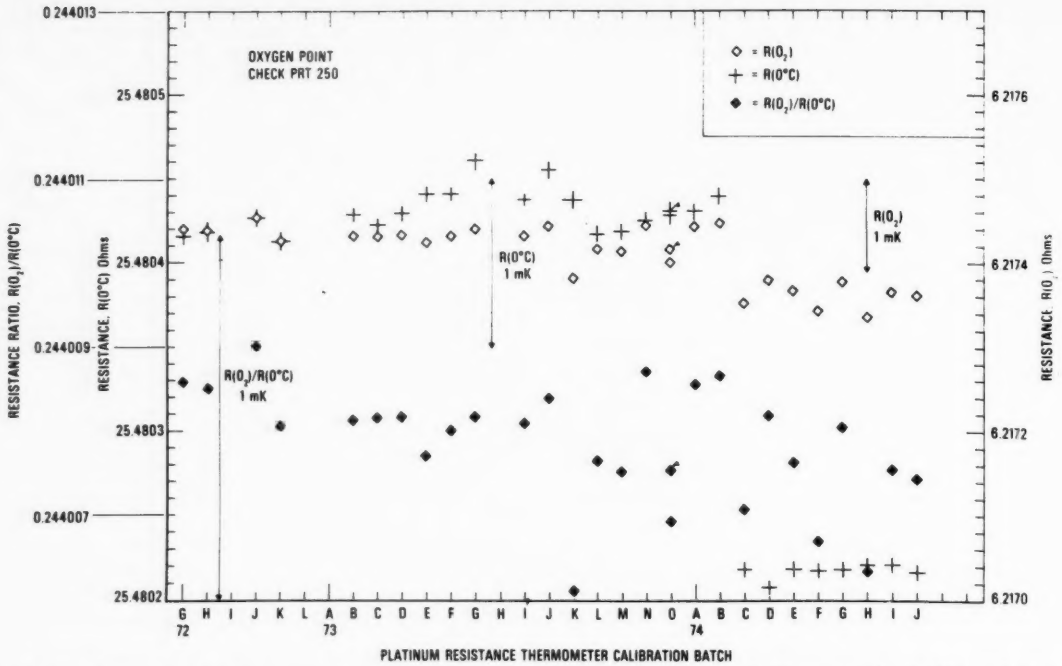


FIGURE 16. *Observed values of resistances for the check SPRT 250 at the oxygen point and at the TP (converted to* R*(0 °C)) and values of* W *calculated from the observations.*

The oxygen-point observations are represented by the symbol◇ and the $R(0\,°C)$ values are represented by the symbol +. The corresponding values of $W(0_2)$ are represented by the symbol

recent work Berry [19] found that the reproducibility of $W(100\,°C)$ of five SPRT's corresponded to 0.1 mK as long as the $R(100\,°C)$ and $R(0\,°C)$ were observed with the platinum of the SPRT in the same oxidation state. The values of $W(t)$ that are obtained in the NBS calibration procedure discussed in this paper correspond essentially to this requirement. Figure 15 shows the plot of $R(Sn)/R(0\,°C)$ or $W(Sn)$ for the check SPRT. The values of $W(Sn)$ are significantly more constant than those of $W(Zn)$ which indicate that the SPRT is not changed as rapidly when used at the tin point as at the zinc point. (The check SPRT's 199 and 200 are essentially alike in construction and were obtained at the same time. Another SPRT may show better or worse stability.) From calibration batch 72K to 74J most of the observed values of $W(Sn)$ are within ±0.3 mK. The noticeable change in the $W(Sn)$ reading after the calibration batch 72K suggests that the check SPRT was "bumped" slightly. (There is a relatively large increase in $R(0\,°C)$ in calibration batch 72L.) The change in the check SPRT indication has no effect on the SPRT's that were being calibrated. The standard deviation of the values of $W(Sn)$ was computed after dividing the data into two intervals: 72G to 72K and 72L to 74J. The pooled standard deviation was found to correspond to ±0.30 mK, which is essentially the same as that (±0.28 mK) found for the values of $W(Zn)$ obtained with the check SPRT 200.

Figure 16 shows the observed $R(0_2)$ and $R(0\,°C)$ for the check SPRT (designated 250) used in the intercomparison calibrations at the oxygen point. The symbol ◇ indicates the check measurements at the oxygen point and the symbol + indicates the $R(0\,°C)$ readings. The "flagged" points for calibration batch 730 indicate that second readings were obtained in the oxygen-point calibration with the group of SPRT's that were calibrated. (The SPRT's of the batch were calibrated on two days; therefore, two check SPRT readings were obtained.) The values of $R(0_2)/R(0\,°C)$ or $W(0_2)$ are also plotted in figure 16. Although there is a small downward trend, the values of $W(0_2)$ are more stable than the values of $W(Zn)$ and $W(Sn)$ of the check SPRT's used with the zinc and tin point cells, respectively. Excluding some outlying observations which are shown to deviate relatively more (see calibration batches 73K, 74F, and 74H), the range of $W(0_2)$ corresponds to not more than 0.7 mK. The standard deviation of the values of $W(0_2)$ corresponds to ± 0.16 mK, which is significantly smaller than that found for $W(Zn)$ and $W(Sn)$ obtained with their respective check SPRT's.

### 7.3 Calibration of "MAP" Thermometers

As part of the NBS Measurement Assurance Program (MAP) on platinum resistance thermometry a set of three calibrated SPRT's has been furnished to participating standards laboratories of the nation. On

receipt of the SPRT's the laboratory first determined $R(TP)$ at 1 and 2 mA currents and then calibrated the SPRT's according to its regular laboratory procedure. After completion of the calibration the laboratory determined $R(TP)$ at 1 and 2 mA currents just before shipping the SPRT's back to the NBS. On return of the SPRT's to the NBS their $R(TP)$'s were first determined at 1 and 2 mA currents; they were then annealed and recalibrated according to the usual retained as the SPRT's are subjected to conditions of use.

For the convenience of the comparison of the successive calibrations at the NBS and, at the same time, to show the degree to which the SPRT's can retain its calibration, the resistance ratios $W$ at −183, 232, and 420 °C obtained through the calibration process are compared relative to the first calibration of the series. The results for SPRT's A, B, C, and D are shown in

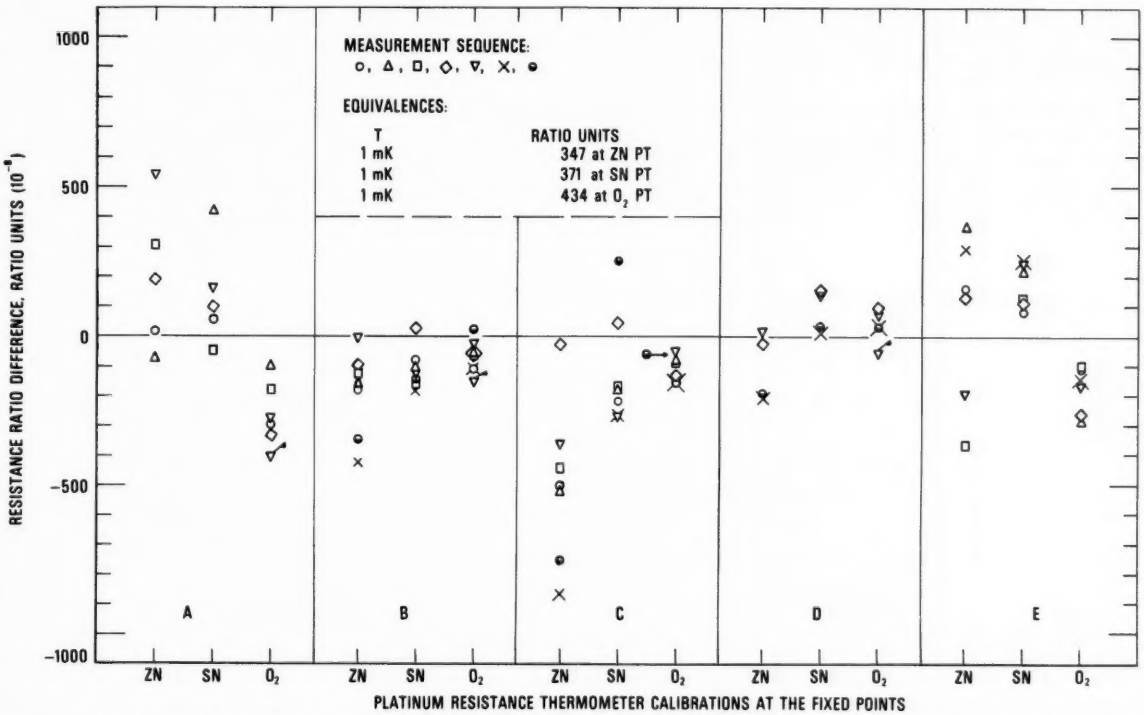


FIGURE 17. *Values of* W *of SPRT's (relative to the first calibration) obtained at the National Bureau of Standards from a series of calibrations at the TP and at the zinc, tin, and oxygen points.*

Thermometers A, B, C, and D were employed in the Measurement Assurance Program and thermometer E was calibrated in successive batches.

procedure. The SPRT's were then shipped to the next participating standards laboratory. The SPRT's were shipped cushioned in soft plastic foam inside a wooden box. When the SPRT's were at the various standards laboratories they were subjected to the annealing temperatures (450 °C to 480 °C) for 4 h and to the various temperatures (about −180, 0, 232, and 420 °C) of the fixed points that were employed in the calibration. While at the NBS the SPRT's were annealed at 480 °C for 4 h and then recalibrated. Therefore, in the interval between the calibrations at the NBS the SPRT's were exposed to temperatures over a wide range, including the higher temperatures where they were "annealed." The successive calibrations that were obtained at the NBS were examined to determine the reproducibility of the calibration and also to determine how well the calibrations of the SPRT's are figure 17.[16] (The first three calibrations of thermometers A, B, and C and the first two calibrations of thermometer D were obtained before shipping them to the standards laboratories that participated in the MAP study.) The calibration sequence after the first calibration is indicated by the symbols ○, △, □, ◇, ▽, ×, and ◒. The flagged points indicate a second measurement using another freeze. There is a tendency for the values of $W(Zn)$ to increase with use which was not the observation with the check SPRT 200 (see fig. 13). The calibration is noticeably more scattered at the zinc point than at the tin point or at the oxygen point. The deviations reflect the combined variations in the

[16] After several successive calibrations the relatively older thermometer A was considered to be less stable than thermometers B and C. Thermometer A was subsequently replaced with thermometer D.

observations of $R(\mathrm{TP})$ and of $R(\mathrm{Zn})$, $R(\mathrm{Sn})$, or $R(0_2)$, the variations in $R(\mathrm{TP})$ being amplified in $W(\mathrm{Zn})$ and $W(\mathrm{Sn})$ (see sec. 7.1). The deviations should reflect also the effect of handling of the SPRT's in the various laboratories and the effect of handling during shipment. Table 1 summarizes the estimated standard deviations of the values of $W(\mathrm{Zn})$, $W(\mathrm{Sn})$, and $W(0_2)$ for thermometers A, B, C, and D and the check SPRT's. The average of the standard deviations of $W(\mathrm{Zn})$ observed for SPRT's A, B, C, and D is shown to be about twice that observed for the check SPRT 200; only the estimated standard deviation of $W(\mathrm{Zn})$ for thermometer D appears to be comparable to that of check SPRT 200.

Figures 18, 19, 20, and 21 show for each SPRT how the values of $W(t)$ (in corresponding values of temperature), based on the various calibrations, deviate over the range $-183\,^{\circ}\mathrm{C}$ to $630\,^{\circ}\mathrm{C}$ relative to the first calibration. The figures indicate the levels of uncertainty of temperature measurement that can be achieved, under the various conditions to which the SPRT's were subjected, relative to the IPTS–68 maintained by the NBS. For example, the degree of repeatability of the measurements at the fixed points indicates the degree of retention of calibration by the SPRT. Since the standard deviations of the values of $W(\mathrm{Sn})$ and $W(0_2)$ are comparable and those of $W(\mathrm{Zn})$ are about twice those observed with the check SPRT's, the calibration of the SPRT's have been retained close to the limit of calibration measurements at the NBS. The user of a SPRT that was calibrated at the NBS can look upon figures 18, 19, 20, and 21 to indicate the level of retention of calibration (after annealing in a similar manner) and repeatability of calibration of a SPRT and, in the analysis of his temperature measurements, should combine the uncertainties shown in the figures with the uncertainties of his measurements to obtain his overall uncertainty relative to the NBS.

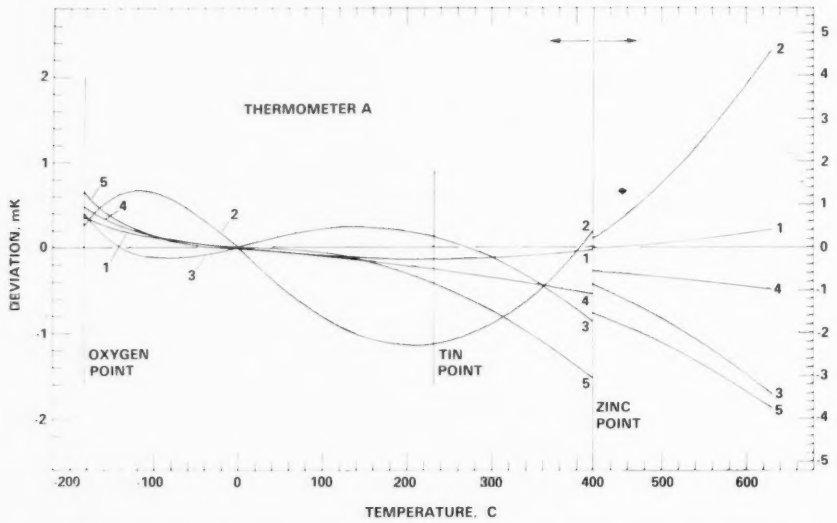


FIGURE 18. *Deviations, relative to the first calibration, of values of* W(t) *(in terms of corresponding values of temperature) of succeeding calibrations of thermometer A.*

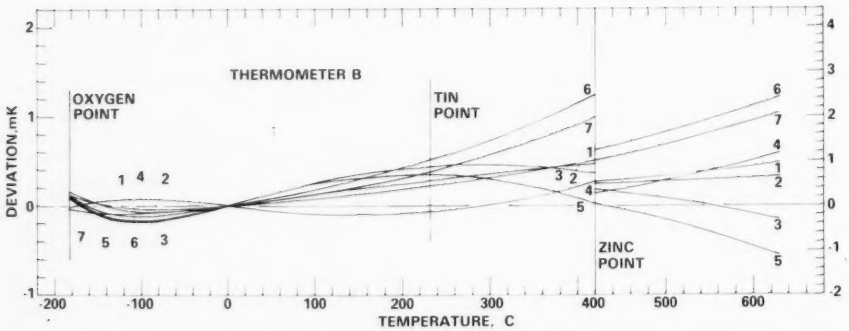


FIGURE 19. *Deviations, relative to the first calibration, of values of* W(t) *(in terms of corresponding values of temperature) of succeeding calibrations of thermometer B.*

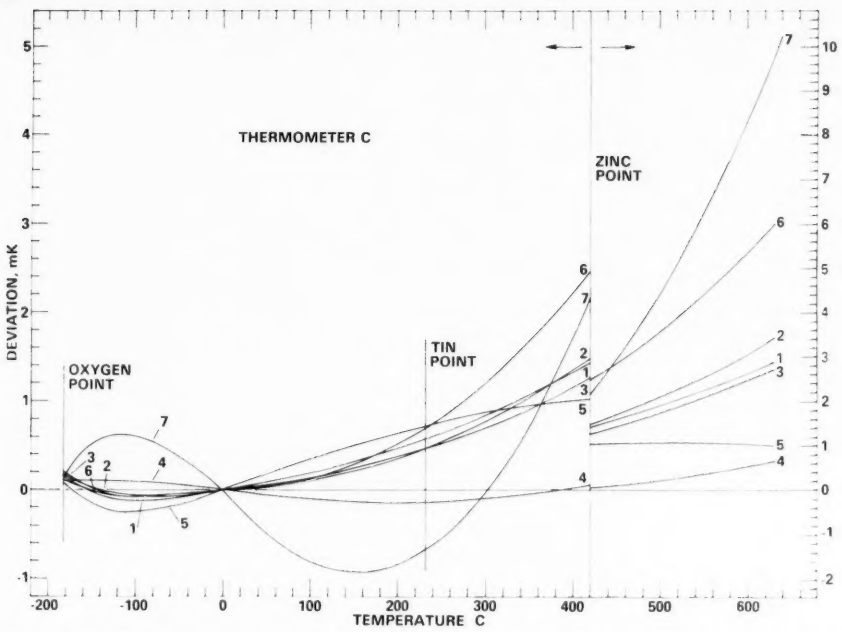


FIGURE 20. *Deviations, relative to the first calibration, of values of* W(t) *(in terms of corresponding values of temperature) of succeeding calibrations of thermometer C.*

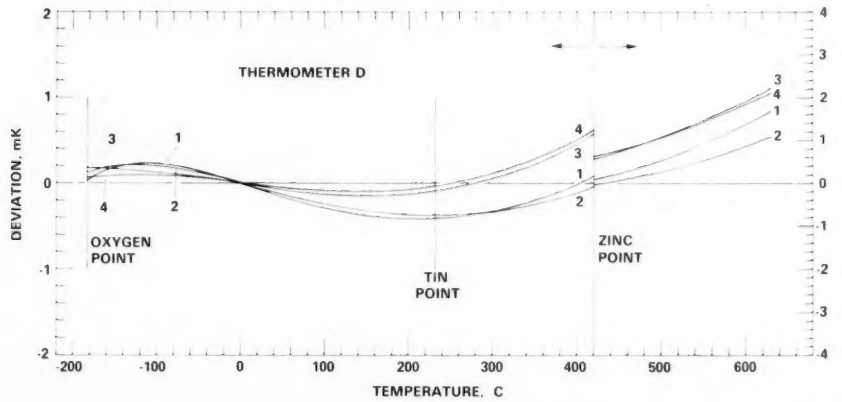


FIGURE 21. *Deviations, relative to the first calibration, of values of* W(t) *(in terms of corresponding values of temperature) of succeeding calibration of thermometer D.*

### 7.4 Repeated calibrations

As another test of reproducibility of the NBS calibrations at the fixed points, a SPRT was repeatedly calibrated (including the initial annealing) in seven successive batches of calibrations. The sequence of calibration of this "test" SPRT (thermometer E) was varied within each batch of SPRT's that were to be calibrated for the customers so that the location of calibration on the freezing "plateau" of the zinc- and tin-point cells was varied for the SPRT. The values of $W$ that were obtained at the zinc, tin, and oxygen points are compared (relative to the first calibration in batch 74D) in figure 17 along with those calibrations obtained for thermometers A, B, C, and D that were used in the NBS–MAP measurements described earlier. The standard deviations of the measurements are summarized in table 1. The results show that the variations in the calibrations of thermometer E are comparable to those obtained for thermometers A, B, C, and D; therefore, the additional handling and "use" of the NBS–MAP therometers did not seem to have affected the calibration of these SPRT's to a large extent. (These measurements were on only one thermometer E; other SPRT's may show better or worse reproducibility.)

Figure 22 shows more clearly how the observations obtained with thermometer E changed with each calibration. The symbols △, □, and ◇ are associated with the measurements at the zinc, tin, and oxygen points, respectively. The same symbols are used to represent the observations at the TP after the measurements at the above three fixed points. The symbol ○ represents the initial measurements at the TP after annealing the SPRT. The filled in symbols represent the values of $W(t)$ at the corresponding fixed points. The plot shows that the values of the SPRT resistances tended to increase with each calibration.[17] However, the values of $W(t)$ obtained at the fixed points do not show any definite trend. Figure 23 shows how the values of $W(t)$ (in terms of equivalent values in $t$) vary relative to those of the first calibration. The measurements of the first calibration were slightly outside of those measurements obtained in the later series of calibrations.

TABLE 1. *Estimated standard deviation of values of* W *at the fixed points of some platinum resistance thermometers*

| SPRT | $W$(Zn) | | $W$(Sn) | | $W$($O_2$) | |
|---|---|---|---|---|---|---|
| | $\pm W \times 10^{-8}$ | $\pm t$ mK | $\pm W \times 10^{-8}$ | $\pm t$ mK | $\pm W \times 10^{-8}$ | $\pm t$ mK |
| A (6)[a] | 230 | 0.66 | 165 | 0.46 | 142 | 0.33 |
| B(8) | 150 | .43 | 76 | .21 | 55 | .13 |
| C (8) | 308 | .88 | 184 | .51 | 55 | .13 |
| D (5) | 109 | .31 | 73 | .20 | 60 | .14 |
| Mean | 199 | .57 | 124 | .33 | 78 | .18 |
| E (7) | 261 | .75 | 92 | .25 | 98 | .23 |
| Mean[b] | 212 | .61 | 118 | .32 | 82 | .19 |
| Check SPRT[c] | 99 | .28 | 110 | .30 | 71 | .16 |

[a] Numbers in parentheses indicate the number of calibrations.
[b] Mean of SPRT's A, B, C, D, and E.
[c] $W$(Zn) was observed with check SPRT 200, $W$(Sn) with check SPRT 199, and $W$($O_2$) with check SPRT 250.

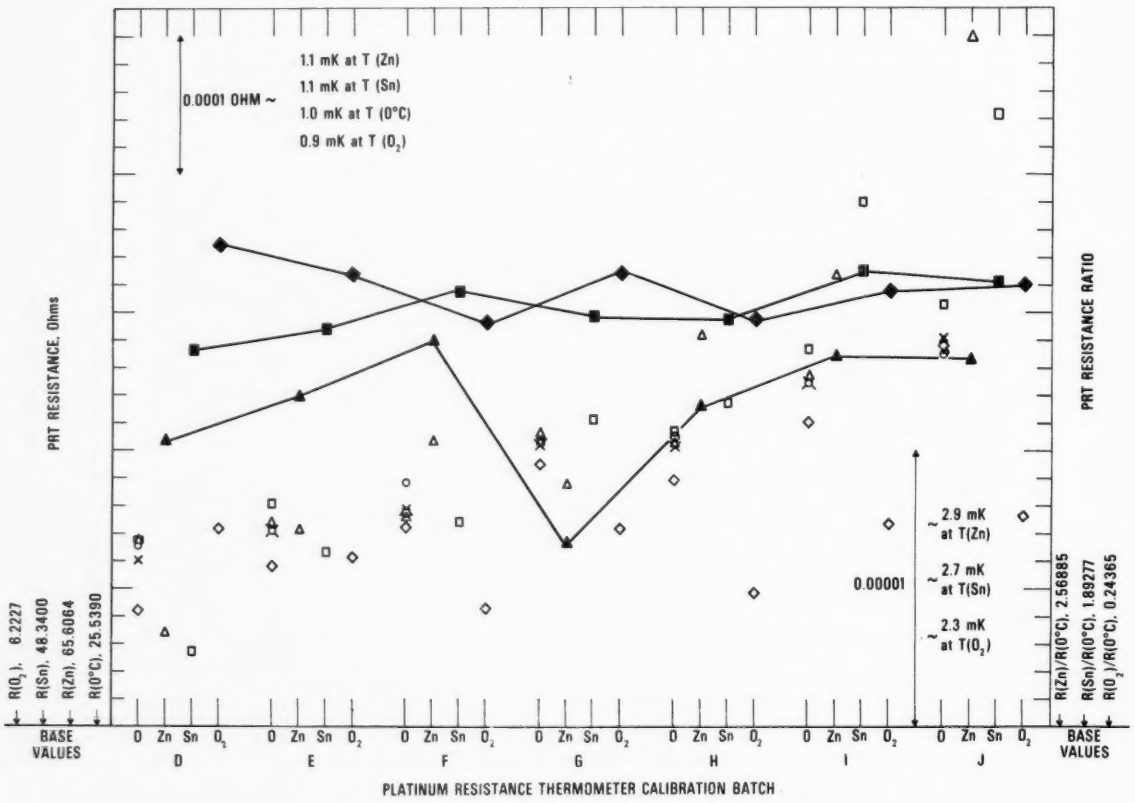


FIGURE 22. *Observed values of resistances at the TP (converted to* R(0 °C)*) and at the zinc, tin, and oxygen points and the values of* W *calculated from the observations for thermometer E calibrated successively in the batches 74D to 74J.*

The sequence of observations at the TP is represented by the symbols in the order ○, △, □, and ◇. The open symbols △, □, and ◇ represent the observations of resistance at the zinc, tin, and oxygen points respectively; the corresponding filled-in symbols represent the values of $W$ at these points.

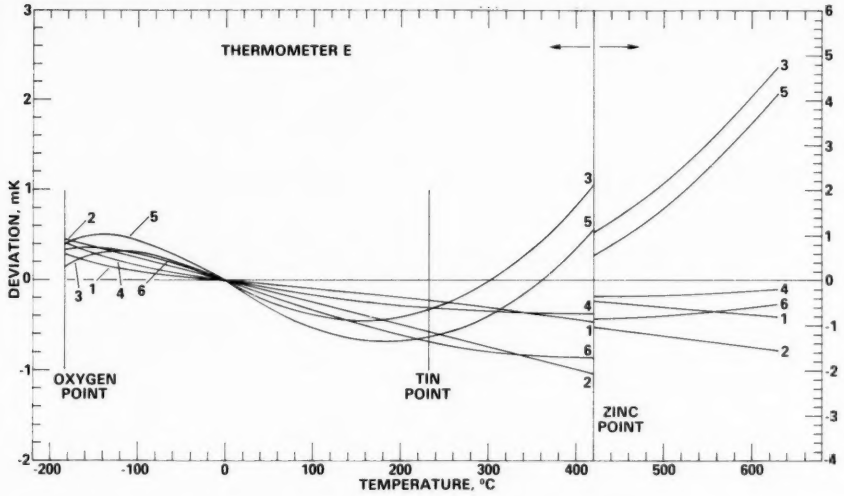


FIGURE 23. *Deviations, relative to the first calibration, of values of* W(t) *(in terms of corresponding values of temperature) of succeeding calibration of thermometer E.*

## 8. Discussion and Conclusion

The calibration data on 213 PRT's (mostly SPRT's) that were received over a two-year period show that the average of the standard deviations of $R$(TP)'s that were observed for each of the thermometers corresponds to $\pm 0.15$ mK. This indicates the precision of the NBS calibration measurements and the high reproducibility of the SPRT's at the TP and the high stability of the SPRT's even after being subjected to temperatures as high as 420 °C or as low as −183 °C. The high reproducibility of values of $W$ of the check SPRT's (serial nos. 199, 200, and 250) that are used for the zinc, tin, and oxygen points (pooled standard deviations: $\pm 0.28$, $\pm 0.30$, and $\pm 0.16$ mK, respectively) shows that SPRT's can be employed in high-precision temperature measurements. [An error in $R$(TP) is amplified (or attenuated) in the value of $W$ at these fixed points by 2.6, 1.9, and 0.24 times, respectively.] The high reproducibility also shows that the tin and zinc points and the reference standard SPRT for the oxygen point are highly stable.

Although both the thermometer resistances and resistance ratios were found to change, the resistance ratios were more stable. The data on the check SPRT's were taken over a two-year period; measurements over a longer period or perhaps other conditions are needed to determine the useful life of a SPRT.[18] The values of $W$(Zn) of the check SPRT used with the zinc point are decreasing slightly with use. An annealing of this SPRT at a higher temperature (e.g., 480 °C) may reduce this trend. The SPRT's that were used in the MAP study and in repeated calibrations were annealed at 480 °C prior to each calibration; the values of $W$(Zn) are either randomly scattered or are increasing slightly with use.

The results with the SPRT's used in the MAP study show that when the thermometers are shipped in a suitable protective container the calibration is retained. (The SPRT's have been shipped and received from a number of laboratories, some located as far as across the continent.) The results show also that SPRT's can be employed reliably in precise temperature measurements. When these SPRT's were heated at 450 °C or 480 °C for 4 h and calibrated at each of the laboratories (5) that participated in the MAP study and were heated again at 480 °C for 4 h at the NBS when the SPRT's were returned from each of the laboratories, the calibrations did not change by more than ±1 mK.[19] The variations in the observed values of $W$ reflect the imprecision in the calibrations superimposed upon whatever changes that have occurred in the SPRT's. The largest scatter was at the zinc point, the average of the standard deviations being $\pm 0.6$ mK. The average of the standard deviations of the observed values of $W$ of the SPRT's at the tin and oxygen points were $\pm 0.3$ mK and $\pm 0.2$ mK, respectively. These standard deviation figures for the tin and oxygen point measurements are comparable to those obtained with the check SPRT's which suggest that the treatments to which the MAP SPRT's were subjected did not significantly

[17] In these measurements the same Mueller bridge calibration was used. Neither the history of the Mueller bridge nor subsequent calibrations indicate that the drift of the bridge was responsible for the drift shown in fig. 22.

[18] A SPRT is usually broken before instabilities resulting from grain growth or other defects cause it to be "retired."

[19] The SPRT's were "annealed" at 480 °C before they were calibrated. The reproducibility of the measurements at the fixed points may have been less if the SPRT's had not been annealed.

affect the thermometers anymore than if the SPRT's had remained at the NBS laboratory and been used. On the other hand, the standard deviation figure obtained on the MAP SPRT's at the zinc point is about twice as large as that obtained with the check SPRT. The values of $W$ that were obtained at the three fixed points in the repeated calibrations of a SPRT were similar to those obtained with the MAP SPRT's. Further work is needed to determine the source of larger imprecision at the zinc point.

The PRT calibration on the IPTS–68 is based on relatively few fixed points. A small error (e.g., corresponding to 1 mK) at any of the fixed points can go undetected and cause large errors above the zinc point (see figures 18, 19, 20, 21, and 23). A fixed point near the upper limit of the PRT scale would be a sensitive means of detecting calibration errors at the tin or the zinc point; or if the PRT is to be used primarily at the higher temperatures, the freezing point of antimony (630.755 °C) or the freezing point of aluminum (660.46 °C) could be included in the calibration [20]. Measurements at the freezing point of cadmium (321.108 °C) could also serve to check the IPTS–68 calibration. Below 0 °C the triple point of xenon (−112 °C) could perhaps be developed for checking the calibration. The comparison calibration of test PRT's in terms of two or three reference standard PRT's, which are periodically "checked" on the IPTS–68, can yield many calibration points that can be analyzed by a least squares method so that the contribution from an error in any one observation would be negligible. Investigations are in progress to improve the calibration accuracy of PRT's.

## 9. References


[1] The International Practical Temperature Scale of 1968. Adopted by the Comité International des Poids et Mesures, Metrologia **5** (No. 2), 35–44 (April 1969).

[2] The International Practical Temperature Scale of 1968 (Amended Edition of 1975), Metrologia, **12,** 7–17 (1976).

[3] The notations employed in the IPTS–68 document have been abbreviated as follows:
$T = T_{68}$
$W(T) = W(T_{68})$
$\Delta W(T) = \Delta W(T_{68})$
$W^*(T) = W_{CCT-68}(T_{68})$
$t = t_{68}$
The other notations have been retained.

[4] Furukawa, G. T., Riddle, J. L., and Bigge, W. R., The International Practical Temperature Scale of 1968 in the region 13.81 K to 90.188 K as maintained at the National Bureau of Standards, J. Res. Nat. Bur. Stand. (U.S.) **77A** (Phys. and Chem.), No. 3, 209–332 (May–June 1973).

[5] Unpublished measurements of the U.S. National Bureau of Standards Platinum Resistance Thermometry Laboratory.

[6] McLaren, E. H., and Murdock, E. G., Radiation effects in precision resistance thermometry. II. Illumination Effect on temperature measurement in water triple-point cells packed in crushed ice, Can. J. Physics **44,** 2653–2659 (1966).

[7] Stimson, H. F., The International Temperature Scale of 1948, J. Res. Nat. Bur. Stand. (U.S.) **42,** 209–217 (1948) RP 1962.

[8] Stimson, H. F., International Practical Temperature Scale of 1948. Text revision of 1960, J. Res. Nat. Bur. Stand. (U.S.), **65A** (Phys. and Chem.), No. 3, 139–145 (May–June 1961).

[9] Powell, R. L., National Bureau of Standards, private communication, May 31, 1966.

[10] Nesmeyanov, A. N., Vapor Pressure of the Elements (Academic Press, Inc., New York, N.Y., 1963).

[11] Furukawa, G. T., Riddle, J. L., and Bigge, W. R., Investigation of freezing temperatures of National Bureau of Standards tin standards, in Temperature, Its Measurement and Control in Science and Industry, Vol. 4, Part 1, 247–263 (Instrument Society of America, Pittsburgh, Pa., 1972).

[12] Riddle, J. L., Furukawa, G. T., and Plumb, H. H., Platinum resistance thermometry, Nat. Bur. Stand. (U.S.), Monogr. 126, 129 pages (April 1973).

[13] Powell, R. L., private communication, November 22, 1968.

[14] Connolly, J. J., and McAllan, J. V., The tin-iron eutectic, Acta Met., **23,** 1209–1214 (1975).

[15] McLaren, E. H., The freezing points of high purity metals as precision temperature standards. II. An investigation of the freezing temperatures of zinc, cadmium, and tin, Can. J. Phys. **35,** 1086–1106 (1957).

[16] Mueller, E. F., and Wenner, F., The Waidner-Wolff and other adjustable electrical-resistance elements, J. Res. Nat. Bur. Stand. (U.S.) **15,** 477–492 (1935) RP842.

[17] Berry, R. J., Oxygen-activated thermal cycling effects in Pt resistance thermometers, Metrologia **10,** 145–154 (1974).

[18] Berry, R. J., The influence of crystal defects in platinum on platinum resistance thermometry, in Temperature, Its Measurement and Control in Science and Industry, Vol. **4,** Part 2, 937–949 (Instrument Society of America, Pittsburgh, Pa., 1972).

[19] Berry, R. J., Control of oxygen-activated cycling effects in platinum resistance thermometers, in Temperature Measurement 1975, edited by B. F. Billing and T. J. Quinn, Institute of Physics Conference Series No. 26, pp. 99–106 (The Institute of Physics, London, 1975).

[20] Furukawa, G. T., Bigge, W. R., Riddle, J. L., and Reilly, M. L., The Freezing Point of Aluminum as a Temperature Standard, in Temperature Measurement 1975, edited by Billing, B. F., and Quinn, T. J., The Institute of Physics Conference Series No. 26 pp. 389–397 (The Institute of Physics, London, 1975).


(Paper 80A3–899)

JOURNAL OF RESEARCH of the National Bureau of Standards – A. Physics and Chemistry
Vol. 80A, No. 3, May–June 1976

# Vapor Pressure of Water at Its Triple Point

**L. A. Guildner, D. P. Johnson, and F. E. Jones**

**Institute for Basic Standards, National Bureau of Standards, Washington, D.C. 20234**

**(January 26, 1976)**

The vapor pressure of water at its triple point was measured with exceptionally high accuracy by realizing it with a special apparatus and measuring the pressure with the NBS precision mercury manometer. The vapor pressure apparatus had a system for circulating the liquid water. Actual triple point conditions were established with a thin sheet of freshly distilled liquid flowing down over an exposed mantle of ice frozen on a vertical well. This technique reduced non-volatile contaminants and the vapor was repeatedly pumped to remove accumulated volatile contaminants. A diaphragm pressure transducer was used to separate the water vapor from the helium used to transmit the pressure to the manometer. The value found for the vapor pressure of water at its triple point was 611.657 Pa with an uncertainty of ± 0.010 Pa from random errors, computed at 99 percent confidence limits. The systematic errors are estimated to be insignificant relative to the random errors.

Key words: Precision mercury manometer; triple point of water; vapor pressure of water.

## 1. Introduction

Water is the stuff of life – the working medium for power generation – the great highway of commerce – the determining factor in the weather. It has such importance to mankind that probably no other single compound has received more attention from the scientific world. Its properties have been measured and remeasured; thermodynamic tables have been constructed and repeatedly revised, and further work of this type is even now commanding worldwide attention. In part, this kind of activity continues because water is not an easy substance to deal with. It is almost a universal solvent, often reacts with the materials of an experiment, and is susceptible to significant changes in its isotopic composition. Consequently, high accuracy in the measurement of many of the properties of water is hard to achieve, and more effort is needed to extend or improve our knowledge of them.

It is our purpose to measure with the highest possible accuracy the vapor pressure of water for $-5\,°C < t_{68} < 100\,°C$. We chose to concentrate initially on the vapor pressure of the triple point, which was known with poor accuracy. Although a "triple point" is a precise designation for a phase diagram, it is not likely to be an actual point in its physical realization. Thermodynamically, a triple point is a system containing matter in three phases with each component in equilibrium throughout the system, i.e., the chemical potential of each component is the same in every phase. If all three phases should happen to be in contact simultaneously (which is not a requirement of the definition), the contact will be along a line producing a closed curve, reducing to a point only in the limit. Furthermore, there are several triple points of water. We shall use the unqualified expression, however, to denote the equality of the chemical potential of pure water in a system containing the three phases: ice I, liquid and vapor. This is the only triple point of water involving the 3 states of matter and the one of most importance. Not only is it the terminus of the ice I-vapor pressure curve and the beginning of the equilibrium liquid-vapor pressure curve,[1] but also its temperature, which can be expected to be invariant by the phase rule, has been assigned a value that, in principle, establishes all thermodynamic temperatures. This unique situation makes a highly accurate value of its vapor pressure, which is also invariant, especially interesting, because it can provide the foundation for exceptionally accurate thermodynamic calculations for water. This is true for this temperature region in particular because thermodynamic temperatures are inherently known with their highest accuracy in the region of the defining value.

Most values reported for the vapor pressure of the triple point have been derived by interpolation or extrapolation of measurements of the two-phase equilibria between the liquid and vapor as a function

[1] Also it is the terminus of the ice I-liquid curve, but this is of no interest for vapor pressure measurements.



206-267 OL - 76 - 9

of temperature. The most significant of these are the values of Thiesen and Scheel, 610.90 Pa [1],[2] Scheel and Heuse, 610.90 Pa [2] and 610.55 Pa [3] and of Douslin, 612.1 Pa [4]. The average of the earlier results fitted along with data over a large temperature range is perhaps best represented, in the sense of a consensus, by the accepted value of the triple point in present day steam tables, viz., 611.2 Pa.

For equal accuracy of pressure measurements, those workers who actually realized the triple point probably attained greater accuracy in the measured vapor pressure. There are only two papers reporting such measurements:

1. The values of Prytz, published in 1931 [5], had an average of 4.5867 mm of Hg pressure, or 611.51 Pa.[3] He realized the triple point statically, i.e., an incomplete layer of ice was formed on the surface of a quiescent pool of water. The pressure was measured by a mercury manometer using interference techniques to locate the menisci with 0.5 $\mu$m Hg (0.065 Pa) imprecision, but the values of the vapor pressure varied by as much as 1.7 $\mu$m Hg (0.22 Pa). Prytz was of the opinion that the average value was about 2 $\mu$m Hg (0.26 Pa) too high.

2. L. Besley and G. Bottomley published two values, 611.29 Pa obtained from direct measurement and 611.11 Pa derived by interpolation [6]. A special mercury manometer was used for the pressure measurements, with the height of the mercury column determined cathetometrically. The vapor pressure cell was connected directly with the manometer, as was also the case in the measurements by Prytz. Considerable effort was made to eliminate dissolved air in the filling of the cell. It was operated statically, being carefully thermostated to realize the 3-phase equilibrium at the surface of the liquid. The total uncertainty of either value was not given. The value derived from direct measurements was based on 148 determinations which varied between 4.579 and 4.590 Torr, and one might thereby regard the variation of $\pm$5.5 m Torr as equivalent to the imprecision at the 99.4 percent confidence level. The residual standard deviation for the polynomial, from which the interpolated value (4.5837 Torr) was derived, was 1.7 m Torr. The two imprecisions are not inconsistent, insofar as three residual standard deviations would approximate the imprecision of the interpolated value at the 99+ percent confidence level, except that in addition the uncertainty would be greater because the triple point was near the lower extreme of the range of the fit.

Our own method also realized the triple point, but in a dynamic system. Liquid water is distilled onto a mantle of ice and falls into a well to be pumped back to the still. This method helps to continuously reduce the concentration of dissolved gases which come out of solution in the still and in the pressure cell and are pumped off periodically. Since the evaporation from the still is quiescent, nonvolatile impurities are retained in the boiler. To maintain the purity of the water vapor in the triple point cell, and of the helium in the manometer line, the vapor pressure system is separated from the manometer line by a diaphragm pressure transducer.

## 2. Equipment

Improved accuracy of the measurements of the vapor pressure of water at the triple point can only be attained by:

(1) Making more accurate pressure measurements.
(2) Realizing the triple point better.
(3) Improving the purity of the water, especially with regard to gases in solution.

The measurements were undertaken in the NBS Gas Thermometry Laboratory because the first problem

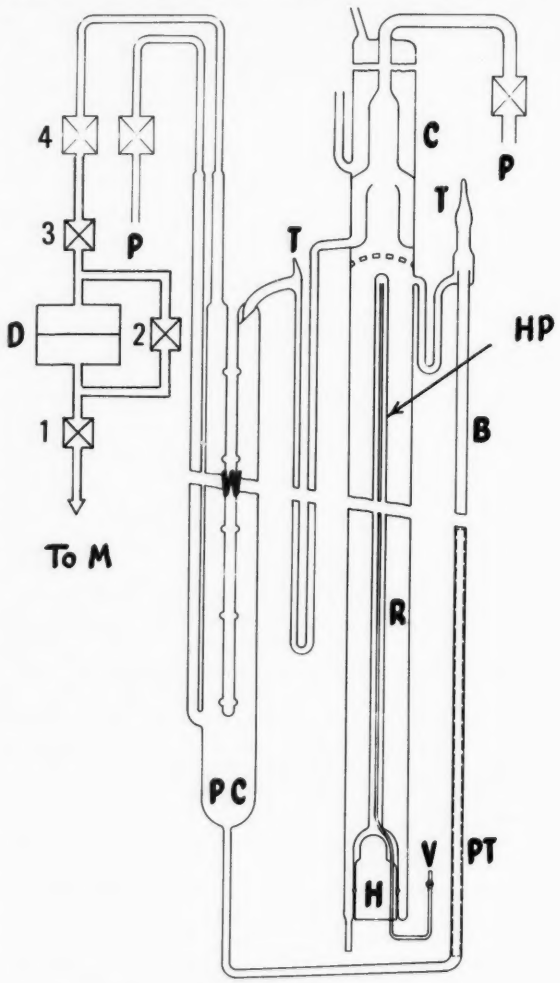


FIGURE 1. *Schematic of equipment.*

[2] Figures in brackets indicate the literature reference at the end of this paper.
[3] Based on the equivalence of 760 mm Hg= 101325 Pa.

was essentially solved by using the NBS precision mercury manometer to measure the pressure. The second and third problems were dealt with by the construction of an elaboration of the triple point cell, and by the use of a metal diaphragm pressure transducer. The arrangement of the equipment is shown schematically in figure 1, where M is the manometer, D is the diaphragm, and the remainder is the valving and the triple point cell. We shall discuss the equipment in terms of these three main elements.

### 2.1. The Manometer

The principles and many of the details of the NBS precision mercury manometer are given in an earlier paper [7]. Essentially it is a W-tube manometer, with the locations of the crowns of very large menisci precisely reproduced by the use of capacitance measurements, and with the height of the mercury column accurately measured by end length standards (gage blocks). The instrumentation of the manometer was designed so that a null signal on a capacitance bridge was observed when the gas pressure in the lower cells balanced the pressure from the mercury column plus the vapor pressure of the mercury in the upper cell. The maintenance of the pressure was made automatic by using the output of the bridge to control a heater in a large ballast (a "thermal injector") so as to restore the pressure.

The pressure to be measured is between 611 and 612 Pa, corresponding to a height of the mercury column close to 4.6 mm. We bought a chromium carbide gage block of that length in the highest quality offered. It was carefully calibrated by J. S. Beers, Deputy Chief for Length in the Dimensional Technology Section. In figure 2 the interference pattern of this block indicates very good flatness and parallelism, with one corner slightly low relative to the gaging point. These properties make meaningful the high precision of the calibration measurement, which had an estimated standard deviation of the mean of $2.6 \times 10^{-6}$ mm. This includes the variability due to wringing.

Because it is impracticable to obtain a gage block of exactly the correct length (particularly in advance of knowing its value) some modification in our usual method of measuring pressure was necessary to provide continuity over the interval between gage block lengths. There is too much uncertainty introduced by measuring an appreciable pressure difference directly by the diaphragm gage. However, the characteristics of the manometer cells are well known, so that an accurately known change of capacitance can be accurately related to a change of meniscus height. The bridge is balanced at "zero level" by adjustment of $C_{Var}$, a 3-lead General Radio variable capacitor, Type 1422–CE,[4] used in the range 0.005 to 0.11 pF, as shown

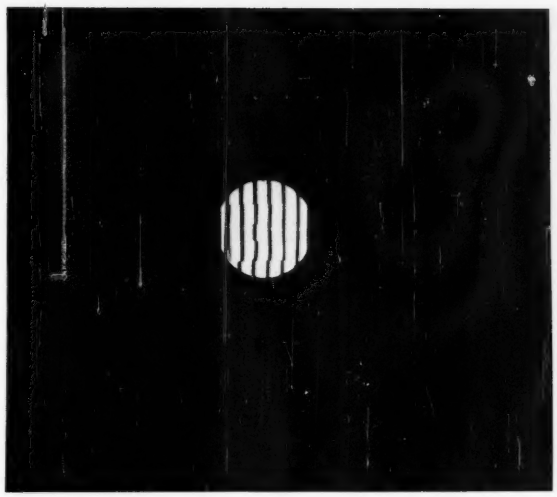

FIGURE 2. *Interference pattern of gage block.*

One fringe equals about 0.25 μm.

in figure 3e. This capacitor has an imprecision of 0.0001 pF and was calibrated at the values used with an uncertainty of the reference estimated at ±0.00003 pF. The uncertainties in the effective areas of the capacitance plates (±0.03% at 99% confidence) limit the attainable accuracy in calculating the change of meniscus height from a change of $C_{Var}$. However, so long as the height of the mercury column differs from the gage block length by no more than 17 μm, the contribution to the error in the measured vapor pressure from this cause will not exceed 1 ppm.

### 2.2. Modified Triple Point Cell

The vapor pressure apparatus, shown in figure 1, provided for circulation of the water. It was pumped from the pressure cell, PC, by a bubble pump, B into a reservoir, R. The reservoir was part of a still with a heater, H, to evaporate water into a condenser, C. The condenser water reentered PC at the top through a trap. The cell was 38 cm deep, with a volume of about 500 $cm^3$. A thermometer well, W, 32 cm deep, was a close fit on the 7 mm diameter case of a platinum resistance thermometer. Seven bulges, 20 mm across, supported the ice mantle when the water was pumped out of the cell. The bubble pump was a vertical tube of 5 mm bore with a piece of perforated PTFE (polytetrafluoroethylene), *PT*, inserted in the lower half. A 50-watt strip heater was taped to the tube and thermally insulated from the bath. The reservoir was 50 mm in diameter and had a volume of about 700 $cm^3$. It had a reentrant tube HP, which extended to the top of the boiler. The tube contained $C_2Cl_3F_3$ and functioned as a heat pipe, transferring heat from the heater, H, to the water surface. It was filled through the valve, V. There were three tubulations: one from the top of the cell to

[4]Certain commercial materials and instruments are identified in this paper in order to adequately specify the apparatus and experimental procedure. Such identification does not imply recommendation or endorsement by the National Bureau of Standards.

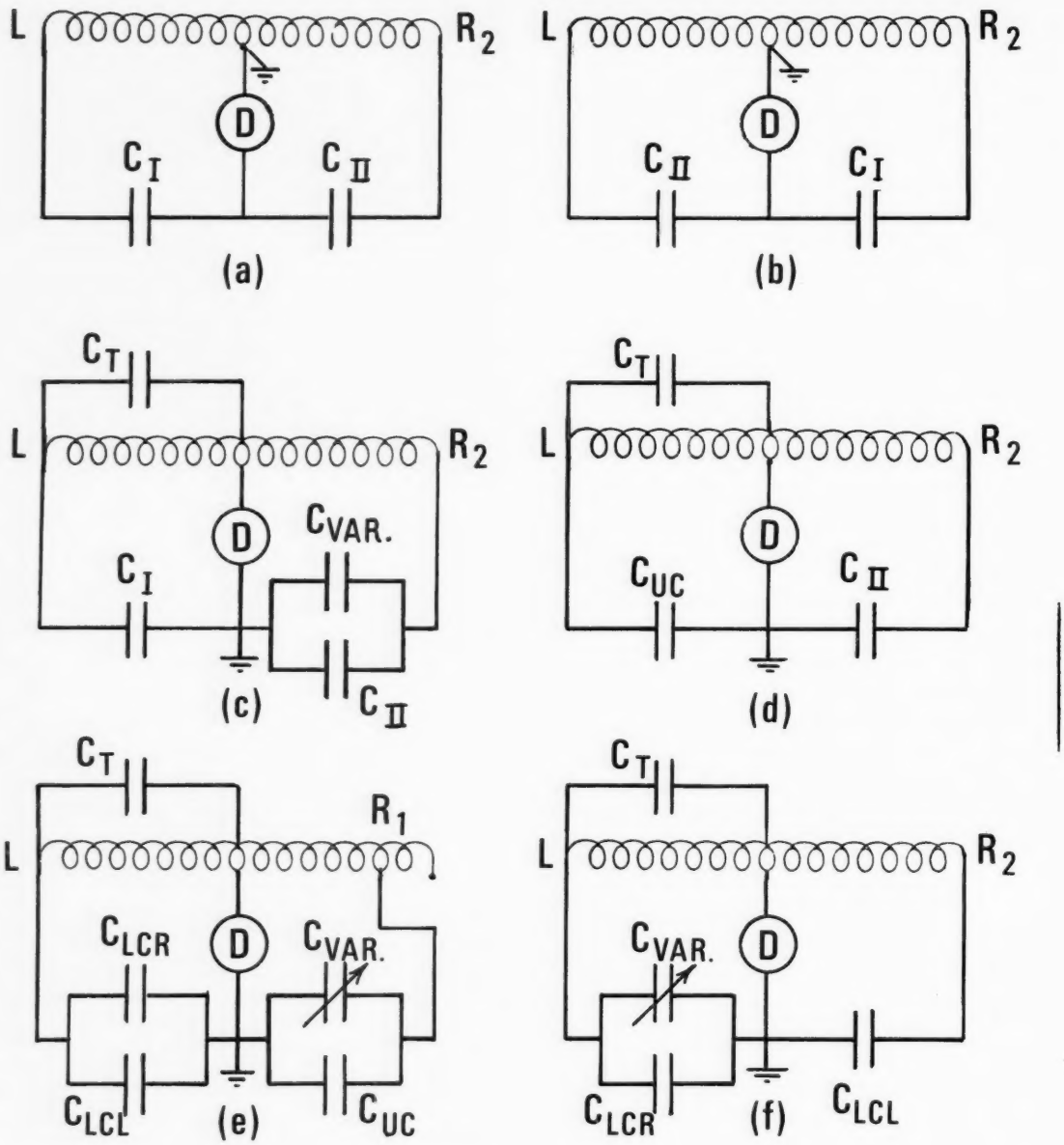


FIGURE 3. *Configurations of circuits used to measure the pressure.*

valve 4 was for the pressure measurements, and two others, *P*, one from the side of the cell and one from the condenser, were for pumping from the gas phase. The tubulations were sealed by PTFE gaskets to stainless steel high-vacuum valves at the top of the assembly.

### 2.3. Pressure Transducer

A special commercial pressure gage with a metal diaphragm, the position of which was sensed on one side by the capacitance between it and an electrode,

was used as a null device to detect equality of pressure between the water vapor on the one side and the helium gas transmitting the measured pressure on the other side. The null reading could be determined before and after measurements by opening the bypass, valve 2 in figure 1, and adequately evacuating both sides. Great care had to be taken in the use of the instrument to achieve the needed stability, both electronic and physical.

## 3. Filling of Vapor Pressure Apparatus

The vapor pressure apparatus was cleaned and filled by the same techniques used in the preparation of conventional triple-point cells. The glass was cleaned with chromic acid, rinsed, lightly etched by hydrofluoric acid, and leached by steaming. Two vapor pressure cells were filled in the course of a production run of triple point of water temperature standards, with water that was purified first by treatment with an ion exchanger and then quadruply distilled, with chemical treatment for removal of organic material between each distillation.

Samples of the purified water were taken for isotopic analysis at the time of filling and also later during operation. Up to the present, there is no measurement of the vapor pressure of the triple point of naturally occurring water for which the maximum reported variation of isotopic composition would make a significant difference. However, the high accuracy of the present measurements being reported in this paper require such a specification to avoid added uncertainty.

## 4. Procedure

The operation of the equipment consisted of preparing the manometer and the vapor pressure apparatus for measurements, determining the null of the evacuated diaphragm gage with the bypass valve open, and then, after closing the bypass valve, back filling the diaphragm with helium on the side of the capacitor electrode and with water vapor on the other. The vapor pressure apparatus was then vacuum pumped for 30 s in each of three successive 2 min periods before any actual measurements were made. We shall expand on these preliminaries and then describe the measurements themselves.

The manometer is "zeroed" with a fixed mercury-to-capacitance-plate separation in the upper cell and for the corresponding separations in the lower cells when all three mercury menisci are on the same level. Under these conditions, the "zero level" capacitance necessary to balance the capacitance bridge (see fig. 3e) is established. The measurement of a vapor pressure consists of generating and measuring in the manometer the equivalent pressure of helium, as evidenced by a zero pressure difference at the diaphragm pressure transducer. To do this, a gage block of appropriate height is inserted between the upper cell and its pedestal, and the pressure of helium in the lower cells and the volume of mercury in the manometer are adjusted until all mercury menisci are at a level relative to the capacitance plates to produce the same capacitances as for zero level. In these measurements, for the first time, we have modified this procedure in order to interpolate between the gage block values. We adjusted the manometer pressure until the diaphragm was balanced, and then we balanced the manometer capacitance bridge by adjusting $C_{Var}$.

The vapor pressure apparatus when not in use is operated in a "Standby" mode, in which the water is continuously circulated by pumping it out of the triple point cell into the still and distilling it back into the triple point cell. Occasionally, the vapor is vacuum pumped, the purpose being to remove gases released from solution, The operating parameters, and even some details of design, of this apparatus were determined by long experimentation. The heat pipe in the condenser reservoir was necessary to avoid overheating the water near the bottom of the reservoir. With the apparatus in a 0 °C thermostat and a heater power of 25 watts, the water temperature in the reservoir was about 25 °C and nearly uniform up to 1 cm below the surface. Distillation occurred at the rate of about 0.01 g/s. The bubble pump, operated with a heater input of 15 W, initially transferred a mixture of water and vapor from the full triple point cell to the reservoir at a rate of about 10 g/min, but the rate dropped as the water level dropped. When the cell was nearly empty, the pump acted as a still with a transfer rate of a few g/h.

To prepare for measurements, the apparatus was placed in a bath, thermostated by circulating liquid close to the triple point temperature and constant within 0.2 mK. The vapor pressure cell was filled by distillation from the condenser (operated at 20 W this required about 24 h). Bath fluid was circulated through the condenser, and was pumped over the top of the cell and also onto the stem of a platinum resistance thermometer inserted into the well of the vapor pressure cell. (When water was being pumped out of the cell, a zone at the top of the reservoir was cooled by pumping bath fluid over it also).

The apparatus was removed from the bath and a mantle of ice was frozen around the thermometer well using powdered solid $CO_2$ as the coolant. The completed mantle was from 5 mm to 10 mm thick.

The apparatus was then returned to the bath, which was regulated at a temperature not more than 1 mK below the triple point temperature and the bubble pump was started. By the next morning, the cell was nearly empty whereupon the reservoir heater was turned on. It distilled water into the pressure cell at about 0.01 g/s (with the bubble pump left on, measurements could be conducted for several hours before enough water accumulated in the cell to touch the ice mantle).

In the meantime, both sides of the diaphragm gage had been evacuated overnight with an ion pump. A "zero" reading was obtained with the gage isolated and

the bypass valve open. Then the bypass valve was closed, the electrode side of the diaphragm cell was filled with helium, and the other with water vapor (with the differential pressure across the gage kept within ±1 mm Hg). Finally, adjustments of the manometer variable capacitor were made in order to balance its bridge when the manometer pressure was such that the reading on the diaphragm gage was very near the "zero" value.

Next, to sweep out gaseous impurities, the water vapor was pumped from the pressure cell, at a rate of approximately 100 $cm^3/s$ (0.6 $cm^3$ S.T.P./s). When the apparatus was in regular use, an initial set of three pumpings, each pumping lasting 30 s over a period of 6 min was sufficient to insure no effect after recovery to a steady state would be observed with further pumping.

Chart records were made of the diaphragm gage output for its zero, and immediately following the last pumpout, readings of the output of the diaphragm gage were recorded. Because the stirring of the thermostat had to be stopped to avoid shaking the diaphragm, the recordings were made for 20 s periods every two minutes. After each set of 3 recordings, the water vapor was again pumped for 30 s. After 4 such sets, the apparatus was closed off, the diaphragm bypass valve opened, and the diaphragm pumped out for 20 min when a new "zero" was recorded. During each measurement, the temperature of the diaphragm was sensed by reading the e.m.f. of a copper-constantan thermocouple referred to ice.

## 5. Measurements

Besides general experimentation to establish effective operating techniques, there were three periods of several weeks during which actual pressure determinations were made. The first period was purely instructive and resulted in vigorous efforts to improve various aspects of the equipment, in particular the diaphragm gage. The results of the second period reflected substantial improvement in the accuracy of the measurements, and were reported at the 1974 meeting of the International Association for the Properties of Steam in Giens, France [8]. The results of the third period are decidedly more accurate than the second, more because of further improvement in the diaphragm gage than anything else. However, numerous possible effects were investigated in addition, and these results will be described here before presenting the final sets of measurements.

Three standard calibrated platinum resistance thermometers were used to measure temperature, one in the well of the vapor pressure cell, the second to measure the temperature of the thermostat bath close to the vapor pressure cell, and the third as a regulator sensor. They were calibrated in a triple point of water cell each day; it is believed the values of the measured temberatures were uncertain by no more than 30 $\mu$K. The temperature registered by the thermometer in the well of the vapor pressure cell could be used as an indication of the state of the mantle. When the ice mantle was dry or nearly so, pumping resulted in a rapid reduction in the pressure, by about 100 Pa, and in the temperature, by about 0.1 K. When an adequate flow of water was maintained over the ice during pumpout, the drop in pressure was no more than 0.5 Pa and in temperature no more than 0.1 mK.

It has also been observed during a run earlier than any being reported that when air in an amount > 100 mm Hg in pressure had entered the cell, the temperature at the mantle was depressed by several tenths of a mK and did not recover fully before a new mantle was frozen.

The effects on the observed vapor pressure resulting from variation of the bath temperature from the temperature of the triple point were studied. For temperatures in the range from 1 mK below the temperature of the triple point to 200 mK above it, scarcely any variation of the vapor pressure was observed. This indicated that the temperature surrounding the apparatus was not very critical, and furthermore, there was probably no undesirable effect from the warmer parts of the tubulations which extended out of the bath. In the final measurements, the bath was thermostated at, or not more than 1 mK above, the temperature of the triple point of water.

The diaphragm unit itself was not thermostated, but was thermally lagged with a thick layer of insulation. Its temperature was measured at frequent intervals, and in its final physical and electronic configuration, a consistent relationship between the copper-constantan e.m.f.'s and the zero readings existed. A straight line was fitted to the data by the method of least squares with the result that the zero can be calculated from the e.m.f. by the following equation: $y = 893.627 - 0.748503\ V$ where $y$ is the chart reading for the diaphragm zero and V is the thermocouple e.m.f. in $\mu$V. The residual standard deviation was 1 chart division, and the standard deviation of a predicted point was about 0.5 chart division. This equation was used to calculate the chart zero pertinent to any given chart pressure reading, from thermocouple e.m.f.'s observed at the same time.

No effect dependent on refreezing the mantle was observed, and in fact, so long as crystals of ice remained, it appeared that the pressure was established, except for the change in the "pressure head", i.e., the pressure due to the weight of the column of vapor above the effective location of the line at which triple-point conditions exist.[5]

The values given in this paper were measured on four successive days and consist of the following five "sets":

1. Set 1: Ten values of diaphragm gage readings in 3 groups, with zeroes before and after the readings.

[5] The calculated variation of the temperature of the ice mantle over its length because of the fluid head was less than 1 $\mu$K.

2. Set 2: Nine values of diaphragm gage readings in 3 groups, with zeroes before and after the readings.
3. Set 3: Eight values of diaphragm gage readings in 3 groups, with zeroes before and after the readings.
4. Set 4: Twelve values of diaphragm gage readings in 4 groups, with zeroes before and after the readings.
5. Set 5: Twenty-five values of diaphragm gage readings in 8 groups, with zeroes before and after each 4 groups.

A group comprises the values measured between pumpouts. After the initial three 30 s pumpouts, the apparatus was pumped about every 10 min. At the conclusion of all the measurements, the value of the capacitance to balance the capacitance bridge for the manometer at zero level was redetermined.

## 6. Equations and Calculations

Because of the effect of the pressure head, there is only a surface, a horizontal plane except for temperature perturbations, at which the triple point pressure can exist. The pressure of the water vapor at the line formed by the intersection of the surface with the mantle is given by the following:

$$P_{tp} = P_{\text{Man}} + \delta P_{\text{Wring}} + \delta P_{\text{CVar}} + \delta P_{\text{Thermp}} + \delta P_{\text{Dia}} + \delta P_{\text{Vap Hd}}.$$

$P_{\text{Man}}$ is given by eq (27) of ref. [7], with temperatures for zero level equal to 20 °C and for helium filling gas. The vapor pressure of mercury and its temperature derivative have been reevaluated at 20 °C as 0.171 Pa and 0.0147 Pa $K^{-1}$, respectively, and the density at zero pressure is evaluated for $t_{68} = 20$ °C (rather than $t_{48}$), as 13,545.82 $Kg/m^3$ [9]. Symbolically,

$$P_{\text{Man}} = -\alpha\rho g\,(h_{\text{UC}}\,\delta t_{\text{UC}} - \bar{h}_{\text{LC}}\delta\bar{t}_{\text{LC}}) + \left(\frac{dP}{dT}\right)_{\text{Hg Vap}}(\delta t_{\text{UC}} - 20) + \rho g h_2\,(1 - \alpha\,[\delta t_{\text{Hg}}]) + P_{20}\,(\text{Hg}) + \rho g h_2\,(2.27 \times 10^{-6}\,h_2 - 2.5 \times 10^{-7} - 4.07 \times 10^{-3}\,M h_0),$$

where $\alpha$ is $\frac{1}{V}\left(\frac{\partial V}{\partial t}\right)_p$ for mercury, $\rho$ is the density of mercury under zero pressure at 20 °C, $g$ is the acceleration due to gravity, the $\delta t$'s are differences of temperature from 20 °C of the upper cell (UC), the average of the lower cells (LC), and the mercury arm (Hg). The height of mercury in all the cells is substantially the same and is symbolized by $h_{\text{UC}}$ for the upper cell or by $\bar{h}_{\text{LC}}$ as the average for the lower cells. The height of the mercury column is $h_2$, and the pressure head is produced by the height of the gas column between the menisci of the lower cells and the center of the diaphragm (which was mounted vertically), designated $h_0$. The pressure head depends upon the molecular weight M. The numbers are consistent for values of the symbolic quantities in S.I.

"Manometer readings," comprising the observations of the resistance of a capsule platinum resistance thermometer located in a thermocouple reference block and the e.m.f.'s of all 4 sets of differential thermocouples for the upper cell, the mercury arm, the left lower cell and the right lower cell, were made once or twice for each set of vapor pressure measurements. The temperatures of the vertical components of the mercury lines were calculated from the thermocouple e.m.f.'s as a difference from the temperature of the reference block. There were twelve copper-constantan thermocouples in series fastened to the upper cell, twenty-five to the mercury arm, ten to the left lower cell and twelve to the right lower cell. The observed e.m.f.'s were converted to temperature differences by a "handbook" sensitivity of 40.5 $\mu$V $°C^{-1}$, per junction at 20 °C, viz., 486, 1013, 405 and 486 $\mu$V $°C^{-1}$, respectively. The platinum resistance thermometer qualified as a standard instrument for the IPTS, with a reading in the triple point cell of $R_{\text{PRT}}/R_{\text{Std}} = 0.25557275$, and calibrated values of

$$A = 3.9855387 \times 10^{-3}\ °C^{-1}$$

and

$$B = -5.8755669 \times 10^{-7}\ °C^{-2}.$$

The values of temperatures were calculated by the program BRIDGE, given in appendix I. The following results (table 1) were obtained when the experimental data were calculated by the program PRSURE, given in appendix II.

The manometer zero was established from 10 determinations made over a period of 10 days. The values

TABLE 1. *Manometer pressure at the diaphragm on the manometer side*

| Set | *PRT* Capsule (Ω) | $t_{\text{cap}}$ °C | Thermocouples | | | | $P_{\text{Man}}$ (Pa) |
|---|---|---|---|---|---|---|---|
| | | | U (μV) | M (μV) | L (μV) | R (μV) | |
| 1 | 27.582052 | 19.9389 | −3 | 21 | 4 | −2 | 610.84306 |
| 2 | 27.582119 | 19.9395 | −6 | 23 | 3 | −4 | 610.84504 |
| 3 | 27.582445 | 19.9428 | −5 | 25 | 5 | −3 | 610.84572 |
| 4 | 27.583308 | 19.9513 | −6 | 24 | 4 | −5 | 610.84403 |
| 5 | 27.583481 | 19.9530 | −8 | 21 | 4 | −6 | 610.84662 |

were adjusted to that which would have been observed if all parts of the manometer were at a uniform temperature of 20 °C. The equation is derived from eq (27) of ref. 7, and as programmed in Basic is given in appendix III. The results in Pa were converted to nm of Hg and in turn the value of the variable capacitor was adjusted on the basis that a change of 1 nm is equivalent to $1 \times 10^{-5}$ pF. The values measured and the calculated results were as follows (see table 2):

TABLE 2. *Observations of manometer zero*

| Date | PRT Capsule (Ω) | $V_{UC}$ (μV) | $V_{LCL}$ (μV) | $V_{LCR}$ (μV) | $C_{Var}$ (pF) | Calc $P$ (Pa) | Corr (nm) | Corr $C_{Var}$ (pF) |
|---|---|---|---|---|---|---|---|---|
| 11/27 | | | | | | | | |
| 11:21 | 27.583362 | −16 | −5 | −21 | 0.02323 | $4.04 \times 10^{-3}$ | +30 | 0.02353 |
| 1:45 | 27.581889 | −17 | −6 | −18 | .02362 | $7.15 \times 10^{-3}$ | +54 | .02416 |
| 2:55 | 27.581750 | −3 | 3 | −8 | .02428 | $1.29 \times 10^{-3}$ | +10 | .02438 |
| 4:15 | 27.581966 | −9 | 0 | −12 | .02409 | $4.88 \times 10^{-3}$ | +37 | .02446 |
| 5:17 | 27.581802 | −14 | −3 | −16 | .02391 | $6.83 \times 10^{-3}$ | +51 | .02442 |
| 12/3 | | | | | | | | |
| 10:10 | 27.593201 | −17 | −6 | −24 | .02356 | $2.24 \times 10^{-3}$ | +17 | .02373 |
| 2:03 | 27.591870 | −18 | −6 | −21 | .02357 | $6.33 \times 10^{-3}$ | +48 | .02405 |
| 12/4 | | | | | | | | |
| 9:25 | 27.587772 | −17 | −5 | −20 | .02343 | $6.49 \times 10^{-3}$ | +49 | .02392 |
| 12/5 | | | | | | | | |
| 9:50 | 27.584449 | −17 | −5 | −19 | .02346 | $7.31 \times 10^{-3}$ | +55 | .02401 |
| 12/6 | | | | | | | | |
| 11:41 | 27.582260 | −15 | −5 | −18 | .02333 | $4.87 \times 10^{-3}$ | +37 | .02370 |
| | | | | | | | | Ave 0.02404 |
| | | | | | | | | Calib. Corr + 0.00031 |
| | | | | | | | | Net 0.02435 |

The estimate of the standard deviation of the mean is $S = 0.00012$ pF.

$\delta P_{Wring}$ is the net correction for imperfectly joined gaging surfaces between the wringing boss on the bottom of each cell and the pedestal or the gage block. The leak rate through the gap formed when two gaging surfaces meet on one edge with a dihedral angle $\phi$ (in $\mu$ rad) was studied [10] and is given for the particular blocks and volume of vacuum system as

$$dp/dt = 0.42\,\phi^2 + 0.022\,\phi^3\ \mu\text{m Hg/min.}$$

The vacuum leak rates were measured, both during the determination of zero level and several times during the course of the vapor pressure measurements. The gaging surfaces are square, of a width $W = 2.41$ cm on a side. The change in height between the measurement of zero level and the pressure measurement was then

$$\delta h = [\phi(\text{UC}) - \phi_0(\text{UC}) - \{\phi(\text{LCL}) + \phi(\text{LCR}) - \phi_0(\text{LCL}) - \phi_0(\text{LCR})\}/2] \times W/2$$

and, with $\delta h$ in nm, the pressure effect in pascals is

$$\delta P_{Wring} = \delta h \text{ x } 1.32763 \text{ x } 10^{-4} \text{ Pa.}$$

The leak rates were measured for each cell separately. It was calculated that the volume of each cell plus thermocouple gage is related to the total volume from which the original equation was derived as

$$V_{LCL}/V_{Tot} = 0.579$$

$$V_{LCR}/V_{Tot} = 0.620$$

$$V_{UC}/V_{Tot} = 0.523.$$

The rates were remeasured after every adjustment of any cell position. The net pressure effect is given in the following:

TABLE 3. *Pressure effect from imperfect gaging joints*

| Set | $dp/dt$ (μm Hg/min) | | | $\delta P_{Wring}$ |
|---|---|---|---|---|
| | LCL | LCR | UC | (Pa) |
| Zero Level | 15 | 39 | 5 | |
| 1, 2 and 3 | 16 | 43 | 23 | 0.00373 |
| 4 and 5 | 16 | 40 | 22 | 0.00357 |

$\delta P_{CVar}$ is derived from the change of mercury level requiring a change of the variable capacitor to maintain the manometer bridge balance. The change of level can be accurately determined because of the coaxial switching arrangement that is part of the manometer instrumentation. The configurations used are shown in figure 3. The manometer transformer has two taps on the right-hand side, and one on the left. The tap $R_1$ has 3/4 the voltage of $L$, and $R_2$ has the same voltage as $L$. The variable capacitor may be switched to any tap.

There is also a switch which changes ground from the center tap to the other side of the detector. There are 3 standard capacitors, labeled $C_I$, $C_{II}$, and $C_{III}$. The values of $C_I$ and $C_{II}$ are $8.2046 \pm 0.0008$ pF, and are equal within 1 ppm. The value of $C_{III}$ is 3.0503 pF, so that it can be used to measure the lower cell capacitances. The capacitances of the various parts of the detection system and the manometer were found from the following sets of measurements at zero level:

TABLE 4. *Measurement scheme to determine manometer capacitance characteristics*

| Figure | Switch Pos. | Tap | Center Tap | $C_{Var}$ | Capacitance Equation |
|---|---|---|---|---|---|
| 3a | I | $R_2$ | Gnd | Out | $C_I = C_{II}$ |
| 3b | II | $R_2$ | Gnd | Out | $C_{II} = C_I$ |
| 3c | I | $R_2$ | UnGnd | 0.04313 pF | $C_T + C_I = C_{II} + C_{Var}$ |
| | | | | Corr. 0.00055 pF | $C_T = 0.04368$ pF |
| 3d | III | $R_2$ | UnGnd | Out | $C_T + C_{UC} = C_{II}$ |
| | | | | | $C_{UC} = 8.16092$ pF |
| 3e | IV | $R_1$ | UnGnd | 0.02373 pF | $C_T + \Sigma C_{LC} = 3/4\ (C_{UC} + C_{Var})$ |
| | | | | Corr. + 0.00006 pF | $\Sigma C_{LC} = 6.13853$ pF $- 0.04368$ pF |
| | | | | .02379 pF | $\Sigma C_{LC} = 6.09485$ pF |
| 3f | VI | $R_2$ | UnGnd | 0.01215 pF | $C_T + C_{LCR} + C_{Var} = C_{LCL}$ |
| | | | | Corr. + .00012 pF | |
| | | | | 0.01227 pF | $C_{LCR} = C_{LCL} - 0.05595$ pF |
| | | | | | $C_{LCL} = 3.07540$ pF |
| | | | | | $C_{LCR} = 3.01945$ pF |

The mercury cell capacitors comprised guarded circular plates facing a grounded surface that was essentially infinite. The capacitance can then be expressed as $C = 1.11267\ A/(4\ \pi\ S)$ pF, where A is the effective area of the plate (in cm$^2$), and S is the separation between the plate and the mercury (in cm). The dimensions of the cells are accurately known; the following separations at zero level can then be calculated (table 5):

TABLE 5. *Characteristics of manometer cells*

| Cell | Cap.[a] (pF) | Eff. Diam. (cm) | $S_0$ ($\mu$m) |
|---|---|---|---|
| UC | 8.16092 | 3.07838 | 807.517 |
| LCL | 3.07540 | 1.88488 | 803.364 |
| LCR | 3.01945 | 1.88509 | 818.432 |

[a] The number of digits is consistent with the imprecision. The total uncertainty is nearly 1 part in $10^4$, but the net changes are known within 3 ppm of the total figure.

In operation, the mercury level is maintained so that $C_{UC} = 8.16092$ pF. The value of the variable capacitor to balance the bridge at zero level, the "manometer zero," corrected for differences of mercury temperature from 20 °C, was 0.02435 pF. The vapor pressure was measured with the variable capacitor in the L arm, so that $C_T + C_{LC} + C_{Var} = 3/4\ C_{UC}$ and the change of capacitance of the lower cells from the balance at zero level is $0.75 \times 0.02435$ pF plus the reading of $C_{Var}$ for the Set. This change of capacitance corresponds to a displacement, $d$, in the separation of the mercury surfaces from the plates in the lower cells, which is

$$\Delta\Sigma C_{LR} = \frac{1.11267}{4\pi}\left[ A_{LCL}\left(\frac{1}{S_0(LCL)+d} - \frac{1}{S_0(LCL)}\right) + A_{LCR}\left(\frac{1}{S_0(LCR)+d} - \frac{1}{S_0(LCR)}\right)\right].$$

The pressure in pascals is related to the displacement in $\mu$m as

$$P_{CVar} = 0.132763 \times d \text{ Pa}.$$

The values obtained are given in table 6.

TABLE 6. *Pressure increment determined by capacitor setting*

| Set | $C_{Var}$ (pF) | $\Delta C$ (pF) | $d$ ($\mu$m) | $\delta P_{CVar}$ (Pa) |
|---|---|---|---|---|
| 1 | 0.02644 | 0.044703 | 5.9911 | 0.79532 |
| 2 and 3 | .02531 | .043573 | 5.8380 | .77507 |
| 4 and 5 | .025306 | .043569 | 5.8376 | .77502 |

$\delta P_{\text{Thermp}}$, the effect of thermomolecular pressure, is expected to be significant only in the pressure transmitting tube of the manometer. This tube, which is 0.1512 cm in radius, ran from the manometer vault, at a temperature very close to 20 °C, to the valves that were physically adjacent to, and assumed to be at the temperature of, the diaphragm unit.

The value of the effect was derived from the equation of Weber, Keesom and Schmidt [11] (the program in Basic for their equation is given in appendix IV). We measured the thermomolecular pressure difference of helium in a tube of 0.0412 cm radius and found the values to be less than the values from Weber's equation by a factor of 0.76. The functional relationship in the Weber equation for the radius of the tube, i.e., that $p\Delta p \propto 1/r^2$, is assumed to be correct. The difference between theory and experiment is thought to occur because of the inadequacy of other assumptions. Therefore, the same factor of 0.76 was used in the calculation because it should still be applicable for the larger tube. (See table 7.)

TABLE 7. *Thermomolecular pressure correction*

| Set | $t_{ave}$ (°C) | $\Delta p$ (Weber) (Pa) | 0.76 $\Delta p$ (Pa) |
|---|---|---|---|
| 1 | 25.05 | 0.02122 | 0.01613 |
| 2 | 25.13 | .02155 | .01638 |
| 3 | 25.13 | .02155 | .01638 |
| 4 | 25.03 | .02105 | .01600 |
| 5 | 24.82 | .02021 | .01536 |

$\delta P_{\text{DIA}}$, the pressure difference at the diaphragm, was derived from sets of charts readings. Following the stated operating procedures, we recorded the diaphragm zero and the copper-constantan thermocouple reading, then pumped three times, after which three sets of measurements, each set consisting of a thermocouple reading and a diaphragm reading for the pressure difference, were recorded. The diaphragm output was recorded for 20 s every 2 min. The thermocouple was read again while the water vapor was repumped from the vapor pressure cell. Three more thermocouple and pressure readings were taken for 20 s at 2 min intervals, and then the diaphragm was evacuated for 20 min and a diaphragm zero recorded. It was experimentally demonstrated that this period of evacuation of the diaphragm was long enough to assure reliable zero values.

Within the imprecision of the instrument, the diaphragm readings were correct on the 10 $\mu$m Hg scale, so that the chart measurements could be calibrated by the diaphragm readings. In order that the uncertainties would be small, the manometer was adjusted so that the difference of the diaphragm from zero was small. The net deflections in chart divisions in Set 1 were $-2, -2.2, -1.7, -6.6, -4.7, -1.7, -5.5, -3.7, -4.7$, and $-5.4$, for an average of $-3.82$ ($S = 1.65$). For set 2, they were $-0.2$, 0.8, $-0.8$, 0.8, 2.8, 2.5, 2.5, 2.5 and 1.5, for an average of 1.38 ($S = 1.31$). For set 3, they were 1.1, 0.1, 0.9, 1.5, 0.5, $-1.5$, $-1.2$ and $-0.8$, for an average of $-0.12$ ($S = 1.04$). For set 4 they were 1.1, 2.2, $-0.1$, $-2.1$, 1.2, $-1.7$, 2.8, 4.3, 0.3, 1.3, $-0.1$, 0.6, for an average of 0.82 ($S = 1.79$). For set 5 they were 2.5, 1, 3.4, 0, 2.5, 1.5, $-0.5$, 1.5, 1.5, $-0.5$, 2.2, 1.2, 3.1, 2.1, 0.2, $-1.8$, $-1.3$, 0.2, 1.1, 1.1, 0.6, 2.6, $-1.9$, 0.2 and 1.6, for an average of 0.89 ($S = 1.39$).

The chart calibration gave a sensitivity of 0.00536 Pa/div so that we have for the five sets (with S denoting the estimate of the standard deviation for a single measurement and $S_m$ the estimate of the standard deviation of the mean) (see table 8):

TABLE 8. *Measured pressure differences at the diaphragm*

| Set | Ave Defl (div) | $\delta P_{\text{DIA}}$ (Pa) | $S$ (div) | $S$ (Pa) | $S_m$ (div) | $S_m$ (Pa) |
|---|---|---|---|---|---|---|
| 1 | −3.82 | −0.0205 | 1.65 | 0.0089 | 0.52 | 0.0028 |
| 2 | 1.38 | .0074 | 1.31 | .0070 | .43 | .0023 |
| 3 | −0.12 | −.0006 | 1.04 | .0056 | .35 | .0019 |
| 4 | .82 | .0044 | 1.79 | .0091 | .52 | .0028 |
| 5 | .89 | .0048 | 1.39 | .0075 | .28 | .0015 |

$\delta P_{\text{VapHd}}$, the pressure head produced by the column of water vapor, is calculated from the estimated vertical distance, $h$, from the midpoint of the diaphragm to the line at the mantle where the triple point is realized. We believe this line to be near the top of the mantle, but its position is not entirely stable, both because the flow of water may vary and because the mantle melts and recedes from the top. The pressure is calculated as

$$\delta P_{\text{VapHd}} = \frac{P_{\text{Man}}\, g\, M}{RK}\left(\frac{h_1}{T_1} + \frac{h_2}{T_2}\right),$$

where $g$ is the acceleration due to gravity, $M$ is the molecular weight of the vapor, $R$ is the molar gas constant, $K$ is the conversion factor between units of pressure, $h_1$ is 0.244 m running between the diaphragm at 25 °C and the bath at 0 °C, and $h_2$ is the distance, 0.07 m, in the bath at 0 °C. Then

$$\delta P_{\text{VapHd}} = 23.31 \times 10^{-6}\, P_{\text{Man}} = 0.01424 \text{ Pa}.$$

The average temperature, $T_1$, was weighted on the high side. The value is bounded by the extremes, of course, and within those limits any reasonable choice would hardly make any significant difference in the final pressure.

## 7. Results

The results are summarized by totalling the elements of pressure for each set (all values in pascals):

TABLE 9. *Total values of the vapor pressure of water at its triple point*

| Set | $P_{Man}$ (Pa) | $\delta P_{Wring}$ (Pa) | $\delta P_{C\,Var}$ (Pa) | $\delta P_{Thermp}$ (Pa) | $\delta P_{DIA}$ (Pa) | $\delta P_{Vap\,Hd}$ (Pa) | $P_{tp}$ (Pa) |
|---|---|---|---|---|---|---|---|
| 1 | 610.84306 | 0.00373 | 0.79532 | 0.01613 | −0.0205 | 0.01424 | 611.6520 |
| 2 | 610.84504 | .00373 | .77507 | .01638 | .0074 | .01424 | 611.6619 |
| 3 | 610.84572 | .00373 | .77507 | .01638 | −.0006 | .01424 | 611.6545 |
| 4 | 610.84403 | .00357 | .77502 | .01600 | .0044 | .01424 | 611.6573 |
| 5 | 610.84662 | .00357 | .77502 | .01536 | .0048 | .01424 | 611.6596 |

The average of the 5 sets is 611.6571 Pa ($S = 3.94$ mPa). The estimate of the standard deviation of the mean is $S_m = 1.76$ mPa.

## 8. Isotopic Composition

The determination of the isotopic content of samples from the vapor pressure cell relative to SMOW (standard mean ocean water) depended upon two steps. First, the isotopic content of cell water was determined relative to NBS–1 standard water [12], the composition of which had, as a second step, been related to SMOW by the work of Craig [13]. The *D/H* absolute abundance ratio of SMOW has been determined very precisely by Hagemann, Nief and Roth as 155.5 ppm [15]. The value for the absolute abundance of $O^{18}$ in SMOW is based on Craig's measurements [13, 14] and as variously interpreted may be taken to be $O^{18}/O^{16} = 1993.4 \times 10^{-6}$ to $1995 \times 10^{-6}$, of which the latter is used here. The compositions of seven samples of the water used in the vapor pressure cell, both relative to SMOW and absolute, are as follows:

TABLE 10. *Isotopic composition of water in the vapor pressure cell*

| | Sample No. | Description | D/H % | D(ppm) | $O^{18}/O^{16}$ % | $O^{18}$(ppm) |
|---|---|---|---|---|---|---|
| | 1 | raw (tap) water | −4.0 | 149 | −0.58 | 1983 |
| 1st cell | 2 | Beginning of cell filling | −4.9 | 148 | −0.71 | 1980 |
| | 3 | End of cell filling | −5.6 | 147 | −0.88 | 1977 |
| | 4 | Beginning of cell filling | −4.6 | 148 | −0.60 | 1983 |
| | 5 | raw (tap) water | −5.5 | 147 | −0.77 | 1980 |
| 2nd cell | 6 | End of cell filling | −5.1 | 148 | −0.64 | 1982 |
| | 7 | Distilled from apparatus 2 weeks after experiment | −6.9 | 145 | | |
| Average | | | | 147 | | 1982 |

All measurements were made with the second cell. The difference between the vapor pressure of the cell water and SMOW because of the reduced compositions of D and $O^{18}$ can be calculated from measurements of Majoub [16], who reported that the ratio of $P_{HDO}/P_{H_2O}$ at 0 °C is 0.8994, and of various authors [16, 17, 18], who reported ratios of $P_{H_2O^{18}}/P_{H_2O^{16}}$ at 0 °C that average about 0.9885. The difference of pressure may then be derived from Raoult's Law, where the pressure of the liquid of the sample at 0.01 °C is 1 ppm more than the corresponding metastable SMOW. The sample triple point temperature is about 40 $\mu$K lower than the triple point of SMOW [19]. Given that $dP/dt$ is about 44.4 Pa/K for water at 0.01 °C, the effect of the difference in temperature of the triple points is about 3 ppm. Thus the vapor pressure at the triple point of the sample, which corresponds closely to the analyses of typical "continental water," can be calculated to be about 2 ppm, or 1.2 m Pa, less than the vapor pressure at the triple point of SMOW.

## 9. Discussion

It is, of course, crucial to the reliability of any data that procedures be established to eliminate or satisfactorily minimize possible errors before any final measurements are made. We believe that the probable difficulties requiring special study were (1) the possible variation of the vapor pressure because of a slow return to equilibrium following a pumpout, or with variation of ambient temperature, (2) the presence of contaminating gas in the system, and (3) the possible errors in determining the diaphragm zero. Each of these problems received special study.

As discussed in section 5, the pressure and temperature were only slightly perturbed by pumpout so long as all three phases were maintained about the mantle. Similarly, in the presence of the mantle, there was at most only a slight change in vapor pressure when the ambient temperature varied from 1 mK below to 0.2 K above the triple point. Thus the

actual realization of the triple point must have contributed great stability to the vapor pressure; the broad expanses of exposed liquid and solid phases could be expected to fulfill the physical necessities for facilitating such an equilibrium.

The procedure of pumping for three 30 s intervals prior to measurements, and subsequently for 30 s every 10 min was adopted because the measured pressure, with lesser amount or frequency of pumping, varied in a way to indicate the accumulation of measurable amounts of contaminating gases. The three recorded diaphragm pressure readings made in each interval between pumping showed no evidence of preferential drift that might indicate the rate of pressure buildup to be significant in that span of time.

An accurate measurement of the diaphragm zero depended upon the evacuation of enough of the sorbed gases (particularly water vapor) that the remainder would not exert a significant pressure difference between the two sides of the diaphragm, with the by-pass valve open. It was observed experimentally that a 20 min evacuation following pressure measurement appeared to be sufficient. These measurements together with the thermocouple e.m.f.'s observed at the same time correlated with those values of zeroes after long pumping and their concomitant thermocouple e.m.f.'s. This fact offered substantial confirmation both that 20 min was an adequate pumpout and that the diaphragm zero could be accurately associated with the thermocouple readings. However, measurements made when the room temperature varied rapidly were not in agreement with the rest of the results, and were not used. The assumption was that the thermocouple, being on the outside of the diaphragm, could not have represented the appropriate temperature when there were substantial gradients.

The reader may note that the corrections for $C_{\mathrm{Var}}$ appear to be inconsistent. This is because a different reference line for reading was used at different times.

## 10. Estimation of the Total Uncertainty

The stated total uncertainty consists of the limits, at 99 percent confidence level for the random errors; and the systematic errors, estimated conservatively enough to warrant about the same confidence level.

The estimates of the values of the errors are expressed initially as one standard deviation. It is useful to treat them in two groups: (A) Those sources of error which contribute to the imprecision calculated from table 9, and (B) those additional sources of error which have a fixed effect on the directly determined value.

The term "systematic error" can be understood, and is used by some authors, to denote any error that introduces a constant bias into the observed results. For example, this is true of each of the items of Part B. However, in all but the last entry the errors were evaluated from well-defined imprecisions, and do not differ in their nature from the imprecisions in Part A. These imprecisions are combined in a sum of the squares addition with those of Part A. In a more restricted definition, we are referring to systematic errors as those which introduce a bias into the results but which are not well enough investigated to be evaluated by statistical techniques, or are not realized to be important. The limits of a systematic error are apt to be less well-defined than for a random error, although there must be some theoretical or experimental results upon which an estimate can be based.

TABLE 11. *Sources of error*

| | (Pa) |
|---|---|
| (A) Random errors Observable in the Final Values | |
| Estimate of the standard deviation in the pressure as a result of imprecision in thermocouple e.m.f.'s | $S = 0.0020$ |
| Estimate of the standard deviation in assignment of the diaphragm zero (1/2 div.) | $S = 0.0027$ |
| Estimate of the standard deviation of the pressure head because of uncertainty in the location of the triple phase line (within 2 cm at 99% confidence) | $S = 0.0003$ |
| Estimate of the standard deviation of the pressure determination (the weighted average of the standard deviations of the diaphragm readings for the 5 sets) | $S = 0.0019$ |

The square root of the sum of the squares of this group is 0.0039 Pa and agrees with the imprecision of the results in table 9 expressed as the estimate of a standard deviation of a single measurement. The estimate of the standard deviation of the mean for 5 sets is 0.0017 Pa.

| | |
|---|---|
| (B) Random Errors and Systematic Errors Not Observed as Imprecision in the Results | |
| Estimate of the standard deviation of the mean of the manometer zero (based on 10 determinations) | $S_m = 0.0016$ |
| Estimate of the standard deviation of the mean of the gage block calibrations (based on 20 determinations) | $S_m = 0.0003$ |
| Estimate of the standard deviation of the mean of calculating the effect of imperfect gage block joints (based on the standard deviation of the calibration) | $S_m = 0.0005$ |
| Estimate of the error from the variable capacitor calibration (based on comparisons with a capacitor calibrated with 10 ppm total uncertainty) | $S = 0.0002$ |
| Estimate of the error in calculating the pressure from the variable capacitor readings (based on the measurement uncertainties of the apparatus dimensions) | $S = 0.0005$ |
| Estimate of the error in the calculation of the thermomolecular pressure effect (the random error based on the standard deviation of the calibration) | Random $S_m = 0.0003$<br>Systematic 0.0003 |

The sum of the random errors in Part B, combined by the square root of the sum of the squares, is 0.0018 Pa. There is also a systematic error of 0.0003 Pa.

We attributed an element of systematic error to the last entry in Part B, inasmuch as neither theory nor experiment for thermomolecular pressure effects is complete. Another important systematic error might be the effect of contaminating gases on the measured pressure. We believe our equipment and procedures were devised in such a way that we were able to prove that this error could not have been significant in our measurements.

The combination of the various random errors for 99 percent confidence limits requires that they be weighted differently according to the number of degrees of freedom. The random errors in Part A were applicable to the 5 final pressures of table 9. With 4 degrees of freedom, the standard deviations were multiplied by 4.6 as given in Student's Table [20], to compute the limits for 99 percent confidence. In Part B, the number of degrees of freedom is nine or more, so that a multiplier of 3.2 was used. The separate weighted standard deviations of Part A and Part B were combined by the sum of the squares, to give an estimated uncertainty of ±10 mPa at the 99 percent confidence limits. The total additional systematic errors are estimated to be relatively insignificant.

---

The authors express their gratitude to James L. Cross for his highly competent efforts in cleaning and filling the vapor pressure apparatus, to John S. Beers for his elegant calibration of the 4.6 mm gage block, and to Irving Friedman for accurately characterizing the isotopic compositions of the water samples.

## Appendix I

Fortran IV program for calculating $t_{68}$ from PRT measurements

```
100 * FORTRAN IV PROGRAM NAMED BRIDGE FOR CALCULATION OF
110 * IPTS-68 VALUES FROM PRT RESISTANCE MEASUREMENTS.
120 DOUBLE PRECISION RT(5),R(5),W,A(10),B(10),T(5),T1,Z
130 DIMENSION N(5)
140 CALL DEFINE (1,7HTCAL74,)
150 CALL DEFINE (2,4HPRT,)
160 READ (1,110)(A(J),B(J),J=1,10)
170 110 FORMAT(D15.8,2X,D15.8)
180 120 READ (2,130)(S1,S2,(N(J),RT(J),R(J),J=1,4))
190 130 FORMAT(2X,F6.2,X,F6.3,(4(/2X,I4,D15.8,D15.8)))
200 WRITE (9,130)(S1,S2,(N(J),RT(J),R(J),J=1,4))
210 WRITE (9,150)S1,S2
220 150 FORMAT(/14X,'STATE'F6.2,2X,F6.3,/)
230 DO 240 J=1,4
240 W=RT(J)/(R(J)-0.996D-03)
250 I=N(J)-700
260 T(J)=(-A(I)+DSQRT(A(I)**2-4.*(1.-W)*B(I)))/(2.*B(I))
270 Z=0.45D-03*T(J)*(T(J)/100.-1.)*(T(J)/419.58-1.)*(T(J)/630.74-1.)
280 T(J)=T(J)+Z
290 WRITE (9,230)N(J),T(J)
300 230 FORMAT('THERM. NO.'I3,3X,'T(INT. 1968) =' D17.10)
310 240 CONTINUE
320 T1 = (T(2) + T(3) + T(4))/3
330 WRITE (9,270)T1
340 270 FORMAT('AVE. T(INT. 1968) ='D17.10,/,/)
350 GO TO 120
360 END
```

TCAL74

```
0.39849575D-02  -0.58762415D-06
0.39850801D-02  -0.58772119D-06
0.39848143D-02  -0.58762185D-06
0.39849917D-02  -0.58769654D-06
0.39849663D-02  -0.58756733D-06
0.39847884D-02  -0.58757724D-06
0.39848898D-02  -0.58760947D-06
0.39850236D-02  -0.58778636D-06
0.39838174D-02  -0.58757363D-06
0.39855387D-02  -0.58755669D-06
```

## Appendix II

### Basic Program for Calculating Pressure From Manometer Readings

```
100 REM BASIC PROGRAM NAMED "PRSURE"
110 REM TO CALCULATE EQ. 27 FOR MANOMETER.
120 REM UNITS ARE SI, RESULTS IN PASCALS.
130 READ R0,G1,M,H0
140 DATA 1.354582E 04,9.801022,0.40026E-2,5.176
150 DATA 486,1013,405,486
160 FOR I =1TO4
170 READ X(I)
180 NEXT I
190 READ S1,S2,T0,H2
200 FOR I=1 TO 4
210 READ E(I)
220 NEXT I
230 FOR I=1TO4
240 LET T(I)=E(I)/X(I)
250 LET T(I)=T(I)+T0
260 NEXT I
270 T1=(T(3)+T(4))/2
280 P=0.8079*(T1-T(1))
290 P=P+0.0147*(T(1)-20)
300 P=P+R0*G1*H2*(1-0.17255E-3*(T(2)-20))
310 LET P=P+R0*G1*H2*(2.27E-6*H2-2.5E-7-4.07E-3*M*H0)
315 P=P+.171
320 PRINT S1;S2;P
330 GO TO 190
340 DATA 1.34,1.1,19.9389,4.6000292E-3
350 DATA -3,21,4,-2
360 DATA 1.34,1.2,19.9395,4.6000292E-3
370 DATA -6,23,3,-4
380 DATA 1.34,1.3,19.9428,4.6000292E-3
390 DATA -5,25,5,-3
400 DATA 1.34,1.4,19.9513,4.6000292E-3
410 DATA -6,24,4,-5
420 DATA 1.34,1.5,19.9530,4.6000292E-3
430 DATA -8,21,4,-6
540 END
```

```
 1.34      1.1      610.84306171
 1.34      1.2      610.84503579
 1.34      1.3      610.84572239
 1.34      1.4      610.84402799
 1.34      1.5      610.84661895
```

## Appendix III

### Basic Program For Calculating Pressure Effects at Zero Level

```
100 REM BASIC PROGRAM NAMED "ZPRES"
110 REM TO CALCULATE EQ. 27 FOR MANOMETER ZERO.
120 REM UNITS ARE SI, RESULTS IN PASCALS.
130 READ R0,G1,M,H0
140 DATA 1.354584E 04,9.801022,0.40026E-2,5.176
150 DATA 486,1013,405,485
160 FOR I =1TO4
170 READ X(I)
180 NEXT I
190 U0 = 20
200 READ S1,S2,T0
210 FOR I=1 TO 4
220 READ E(I)
230 NEXT I
240 FOR I=1TO4
250 LET T(I)=E(I)/X(I)
260 LET T(I)=T(I)+T0
270 NEXT I
280 T1=(T(3)+T(4))/2
290 P=0.8079*(T1-T(1))
300 P=P+0.0147*(T(1)-T1)
310 PRINT S1;S2;P
320 GO TO 200
330 DATA 1048,1.0,19.9567
340 DATA -16,5,-5,-21
350 DATA 1048,1.1,19.8094
360 DATA -17,7,-6,-18
370 DATA 1048,1.2,19.7855
380 DATA -3,19,3,-8
390 DATA 1048,1.3,19.8169
400 DATA -9,11,0,-12
410 DATA 1048,1.4,19.8007
420 DATA -14,8,-3,-16
430 DATA 1048,1.5,20.0502
440 DATA -17,7,-6,-24
450 DATA 1048,1.6,20.0369
460 DATA -18,6,-6,-21
470 DATA 1048,1.7,19.9959
480 DATA -17,7,-5,-20
490 DATA 1048,1.8,19.9627
500 DATA -17,9,-5,-19
510 DATA 1048,1.9,19.9408
520 DATA -15,7,-5,-18
530 END
```

```
 1048        1    .404552E-02
 1048        1.1  .715303E-02
 1048        1.2  .129202E-02
 1048        1.3  .487762E-02
 1048        1.4  .682625E-02
 1048        1.5  .224516E-02
 1048        1.6  .633001E-02
 1048        1.7  .649643E-02
 1048        1.8  .731340E-02
 1048        1.9  .486854E-02
```

## Appendix IV

### Basic Program For Calculating Thermomolecular Pressure

```
100 REM BASIC PROGRAM "THERMP", DERIVED FROM WEBER-SCHMIDT EQ. FOR
110 REM CALCULATING THE THERMOMOLECULAR PRESSURE DEVELOPED BY
120 REM HELIUM IN A TUBE OF RADIUS R RUNNING BETWEEN TEMPERATURES OF
130 REM T1 TO T2.  UNITS CGS, PRESSURE IN DYNES/CM↑2.
140 READ L0,T0,K1,K2,N0,N
150 READ R,M,R0
160 DATA 17.85,273.15,1.36,1.68,1.86885E-04,0.1866
170 DATA .1492,1.25,1.7846E-10
180 P=6116.4
190 PRINT "P =" P
200 READ T2,T1
210 T1=T1+273.15
220 T2=T2+273.15
230 PRINT "T1 =" T1,"   T2 =" T2
240 LET S=(T1/T2)**(N+1)
250 LET S0=(T1/T0)**(N+1)
260 LET L1=L0*S0
270 LET E=4*K2*L1/R
280 LET F=M-1/(2*(N+1))
290 LET D=3*F*K1/(2*3.14159*K2)
300 LET G=0.5*((E/P)↑2)*(1+S↑2)*(1-D)
310 LET H=2*E*(1+S↑2/(S+1))/(3*F)
320 LET C=1-H+G
330 LET U=(T1**(2+2*N)-T2**(2+2*N))/(T0**(2+2*N))
340 LET W=6*K1*(N0↑2)*U*C
350 LET V=(1+N)*P0*P↑2
360 LET X =W/V
370 PRINT "P1↑2 -P2↑2 =" X
380 LET P3=X/(2*P)
390 LET Y=P/(P+P3/2)
400 LET P3=P3*Y
410 PRINT "DELTA P =" P3
420 PRINT
430 GO TO 200
440 DATA 19.94,25.05,19.94,25.13,19.96,25.03
450 DATA 19.95,24.82
460 STOP
470 END


?XBASIC THERMP DB
RUN
P =      6116.4
T1 =       298.2       T2 =       293.09
P1↑2 -P2↑2 =      2595.48711
DELTA P =          .21217073

T1 =       298.28      T2 =       293.09
P1↑2 -P2↑2 =      2636.4391679
DELTA P =          .21551834

T1 =       298.18      T2 =       293.11
P1↑2 -P2↑2 =      2575.2255458
DELTA P =          .21051446

T1 =       297.97      T2 =       293.1
P1↑2 -P2↑2 =      2472.7760644
DELTA P =          .20213976
```

## 11. References


[1] Thiesen, M., and Scheel, K., Wiss. Abh. Physik-Techn. Reichsanst. **3,** 71 (1900).
[2] Scheel, K., and Heuse, W., Ann. Phys. Leipzig **29,** 729 (1909).
[3] Scheel, K., and Heuse, W., Ann. Phys. IV **26,** 54 (1908).
[4] Douslin, D. R., J. Chem. Therm. **3,** 187 (1971).
[5] Prytz, K., Mat.-fysik. Medd. Danske Vidensk. Selskab. **11,** 1 (1931).
[6] Besley, L., and Bottomley, G. A., J. Chem. Therm. **5,** 397 (1973).
[7] Guildner, L. A., Stimson, H. F., Edsinger, R. E., and Anderson, R. L., Metrologia **6,** 1 (1970).
[8] Johnson, D. P., Guildner, L. A., and Jones, F. E., The Vapor Pressure of Water at its Triple Point, Proc. 8th Int., Conf. on the Properties of Steam, in press.
[9] Guildner, L. A., and Terrien, J., *Experimental Thermodynamics, Vol.* **2,** Ch. 4, Part 1, p. 115 (Butterworth and Co., London, 1975).
[10] Guildner, L. A., Anderson, R. L., and Edsinger, R. E., J. Res. Nat. Bur., Stand. (U.S.), **77A** (Phys. and Chem.), No. 5, 667–670 (Sept-Oct. 1973).
[11] Weber, S., Keesom, W. H. and Schmidt, G., Comm. No. 246a, Kamerlingh Onnes Laboratory, Univ. of Leiden, 1937.
[12] Friedman, I., Hardcastle, K., and Gleason, J., private communication.
[13] Craig, H., Science **133,** 1833 (1961).
[14] Craig, H., Geochim. Cosmochim. Acta **12,** 133 (1957).
[15] Hagemann, R., Nief, G., and Roth, E., Tellus **226,** 712 (1970).
[16] Majoub, M., J. Chim. Phys. Physicochim. Biol. **68,** 625 (1971).
[17] Baertschi, P., and Thuerkauf, M., Helv. Chim. Acta **43,** 80 (1960).
[18] Szapiro, S., and Steckel, F., Trans. Faraday Soc. **63,** 883 (1967).
[19] The International Practical Temperature Scale of 1968, Metrologia **5,** 35 (1969).
[20] Nat. Bur. Stand. (U.S.), Spec. Pub. 300, Vol. **1,** p. 307 (1969).


(Paper 80A3–900)



206-267 OL - 76 - 10

JOURNAL OF RESEARCH of the National Bureau of Standards — A. Physics and Chemistry
Vol. 80A, No. 3, May-June 1976

# Publications of the National Bureau of Standards*

## Citations with Selected Abstracts

*J. Res. Nat. Bur. Stand. (U.S.)*, **80A** *(Phys. and Chem.)*, No. 2 (Mar.-Apr. 1976), SD Catalog No. C13.22/sec.A:80/2.

**Extinction coefficients of $NO_2$ and $N_2O_4$,** A. M. Bass, A. E. Ledford, Jr., and A. H. Laufer.

**A study of the chemiluminescence of the $Pb+O_3$ reactions,** M. J. Kurylo, W. Braun, S. Abramowitz, and M. Krauss.

**Structure- and solvent-property relationships for the electronic energies of charge-transfer complexes between certain benzene derivatives,** H. Argentar.

**Bidirectional reflectometry. Part. I. A high resolution laser bidirectional reflectometer with results on several optical coatings,** J. J. Hsia and J. C. Richmond.

**Bidirectional reflectometry. Part II. Bibliography on scattering by reflection from surfaces,** J. C. Richmond and J. J. Hsia.

**Energy levels, classified lines, and Zeeman effect on neutral thorium,** R. Zalubas.

*J. Res. Nat. Bur. Stand. (U.S.)*, **80B** *(Math. Sci.)*, No. 2, April-June 1976), SD Catalog No. C13.22/sec.B:80/2.

**The dependence of inspection-system performance on levels of penalties and inspection resources,** A. J. Goldman and M. H. Pearl.

**A minimax-measure intersection problem,** P. R. Meyers.

**Inverting sparse matrices by tree partitioning,** D. R. Shier.

**The structure of higher degree symmetry classes of tensors,** R. Merris.

**The Kronecker power of permutation,** R. Merris

**On Iohvidov's proofs of the Fischer-Frobenius theorem,** R. C. Thompson.

**Matrix algebra and eigenvalues for the bead/spring model of polymer solutions,** J. T. Fong and A. Peterlin.

**Predictable regular continued cotangent expansions,** J. Shallitt.

**Automatic computing methods for special functions. Part III. The sine, cosine, exponential integrals, and related functions,** I. A. Stegun and R. Zucker.

**Definite integrals of the complete elliptic integral K,** M. L. Glasser.

Monogr. 150. **Liquid-in-glass thermometry,** J. A. Wise, *Nat. Bur. Stand. (U.S.), Monogr. 150*, 30 pages (Jan. 1976) SD Catalog No. C13.44:150, 85 cents.

Key words: calibration; emergent stem; liquid-in-glass thermometer; reference point; stirred liquid comparison bath; temperature scale.

This Monograph, which supersedes NBS Monograph 90, contains information of general interest to manufacturers and users of liquid-in-glass thermometers. Instructions explaining how to submit a thermometer to the National Bureau of Standards for calibration are provided, and the techniques and equipment, such as stirred liquid comparison baths, used in the calibration procedures are described. A discussion of important principles of acceptable thermometer design and factors affecting their use is included. Listed are tables of tolerances reflecting good manufacturing practices and reasonably attainable accuracies expected with liquid-in-glass thermometers. The calculation of corrections for the temperature of the emergent stem is given in detail for various types of thermometers and conditions of use.

SP386, 1976 Edition. **Standards on noise measurements, rating schemes, and definitions: A compilation,** T. L. Quindry, Ed., *Nat. Bur. Stand. (U.S.), Spec. Publ. 386, 1976 Edition*, 84 pages (Apr. 1976) SD Catalog No. C13.10:386, $1.90.

Key words: acoustics; noise; rating scheme; sound; standards organization.

This compilation deals with material assembled from the various standards, industrial and trade organizations, or technical and scientific societies concerned with acoustics. There has been no attempt to review or evaluate the standards, but rather just to list documents covering measurement techniques, calibration methods, definitions, rating schemes, and equipment and product specifications concerned with noise. Those standards dealing solely with ultrasonics, audio equipment, or shock and vibration have not generally been included. The paragraphs describing the standards give a brief summary of intent and/or scope of the standard. In some cases the paragraph is the official description of the standard as issued by the organization or society promulgating the standard, while in others the paragraph merely describes the intent of the standard. Proposed standards are also listed where available. Not listed are proposed revisions of current standards and those which must be reapproved to remain in effect. For the convenience of those readers wishing to purchase copies of standards, names and addresses for the various organizations and/or societies are provided. Federal Regulations directly involving noise measurements are given in Appendix A. Appendix B lists active committees for each organization and names and addresses of appropriate committee chairmen or technical contacts. This compilation includes all information available as of January 1, 1976.

SP396-3. **Critical survey of data sources: Corrosion of metals,** R. B. Diegle and W. K. Boyd, *Nat. Bur. Stand. (U.S.), Spec. Publ. 396-3*, 38 pages (Jan. 1976) SD Catalog No. C13.10:396-3, $1.30.

Key words: commercial alloys; corrosion; data sources; metals.

This survey was undertaken to provide a directory of authoritative sources of information on corrosion of metals. It assesses the scope,

**Publications with prices and SD Catalog numbers may be purchased directly from the Superintendent of Documents, U.S. Government Printing Office, Washington, D.C. 20402 (foreign: one-fourth additional). Microfiche copies of the above, plus paper copy and microfiche versions of NBS Interagency Reports (NBSIR's), may be purchased from the National Technical Information Service (NTIS), Springfield, Va. 22161. Prices are subject to change. Reprints from the NBS Journal of Research and non-NBS publications may often be obtained directly from the authors.*

assets, and deficiencies of about thirty-eight of the most important sources. These include handbooks and technical compilations, information centers, technical societies, and trade associations and institutes. The initial listing of sources to be included was drafted by the authors and submitted to members of the Publications Committee of the National Association of Corrosion Engineers. This Committee thus served as an ad hoc review group for the sources which appear herein. The Directory is indexed by materials and types of corrosion.

SP400-18. **Semiconductor measurement technology: The destructive bond pull test,** J. Albers, Ed., *Nat. Bur. Stand. (U.S.), Spec. Publ. 400-18,* 52 pages (Feb. 1976) SD Catalog No. C13.10:400-18, $1.25.

Key words: bond angle; bonding; bond pull test; bond-to-bond spacing; large wire; loop height; microelectronics; nondestructive bond pull test; position of hook; pull rate; pull strength; resolution-of-forces; semiconductor devices; ultrasonic bonding; wire bond.

This report summarizes the work done at NBS on the destructive bond pull test as applied to small-diameter (approximately 1 mil or 25 μm) ultrasonically bonded aluminum wire. This work was performed during the period from 1969 to 1974. The report begins with a brief summary of the calculation of the resolution-of-forces operative in the bond system during the application of the pulling force. Next, comparisons of the theoretical and experimental dependencies of the pull strength on the variables involved in the resolution-of-forces calculation are given. Some of the variables which are not directly involved in this calculation are then considered and their effects on the measured pull strength are presented. The report ends with a sensitivity calculation as to how well the variables must be controlled to maintain the variability of the pull strength to within given limits. Bond pull specifications for large-diameter wire as well as recommended force levels to be used in the application of the nondestructive bond pull test, both of which have resulted from the pull test work, are considered in the appendices.

SP400-19. **Semiconductor measurement technology: Progress report, January 1 to June 30, 1975,** W. M. Bullis, Ed., *Nat. Bur. Stand. (U.S.), Spec. Publ. 400-19,* 95 pages (Apr. 1976) SD Catalog No. 13.10:400-19, $2.10.

Key words: acoustic emission; beam-lead bonds; bias-temperature stress test; boron redistribution; capacitance-voltage methods; charge-coupled device structures; Darlington pairs; deep depletion; dopant profiles; electrical properties; electron beam induced current; electron beam induced damage; electronics; epitaxial layer thickness; four-probe method; hermeticity; leak tests; measurement methods; microelectronics; moisture infusion; optical flying-spot scanner; oxide films; passivation overcoats; photomask metrology; pull test; resistivity; Rutherford backscattering; scanning electron microscope; scanning low energy electron probe; semiconductor devices; semiconductor materials; semiconductor process control; shear test; sheet resistors; silicon; silicon on sapphire; spreading resistance; test patterns; thermal resistance; thermal response; transistors; ultrasonic bonding; wire bonds; x-ray photoelectron spectroscopy.

This progress report describes NBS activities directed toward the development of methods of measurement for semiconductor materials, process control, and devices. Both in-house and contract efforts are included. The emphasis is on silicon device technologies. Principal accomplishments during this reporting period included (1) completion and analysis of an interlaboratory evaluation of standard reference wafers for resistivity measurement by the four-probe method, (2) analysis of the effect of finite contact size on sheet resistance as measured with a van der Pauw structure, (3) calculation of errors introduced in measuring line width with typical microscope systems, (4) development of procedures for predicting the magnitude of electron beam induced current in silicon device structures, (5) application of the optical flying-spot scanner to observation of hot spots and nonlinearities in rf power transistors and of logic patterns in an MOS shift register, and (6) determination of a more accurate electrical method, based on peak junction temperature measurement, for establishing safe operating area curves for medium power transistors. Also reported are the results of work on spreading resistance measurements, ionization of dopant impurities in silicon, Rutherford backscattering measurements, x-ray photoelectron spectroscopy, ion microprobe mass analysis, tests for determining the surface quality of sapphire substrates, reevaluation of Irvin's curves, mathematical models of dopant profiles, deep depletion measurements of resistivity profiles, measurement of epitaxial layer thickness by the deep depletion method, bias-temperature stress test measurements on MOS capacitors, a high voltage capacitance-voltage method for measuring characteristics of thick insulator films, ion implantation parameters, methods for determining integrity of passivation overcoats, optical imaging and calibration standards for photomask metrology, line-width measurements, charge-coupled device test structures, test pattern design and analysis for silicon on sapphire MOS device technologies, nondestructive acoustic emission test for beam-lead bonds, pull and shear tests for wire bonds, a rapid cycle dry gas gross leak test, leak detection by helium mass spectrometry, correlation of moisture infusion in semiconductor packages with leak size and device reliability, an automated scanning low-energy electron probe, electron beam induced damage in silicon device structures, and thermal resistance measurements on Darlington transistors. Supplementary data concerning staff, publications, workshops and symposia, standards committee activities, and technical services are also included as appendices. A sixth appendix is included to summarize the results of a study which was carried out to assess the impact of automation of integrated circuit processing and assembly on future measurement requirements in the industry.

SP400-21. **Semiconductor measurement technology: Planar test structures for characterizing impurities in silicon,** M. G. Buehler, J. M. David, R. L. Mattis, W. E. Phillips, and W. R. Thurber, *Nat. Bur. Stand. (U.S.), Spec. Publ. 400-21,* 32 pages (Jan. 1976) SD Catalog No. C13.10:400-21, $1.30.

Key words: MOS capacitors; *p-n* junctions; resistivity of silicon; semiconductor devices; semiconductor process control; sheet resistors; test patterns; thermally stimulated currents.

Various test structures such as sheet resistors, *p-n* junctions, and MOS capacitors and their associated physical models have been developed to characterize dopants and defects in silicon. These structures address various needs within the semiconductor industry for (a) well-designed and miniaturized test structures such as an orthogonal van der Pauw sheet resistor, (b) simple and economical measurements such as the oxide window width of a diffused layer, (c) updated values for the resistivity versus dopant density relation, and (d) improved detection methods for identifying defect centers which control the lifetime and leakage currents of devices.

SP400-27. **Semiconductor measurement technology: Laser scanning of active semiconductor devices—Videotape script,** D. E. Sawyer and D. W. Berning, *Nat. Bur. Stand. (U.S.), Spec. Publ. 400-27,* 26 pages (Feb. 1976) SD Catalog No. C13.10:400-27, $1.20.

Key words: failure analysis; hot spots; integrated circuits; laser scanner; measurement method; nondestructive test; nonlinear operation; optical scanner; reliability; transistors.

This is the script of a videotape presentation which describes new and powerful applications for laser scanning in semiconductor device design and reliability work. The design of the scanner is described in

detail and many of its applications are displayed and discussed. The optical scanner can, in a completely nondestructive way, reveal the inner workings of semiconductor devices. For example, it is shown that the scanner can (1) map dc and high-frequency gains in transistors, (2) reveal areas of the device operating in a nonlinear manner, (3) electronically map temperature in the transistor, and (4) detect the location of hot spots that can develop for certain operating conditions. The vehicle used to show these capabilities of the scanner is a bipolar interdigitated UHF transistor. A dual input NAND gate is used to demonstrate the use of the scanner to determine internal logic states and otherwise observe internal operation of the circuit. To show the ability of the scanner to examine MOS devices without detectable degradation, a MOS shift register is used. The location and progress of internal logic in the register is clearly shown by the scanner. Not only can internal logic be mapped and marginally-operating logic cells detected, but individual logic states can be changed by the scanner without affecting other elements.

SP416, 1976 Edition. **Attacking the fire problem: A plan for action—1976 Edition,** F. B. Clarke and D. W. Raisher, Eds., (Supersedes NBS Special Publication 416, 1975 Edition) *Nat. Bur. Stand. (U.S.), Spec. Publ. 416, 1976 Edition,* 41 pages (Jan. 1976) SD Catalog No. C13.10:416, 1976 Ed., $1.00.

Key words: building design; consumer protection; fire control; fire detection; fire research; fire spread; flammability.

The mission of the Center for Fire Research is to insure the development of the technical base for the standards and specifications needed in support of the National goal to reduce fire losses by 50 percent over the next generation. A systems approach to accomplish this mission is described. The Center consists of four basic programs in the area of Fire Science and five applied research programs in the area of Fire Safety Engineering. Each applied program addresses an aspect of the Fire Problem, using fundamental information supplied by the basic research function. Active participation by staff members in voluntary standards organizations is the principal means of making this technology available for codes and standards needed to reduce the Nation's fire loss.

SP426. **Bibliography of low energy electron and photon cross section data (through December 1974),** L. J. Kieffer, *Nat. Bur. Stand. (U.S.), Spec. Publ. 426,* 219 pages (Mar. 1976) SD Catalog No. C13.10:426, $3.30.

Key words: atom; collision cross section; detachment; dissociation; elastic scattering; electron; excitation; fluorescence; ion; ionization; molecule; photon; positron.

A bibliography of original reports of measurements or calculations of electron, positron and photon cross sections and their ions is presented. A detailed index to the bibliography allows retrieval of cross section data for specific processes and atomic or molecular species. A comprehensive author index is included. The bibliography covers the period 1921 through calendar year 1974 but some references late in 1974 may not have been found and included. No references were found prior to 1921.

SP438. **Testing and certification for export products in industralizing countries.** Proceedings of a Regional Seminar held at the Regional English Language Centre and International House, Singapore, May 19-20, 1975, H. S. Peiser and R. S. Marvin, Eds., *Nat. Bur. Stand. (U.S.), Spec. Publ. 438,* 160 pages (Feb. 1976) SD Catalog No. C13.10:438, $2.40.

Key words: certification; developing countries; exports; industrializing countries; labeling; seminar; South Asia trade; testing.

A regional seminar sponsored by the Singapore Institute of Standards and Industrial Research, the National Bureau of Standards, and the Agency for International Development was held in Singapore in May of 1975. The participants represented most of the countries in South Asia concerned with increasing their exports, and concentrated on various problems connected with the testing and certification of such exports. Most of the prepared papers reviewed the practice and future plans of these countries. During the discussion a number of specific problems and issues were raised, with a good deal of attention focused on the extent to which the standards and certification of goods by an exporting country can be and are recognized by the importer. This report includes both the prepared papers and a mildly edited version of the discussions following each.

SP439. **The Center for Building Technology: A perspective,** M. Olmert, *Nat. Bur. Stand. (U.S.), Spec. Publ. 439,* 30 pages (Jan. 1976) SD Catalog No. C13.10:439, 95 cents.

Key words: building research; criteria; energy; engineering; industry construction; measurement techniques; standards.

The mission of the Center for Building Technology is threefold. They are (1) advance building technology by providing technical and scientific bases for criteria and standards that improve the usefulness, safety, and economy of buildings; (2) facilitate, for the public benefit, the implementation of improved building technology by providing technical assistance to all sectors of the building community; and (3) develop improved techniques by which the end-users in buildings, communities and industrial processes conserve energy. This report presents an overview of the Center for Building Technology's research areas through its accomplishments and ongoing projects.

SP441. **Successful experiences in teaching metric.** A Conference in Celebration of the One Hundredth Anniversary of the Metric Convention, 1875-1975, held at the National Bureau of Standards, Gaithersburg, Maryland, May 20-21, 1975, J. V. Odom, Ed., *Nat. Bur. Stand. (U.S.), Spec. Publ. 441,* 115 pages (Jan. 1976) SD Catalog No. C13.10:441, $2.30.

Key words: education; International System of Units; metrication; metric education; metric system; training; Treaty of the Meter.

These proceedings contain the texts of the presentations made at a recent conference on Successful Experiences in Teaching Metric. Specific experiences in introducing the metric system in all areas of educational interest were presented. These ideas will be especially useful to educators just beginning to prepare for their change to the metric system.

BSS83. **Polymer impregnated hardened cement pastes and mortars,** J. R. Clifton, J. E. Fearn, and E. D. Anderson, *Nat. Bur. Stand. (U.S.), Bldg. Sci. Ser. 83,* 21 pages (Apr. 1976) SD Catalog No. C13.29/2:83, 55 cents.

Key words: cement; compressive strength; flexural strength; fracture mechanics; polymer impregnated cement; polymer impregnated mortar; porosity; scanning electron microscopy.

Polymer impregnated hardened cement pastes and mortars have been prepared and their properties compared to those of control specimens. Specimens were made by impregnating dried and evacuated precast hardened cement pastes and mortars with methyl methacrylate, under pressure, which was thermally polymerized. The effects of the microstructure of the cement pastes and mortars on the performance of polymer impregnated mortars were determined by preparing specimens with a wide range of porosities by varying the water to cement ratio and the curing times prior to impregnation.

The properties of impregnated and control specimens were investigated by: scanning electron microscopy; porosity determinations; fracture mechanics studies; and strength determinations. The polymer impregnated materials had compressive and flexural strengths, moduli of elasticity, and fracture toughnesses which were substantially higher than unimpregnated materials.

FIPS PUB 38. **Guidelines for documentation of computer programs and automated data systems,** B. Marron, Standards Coordinator, *Nat. Bur. Stand. (U.S.), Fed. Info. Process. Stand. Publ. (FIPS PUB) 38*, 50 pages (1975) SD Catalog No. C13.52:38, $1.35.

Key words: automated data systems; computer programs; documentation; documentation content guidelines; FIPS guidelines; software.

These guidelines provide a basis for determining the content and extent of documentation for computer programs and automated data systems. Software development phases and related document types are identified, several examples of documentation options are given, and content guidelines for ten document types are provided. The ten document types are: Functional Requirements Document; Data Requirements Document; System/Subsystem Specification; Program Specification; Data Base Specification; Users Manual; Operations Manual; Program Maintenance Manual; Test Plan; Test Analysis Report.

The guidelines are intended to be a basic reference and a checklist for general use throughout the Federal Government to plan and evaluate documentation practices.

FIPS PUB 39. **Glossary for computer systems security,** D. Branstad and R. Krell, *Nat. Bur. Stand. (U.S.), Fed. Info. Process. Stand. Publ. (FIPS PUB) 39*, 19 pages (Jan. 1976) SD Catalog No. C13.52:39, 60 cents.

Key words: computer; data processing; definitions; Federal Information Processing Standards Publication; information processing; privacy; security; terms; vocabulary.

This glossary provides an alphabetic listing of approximately 170 terms and definitions pertaining to privacy, and security related to data, information systems hardware and software. Multiple word terms are listed in natural order, synonyms are referenced, and glossary terms appearing within a definition are indicated.

PS64-75. **School paste.** *(ANS Z 297.2-1975)*, C. W. Devereux, Technical Standards Coordinator, *Nat. Bur. Stand. (U.S.), Prod. Stand. 64-75*, 6 pages (Apr. 1976) SD Catalog No. C13.20/2:64-75, 35 cents.

Key words: paste, water-based, semi-liquid; school paste.

The purpose of this Voluntary Product Standard is to establish nationally recognized quality, safety, and packaging requirements for school paste and to provide a basis for common understanding among producers, distributors, and users of this product.

PS65–75. **Paints and inks for art education in schools.** *(ANS Z297.1-1975)*, G. S. Chaconas, Technical Standards Coordinator, *Nat. Bur. Stand. (U.S.), Prod. Stand. 65-75*, 7 pages (Mar. 1976) SD Catalog No. C13.20/2:65-75, 35 cents.

Key words: art education; inks for art education; paints and inks; schools, paints and inks.

This Voluntary Product Standard covers the establishment of requirements for preservatives, toxicity, course particle content, performance, working qualities, and packaging for school paints and inks, and provides producers, distributors, and users with a basis for common understanding of the characteristics of this product.

TN670. **An infrared spectrometer utilizing a spin flip Raman laser, IR frequency synthesis techniques, and $CO_2$ laser frequency standards,** J. S. Wells, F. R. Petersen, G. E. Streit, P. D. Goldan, and C. M. Sadowski, *Nat. Bur. Stand. (U.S.), Tech. Note 670*, 54 pages (Jan. 1976) SD Catalog No. C13.46:670, $1.60.

Key words: air quality measurements; improved resolution spectroscopy; infrared frequency measurements; infrared spectrometer; spin flip laser; tunable IR laser.

The central part of this spectrometer is a cw spin flip Raman laser which operates between 1900 and 1800 $cm^{-1}$. The spin flip laser has so far demonstrated capabilities of resolving spectra separated by 0.01 $cm^{-1}$ and shows promise of exceeding this resolution capability. When used with an opto-acoustic detector or with a detector and a flow system, it is capable of making a variety of measurements of environmental interest. Many of these environmental applications require only wavelength metrology.

By using $CO_2$ laser standards as frequency references and incorporating infrared frequency synthesis techniques, spectroscopy with the spin flip Raman laser can be put on a frequency metrology basis. A $CO_2$ laser has been used with a metal-oxide-metal diode to synthesize a known frequency reference which was used to stabilize the CO pump laser. The MOM diode also has the potential for measuring the frequency difference between the SFRL and the CO pump laser, a step which will complete absolute frequency measurements with the SFRL. The progress toward achieving this goal, the potential capabilities of this unique spectrometer, and some future applications are discussed.

TN675. **Heat transfer and flow of helium in channels—Practical limits for applications in superconductivity,** M. C. Jones and W. W. Johnson, *Nat. Bur. Stand. (U.S.), Tech. Note 675*, 45 pages (Jan. 1976) SD Catalog No. C13.46:675, $1.30.

Key words: buoyancy; channels; film boiling; forced convection; helium I; helium II; mixed convection; nucleate boiling; subcritical; supercritical; transition; turbulent flow.

Heat transfer and fluid mechanics of helium flowing in channels are reviewed. Emphasis is placed on observed or anticipated limits of operation which might be expected to apply in applications of superconductivity. Topics included are: the high-heat-flux degradation of heat transfer and possible effects of buoyancy forces in supercritical helium; transition to film boiling in subcritical helium; limiting heat currents in helium II; and the possibility of oscillations in forced flow helium systems.

TN677. **Laser attenuators for the production of low power beams in the visible and 1.06 $\mu$m regions,** B. L. Danielson and Y. Beers, *Nat. Bur. Stand. (U.S.), Tech. Note 677*, 25 pages (Jan. 1976) SD Catalog No. C13.46:677, $1.20.

Key words: beam splitter; laser attenuation; neutral density filter.

Some methods were investigated for the accurate attenuation of laser beams to very low levels; approximately $10^{-11}$ watts. This work was done at 1.06 and 0.6471 $\mu$m, but the conclusions are applicable throughout the visible region as well. Two types of devices were considered: wedged beam splitters and neutral density filters. The theory of the attenuation of a wedged beam splitter was described and some of the errors associated with these devices were discussed.

TN889. **Trace hydrocarbon analysis: The National Bureau of Standards Prince William Sound/Northeastern Gulf of Alaska baseline study,** S. N. Chesler, B. H. Gump, H. S. Hertz, W. E. May, S. M. Dyszel, and D. P. Enagonio, *Nat. Bur. Stand. (U.S.), Tech. Note 889*, 73 pages (Jan. 1976) SD Catalog No. C13.46:889, $1.80.

Key words: baseline studies; gas chromatography; gas chromatography-mass spectrometry; hydrocarbons; liquid chromatography; petroleum analysis; trace analysis.

The low concentration of hydrocarbons anticipated in pollution baseline studies necessitates the development of analytical techniques sensitive at the submicrogram per kilogram concentration

level. The method of analysis developed in this laboratory involves dynamic headspace sampling for volatile hydrocarbon components of the sample followed by coupled-column liquid chromatography for the nonvolatile components. These techniques require minimal sample handling, reducing the risk of sample component loss and/or sample contamination. Volatile sample components are separated from the matrix in a closed system and concentrated on a TENAX-GC packed precolumn, free from large amounts of solvent and ready for GC/GC-MS analysis. Nonvolatile compounds, such as the benzpyrenes, may be extracted from large volumes of water and concentrated on a Bondapak C18 packed precolumn for coupled-column liquid chromatographic separation and analysis. Results of the application of these techniques are presented and discussed.

TN891. **Issues in fire vehicle replacement: Users' views and synthesis,** P. B. Saunders, R. H. F. Jackson, P. R. Meyers, and M. H. Pearl, *Nat. Bur. Stand. (U.S.), Tech. Note 891*, 19 pages (Jan. 1976) SD Catalog No. C13.46:891, $1.10.

Key words: engine pumper; fire vehicle; ladder truck; maintenance; replacement; specifications; standards.

This report documents the findings and recommendations from a study of fire vehicle replacement procedures. Exploration of that subject proved to require consideration of related issues arising in: (1) writing apparatus specifications, (2) maintaining and repairing vehicles, and (3) obtaining spare parts. The topics and most of the recommendations described herein are synthesized directly from visits and/or telephone interviews with fire department officials across the country. The recommendations of the study call for greatly increased communication among departments, the development of standards for vehicle performance, maintenance staff size, etc., and national and/or regional centers for training personnel and establishing standard vehicle testing procedures.

TN894. **Apparatus for testing oceanographic resistance thermometers,** G. T. Furukawa and J. L. Riddle, *Nat. Bur. Stand. (U.S.), Tech. Note 894*, 59 pages (Jan. 1976) SD Catalog No. C13.46:894, $1.60.

Key words: bridge; deep-sea thermometer; high pressure; oceanographic thermometer; platinum resistance thermometer; pressure; pressure intensifier; pressure seal; pressure vessel; resistance; resistance thermometer; test; thermometer; thermometer leads; thermostated bath; vacuum; water tight.

The design and construction of an apparatus for testing resistance-type oceanographic thermometers to $6.89 \times 10^4$ kPa(10,000 psi) are described. Detailed operating procedures for the apparatus are given. The results of performance tests with the apparatus are discussed.

TN897. **Interpretation of data in the network measurement system,** S. W. Watkins and M. D. Abrams, *Nat. Bur. Stand. (U.S.), Tech. Note 897*, 46 pages (Mar. 1976) SD Catalog No. C13.46:897, $1.15.

Key words: computer networks; data analysis; interactive; network service; performance evaluation; performance measurement; service.

The Network Measurement System (NMS) represents an implementation of a new approach to the performance measurement and evaluation of computer network systems and services. In this report, the interpretation of data within the NMS is described. These data have been acquired by the Network Measurement Machine (NMM) component of the NMS and are then interpreted by a Data Analysis Package (DAP), which produces meaningful information concerning the quality of network service delivered to interactive terminal users as well as a characterization of user demands and network communication facility utilization.

This report traces the flow of data from the time of capture by the minicomputer-based NMM through the several phases of modeling and structuring in the DAP. Included in this description is the statistical treatment of the data which provides quantitative measures of various aspects of network performance.

TN898. **A prototype semi-automated system for measuring air infiltration in buildings using sulfur hexafluoride as a tracer,** C. M. Hunt and S. J. Treado, *Nat. Bur. Stand. (U.S.), Tech. Note 898*, 24 pages (Mar. 1976) SD Catalog No. C13.46:898, 55 cents.

Key words: air infiltration instrumentation; air infiltration measurement; building ventilation rates; sulfur hexafluoride tracer.

A system is described which automatically operates a small gas chromatograph and measures parts per billion concentrations of sulfur hexafluoride ($SF_6$) in air. It samples air on a 10 minute cycle and records the response on a strip chart recorder. When $SF_6$ is distributed in the air of a building, data is obtained from which air infiltration rates may be determined.

TN901. **Comparison of theoretical and experimental photoeffect data 0.1 keV to 1.5 MeV,** J. H. Hubbell and W. J. Veigele, *Nat. Bur. Stand. (U.S.), Tech. Note 901*, 43 pages (Apr. 1976) SD Catalog No. C13.46:901, $1.15.

Key words: attenuation coefficients; cross sections; gamma rays; photoelectric effect; photons; x rays.

Graphs of calculated and experimental atomic photoeffect cross sections as a function of photon energy 0.1 keV to 1.5 MeV are presented for all elements Z=1 to 94. The calculated results presented are (a) the nonrelativistic Hartree-Fock self-consistent-field (SCF) results of Veigele, Henry, et al., over the range 0.1 keV to between 1.0 and 8.0 keV for all elements Z=1 to 94 and (b) the relativistic Hartree-Slater SCF results of Scofield over the range 1.0 keV to 1.5 MeV for all elements Z=1 to 101. The "experimental" data-points are derived by subtracting theoretical scattering cross sections from total attenuation coefficient measurements in the literature. Differences between theoretical and experimental photoeffect data are typically a factor of two from 0.1 to 1.0 keV, 5-10 percent from 1.0 to 5.0 keV and 1-5 percent from 5.0 keV up to energies, ranging from 20 keV for carbon up to 500 keV for lead, above which the photoeffect cross section becomes fractionally too small to be accurately determined from the total attenuation coefficient.

TN902. **Evaluation, revision and application of the NBS stylus/computer system for the measurement of surface roughness,** E. C. Teague, *Nat. Bur. Stand. (U.S.), Tech. Note 902*, 151 pages (Apr. 1976) SD Catalog No. C13.46:902, $2.70.

Key words: amplitude density function; arithmetic average; autocorrelation function; average wavelength; kurtosis; minicomputer software; random error; skewness; surface microtopography; surface roughness; surface texture; systematic error.

This report describes in detail the hardware and software used at NBS to implement on a stylus instrument/minicomputer system the process of calibrating the system with an interferometrically measured step and the calculation of important characterizations of surface profiles. The characterizations of a profile which may be calculated include the arithmetic average value, the mean square value, the amplitude density function, the autocorrelative function and the average wavelength. The report also includes a statistical evaluation, using empirical and analytical techniques, of the calibration procedures' long term stability.

TN903. **The NIRA computer program package (Photonuclear Data Center),** H. J. Vander Molen and H. M. Gerstenberg, *Nat. Bur. Stand. (U.S.), Tech. Note 903*, 30 pages (Feb. 1976) SD Catalog No. C13.46:903, 85 cents.

Key words: central computer; computer programs; data manipulation; digital data; mass storage; NIRA; Photonuclear Data Center.

The Photonuclear Data Center's NIRA library of programs, executable from mass storage on the National Bureau of Standard's central computer facility, is described. Detailed instructions are given (with examples), for the use of the library to analyze, evaluate, synthesize, and produce for publication, camera-ready tabular and graphical presentations of digital photonuclear reaction cross-section data. NIRA is the acronym for Nuclear Information Research Associate.

TN910-1. **Self-study manual on optical radiation measurements: Part I—Concepts, Chapters 1 to 3,** F. E. Nicodemus, Ed., *Nat. Bur. Stand. (U.S.), Tech. Note 910-1,* 93 pages (Mar. 1976) SD Catalog No. C13.46:910-1, $2.10.

Key words: optical radiation measurement; photometry; radiometry; spectroradiometry.

This is the initial publication of a new series of Technical Notes (910) entitled "A Self-Study Manual on Optical Radiation Measurements." It contains the first three chapters of this Manual. Additional chapters will be published, similarly, as they are completed. The Manual is a definitive tutorial treatment of the measurement of incoherent optical radiation that is complete enough for self instruction. Detailed chapter summaries make it also a convenient authoritative reference source.

The first chapter is an introduction that includes a description of optical radiation and the ray approach to its treatment in this Manual (based on geometrical optics), a discussion of relevant parameters and their use in a measurement equation as a systematic technique for analyzing measurement problems, and a presentation of the system of units and nomenclature used.

The second chapter, on the distribution of optical radiation with respect to position and direction, introduces the basic radiometric quantity, radiance, and its important invariance properties. It is shown how to determine the total power in a beam from the radiance distribution and to determine the distribution of radiance at any surface, through which the beam passes, in terms of the distribution at any other surface that also intersects the entire beam.

NBSIR 75-692. **A minicomputer-based system for the measurement and analysis of community noise,** R. L. Fisher, D. S. Blomquist, J. S. Forrer, and D. M. Corley, 106 pages (May 1975). Order from NTIS as PB250385, $5.50.

Key words: community noise; computer interface; instrumentation; minicomputer; noise.

An operating system for the measurement and analysis of community noise was turned over to the Army for their use in February 1975, thus accomplishing the transfer of technology developed by NBS to the Bioacoustics Division, U.S. Army Environmental Hygiene Agency. This report documents the hardware and software packages prepared by NBS in support of this system.

NBSIR 75-788. **Evaluation of the fire hazard in a mobile home resulting from an ignition on the kitchen range,** E. K. Budnick and D. P. Klein, 28 pages (Feb. 1976). Order from NTIS as PB250843, $4.00.

Key words: fire test; flame spread; kitchen cabinets; kitchen range; kitchen range hood; limited combustibility; mobile home.

A series of fire tests was conducted in a typical mobile home to evaluate the potential fire hazard resulting from an accidental ignition from cooking on the kitchen range. Specific attention was directed to (a) ease of ignition of the kitchen cabinets as a function of the clearance between the range and the underside of the cabinets with and without the presence of a metal hood and (b) flame spread following the ignition.

The tests, which used a preheated pan of cooking oil as an ignition source, were conducted in a mobile home kitchen area. The materials tested were printed lauan plywood, printed particle board, and molded polystyrene, representative of materials used in kitchen cabinet construction in mobile homes.

Under the test conditions employed, it was found that ignition of the kitchen cabinets occurred in all cases in which a metal hood was not used. The time to ignition of the materials was only slightly affected by the clearance between the specimen (cabinet bottom) and the range. A significant time delay or no ignition resulted from the installation of a metal range hood.

An additional problem area revealed by the tests was the ignition and burn-through of the partition directly behind the range.

Specific design recommendations based on test results are presented along with suggestions for further investigation.

NBSIR 75-790. **FY75 progress report on design criteria and methodology for construction of low-rise buildings to better resist typhoons and hurricanes,** R. D. Marshall and N. J. Raufaste, Jr., 362 pages (Nov. 1975). Order from NTIS as PB250848, $10.50.

Key words: buildings; codes and standards; housing; hurricanes; low-rise buildings; natural disaster; structural connections; typhoons; wind loads.

This report represents the major accomplishments conducted during the third phase (FY75) of a three year project to develop improved design criteria for low-rise buildings in developing countries to better resist extreme winds. The research study sponsored by the Agency for International Development commenced in March 1973. Two other reports were prepared: NBSIR 74-582 FY73 Progress Report (first phase of the research—4 months) and NBSIR 74-567 FY74 Progress Report (second phase of the research—12 months). During FY75, 6 major tasks were completed (instrumentation of fifth and sixth of six test houses to collect full scale field wind data, continuation of technician training at the field sites and at the wind tunnel facility, analyzed of extreme wind data, development of draft improved design criteria reports, participation in regional conferences in Manila and scheduling of regional dissemination of project results conference in Jamaica for November 1975). Research activities will be completed in December 1975. A final report will be published by the end of FY76.

NBSIR 75-827. **Report on NBS dual mixer time difference system (DMTD) built for time-domain measurements associated with Phase 1 of GPS,** D. W. Allan, 21 pages (Jan. 1976). Order from NTIS as PB247938, $3.50.

Key words: frequency measurement; frequency mixing; global positioning system; isolation amplifiers; low-noise amplifiers; precision frequency measurements; precision time measurements; time difference measurements; time-domain frequency stability; time interval.

Based on a previous work reported at the 1975 Frequency Control Symposium, the National Bureau of Standards was asked to build a Dual Mixer Time Difference (DMTD) measuring system. This report includes the design, construction, and testing of this DMTD system in fulfillment of this request. The precision of time difference measurement with this system was shown to be about 0.1 picosecond and the accuracy about 10 ps; similarly, the frequency stability precision was shown to be described by $\sigma_y(\tau) \simeq 10^{-13}\,\tau^{-1}$, $0.1\text{s} < \tau < 10^5\text{s}$ and equal to $10^{-16}$ at $\tau$ equal about half a day.

The request for this DMTD system was for measuring the clocks that will go on board the satellites for Phase 1 of the Global Positioning System (GPS) program. The DMTD system described in this re-

port is the only system that can easily meet all of the time-domain measurement requirements for this program.

NBSIR 75-828. **Semi-annual report on materials research in support of superconducting machinery,** R. P. Reed, J. G. Hust, M. B. Kasen, H. M. Ledbetter, D. T. Read, E. R. Naimon, R. E. Schramm, L. L. Sparks, R. L. Tobler, and W. F. Weston, 193 pages (Jan. 1976). Order from NTIS as PB249041, $7.50.

Key words: composites; copper alloys; cryogenic temperatures; elastic properties; engineering materials; fatigue; fracture; iron alloys; mechanical properties; nickel alloys; superconducting machinery; thermal conductivity.

Results are reported of a six-month study, March through August 1975, on candidate materials for superconducting machinery. The results cover five areas—advanced composites, elastic properties, fatigue resistance and fracture toughness, magnetothermal conductivity, and thermal conductivity. Material properties were studied over the temperature range 4 to 300 K. Materials studied include: oxygen-free copper; copper-nickel alloys; a precipitation-hardening copper alloy; invar; nickel-chromium-iron alloys; stainless steels; and the composite materials boron/aluminum, boron/epoxy, S-glass/epoxy, graphite/epoxy, and an organic-fiber/epoxy. Some notable results of the study are: the first 4 K fatigue data on a composite material; a ten-fold increase in the fatigue life of a uniaxial glass/epoxy composite between room temperature and liquid-helium temperature; the first 4 K fatigue fracture toughness studies on a nitrogen-strengthened chromium-nickel-manganese steel, which show this material has higher yield strength and adequate toughness compared to conventional stainless steels; room-temperature elastic properties of a copper-cadmium-chromium precipitation-hardening alloy, which are quite different from those of unalloyed copper and show a non-parallel behavior of the shear modulus and the bulk modulus; the thermal conductivity of 304 stainless steel may be reduced one third at 4 K by a 6 MA/m (80 kOe) magnetic field; the first systematic study of the tensile properties of fiber-reinforced composite materials between room temperature and liquid-helium temperature.

This work was supported by the Advanced Research Projects Agency of the U.S. Department of Defense.

NBSIR 75-829. **Radiation characteristics of dipole sources located inside a rectangular, coaxial transmission line,** J. C. Tippet and D. C. Chang, 35 pages (Jan. 1976). Order from NTIS as PB248855, $4.00.

Key words: EMC measurements; radiation resistance; rectangular coax; shielded strip line; TEM cell.

When making EMC measurements inside a shielded enclosure, the radiation characteristics of the device being tested changes. In this report the change in radiation resistance of dipole sources located inside a National Bureau of Standards TEM transmission cell is determined. In many cases a practical device can be modeled by dipole sources. In these cases, the analysis allows one to predict the device's radiation characteristics in other environments, e.g., free space.

NBSIR 75-900. **Liquid level instrumentation in volume calibration,** R. M. Schoonover, H. H. Ku, J. R. Whetstone, and J. F. Houser, 37 pages (Oct. 1975). Order from NTIS as PB250859, $4.00.

Key words: density measurement; electromanometer; large volume calibration.

The technique of pressure head measurement for determining liquid levels in tanks has been used for the intercomparison of commercially available electromanometers with themselves and a sight glass. In addition to obtaining intercomparison information, the high precision of these devices coupled with that of volumetric transfer techniques demonstrates the applicability of the calibration method in determining departures of the actual tank geometry from that of a model straight-walled geometry. It is shown that the calibration of the volume-to-height relationship of a 3300 liter tank may be accomplished with an uncertainty in this relationship of ~4 parts in 10,000.

NBSIR 75-902. **A survey of fire accidents involving curtains and draperies—deaths, injuries and financial loss,** L. D. Moore and A. K. Vickers, 35 pages (Dec. 1975). Order from NTIS as PB249539, $4.00.

Key words: curtains; draperies; FFACTS system; fire; flammable fabrics; NFPA.

A case history survey of 286 fire accidents was conducted. This survey was composed of three groups of case histories in which curtains or draperies (C/Ds) were involved. The cases were analyzed in detail, attempting to ascertain the extent to which these products represented fire hazards.

As none of the three files were chosen on a statistical basis, projection of the data to the overall fire hazard situation is not technically feasible.

To learn more of the physical nature of burning C/Ds, and to supply information that may be utilized to judge the extent of hazard, it is recommended that full-scale experiments be conducted.

NBSIR 75-913. **Structural test procedures for bicycles,** D. E. Marlowe, 50 pages (Oct. 1975). Order from NTIS as PB248911, $4.00.

Key words: bicycle; consumer safety; regulations; safety; structural testing.

Tests for several structural performance criteria have been included in a mandatory regulation on bicycle safety which has been proposed by Consumer Product Safety Commission. The apparatus and procedures developed to conduct these tests and results from 15 representative bicycles are described. Several of the bicycles tested failed to meet the requirements for the seat and handlebar stem friction clamp strength.

NBSIR 75-915. **A source of error in paper extract pH determinations: Contact between paper and reference electrodes,** E. J. Parks and R. L. Hebert, 17 pages (Jan. 31, 1975). Order from NTIS as PB249775, $3.50.

Key words: acidity; contact; decantate; electrode; error; extract; paper; pH; suspension.

If the reference electrode of a pH meter is permitted to contact paper suspended in an aqueous medium, the pH observed is lower than that observed with no contact. The effect has been observed with papers of widely different pH, and varies in magnitude with the proximity of contact and with different papers. The problem can be avoided by taking measurements on decanted equilibrium solutions instead of suspensions of paper.

The cause of this effect may be analogous to the suspension effect in colloidal systems.

NBSIR 75-916. **The role of passive film growth kinetics and properties in stress corrosion and crevice corrosion susceptibility,** J. Kruger, J. R. Ambrose, and T. Kodama, 85 pages (Oct. 1975). Order from NTIS as ADA019648, $5.00.

Key words: chemical breakdown of passivity; chloride; crevice corrosion; ellipsometry; iron; molybdenum; repassivation kinetics; stress corrosion.

This report consists of four parts as follows: Part I—A study of the influence of molybdate ions on the repassivation kinetics of iron in chloride solutions. Results indicate that molybdate ions precipitated

as ferrous molybdate in pits inhibit propagation but not initiation. Part II—Using a technique that allows ellipsometric studies to be made in a crevice, this work has found significantly lower film growth rates in a crevice on iron as compared to the rates observed outside the crevice. Part III—A review of the current state of our understanding of chemical breakdown of passivity is given with a listing of critical questions that remain to be resolved. A short bibliography on the subject is included. Part IV—A review of the qualitative applications of ellipsometry to study localized corrosion that have been developed at NBS is given.

NBSIR 75-923. **Corrosion of metallic piping on military bases—A survey,** P. W. Brown and J. R. Clifton, 21 pages (Nov. 1975). Order from NTIS as PB250767, $3.50.

Key words: corrosion; corrosion control; metallic piping; nondestructive evaluation; survey; water hardness.

The results of surveys of the extent of corrosion of metallic piping systems at selected military installations have been analyzed. Potable water, fire protection, heat distribution, cooling, and natural gas distribution systems are included in these surveys. The corrosion evaluation techniques used in these surveys and the types of protection applied are discussed. General recommendations regarding continuation and extension of these surveys are given.

NBSIR 75-933. **A study of the national humidity and moisture measurement system,** A. Wexler, 52 pages (Aug. 1975). Order from NTIS as PB248983, $4.50.

Key words: humidity; humidity measurement system; measurement of humidity; measurement of moisture; moisture; moisture measurement system; water vapor.

This study analyzes and assesses the status of the National Measurement System for humidity and moisture. It focuses on the physical process of measuring and controlling water vapor and moisture. It describes the nature, extent and economic dimensions of the system. It indicates impacts and trends, identifies deficiencies and shortcomings and shows the role NBS plays in the system. The study presents an overview of the complex structure of interrelated scientific, technological, social and economic components that form the basis of this system.

NBSIR 75-950. **Proposed criteria for use of the critical radiant flux test method,** I. A. Benjamin and C. H. Adams, 49 pages (Dec. 1975). Order from NTIS as PB250664, $4.00.

Key words: fire hazard; fire safety; flooring test; radiant panel.

The objective of this discussion is to present background and other technical data that will help in suggesting criteria to be used in conjunction with the Flooring Radiant Panel Test to determine the potential contribution to fire growth of floor covering systems for use in corridors and exitways.

NBSIR 75-951. **Correlation of floor vibration to human response,** J. R. Shaver, 32 pages (Dec. 1975). Order from NTIS as PB249094, $4.00.

Key words: analysis; experimental; floor systems; human response; random process; spectral analysis; vibration.

A new approach to the problem of perceptible floor vibrations is presented predicated on the realization that human activity and human response to this activity are random variables. Techniques for data reduction are discussed and a detailed description of one approach is given along with the associated computer program. Data from floor vibrations is compared with current criteria for human response to vibration.

NBSIR 75-957. **Finite element analysis of spotwelded, bonded and weldbonded lap joints,** R. A. Mitchell, R. M. Woolley, and S. M. Baker, 25 pages (Dec. 1975). Order from NTIS as PB250769, $3.50.

Key words: adhesive-bonded joints; bonded joints; double-lap joint analysis; finite element analysis; joining; joints; single-lap joint analysis; single-lap-joint bending; spotwelded joints; weld-bonded joints.

Finite element computer analyses of single-lap and double-lap structural joints are described. A planform analysis articulates the in-plane deformation of the joined sheet material and the lap-shear stresses acting through the spotwelds and/or adhesive. A longitudinal cross-section analysis computes out-of-plane bending effects, particularly important in single-lap joints, and adhesive peel stresses. Numerical results are presented that suggest a reasonable degree of mutual consistency between the planform analysis and the cross-section analysis. Although the basic finite element formulation is linear, nonlinear deformation can be simulated by a series of linear solutions. The computer output includes contour plots of stress and strain fields and exaggerated-scale plots of displacements.

NBSIR 75-960. **The police patrol car: State of the art,** R. G. Massey, 61 pages (Nov. 1975). Order from NTIS as PB249774, $4.50.

Key words: functional requirements; patrol cars; performance of patrol cars; police patrol cars; problems with patrol cars; state of the art survey.

This report, entitled "The Police Patrol Car: State of the Art" describes the functional requirements of police agencies for patrol cars, the manner in which these requirements are met, or not met, by vehicles currently in use, and a discussion of new automotive technology which might affect patrol car performance in the future.

NBSIR 75-966. **Measurements and observations of the toxicological hazard of fire in a Metrorail interior mock-up,** M. M. Birky, A. W. Coats, S. E. Alderson, J. E. Brown, M. Paabo, and B. Pitt, 20 pages (Feb. 1976). Order from NTIS as PB250768, $3.50.

Key words: blood; carbon dioxide; carbon monoxide; cyanide; fire; hydrogen chloride; hydrogen cyanide; oxygen; rats.

Oxygen depletion, carbon monoxide, carbon dioxide, hydrogen chloride and hydrogen cyanide were selected for measurement and identification in Metrorail fire tests.

Male rats exposed to the combustion products were examined for changes in blood chemistry, gross pathology and loss of function. Hydrogen cyanide and carbon monoxide levels in blood were elevated and functional changes were noted.

NBSIR 75-968. **Selected thermochemical data compatible with the CODATA recommendations,** V. B. Parker, D. D. Wagman, and D. Garvin, 35 pages (Jan. 1976). Order from NTIS as PB250845, $4.00.

Key words: CODATA compatible values; enthalpies of formation; entropy; Gibbs energy of formation; selected thermodynamic values; thermodynamic properties.

Selected thermochemical properties data at 298.15 K are given for 384 substances. The data are compatible with the current recommendations of the CODATA Task Group on Key Values for Thermodynamics. The set of values provided here is suitable for use as auxiliary data in evaluations of the thermochemical properties of compounds of the actinide elements. Rules used in the conversion of units and the rounding of numbers are stated.

NBSIR 75-971. **A fire hazard evaluation of the interior of WMATA Metrorail cars,** E. Braun, 34 pages (Dec. 1975). Order from NTIS as PB249776, $4.00.

Key words: flame spread; flammability; full-scale fire tests; laboratory fire tests; Metrorail cars; neoprene; smoke; transportation; urethane.

A series of fire tests was conducted for the Washington Metropolitan Area Transit Authority to assist them in assessing the potential for fire hazard in the new Metrorail subway cars. Results of small-scale laboratory tests were found inadequate for this assessment. Results of full-scale tests on mock-ups of the interior (and on a real car for a smoke penetration test) show that the potential for hazard arises primarily from the seat padding and covering and from the plastic wall lining. The hazard arises both from smoke development and from spread of flame and heat. The times to reach unacceptable conditions has been determined for several test conditions. It is recommended that the authorities review these times in the context of what they consider to be appropriate times for safe escape. Recommendations are made for increasing the amount of time available for escape. These would require changes in the seating and wall lining materials.

NBSIR 75-973. **Guide to improving the performance of a manipulator system for nuclear fuel handling through computer controls,** J. M. Evans, Jr., J. S. Albus, A. J. Barbera, R. Rosenthal, and W. B. Truitt, 53 pages (Nov. 1975). Order from NTIS as PB249255, $4.50.

Key words: computer control of automation systems; computer interface; computer software for robot control; hierarchical control of manipulators; position servos; trajectory control.

The Office of Developmental Automation and Control Technology of the Institute for Computer Sciences and Technology of the National Bureau of Standards provides advising services, standards and guidelines on interface and computer control systems, and performance specifications for the procurement and use of computer controlled manipulators and other computer based automation systems. These outputs help other agencies and industry apply this technology to increase productivity and improve work quality by removing men from hazardous environments.

In FY 74 personnel from the Oak Ridge National Laboratory visited NBS to discuss the feasibility of using computer control techniques to improve the operation of remote control manipulators in nuclear fuel reprocessing. Subsequent discussions led to an agreement for NBS to develop a conceptual design for such a computer control system for the PaR Model 3000 manipulator in the Thorium Uranium Recycle Facility (TURF) at ORNL. This report provides the required analysis and conceptual design. Complete computer programs are included for testing of computer interfaces and for actual robot control in both point-to-point and continuous path modes.

NBSIR 75-974. **The demonstration of experimental lead paint hazard abatement in Atlanta, Georgia,** T. H. Boone, H. W. Berger, A. P. Cramp, and H. A. Jackson, 121 pages (Dec. 1975). Order from NTIS as PB249777, $5.50.

Key words: abatement; barrier materials; building materials; children; housing; lead-based paint; lead poisoning; paint removal.

This report describes the second stage of an experimental lead paint hazard abatement program carried out in 80 dwelling units in Atlanta, Georgia. The entire program will ultimately involve the abatement of lead paint hazards in a total of approximately 250 dwelling units distributed over three or more cities.

The procedures demonstrated in this field testing program were: paint removal using chemical solvents; paint removal using three heat producing devices; the replacement of components such as windows, doors, and wood trim and the installation of flexible sheet materials, rigid boards, plaster products and aggregate filled coatings, over existing lead paint on walls. Also evaluated was the covering of deteriorated, lead paint coated floors with plywood.

The report includes procedures for inspecting and selecting dwellings for lead paint hazard abatement, evaluations of the suitability and implementation characteristics of the abatement methods, and recommendations for their use.

Subsequent reports will present the results of comparable programs in additional cities and a final report will compare the cost-effectiveness of the alternative abatement methods.

NBSIR 75-976. **Standards and measurement capabilities in the Kingdom of Saudi Arabia,** A. A. Bates, 37 pages (Spring 1975). Order from NTIS as PB248986, $4.00.

Key words: building codes; industrialization; less-developed country; SASO; Saudi Arabia; standardization; tentative standards.

The Saudi Arabian Standards Organization (SASO) is operating under uniquely difficult circumstances. Basic sources of difficulties are: (1) almost total lack of any industries for consultation and cooperation, (2) extreme speed at which Saudi Arabia is attempting transformation into an urban-industrial state, (3) unavailability of well-trained indigenous Saudi personnel, either scientific-technical or secretarial-clerical, and (4) lack of SASO laboratory facilities for standardization research work.

Operating procedures which SASO has adopted are based on consensus principles utilized in countries with advanced industrial economies. Such procedures are not now applicable in Saudi Arabia. Only the Saudi Portland Cement industry now offers opportunity for consensus standardization.

Until industrialization has advanced in the Kingdom, SASO should use Interim Procedures to produce Tentative Standards for national use. The Interim Procedures should permit direct and immediate adoption of necessary standards from reliable national and international sources with minimum modification. The nature and terms of use of Tentative Standards must be defined for public understanding.

SASO should not play the central role in the enforcement of SASO standards. SASO should have an advisory relationship with authorities charged with mandatory standards enforcement. SASO should not now undertake the development of a national Saudi building code, although it must produce the standards upon which a building code may be promulgated by a related agency appointed for that purpose.

NBSIR 75-977. **Development of solid state samplers for work atmospheres: Phosphine,** B. Greifer and J. K. Taylor, 32 pages (Jan. 1976). Order from NTIS as PB251220, $4.00.

Key words: air analysis; air sampling; gas analysis; industrial hygiene; phosphine; sorber; work atmosphere.

Investigations to find suitable solid-state sorber materials for phosphine in work atmospheres at the ppm level are described. The best sorber to date is silver nitrate-impregnated silica gel. Some difficulties remain to be overcome before a procedure for determining the amount of phosphine adsorbed can be recommended.

NBSIR 76-979. **Intercomparison procedures for gage blocks using electromechanical comparators,** J. S. Beers and C. D. Tucker, 23 pages (Jan. 1976). Order from NTIS as PB248992, $3.50.

Key words: calibration; comparator; gage blocks; length; measurement process.

The widely used procedures for calibrating gage blocks by comparison with blocks of known length generally lack the redundancy needed to evaluate measurement uncertainty or the controls needed to monitor the process on a continuing basis. A detailed description

is given here for the systematized intercomparison of groups of four nominally equal gage blocks using an electromechanical comparator. Two of the blocks are unknowns and two are standards. The process provides the redundancy needed for evaluating uncertainty and for continuous monitoring. Gage block thermal effects, equalization time, handling techniques, and observation sequence are described.

NBSIR 76-980. **NBS space processing research,** E. Passaglia and R. L. Parker, 217 pages (Feb. 1976). Order from NTIS as PB250849, $7.75.

Key words: convection; crystal growth; crystal perfection; microgravity; purification; space processing.

This report describes NBS work for NASA in support of NASA's Space Processing Program covering the period November 1, 1974 to December 31, 1975. The objectives of the NBS program are to perform ground-based studies (and, where appropriate, space-based studies) of those aspects of space that could possibly provide a unique environment for making materials more perfect or more pure. The approach taken deals primarily with experimental and theoretical studies of the possible effects of the absence of gravitational forces on those materials preparation processes where the presence of gravity may be important in reducing perfection or purity. The materials preparation processes studied comprise six tasks in the areas of crystal growth, purification and chemical processing, and the preparation of composites.

NBSIR 76-983. **A survey of manufacturers' views on the ETIP procurement experiment. Volume two: Water heaters,** P. C. Goodman, 34 pages (Jan. 1976). Order from NTIS as PB251213, $4.00.

Key words: energy-efficient products; Experimental Technology Incentives Program; life-cycle costing; procurement experiments; water heaters.

This report describes the findings of a survey of seven water heater manufacturers by the Center for Consumer Product Technology. The survey was conducted for the Experimental Technology Incentives Program (ETIP) as part of its evaluation of the Federal Supply Service (FSS) procurement of water heaters. Survey questions were designed to obtain manufacturers' views on the use of Government procurement policies as a means of increasing the rate of introduction of new technologies into the consumer marketplace. The questions covered the following areas: (1) reasons for participation or nonparticipation of a manufacturer in the ETIP experiment; (2) problems that a manufacturer encounters with existing Federal procurement practices; (3) acceptability of using life-cycle costing in the bidding procedure; and (4) effect of the most recent Government procurement on present and future company operations, including support for engineering and investment in research, types of themes used in advertising campaigns, etc. Results of the survey are reported, and implications are drawn for future ETIP involvement in Government procurement activities.

NBSIR 76-986. **Building energy authority and regulations survey: State activity,** R. M. Eisenhard, 52 pages (Jan. 1976). Order from NTIS as PB250858, $4.50.

Key words: authority; building; energy; legislation; regulations; state.

This report provides the status of State authority to regulate energy use in new buildings and the status of bills creating such authority that were pending in the 1975 legislative session. Regulations that have been developed are identified and described. Legislation relating to solar energy, retrofitting, insulation and other building energy matters, is identified and the status indicated.

NBSIR 76-987. **Effect of insulation on the surface temperature of roof membranes,** W. J. Rossiter, Jr. and R. G. Mathey, 20 pages (Feb. 1976). Order from NTIS as PB250857, $3.50.

Key words: built-up roofing; insulation; performance; radiative cooling; roofing; solar heating; surface temperature.

The surface temperatures of black, gray and white roofs were calculated for various thicknesses of insulation located between the membrane and roof deck. The calculations were performed using a steady-state heat balance equation to illustrate the increase in roof surface temperatures due to solar radiation.

The calculations indicate that the first increment, about 1 inch (25 mm), of insulation causes a significant rise in the roof surface temperature due to solar radiation. Increasing the amount of insulation above this first increment to greater thicknesses does not appreciably increase the roof surface temperature.

NBSIR 76-991. **Evaluation of transparent electro-photographic film and camera system,** T. C. Bagg, 8 pages (Jan. 1976). Order from NTIS as ADA021255, $3.50.

Key words: add-on films; information storage; microforms; transparent electrophotographic material.

On behalf of the Naval Supply Systems Command, the National Bureau of Standards was requested to assist in the evaluation of new microfilm techniques and materials which permit the adding-on of images at various times. This is an interim report on the initial evaluation of the AB Dick/Scott System 200 which uses transparent electrophotographic materials.

NBSIR 76-992. **Studies of deformation at sliding wear tracks in iron,** A. W. Ruff, 70 pages (Feb. 1976). Order from NTIS as ADA021295, $4.50.

Key words: electron channeling; iron; metals; plastic deformation; surfaces; wear.

Determinations of strains have been made on the surface and subsurface on specimens of high purity iron after different amounts of sliding wear have taken place. The method involved the measurement of loss of intensity (contrast) of particular electron channeling lines obtained from small selected areas near the wear track. Through the use of a calibration specimen deformed plastically to a range of strain values, the channeling line contrast loss was related to plastic strain. Strain maps lateral to the wear track and below the original surface were obtained for different total sliding distances by removing controlled thicknesses of iron using electropolishing. In all cases the maximum strain was found at the track center location at the surface and the strains decreased steadily with depth below the track. At 50 g load the strains vanished at about 40 $\mu$m depth. Significant strains were found to exist outside the wear track boundaries. The results are compared with other studies previously reported. There was no indication of a soft or less hardened surface layer in any of the specimens studied.

NBSIR 76-1000. **The construction, operation and performance of a reactive gas generator; with specific application to HCHO, $CH_3CHO$, $CH_2CHCHO$, $SO_2$, HCN and HCl production,** J. A. Walker and W. Tsang, 55 pages (Jan. 1976). Order from NTIS as PB251219, $4.50.

Key words: acetaldehyde; acrolein; formaldehyde; gas chromatography; hydrogen chloride; hydrogen cyanide; pollution; pyrolysis; reactive gas generator; sulfur dioxide.

An instrument capable of generating a variety of reactive gases in trace levels has been constructed and tested. Operational details, with specific application to HCHO, $CH_3CHO$, $CH_2CHCHO$, $SO_2$, HCN and HCl production are discussed.

NBSIR 76-1003. **Thermal conductivity and electrical resistivity of six copper-base alloys,** M. C. I. Siu, W. L. Carroll, and T. W. Watson, 22 pages (Mar. 1976). Order from NTIS as PB251211, $3.50.

Key words: copper-base alloy properties; electrical resistivity; Smith-Palmer equation; thermal conductivity.

Measurements of the thermal conductivity, $\lambda$ and electrical resistivity, $\rho$, of oxygen free copper and six copper-base alloys in the temperature range 298 to 924 K are presented. Except for copper, the $\lambda$ and $\rho$ values of copper alloys having the same chemical composition as those given in this paper have not been previously reported. The measured values of $\lambda(W \cdot m^{-1} \cdot K^{-1})$ and $\rho(\Omega \cdot m)$ were found to conform, within 10 percent, to the predictions of the Smith-Palmer equation, $\lambda = 2.39 \times 10^{-8}\ T/\rho + 7.50$ $[W \cdot m^{-1} \cdot K^{-1}]$, where T is the thermodynamic temperature expressed in kelvins.

NBSIR 76-1008. **Energy conservation through the facilitation of increased blended cement use,** P. W. Brown, J. R. Clifton, and G. Frohnsdorff, 28 pages (Feb. 1976). Order from NTIS as PB251218, $4.00.

Key words: blast furnace slag; blended cements; energy conservation; fly ash.

About 95 percent of the cement produced in the United States is portland cement and its manufacture requires about 2 percent of the energy consumed annually in the nation's industrial processes. The production of blended cements containing substantial amounts of fly ash or blast furnace slag and their substitution for portland cement appears attractive from the standpoint of energy conservation. While production and utilization of blended cements in other industrialized countries is extensive, blended cements account for less than 1 percent of the total cement production in the U.S. The reasons for the small U.S. production of blended cements are discussed in the contexts of standards revision and the need for the development of additional data as a basis for this revision.

NBSIR 76-1010. **Optical materials characterization,** A. Feldman, D. Horowitz, R. M. Waxler, I. H. Malitson, and M. J. Dodge, 27 pages (Feb. 1976). Order from NTIS as PB250654, $4.00.

Key words: birefringence; elastooptic constants; infrared-laser window materials; interferometry; KCl; photoelasticity; piezooptic constants; refractive index; stress-optical constants; thermal coefficient of refractive index.

Refractive index and the photoelastic constants have been measured on specimens of reactive atmosphere processed (RAP) KCl and KCl nominally doped with 1 percent KI. The refractive indices were measured by the minimum deviation method in the wavelength range 0.25 $\mu$m to 15.5 $\mu$m. Measurements were made near 20 and near 34 °C on the RAP specimen and near 20 °C on the doped specimen. Each set of experimental data was fitted to a three term Sellmeier-type dispersion equation. The temperature coefficient of index was then computed for the RAP KCl. The data for the different types of KCl were compared to each other and to earlier reported data on commercial KCl. The piezo-optical constants $q_{11}$, $q_{12}$ and $q_{44}$ and the elasto-optical constants $p_{11}$, $p_{12}$ and $p_{44}$ were obtained at 10.6 $\mu$m for the RAP and doped KCl. The measurements required the use of a modified Twyman-Green interferometer capable of measuring fringe shifts ~0.002 of a wave. Within experimental error the coefficients of the two materials agree. Negligible dispersion was found for $q_{11}$, $q_{12}$, $p_{11}$ and $p_{12}$ between the visible and 10.6 $\mu$m while a small dispersion was found for $q_{44}$ and $p_{44}$.

*This column lists all outside publications by the NBS staff, as soon as possible after issuance as practical. For completeness, earlier references not previously reported may be included from time to time.*

15707. Morrissey, B. W., Stromberg, R. R., **Bound fraction measurements of adsorbed blood proteins,** (Proc. American Chemical Society Meeting on Biomedical Applications of Polymers, Chicago, Ill., Aug. 25-29, 1973), Paper in *Biomedical Applications of Polymers*, H. P. Gregor, Ed., **7,** 57-68 (Plenum Press, New York, N.Y., 1975).

Key words: blood proteins; infrared bound fraction; protein adsorption; protein conformation.

The likelihood that surface-induced blood coagulation results from specific protein-material interactions has led to a study of the conformation of adsorbed blood proteins. Infrared difference spectroscopy was used to determine the bound fraction, i.e., the fraction of carbonyl groups of an adsorbed molecule directly interacting with the surface, of serum albumin, prothrombin, and fibrinogen in situ. Measurements were carried out on individual proteins as a function of the amount adsorbed, time of adsorption, pD, and ionic strength using a silica surface.

The results obtained for serum albumin and prothrombin indicate that the internal bonding of these globular proteins is sufficient to prevent changes in the structure while adsorbed, even at low surface population. The bound fraction of fibrinogen increases with increasing adsorbance suggesting possible interfacial aggregation. The conformation of all three proteins was found to be independent of the time of adsorption, although major differences in the rates of adsorption were observed.

15708. Flynn, D. R., Pallett, D. S., **Simplified method for alculating the transmission loss of two-element partitions,** *J. Acoust. Soc. Am.* **58,** No. 6, 1341-1342 (Dec. 1975).

Key words: airborne sound transmission; architectural acoustics; building acoustics; sound reduction index; sound transmission loss; transmission loss.

Three alternative procedures—a table look-up, a nomograph, and a specially devised slide rule, depending on the preference of the user—are given for rapid computation of the sound transmission loss of a composite partition.

15709. Cezairliyan, A., Beckett, C. W., **Measurement of thermal properties at high pressures by transient techniques,** Chapter 7 in *Thermochemistry and Thermodynamics*, H. A. Skinner, Ed., **10,** 247-260 (Butterworths, London, 1975).

Key words: heat capacity; high pressures; thermal conductivity; thermal diffusivity; thermal properties; transient techniques.

Measurements of selected thermal properties (heat capacity, thermal conductivity and thermal diffusivity) at high pressures (up to 100 kbars) using transient techniques are reviewed.

15710. Feldman, A., **Relations between electrostriction and the stress-optical effect,** *Phys. Rev. B* **11,** No. 12, 5112-5114 (June 15, 1975).

Key words: electrostriction; electrostrictive coefficients; free energy; stress-optical constants; stress-optical effect.

Relationships are obtained between the stress-optical constants and the electrostrictive coefficients of solid materials. These results, which are dependent upon the geometric boundary conditions, encompass the apparent differences in the relationships derived by different authors.

15711. Geist, J., **The role of radiometry in solar energy utilization,** *Proc. Smithsonian-Eppley Symp. on Solar Radiation Measurement and Instrumentation, Rockville, Md., Nov. 13-14, 1973,* pp. 79-94 (1973).

Key words: effective irradiance; radiometry; solar energy conversion.

This paper identifies the various radiometric problems that are of importance to solar energy utilization. Some basic definitions are presented, and the effective irradiance is shown to be a fruitful concept. Three different activities of the solar energy community that require effective irradiance data are discussed. Finally, it is shown that these different activities apply different constraints to effective irradiance data; the optimum type of data for one activity not necessarily being at all suitable for the other two activities.

15712. Kelly, G. E., Didion, D. A., **A laboratory test of the modular concept as applied to gas-fired boilers,** (Proc. Conf. on Improving Efficiency in HVAC Equipment and Components for Residential and Small Commercial Buildings, Oct. 7-8, 1974), Paper in *Proceedings of Conference on Improving Efficiency in HVAC Equipment and Components for Residential and Small Commercial Buildings*, D. A. Didion and V. Goldschmidt, Eds., pp. 18-30 (Purdue Research Foundation, Lafayette, Ind., Oct. 1974).

Key words: boiler oversizing; efficiency vs. heating load; modular boilers; modular concept; seasonal efficiency.

The modular concept of boiler operation was examined in a laboratory test of five gas-fired, cast iron, hydronic boilers. Four of the boilers, each having an input rating of 85,000 Btu per hour, were arranged so that they could either be operated like a single boiler (i.e., all of the boilers either on or off) or as a modular installation in which the boilers are sequentially fired to match the number in operation with the heating load. The fifth boiler had an input rating of 300,000 Btu per hour and was operated as a single boiler installation. Efficiency vs. heating load curves were obtained for the single boiler installation, the four small boilers run like a single boiler and the modular installation operated with and without water flowing through the "idle" modules. These efficiency curves were then used to theoretically predict the effect of the modular concept and boiler oversizing on the seasonal efficiency of gas-fired heating plants.

15713. Achenbach, P. R., **Status of energy standards for heating, ventilating and air-conditioning systems in buildings,** (Addendum to Proc. of Conf. on Improving Efficiency in HVAC Equipment and Components for Residential and Small Commercial Buildings, Oct. 7-8, 1974), Paper in *Addendum to Proceedings of Conference on Improving Efficiency in HVAC Equipment and Components for Residential and Small Commercial Buildings*, P. Newman, Ed., pp. A134-A142 (Purdue Research Foundation, Lafayette, Ind., 1975).

Key words: energy conservation; energy standards for mechanical systems; heating and air-conditioning systems; state energy regulations.

The circumstances in energy supply are described which caused the National Conference of States on Building Codes and Standards to request the National Bureau of Standards in 1973 to develop an interim standard for energy conservation in new buildings. The progress in development of such a standard by NBS and the American Society of Heating, Refrigerating and Air-Conditioning Engineers is chronicled to October 1974. The principal policy issues raised by the preparation of an energy conservation standard which could become the basis for State and local regulations are discussed. The components of heating and air-conditioning systems which are at issue between the NBS and ASHRAE documents for inclusion in the energy conservation standard are identified. The long-range objectives of the Federal Energy Administration in developing energy conservation requirements for buildings are summarized.

15714. Hummer, D. G., Kunasz, P. B., **Migration of excitation in transfer of spectral-line radiation,** *J. Quant. Spectrosc. Radiat. Transfer* **16,** 77-96 (1976).

Key words: diffusion; excitation exchange; radiative transfer; spectral line profiles.

A simple mathematical model is developed for the transfer of energy through a gas by the combined effect of radiative transfer and migration of excitation. The "excitation" is carried through the gas by a succession of atoms which experience resonant excitation exchange; it thus appears to random walk through the medium. The theory developed here is valid when the distance traveled by an atom while excited is much larger than the typical distance at which two atoms can exchange excitation (roughly $10^{-6}$ cm). The model is expressed in terms of a pair of coupled transport equations for the intensity of radiation and the density of excited atoms, which are solved by means of a generalized discrete-ordinate technique. Extensive numerical results are obtained and discussed in terms of characteristic lengths for the various transfer processes. Substantial effects of migration are seen in both the distribution of excited atoms near the cell windows and the line profile of the emergent radiation for typical laboratory conditions.

15715. Fiori, C. E., Myklebust, R. L., Heinrich, K. F. J., Yakowitz, H., **Prediction of continuum intensity in energy-dispersive x-ray micro-analysis,** *Anal. Chem.* **48,** No. 1, 172-176 (Jan. 1976).

Key words: background; continuous x rays; electron probe microanalysis; energy-dispersive x-ray analysis; lithium-drifted silicon detector.

A method for background prediction in electron-excited energy-dispersive x-ray spectrometry (EDS) is described. This method yields the intensity of the continuous radiation which would be observed by the detector as a function of x-ray photon energy. The method can be incorporated into existing electron probe microanalysis data reduction programs. Tests indicate that the proposed background correction scheme is satisfactory for quantitative analysis.

15716. Chabay, I., Klauminzer, G. K., Hudson, B. S., **Coherent anti-Stokes Raman spectroscopy (CARS): Improved experimental design and observation of new higher-order processes,** *Appl. Phys. Lett.* **28,** No. 1, 27-29 (Jan. 1, 1976).

Key words: CARS; diphenyloctatetraene (dilute solution); four-wave numbering; HORSES; nonlinear optics; Raman spectroscopy.

The development of the optical and electronic arrangement which has permitted the straightforward measurement of coherent anti-Stokes Raman spectra (CARS) and of higher order processes not previously reported is described in this paper. The CARS spectrum of a dilute solution of diphenyloctatetraene in benzene is presented. This spectrum demonstrates the significantly greater signal-to-noise ratio possible with CARS as compared to conventional Raman techniques. Higher-order Raman spectral excitation studies (HORSES) are described which indicate the presence of a six-wave or a second-order four-wave mixing process.

15717. Shine, R., Gerola, H., Linsky, J. L., **Diffusion effects on the line intensities of He I and He II in the solar transition region,** *Astrophys. J.* **202,** L101-L105 (Dec. 1, 1975).

Key words: chromosphere-sun; coronal holes; diffusion; transition region-sun; ultraviolet spectrum-sun.

We develop a heuristic treatment of diffusion in the solar chromosphere-corona transition region. We find that diffusion becomes increasingly important with steeper temperature gradients, in active and quiet regions relative to coronal holes, and with increasing excitation potential. Numerical calculations are made for the resonance lines of He I and He II and show that diffusion can enhance these lines. Thus the helium lines may appear relatively weak in coronal holes due to a weakening of the enhancement mechanism. Most transition region lines will be less affected by diffusion than He I or He II.

15718. Hebner, R. E., Jr., Cassidy, E. C., Jones, J. E., **Improved techniques for the measurement of high-voltage impulses using the electrooptic Kerr effect,** *IEEE Trans. Instrum. Meas.* **IM-24,** No. 4, 361-366 (Dec. 1975).

Key words: automation; electrical measurements; electrooptics; high voltage measurement; Kerr effect; optical coupling; pulse measurement.

The purpose of this paper is to present two methods of accumulating, analyzing, and presenting in real time the data generated by a Kerr system in response to a high-voltage impulse. These methods provide immediate information concerning selected electrical parameters in a form which is easily interpretable by most personnel. The first method uses an electronic counter to determine the number of optical transmittance maxima, i.e., light pulses, during the high-voltage impulse. From this count, the peak value of impulse can be calculated. The second method, which can be more accurate and does provide information concerning waveshape, uses a digital recorder to store the output waveform from the Kerr system. A computer is then used to reconstruct the voltage impulse and to determine such parameters as the peak value and risetime of the impulse.

15719. Hellwig, H., **A review of precision oscillators,** *Proc. 6th Precise Time and Time Interval (PTTI) Meeting, Washington, D.C., Dec. 3-5, 1974,* pp. 59-81 (Dec. 1974).

Key words: accuracy; atomic clocks; clocks; crystal oscillator; frequency standards; stability; survey of clocks.

Precision oscillators used in PTTI applications include quartz crystal, rubidium gas cell, cesium beam, and hydrogen maser oscillators. A general characterization and comparison of these devices is given including accuracy, stability, environmental sensitivity, size, weight, power consumption, availability and cost. Areas of special concern in practical applications are identified and a projection of future performance specifications is given. An attempt is made to predict physical and performance characteristics of new designs potentially available in the near future.

15720. Petersons, O., Anderson, W. E., **A wide-range high-voltage capacitance bridge with one PPM accuracy,** *IEEE Trans. Instrum. Meas.* **IM-24,** No. 4, 336-344 (Dec. 1975).

Key words: capacitance measurements; current comparators; current transformers; high voltage bridges; high voltage capacitors; high voltage measurements; impedance bridges.

An impedance bridge for high-voltage capacitance and related measurements to an accuracy of 1 ppm is described and the background research and development which made it possible is documented. The bridge is of the transformer-ratio-arm type, the principal components of which are a comparator and several two-stage transformers. The bridge can be used to measure capacitance ratios over a range from 1/1 to $10^7$/1 with a resolution between 0.1 and 0.25 ppm. The highest accuracies are obtained at the principal power frequencies of 50-60 Hz, but the bridge is usable up to 400 Hz. The factors which limited the accuracy of previously developed bridges of this type were reexamined and their influence reduced. Two independent methods were developed for the calibration of the bridge.

15721. DiMarzio, E. A., Bishop, M., **The nature of the helix-random coil transition of biological macromolecules attached to a surface,** *Biopolymers* **13,** 2331-2348 (1974).

Key words: biopolymers; helix-coil transition; phase transitions in biopolymers; self-assembly; structural transformations; surface adsorption.

The effect of the presence of a surface on the helix-random coil transition is investigated. It is found that a grand canonical ensemble formation used previously to solve exactly the problem of a polymer between two plates can be used to solve approximately the problem of DNA near a plane surface. The formalism is applied to the homogeneous perfect-matching model of infinite molecular weight. A crucial part of the calculation for double-stranded molecules involves the evaluation of the entropy of the loops connecting the helical portions of the double-stranded chains. One obtains as a measure of the configurational freedom of a loop $As^j/j^c$ where $c$ has the following values: for a loop connecting two helical regions both off the surface $c=3/2$; for a loop connecting a helical region on the surface to a helical region off the surface $c=5/2$; for a loop connecting helixes both on the surface $c=4$. Corresponding values for an $n$-stranded molecule are $c=(3n-3)/2$, $c=(4n-3)/2$, $c=(5n-2)/2$. In all cases, the effect of the surface is to sharpen the transition. In the case of double-stranded molecules, the transition becomes first order. We take the view that self-assembly of biological macromolecules can be considered as a sharp thermodynamic phase transition. Thus, the above systems become models of self-assembling systems. They are also relevant to the problem of surface-induced enzymatic activity.

15722. Heinrich, K. F. J., Yakowitz, H., **Absorption of primary x rays in electron probe microanalysis,** *Anal. Chem.* **47,** No. 14, 2408-2411 (Dec. 1975).

Key words: absorption correction; primary emission; quantitative electron probe analysis; x-ray absorption factor.

Available experimental evidence concerning absorption in x-ray targets, corrected for fluorescence due to the continuum, is generalized to give the formula, $f_p=(1+a\gamma\chi)^{-2}$, in which $f_p$ is the primary x-ray absorption factor, $\gamma=(E_o^{1.65}-E_q^{1.65})$, $E_o$(kV) is the operating voltage, $E_q$(kV) the critical excitation voltage, $\chi=\mu$ cosec $\psi$, $\mu$ is the mass absorption coefficient for the respective target and line, $\psi$ is the x-ray emergence angle, and $a=1.2\times10^{-6}$ g/cm$^2$. The presumed effect of the atomic number of the target on $f_p$ is overestimated by Philibert's formula. It is smaller than the statistical spread of experimental data, and can therefore be neglected.

15723. Mihalas, D., Kunasz, P. B., Hummer, D. G., **Solution of the comoving-frame equation of transfer in spherically symmetric flows. I. Computational method for equivalent-two-level-atom source functions,** *Astrophys. J.* **202,** 465-489 (Dec. 1, 1975).

Key words: atmospheres, stellar; atomic and molecular processes; line formation; radiative transfer.

The equation of radiative transfer in the comoving frame makes possible an economical solution of the line formation problem in spherical atmospheres expanding with arbitrarily large velocities. A stable differencing scheme and a frequency-by-frequency elimination procedure have been developed to solve the partial differential equations that describe the radiation field in the comoving frame. Numerical results were obtained for a large number of illustrative models involving line formation by two-level atoms, electron scattering, and continuous absorption. Selected results that simulate situations in the stellar winds of hot stars and similar objects are discussed. In addition to P Cygni and other very broad profiles, extreme center-to-limb variations are obtained that show both limb darkening and limb brightening. For very high velocity flows with very weak or nonexistent continuum and electron-scattering opacities, the flux profiles are very nearly symmetric about the laboratory wavelength and have shapes reminiscent of those observed in the nuclei of Seyfert galaxies. Comparisons are presented between the results of Sobolev-type escape probability calculations and those obtained here. The force of radiation on the gas is examined in a number of situations; the mechanism mentioned by Noerdlinger and Rybicki for the disruption of radiatively driven envelopes in planar geometries is shown to become inoperative for even slightly extended spherical systems.

15724. McQueen, J. T., Levinsohn, D. M., Waksman, R., Miller, G. K., **The evaluation of the Shirley Highway Express-Bus-on-Freeway Demonstration Project,** *Report DOT/UMTA* **7,** 133 pages (Available as PB247637 from the National Technical Information Service, Springfield, Va. 22151, Aug. 1975).

Key words: bus transit; busways; carpools; energy impacts; mode choice; pollution reduction.

The Shirley Highway Express Bus-on-Freeway Project began in June 1971 and ended December 31, 1974. The principal goal of the project was to demonstrate that express bus-on-freeway operations can improve the quality of bus service and lead to an increase in the people moving capability of peak period transportation facilities for an entire urban corridor. Secondary project goals were to demonstrate the effectiveness of this technology as a means of reducing auto pollutant emissions and gasoline consumption, improving the mobility of the transportation disadvantaged and the economic condition of the transit operator.

This report summarizes project performance with respect to the attainment of the above goals. An analysis of bus operations is presented which shows that the project effected an improvement in the quality of the Shirley Highway Corridor bus service as evidenced by the reduction in travel times by bus, and the increase in both the reliability and the coverage of the bus systems. Trends in peak period traffic volumes are presented which show that the subsequent increase in bus patronage and bus' share of Corridor commuters led to an increase in the peak period people moving capability of the Corridor. Corridor people moving capability was also increased by project stimulated growth in carpooling.

Data from surveys of Corridor commuters were used in identifying factors important in commuters' decision to use bus or to carpool. Bus users who formerly had commuted by auto reported that the most important factors in their decisions to switch from auto were the expense and discomfort of commuting by auto, and the express features of project bus service. Factors reported as most important in decisions to join or form a carpool were reduction in commuting costs, special parking privileges for carpools, and availability of the express busway to carpools.

The report concludes with an analysis of project performance with respect to the secondary goals. The project resulted in significant reductions in peak period auto usage, auto pollutant emissions and gasoline consumption. The utilization of project bus service by transportation disadvantaged persons is discussed and project costs and revenues are analyzed.

15725. Zalubas, R., Reader, J., Corliss, C. H., **$4s^24p^4$-$4s4p^5$ transitions in five-times-ionized yttrium (YVI),** *J. Opt. Soc. Am.* **66,** No. 1, 35-36 (Jan. 1976).

Key words: spectra; ultraviolet; wavelengths; yttrium.

The spectrum of yttrium has been observed in a sliding spark discharge at peak currents up to 2000 Å on the 10.7 m normal and grazing incidence vacuum spectrographs at NBS. From these observations, the group of $4s^24p^4$-$4s4p^5$ transitions in YVI, which lie in the region 457-766 Å, has been identified and measured, thus yielding values for the 4 levels of the $4s4p^5$ configuration and revised values for the 5 levels of the $4s^24p^4$ configuration. The energy parameters obtained from a least-squares fit to the observed levels are compared with Hartree-Fock calculations.

15726. Mulholland, G. W., **Self-diffusion through a liquid-vapor interface,** *J. Chem. Phys.* **64,** No. 2, 862-870 (Jan. 15, 1976).

Key words: continuous interface profile; diffusion equation; hypergeometric differential equation; interfacial force; liquid-vapor interface; Markov Stochastic model; self-diffusion.

A diffusion equation containing information about the structure of the liquid-vapor interface is constructed to describe self-diffusion in a one component, two phase fluid. Analysis of the diffusion equation in the limit of vanishing interface thickness leads to interfacial matching conditions, one of which was previously assumed ad hoc. From a study of the asymptotic long time behavior of the equation, it is found that an ordinary self-diffusion experiment can not be expected to provide information about the interface structure. A numerical study of the diffusion equation shows that the reduced time to diffuse through the interface is independent of the ratio of the vapor and liquid densities, which is the one free parameter in the diffusion equation. An experimental test of our prediction that it takes the same time to diffuse from the liquid to the vapor as vice versa is suggested.

15727. Dyer, C. S., Trombka, J. I., Schmadebeck, R. L., Eller, E., Bielefeld, M. J., O'Kelley, G. D., Eldridge, J. S., Northcutt, K. J., Metzger, A. E., Reedy, R. C., Schonfeld, E., Seltzer, S. M., Arnold, J. R., Peterson, L. E., **Radioactivity observed in the sodium iodide gamma-ray spectrometer returned on the Apollo 17 mission,** *Space Sci. Instrum.* **1,** 279-288 (1975).

Key words: Apollo 17; background; cosmic-ray proton; induced radioactivity; secondary neutrons; sodium iodide detector.

In order to obtain information on radioactive background induced in the Apollo 15 and 16 gamma-ray spectrometers (7 cm × 7 cm NaI) by particle irradiation during spaceflight, an identical detector was flown and returned to earth on the Apollo 17 mission. The induced radioactivity was monitored both internally and externally from one and a half hours after splashdown. When used in conjunction with a computation scheme for estimating induced activation from calculated trapped proton and cosmic-ray fluences, these results show an important contribution resulting from both thermal and energetic neutrons produced in the heavy spacecraft by cosmic-ray interactions.

15728. Leep, D., Gallagher, A., **Excitation of the Mg and $Mg^+$ resonance lines by electron impact on Mg atoms,** *Phys. Rev. A* **13,** No. 1, 148-155 (Jan. 1976).

Key words: electron excitation; magnesium.

We have measured the optical excitation functions and polarizations of the Mg resonance line (2852 Å) and of the $Mg^+$ resonance lines (2796 Å, 2803 Å, unresolved) arising from ionizing excitation of magnesium atoms, for electron-impact energies from the excitation threshold to 1400 eV. In our crossed-beam apparatus, the electron-beam energy resolution was ≈0.25 eV for energies below 10 eV, and the atom beam was optically thin. The excitation function of the ionic lines was normalized to that of the atomic line by relative intensity measurements. The 2852-Å excitation function, when normalized to Born theory in the high-energy limit, has a maximum cross section of $17.3\pi a_0^2 \pm 3$ percent 18.5 eV. This excitation function is graphically compared with the resonance-line excitation functions of Na, Ca, and Li previously measured in this laboratory. The 2852-Å polarization function is consistent with the theoretical threshold limit of +100 percent, and has a sharp feature near 5 eV which cannot be due to cascading.

15729. Mahan, A. H., Gallagher, A., Smith, S. J., **Electron impact excitation of the 3S, 3P, and 3D states of H,** *Phys. Rev. A* **13,** No. 1, 156-166 (Jan. 1976).

Key words: electron excitation; hydrogen.

The relative excitation function for electron-impact excitation of H to yield Balmer $\alpha$ has been measured from threshold to 500-eV collision energy in a crossed-beam apparatus. The relative contributions of the 3S, 3P, and 3D states to this excitation function have been measured by modulating the electron beam and discriminating on the

basis of their different lifetimes for radiative decay after excitation. The resulting set of relative 3*S*, 3*P*, and 3*D* cross sections has been normalized by equating the total measured Balmer-$\alpha$ cross section at 500 eV to the Born approximation. The normalized cross sections are then compared to available theories at lower energies. In contrast to virtually all known excitation cross sections of neutral atoms, which fall below the Born theory at low energies, the H ($1S \rightarrow 3D$) cross section exceeds the Born theory, apparently owing to coupling between the 3*D* and 2*P* states.

15730. Murphy, T. A., Sengers, J. V., Sengers, J. M. H. L., **Scaled parametric equation of state for steam in the critical region,** (Proc. 8th Int. Conf. on the Properties of Water and Steam, Giens, France, Sept. 23-27, 1974), Paper in *Proceedings of the 8th International Conference on the Properties of Water and Steam*, P. Bury, H. Perdon, and B. Vodar, Eds., **1**, 603-613 (Ministère de l'Industrie et de la Recherche, Paris, France, 1975).

Key words: critical density; critical exponents; critical pressure; critical region; critical temperature; equation of state; linear model; scaled equation; steam.

The anomalous thermodynamic behavior of fluids near the critical point can be described in terms of scaling laws. In recent years a parametric equation of state, the so-called Linear Model, has been proposed that satisfies the scaling laws and contains only a small number of adjustable parameters. It is shown that the Linear Model yields a satisfactory representation of the experimental P-V-T data for steam in the critical region.

15731. McCarty, R. D., **The correlation of equilibrium and transport properties of fluids,** (Proc. 8th Int. Conf. on the Properties of Water and Steam, Giens, France, Sept. 23-27, 1974), Paper in *Proceedings of the 8th International Conference on the Properties of Water and Steam*, P. Bury, H. Perdon, and B. Vodar, Eds., **1**, 537-556 (Ministère de l'Industrie et de la Recherche, Paris, France, 1975).

Key words: correlation; equation of state; excess function; hydrogen; interpolation methods; least squares; methane; thermodynamic properties; transport properties.

The practice of using a mathematical model for correlating the transport and thermodynamic properties of fluids is reviewed. Changes which are currently taking place in the field are analyzed from both the correlator's point of view and the people who are going to use the results of the correlation. The present state-of-the-art indicates present and future correlations must be more user oriented than those of the past. A review of correlation methods is given with emphasis on model selection. A new model for the transport property excess function is given. An example of simultaneous data fitting demonstrates the value of this technique.

15732. Johnson, D. P., Guildner, L. A., Jones, F. E., **Vapor pressure of water at its triple point,** (Proc. 8th Int. Conf. on the Properties of Water and Steam, Giens, France, Sept. 23-27, 1974), Paper in *Proceedings of the 8th International Conference on the Properties of Water and Steam*, P. Bury, H. Perdon, and B. Vodar, Eds., **1**, 365-377 (Ministère de l'Industrie et de la Recherche, Paris, France, 1975).

Key words: mercury manometer; triple point of water; vapor pressure.

The vapor pressure of water has been measured at its triple point with a newly constructed apparatus. It was designed to provide a dynamic system with a thin stream of water flowing down an ice mantle, the temperature of which was determined by a standard platinum resistance thermometer. The pressure was measured by the NBS precision mercury manometer, with a diaphragm unit to separate the helium in the manometer from the water vapor. The value found from a series of measurements was 611.636 Pa with an estimated total uncertainty (3 $\sigma$ limits plus estimate of systematic error) of $\pm 0.061$ Pa.

15733. Sengers, J. M. H. L., **Universality of critical behavior in fluids,** (Proc. 8th Int. Conf. on the Properties of Water and Steam, Giens, France, Sept. 23-27, 1974), Paper in *Proceedings of the 8th International Conference on the Properties of Water and Steam*, P. Bury, H. Perdon, and B. Vodar, Eds., **1**, 56-78 (Ministère de l'Industrie et de la Recherche, Paris, France, 1975).

Key words: critical exponents; critical region; homogeneity; polar fluids; scaling; steam; universality.

Modern developments in the description of critical-region anomalies are reviewed. The concepts of critical exponents, homogeneity, scaling and universality are introduced. The question is raised whether the critical behavior of steam, a polar fluid, can be expected to be the same as that of nonpolar fluids. Theoretical and experimental evidence for an affirmative answer to this question is presented. The consequences for the correlation of properties of steam in the critical region are drawn.

15734. Lide, D. R., Jr., **Cooperation between professional societies and a government agency: The Journal of Physical and Chemical Reference Data,** *IEEE Trans. Prof. Commun.* **PC-18,** No. 3, 127-129 (Sept. 1975).

Key words: journal; professional societies; publications; reference data.

The National Standard Reference Data System consists of data centers and other projects funded or coordinated by the National Bureau of Standards (NBS) which compile and evaluate data on physical and chemical properties of well-defined materials. The output is then published in the form of tables of recommended data and critical reviews. In 1972 an agreement was reached with the American Chemical Society (ACS) and the American Institute of Physics (AIP) for establishing a new publication channel for the material, the *Journal of Physical and Chemical Reference Data*. Editorial work and preparation of camera-ready copy is handled by NBS, while ACS and AIP divide the other responsibilities. The progress of this journal is reviewed.

15735. Choi, C. S., Santoro, A., Marinkas, P. L., **1,3,5-Triacetyl-2,4,6-hexahydro-*s*-triazine (TRAT),** *Acta Crystallogr.* **B31,** Part 12, 2934-2937 (Dec. 15, 1975).

Key words: diffractometer; direct methods; explosives; single-crystal; triazine; x ray.

$C_9H_{15}N_3O_3$, monoclinic, $P2_1/c$, $a = 7.772$ (2), $b = 15.521$ (4), $c = 10.101$ (2) Å, $\beta = 116.34$ (2)°, $Z = 4$, $D_x = 1.30$, $D_m = 1.31$ g cm$^{-3}$, $F(000) = 456$. All x-ray measurements were made with Mo $K\alpha$ radiation ($\lambda = 0.71069$ Å). The structure was solved by direct methods and refined by full-matrix least-squares calculations to final $R$ and $R_w$ values of 0.051 and 0.035, respectively, for 777 observed reflections.

15736. Hellwig, H. W., **Atomic frequency standards: A survey,** *Proc. IEEE* **63,** No. 2, 212-229 (Feb. 1975).

Key words: application of standards; basic standards; cesium standards; frequency accuracy; frequency stability; frequency standards; hydrogen standards; ion storage; laser stabilization; rubidium standards; saturated absorption; time standards.

The last comprehensive survey on atomic frequency standards was done by McCoubrey. This survey reviews the more recent historical background of atomic frequency standards leading to the present developments. A discussion of the underlying physical and engineering principles is given. Modern atomic frequency standards, including their performance, are compared quantitatively, and projections are attempted at likely future developments and performance characteristics.



206-267 OL - 76 - 11

As in 1966, the standards principally used in technical and scientific applications are rubidium gas cell devices, cesium beam tubes, and hydrogen maser oscillators. However, substantial advances in physical and performance characteristics can be reported.

New developments include passive hydrogen devices, saturated absorption stabilized lasers, ion storage devices, and atomic beams in the far infrared and infrared region, as well as new techniques to evaluate frequency biases such as those encountered in cesium and hydrogen standards.

The survey includes a discussion of the effects of past and current developments in atomic frequency standards on the technical and scientific user community.

15737. Snyder, N. S., **The Kapitza conductance of the (100) surface of copper,** *J. Low Temp. Phys.* **22,** No. 3/4, 257-284 (1976).

Key words: heat transfer to helium II; interfacial thermal resistance; Kapitza conductance; Kapitza conductance of copper; x-ray diffraction examination of single crystal lattice damage; (100) surface of copper.

Measurements of the Kapitza conductance to liquid helium II across the (100) surface of single crystals of copper are presented. The temperature range of these measurements was 1.6-2.1 K. The sample surfaces were subjected to several different treatments. Some surfaces were cleaned by low-energy argon ion bombardment, annealed in an ultrahigh-vacuum system, and preserved under vacuum until purified liquid helium was admitted. Other surfaces were intentionally damaged by machining and/or exposure to the atmosphere. The conductance after these latter treatments was found to be about a factor of three higher than that of the more ideally cleaned and annealed surfaces, and a significant difference in the temperature dependence of the conductance was also observed. Conductances were reproducible for similarly treated surfaces and could be correlated with surface damage determined by x-ray diffraction. The relationship of these results to the numerous current theories of the Kapitza conductance is discussed. Conductance measurements of polycrystalline indium, which was used as a sealant, are presented.

15738. Kulin, G., **Simplified application of Palmer-Bowlus flow meters,** *J. Water Pollut. Control Fed. Discussion* **48,** No. 1, 200-201 (Jan. 1976).

Key words: flow measurement, water; flumes, measuring; open channel flow measurement; Palmer-Bowlus flumes; sewage flow measurement.

Possible errors associated with the use of the customary theoretically derived rating curves for Palmer-Bowlus flumes are identified and evaluated.

15739. Lieberman, A. G., **Problems in using surface analysis techniques for the depth profiling of microelectronic materials,** *Technical Digest of International Electron Devices Meeting, Washington, D.C., Dec. 1-3, 1975,* pp. 126-129 (1975).

Key words: Auger electron spectroscopy; depth impurity profiling; ion implantation; ion sputtering; microelectronic materials; Rutherford backscattering; secondary ion mass spectroscopy; silicon; silicon dioxide; surface analysis; x-ray photoelectron spectroscopy.

Practical problems associated with the depth profiling of impurity distributions in silicon and silicon dioxide are illustrated for several widely used surface analysis techniques as applied at a number of laboratories. The methods used for depth profiling were Rutherford backscattering spectroscopy, Auger electron spectroscopy and x-ray photoelectron spectroscopy.

15740. Allan, D. W., **The measurement of frequency and frequency stability of precision oscillators,** *Proc. Sixth Annual Precise Time and Time Interval (PTTI) Planning Meeting, U.S. Naval Research Laboratory, Washington, D.C., Dec. 3-5, 1974,* pp. 109-142 (Goddard Space Flight Center, Greenbelt, Md., 1974).

Key words: accurate frequency measurement; accurate time measurement; frequency; frequency stability; frequency stability analysis; models of frequency stability; picosecond time difference measurements.

The specification and performance of precision oscillators is a very important topic to the owners and users of these oscillators. This paper presents at the tutorial level some convenient methods of measuring the frequencies of precision oscillators—giving advantages and disadvantages of these methods.

Conducting such measurements, of course, gives additional understanding into the performance of the given pair of oscillators involved. Further it is shown that by processing the data from the frequency measurements in certain ways, one may be able to state more general characteristics of the oscillators being measured. The goal in this regard is to allow the comparisons of different manufacturers' specifications and more importantly to help assess whether these oscillators will meet the standard of performance the user may have in a particular application.

The methods employed for measuring frequency are designed for state-of-the-art oscillators, and an effort has been made to allow for fairly simple, inexpensive, and/or commonly available componentry to be used in the measurement systems. The method for measuring frequency stability is basically that recommended by the IEEE subcommittee which wrote the paper "Characterization of Frequency Stability," IEEE Transactions on Instrumentation and Measurement, IM-20, No. 2, pp. 105-120, (May 1971).

15741. Powell, F. J., **The Manchester, N.H., experimental energy office building,** (Proc. Seminar on Energy Conservation by Design, Orlando, Fla., March 20-21, 1974), Paper in *Proceedings Energy Conservation—By Design,* Section 14, 1-14 (Harry Phipps, Energy Systems Consultants, St. Petersburg, Fla., 1974).

Key words: energy conservation; energy consumption prediction; experimental office building.

A brief background of the experimental 7-story Federal Energy Demonstration Office Building to be Constructed at Manchester, N.H. is given. A summary of the results of a predesign energy analysis done at NBS is presented as a comparison of normal General Services Administration practice in 1972 with changes made for a new energy conservation design approach. A similar comparison is made for the same building if the location were changed to Orlando, Fla. The results indicate annual energy savings of 52 percent for Manchester and 39 percent for Orlando are possible by using additional thermal insulation in the roof, walls and floor, reducing the window area, reducing the quantity of ventilation and lighting power, and using energy efficient heating, ventilating and air-conditioning systems.

15742. Fowlkes, C. W., **Crack opening interferometry—The effects of optical refraction,** *Eng. Fract. Mech.* **7,** 689-692 (1975).

Key words: cracks; experimental mechanics; fracture; fracture toughness; interferometry; model experiments; stress; stress intensity.

This paper contains an analytical prediction of the distortions of interference fringes near a crack tip resulting from refraction of the light rays due to the stress field. The effects of these distortions on the results of crack opening interferometry (COI) experiments for determining stress intensity factors are discussed.

15743. Howard, C. J., Evenson, K. M., **Rate constants for the reactions of OH with $CH_4$ and fluorine, chlorine, and bromine substituted methanes at 296 K,** *J. Chem. Phys.* **64,** No. 1, 197-202 (Jan. 1, 1976).

Key words: gas reactions; hydroxyl radical; kinetics.

The absolute rate constants for the reactions of OH radicals with $CH_4$ and fifteen fluorine, chlorine, and bromine substituted methane molecules have been measured using a discharge flow system and laser magnetic resonance detection of OH. Measurements were made at 296 K and at pressures between 107 and 1300 Pa. The results indicate that the reaction mechanism involves the abstraction of a hydrogen atom and formation of $H_2O$ and a methyl type radical product. Completely halogenated methane molecules are found to be relatively unreactive. Hydrogen containing molecules react with rate constants ranging from about 0.2 to $160 \times 10^{-15}$ cm$^3$/molecule·sec. The reactivity increases with decreasing carbon-hydrogen bond energies. Rough estimates are made of the Arrhenius parameters for the reactions.

15744. Currie, L. A., Lindstrom, R. M., **The NBS measurement system for natural argon-37,** (Proc. Noble Gases Symp., Las Vegas, Nev., Sept. 24-28, 1973), Paper in *Noble Gases*, R. E. Stanley and A. A. Moghissi, Eds., CONF-730915, pp. 40-57 (U.S. Environmental Protection Agency, Las Vegas, Nev., Dec. 1975).

Key words: Ar-37; atmospheric radioactivity; cosmic-ray reactions; exponential distribution; low-level counting; noble gas separation; on-line computer; pulse shape discrimination; tropospheric mixing.

A project to determine the cosmic-ray production rate and the natural levels of 35-day half-life $^{37}$Ar in the atmosphere has been underway at the National Bureau of Standards for about the past year. The prime objective of this project is to determine the spatial dependence of $^{37}$Ar production in the atmosphere, and the spatial distribution of the naturally-produced $^{37}$Ar (observed concentrations). The results of this study are to be used, in cooperation with L. Machta (National Oceanographic and Atmospheric Administration), to derive information about atmospheric mixing. The purpose of this communication, however, is to present a general description of the various components of the measurement system.

As the lowest concentrations of interest are but $\cong 10^{-3}$ dpm ($^{37}$Ar)/l-Ar, very high sensitivity measurement techniques are required. Among the techniques which we have adopted are: quantitative separation of the noble gases from about 1 m$^3$ of air, using a $CaC_2$ reactor; gas chromatographic separation of the argon fraction; isotopic enrichment (by a factor of $\cong 100$) of purified argon; use of specially selected low-level gas proportional counters together with massive shielding and anticoincidence meson cancellation; and the application of pulse discrimination based upon both amplitude (energy) and pulse shape. Finally, on-line computer techniques are being applied for data acquisition and system control.

15745. Kasen, M. B., **Properties of filamentary-reinforced composites at cryogenic temperatures,** *Am. Soc. Testing Mater. Spec. Tech. Publ.* **580,** pp. 586-611 (1975).

Key words: boron; cryogenics; glass; graphite; literature review; PRD-49; reinforced aluminum; reinforced plastics; structural composites; tensile moduli; tensile strength; thermal conductivity; thermal contraction.

This paper presents a review of a series of significant publications on the mechanical and thermal properties of filamentary-reinforced structural composites in the cryogenic temperature range. The objective, scope of work, and significant conclusions of the selected works are discussed. The temperature dependence of the ultimate tensile strength, tensile modulus, thermal conductivity, and thermal contraction (expansion) is presented for selected composites developed in each program. Problem areas are defined and suggestions are made for future work.

15746. Mies, F. H., **Optical pumping by solar radiation in comets: Polarization of the Na resonance lines,** *Astrophys. J.* **202,** 823-831 (Dec. 15, 1975).

Key words: atomic and molecular processes; comets; line formation; polarization; quantum mechanics.

At some distance from the nucleus of a comet, the rate of fluorescent scattering of solar radiation by an atom or molecule will be comparable to, or exceed, the rate of collisional relaxation. This is the condition for optical pumping. If the ground state has fine structure or hyperfine structure, then significant nonequilibrium distributions of these levels can result, and the fluorescence spectrum can deviate markedly from the laboratory spectrum. In particular, since the incident solar radiation is unidirectional, the pumping causes an *alignment* of the hyperfine magnetic sublevels along the incident axis, and observations from the Earth should exhibit an enhanced linear polarization in the Sun-comet-Earth plane. Therefore, polarization measurements can be used as a diagnostic for the presence or absence of collisional relaxation. Conditions are especially favorable for the enhanced polarization of the Na $D_2$ resonance line, and, at a scattering angle of 90°, detailed calculations are presented which predict a polarization of 16 percent, and under favorable circumstances as much as 21 percent, as compared with 10.5 percent for a collisionally equilibrated Na gas.

15747. Kuyatt, C. E., **Observation of polarized electrons by Davisson and Germer,** *Phys. Rev. B* **12,** No. 10, 4581-4583 (Nov. 15, 1975).

Key words: electron polarization; electron scattering; low energy; nickel; single crystals; tungsten.

Early attempts to observe electron polarization in the scattering of low-energy electrons from solids are reviewed. It is found that results published by Davisson and Germer in 1929 were analyzed incorrectly, and that they had in fact observed significant electron polarizations in the diffraction of low-energy electrons from single-crystal nickel.

15748. Gadzuk, J. W., **Angle-resolved photoemission from crystal-field split *d* shells of adsorbed atoms,** *Phys. Rev. B* **12,** No. 12, 5608-5614 (Dec. 15, 1975).

Key words: adsorption; angular distributions; photoemission; photoionization.

A theory of the angular distribution (AD) of photoemitted electrons from filled *d* shells of atoms adsorbed on solid surfaces is presented. The crystal field at the surface of the substrate splits the degenerate *d* states of the adsorbate into at least $e_g$ and $t_{2g}$ components. The angular distribution is then calculated for photoemission from the $e_g$ group (since the distribution from the $t_{2g}$ group is easily related to this). The final state is written as a partial-wave sum. For photoelectron kinetic energies less than about 10 eV, transitions from *d* to *p* partial waves dominate the AD and these AD's are azimuthally symmetric (for unpolarized light at normal incidence). Above 10 eV, the delayed onset (due to passing over the centrifugal barrier) of *d* to continuum *f* partial-wave emission occurs and this channel then dominates. The $d_{x^2-y^2}$ initial state, composed of spherical harmonics $Y_{2\pm2}$ is connected to $Y_{3\pm3}$ and $Y_{3\pm1}$ partial waves by the dipole operator. The calculated differential cross section, of the form $d\sigma/d\Omega = a(\theta) - b(\theta)\cos 4\phi$, is fourfold symmetric, as expected, owing to interference effects between the $m = \pm 1$ and $m = \pm 3$ partial waves. The anisotropy parameter $\alpha(\theta) \equiv b(\theta)/a(\theta)$ changes sign at $\theta = 63.43°$ and this manifests itself as a 45° azimuthal rotation of the fourfold pattern. Specific systems for studying this effect experimentally are discussed. The deposition of Cu, Ag, or Au on a wide-band-gap insu-

lator such as LiF appears promising as LiF should provide a large crystal field and the noble-metal *d* states should fall within the gap, thus remaining sharp and resolvable. The importance of the partial-wave interferences in other angle-resolved photoemission studies of oriented atoms, molecules, and surfaces is noted.

15749. Gadzuk, J. W., **Extra-molecular relaxation energies for $H_2$ embedded in an electron gas,** *Chem. Phys. Lett.* **36,** No. 5, 606-610 (Dec. 15, 1975).

Key words: molecular hydrogen; photoelectron spectroscopy; polarization energy; relaxation energy; screening energy.

The screening energy associated with a bonding orbital hole state in an $H_2$ molecule embedded in an electron gas has been calculated, within a linear response formalism. The relationship between this energy and the atomic screening energy is determined and the role of the bonding charge density is emphasized.

15750. Swanson, N., Celotta, R. J., **Observation of excited states in ozone near the dissociation limit,** *Phys. Rev. Lett.* **35,** No. 12, 783-785 (Sept. 22, 1975).

Key words: electron energy loss; forbidden transitions; ozone; triplet states.

Several calculations suggest that the lowest triplet states of ozone lie near the dissociation limit. Using electron energy-loss spectroscopy, we have observed a broad feature beginning at 1.3 eV, with a maximum at 1.65-eV energy loss. This structure is present only under large momentum-transfer conditions, indicative of the excitation of optically forbidden states. Together with the calculations, these data demonstrate that one or more excited states of ozone exist which are stable against dissociation.

15751. Huebner, R. H., Celotta, R. J., Mielczarek, S. R., Kuyatt, C. E., **Energy absorption by $N_2O$ in the 4 to 14 eV region,** *J. Chem. Phys.* **63,** No. 10, 4490-4494 (Nov. 15, 1975).

Key words: electron energy loss; energy absorption; $N_2O$; nitrous oscillator strength; photoabsorption.

Apparent oscillator-strength values for transitions in the 4 to 14 eV region in nitrous oxide have been derived from electron energy-loss measurements. Detailed comparison with photoabsorption measurements in the ultraviolet region indicates a weak transition below the $^1\Delta \leftarrow X^1\Sigma^+$ transition at 6.8 eV not observed optically. This analysis also provides oscillator-strength values in the region between 11.5 and 12.4 eV, where no quantitative photoabsorption data are available.

15752. Penn, D. R., **Measurement of the surface density of states by field ionization,** *Surf. Sci.* **52,** 270-276 (1975).

Key words: field ion energy distribution; field ionization; surface density of states; tungsten.

It is shown that recent measurements of field ion energy distributions from clean tungsten surfaces probe the density of metal states in the vicinity of the surface. We find $j(\omega) = (2\pi/\hbar)\Sigma_m |\int d^3r \psi_m(\mathbf{r}) \gamma(z)|^2 \delta(\omega - \epsilon_m)$, where $j(\omega)$ is the ion current at energy $\omega$, $\psi_m$ and $\epsilon_m$ are electronic metal eigenfunctions and eigenvalues in the presence of the external electric field used in field ionization and $\gamma(z)$ is a function which is large near the noble gas atom. An explicit expression for $\gamma(z)$ is given in the text. It is estimated that tungsten metal states with values of $\mathbf{k}_{||}$ at least as large as 0.5 $Å^{-1}$ make an appreciable contribution to $j(\omega)$ where $\mathbf{k}_{||}$ is the electron momentum parallel to the surface.

15753. Cabana, A., Laurin, M., Pépin, C., Lafferty, W. J., **High-resolution infrared spectrum of the $\nu_3$ and $\nu_2 + \nu_3 - \nu_2$ bands of $^{14}N^{16}O_2$,** *J. Mol. Spectrosc.* **59,** 13-27 (1976).

Key words: infrared spectrum; nitrogen dioxide, $\nu_3$ band; nitrogen dioxide, $\nu_3 + \nu_2 - \nu_2$ band; rotational constants; spectroscopic constants; spin-rotation constants.

The infrared absorption spectrum of the $\nu_3$ band of $^{14}NO_2$ has been recorded with a resolution and a frequency accuracy much improved over the previous investigations. The *K*- and *N*-line assignments have been greatly extended and a more accurate set of spectroscopic constants derived. Several lines in the subbands with $K_a \geq 3$ have been observed to be doubled by spin-rotation interaction and spin-rotation interaction constants have been obtained. Several weak series of lines in the spectrum ($K_a = 0$, 1, 2, and 3) have been unambiguously assigned to the "hot band" $\nu_2 + \nu_3 - \nu_2$. Lines of the $K_a = 3$, 4, 5, and 6 subbands of $\nu_3$ have been found to be perturbed by a Coriolis interaction with the $K_a = 4$, 5, 6, and 7 levels of $2\nu_2$.

15754. Mielenz, K. D., Cehelnik, E. D., McKenzie, R. L., **Elimination of polarization bias in fluorescence intensity measurements,** *J. Chem. Phys.* **64,** No. 1, 370-374 (Jan. 1, 1976).

Key words: emission anisotropy; fluorescence; fluorescence decay; fluorescence quantum yields; polarization; spectrofluorimetry; viewing angle.

It is proposed theoretically and confirmed experimentally that, if the fluorescence emission from a polarized sample is viewed in the horizontal plane at an angle of 45° (or 135°) to the direction of propagation of the exciting radiation with a polarizer set at 54.75° (or 125.25°) from the vertical direction, then, the reading obtained is proportional to the total flux emitted by the sample and is independent of the state of polarization of the exciting radiation and the emission anisotropy of the sample. The polarization sensitivity of the emission detection system then becomes a factor which is included in the spectral sensitivity curve of the emission detection system.

15755. Huebner, R. H., Bushnell, D. L., Jr., Celotta, R. J., Mielczarek, S. R., Kuyatt, C. E., **Ultraviolet photoabsorption by halocarbons 11 and 12 from electron impact measurements,** *Nature* **257,** No. 5525, 376-378 (Oct. 2, 1975).

Key words: electron energy loss; electron impact; Freon 11; Freon 12; uv photoabsorption.

Electron energy loss measurements are made of Freons 11 and 12. The data is converted to oscillator strength distributions and compared to the existing photoabsorption data in the energy range relevant to atmospheric photodissociation.

15756. Hahn, M. H., Robinson, H. E., Flynn, D. R., **Robinson line-heat-source guarded hot plate apparatus,** *Am. Soc. Test. Mater. Spec. Tech. Publ. 544,* pp. 167-192 (1974).

Key words: conduction; energy conservation; heat transfer; insulation; thermal conductivity; thermal insulation.

This paper presents a description of the line-heat-source guarded hot plate apparatus conceived by the late H. E. Robinson, the results of mathematical analyses of potential sources of uncertainty, and the design of an apparatus of this type being constructed at the National Bureau of Standards. This design utilizes a line source heater, from which heat diffuses laterally in the plate. Such a design does not produce a wholly uniform plate temperature, but does enable calculation of average plate surface, and edge, temperatures utilizing only a few temperature sensors.

15757. Jacox, M. E., **Matrix isolation study of the products of the interaction between metastable Ar and Kr atoms and chloroform. Photodecomposition of $HCCl_2^+$ and $HCCl_2^-$,** *Chem. Phys.* **12,** 51-63 (1976).

Key words: Ar metastable interactions; $ClHCl^-$; emission spectrum; $HAr_n^+$; $HCCl_2^+$; $HCCl_2^-$; $HCCl_3$; infrared spectrum;

matrix isolation; molecular rotation in solid Ar; photoinduced proton transfer; ultraviolet spectrum.

The emission spectrum of a microwave discharge through argon and the infrared and ultraviolet spectra of the products of the interaction of $HCCl_3$ with the periphery of such a discharge, observed after rapid quenching in an argon matrix at 14 K, indicate that metastable argon atoms play an important role in matrix isolation experiments using such a discharge configuration to produce free radicals and molecular ions. Exceptionally high yields of $HCCl_2^+$ and $HCCl_2^-$ and a significant concentration of $CCl_3^+$ were stabilized in these experiments. The observations support the earlier assignment of the 1037 $cm^{-1}$ peak to "isolated" $CCl_3^+$. Upon exposure of the sample to 370-280 nm radiation, a prominent, slightly perturbed absorption of $ClHCl^-$ appeared at 705 $cm^{-1}$. This absorption was destroyed by 280-260 nm radiation. The relative stability of both $HCCl_2^+$ and $CCl_3^+$ upon exposure of the sample to radiation of wavelength longer than 280 nm is attributed to electron scavenging by the $HCCl_3$ in the matrix; this species is present in considerably greater concentration than are the ion products. Evidence is presented for the photodecomposition of $HCCl_2^+$ at wavelengths shorter than about 280 nm. A marked increase in the concentration of $HAr_n^+$ when $HCCl_2^+$ was photolyzed by radiation of wavelength shorter than 260 nm is consistent with the calculated threshold energy for proton transfer from $HCCl_2^+$ to Ar. The results of krypton matrix experiments are also consistent with this mechanism. Unstructured absorption bands near 285 and 250 nm are tentatively attributed to $ClHCl^-$ and $HCCl_2^+$, respectively. An increase in the concentration of "nonrotating" $H_2O$, compared to $H_2O$ molecules free to undergo rotational transitions, when ions are present in the matrix can be attributed to the electric field produced by ionic interactions.

15758. Gadzuk, J. W., **Interaction of atoms and molecules with surfaces,** Chapter 7 in *Surface Physics of Materials*, J. M. Blakeley, Ed., **II,** 339-375 (Academic Press, Inc., New York, N.Y., 1975).

Key words: adsorption; chemisorption; electronic properties of solids; molecules; surfaces.

The theory of chemisorption of atoms and molecules on surfaces is considered. Emphasis is directed towards the Anderson model (self-consistent molecular orbital theory) and the dielectric screening models. The techniques of group orbitals are used to reduce the many atom problems to one involving a surface molecular complex. Specific cases of H adsorbed on the (100) face of W, alkali atoms on metals, and 5d transition metal atoms on W are treated.

15759. Gadzuk, J. W., **Angle resolved photoemission from chemisorbed layers: Further theoretical considerations,** *Surf. Sci.* **53,** 132-143 (1975).

Key words: angular distributions; chemisorption; electron spectroscopy; photoemission.

In recent theoretical work by Gadzuk and by Liebsch, the importance of angle resolved photoemission studies of surfaces and chemisorbed atoms has been demonstrated. In the theory due to Gadzuk, the role of the initial state in the photoemission process has been emphasized, whereas in the theory due to Liebsch, the role of the final state is stressed in determining a photoemission angular distribution (PAD) from chemisorbed atoms. Here it is shown what conditions favor initial versus final state dominance. In both theories, the PAD is calculated for an isolated chemisorbed atom or surface molecule complex. It is shown how two-dimensional band effects due to adatom–adatom interactions modify (or do not modify) the PAD.

15760. Mahan, A. H., Gallagher, A., **Transition radiation for the diagnosis of low-energy electron beams,** *Rev. Sci. Instrum.* **47,** No. 1, 81-83 (Jan. 1976).

Key words: electron optics; transition radiation.

Electron bombardment of metallic silver is known to produce "transition radiation," predominantly at 300-450 nm wavelengths. In reported measurements at 15-500 eV impact energies, transition radiation was used to diagnose the shape and time dependence of an rf modulated electron beam. It is suggested that this is a superior target, as opposed to phosphors or gases normally used, to determine instrumental time response functions and electron beam imaging.

15761. Truhlar, D. G., Poling, R. E., Brandt, M. A., **Infinite-order sudden approximation for rotational excitation of hydrogen molecules by electrons in the energy range 10-40 eV,** *J. Chem. Phys.* **64,** No. 2, 826-829 (Jan. 15, 1976).

Key words: differential cross sections; elastic scattering; electron scattering; hydrogen molecules; momentum transfer; rotational excitation; scattering theory; sudden approximation.

Electron scattering by $H_2$ is treated using a noncentral interaction potential including short-range and long-range static contributions, exchange, and polarization effects. The molecule is treated as a rigid rotator and the scattering is treated in the infinite-order sudden approximation. The results show that the rotational excitation cross section exceeds the elastic scattering cross section at large scattering angles at intermediate energies but not at small angles at low energies.

15762. Burch, D. M., Peavy, B. A., Powell, F. J., **Comparison between measured and computer-predicted hourly heating and cooling energy requirements for an instrumented wood framed townhouse,** *ASHRAE Trans.* **81,** Part II, Paper No. 2363, 70-88 (1975).

Key words: building heat transfer; computer programs; dynamic thermal performance; heat flow analysis; heating and cooling loads; thermal analysis; transient heat flows.

A sophisticated computer program called NBSLD was validated for predicting the hourly heating and cooling loads of a residence. An instrumented four-bedroom townhouse was exposed to simulated winter and summer conditions inside a large environmental laboratory. During the tests, the activities of a six member family were simulated, and the inside temperature of the test house was maintained at approximately 75 °F (23.9 °C). Hourly heating and cooling input energy was measured and compared with corresponding computer-predicted values. The NBSLD computer program predicted maximum heating and cooling input loads within 9.2 percent, and energy requirements within 8.2 percent.

15763. Johnson, C. R., **A local Lyapunov theorem and the stability of sums,** *Linear Algebra and Appl.* **13,** 37-43 (1976).

Key words: cone; Lyapunov's theorem; stable matrix.

We present a "local" analog of Lyapunov's theorem which characterizes $n$ by $n$ matrices whose eigenvalues lie in the open left half plane. This allows the characterization of pairs of stable matrices $A$, $B$ such that the sum $A + \alpha B$ is stable for all real $\alpha > 0$.

15764. Ives, L. K., Ruff, A. W., Reed, R. P., **An electron microscope study of the Tishomingo meteorite,** (Proc. 32d Annual Meeting of Electron Microscopy Society of America, St. Louis, Mo., Aug. 13-15, 1974), Paper in *Proceedings Electron Microscopy Society of America, 32d Annual Meeting*, C. J. Arceneaux, Ed., pp. 520-521 (Claitor's Publ. Div., Baton Rouge, La., 1974).

Key words: alloy; austenite; electron microscopy; iron-nickel; martensite; meteorite; Tishomingo.

Transmission electron microscope studies have been performed on the Tishomingo meteorite. The microstructure consists of original austenite material and transformed martensite. Deformation twins have been observed. High dislocation density was found within the austenite. Heating stage experiments were performed to investigate thermal response of the material.

15765. Fraker, A. C., **Microstructural and corrosion studies of the Ti-2 wt.% Ni alloy,** (Proc. 32d Annual Meeting of Electron Microscopy Society of America, St. Louis, Mo., Aug. 13-15, 1974), Paper in *Proceedings Electron Microscopy Society of America, 32d Annual Meeting*, C. J. Arceneaux, Ed., pp. 516-517 (Claitor's Publ. Div., Baton Rouge, La., 1974).

Key words: corrosion; microstructures; titanium.

The influence of heat treatment on the Ti-2wt.% Ni alloy microstructure was studied. Heat treating above the $\alpha+\beta$ temperature region and quickly cooling produces a martensite type microstructure with a highly segregated $Ti_2Ni$ precipitate phase. Heat treating at lower temperatures results in an enlarged $\alpha$-titanium grain structure with large randomly dispersed $Ti_2Ni$ precipitates. Transmission electron microscopy, electron diffraction and light microscopy were used to show these microstructural differences as well as examples of local corrosion at the precipitate.

15766. Coriell, S. R., Hurle, D. T. J., Sekerka, R. F., **Interface stability during crystal growth: The effect of stirring,** *J. Cryst. Growth* **32,** No. 1, 1-7 (Jan. 1976).

Key words: alloy; boundary layer; fluid flow; interface; solidification; stability.

The influence of stirring on the morphological stability of a solid-liquid interface during the unidirectional solidification of a binary alloy at constant velocity is calculated on the basis of a model that employs a stagnant solute boundary layer. For fixed values of the growth velocity, temperature gradient, and concentration gradient at the interface, stirring decreases morphological stability. Further, the wavelength at which instability first occurs is greater with stirring than in the absence of stirring. For a fixed growth velocity and temperature gradient, and a bulk liquid of given composition, the effect of stirring decreases morphological stability for a distribution coefficient $k > 1$ but can either increase or decrease stability for $k < 1$. The dependence of critical wavelength on growth velocity measured by Morris and Winegard for Pb-Sb alloys can be explained by this theory.

15767. deWit, R., **Partial disclinations,** *J. Phys. C: Solid State Phys.* **5,** 529-534 (1972).

Key words: crystal; disclination; dislocation; pseudopentagonal; stacking fault; twin; wedge.

A twin in a crystal can terminate at a partial wedge disclination. This is the analogue to a stacking fault terminating at a partial dislocation. It is illustrated for an FCC crystal. Similarly, several twins can terminate at a partial disclination. This is also illustrated for an FCC crystal. Crystals with such defects, which are called pseudopentagonal twins, have been observed. Their x-ray diffraction pattern should show the elastic distortion of the disclination.

15768. Bennett, L. H., McAlister, A. J., Cuthill, J. R., Erickson, N. E., Watson, R. E., **Electronic density of states of lanthanum-transition-metal alloys of $CaCu_5$ type,** *Phys. Rev. B Comments and Addenda* **12,** No. 11, 5335-5337 (Dec. 1, 1975).

Key words: alloys; copper; electronic density of states; lanthanum; nickel; nuclear magnetic resonance; platinum; x-ray photoemission.

Pt-site Knight shifts for the alloy system $LaCu_{5-x}Pt_x$ ($0 < x \leq 5$), and x-ray photoemission data for Pt, $LaNi_5$, and $LaPt_5$ are presented. Variation of the electronic structure of La-transition-metal alloys of $CaCu_5$ type with alloying at the transition-metal sites is discussed in the light of these results and earlier data on the $LaNi_{5-x}Pt_x$ system.

15769. Berger, R. E., **Impact testing of ophthalmic lenses: Stress distribution and the "search" theory,** *J. Am. Optom. Assoc.* **47,** No. 1, 86-92 (Jan. 1976).

Key words: fracture; glass; impact; ophthalmic lenses; stress distributions.

Elementary concepts in fracture mechanics, stress analysis, and impact are discussed as they pertain to fracture of lenses in drop ball testing. Quasi- tatic estimates for stress distributions during impact are obtained. These profiles show a sharp peak in the tensile stress under the impact point.

Identical groups of lenses were impact tested in two different modes: (1) 25 impacts at a single spot on the lens, (2) 1 impact at each of 25 different spots. Much more breakage was observed in the latter group.

Both the experimental and analytical considerations lend support to the "search" theory of drop ball testing—fracture occurs when the ball strikes a weak spot (where there exists a sufficiently severe flaw) on the lens. Lenses which pass an impact test may well have dangerous flaws away from the impact point.

15770. Johnson, C. R., **Numerical location of the field of values,** *Linear and Multilinear Algebra* **3,** 9-14 (1975).

Key words: *D*-stable matrix; field of values; Gersgorin's theorem; nonnegative matrix; Perron-Frobenius eigenvalue; spectrum of a square complex matrix.

We give an estimate of the angular location of the *field of values*

$$F(A) = \{x^*Ax : x^*x = 1, x \in C^n\}$$

via the Perron-Frobenius root of a nonnegative matrix obtained from $A$. This estimate is invariant under diagonal congruences of $A$ and may be used to sharpen an existing inclusion region for $F(A)$. Employing a result of Wielandt, an application is also made to the location of spectra of products of matrices based only on regions simply obtained from the factors individually.

15771. Yakowitz, H., **Energy dispersive x-ray spectrometry,** *J. Microscopie Biol. Cell.* **22,** No. 2-3, 137-150 (1975).

Key words: elemental distribution; energy dispersive x-ray analysis; light element analysis; scanning electron microscopy; thin film x-ray analysis; x-ray continuum radiation.

An energy dispersive x-ray spectrometer (EDS) was first used for electron microanalysis in 1968. Since then the number and quality of EDS systems has steadily and rapidly increased. Today a large majority of scanning electron microscopes (SEM) and many transmission electron microscopes (TEM) are equipped with EDS facilities. Thus, the electron microscopist can perform qualitative and quantitative analyses and can also map elemental distribution in the area scanned by the electron beam.

This paper will provide only a brief overview of the operating principles and required equipment for EDS systems. Major emphasis will be placed on data interpretation including background correction, pulse pile-up effects, peak interferences and analytical schemes for quantitation.

15772. Peterlin, A., Olf, H. G., **Environmental effects on low temperature crazing of crystalline polymers,** *J. Polym. Sci. Part C:* No. 50, 243-264 (1975).

Key words: crazing; cryogenic temperatures; crystalline polymers; environmental effects on crazing; fractional free volume; glass transition temperature; smectic polypropylene; spherulitic polypropylene.

The ductile behavior of crystalline polymers between liquid nitrogen and room temperatures is primarily due to enhancement of crazing by the presence of gases ($N_2$, $A_2$, $O_2$, $CO_2$) of high thermodynamic activity, i.e., close to their condensation point. Without the presence of such a gas, at temperatures sufficiently above its condensation point so that its activity has dropped to a few percent, the crystalline material is rather brittle although some very limited crazing can be detected. As expected, the ductility and the amount of crazing are very nearly the same in helium as under vacuum. The crazes in smectic PP are extremely long, often traversing the entire width (0.5 cm) of the sample, and generally very similar to crazes in glassy amorphous polymers. They are thin and become thicker at higher temperatures. In monoclinic PP with well developed spherulitic structure, crazing occurs along spherulite diameters that are perpendicular to the stress direction but not along the boundaries between spherulites. In general, the length of a craze equals the spherulite diameter. At low temperatures all crazes originate on the outer surface of the sample which is in direct contact with the gas.

The action of the gas is due to two mechanisms. First, the adsorbed gas reduces the surface energy of the polymer, facilitating the creation of a new surface in the holes and voids of the craze. Second, the gas becomes highly absorbed at the tip of an incidental flaw or of an existing craze, since these are regions of high dilatant stress. The locally absorbed gas acts as a plasticizer easing the flow involved in the nucleation and growth of the craze, i.e., in the formation of fibrillar material of the craze.

15773. Carroll, J. J., Smit, J., Melmed, A. J., **Field-ion imaging of titanium and effects due to hydrogen,** *Surf. Sci.* **45,** No. 2, 640-648 (Oct. 1974).

Key words: field-ion microscopy; hydrogen; titanium.

Titanium specimens of nominal 99.99+ percent purity were prepared and imaged in the field-ion microscope between 23-30 K using hydrogen, hydrogen-helium mixtures, and neon imaging gases. Micrographs obtained in the presence of hydrogen show features that may indicate the early stage development of cracks and hydrides, mostly on and between the $\{11\bar{2}0\}$ and $\{10\bar{1}0\}$ plane regions. Neon field-ion microscopy shows that the image features due to hydrogen-titanium interactions in the field-ion microscope are confined to about 10-15 topmost metal layers.

15774. McKee, R. A., Stark, J. P., **Interpretations for thermomigration results in aluminum and aluminum alloys,** *Acta Metall.* **23,** 1145-1148 (Oct. 1975).

Key words: alloys; aluminum; copper-aluminum; nonisothermal diffusion; silver-aluminum; thermomigration; vacancies.

Recent anomalies have been reported for thermomigration results in aluminum and aluminum alloys. A sign reversal for the measured heat of transport and consequently a mass flux reversal in the thermomigration experiment was reported for self-thermomigration in pure aluminum and for thermomigration of copper in aluminum. These events occurred as a result of varying the grain or crystal size in the experiment. A grain size effect on the measured heat of transport for silver in aluminum has also been reported. Experimental data for nonisothermal diffusion of $Ag^{110}$ in aluminum has established the existence of stable point defect concentrations in excess of those predicted for thermal equilibrium and the explanation for the anomalies in aluminum thermomigration experiments is now possible.

15775. Peterlin, A., **Optical effects in flow,** *Annu. Rev. Fluid Mech.* **8,** 35-55 (1976).

Key words: flow with longitudinal gradient; flow with transverse gradient; optical anemometry; optical birefringence; optical excess tensor; optical mapping of flow; stress excess tensor; two-dimensional flow.

A critical survey of optical effects induced by flow is given for pure liquids, liquid mixtures, suspension and polymer solutions. The optical and stress excess tensors are proportional in pure liquids, mixtures, and polymer solutions and melts in almost the full range of flow gradient (rheo-optical law). Such a proportionality exists also for suspensions at small gradient as long as the birefringence is a linear function of the gradient.

Optical birefringence is used for the mapping of stresses on a flow field in complicated flow geometry and particularly with non-Newtonian fluids. The Doppler effect of scattered light is used for optical anemometry.

15776. Manning, J. R., Stark, J. P., **Complete-path matrix equations for tracer diffusion coefficients and correlation factors,** *Phys. Rev. B* **12,** No. 6, 2075-2079 (Sept. 15, 1975).

Key words: atom migration; correlation factor; crystal defect; diffusion coefficient; matrix equations; nonrandom walk equation.

General complete-path matrix equations are derived for the tracer diffusion coefficient and correlation factor by taking into account the frequency with which defects encounter a tracer atom and the possibility of multiple exchanges of a defect with the atom. These equations apply even when mirror symmetry and rotational symmetry of the crystal and defect are lacking, as for example when diffusion occurs via complex defects in noncubic crystals. They also are valid for diffusion along any diffusion direction and where the individual atom jumps provide a variety of jump distances. It is shown that the general equations reduce to those of Stark and of Howard in the special case where there is mirror symmetry across the diffusion place.

15777. Fraker, A. C., **Microstructures of Ti-1.5 w/o Ni alloys with Mo and Al additions,** (Proc. 33d Annual Electron Microscopy Society of America, Las Vegas, Nev., Aug. 11-15, 1975), Paper in *Proceedings Electron Microscopy Society of America, 33d Annual Meeting*, G. W. Bailey, Ed., pp. 54-55 (Claitor's Publ. Div., Baton Rouge, La., 1975).

Key words: microstructures; titanium; transmission electron microscopy.

Small additions of Mo to Ti-0.8 to 1 w/o Ni alloys produce good crevice corrosion resistance and improved fabrication properties. This work shows how the Ti-1.5 w/o Ni alloy microstructure is altered by adding 2 w/o Mo or 2 w/o Al. It was concluded that the Mo addition produces a more elongated microstructure with smaller sized $Ti_2Ni$ precipitates, enhances the martensitic reaction and increases the hardness of the material. The Al addition does not change the microstructure markedly but does cause an increase in microhardness.

15778. Ruff, A. W., Ives, L. K., **Measurement of solid particle velocity in erosive wear,** *Wear Short Commun.* **35,** 195-199 (1975).

Key words: erosive wear; particle impingement; particle velocity measurement; wear; wear testing.

A method is described for determining the velocity of solid particles in a gas-particulate stream applied to erosion testing of materials. A simple mechanical configuration allows the measurement to be made under a wide range of equipment conditions. The time-of-flight of the particles is determined over a controlled path length between two rotating disks. Examples of measurements on several test apparatus are presented. The importance of nozzle design is discussed. A comparison between particle and gas stream velocity is presented.

15779. Kuriyama, M., **A classical derivation of the dynamical diffraction equation for imperfect crystals based on the Ewald-Laue-Bethe theory,** *Acta Crystallogr.* **A31,** Part 6, 774-779 (Nov. 1975).

Key words: dynamical diffraction equation; imperfect crystals; scattering matrix theory.

The basic equation of dynamical diffraction for imperfect crystals, which has been derived previously by a general dynamical theory of diffraction, is rederived classically based on the Ewald-Laue-Bethe concept, thus completing the formulation of a "scattering matrix" theory. It is shown in this classical derivation that a series of assumptions is required at each stage of the mathematical formulation to allow it to proceed further. These assumptions are then viewed in terms of the general dynamical theory of diffraction, and found unnecessary in the rigorous formulation. This classical formulation provides a conceptual relation between the traditional Ewald-Laue-Bethe dynamical theory and the general dynamical theory, one that has been derived with the aid of quantum-field theory.

15780. McAlister, A. J., Cuthill, J. R., Dobbyn, R. C., Williams, M. L., Watson, R. E., **Band structure of face-centered and body-centered-cubic 3*d* transition metals,** *Phys. Rev. B* **12,** No. 8, 2973-2983 (Oct. 15, 1975).

Key words: Co; Cr; *d*-band widths; electronic structure; Fe; ferromagnetism; soft x-ray emission; soft x-ray spectra; transition metals.

Measurements of the soft-x-ray $M_{2,3}$ emission spectra of face-centered Fe and Co, and body-centered Fe, Cr, and V are reported and $M_3$ single-hole excitation profiles are estimated. 3*d* bandwidths inferred from these results and earlier data on Cu and Ni are compared with band-theory predictions. As has been seen previously with x-ray and ultraviolet photoemission, the experimental Ni bandwidth is markedly narrower than theory predicts; there is a suggestion that the bandwidth of Cu is somewhat broader; theory and the present results are in fair agreement for the other metals. Fine structure is seen in the spectra; correlations are noted in the weak structure of metals of common crystal structure; and structural correlations with x-ray and ultraviolet photoemission data are seen as well.

15781. Sawyer, D. E., Berning, D. W., **Laser scanning of active semiconductor devices,** *Proc. Technical Digest, International Electron Devices Meeting, Washington, D.C., Dec. 1-3, 1975, IEDM Technical Digest,* pp. 111-114 (1975).

Key words: active devices; hot spots; laser scanning; logic flow observation; LSI testing; nondestructive test; nonlinearity measurement; UHF transistor measurement.

A laser scanner is described which can nondestructively explore electrical characteristics of semiconductor devices on a point-by-point basis. The results of applying the scanner to electronically map temperature distributions and hot spots in a power transistor are given. The results of mapping localized nonlinearities in electrical operation and 0.5 GHz response are also presented. Pictures show the progress of logic in a MOS shift register and demonstrate the ability to change at will the logical state of an embedded active cell with the laser.

15782. Mathey, R. G., Clifton, J. R., **Bond of coated reinforcing bars in concrete,** *J. Struct. Div. Proc. Am. Soc. Civil Eng.* **102,** No. ST1, 215-229 (Jan. 1976).

Key words: bond strength; coated reinforcing bars; evaluation; organic coatings; pullout tests.

The bond strengths were determined for 23 epoxy-coated (10 different epoxy coatings), six polyvinyl chloride-coated (three different coating materials), and five uncoated reinforcing bars. The length of embedment of the reinforcing bar in the concrete was 12 in (305 mm). The loads or bond stresses corresponding to a loaded-end slip of 0.01 in (0.25 mm) or a free-end slip of 0.002 in (0.051 mm) were considered as critical values in determining the bond strength, depending on which of these values of slip developed first. For coating film thicknesses ranging from 0.001 in to 0.011 in, the epoxy-coated bars developed bond strengths essentially equal to the bond strengths for uncoated bars. Experimental values were higher than minimum acceptable values in building code and highway bridge requirements. Bond strengths of the polyvinyl chloride-coated bars and bars with thick epoxy coatings were unacceptable.

15783. Harrison, S. H., **Neutron activation analysis: A useful tool for evaluating water sampling and analysis techniques,** *Proc. Transactions American Nuclear Society, New Orleans, La., June 6-13, 1975,* **21,** 110-111 (1975).

Key words: neutron activation analysis; particulates; sampling; species; trace element concentrations.

Neutron activation analysis (NAA) was used to determine the natural variability of trace element concentrations at a single sampling location over a short time (2 or 3 hours) and to compare the performance of two different water sampling devices. Data for both dissolved species and suspended particulates are presented. A normalizing technique for evaluating suspended particulate data is described.

Unique results obtained with this normalizing technique are demonstrated on data from a highly polluted tributary of the Chesapeake Bay.

15784. McClintock, W., Henry, R. C., Moos, H. W., Linsky, J. L., **Ultraviolet observations of cool stars. IV. Intensities of Lyman-$\alpha$ and Mg II in Epsilon Pegasi and Epsilon Eridani, and line width-luminosity correlations,** *Astrophys. J.* **202,** No. 3, 733-740 (Dec. 15, 1975).

Key words: chromospheres, stellar; *Copernicus* observations; ultraviolet stellar spectra; Wilson-Bappu effect.

The Princeton spectrometer on the *Copernicus* satellite has been used to confirm the existence of a line width-luminosity relation for the L$\alpha$ and Mg II $\lambda$2800 chromospheric emission lines in K-type stars, by observation of a K2 dwarf ($\epsilon$ Eri) and of a K2 supergiant ($\epsilon$ Peg). Combined with previously reported observations of lines in three K giants ($\alpha$ Boo, $\alpha$ Tau, and $\beta$ Gem), the data are consistent with an identical dependence of line-width on absolute visual magnitude for the Ca II K, L$\alpha$, and Mg II $\lambda$2795 lines. Surface fluxes of L$\alpha$, Mg II $\lambda$2800, and O V $\lambda$1218 (upper limit) for $\epsilon$ Eri, and of Mg II $\lambda$2800 for $\epsilon$ Peg are also compared with values reported previously for the three giant stars.

15785. Pease, R. L., Galloway, K. F., Stehlin, R. A., **Radiation damage to integrated injection logic cells,** *IEEE Trans. Nucl. Sci.* **NS-22,** No. 6, 2600-2604 (Dec. 1975).

Key words: digital bipolar circuits; integrated injection logic; radiation damage; radiation effects.

The effects of neutron and total dose gamma irradiations on the electrical characteristics of an integrated injection logic ($I^2L$) cell and an $I^2L$ multiple inverter circuit were investigated. These units were designed and fabricated to obtain circuit development information and did not have radiation hardness as a goal. The following parameters of the test structures were measured as a function of total dose and neutron fluence: the dc common-base current gain of the lateral *pnp* transistor; the dc common-emitter current gain of the vertical *npn* transistor; the forward current-voltage characteristics of the injector-substrate junction, and the propagation delay versus power dissipation per gate for the multiple inverter circuit. The limitations of the present test structures in a radiation environment and possible hardening techniques are discussed.

15786. Galloway, K. F., Keery, W. J., Leedy, K. O., **Integrated circuit damage resulting from SEM examination,** *Proc. 25th Annual Electronic Components Conf., Washington, D.C., May 12-14, 1975,* pp. 263-266 (Institute of Electrical and Electronics Engineers, New York, N.Y., 1975).

Key words: electron beam damage; electron beam energy deposition; integrated circuits; ionizing radiation effects; scanning electron microscope; surface effects.

The scanning electron microscope utilizes a well controlled low-energy electron beam which is a potential source of damage to specimens under investigation. In particular, the energy deposited by the electron beam can alter the surface oxide properties of semiconductor devices which can, in turn, lead to a change in device electrical parameters. The energy deposition and the resulting oxide changes are reviewed in this paper, and the effects of the scanning electron beam are illustrated.

15787. Heinrich, K. F. J., **Scanning electron probe microanalysis,** Chapter in *Advances in Optical and Electron Microscopy* **6,** 275-301 (Academic Press, Inc., London, England, 1975).

Key words: color composite technique; counting statistics; electron beam scanning; electron probe microanalysis; x-ray analysis.

Scanning electron probe microanalysis is related to microscopy as well as to chemical analysis. The present techniques can be considered as incomplete variations of a hypothetical model of quantitative elemental characterization of a microscopic area. Such a "complete scanning analysis" is at present limited by statistics of achievable count rates, and by the requirements for applying complicated transformations or "corrections" to the experimental results. The use of color composites and of data collection and evaluation systems which are becoming more readily available provides improved techniques for the presentation of information. Further progress depends upon the development of x-ray detectors having low coincidence losses and of extensive storage and manipulation of digital information.

15788. Freund, S. M., Hougen, J. T., Lafferty, W. J., **Laser magnetic resonance spectra of $^{14}NO_2$ and $^{15}NO_2$ near 1600 cm$^{-1}$,** *Can. J. Phys.* **53,** No. 19, 1929-1938 (1975).

Key words: band center; intensities; laser magnetic resonance; nitrogen dioxide; rotational assignment; spin-rotation splittings.

Two laser magnetic resonance patterns for $^{14}NO_2$ and six patterns for $^{15}NO_2$, observed using six CO laser transitions, have been analyzed to yield spin corrected zero-field vibration–rotation transition wave numbers and zero-field spin–rotation splittings. The $^{14}NO_2$ results are in good agreement with results obtained from conventional infrared grating studies. The $^{15}NO_2$ results allow new values of $\nu_0 = 1582.107 \pm 0.008$, $A' - A'' = -0.2116 \pm 0.0011$, and $D_K' - D_K'' = -1.39 \pm 0.20 \times 10^{-4}$ cm$^{-1}$ to be determined for the $\nu_3$ fundamental of that molecule (errors are 3 standard deviations). Two spectral figures and a list of assigned Zeeman lines are presented to permit using this stable molecule as an aid in adjusting newly constructed instruments. Closed form approximate intensity expressions are given for Zeeman transitions of the type observed in this work, i.e., for sharp partially spin forbidden Zeeman transitions in $A$ type bands of near prolate asymmetric rotors.

15789. Carpenter, B. S., Myklebust, R. L., **Comparative analysis for boron in steel by ion microprobe mass analyzer and the nuclear track technique,** *Anal. Chim. Acta Short Commun.* **81,** 409-411 (1976).

Key words: alpha particles; boron; ion microprobe mass analyzer; nuclear track technique; standard reference material; steel.

This work describes the analytical capabilities of the NBS Ion Microprobe Mass Analyzer for determining trace concentrations of boron in a steel matrix. In addition, the boron concentration values obtained in this way are compared with those obtained by the Nuclear Track Technique, in which the boron concentration and distribution are determined by counting the alpha tracks produced by the nuclear reaction $^{10}B(n, \alpha)^7Li$ in plastic solid-state recorders. Both methods are surface, or limited depth, microtechniques that perform analyses through interaction with individual atoms; thus, comparison of the results from both methods is useful in revealing the spatial homogeneity of the boron in the steels.

15790. Newman, M., **Some results on symplectic matrices,** *Linear and Multilinear Algebra* **3,** 95-98 (1975).

Key words: generalized permutations; $p$th roots; symplectic matrices.

The principal results are that if $A$ is an integral matrix such that $AA^T$ is symplectic then $A = CQ$, where $Q$ is a permutation matrix and $C$ is symplectic; and that if $A$ is a hermitian positive definite matrix which is symplectic, and $B$ is the unique hermitian positive definite $p$th root of $A$, where $p$ is a positive integer, then $B$ is also symplectic.

15791. Carlsten, J. L., Peterson, J. R., Lineberger, W. C., **Binding of an electron by the field of a molecular dipole–LiCl$^-$,** *Chem. Phys. Lett.* **37,** No. 1, 5-8 (Jan. 1, 1976).

Key words: alkali-halide; negative ions; photoelectron spectroscopy; polar molecules.

We present direct experimental evidence for the binding of an electron by the dipole moment of a neutral molecule. The photoelectron spectrum of $LiCl^-$ was obtained and analyzed to determine that the binding energy of the electron in the $LiCl^-$ ion is $(0.61 \pm 0.02)$ eV. This result is an order of magnitude smaller than the predictions of the fixed dipole theoretical model, but is consistent with a recent calculation, which allows for distortion of the dipolar core.

15792. Kilmer, R. D., Leasure, W. A., Jr., Mathews, D. E., **Truck Noise I-C: Pavement surface effects on the generation of truck tire noise,** *Report No. DOT-TST-76-49,* 111 pages (Available from the National Technical Information Service, Springfield, Va. 22161, Oct. 1975).

Key words: acoustics; noise measurement; noise (sound); tire noise; transportation noise; truck.

This report presents data showing the effect that pavement surface has on the generation of truck tire noise. Three different tread designs–rib, cross-bar and pocket–were tested at speeds of 40, 50 and 60 mph (64.4, 80.5 and 96.5 km/hr) while coasting on eight different pavement surfaces at the Texas Transportation Institute. These surfaces represent a wide range of surface texture. Also presented are the results of one method of quantitatively characterizing pavement surface texture; namely, the mean square value of the macrotexture profile, obtained utilizing a macrotexture profile tracer. Plots of tire noise versus this particular measure of surface texture show that up to a certain macrotexture the generated noise is tire dependent while above this value the pavement macrotexture appears to be the controlling parameter. Because of the wide variation in noise level with changes in surface texture for the pocket retread, this tire is investigated as a possible simple calibrator of surface texture. These investigations serve as the basis for evaluation of the effect of surface texture on the generation of tire noise.

15793. Lofquist, K. E. B., **An effect of permeability on sand transport by waves,** *Technical Memorandum No. 62,* 74 pages (U.S. Army Corps of Engineers, Coastal Engineering Research Center, Fort Belvoir, Va., Dec. 1975). (Available from the National Technical Information Service, Springfield, Va. 22161).

Key words: beach accretion; coastal processes; offshore zone; oscillatory water tunnel; permeability effect on sand transport; ripples, sand; sand motion under waves.

Permeability effects on the movement of sand in oscillatory flows are observed in laboratory experiments which approximate prototype conditions at the seabed under progressive waves. A natural sand is used, wave periods range between three and fourteen seconds, and the sand surfaces are naturally rippled. The apparatus has a symmetry which removes all effects, except those of permeability, which might cause a net movement of the sand. Onshore and offshore directions are determined by the phase relationships between the horizontal flows and superposed vertical permeability flows. A positive permeability effect is found, in that the ripple profiles move in the onshore direction. The velocity of this motion is measured and described in a simple dimensionless plot. The associated net transport of sand is not observed directly, but can be inferred, to an extent, from the motions of the ripple profiles. The effects of permeability are cumulative and can be significant in coastal processes of long duration. Any estimate of the local rate of sand transport onshore due to permeability involves the distribution of permeabilities within the seabed which are largely unknown. An overall estimate is less than 1 cubic meter per meter of shoreline per year, which is negligible for most engineering considerations.

15794. Bender, P. L., Silverberg, E. C., **Present tectonic-plate motions from lunar ranging,** *Tectonophysics* **29,** 1-7 (1975).

Key words: geodesy; geodynamics; lasers; metrology; moon; tectonics.

Measurements to determine the motion of the Pacific Plate with respect to North America are planned to start within a few months. The University of Hawaii Lunar Ranging Station on Maui is expected to begin operating, and to achieve an accuracy of 2 or 3 cm soon for a single run. The University of Texas McDonald Observatory has been achieving an accuracy of 8-15 cm on a routine basis since late 1971. Work on further improving the McDonald accuracy is planned. Using data from many runs, an accuracy of 1 cm/yr is expected for the relative motion within the first few years.

A transportable lunar-ranging station has been proposed which could be constructed in about eighteen months. The station could observe for 3-6 weeks at a chosen site, and determine the location of the site with respect to the fixed lunar-ranging stations. The accuracy expected is 1-3 cm in each coordinate. If approved, a possible initial itinerary for the station might be as follows: (a) two or three sites in California, including Goldstone, plus one site in Utah; (b) sites in Baja California and Mexico, plus several others in the U.S.; (c) several sites in Central America, the Caribbean, and South America; (d) repeat measurements in California, Utah, and Baja California, plus initial measurements at sites in Africa, India, and the Pacific. It is expected that data on plate motions also will become available from satellite range measurements and VLBI.

15795. Madden, R. P., **Atomic physics with synchrotron radiation,** (Proc. IX Int. Conf. on The Physics of Electronic and Atomic Collisions, Seattle, Wash., July 24-30, 1975), Paper in *The Physics of Electronic and Atomic Collisions*, J. S. Risley and R. Geballe, Eds., pp. 563-583 (University Washington Press, Seattle, Wash., 1976).

Key words: atomic physics; synchrotron radiation; vacuum ultraviolet.

The availability of synchrotron radiation sources is increasing steadily and their application to problems in atomic physics is growing rapidly. This paper reviews the work in absorption spectroscopy, photoelectron spectroscopy, fluorescence, mass spectroscopy lifetime measurements and time resolved spectra which is currently being done with this powerful source of polarized continuum radiation.

15796. Berger, H., **Detection systems for neutron radiography,** (Proc. American Society for Testing and Materials Symp. on Neutron Radiography and Gaging, Gaithersburg, Md., Feb. 10, 1975), Paper in *Practical Applications of Neutron Radiography and Gaging, Am. Soc. Test. Mater. Spec. Tech. Publ. 586*, pp. 35-57 (Jan. 1976).

Key words: films; images; neutron radiography; nondestructive tests; real-time imaging; thermoluminescence; track-etch.

Image detection methods for neutron radiography are described and capabilities of the methods in terms of exposure requirements, spatial resolution, and contrast are given. Neutron energy ranges cold, thermal, epithermal, and fast are included, but emphasis is on detectors for thermal neutron images. Image methods include photographic film, real-time, track-etch, gas-cell, and thermoluminescent; major emphasis is on film techniques, both direct exposure and transfer.

15797. Burns, G. W., Hurst, W. S., **Highly stable, sheathed, beryllia insulated, tungsten-rhenium alloy thermocouples,** (Proc. Int. Colloquium on High-Temperature In-Pile Thermometry, JRC Petten, Netherlands, Dec. 12-13, 1974), Paper in *International Colloquium on High-Temperature In-Pile Thermometry*, P. von der Hardt, P. Zeisser, and F. Mason, Eds., EUR 5395 **1,** 1-23 (Commission of the European Communities Directorate-General Scientific and Technical Information and Information Management, Luxembourg, Belgium, 1975).

Key words: beryllium oxide; refractory metals; sheathed thermocouples; tantalum; temperature measurements; thermal emf drift; tungsten-rhenium alloys.

The fabrication and performance testing of 1.6 mm diameter tantalum sheathed, beryllium oxide (BeO) insulated, W-3% Re/W-25% Re thermocouples are reported. Fully assembled thermocouples constructed from aged thermoelements, specially heat treated, sintered BeO insulators, and specially cleaned and etched tantalum sheaths were tested for 2059 h at 1800 °C in a helium environment. The measured thermal emf drifts were less than the equivalent of 1 °C per thousand hours of exposure at 1800 °C. No gross chemical attack or degradation of the component materials was evident. The fabrication techniques, thermal emf test results, and post-test analyses of the component materials are discussed.

15798. Reader, J., **Energy levels of singly ionized cesium (Cs II),** *Phys. Rev. A* **13,** No. 2, 507-516 (Feb. 1976).

Key words: cesium; energy levels; spectra.

The system of observed energy levels of Cs II of Wheatley and Sawyer has been reinterpreted through the use of Hartree-Fock calculations and published Zeeman effect and hyperfine-structure measurements. Of the 80 known levels, 30 have been rejected as being not real. A revised list of 54 observed levels of Cs II is presented that includes the $5p\ ^5 5d^1P_1$ level recently found by Reader and Epstein and three levels of the $5p^5 6d$ configuration that were located with the aid of Sommer's line list. Percentage compositions and Slater parameters are given for the $5p^5(5d+6s)$, $6p$, and $(6d+7s)$ configurations. Severe configuration mixing is found for levels of the $5p^5(5d+6s)$ group. The measured $g$ values of the $5p^5(5d+6s)$ levels provide evidence of a strong term dependence for the parameter $G^1(5p5d)$. By taking into account displacements of the $5p^5ns$ levels due to configuration interaction, the ionization energy is revised to be $186\,600 \pm 150$ $cm^{-1}$ ($23.14 \pm 0.02$ eV).

15799. Bender, P. L., **Applications of PTTI to new techniques for determining crustal movements, polar motion, and the rotation of the earth,** *Proc. 6th Annual Precise Time and Time Interval (PTTI) Planning Meeting, Washington, D.C., Dec. 3-5, 1974*, pp. 39-55 (U.S. Naval Research Laboratory, Washington, D.C., Dec. 1975).

Key words: crustal moments; earth rotation; geodynamics; lunar distance; microwave interferometry; plate tectonics; satellite geodesy.

New extra-terrestrial techniques for geodesy and geodynamics include laser range measurements to the moon or to artificial satellites, Doppler measurements with the Transit satellite system, and both independent-clock and linked-antenna microwave interferometry. The ways in which PTTI measurements are used in these techniques will be reviewed, and the accuracies expected during the latter half of the 1970's will be discussed. At least 3 of the techniques appear capable of giving accuracies of 5 cm or better in each coordinate for many points on the Earth's surface, and comparable accuracies for the Earth's rotation and polar motion. For fixed stations or for sites a few hundred km apart, baseline lengths accurate to 1 cm may be achieved. Ways in which the complementary aspects of the different techniques can be exploited will be discussed, as well as how they tie in with improved ground techniques for determining crustal movements. Some recent results from the extra-terrestrial methods will be mentioned.

15800. Hoer, C. A., Engen, G. F., **Analysis of a six-port junction for measuring** $v$, $i$, $a$, $b$, $z$, $\Gamma$, **and phase,** (Proc. 6th Conf. of the Int. Measurement Confederation, Dresden, Germany, June 17-23, 1973), Paper in *Measurement and Instrumentation, Acta IMEKO 1973*, **1**, 213-222 (Publishing House of the Hungarian Academy of Sciences, Akadémiai Kiadó, Budapest, Hungary, 1973).

Key words: admittance; current; impedance; phase angles; power; reflection coefficient; six-port; voltage.

This theoretical paper shows how complex voltage, current, incident and emergent wave amplitudes, immittance, reflection coefficients, and phase angles can all be measured with an arbitrary six-port junction. Four ports are terminated with power meters or other detectors from which power values can be obtained.

In particular, if v represents voltage, $|v|^2$ is given as a linear function of the four power meter indications. The same is true for current and the wave amplitudes. Complex immittance, or reflection coefficient, on the other hand, is given by the ratio between two linear combinations of the power meter readings.

Some practical design considerations are also given.

15801. Bender, P. L., **Reference coordinate system requirements for geophysics,** (Proc. IAU Symposium No. 26 on Reference Coordinate Systems for Earth Dynamics, Torun, Poland, Aug. 26-31, 1974), Paper in *Reference Coordinate Systems for Earth Dynamics*, B. Kolaczek and G. Weiffenbach, Eds., pp. 85-92 (Polish Academy of Sciences, Warsaw, Poland, Apr. 1975).

Key words: coordinate systems; geodesy; geodynamics; lasers; tectonics; VLBI.

Five important geodynamical quantities which are closely linked are: (1) motions of points on the Earth's surface; (2) polar motion; (3) changes in UT1-UTC; (4) nutation; and (5) motion of the geocenter. For each of these we expect to achieve measurements in the near future which have an accuracy of 1 to 3 cm or 0.3 to 1 milliarcsec.

From a metrological point of view, one can say simply: "Measure each quantity against whichever coordinate system you can make the most accurate measurements with respect to." I believe that this statement should serve as a guiding principle for the recommendations of the colloquium. However, it also is important that the coordinate systems help to provide a clear separation between the different phenomena of interest, and correspond closely to the conceptual definitions in terms of which geophysicists think about the phenomena.

In any discussion of angular motion in space, both a "body-fixed" system and a "space-fixed" system are used. Some relevant types of coordinate systems, reference directions, or reference points which have been considered are: (1) celestial systems based on optical star catalogs, distant galaxies, radio source catalogs, or the Moon and inner planets; (2) the Earth's axis rotation, which defines a line through the Earth as well as a celestial reference direction; (3) the geocenter; and (4) "quasi-Earth-fixed" coordinate systems.

When a geophysicist discusses UT1 and polar motion, he usually is thinking of the angular motion of the main part of the mantle with respect to an inertial frame and to the direction of the spin axis. Since the velocities of relative motion in most of the mantle are expected to be extremely small, even if "substantial" deep convection is occurring, the conceptual "quasi-Earth-fixed" reference frame seems well defined. Methods for realizing a close approximation to this frame fortunately exist. Hopefully, this colloquium will recommend procedures for establishing and maintaining such a system for use in geodynamics. Motion of points on the Earth's surface and of the geocenter can be measured against such a system with the full accuracy of the new techniques.

The situation with respect to celestial reference frames is different. The various measurement techniques give changes in the orientation of the Earth relative to different systems, so that we would like to know the relative motions of the systems in order to compare the results. However, there does not appear to be a need for defining any new system. Subjective figures of merit for the various systems depend on both the accuracy with which measurements can be made against them and the degree to which they can be related to inertial systems.

The main coordinate system requirement related to the 5 geodynamic quantities discussed in this talk is thus for the establishment and maintenance of a "quasi-Earth-fixed" coordinate system which closely approximates the motion of the main part of the mantle. Changes in the orientation of this system with respect to the various celestial systems can be determined by both the new and the conventional techniques, provided that some knowledge of changes in the local vertical is available. Changes in the axis of rotation and in the geocenter with respect to this system also can be obtained, as well as measurements of nutation.

15802. Clough, R. B., **A note on the measurement of proportional limit under multiaxial stresses,** *J. Test. Eval.* **4**, No. 2, 139-140 (1976).

Key words: flow surface; multiaxial stresses; plasticity; proportional limit.

Theoretical definitions of the multiaxial plastic flow surface are exact; however, ambiguities arise in the experimental measurement. A new method for measuring the multiaxial flow surface based on maximum elastic stress rate is proposed which eliminates these ambiguities. It is applied to biaxial yielding.

15803. Bowman, R. R., **A probe for measuring temperature in radio-frequency-heated material,** *IEEE Trans. Microwave Theory Tech. Short Papers* **MTT-24**, No. 1, 43-45 (Jan. 1976).

Key words: high-resistance leads; radio frequency heating; temperature measurements; thermistor probe.

Measuring temperature in material being heated by radio-frequency (RF) fields is difficult because of field perturbations and direct heating caused by any conventional leads connected to the temperature sensor. A temperature probe consisting simply of a thermistor and plastic high-resistance leads appears to practically eliminate these problems. The design goals are described, and the performance of an initial test model of this type of probe is discussed.

15804. Yaghjian, A. D., **Direct integration of the field equations for electroacoustic transducers,** *Proc. IEEE Letters* **62,** No. 6, 858-859 (June 1974).

Key words: electroacoustic; integration; transducer.

Expressions are derived for the electroacoustic fields inside a linear transducer in terms of the volume sources and the fields on the surface of the transducer.

15805. Straty, G. C., Tsumura, R., **Phase transition and melting pressures of solid ethane,** *J. Chem. Phys.* **64,** No. 2, 859-861 (Jan. 15, 1976).

Key words: ethane; melting line; melting pressures; solid ethane; solid phase transition.

The melting pressures of ethane at 14 temperatures from near the triple point to 95.50 K and pressures to 32.0 MPa are reported. A triple point temperature of $90.348 \pm 0.005$ K is obtained from the data which is in agreement with the determination of Clusius and Weigand (1940) but in substantial disagreement with other determinations. Qualitative evidence has been obtained which indicates the existence of a previously unrecognized solid phase transition along a boundary roughly parallel to the melting line at a temperature about 0.5 K below the melting temperature, suggesting that some previous melting point determinations may have been influenced by misinterpretation of the effects of this transition.

15806. Bender, P. L., **Prospects for rapid realization of a quasi-Earth-fixed coordinate system,** (Proc. IAU Symposium No. 26 on Reference Coordinate Systems for Earth Dynamics, Torun, Poland, Aug. 26-31, 1974), Paper in *Reference Coordinate Systems for Earth Dynamics,* B. Kolaczek and G. Weiffenbach, Eds., pp. 297-302 (Polish Academy of Sciences, Warsaw, Poland, Apr. 1975).

Key words: coordinate systems; geodesy; geodynamics; lasers; tectonics; VLBI.

It appears that a combination of VLBI, lunar ranging, and satellite ranging can provide a quasi-Earth-fixed coordinate system with high accuracy and good coverage more rapidly than any one technique alone. In considering this possibility, the conceptual separation of the job into two parts seems useful. There are: (1) establishment of a global network of at least three fundamental reference points on major plates, and (2) the determination of a larger number of regional reference points of geodynamic interest. The example of lunar ranging plus satellite ranging is used to illustrate one way in which an accurate realization of an initial terrestrial system could be achieved quickly.

15807. Hutchinson, J. M. R., Lucas, L. L., Mullen, P. A., **Study of the scattering correction for thick uranium-oxide and other α-particle sources—II: Experimental,** *Int. J. Appl. Radiat. Isot.* **27,** No. 1, 43-45 (Jan. 1976).

Key words: alpha particles; backscattering; gadolinium-148; polonium-210; self absorption; uranium-oxide.

Experimental values of the $2\pi$ α-particle counting rate, $C_{2\pi}$, including scattering, divided by the disintegration rate, $N_0$, are reported for uranium dioxide, $^{210}$Po and $^{148}$Gd sources mounted on platinum backings, and a $^{210}$Po source on a $U_3O_8$ backing. The $^{235}UO_2$ source thicknesses varied from 0.05 to 1.1 mg/cm$^2$. The experimental values of the scattering are in agreement with theoretical values given in Part I (this issue), which take into account source thickness, α-particle energy, and composition of the backing material.

15808. Lucas, L. L., Hutchinson, J. M. R., **Study of the scattering correction for thick uranium-oxide and other α-particle sources—I: Theoretical,** *Int. J. Appl. Radiat. Isot.* **27,** No. 1, 35-42 (Jan. 1976).

Key words: alpha particles; backscattering; disintegration rate; ranges; self-absorption; uranium oxide.

Theoretical values of the $2\pi$ α-particle counting rate, $C_{2\pi}$, including scattering, divided by the disintegration rate, $N_0$, are calculated for α-particle sources mounted on flat backing materials. The theoretical values (Part I) and experimental values (Part II) are in good agreement, and show that: (a) $C_{2\pi}/N_0$ values as a function of α-particle energy and source thickness can be calculated on the basis of a simple physical model; (b) The scattering correction, expressed as a fraction of the disintegration rate, decreases with increasing source thickness; and (c) The α-particle scattering in uranium-oxide is much less than the scattering in platinum, in disagreement with previous estimates. The calculations are readily extended to other source compositions and α-particle energies.

15809. Jones, M. C., Peterson, R. G., **A study of flow stability in helium cooling systems,** *J. Heat Transfer* **97,** No. 4, 521-527 (Nov. 1975).

Key words: computations; cooling system; cryogenics; electric power transmission; flow stability; helium; oscillations; superconductors; theory.

Methods have been developed for the computation of the frequency response and stability of helium cooling systems in the frequency range of the density wave instability. While more generally applicable, these methods were developed for a study of superconducting power transmission. Special features are the use of helium thermodynamic properties derived at every point from the exact equation of state, and the full accounting of the effect of compressibility. Classical linear control theory is employed throughout. By using a finite difference approach to the integration of the conservation equations over the space coordinate, the accuracy obtainable is limited only by the computation time available. Examples are given for representative transmission line parameters with the helium at a variety of supercritical pressures. It is concluded that, while density wave instability is a real potential problem in superconducting power transmission lines, it is not difficult to select operating parameters in a safe stable regime.

15810. Marshall, H. E., Ruegg, R. T., **Cost sharing to induce efficient techniques of abating wastewater pollution,** *J. Environ. Econ. Manage.* **2,** 107-119 (1975).

Key words: cost sharing; efficiency; environment; financing; grants; pollution abatement; wastewater; water pollution; water resources.

This paper analyzes existing cost-sharing rules for wastewater pollution grants administered by the Environmental Protection Agency under the 1972 Amendments to the Federal Water Pollution Control Act. It identifies and measures biases in the existing cost-sharing rules that encourage nonfederal interests to select particular techniques (e.g., capital-intensive techniques) over others even when the selected techniques are not the least costly to the nation. The paper develops theoretically a cost-sharing condition—that the same percentage cost share be applied to all abatement techniques—that would eliminate the cost-sharing bias. Alternative cost-sharing approaches are evaluated in terms of their biasing effects and their absolute dollar costs for federal and nonfederal project participants.

15811. Lias, S. G., Eyler, J. R., Ausloos, P., **Hydride transfer reactions involving saturated hydrocarbons and $CCl_3^+$, $CCl_2H^+$, $CCl_2F^+$, $CF_2Cl^+$, $CF_2H^+$, $CF_3^+$, $NO^+$, $C_2H_5^+$, sec-$C_3H_7^+$ and t-$C_4H_9^+$,** *Int. J. Mass Spectrom. Ion Phys.* **19,** 219-239 (1976).

Key words: collision processes; halocarbon ions; hydrocarbons; ion-molecule reactions; kinetics; rate constants.

The compounds $CCl_4$, $CCl_3H$, $CCl_3F$, $CCl_2F_2$, $CF_3H$, $CF_4$, NO, $C_2H_6$, neo-$C_5H_{12}$, and $C_3H_8$ were ionized by low energy electrons in a

pulsed ion cyclotron resonance spectrometer to produce $CCl_3^+$, $CCl_2H^+$, $CCl_2F^+$, $CF_2Cl^+$, $CF_2H^+$, $CF_3^+$, $NO^+$, $C_2H_5^+$, t-$C_4H_9^+$, and sec-$C_3H_7^+$ ions, respectively. In these pure compounds, the respective ions formed are all unreactive, and can be trapped with essentially no loss in the ICR analyzer cell for up to 0.2 s after their formation, at a pressure of $10^{-7}-10^{-5}$ torr. When alkanes or cycloalkanes are added to these compounds, the predominant ions formed in each case undergo a hydride transfer reaction with the added alkane. This is the only reaction channel:

$$A^+ + RH \rightarrow AH + R^+$$

(where $A^+$ is the initial ion formed and RH is the added alkane or cycloalkane). By following the abundances of the reactant ions as a function of time in these dilute mixtures, approximately one hundred rate coefficients of hydride transfer reactions of thermal ions (in the range $10^{-12}-10^{-9}$ cm$^3$ molecule$^{-1}$ s$^{-1}$) have been determined. For several of these ions, it is demonstrated that even when reaction is very exothermic at every site in the molecule the reacting ion exhibits positional selectivity. Detailed examination of the reaction probabilities for these ions reacting with alkanes of different chain lengths and structures leads to the conclusion that the rates of hydride transfer reactions depend in part on the exothermicity of the reaction and in part on the lifetime of the ion-molecule complex. For large reactant ions such as t-$C_4H_9^+$, steric effects may also play a role. The product ions formed in these hydride transfer reactions undergo further fragmentation to an extent which depends on the exothermicity of the reaction; the most important fragmentation paths correspond to loss of $C_2-C_4$ olefins from the product alkyl ions.

15812. Powell, C. J., **Cross sections for ionization of inner-shell electrons by electrons,** *Rev. Mod. Phys.* **48,** No. 1, 33-47 (Jan. 1, 1976).

Key words: Bethe theory; cross sections; electron; inner-shell electrons; ionization; *K*-shell; *L*-shell; photoabsorption.

A survey is given of the available cross-section data for ionization of inner-shell electrons by incident electrons in the range of interest for electron-probe microanalysis and for Auger-electron spectroscopy of solid surfaces. Owing to the paucity of data, the bulk of the discussion is limited to *K*-shell and *L*-shell ionization of light atoms. Calculated, semiempirical, and experimental cross-section data have been intercompared graphically and through fits to the linearized Bethe equation for inner-shell ionization (the Fano plot). Almost all of the data could be satisfactorily fitted over the range $4 \leq U_{nl} \leq 30$, where $U_{nl}=E_0/E_{nl}$, $E_0$ is the incident electron energy, and $E_{nl}$ the binding energy of electrons in the $nl$ shell. From these fits, values could be obtained of the "effective" Bethe parameters $b_{nl}$ and $c_{nl}$. Values of the parameter $b_{nl}$ have also been derived from photoabsorption data and were found to be generally consistent with the ionization data if account was taken of the distribution of differential oscillator strength with respect to excitation energy and the consequent expected variation of $b_{nl}$ with incident electron energy. The derived "effective" Bethe parameters should not therefore be used outside the range of each fit.

15813. Waclawski, B. J., Herbst, J. F., **Photoemission for Xe physisorbed on W(100): Evidence for surface crystal-field effects,** *Phys. Rev. Lett.* **35,** No. 23, 1594-1596 (Dec. 8, 1975).

Key words: crystal field; photoemission; physisorption; tungsten (100); xenon.

Photoemission spectra at $h\nu=21.2$ eV reveal two $5p$ levels for xenon physisorbed on a tungsten (100) surface. The spin-orbit splitting of the two levels and their intensity ratio correspond closely to gas-phase measurements, while the $5p_{3/2}$ peak is significantly broadened with respect to the $5p_{1/2}$. We interpret the broadened structure as an unresolved doublet resulting from splitting the Xe $5p_{3/2}$ states in the tungsten-surface crystal field.

15814. Fuggle, J. C., Madey, T. E., Steinkilberg, M., Menzel, D., **Photoelectron spectroscopic studies of adsorption of CO and oxygen on Ru(001),** *Surf. Sci.* **52,** 521-541 (1975).

Key words: adsorbate; chemisorption; ruthenium; ultraviolet photoelectron spectroscopy; x-ray photoelectron spectroscopy.

XPS and UPS have been used for a detailed study of the adsorption and coadsorption of CO and oxygen on a clean Ru(001) single crystal. The measured substrate and adsorbate core level binding energies and valence levels are discussed. The O 1s XPS peak intensity has been used for kinetic studies of adsorption and coadsorption. Some studies of the angular dependence of adsorbate and substrate peak intensity ratios are presented. We also present data on the shifts of XPS peaks and changes in UPS spectra as a function of adsorbate coverage. The data are correlated with the results of earlier measurements with other methods.

15815. Bardsley, J. N., Junker, B. R., Norcross, D. W., **Pseudopotential calculations for $Na_2^+$, Na and $Na_2^-$,** *Chem. Phys. Lett.* **37,** No. 3, 502-506 (Feb. 1, 1976).

Key words: molecular structure; pseudopotentials.

Potential curves have been computed for five states of $Na_2^+$, five states of $Na_2$ and two states of $Na_2^-$ using a pseudopotential approach. The results are consistent with the accepted attribution to a $^3\Pi$ state of the perturbations observed in transitions involving the $A^1\Sigma_u$ state of $Na_2$, and the stability of the $Na_2^-$ ion is established.



U. S. GOVERNMENT PRINTING OFFICE: 1976 OL - 206-267

# NBS TECHNICAL PUBLICATIONS

## PERIODICALS

**JOURNAL OF RESEARCH** reports National Bureau of Standards research and development in physics, mathematics, and chemistry. It is published in two sections, available separately:

- **Physics and Chemistry (Section A)**

Papers of interest primarily to scientists working in these fields. This section covers a broad range of physical and chemical research, with major emphasis on standards of physical measurement, fundamental constants, and properties of matter. Issued six times a year. Annual subscription: Domestic, $17.00; Foreign, $21.25.

- **Mathematical Sciences (Section B)**

Studies and compilations designed mainly for the mathematician and theoretical physicist. Topics in mathematical statistics, theory of experiment design, numerical analysis, theoretical physics and chemistry, logical design and programming of computers and computer systems. Short numerical tables. Issued quarterly. Annual subscription: Domestic, $9.00; Foreign, $11.25.

**DIMENSIONS/NBS (formerly Technical News Bulletin)**—This monthly magazine is published to inform scientists, engineers, businessmen, industry, teachers, students, and consumers of the latest advances in science and technology, with primary emphasis on the work at NBS. The magazine highlights and reviews such issues as energy research, fire protection, building technology, metric conversion, pollution abatement, health and safety, and consumer product performance. In addition, it reports the results of Bureau programs in measurement standards and techniques, properties of matter and materials, engineering standards and services, instrumentation, and automatic data processing.

Annual subscription: Domestic, $9.45; Foreign, $11.85.

## NONPERIODICALS

**Monographs**—Major contributions to the technical literature on various subjects related to the Bureau's scientific and technical activities.

**Handbooks**—Recommended codes of engineering and industrial practice (including safety codes) developed in cooperation with interested industries, professional organizations, and regulatory bodies.

**Special Publications**—Include proceedings of conferences sponsored by NBS, NBS annual reports, and other special publications appropriate to this grouping such as wall charts, pocket cards, and bibliographies.

**Applied Mathematics Series**—Mathematical tables, manuals, and studies of special interest to physicists, engineers, chemists, biologists, mathematicians, computer programmers, and others engaged in scientific and technical work.

**National Standard Reference Data Series**—Provides quantitative data on the physical and chemical properties of materials, compiled from the world's literature and critically evaluated. Developed under a world-wide program coordinated by NBS. Program under authority of National Standard Data Act (Public Law 90-396).

NOTE: At present the principal publication outlet for these data is the Journal of Physical and Chemical Reference Data (JPCRD) published quarterly for NBS by the American Chemical Society (ACS) and the American Institute of Physics (AIP). Subscriptions, reprints, and supplements available from ACS, 1155 Sixteenth St. N.W., Wash. D. C. 20056.

**Building Science Series**—Disseminates technical information developed at the Bureau on building materials, components, systems, and whole structures. The series presents research results, test methods, and performance criteria related to the structural and environmental functions and the durability and safety characteristics of building elements and systems.

**Technical Notes**—Studies or reports which are complete in themselves but restrictive in their treatment of a subject. Analogous to monographs but not so comprehensive in scope or definitive in treatment of the subject area. Often serve as a vehicle for final reports of work performed at NBS under the sponsorship of other government agencies.

**Voluntary Product Standards**—Developed under procedures published by the Department of Commerce in Part 10, Title 15, of the Code of Federal Regulations. The purpose of the standards is to establish nationally recognized requirements for products, and to provide all concerned interests with a basis for common understanding of the characteristics of the products. NBS administers this program as a supplement to the activities of the private sector standardizing organizations.

**Consumer Information Series**—Practical information, based on NBS research and experience, covering areas of interest to the consumer. Easily understandable language and illustrations provide useful background knowledge for shopping in today's technological marketplace.

*Order* **above** *NBS publications from: Superintendent of Documents, Government Printing Office, Washington, D.C. 20402.*

*Order* **following** *NBS publications—NBSIR's and FIPS from the National Technical Information Services, Springfield, Va. 22161.*

**Federal Information Processing Standards Publications (FIPS PUBS)**—Publications in this series collectively constitute the Federal Information Processing Standards Register. Register serves as the official source of information in the Federal Government regarding standards issued by NBS pursuant to the Federal Property and Administrative Services Act of 1949 as amended, Public Law 89-306 (79 Stat. 1127), and as implemented by Executive Order 11717 (38 FR 12315, dated May 11, 1973) and Part 6 of Title 15 CFR (Code of Federal Regulations).

**NBS Interagency Reports (NBSIR)**—A special series of interim or final reports on work performed by NBS for outside sponsors (both government and non-government). In general, initial distribution is handled by the sponsor; public distribution is by the National Technical Information Services (Springfield, Va. 22161) in paper copy or microfiche form.

## BIBLIOGRAPHIC SUBSCRIPTION SERVICES

**The following current-awareness and literature-survey bibliographies are issued periodically by the Bureau:**

**Cryogenic Data Center Current Awareness Service.** A literature survey issued biweekly. Annual subscription: Domestic, $20.00; Foreign, $25.00.

**Liquified Natural Gas.** A literature survey issued quarterly. Annual subscription: $20.00.

**Superconducting Devices and Materials.** A literature survey issued quarterly. Annual subscription: $20.00. Send subscription orders and remittances for the preceding bibliographic services to National Bureau of Standards, Cryogenic Data Center (275.02) Boulder, Colorado 80302.

U.S. DEPARTMENT OF COMMERCE
National Bureau of Standards
Washington, D.C. 20234

OFFICIAL BUSINESS
Penalty for Private Use, $300

POSTAGE AND FEES PAID
U.S. DEPARTMENT OF COMMERCE
COM–215
SPECIAL FOURTH-CLASS RATE
BOOK

JOURNAL OF RESEARCH of the National Bureau of Standards
A. Physics and Chemistry

Vol. 80A, No. 3 May–June 1976

[illegible]

Page

**Standardization [illegible] surements**

Proceedings of a Workshop Seminar held at the National Bureau of Standards

Gaithersburg, Md., November 19–20, 1975

Part 1. Luminescence Quantum Yields—Lectures and Panel Papers

Fluorescence quantum yield measurements. J. B. Birks. 389

Some methods of luminescence efficiency measurements. Alfred Bril and A. Willy de Jager-Veenis. 401

On the actinometric measurement of absolute luminescence quantum yields. J. N. Demas and B. H. Blumenthal. 409

The calorimetric detection of excited states. James B. Callis. 413

Fluorescence efficiency of laser dyes. K. H. Drexhage. 421

Other NBS Papers

Oscillator strengths for lines of ionized uranium (U II). Charles H. Corliss. 429

Cancer detection by NMR in the living animal. L. D. Weisman and L. H. Bennett, L. R. Maxwell, Sr., and D. E. Henson. 439

Modulus of natural rubber cross-linked by dicumyl peroxide. III. Some molecular interpretations, possible refinements of theory, and conclusions. Lawrence A. Wood. 451

Calculations of configurations of doubly ionized copper (Cu III). J. Sugar and W. C. Martin. 465

The International Practical Temperature Scale of 1968 in the region 90.188 K to 903.89 K as maintained at the National Bureau of Standards, George T. Furukawa, John L. Riddle, and William R. Bigge. 477

Vapor pressure of water at its triple point. L. A. Guildner, D. P. Johnson, and F. E. Jones. 505

Publications of the National Bureau of Standards. 523

Library of Congress Catalog Card Number: 62–37059

For sale by the Superintendent of Documents, U.S. Government Printing Office, Washington, D.C. 20402. (Order by SD Catalog No. C 13.22/sec. A:80/3). Single copy price varies. Subscription price: $17.00 a year; $4.25 additional for foreign mailing.

UNITED STATES GOVERNMENT PRINTING OFFICE, WASHINGTON : 1976